

SLAC-R-354
SLAC-354
CONF-8907149
UC-414
(M)

SLD PHYSICS STUDIES
PROCEEDINGS OF THE SLD PHYSICS WEEK
Kirkwood, California
July 31–August 4, 1989

Stanford Linear Accelerator Center
Stanford University
Stanford, California 94309

October 1989

Prepared for the Department of Energy
under contract number DE-AC03-76SF00515

Printed in the United States of America. Available from the National Technical Information Service, U.S. Department of Commerce, 5285 Port Royal Road, Springfield, Virginia 22161. Price: Printed Copy A99, Microfiche A01.

PREFACE

The SLD Collaboration met at Kirkwood, California during the week of July 31 to August 4, 1989 to discuss the physics program of the SLD detector at the SLAC Linear Collider (the SLC). This volume contains the talks presented at this meeting.

The discussions at Kirkwood were based on the physics studies carried out over the past year by the SLD Physics Working Groups. These groups and their leaders were the following:

1. Electroweak Parameter and QCD Tests
T. Hansl-Kozanecki and T. Burnett
2. Heavy Quark Spectroscopy
I. Peruzzi and M. Witherell
3. $B\bar{B}$ Mixing and CP Violations
R. Schindler and G. Gladding
4. Search for Supersymmetry
R. Dubois and S. Whitaker
5. Higgs Search
P. Mockett
6. Search for Technicolor
U. Nauenberg
7. Search for New Quarks, Leptons and Z's
P. Rowson and J. Brau
8. Neutrino Counting
U. Nauenberg

The agenda for the week at Kirkwood and the list of attendees at the meeting are included at the end of this volume. The agendas for the various sessions were developed by the working group leaders.

This volume is organized into nine sections. The first is a general overview and summary of some of the most interesting physics topics for SLD. This is followed by a section for the topics of each of the eight working groups. The working group leaders served as the editors for each of these sections.

Many interesting and beautiful analyses of the various physics topics emerged. Most of these were based on the SLD Monte Carlo and event reconstruction software package. It was very gratifying to see that, although with some problems and rough spots, the software package more or less was in working and useable shape, and is even becoming moderately user friendly as evidenced by the fact that many new graduate students who joined the collaboration just recently were able to use the package in a short time.

It should be emphasized that this Kirkwood meeting was the first SLD physics meeting. Therefore the articles in this volume should be regarded as preliminary progress reports. Also, emphasis was placed on speedy publication of this volume rather than meticulous care in completeness of references, drafting of figures, etc. The physics studies are continuing and more complete reports will be presented at later meetings.

We would like to thank Juanita O'Malley and Karen Krieger for making all of the arrangements for the meeting and for making sure that the meeting was not only operating smoothly but was enjoyable as well. Our special thanks go to Mary Kraus for putting this volume together for us.

Charlie Baltay

Marty Breidenbach

Photographs in this volume were taken by Karen Krieger and Ginny Baltay.

PROCEEDINGS OF THE 1989 SLD KIRKWOOD PHYSICS MEETING

TABLE OF CONTENTS

	Page
OVERVIEW	
An Overview of the Physics Potential of SLD C. Baltay	1
ELECTROWEAK PARAMETER AND QCD TESTS	
The Electroweak Parameters at the Z^0 T. Hansl-Kozanecka	50
QED Radiative Corrections at the Z^0 : Theory versus Implementation R. Battiston, G. Bilei, G. Mantovani, M. Pauluzzi, A. Santocchia and L. Servoli	84
Precision Measurements of Electroweak Observables and Testing of the Standard Model R. Battiston	96
High-precision Measurement of Γ_Z in SLD Using Large-angle e^+e^- Events R. Battiston, M. Pauluzzi, L. Servoli and A. Santocchia	103
A Test of Electron-Muon Universality Using Polarization Cross Section Asymmetries J.M. Yamartino	115
Prospects of Tau Physics with the SLD Detector U. Schneekloth	122

A Geometric Method of Tagging B Flavor Events	
D.C. Williams and L.S. Osborne	129
Charged Tracking Acceptance for Hadronic Events	
G.J. Baranko	137
QCD at the Z^0	
P.N. Burrows	142

HEAVY QUARK SPECTROSCOPY

B Decays and Spectroscopy	
I. Peruzzi, M. Witherell, P. Antilogus, T. Browder, S. Dasu, G. Eigen, G. Gladding, D. Hitlin, M. Kelsey, J. Labs, L. Mathys, J. McGowan, S. McHugh, L. Osborne, R. Panvini, J. Richman C. Simopoulos, P. De Simone, M. Strauss, D. Williams and G. Word	175
Semileptonic Decays and Measurement of the B-Meson Lifetimes	
T.E. Browder and M.S. Witherell	186
Study of the $B \rightarrow J/\psi$ Decays with the SLD	
A. Calcaterra, R. De Sangro, P. DeSimone, I. Peruzzi and M. Piccolo	201
Tagging D_s Mesons in $b\bar{b}$ Events Produced in Z^0 Decays	
M.H. Kelsey and G. Eigen	213
Particle Identification with the CRID	
P. Antilogus	233
Calculation of Track-Error Matrices for the SLD Fast Monte Carlo	
J.D. Richman and L. Mathys	244
B-Meson Reconstruction	
L. Osborne and D. Williams	253

Identification of D^0 , D^+ , and D^* Mesons with the SLD	
M. Strauss, T. Browder and S. McHugh	272

Reconstruction of D's, F's, and Neutrals with the SLD Detector	
J.M. Izen	283

$B\bar{B}$ MIXING AND CP VIOLATIONS

Preliminary Report of the $B\bar{B}$ Mixing and CP Violation Group	
T. Browder, G. Eigen, G. Gladding, J. Izen, P. Kim, J. Labs, R. Schindler and C. Simopoulos	294

\bar{B}_s, B_s Oscillations Seen from $e^+e^- \rightarrow Z^0 \rightarrow \bar{b}b$ with the SLD at the SLC	
T.W. Reeves, R.S. Panvini and G.B. Word	358

On the Use of Charged Fragmentation Kaons for Tagging B_s Mesons	
T.W. Reeves and R.S. Panvini	370

Aspects of B Physics from $e^+e^- \rightarrow Z^0 \rightarrow \bar{b}b$	
L-P Chen, R.S. Panvini, T.W. Reeves and G.B. Word	375

CP Violation at the Z^0	
S. Manly	393

SEARCH FOR SUPERSYMMETRY

SUSY and the SLD	
S. Whitaker	410

SUSY Searches for \tilde{e} , $\tilde{m}u$, \tilde{q}	
R. Dubois	419

Production of Supersymmetric Higgs Scalars in Z^0 Decays	
S. Whitaker, C. Baltay, S. Manly and J.D. Turk	426

HIGGS SEARCH

Search for Higgs Bosons using a Missing Energy Signature	
A.S. Johnson	438

SEARCH FOR TECHNICOLOR

A Search for Technicolor Particles Using the SLD Detector	
I. Abt, C. Baltay, G. Chadwick, S. Manly, U. Nauenberg, U. Schneekloth, M. Sokoloff, J. Turk, R. Webber and L.C.R. Wijewardhana	447
Jet-Jet Invariant Mass Reconstruction	
C. Baltay, S. Manly and J.D. Turk	495

SEARCH FOR NEW QUARKS, LEPTONS AND Z's

The Search for New Particles with the SLD at the Stanford Linear Collider	
P.C. Rowson, C. Arroyo, A.O. Bazarko, T. Bolton, J. Brau, M.H. Shaevitz, S.R. Smith, R.V. Steiner, A. Weidemann, R. White and C. Zeitlin	513
Fourth Generation Sequential Lepton Searches at SLD	
T. Bolton	528
A Fourth-Generation Charge $-\frac{1}{3}$ Quark at SLD	
A.W. Weidemann and C.J. Zeitlin	546
Singly Produced Neutral Heavy Leptons and the Search for Monojets	
A.O. Bazarko and M.H. Shaevitz	559
Search for Excited Muons in SLD	
C.G. Arroyo and R.V. Steiner	568
Additional Neutral Vector Bosons	
P.C. Rowson	578

NEUTRINO COUNTING

A Study of Neutrino Counting with the SLD Detector

H. Band, W. Bugg, G. Chadwick, D. Coyne, M. Gyure,
S. Hertzbach, R. Messner, A. Mincer, P. Mockett,
U. Nauenberg, P. Reutens, J. Rothberg, P. Rowson,
M. Shaevitz, R. Sobie, J. Thaler, B. Wilson,
C. Young and K. Young

587

An Overview of the Physics Potential of SLD

C. Baltay
Yale University

1 Introduction

An impressive amount of very nice analysis on a wide range of physics topics that are relevant to the SLD detector running at the SLAC SLC has been presented at this meeting. This overview is not intended as a review or summary of all of the topics that were discussed here. Instead the aim is to concentrate on those topics where, because of the special features of the SLD detector or of the SLC collider, we expect the SLD physics program to be at some advantage compared to other detectors running at e^+e^- colliders in a similar energy range. Thus some topics will not be discussed in this overview at all; for these the reader is referred to the detailed articles in the rest of these proceedings.

1.1 Most likely SLD turn on scenario

In order to focus the physics discussion that follows, we have assumed the following scenario for the initial running of the SLD:

- SLD will move onto beamline some time during the summer of 1990.
- During the first year of SLD physics running, we expect 10^5 Z's/year with 45% polarized electron beams.

- We expect that during this year the LEP collider at CERN will be running with about 10^6 Z's/year but with no polarization.
- During later years, the SLC event rate will be increasing slowly, and the beam polarization will be improved to a possible maximum of 90%. The LEP event rate will also be increasing slowly, but polarization will remain a very difficult, if not impossible, problem at LEP.

1.2 Comparison with other detectors

1.2.1 Mark II at the SLC

The main advantage of the Mark II over SLD is that the Mark II is a well-tested and understood detector that is now actually on beamline taking data. The advantages of the SLD are:

- Finely segmented, projective tower hadron calorimetry (the Mark II has no hadron calorimetry at all)
- Better vertex detector (three dimensional CCD detector of the SLD, silicon strips at the Mark II)
- Particle identification with the Cerenkov Ring Imaging Detector (CRID)
- Better acceptance: $\sim 4\pi$ muon detection, forward drift chambers, and similar technology in the forward and barrel regions

1.2.2 Comparison with the LEP program

The LEP program will have some considerable advantages compared to that at SLC:

- Higher luminosity
- 4 state of the art detectors
- Better resolution for electrons and muons in the L3 detector

The advantages of SLD at the SLC are:

- Polarized beam at the SLC
- The SLD has better hadron calorimetry than any of the LEP detectors
- Better vertex detection, due to the very small beam sizes at the SLC and the three-dimensional space points of the SLD CCD vertex detector. Thanks to the small SLC beampipe the SLD vertex detector can be placed a factor of 3 to 4 times closer to the interaction point than is possible at LEP.

The various features of all of these detectors are summarized in Tables I and II. The way in which the advantages mentioned above for the SLD translate into physics is the main topic of the rest of this overview.

1.3 Summary of physics topics relevant to SLD

The special features of the SLD at the SLC discussed above help in the physics analysis in many ways.

- a) Good hadron calorimetry is important in searches for new particles decaying into $q\bar{q}$ jets (jet-jet effective mass reconstruction) and missing energy signatures
- b) Polarized beams allow much higher precision in the measurement of electroweak parameters and tests of the standard model
- c) Good vertex resolution is crucial for B decay studies where the detection and separation of secondary vertices is essential
- d) The combination of polarized beams and good vertex detection is important in several areas such as the study of the time development of $B - \bar{B}$ mixing

The physics capabilities of SLD relative to the other detectors is summarized briefly in Table III. The checkmarks in the last two columns of this table indicate the topics where SLD has some advantage over other detectors.

2 Vertex Detection

Good vertex detection is very important in the study of Z^0 decays because many of the most interesting decay products, such as the τ lepton and the b and the c quarks

have lifetimes in the range of 10^{-12} to 10^{-13} seconds. The mean decay length of these particles is thus in the range of a hundred microns to a few millimeters. To detect and separate these secondary vertices from each other, spatial resolution of the order of tens of microns is required.

Of the detectors under discussion here silicon detectors provide the highest resolution. These come in various geometries (see Fig. 1). Silicon strips (Fig. 1a) running in one direction only (usually axial) measure only one coordinate, which is not very good in a high multiplicity environment. Strips running in two directions (Fig. 1b) provide two coordinates, but ambiguities in associating x hits with y hits are a problem in a high multiplicity jet environment. Charge coupled devices (CCD chips) have a large number of individual pixels which are independently read out, so that actual two dimensional points are measured. The readout time for CCD's is slow (~ 50 msec) but this is not a problem at the SLC. Furthermore the availability of high quality CCD chips is limited and they are expensive. The small radius beam pipe at the SLC allowed SLD to have a unique CCD vertex detector.

The properties of the vertex detectors at SLC and LEP are summarized in Table II. The unique advantages of the SLD vertex detector are apparent: it has high spatial resolution, three dimensional points, and is close to the interaction point. Figure 12 shows an actual event in a prototype of our CCD vertex detector in CERN Experiment NA32. The advantages of the high resolution three dimensional readout are apparent.

The impact parameter resolution σ_p is the resolution in the closest approach to the interaction point of a reconstructed track extrapolated back to the interaction point. This resolution has been extensively studied for the SLD vertex detector and is a complicated function of the momentum and angle of each track. It can be roughly parametrized as

$$\sigma_p \sim 6 \oplus \frac{30}{p} \text{ for a 16 mm radius beam pipe}$$

$$\sigma_p \sim 10 \oplus \frac{50}{p} \text{ for a 25 mm radius beam pipe}$$

where σ_p is in microns, p is the momentum of the track in GeV/C, and the \oplus denotes addition in quadrature.

This result can be qualitatively understood in terms of the extrapolation distance ℓ from the innermost detector layer to the interaction point (see Fig. 2). The dominant term is

$$\sigma_p \sim \ell \times \delta\theta$$

where $\delta\theta$ is the error on the angle of the track, which is measured in the outer layers of the vertex detector and the central drift chamber. At infinite momentum $\delta\theta \sim 1/3$ milliradian. At lower momenta multiple scattering dominates $\delta\theta$,

$$\delta\theta_{rms} \sim \frac{15 MeV/C}{P\beta} \sqrt{t/x_o} \sim \frac{1.5 mrad}{P(GeV/C)}$$

where t/x_o , the thickness of material traversed, is of the order of 0.01 up to the first layer for all of the detectors.

The resolution in the decay length of a particle, σ_d , is related to the impact parameter by (see Fig. 3)

$$\sigma_d = \frac{\sigma_p}{\sin\theta}$$

where θ is the decay angle of the detected track. From a monte carlo study of $Z^0 \rightarrow b\bar{b}$ events, typical parameters of B decay are:

$$P_B \sim 35 GeV$$

$$P_B/m \sim 7$$

$$\text{average } \theta \sim 8^\circ$$

typical momentum of decay product $\sim 5 GeV/C$, and m is the mass of the B.

Thus, for the 25 mm beampipe,

$$\sigma_p \sim 14 \text{ microns, and}$$

$$\sigma_d \sim 100 \text{ microns}$$

This is to be compared to the typical decay length $\lambda = (P/m)c\tau \sim 2500$ microns for a B decay. To get clean vertex separation a cut of around $3\sigma_d$ or 300μ might be required, which allows fairly high efficiencies. However, if the vertex detector were a factor of 3 or 4 further from the interaction point, and the resolution were linear in this distance, the vertex finding efficiency would suffer considerably.

3 Precision Tests of the Standard Model

One of the most precise tests of the standard model in e^+e^- collisions at the Z^0 mass come from the measurement of the various asymmetries. The various asymmetries can be defined in the following way.

3.1 Definition of the asymmetries

- a) The forward-backward asymmetry A_{FB} for the process $e^+e^- \rightarrow f\bar{f}$, where $f\bar{f}$ is any fermion-antifermion pair is defined as

$$A_{FB} = \frac{\sigma(f \text{ forward}) - \sigma(f \text{ backward})}{\sigma(f \text{ forward}) + \sigma(f \text{ backward})}$$

where σ (f forward) is the cross section for the fermion f to be produced in the forward hemisphere with respect to the incident e^- , and σ (f backward) is the cross section for f to be produced in the backward hemisphere. Two points are worth noting:

- A_{FB} is nonzero even with unpolarized beams due to parity violation in Z^0 decays
- A_{FB} is much larger with polarized incident electrons

- b) The “Improved” Polarization forward-backward asymmetry \tilde{A}_{FB} for the process $e^+e^- \rightarrow f\bar{f}$ can be defined as

$$\tilde{A}_{FB} = \frac{(\sigma_L(\text{forward}) - \sigma_R(\text{forward})) - (\sigma_L(\text{backward}) - \sigma_R(\text{backward}))}{(\sigma_L(\text{forward}) + \sigma_R(\text{forward})) + (\sigma_L(\text{backward}) + \sigma_R(\text{backward}))}$$

where σ_L (forward) is the cross section for producing the fermion forward with left handed incident electrons, σ_R are the cross sections with right handed incident electrons, etc.

- c) The left-right asymmetry A_{LR}

$$A_{LR} = \frac{\sigma_L - \sigma_R}{\sigma_L + \sigma_R}$$

where σ_L, σ_R are the total e^+e^- cross sections with left handed or right handed incident electrons, respectively. Note that this asymmetry can be measured by summing all final states.

These asymmetries can be written in terms of the vector and axial vector couplings of the fermions to the Z^0 , which in turn can be expressed in terms of the Weinberg angle θ , as follows:

<u>Fermion</u>	<u>a_f</u>	<u>v_f</u>	<u>$A_f(\sin^2\theta = 0.23)$</u>
ν_i	-1	+1	-1.0
e, μ, τ	+1	$-1 + 4 \sin^2\theta$	-0.16
u, c, t	-1	$+1 - 8/3 \sin^2\theta$	-0.68
d, s, b	+1	$-1 + 4/3 \sin^2\theta$	-0.94

In the last column, A_f is an abbreviation for a frequently occurring combination of the couplings

$$A_f \equiv \frac{2a_f v_f}{a_f^2 + v_f^2}$$

in particular,

$$A_e = \frac{2a_e v_e}{a_e^2 + v_e^2}$$

Without polarization, we have, for $e^+ e^- \rightarrow f \bar{f}$

$$A_{FB} = 3/4 \left(\frac{2a_e v_e}{a_e^2 + v_e^2} \right) \left(\frac{2a_f v_f}{a_f^2 + v_f^2} \right) = 3/4 A_e A_f$$

The other asymmetries are zero without polarization.

With polarization, if we write P for the polarization of the incident e^- beam, we have

$$\begin{aligned} A_{LR} &= \frac{2a_e v_e}{a_e^2 + v_e^2} P = A_e P \\ A_{FB} &= 3/4 \frac{A_e + P}{1 + A_e P} \times \frac{2a_f v_f}{a_f^2 + v_f^2} = 3/4 \frac{A_e + P}{1 + A_e P} \times A_f \\ \tilde{A}_{FB} &= 3/4 \frac{2a_f v_f}{a_f^2 + v_f^2} P = 3/4 A_f P \end{aligned}$$

Note that A_{LR} depends on the incident electron couplings only, \tilde{A}_{FB} on the final state fermion couplings only, while A_{FB} depends on both.

3.2 Measurement of the left-right asymmetry

In terms of the Weinberg angle, A_{LR} can be written as

$$A_{LR} = A_e P = \frac{2(1 - 4 \sin^2 \theta)}{1 + (1 - 4 \sin^2 \theta)^2} P$$

Near $\sin^2 \theta \sim 1/4$, A_{LR} is very sensitive to $\sin^2 \theta$ (see Figure 10)

$$\delta \sin^2 \theta = 1/8 \delta A_e$$

where $\frac{\delta A_e}{A_e} = \sqrt{(\frac{\delta A_{LR}}{A_{LR}})^2 + (\frac{\delta P}{P})^2}$

In addition, A_{LR} is very easy to measure since it depends on the total cross sections only, so that systematics connected with final state selection are minimized and all events can be used. For N Z^0 decays,

$$\delta A_{LR} \cong 1/\sqrt{N}$$

We can thus expect the following precision as a function of the total Z^0 sample, with 45% beam polarization:

N_Z	$\delta P/P$	δA_e	$\delta \sin^2 \theta$
10^4	3%	0.022	0.003
10^5	2%	0.008	0.001
10^6	1%	0.0027	0.0003

We have assumed here that as time goes on the systematic error on the knowledge of the polarization will improve from around 3% to 1%.

The tests of the Standard Model that can be performed with this high precision measurement of $\sin^2 \theta$ can be formulated in a number of ways. The Standard Model has 3 basic free parameters which can be taken to be

$$\alpha, G_F, \text{ and } M_Z$$

or

$$\alpha, G_F, \text{ and } \sin^2 \theta$$

Thus measuring $\sin^2 \theta$ and M_Z to a corresponding high precision and comparing the two measurements is a critical test of the model. One way to do the comparison is via the Standard Model relation

$$M_Z^2 = \frac{\pi \alpha}{\sqrt{2} G_F \sin^2 \theta (1 - \sin^2 \theta)}$$

The most precise measurement of M_Z will come from SLC/LEP, and will probably be limited to $\delta M_Z \sim 30$ to 50 MeV by systematic errors. The precision on $\sin^2 \theta$ that corresponds to this is (see Fig. 11)

$$\delta \sin^2 \theta = 0.0003$$

3.2.1 Sensitivity to the top and the Higgs masses

Because of loop corrections large masses for the top quark or the Higgs boson will induce deviations from the above Standard Model prediction. These effects can be parametrized as a deviation Δr

$$M_Z^2 = \frac{\pi\alpha}{\sqrt{2} G_F \sin^2\theta(1-\sin^2\theta)} \times \left(\frac{1}{1+\Delta r}\right)$$

where

$$\Delta r_{top} = 6.3 \times 10^{-3} (M_t/M_W)^2$$

$$\Delta r_{Higgs} = 2.3 \times 10^{-3} \ln(M_H/M_W)^2$$

Figure 4 shows the dependence of A_{LR} on the top mass.

It is possible that by the time this measurement is done the top quark will have been discovered and its mass measured at hadron colliders. In that case a difference between the t mass inferred from our A_{LR} measurement and the direct measurement of the top mass would be an indication of new physics.

3.2.2 Sensitivity to New Physics

The existence of various new particles beyond the Standard Model will induce shifts in the left right asymmetry from the predictions of the Standard Model. A precise measurement of A_{LR} is sensitive to masses in the several hundred GeV mass range which would otherwise be beyond the kinematic reach of SLC or LEP. Examples of such new particles are new heavy quarks, new heavy leptons, scalar quarks or leptons, new Z'' 's, etc. The sensitivity attainable with a sample of $10^5 Z^0$ decays and 45% beam polarization are shown in Figs. 5 to 9.

3.2.3 Comparison with e^+e^- collisions without polarization

If polarization were not available in e^+e^- collisions at the Z^0 mass, then, of course, the left right asymmetry vanishes, by definition. The most precise measurement of $\sin^2\theta$ for tests of the Standard Model then would probably come from the measurement of

the forward backward asymmetry. In this measurement a specific final state must be used; $e^+e^- \rightarrow \mu^+\mu^-$ would probably be the most precise because it is the cleanest systematically.

$$A_{FB}^\mu = 3/4 \left(\frac{2a_e v_e}{a_e^2 + v_e^2} \right) \left(\frac{2a_\mu v_\mu}{a_\mu^2 + v_\mu^2} \right)$$

The disadvantages of this measurement compared to the A_{LR} measurement is that A_{FB} is much less sensitive to $\sin^2\theta$, as shown in Figure 10, and since a unique final state has to be used only $\sim 3\%$ of the Z decays are useful.

A comparison of the total number of Z decays needed to reach a similar precision in $\sin^2\theta$ in the two cases is as follows.

Precision $\delta \sin^2\theta$	Total no. of Z decays needed	
	with $P = 45\%$	with $P = 0$
0.003	10^4	$\geq 10^6$
0.001	10^5	$\geq 10^7$
0.0003	10^6	

Thus having beams with 45% polarization gives more than a factor of 100 advantage in luminosity to reach a similar precision. This comparison is shown in Figure 11. An additional factor that the above numbers do not include is that the systematic errors could be quite a problem without polarization since the asymmetry being measured is a lot smaller, and there must be larger systematic errors due to efficiencies and backgrounds associated with the selection of a unique channel such as $e^+e^- \rightarrow \mu^+\mu^-$.

3.3 Measurement of the couplings a_f, v_f

The various asymmetries, as discussed above, are a sensitive way to measure the axial vector and the vector couplings a_f and v_f of the fermions to the Z .

3.3.1 The couplings of the electron to the Z

The most sensitive way to measure the electron couplings is via the left-right polarization asymmetry

$$A_{LR} = \frac{2a_e v_e}{a_e^2 + v_e^2}$$

For $\sin^2\theta = 0.23$, we expect $a_e \sim 1$, $v_e \sim 0.08$. With a sample of $10^5 Z$'s with a beam polarization of 45%, we expect a precision on v_e of

$$\delta v_e = 0.004$$

To do the same measurement without polarized beams we would have to use the forward backward asymmetry

$$A_{FB}^e = 3/4 \left(\frac{2a_e v_e}{a_e^2 + v_e^2} \right)^2$$

which is expected to be very small, $A_{FB}^e \sim 0.02$ for $\sin^2\theta \sim 0.23$, and therefore not easy to measure. A total of $\geq 10^7 Z$ decays would be needed to reach the precision of $\delta v_e \sim .004$ which can be achieved with $10^5 Z$'s with 45% polarized beams. In addition the systematic errors associated with using the single channel $e^+e^- \rightarrow e^+e^-$ (event selection efficiencies, interference with Bhabba scattering, etc.) could be quite serious.

3.3.2 Couplings of the other fermions to the Z

With polarized beams one can measure the couplings of the fermions to the Z in the processes $e^+e^- \rightarrow Z^0 \rightarrow f\bar{f}$ via the “improved” polarization forward-backward asymmetry defined above:

$$\tilde{A}_{FB} = 3/4 \times \frac{2a_f v_f}{a_f^2 + v_f^2} \times P$$

These have the advantage of being large and independent of the electron couplings.

Without polarization one would have to use the usual forward-backward asymmetry

$$A_{FB} = 3/4 \frac{2a_e v_e}{a_e^2 + v_e^2} \frac{2a_f v_f}{a_f^2 + v_f^2}$$

which are much smaller and depend on both the e and the f couplings.

The relative luminosity needed to achieve the same precision with or without polarization is roughly

$$(\tilde{A}_{FB}/A_{FB})^2$$

The sizes of these asymmetries and the luminosity advantage due to polarization are as follows:

<u>Fermion</u>	<u>\tilde{A}_{FB} with 45% polarization</u>	<u>A_{FB} with no polarization</u>	<u>Luminosity advantage with polarization</u>
μ, τ	0.054	0.019	8
u, c	0.23	0.082	8
d, s, b	0.32	0.113	8

In reality the advantage due to polarization will be much larger because there will be non-negligible errors in selecting the fermion final states such as $c\bar{c}$, $b\bar{b}$, etc. and these systematic errors will hurt much more in measuring the smaller forward backward asymmetry with no polarization.

4 Heavy Quark Spectroscopy

B spectroscopy, i.e. the study of mesons and baryons containing a b quark, will be a very interesting field in the next few years. Because of this interest there have been and will be in the future a large number of facilities involved in b studies. These include the CLEO and ARGUS detectors at the lower energy e^+e^- colliders at Cornell and DESY respectively. These detectors have already done some very nice things. One of the limitations they have is that their B 's are produced essentially at rest, which make it difficult to study some topics such as lifetimes and Dalitz plot analyses of semileptonic decays. They make B^\pm and B_d mesons prolifically, but have much lower rates for B_s mesons and baryons. Thus on many interesting questions the higher energies in Z decays provide a considerable advantage. There are plans at hadron accelerators and colliders to do B studies, and there is much talk about B factories. However the time frame in which these facilities will make a contribution is very likely to be beyond the next two or three years which are of interest in this discussion. Other detectors studying Z decays are the Mark II at the SLC and the four detectors at LEP. For detailed studies of B decays good vertex resolution and good particle identification (i.e., $K/\pi/p$ separation) are very important. With the combination of the superior CCD vertex detector and the ring imaging Cerenkov counters SLD should have a considerable advantage over the other detectors for many interesting topics in B spectroscopy. An actual event recorded in a "prototype" of our CCD vertex detector in experiment NA32 at CERN is shown in Figure 12. The advantages of high resolution three dimensional readout is apparent. Track 3, whose vertex assignment is ambiguous in the first projection (Figure 12a) is unambiguous with three dimensional points (Figures 12b and 12c). The density of points shown in one square millimeter

of Figure 12c is similar to what we expect in a jet in Z decays. The potential for ambiguities and confusion without high resolution three dimensional readout could be quite large. The SLD Cerenkov counters provide good particle separation over most of the momentum range of interest, as shown in Figure 13. The $K-\pi$ separation at a momentum of 11 GeV/C that was measured in an SLD CRID prototype is shown in Figure 14.

4.1 Topics in B spectroscopy

Considering the special features of SLC and SLD, the following list provides some examples of the topics in B spectroscopy where SLD should excel.

- a) B^\pm , B_d^0 , B_s^0 lifetimes and lifetime ratios
- b) Measurement of the K-M matrix element V_{cb} by analysis of the Dalitz plot for the decays $B \rightarrow D\ell\nu$
- c) Measurement of V_{ub} by analysis of the Dalitz plot for $B \rightarrow \rho\ell\nu$
- d) Rare hadronic decays like $B \rightarrow \psi + x$
- e) Study of B_s and baryons

All of these topics rely heavily on the following features

- B 's produced with high velocity in Z decays
- Good vertex resolution with CCD's
- Good particle identification with CRID's

4.2 Comparison with other detectors

4.2.1 CLEO and ARGUS

As mentioned above, CLEO and ARGUS have already done some beautiful work on B mesons, and are in a good position to continue that in the future. Their major limitations are in two areas where SLD will have an advantage:

- a) The B mesons are produced essentially at rest at the $\gamma(4s)$ resonance. This causes severe systematic problems in
 - Lifetime measurements
 - Dalitz plot analysis in semileptonic decays like $B \rightarrow D e \nu$ and $B \rightarrow \rho e \nu$
- b) The high cross section running at the $\gamma(4s)$ resonance is below threshold for producing the B_s and baryons. The cross sections above the $\gamma(4s)$ are much smaller and the backgrounds are thus much more severe.

4.2.2 Mark II

The effectiveness of the Mark II detector at the SLC in studying B spectroscopy will be limited by

- a) Poor particle identification compared to the CRID's in SLD
- b) Poorer vertex detection due to ambiguities in their silicon strips, compared to the CCD detectors of SLD

4.2.3 The LEP Detectors

- a) The SLD has considerably better vertex detection than any of the four LEP detectors, as has been discussed in section 2 above (see Table II). This should give at least a factor of 3 to 5 advantage in vertex detection efficiencies.
- b) Of the four detectors only DELPHI has good high momentum $K/\pi/p$ identification in their RICH counters. However, at least at the present, they have only a one dimensional silicon strip vertex detector which will lead to much lower vertex finding efficiencies.
- c) ALEPH has a silicon vertex detector with crossed strips, but they have much more limited particle identification ($K/\pi/p$ separation) without a Cerenkov counter.
- d) SLD has significantly better vertex resolution and particle identification than the other two LEP detectors, which have chosen to sacrifice these features in favor of others where they excel (see Tables I and II).

It is not easy to evaluate the luminosity advantage that the above features give the SLD detector for the physics topics in B spectroscopy listed above, but an order of magnitude seems plausible, i.e., the SLD with $10^5 Z$'s should be able to compete favorably with LEP with $10^6 Z$'s.

5 $B^0 - \bar{B}^0$ Mixing

The quantum mechanical mixing of the B^0 and \bar{B}^0 states is one of the most important topics in B physics. The mixing has been observed for B_d^0 in the ARGUS, CLEO, and UA1 detectors. However the time evolution of B_d^0 mixing has not been studied and there have been no studies of B_s^0 mixing. Because of the availability of polarized beams at SLC and the good vertex resolution and particle identification, SLD is in a uniquely advantageous position to study all of these effects.

5.1 Summary of the Nomenclature for $B - \bar{B}$ Mixing

The quark content of the six B meson states of interest are

$$\begin{array}{ll} B^+ = \bar{b}u & B^- = b\bar{u} \\ B_d^0 = \bar{b}d & \bar{B}_d^0 = b\bar{d} \\ B_s^0 = \bar{b}s & \bar{B}_s^0 = b\bar{s} \end{array}$$

The decays of the B mesons proceed via the weak interactions. The weak eigenstates of the B_d and the B_s are (assuming no CP violation for this discussion)

$$\begin{aligned} B_1 &= 1/\sqrt{2}(B^0 + \bar{B}^0) \\ B_2 &= 1/\sqrt{2}(B^0 - \bar{B}^0) \end{aligned}$$

The time dependent amplitudes for these states can be written as

$$\begin{aligned} B_1 &= e^{-(1/2\Gamma_1 + im_1 t)} \\ B_2 &= e^{-(1/2\Gamma_2 + im_2 t)} \end{aligned}$$

Then we have the amplitudes

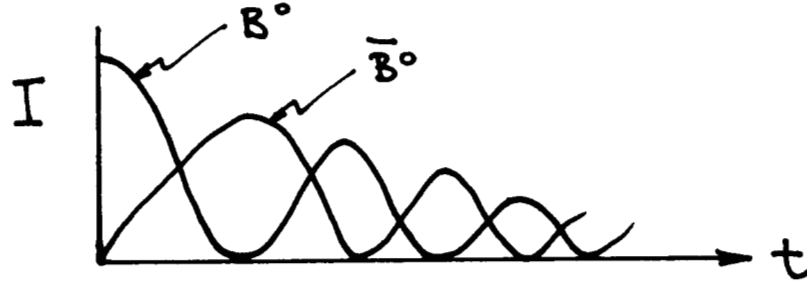
$$\begin{aligned} B^0 &= 1/\sqrt{2}(B_1 + B_2) \\ \bar{B}^0 &= 1/\sqrt{2}(B_1 - B_2) \end{aligned}$$

If we have a pure B^0 at $t=0$, then the intensities of B^0 and \bar{B}^0 as a function of time are

$$I(B^0) = 1/4(e^{-\Gamma_1 t} + e^{-\Gamma_2 t} + 2e^{-1/2(\Gamma_1 + \Gamma_2)t} \cos \Delta m t)$$

$$I(\bar{B}^0) = 1/4(e^{-\Gamma_1 t} + e^{-\Gamma_2 t} - 2e^{-1/2(\Gamma_1 + \Gamma_2)t} \cos \Delta m t)$$

where $\Delta m = m_2 - m_1$ is the mass difference between the B_2 and the B_1 states. This produces $B^0 - \bar{B}^0$ oscillations with a frequency $\nu = 2\pi/\Delta m$, as shown below.



If we do not measure the time dependence but integrate over time, the intensities are

$$I = \int I(B^0) dt = 1/4(\frac{1}{\Gamma_1} + \frac{1}{\Gamma_2} + \frac{2\Gamma}{\Gamma^2 + \Delta m^2})$$

$$\bar{I} = \int I(\bar{B}^0) dt = 1/4(\frac{1}{\Gamma_1} + \frac{1}{\Gamma_2} - \frac{2\Gamma}{\Gamma^2 + \Delta m^2})$$

where $\Gamma = 1/2(\Gamma_1 + \Gamma_2)$. Later on we will also use $\Delta\Gamma = \Gamma_2 - \Gamma_1$.

The mixing parameter X is defined as

$$X = \frac{\text{Mixed}}{\text{Mixed} + \text{Unmixed}} = \frac{I}{I + \bar{I}}$$

where Mixed is the intensity of \bar{B}^0 when we start with a pure B^0 state. Then

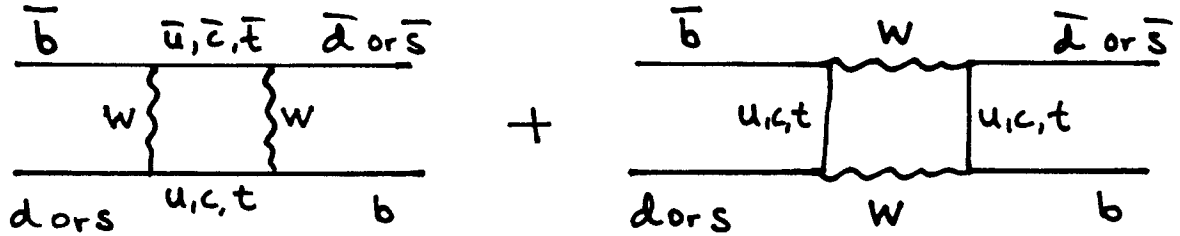
$$X = \frac{(\Delta m/\Gamma)^2 + (1/2\Delta\Gamma/\Gamma)^2}{2 + 2(\Delta m/\Gamma)^2}$$

It is usually assumed that $\Delta\Gamma/\Gamma \ll \Delta m/\Gamma$. The expression for the mixing parameter then simplifies to

$$X = 1/2 \frac{(\Delta m/\Gamma)^2}{1 + (\Delta m/\Gamma)^2}$$

We can see that for large $\Delta m/\Gamma$ the mixing parameter approaches its asymptotic value of $1/2$.

The parameter of physical interest is $\Delta m/\Gamma$. It is related to the KM matrix parameters V_{ts} and V_{td} in the following way. The two box diagrams responsible for the mixing are



Since the strength of these diagrams depend on the square of the mass of the intermediate quarks, they are expected to be dominated by the t quark contribution

$$(\Delta m/\Gamma)_{B_d} \sim \tau_{B_d} |V_{tb}|^2 |V_{td}|^2 M_t^2 \dots$$

$$(\Delta m/\Gamma)_{B_s} \sim \tau_{B_s} |V_{tb}|^2 |V_{ts}|^2 M_t^2 \dots$$

where V_{tb} etc are the K-M matrix elements, τ_B are the lifetimes, M_t is the mass of the top quark, and the stand for other factors expected to be similar for B_d and B_s . In that case, and assuming that the B_d and the B_s lifetimes are similar, one might expect that the B_s mixing will be larger than B_d mixing

$$\frac{(\Delta m/\Gamma)_{B_s}}{(\Delta m/\Gamma)_{B_d}} \sim \frac{|V_{ts}|^2}{|V_{td}|^2} > 1$$

since we expect that $V_{ts} > V_{td}$ because V_{ts} is one generation gap closer than V_{td} . From the ARGUS and CLEO measurement of $B_d^0 - \bar{B}_d^0$ mixing we infer that

$$(\Delta m/\Gamma)_{B_d} \sim 0.7$$

and, using the B lifetime of $\sim 10^{-12}$ sec, $\Delta m(B_d) \sim 3 \times 10^{-10}$ MeV. Accordingly we would expect for the B_s mixing

$$(\Delta m/\Gamma)_{B_s} > 1$$

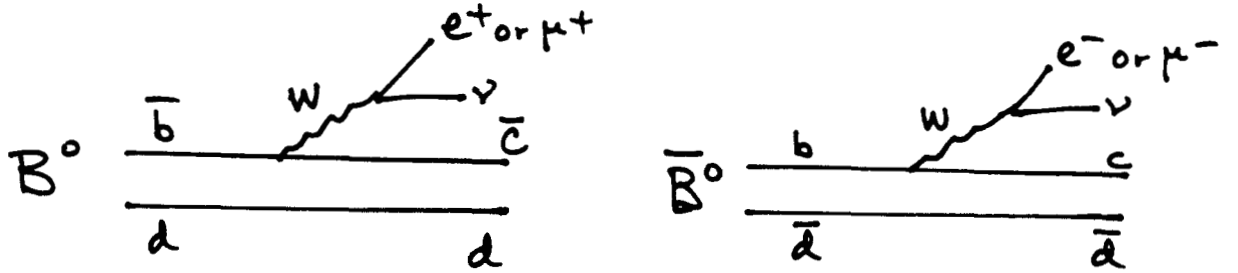
$$X_{B_s} \sim 1/2$$

However, at this time nothing is known experimentally about B_s mixing.

The dependence of the mixing parameter X on $\Delta m/\Gamma$ is shown graphically in Figure 15. As discussed above, X can be measured experimentally without measuring any time dependence, i.e., integrating over time like the ARGUS and CLEO measurements. However, as the mixing is large, $X \rightarrow 1/2$, and a measurement of X gives a very poor determination of the physically interesting parameter $\Delta m/\Gamma$. Thus for large mixing, as we expect to be the case for the B_s^0 , measuring the time dependence of the $B - \bar{B}$ mixing is the only good way to measure $\Delta m/\Gamma$.

5.2 The conventional method to look for $B - \bar{B}$ mixing

Both ARGUS and CLEO used the double lepton tag method to observe $B_d^0 - \bar{B}_d^0$ mixing using the reaction $e^+e^- \rightarrow B^0 + \bar{B}^0$. In this method one uses only those events in which both B's decay into an e or a μ . The sign of the lepton determines whether the B was a B^0 or a \bar{B}^0 at the decay point, since $B^0 \rightarrow e^+$ or μ^+ and $\bar{B}^0 \rightarrow e^-$ or μ^- , as can be seen from the diagrams below.



Like sign dileptons, i.e., leptons with the same sign from both B decays in the event is evidence for mixing. This can be easily seen by considering for example the case where one side decays into an e^- , indicating a \bar{B}^0 decay. Then the other side must have been a B^0 , and should decay into an e^+ if there is no mixing. An e^- on both sides means that on one or the other side mixing occurred. The mixing parameter, aside from small corrections, then is

$$X = \frac{l^+l^+ + l^-l^-}{l^+l^- + l^+l^+ + l^-l^-}$$

The problem with this double tag method (where both sides are tagged by a flavor specific decay mode) is that the lepton tag efficiency comes in squared, giving a very low event rate. ARGUS and CLEO observed three to five hundred like sign dilepton events in samples of 100,000 to 200,000 total $B\bar{B}$ events. These numbers are given in Table IV. The lepton tag efficiency on each side was around 5 to 6%, which comes

in squared. The 5 or 6% can be understood as the product of the leptonic branching ratios, $(B \rightarrow e) + (B \rightarrow \mu) \cong 22\%$, the lepton detection efficiency, and the fraction of the leptons that survive the $P \geq 1.5$ GeV/C cut to separate leptons from B decays and D decays, as shown in Figure 16.

5.3 $B\bar{B}$ Mixing in Z Decays

We expect the process $e^+e^- \rightarrow Z^0 \rightarrow b\bar{b}$ to be about 14% of all Z decays. We thus expect a total of 14,000 $b\bar{b}$ pair events in a sample of 10^5 Z decays. If we then assume that a \bar{b} hadronizes to mesons and baryons with the following probabilities

$$\begin{array}{lll} \bar{b} \rightarrow & B^+ & \sim 40\% \\ & B_d^0 & \sim 40\% \\ & B_s^0 & \sim 10\% \\ & \text{baryons} & \sim 10\% \end{array}$$

we expect the numbers of pairs summarized in Table V.

5.3.1 Using the conventional double lepton tag method

Consider using the double lepton tag method described in section 5.2 with a sample of 10^6 Z decays. From Table V we then expect

$$\begin{array}{l} 78,000 \text{ events with } B_u + \bar{B}_{u,d,or s} + \text{charge conj} \\ 78,000 \text{ events with } B_d + \bar{B}_{u,d,or s} + \text{charge conj} \\ 23,000 \text{ events with } B_s + \bar{B}_{u,d,or s} + \text{charge conj} \end{array}$$

If we assume a single lepton tag efficiency of 6% as in ARGUS or CLEO, we expect

$$\begin{array}{l} 280 \text{ } B_u \text{ events with double lepton tag} \\ 280 \text{ } B_d \text{ events with double lepton tag} \\ 80 \text{ } B_s \text{ events with double lepton tag} \end{array}$$

These numbers are smaller than what has already been published by ARGUS or CLEO. However, there are two differences. The ARGUS And CLEO samples did not contain

any B_s events, and the B 's from Z decays have high momentum so that in principle time dependences can be studied. The trouble is that the B_u , B_d , and B_s events are not distinguished from one another by the lepton tags. To separate out the B_s sample requires cuts that will reduce the 80 event sample by a factor of 5 or so. To study time dependence one has to find vertices; with the expected vertexing efficiencies the sample once again will be reduced to a small number.

We thus conclude that the usual double lepton tag method does not produce an interesting number of events even with a sample of 10^6 Z 's. We have considered B decay modes other than the leptonic one to use in a double tag method. However all useful decay modes we could think of have branching ratios smaller than the leptonic one (which is 22%) and thus are even less promising. One might do slightly better by summing over several flavor specific decay modes.

5.3.2 Method using polarization and inclusive vertex tagging

Availability of polarized beams and very good vertex resolution allows us to consider a different method of studying the time evolution of $B\bar{B}$ mixing, which was proposed for SLD by Bill Atwood. The large forward backward asymmetry for $e^+e^- \rightarrow Z \rightarrow b\bar{b}$ with polarized electrons can be used to tag the flavor of the B at $t=0$. One can then do an experiment looking at only one B in the event decaying in a flavor specific way. To maximize the useful number of events and to allow study of the decay time evolution of the mixing an inclusive vertex tagging scheme can be used that consists of looking for two separated secondary decay vertices corresponding to the B decay followed by a D decay.

The forward-backward asymmetry in this case can be written as

$$A_{FB} = \frac{(B^0 \text{ in } e^- \text{ direction}) - (\bar{B}^0 \text{ in } e^- \text{ direction})}{(B^0 \text{ in } e^- \text{ direction}) + (\bar{B}^0 \text{ in } e^- \text{ direction})}$$

where e^- direction stands for the whole forward hemisphere with respect to the incident e^- . This asymmetry is predicted by the Standard Model to be (see section 3.1)

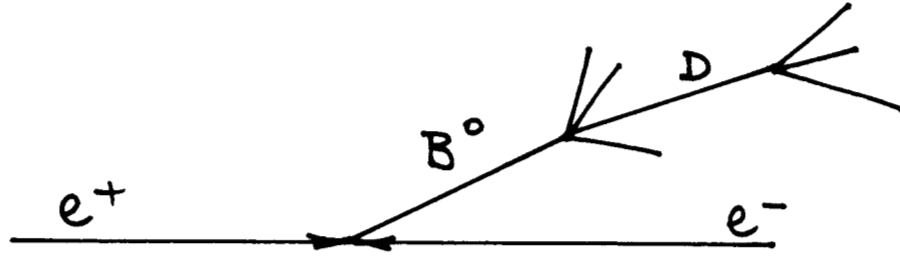
$$\begin{aligned} A_{FB} &= 71\% \text{ for } 100\% \text{ polarization} \\ &= 42\% \text{ for } 45\% \text{ polarization} \end{aligned}$$

These standard model predictions can be verified by using $e^+e^- \rightarrow Z^0 \rightarrow B^+B^-$ events where there can be no mixing. For B^0 , mixing will dilute the asymmetry

$$A_{FB}(B^0) = (1 - 2X)A_{FB}(B^\pm)$$

where $A_{FB}(B^0)$ is the forward-backward asymmetry measured with B^0 , $A_{FB}(B^\pm)$ is the asymmetry measured by B^\pm , and X is the mixing parameter for $B^0 - \bar{B}^0$ mixing. Thus the mixing parameter can be measured by the asymmetry dilution. The time dependence of the mixing can be measured by looking at $A_{FB}(B^0)$ in bins of the B^0 proper decay time. The asymmetry should exhibit decay time dependent oscillations with frequency $\nu = 2\pi/\Delta m$ as discussed in section 5.1 and shown in Figures 17 to 19.

The inclusive vertex tag consists of looking for a chain of two decay vertices.



- a) The observation of two such vertices clearly identifies the event as a B decay.
- b) The multiplicity at the B decay vertex is expected to be around 3.5 charged tracks so that counting the charge should be fairly reliable and B^\pm can be separated from B^0 decays.
- c) Looking for a charged lepton from either the B or the D vertex will identify the decay as a B^0 or a \bar{B}^0 (a B^0 will give an ℓ^+ at the B decay vertex or an ℓ^- at the D decay vertex). Thus instead of having to make a momentum cut (with a large loss of efficiency) to separate leptons from B and D decays, we can get a high efficiency by using both the B and the D decay leptons by seeing which decay vertex they come from
- d) One can separate B_s^0 from B_d^0 decays by counting the number of kaons in the decay chain. B_s^0 should often produce two kaons, one from the $\bar{b} \rightarrow \bar{c} \rightarrow \bar{s}$ decay chain, the other from the “spectator” s in the B_s^0 . The B_d^0 will usually have only one K in the decay chain.

We are now in the process of developing algorithms and doing Monte Carlo calculations to estimate the efficiencies for steps a) to d) above. Our ability to estimate some of the

efficiencies at this time will be limited by the fact that the B_s^0 has not been observed yet and thus there are no experimental measurements about any of its decay modes or branching ratios. For the purposes of this discussion we make the following plausible estimates for the efficiencies of the steps a) to d) above:

a) Double vertex finding 40%

b) Charge counting 90%

c) Lepton tag

$$2 \times (12\% + \frac{7\%+18\%}{2}) \times 0.9 \cong 45\%$$

where the factor of 2 is for sum of e^\pm and μ^\pm

12% is the $B \rightarrow e$ or μ branching ratio

$\frac{7\%+18\%}{2}$ is the average D^0 or $D^+ \rightarrow e$ or μ

0.9 is lepton detection efficiency

d) Double K tag for B_s 20%

0 or 1 K tag for B_d 80%

For a sample of 10^5 Z decays, we expect the following numbers of B produced

$$11,000 B_d$$

$$2,800 B_s$$

We thus expect

$$11,000 \times .4 \times .9 \times .45 = 1800 B_d^0 \text{ or } \bar{B}_d^0$$

$$2800 \times .4 \times .9 \times .45 = 450 B_s^0 \text{ or } \bar{B}_s^0$$

which are separated from B^\pm , and B^0 or \bar{B}^0 flavor identified. If we need to separate B_s from B_d we expect

$$1800 \times 0.8 \cong 1400 B_d$$

$$450 \times 0.2 \cong 100 B_s$$

Note: If the efficiencies turn out to be different from the above assumptions by a factor of f , we will need $(1/f) \times 10^5$ Z decays to collect these samples of events.

With these samples we can carry out a variety of measurements:

- a) With 1400 clean B_d^0 events we can measure the time evolution of $B_d^0 - \bar{B}_d^0$ mixing. Figure 17 shows a Monte Carlo simulation of the time dependence of A_{FB} for B_d with 1000 events.
- b) We can do measurements of the time evolution, and thus $\Delta m/\Gamma$, for $B_s^0 - \bar{B}_s^0$ mixing. Consider two possible scenarios:

1. As expected, B_s mixing is much larger than B_d mixing i.e.,

$$(\Delta m/\Gamma)_{B_s} \gg (\Delta m/\Gamma)_{B_d}$$

then the asymmetry oscillations for B_s will have a much higher frequency than the B_d oscillations. In this case we can use the full 450 event B_s and 1800 event B_d samples (which are not separated from each other) since the high frequency $B_s - \bar{B}_s$ oscillations can be clearly observed on top of the slowly varying $B_d - \bar{B}_d$ oscillations. The case for $(\Delta m/\Gamma)_{B_d} \cong 0.7$ and $(\Delta m/\Gamma)_{B_s} \cong 7$ is shown in Figure 18. The expected precision in $(\Delta m/\Gamma)_{B_s}$ from this fit is

$$(\Delta m/\Gamma)_{B_s} \cong 7 \pm 0.3$$

2. If the unexpected should occur and $(\Delta m/\Gamma)_{B_s}$ is closer to $(\Delta m/\Gamma)_{B_d}$, we can use the 100 event B_s sample which is separated from the B_d sample.
3. It may be better to be between the two extremes given above, i.e., use milder cuts to separate B_d from B_s . For example we might get a factor of 9 reduction of B_d with a 40% efficiency for B_s . This would give a sample of ~ 200 B_d and ~ 200 B_s . The fit in this case is shown in Figure 19.

5.3.3 Conclusions about $B - \bar{B}$ Mixing

- a) The capabilities of the SLD with a 45% polarized e^- beam should allow us to
 - measure the time dependence of B_d mixing with 10^5 Z 's or less
 - measure the time dependence of B_s mixing, but we need at least 10^5 Z 's or slightly more.
- b) Comparison with LEP

- A sample of 10^7 Z 's or more are needed to look at the time development of B_s mixing without polarization using the double lepton tag method.
- The method using A_{FB} with polarized beams is much more advantageous. We do not know all of the efficiencies very well at this time. However some of the relative factors in the luminosity required at SLC or LEP seem clear.
 - i) Vertexing efficiency at SLC due to the close in CCD vertex detectors should be better by a factor of 3 to 5 for the two vertex chain.
 - ii) A_{FB} without polarization is $\sim 10\%$, with 45% polarization it is around 42%. The number of events needed to obtain the same precision in $\Delta m/\Gamma$ goes like $(1/A_{FB})^2$, so this is an advantage of a factor of 16 in luminosity.
 - iii) We thus expect that SLD can do a similar measurement by this particular method with a factor of 50 to 80 less luminosity than LEP.
- c) As $\Delta m/\Gamma$ increases the frequency of the A_{FB} oscillations in proper time, and therefore decay distance, increases, requiring increasingly better vertex resolution to see the effect. Figure 20 shows the resolution required to observe A_{FB} oscillations as a function of $\Delta m/\Gamma$. The better vertex resolution of SLD will allow us to explore a larger range of this parameter, up to $\Delta m/\Gamma = 15$ or 20.

6 Summary and Conclusion

There are a set of interesting and forefront areas of physics, such as

- Precision tests of the Electroweak Theory
- B Spectroscopy
- $B\bar{B}$ Mixing

where SLD at the SLC with 10^5 Z 's per year with polarization can compete favorably, and in some cases do better, than LEP with 10^6 Z 's per year without polarization.

Many interesting and beautiful analyses were presented here throughout this week. However, we should remember that this is the first SLD physics meeting, and many of the results are preliminary. We have to continue these physics studies in the next year, and most important, we have to complete the assembly and commissioning of SLD so we can move onto the beamline next summer.

Table I. Summary of Z-factory Detectors*

	ALEPH (LEP)	DELPHI (LEP)	L3 (LEP)	OPAL (LEP)	Mark II (SLC)	SLD (SLC)
Vertex Detector	chamber + μ -strips	chamber + μ -strips	TEC	chamber	chamber + μ -strips	CCD's
Tracking Device	TPC 1 atm $r = 1.8$ m $n = 300$	TPC 1 atm $r = 1.2$ m + outer	TEC	DC 4 atm $r = 1.6$ m $n = 160$	DC 1 atm $r = 1.5$ m $n = 72$	DC 1 atm $r = 1.0$ m $n = 80$
Coil	s.c. 1.5 T	s.c.	warm 0.4 T	warm 0.4 T	warm 0.5 T	warm 0.6 T
Tracking Resolution	0.13% p	0.15% p	0.03% p μ only	0.15% p	0.12% p	0.13% p
Particle Id	dE/dx 4.5% σ	dE/dx + RICH	—	dE/dx 3.5% σ	dE/dx 7% σ	CRID
EM calor.	Pb-gas	HDPC	BGO	Pb glass	Pb-LA	PB-LA
EM resolution	$18\%/\sqrt{E}$	$18-20\%/\sqrt{E}$	1%	$6.5\%/\sqrt{E}$	$12\%/\sqrt{E}$	$8\%/\sqrt{E}$
Hadron cal. Resolution	$100\%/\sqrt{E}$	$100\%/\sqrt{E}$	$50\%/\sqrt{E}$ +10%	$100\%/\sqrt{E}$	—	$55\%/\sqrt{E}$
Muon Det.	full	full	high res	full	55%	full

*Taken from the 1985 HEPAP Study at Coolfont

Table II. Vertex Detector Comparison

Vertex Detector	ALEPH	DELPHI	OPAL	L3	SLD
Type: Initial	Silicon strips	Silicon strips	Drift chamber	TEC	CCD's
Later			Silicon strips		
Beam Pipe Radius					
Initial	8 cm	8 cm	8 cm	8 cm	2.5 cm
Later	6 cm	6 cm	6 cm	6 cm	1.6 cm
Beam size	$\sim \frac{1}{2}$ mm	$\sim \frac{1}{2}$ mm	$\sim \frac{1}{2}$ mm	$\sim \frac{1}{2}$ mm	$1\frac{1}{2}\mu$
Vertex det. pitch or pixel size	$250\mu^*$	25μ			$2.2 \times 22\mu$
Resolution: ϕ	$25\mu^*$	5μ	50μ	30μ	5μ
\ominus	$25\mu^*$	—	300μ	mm's	5μ
Two track resolution	$\sim 500\mu$		2 mm	500μ	40μ

*1983 Design report
has it changed since?

Table III. Physics Topics of Interest for the SLD

Physics Topic	Some SLD Advantage	
	Over Mark II	Over LEP
1. Electroweak Tests		
• Precision tests ALR vs. M_Z		X
• Precision meas of Γ_Z via Bhabbas	X	
• Measurements of $Z \rightarrow f\bar{f}$ Couplings via $A_{FB}^{(Pol)}$	X	X
2. B Spectroscopy		
• B^\pm, B^0 Lifetimes	X	X
• V_{cb}, V_{ub} meas. via semileptonic decays	X	X
• B_s and B-baryons	X	X
3. $B - \bar{B}$ Mixing	X	X
4. Supersymmetry	X	
5. Higgs Search	X	
6. Technicolor, extended Higgs	X	
7. New Quarks, Leptons, Z's	X	
8. Neutrino Counting		

Table IV. $B_d - \bar{B}_D$ Mixing Samples in the ARGUS and CLEO Detectors

	ARGUS	CLEO
$N(\Upsilon(4S))$	96000	220000
Like - sign dilepton candidates		
Total	50	73
Fakes	12.3	12.7
Secondaries	12.9	27.8
Signal	$24.8 \pm 7.6 \pm 3.8$	$32.5 \pm 8.5 \pm 5.5$
Unlike - sign dilepton candidates		
Total	302	475
Fakes	24.7	32.9
Secondaries	7.2	6.4
Signal	$270 \pm 19.4 \pm 5.0$	431 ± 24
r	0.22 ± 0.10	0.18 ± 0.08

Table V. $B - \bar{B}$ Pairs Produced in $10^5 Z^0$ Decays

Pair	%	Events/ $10^5 Z$
$B_u \bar{B}_u + \text{c.c.}$	16	2200
$B_d \bar{B}_d$	16	2200
$B_u \bar{B}_d$	32	4500
$B_u \bar{B}_s$	8	1100
$B_d \bar{B}_s$	8	1100
$B_s \bar{B}_s$	1	140
B_u B baryon	8	1100
B_d B baryon	8	1100
B_s B baryon	2	280
$B_{bar} \bar{B}_{bar}$	1	140

Totals

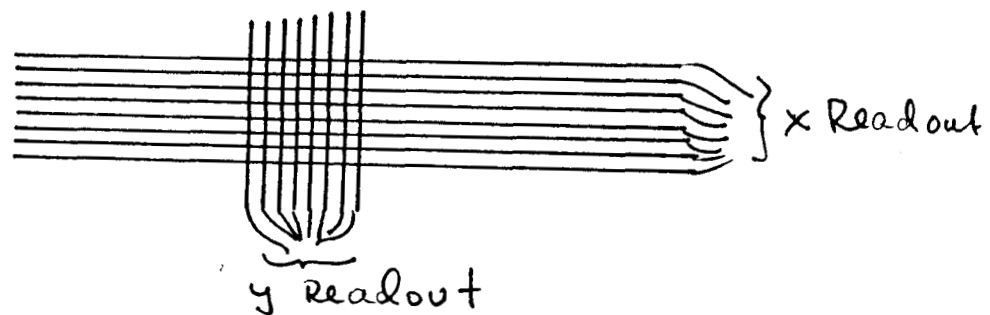
B_u - 11,000

B_d - 11,000

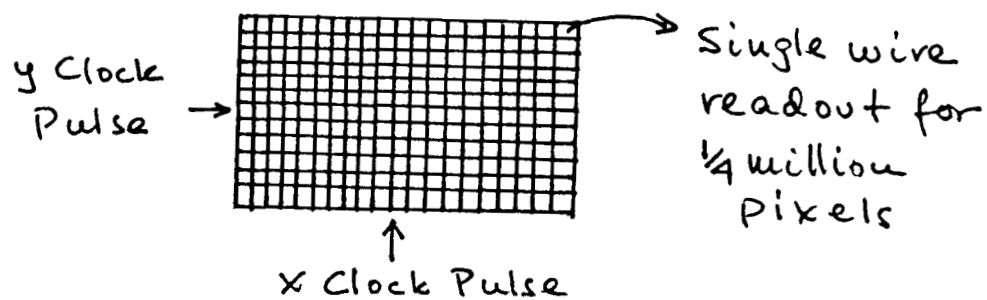
B_s - 2,800



a) One dimensional Silicon Strips



b) Crossed x and y Silicon Strips



c) Charge Coupled Devices (CCD's)

Figure 1. Silicon vertex detectors. a) One dimensional strips. b) Crossed x and y strips. c) CCD chips.

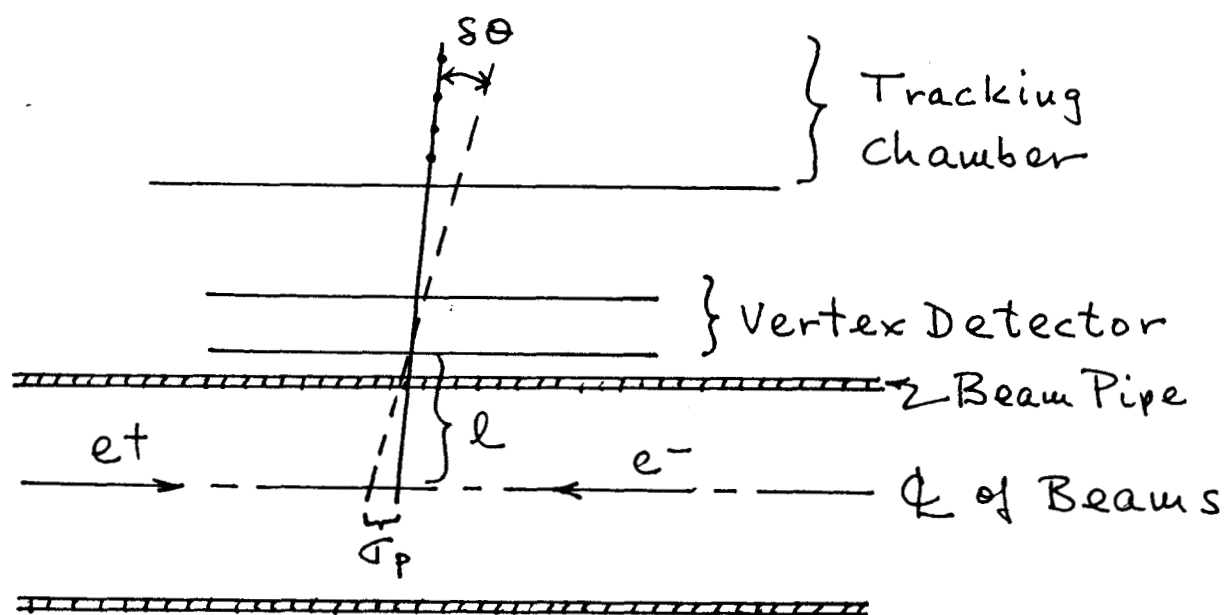


Figure 2. Common vertex detector geometry.

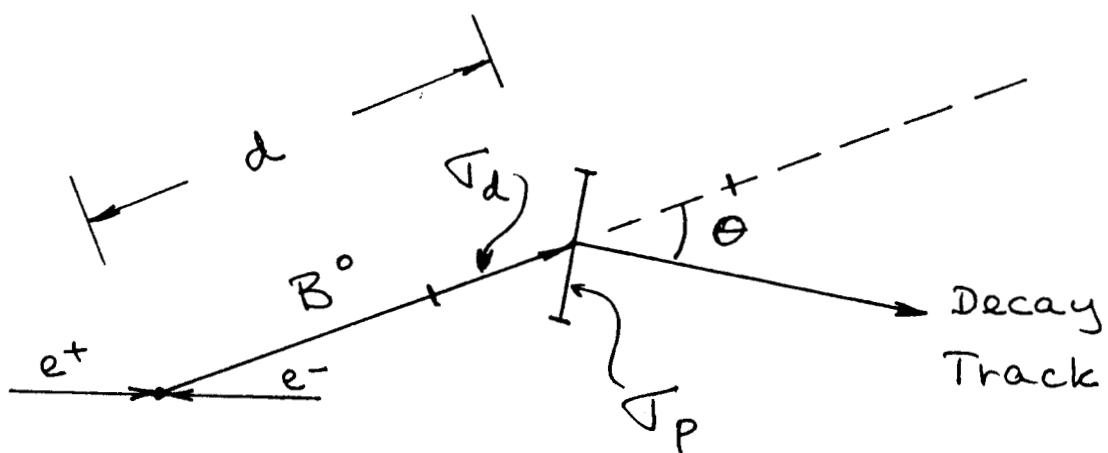


Figure 3. Dependence of σ_d , the resolution in the decay distance d , on σ_p , the resolution in the impact parameter.

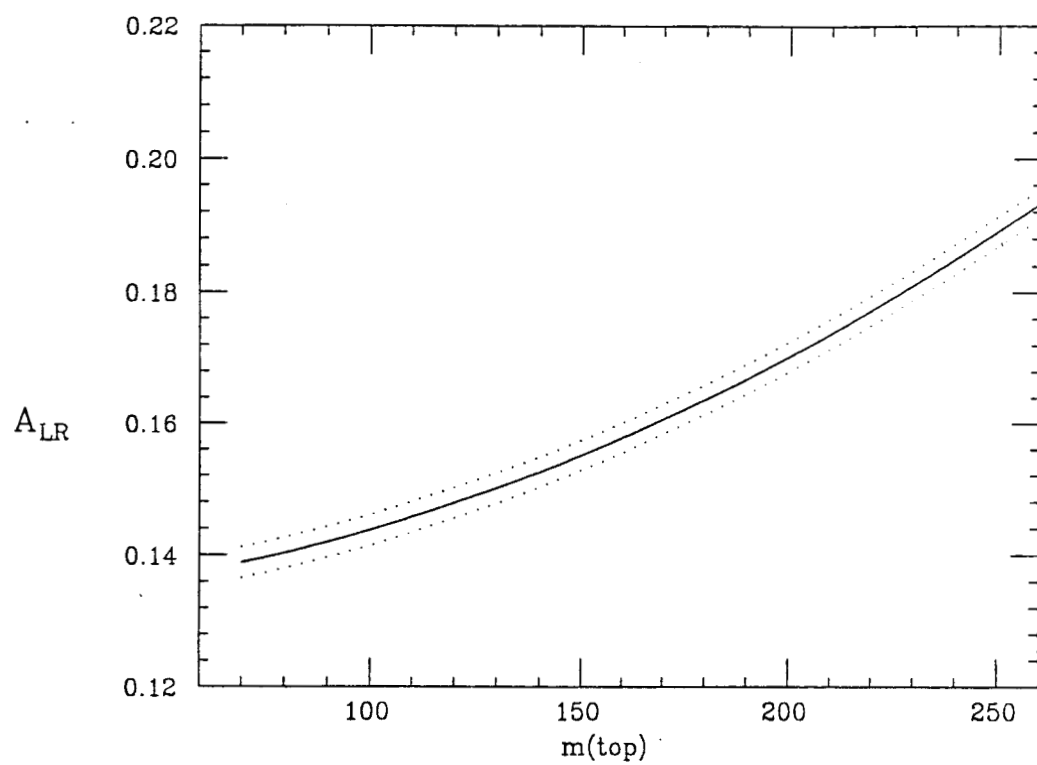
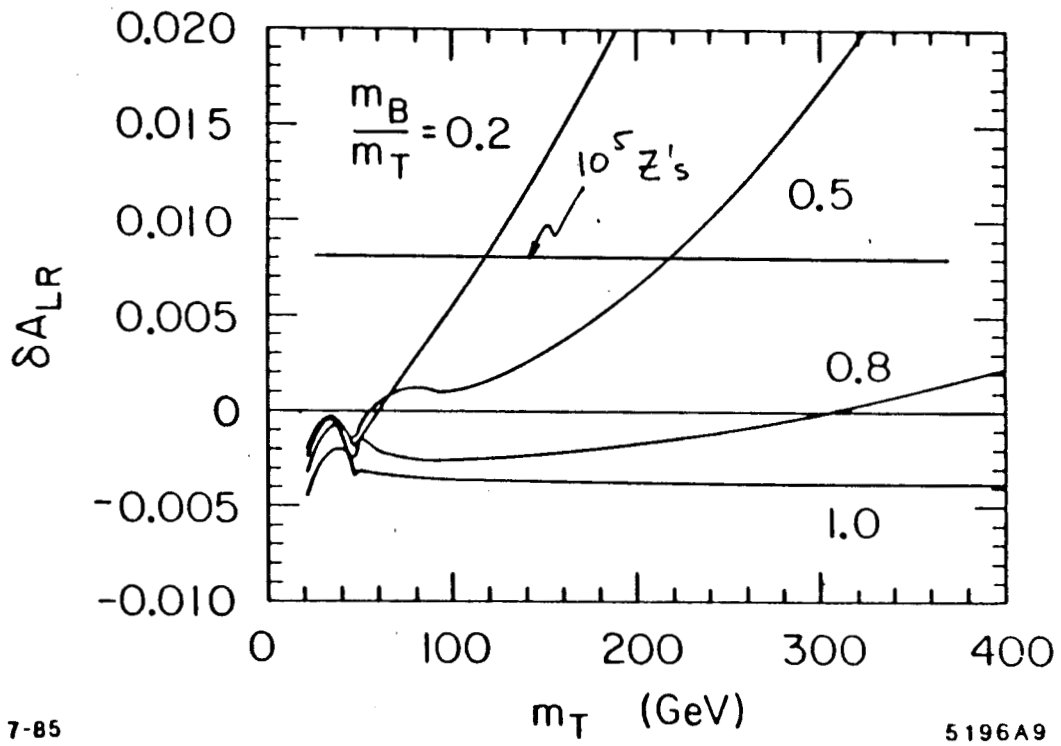


Figure 4. Dependence of A_{LR} on the top mass. The dependence on the Higgs mass is small (Figure from Traudl Hansl Kozaněcka)



7-85

5196A9

Figure 5. The shift in the left-right asymmetry caused by new heavy quark doublets of various masses. The solid horizontal line indicates the experimental precision that can be obtained on A_{LR} with $10^5 Z's$. Figure from article by Morris Schwartz.

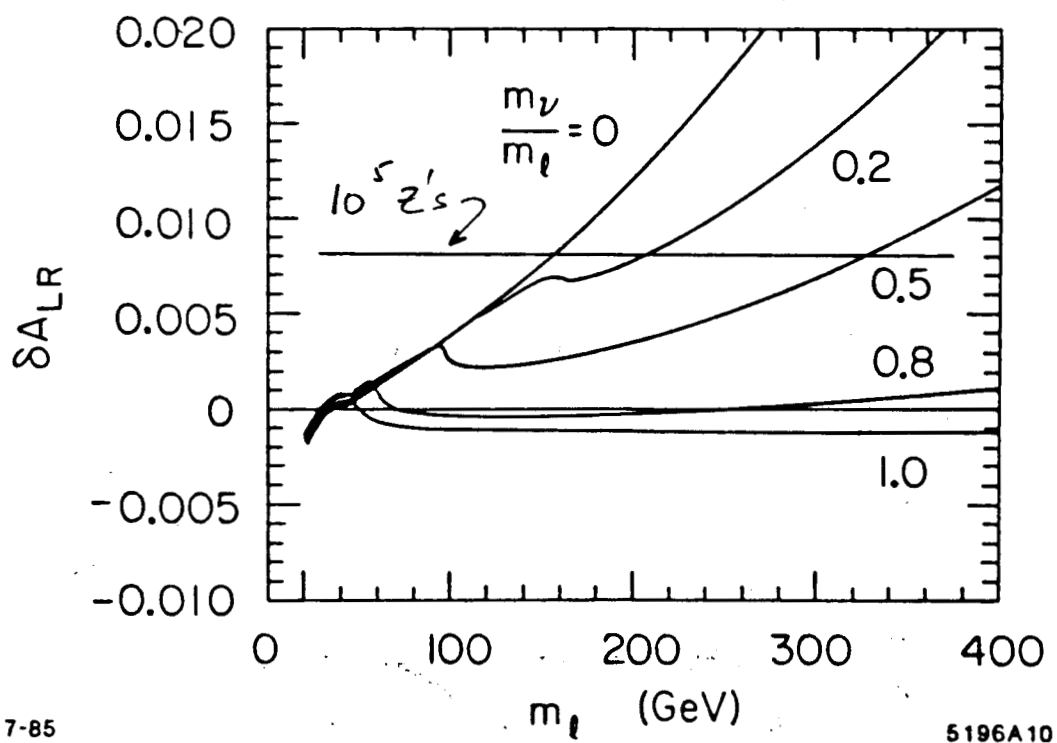


Figure 6. The shift in the left-right asymmetry caused by new heavy leptons with various masses. The solid horizontal line indicates the experimental precision that can be obtained on A_{LR} with $10^5 Z$'s. Figure from article by Morris Schwartz.

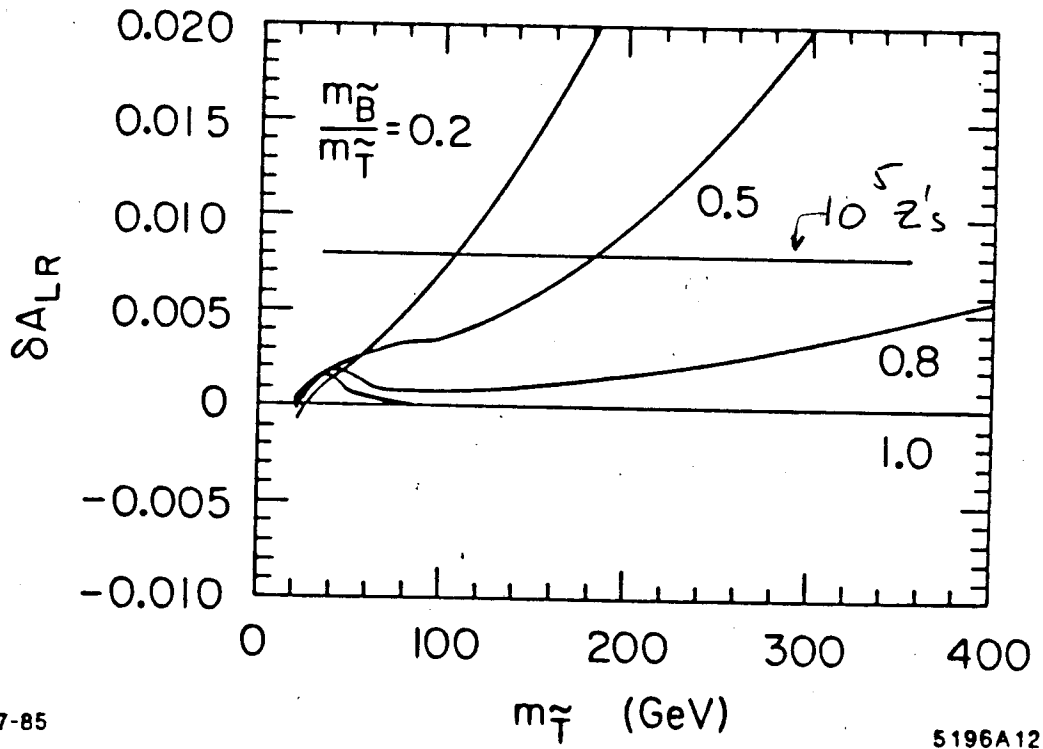


Figure 7. The shift in the left-right asymmetry caused by new heavy scalar quark doublets of various masses. The solid horizontal line indicates the experimental precision that can be obtained on A_{LR} with $10^5 Z$'s. Figure from article by Morris Schwartz.

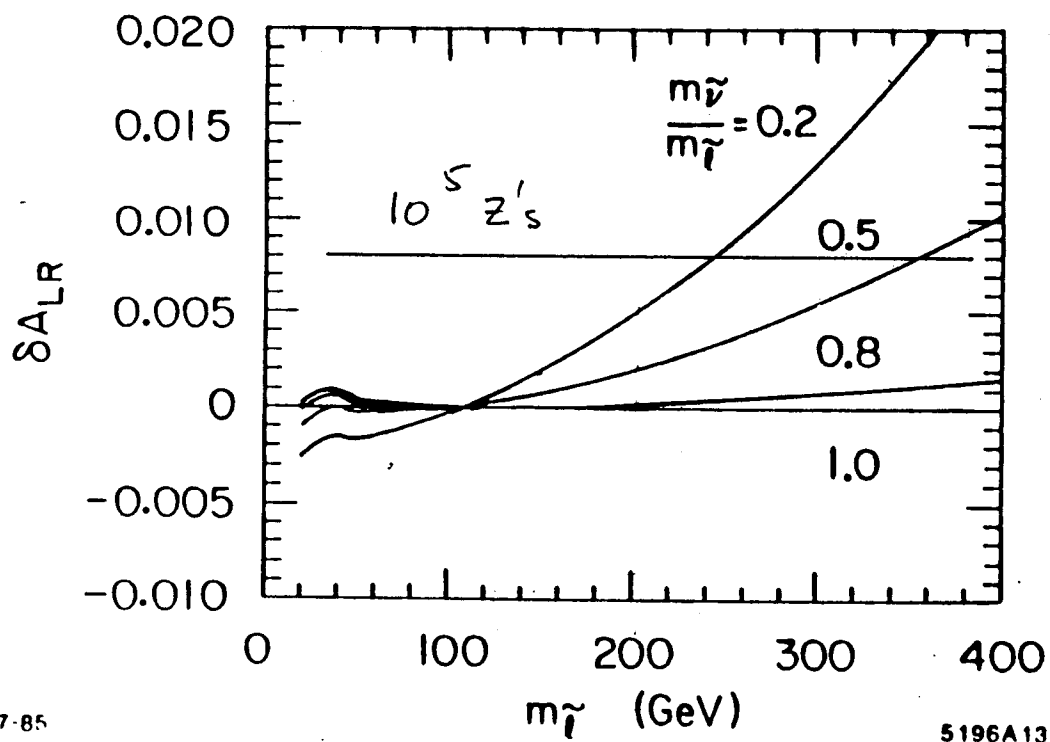


Figure 8. The shift in the left-right asymmetry caused by new heavy scalar lepton doublets of various masses. The solid horizontal line indicates the experimental precision that can be obtained on A_{LR} with $10^5 Z$'s. Figure from article by Morris Schwartz.

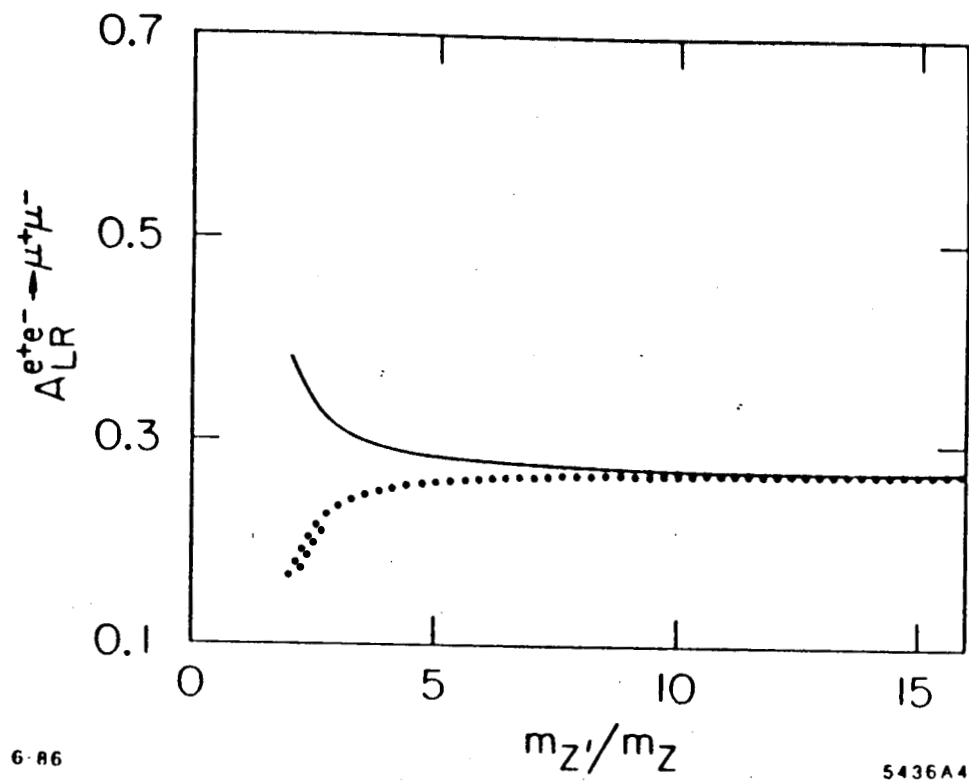


Figure 9. The effect of a new heavy Z' boson on the left-right asymmetry as a function of the Z' mass. Figure from outside by Morris Schwartz.

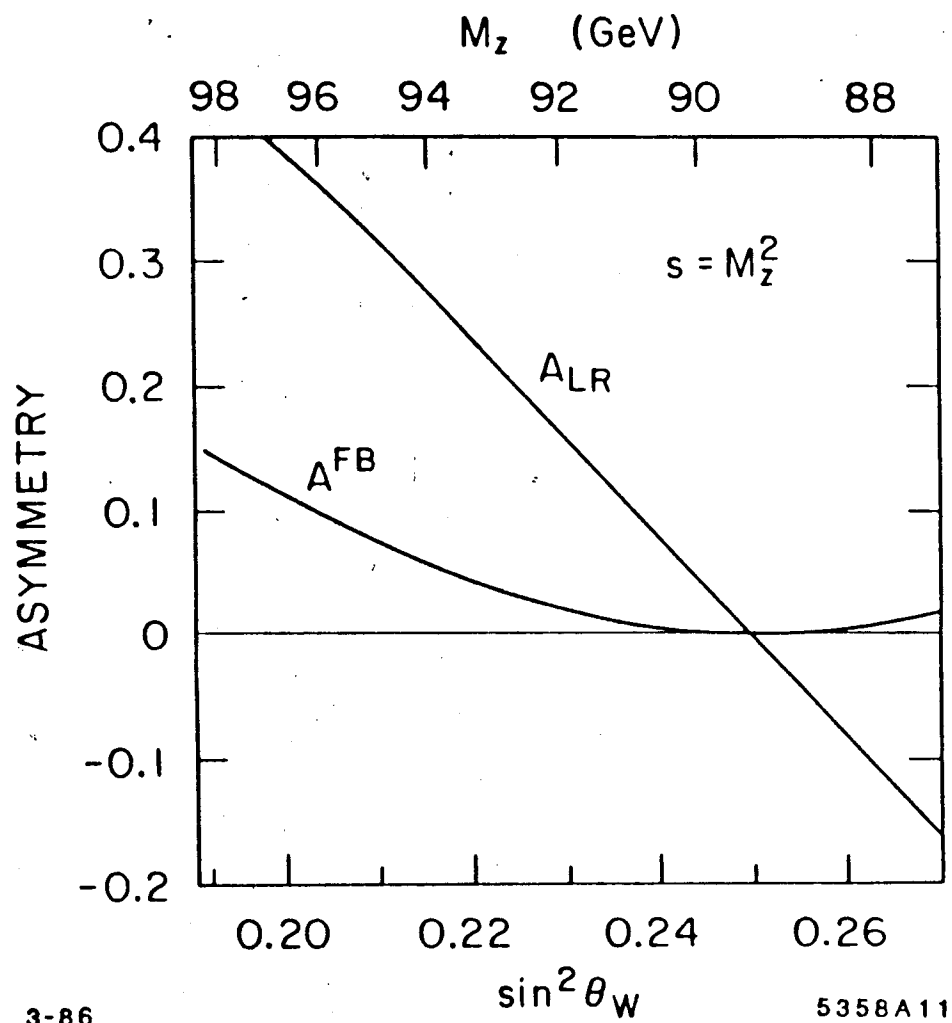


Figure 10. Sensitivity of the left-right asymmetry A_{LR} and the forward-backward asymmetry A_{FB} on $\sin^2 \theta$.

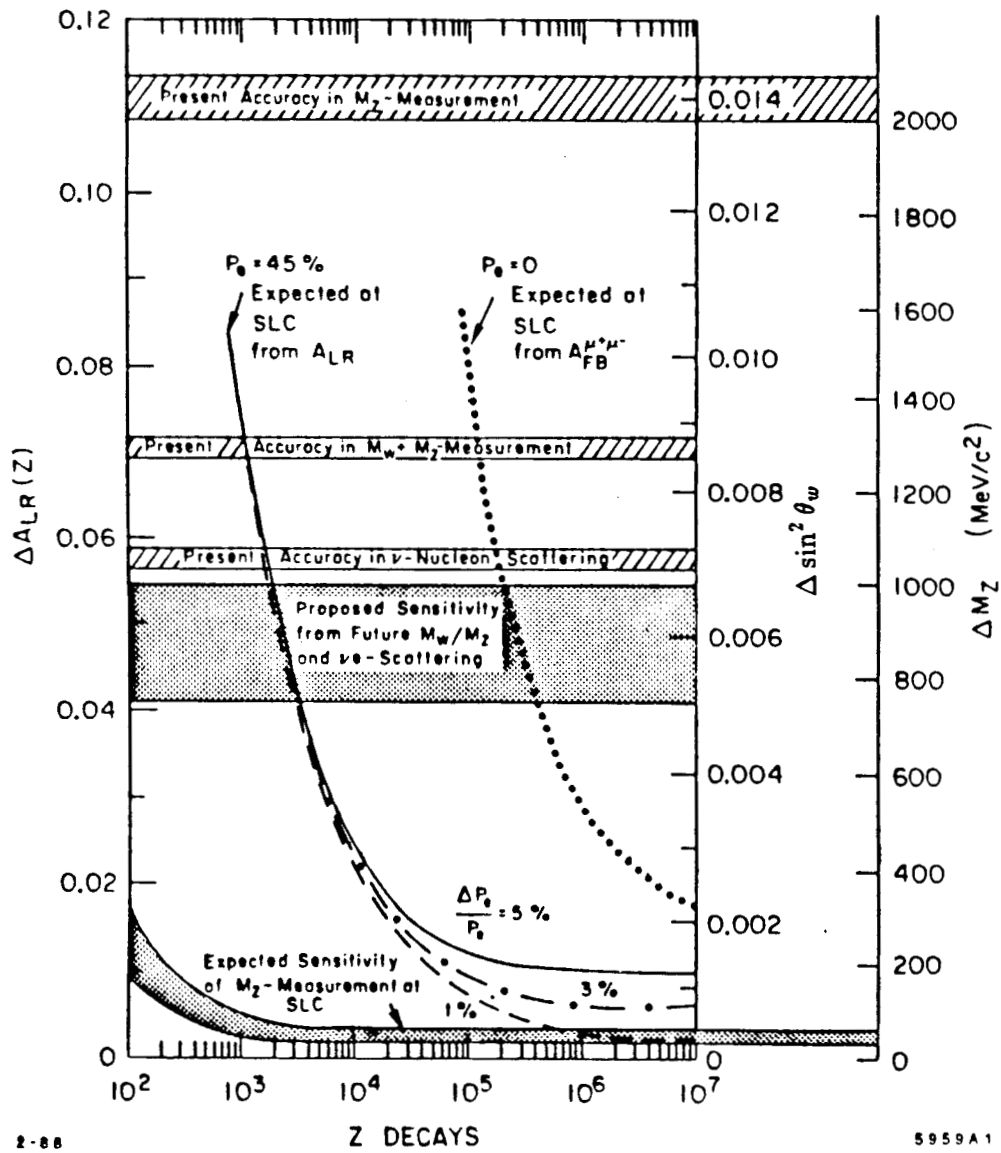
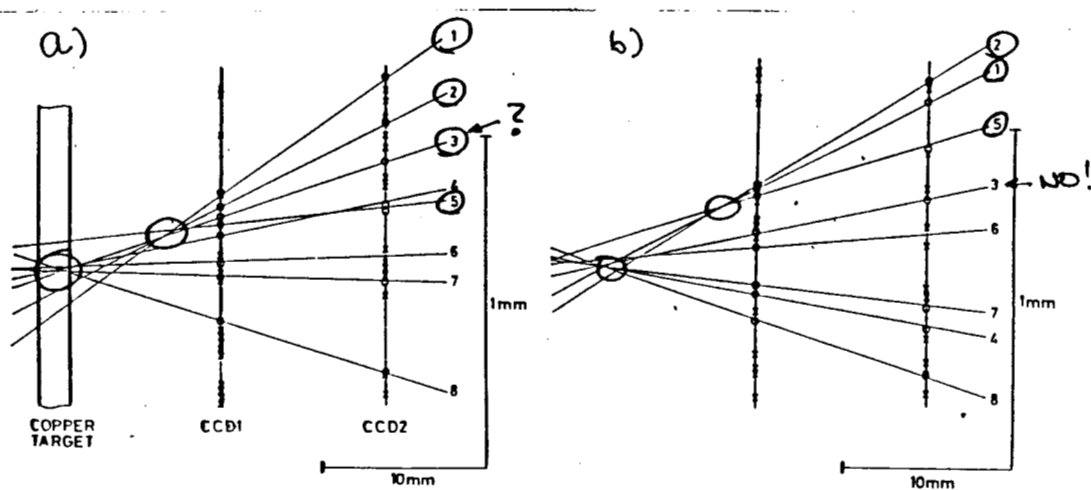
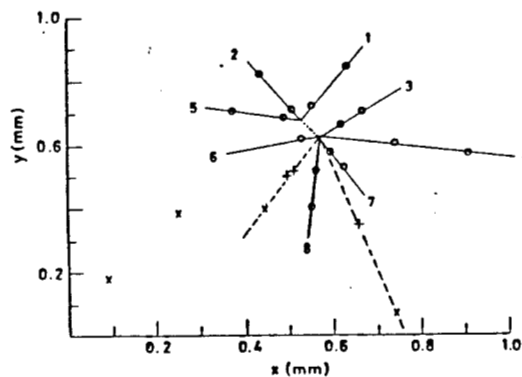


Figure 11. Precision of the test of the standard model as a function of the size of the Z decay sample with and without polarization of the incident electrons.



3 dimensional points are important for clean vertex I.D



c) Beams eye view of one square millimeter!!

Figure 12. A typical event in a two plane CCD vertex detector in experiment NA32 at CERN. a) side view. b) top view. c) beams eye view of one square millimeter.

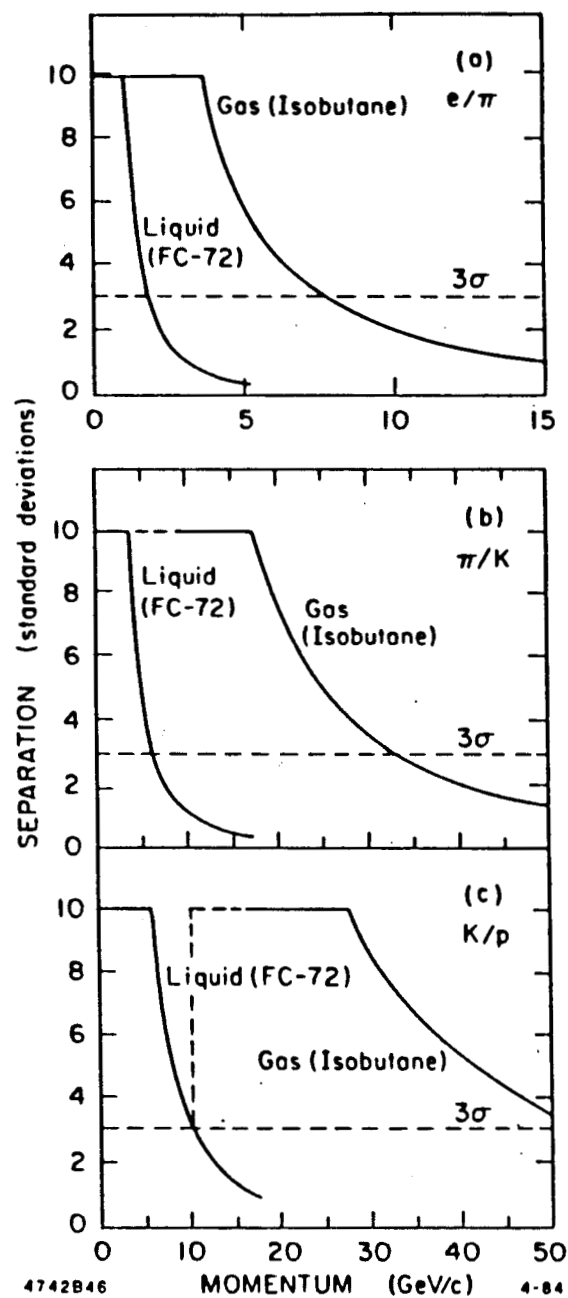


Figure 13. Particle separation capability of the SLD CRID detector as a function of the particle momentum. a) $e - \pi$ separation. b) π -K separation. c) K-P separation.

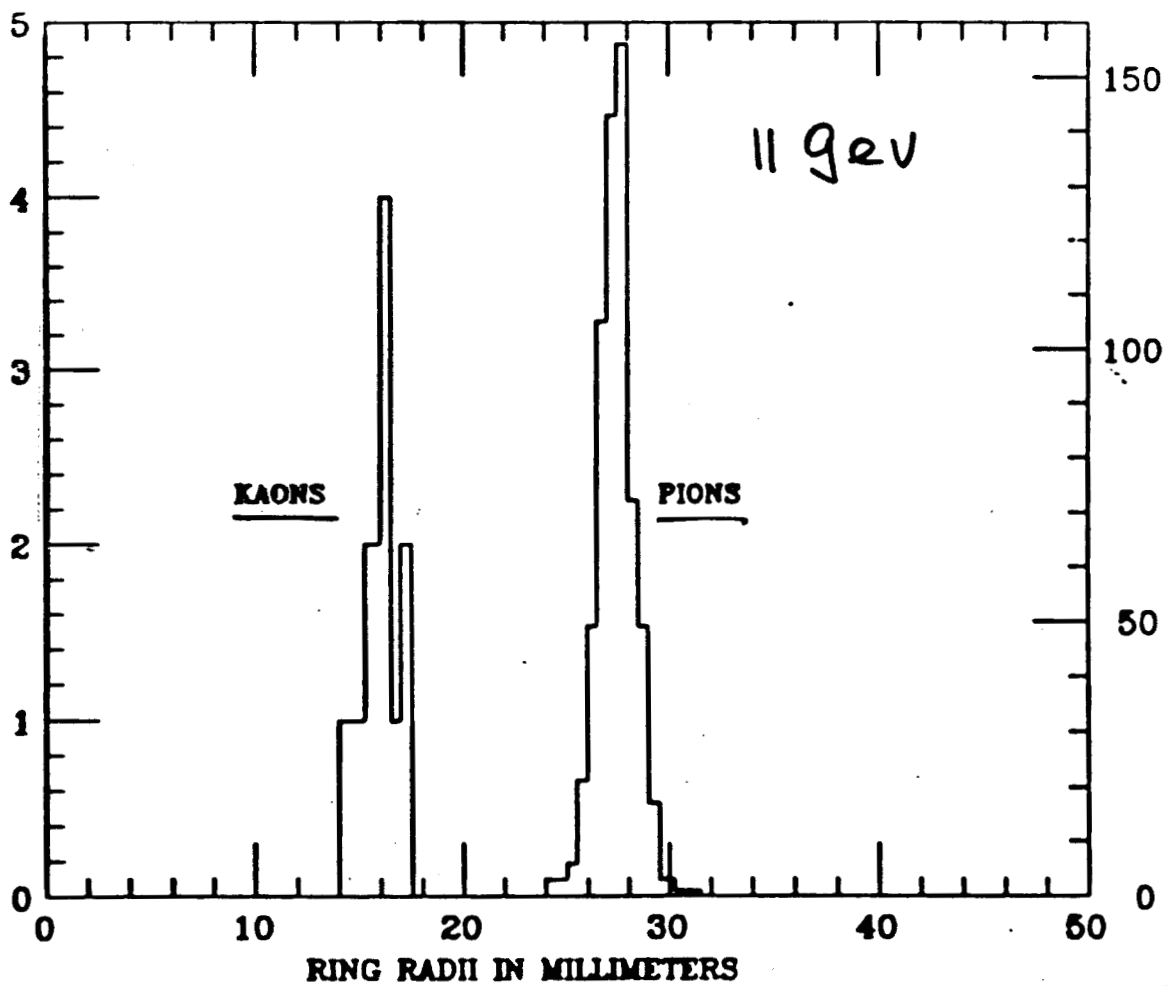


Figure 14. Separation of kaons and pions at 11 GeV/c in a prototype of the SLD CRID detector.

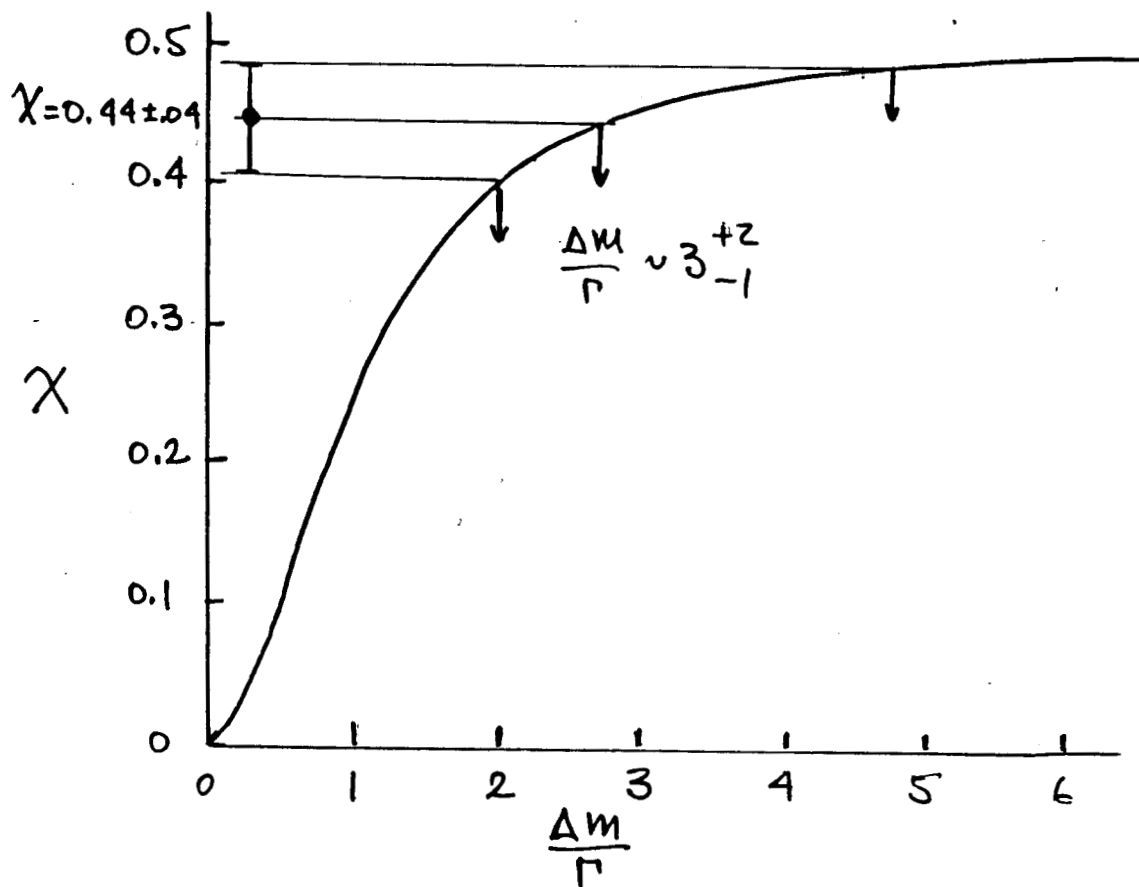


Figure 15. Dependence of the mixing parameter X on the parameter $\Delta m/\Gamma$.

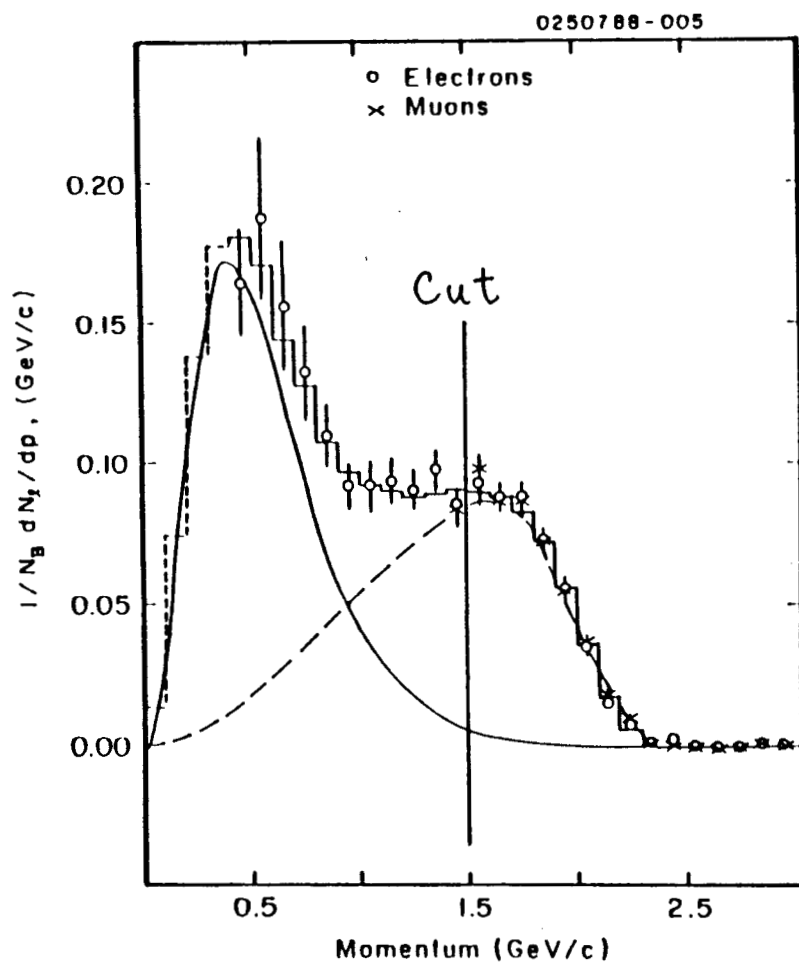


Figure 16. Momentum distribution of the electrons and muons from the semileptonic decays of D mesons (solid curve) and B mesons (dashed curve) in the CLEO detector.

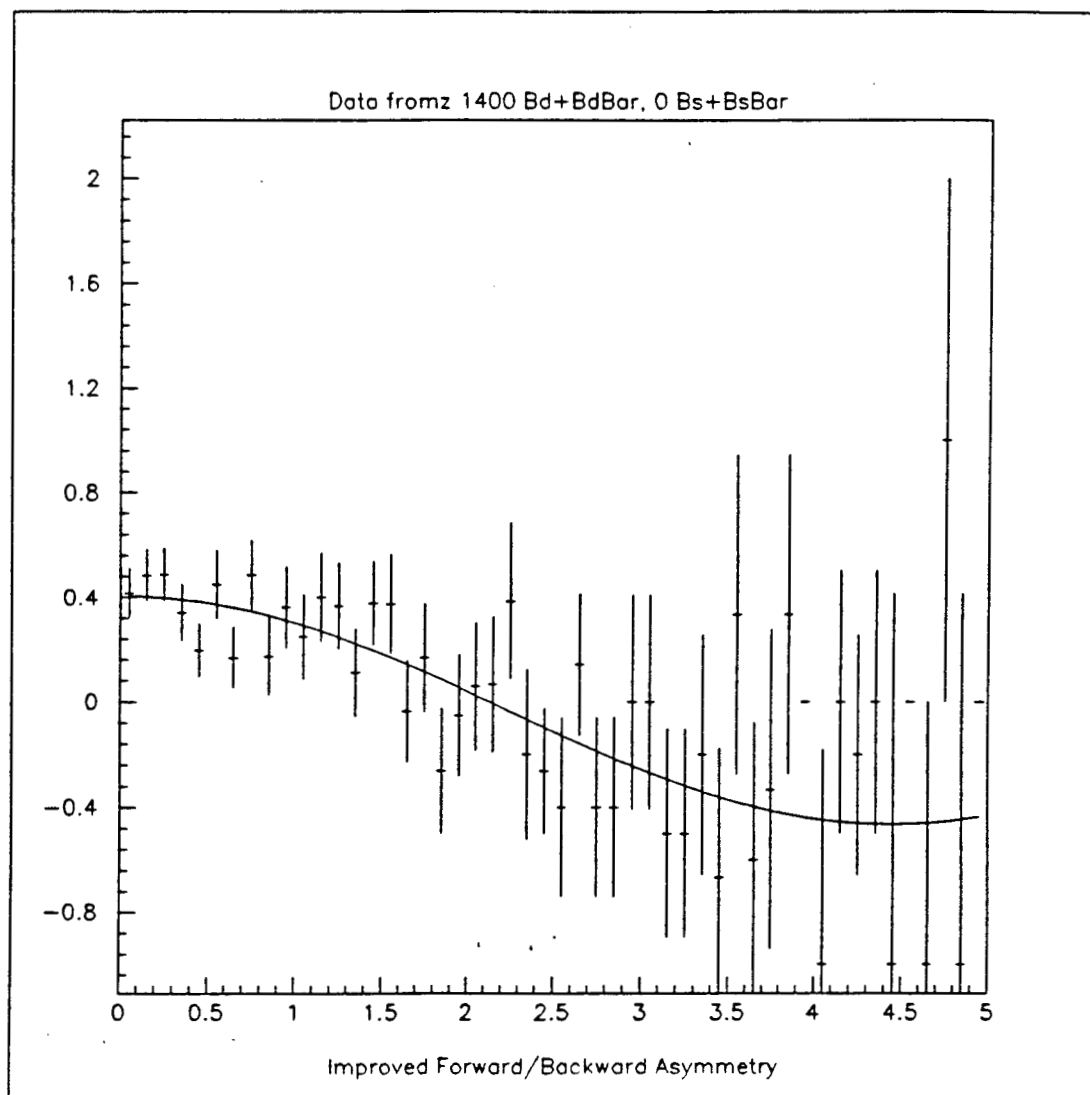


Figure 17. The forward-backward asymmetry A_{FB} as a function of proper decay time for a sample of 1400 B_d^0 and \bar{B}_d^0 decays with $(\Delta m/\Gamma)B_d = 0.7$.

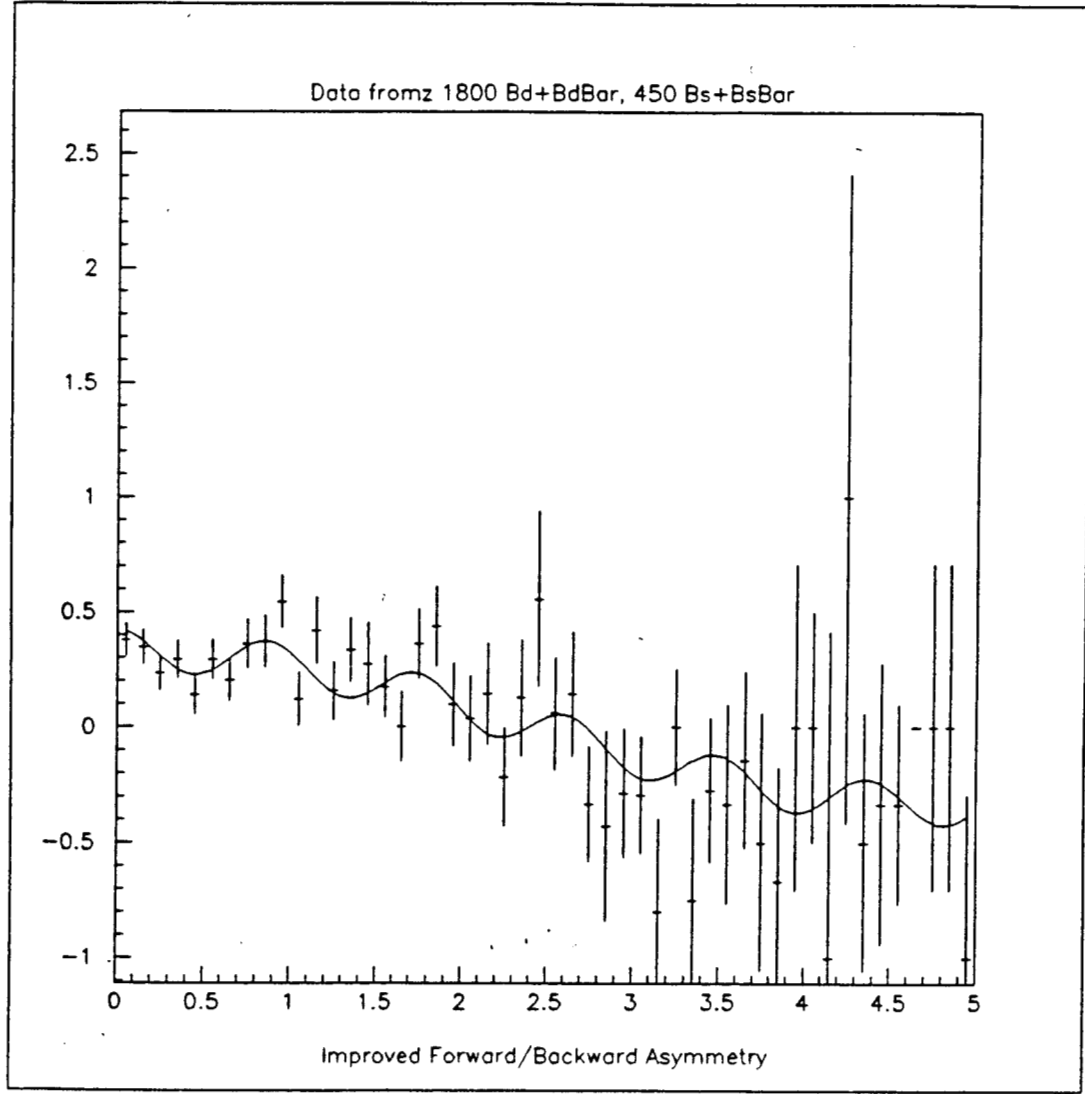


Figure 18. The forward-backward asymmetry A_{FB} as a function of proper decay time for a sample of 1800 ($B_d^0 + \bar{B}_d^0$) and 450 ($B_s^0 + \bar{B}_s^0$) decays with $(\Delta m/\Gamma)B_d = 0.7$ and $(\Delta m/\Gamma)B_s = 7.0$.

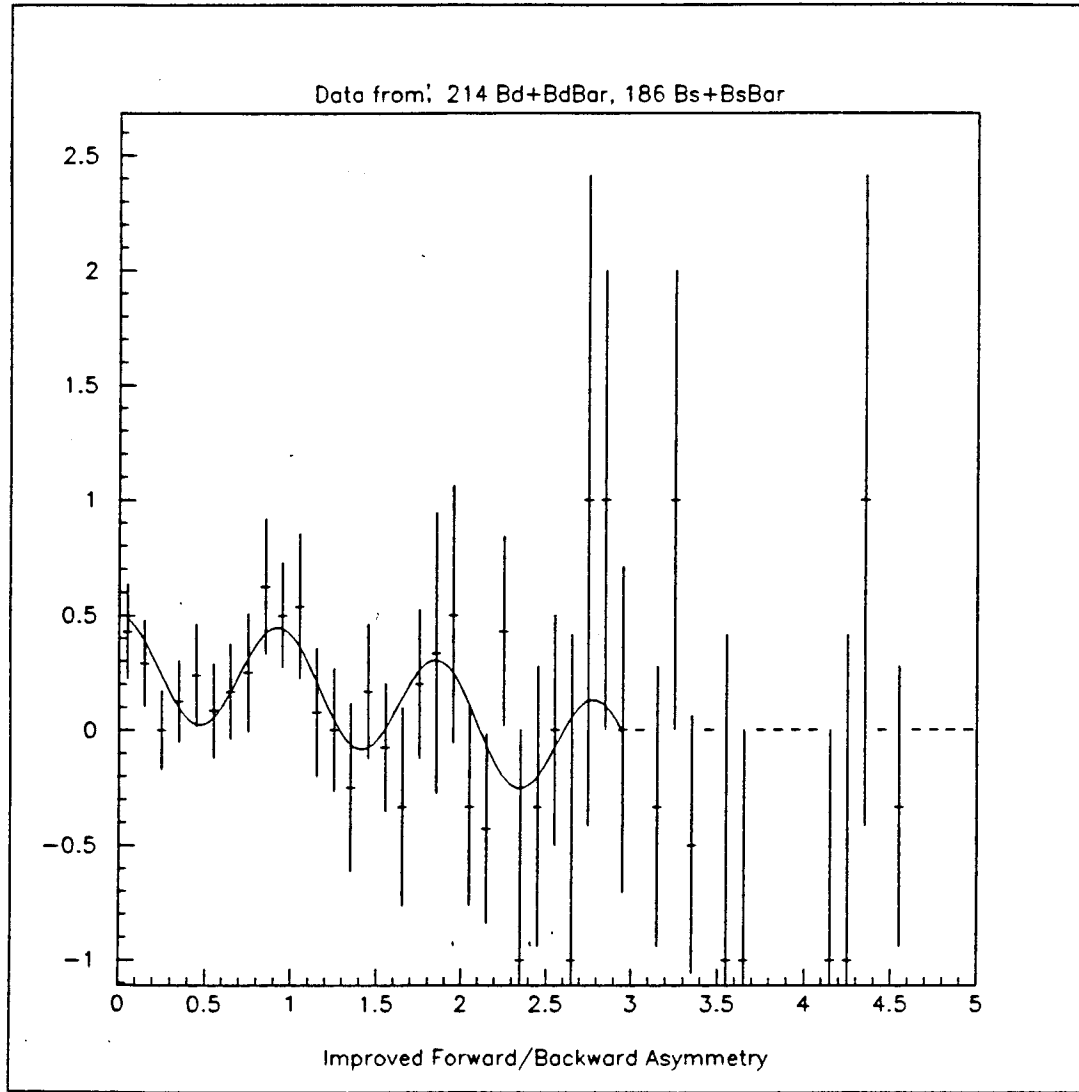


Figure 19. The forward-backward asymmetry A_{FB} as a function of proper decay time for a sample of 214 ($B_d^0 + \bar{B}_d^0$) and 186 ($B_s^0 + \bar{B}_s^0$) decays with $(\Delta m/\Gamma)B_d = 0.7$ and $(\Delta m/\Gamma)B_s = 7.0$.

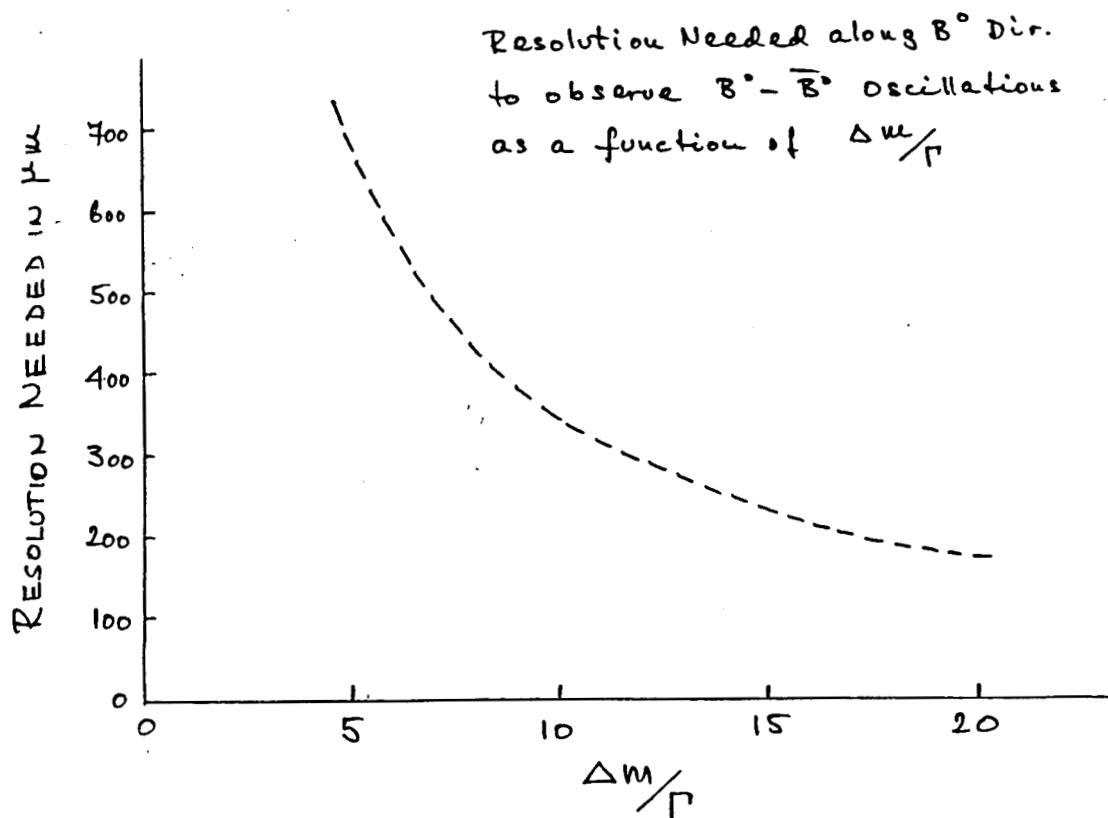


Figure 20. Resolution needed in the B^0 decay length to observe $B^0 - \bar{B}^0$ oscillations as a function of $\Delta m/\Gamma$.

The Electroweak Parameters at the Z^0

T. Hansl-Kozanecka

1. Introduction.

This note is organized as follows. In section 2 we recollect some basic formulas for electroweak parameters. In the subsequent sections we discuss the measurements of electroweak parameters in three groups:

- Measurement of the mass of the Z^0 ;
- Measurements of the type $(v^2 + a^2)$: cross section, partial widths and total width. Lifetime measurements, which also belong in this category, will not be discussed.
- Measurements of the type $va/(v^2 + a^2)$; these are the various asymmetry measurements and the τ -polarization. These are in fact measurements of the ratio v/a and could be combined with the $(v^2 + a^2)$ measurements to extract v and a , the vector and axial vector couplings, separately.

Throughout this paper we will restrict ourselves to the standard model with five flavours, assuming $m_t > M_Z/2$. The accuracy of the different measurements will be summarized in the final Table 12.

2. The electroweak parameters

The standard model of the electroweak interactions [1] is a gauge theory based on the Group $SU(2)_L \times U(1)$. Its interaction Lagrangian

$$L(g_0, g'_0, v_0, \lambda_0, g_f^0) \tag{2.1}$$

is a function of g_0 and g'_0 , the coupling constants associated with $SU(2)$ and $U(1)$, respectively; v_0 is related to the vacuum expectation value of the Higgs field, which gives rise to mass terms for three out of the four $SU(2) \times U(1)$ gauge fields.

$$M_W^0 = \frac{1}{2}g_0 v_0, \quad M_Z^0 = \frac{1}{2}\sqrt{g_0^2 + g_0'^2} v_0.$$

$$\frac{M_W^0}{M_Z^0} = \frac{g_0}{\sqrt{g_0^2 + g_0'^2}} = \cos\Theta_0 \equiv c_0, \quad (s_0^2 = 1 - c_0^2).$$

The unification condition

$$e_0 = g_0 s_0 = g'_0 c_0 \quad (s_0 = \sin\theta_W^0)$$

relates the electric charge e_0 to the $SU(2)$ coupling and the weak mixing angle. In the case

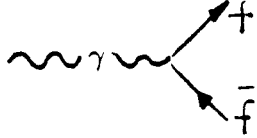
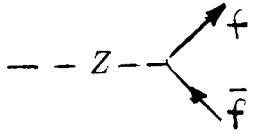
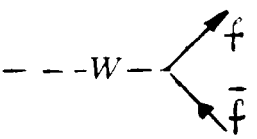
of Higgs doublets, the ρ parameter, typifying the strength of the neutral current interactions relative to the charged current, is unity:

$$\rho_0 = \frac{M_W^{\circ 2}}{M_Z^{\circ 2} c_0^2} = 1.$$

By comparing with the Fermi theory of the muon decay one has

$$\frac{G_\mu^0}{\sqrt{2}} = \frac{g_0^2}{8M_W^{\circ 2}} = \frac{e_0^2}{8M_W^{\circ 2} s_0^2} = \frac{1}{2v_0^2}.$$

The index "0" indicates the bare parameters of the processes:

	e_0
	$M_Z^{\circ}, \quad \frac{g_0}{c_0} \gamma^\mu \frac{1}{2} (c_V^f - c_A^f \gamma^5)$ $c_V^f = I_3^f - 2Q^f s_0^2, \quad c_A^f = I_3^f$
	$M_W^{\circ}, \quad -i \frac{g_0}{\sqrt{2}} \gamma^\mu \frac{1}{2} (1 - \gamma^5), \quad G_\mu^0$

The Lagrangian (2.1) has three fundamental parameters g_0 , g_0' and v_0 . There are many more parameters, like the fermion masses $m_f = g_f^0 \cdot v_0$ and the elements of the Kobayashi–Maskawa matrix. These are the subject of other studies in these proceedings.

The three parameters g , g' and v cannot be measured directly, nor are the bare quantities directly accessible to experiment. The experiments measure the renormalized physical quantities: the electron charge e (from Thomson scattering), the Fermi constant G_μ (from muon decay), the masses of the intermediate vector bosons M_W (at $\bar{p}p$ colliders or LEP2) and M_Z (at SLC/LEP), and the weak mixing angle θ_W from $\nu(\bar{\nu})$ scattering experiments and asymmetries:

$$e_0 = e + \delta e, \quad M_W^{\circ} = M_W + \delta M_W, \quad M_Z^{\circ} = M_Z + \delta M_Z,$$

$$G_\mu^0 = G_\mu + \delta G_\mu, \quad s_0^2 = s_W^2 + \delta s_W^2.$$

For the measured quantities the bare relations are modified [8],

$$\begin{aligned} \frac{G_\mu}{\sqrt{2}} &= \frac{1}{2v^2}(1 + \Delta r) \quad \Delta r = \Delta r(\epsilon, G_\mu, M_Z, m_t, m_H, \dots), \\ M_W^2 &= \frac{\pi\alpha}{\sqrt{2}G_\mu \sin^2\theta_W} \times \frac{1}{1 - \Delta r}, \\ \sin^2\theta_W \cos^2\theta_W &= \frac{\pi\alpha}{\sqrt{2}G_\mu M_Z^2} \times \frac{1}{1 - \Delta r}. \end{aligned} \quad (2.2)$$

To calculate the physical quantities, contributions of the type shown in Fig. 1 have to

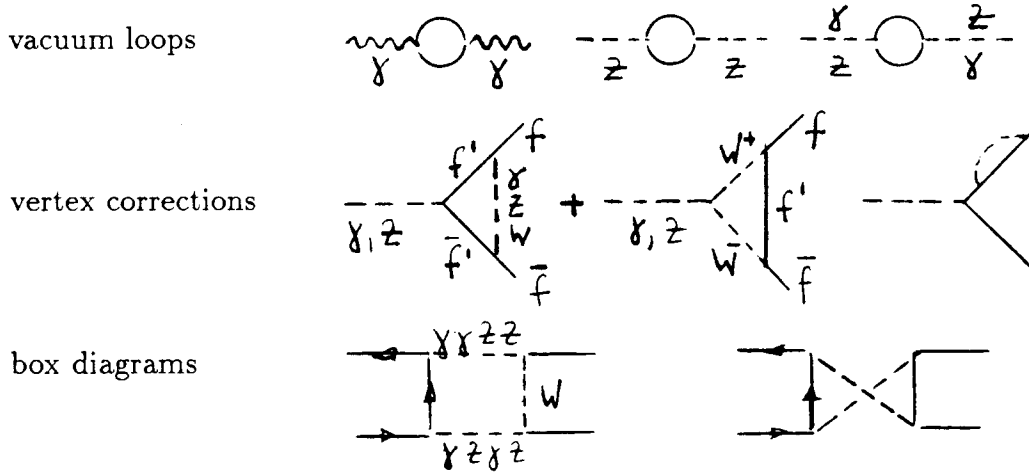


Figure 1. Electroweak radiative corrections to $e^+e^- \rightarrow f\bar{f}$

be taken into account. The contributions from vacuum loops and vertex corrections are most important, contributions from box diagrams involving weak bosons have been shown to be very small [9]. Vertex and box diagrams involve virtual W^\pm , Z and Higgs bosons. Corrections due to the vacuum loops (gauge boson self energy) are often referred to as “oblique” corrections. They are responsible for the large shifts in W and Z masses. To these loop diagrams contribute any particles coupled to the vector bosons. Results become dependent on other parameters like top-quark mass m_t and Higgs mass m_H .

G_μ and $\alpha = e^2/4\pi$ are the most accurately measured electroweak constants. SLC/LEP will soon measure M_Z to 4 significant digits. The appropriate choice of parameters at SLC/LEP is therefore (α, G_μ, M_Z) . These can be taken to define the theory. Then $\sin^2\theta_W$ and M_W can be predicted in terms of α, G_μ , and M_Z , eqns. (2.2). The precise measurement of $\sin^2\theta_W$ or M_W then becomes a test of the standard model and a measurement of the two main unknown parameters, m_t and m_H .

There exist other choices of parameters, for example the choice (e_0, G_μ^0, s_0^2) , which is suitable for low energy processes [10]. The so-called “starred scheme” fixes s_0^2 by M_Z^2 [9]. A generally accepted scheme is the on-shell renormalization scheme based on the boson masses M_W, M_Z together with the electromagnetic fine-structure constant α [11]. The

different schemes should predict the same values for physical quantities. In practice the results differ because the calculations are not carried out to all orders. A large effort has been made in recent years to reach the theoretical accuracy that will be comparable with the expected experimental accuracy at SLC/LEP [3– 7].

We return now to eqns. (2.2). If one replaces α and G_μ by their running values, $\alpha(M_Z^2)$, $G_\mu(M_Z^2)$, since all values are now evaluated at the same scale, the bulk of the radiative effects is accounted for [12, 9]. G_μ is approximately independent of the scale, $G_\mu(M_Z^2) \approx G_\mu(0)$, such that the main effect is due to $\Delta\alpha = \alpha(M_Z^2) - \alpha(0)$.

The contributions to $\Delta\alpha$ from the photon vacuum polarization can be computed exactly in the case of lepton loops. The contribution from light quarks was evaluated through dispersion relations that are integrals of the measured total cross section of $e^+e^- \rightarrow \text{hadrons}$ [13],

$$\begin{aligned}\Delta\alpha_{udscb}(s=M_Z^2) &= 0.0288 \pm 0.0009, \\ \Delta\alpha_{udscb+e\mu\tau}(s=M_Z^2) &= 0.0602 \pm 0.0009.\end{aligned}\tag{2.3}$$

The error in $\Delta\alpha$ corresponds to an uncertainty in the prediction of $\sin^2\theta_W$ of

$$\delta^{(\alpha)} s_W^2 \approx 0.3 \delta\Delta\alpha \approx \pm 0.0003$$

and will ultimately limit the high-precision measurements. Having absorbed the large effects in $\alpha(M_Z^2)$, the dependence on masses $m \geq M_Z$ becomes more explicit,

$$s_W^2 c_W^2 = \frac{\pi\alpha(M_Z^2)}{\sqrt{2}G_\mu M_Z^2} \cdot \frac{1}{1 - \Delta r_{(2)}}, \quad \alpha(M_Z^2) = \frac{1}{127.6}.$$

The remaining $\Delta r_{(2)} = -\frac{c_W^2}{s_W^2} \Delta\rho$ contains the dependence on the top mass and the Higgs mass [11]

$$\begin{aligned}\Delta r_{(2)}^{top} &= -\frac{c_W^2}{s_W^2} \cdot \frac{\alpha}{4\pi} \frac{3}{4s_W^2 c_W^2} \left(\frac{m_t}{M_Z}\right)^2 \approx -0.0088 \times \left(\frac{m_t}{M_Z}\right)^2, \\ \Delta r_{(2)}^{Higgs} &= -\frac{c_W^2}{s_W^2} \cdot \frac{\alpha}{4\pi} \frac{3}{4c_W^2} \ln\left(\frac{m_H}{M_W}\right)^2 \approx 0.0023 \times \ln\left(\frac{m_H}{M_W}\right)^2.\end{aligned}\tag{2.4}$$

Δr is quite sensitive to m_t but rather insensitive to m_H . Indeed, the variation of Δr with m_t is quadratic while its dependence on m_H is only logarithmic.

The amplitude for Z^0 exchange expressed in bare quantities (tree level) is

$$\frac{\sqrt{2}G_\mu^0 M_Z^0{}^2}{D(s)} \rho_0 (J_3^i - s_0^2 J_{em}^i) (J_3^f - s_0^2 J_{em}^f),$$

where i = initial, f = final fermion and $D(s) = s - M_Z^2 - iM_Z\Gamma_Z$. The effect of electroweak

radiative corrections can be absorbed in “effective parameters”,

$$\rho_0 \longrightarrow \rho = \rho_0(1 + \delta\rho),$$

$$s_0^2 \longrightarrow \sin^2\theta_{eff} = ks_0^2,$$

which are in general process-dependent and different for initial and final states,

$$\frac{\sqrt{2}G_\mu^0 M_Z^{\circ 2}}{D(s)} \rho (J_3^i - k_i s_0^2 J_{em}^i) (J_3^f - k_f s_0^2 J_{em}^f),$$

$$\rho = \frac{M_W^2}{M_Z^2 c_W^2} = \rho_0(1 + \delta\rho)$$

$$\rho_{\nu e} = \rho_0(1 + \delta\rho_{\nu e}), \quad \rho_{\nu q} = \rho_0(1 + \delta\rho_{\nu q}), \dots$$

$$k_i = 1 + \delta k_i, \quad k_f = 1 + \delta k_f.$$

$\delta\rho, \delta\rho_{\nu e}, \dots, \delta k_i, \delta k_f$ can be computed given $\alpha, G_\mu, M_Z, m_t, m_H$.

Longitudinally polarized beams are the unique tool to isolate the initial state couplings from the final state couplings. This will be exploited in more detail in section 3.

The electroweak mixing angle θ_W is no longer a free parameter of the theory. Sirlin [14] has introduced the convention of defining $\sin^2\theta_W$ in terms of the measured W and Z boson masses,

$$\sin^2\theta_W^{(Sirlin)} = 1 - \frac{M_W^2}{M_Z^2}, \quad (2.5)$$

which is equivalent to $\delta\rho \equiv 0$. $\sin^2\theta_W^{(Sirlin)}$ has a different value and different functional dependence on, for example the top mass, than $\sin^2\theta_{eff}$, where the latter is determined from the measurement of the asymmetries or the partial decay width of a decay channel $Z \rightarrow \bar{f}f$.

Two examples may illustrate the above discussion.

Example 1: The Mark II Collaboration has recently published the first high accuracy measurement at an e^+e^- collider of the mass of the Z^0 boson [15],

$$M_Z = 91.17 \pm 0.18 \text{ GeV}/c^2.$$

This measurement corresponds to a range of $\sin^2\theta_W$ values. The $\sin^2\theta_W^{(Sirlin)}$ is shown in Fig. 2 as function of the top mass and for two values of the Higgs mass. A value of $\sin^2\theta_W$ can only be extracted, when also m_t and m_H are specified:

$$\sin^2\theta_W^{(Sirlin)} = 0.2307 \pm 0.0013 \quad \text{for } m_t = 100 \text{ GeV}/c^2, \\ m_H = 100 \text{ GeV}/c^2.$$

Example 2: The partial width for $Z \rightarrow \bar{f}f$ shows an increase with increasing top mass due to the quadratic top mass term in (2.4). An exception is the $Z \rightarrow \bar{b}b$ decay. The

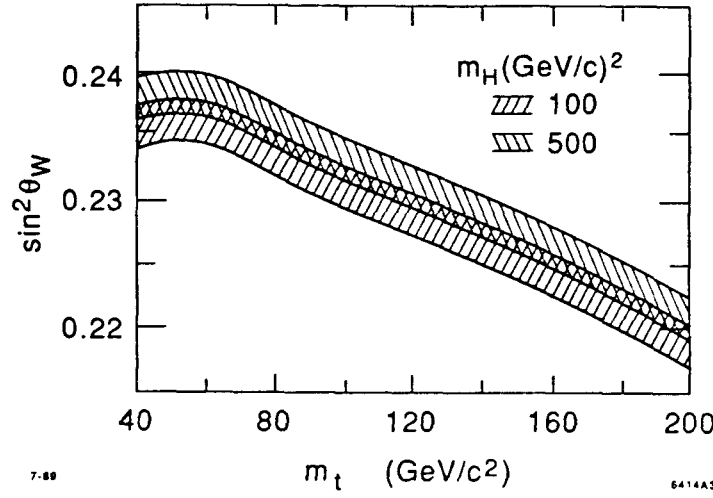


Figure 2. Value of $\sin^2 \theta_W^{\text{Sirlin}}$ as function of the top mass, for Higgs masses of 100 and 500 GeV. The width of each band represents the uncertainty in $\sin^2 \theta_W$ corresponding to the uncertainty in M_Z [14] (curves from Expostar).

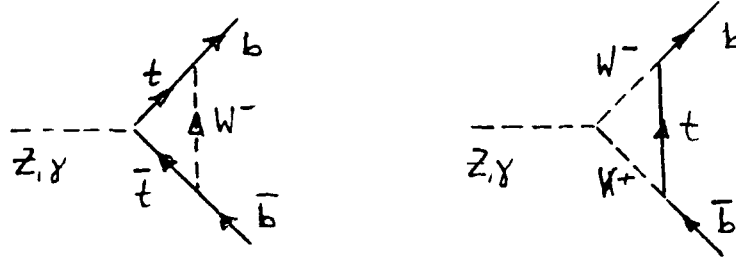


Figure 3. Corrections for the $Z \rightarrow \bar{b}b$ vertex.

reason for this is the additional top dependence of the vertex corrections in $Z \rightarrow \bar{b}b$ [15], see Fig. 3. This vertex contribution cancels partly the top contribution from the vacuum loop. As a consequence the partial width $Z \rightarrow \bar{b}b$ is constant within 2 MeV in the whole top mass range up to 250 GeV, Fig. 4. For non- b decay channels $Z \rightarrow \bar{f}f$, $f \neq b$, the vertex contributions are practically independent of m_t and no cancellation of the vacuum loops occurs. A parametrization of the effective couplings is given in [16], which is instructive for the rôle of $\sin^2 \theta_{\text{eff}}$,

$$G_\mu \longrightarrow G_\mu(1 + \delta\rho_t), \quad \delta\rho_t = \frac{3\sqrt{2}G_\mu}{(4\pi)^2} m_t^2$$

$$\sin^2 \theta_{\text{eff}} = \sin^2 \theta_W + \cos^2 \theta_W \delta\rho_t + \frac{\alpha}{4\pi} \left[\ln\left(\frac{m_H}{17.3}\right) + 1 \right] - 2$$

$$c_V^f = I_3^f - 2Q_f \sin^2 \theta_{\text{eff}} + \delta b \frac{1}{3} \delta\rho_t$$

$$c_A^f = I_3^f + \delta b \frac{1}{3} \delta\rho_t$$
(2.6)

($\delta b = 1$ for b quarks, $= 0$ otherwise). In general one can expect the corrections entering via

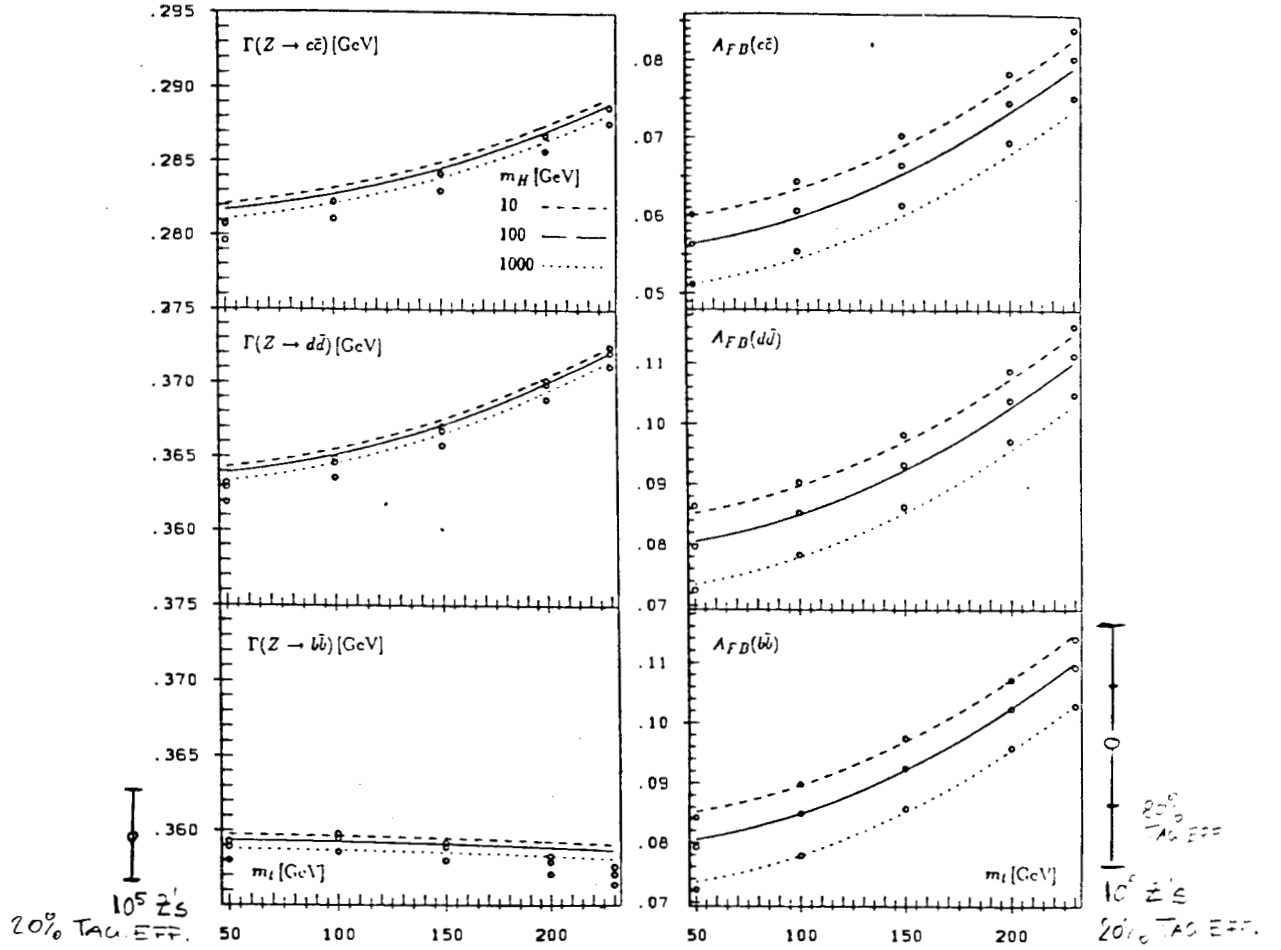


Figure 4. The dependence of the partial widths Γ_f and the forward-backward asymmetries on the top and Higgs masses. The measurement accuracy expected for a tagging efficiency of 20% for b-quarks is indicated also. Curves: approximate equations [16], see text; points: full one-loop calculation from [15];

the Z-Z and the Z- γ propagators to be identical for different decay channels $Z \rightarrow \bar{f}f$, whereas the vertex and quark self-energy diagrams yield different corrections.

3. Measurement of the Mass and Width of the Z boson.

One of the basic measurements at the e^+e^- colliders SLC/LEP is the determination of the Z^0 resonance. This provides two of the important electroweak parameters: the mass and the width of the neutral vector boson. The mass is one of the basic parameters for the prediction of electroweak physical quantities as was discussed in the previous section. The width is related to the fundamental question of the number of generations. Being a prediction of the standard model after the Z mass is known, the width serves as a test of the theory. The partial widths for $Z \rightarrow \bar{f}f$ will allow the investigation of the weak coupling constants of the various fermions. Because of its importance, detailed studies have been

made of the line shape. The theoretical predictions are accurate to 10 MeV in the shape (position and width of the peak); the absolute scale is determined within 0.3% [18].

We discuss first the line shape measurement and the measurement errors and turn then to the theoretical predictions and the QED and QCD corrections. The effect of electroweak corrections, which were already explained in the introduction, will be summarized for the special case of mass and width measurements.

3.1. SCANNING STRATEGY AND MEASUREMENT ERRORS

The mass and width will be measured using all visible final states $Z \rightarrow \bar{f}f$, except electrons ($f \neq e$). Analytic formulas exist that describe the Z^0 -line shape in terms of the three shape parameters position, width and height (M_Z , Γ_Z , Γ_{inv} or number of neutrinos).

$$\sigma(\sqrt{s}) = \frac{12\pi}{M_Z^2} \frac{s\Gamma_e(\Gamma_Z - \Gamma_{inv})}{(s - M_Z^2)^2 + (s\Gamma/M_Z)^2} (1 + \delta(s)), \quad (3.1)$$

$$\Gamma_Z = \Gamma_q + (\Gamma_\mu + \Gamma_\tau + \Gamma_e) + \Gamma_{inv}.$$

More details of the presentation of $\sigma(\sqrt{s})$ and the radiative corrections $(1 + \delta(s))$ will be discussed below.

The Mark II group has developed a scanning strategy that chooses the scan points in energy steps around the (approximately known) position of the Z^0 peak such that the errors of the parameters and their correlations are minimal [19]. These conditions are satisfied if the scan points are chosen at the points of maximum sensitivity. Fig. 5 shows the points and the sensitivity of the cross section for the three parameters. The positions of optimum sensitivity to M_Z are at -0.8 and $+1$ GeV; to measure the width, the optimum scan positions should be chosen at ± 2 GeV; Γ_{inv} depends directly on the absolute normalization and all information comes from a scan point close to the peak.

This method allows a direct estimate of the errors. For a five-point scan with spacing of ~ 750 MeV and luminosity $L_m \propto \sigma^{\frac{1}{2}}(E_m)$ the errors are [19]

$$\delta M_Z = \frac{2}{\sqrt{N}} \text{ GeV},$$

$$\delta \Gamma_Z = \frac{6}{\sqrt{N}} \text{ GeV},$$

$$\delta \Gamma_{inv} = \frac{2.1}{\sqrt{N}} \text{ GeV}.$$

N is the number of visible Z^0 events collected at the scan points; the number of equivalent Z^0 events produced at the peak with the same luminosity is about 15% higher. With 2500 visible Z^0 events the mass can be determined to 40 MeV and with 30 k events the width will be determined to 35 MeV. The measurements will not be limited by statistics but by the systematic errors, especially the accuracy with which the beam energy can be determined, Table 1.

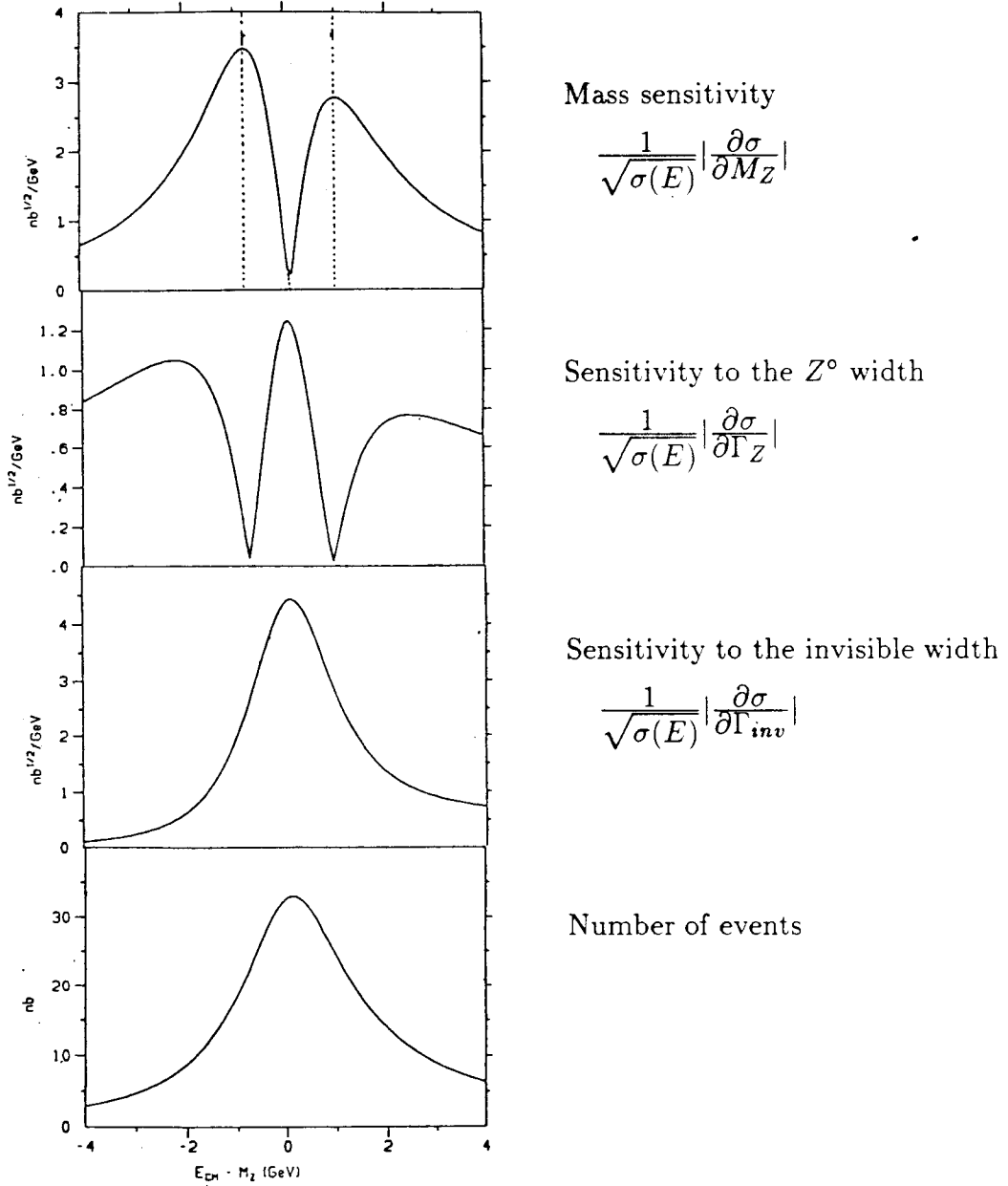


Figure 5. The sensitivity of the cross section (3.1) to the Z^0 mass, Z^0 width and the partial width Γ_{inv} of the invisible (neutrino) cross section.

Systematic errors

The experimental accuracy in the determination of the line shape is limited by uncertainties on the collider energy scale and the normalization of the cross section measurement.

Beam energy measurement.

The determination of weak parameters requires absolute and relative measurements of the center-of-mass energy to high precision over long periods of time. Spectrometers have been installed in both the electron and positron extraction lines of the SLC. The method

Table 1
Systematic errors of the beam energy measurement at SLC [21, 15]

Source of error	Size of error (MeV)
Magnetic measurement	5
Detector resolution	10
Magnet rotation	16
Survey	5
Total (per beam)	20

of measurement is to observe indirectly the deflection of charged beams via the narrow beams of synchrotron radiation they emit [20]. The systematic errors in each beam energy measurement are 20 MeV. Including an allowance for offset beams and a finite dispersion the absolute error on E_{cm} is 40 MeV, the relative error relevant for the line-shape measurement is 35 MeV [21]. The energy spread within each beam is at present about $\pm 0.3\%$ [15].

The polarization facility at SLC [22] will eventually give a complementary measurement of the electron beam energy with comparable or slightly better accuracy. This provides an important systematic check [23].

Normalization.

The cross section normalizations are dominated by the systematic uncertainties on the luminosity measurement. For the line-shape scan of the Z only the relative luminosity between different energy points is of importance.

Table 2
Energy resolution and readout geometry of the SLD Luminosity monitors

calorimeter (absorber)	$\sigma(E)\sqrt{E}$ (%)	depth x_{rad} or Λ_{abs}	tower size	$\sigma(pos)$ (e.m. only)	coverage (mrad)
LMSAT e.m. (3.5 mm tungsten)	18	$(6 + 17)x_{rad}$	$1 \times 1 \text{ cm}^2$ $\Delta\vartheta \sim 6 \text{ mrad}$	$0.6 \text{ mrad}/\sqrt{\frac{46.5}{E}}$	28 to 65
MASC e.m. (7 mm tungsten)	18	$(6 + 17)x_{rad}$	$1 \times 1 \text{ cm}^2$ $\Delta\vartheta \sim 30 \text{ mrad}$	$2.8 \text{ mrad}/\sqrt{\frac{46.5}{E}}$	65 to 190

The parameters of the SLD luminosity monitors are summarized in Table 2 [24]. At small angles, the differential cross section for Bhabha scattering is given to a very good

approximation by

$$\frac{d\sigma}{d\vartheta} = \frac{k}{\vartheta^3}, \quad (3.2)$$

$$k = \frac{32\pi\alpha^2}{s} = 0.251 \left(\frac{45.5}{E_{beam}} \right)^2 nb \quad (E_{beam} \text{ in GeV}).$$

The Bhabha rate recorded in the SLD luminosity monitor (LMSAT + MASC), is ~ 4 times the peak rate of visible Z 's. The statistical error of the Bhabha rate is therefore small compared to the statistical error of the event rate.

Systematic errors of the luminosity measurement are of three sources:

- The differential cross section predicted by theory: The cross section for Bhabha scattering has been computed to $\mathcal{O}(\alpha^3)$ [25]. Several Monte Carlo programs exist for small angle Bhabha scattering and agree in their results [26]. Electroweak effects are small ($\leq 0.2\%$).
- The detector acceptance : The fiducial volume has to be well understood in terms of angular resolution, positioning accuracy of the detector and monitoring of the beam position. The small size of the interaction point ($\sigma_{x,y} = 1.8 \mu m$) and short bunch length ($\sigma_z = 0.4 mm$) make monitoring of the Bhabha rate easier at SLC than LEP.
- The counting rate: Because of the steep dependence on the polar angle, trigger conditions and reconstruction efficiency have to be understood very well. A detailed study has still to be done.

3.2. THE Z^0 LINE-SHAPE

At lowest order, the partial width of a Z decaying into a fermion pair is given by [27]

$$\Gamma_{Z \rightarrow \bar{f}f}^0 = \frac{\alpha}{3} \frac{N_c^f M_Z}{4s_W^2 c_W^2} \sqrt{(1 - 4\mu_f)} \left[(c_V^f)^2 (1 + 2\mu_f) + (c_A^f)^2 (1 - 4\mu_f) \right],$$

$$\text{with } \mu_f = \frac{m_f^2}{M_Z^2}, \quad N_c^f = \text{colour factor } (= 3 \text{ for } q, = 1 \text{ for leptons}).$$

It can also be expressed as (replacing α)

$$\bar{\Gamma}_{Z \rightarrow \bar{f}f}^0 = N_c^f \frac{G_\mu M_Z^3}{96\pi\sqrt{2}} \sqrt{(1 - 4\mu_f)} \left[(c_V^f)^2 (1 + 2\mu_f) + (c_A^f)^2 (1 - 4\mu_f) \right]. \quad (3.3)$$

$\bar{\Gamma}_{Z \rightarrow \bar{f}f}^0$ turns out to be a sufficiently good approximation, at least for $m_t < 150 GeV$, including already the major part of the weak one-loop correction [27].

The total width is given by

$$\Gamma_Z^0 = \sum_f \Gamma_{Z \rightarrow f\bar{f}}^0.$$

In the massless fermion case the partial width reduces to

$$\Gamma_{Z \rightarrow f\bar{f}}^0 = \Gamma_f^- + \Gamma_f^+ = \frac{\alpha}{3} \frac{N_c^f M_Z}{4s_W^2 c_W^2} \left[(c_V^f - c_A^f)^2 + (c_V^f + c_A^f)^2 \right];$$

the $-$, $+$ sign refers to the helicity of f , the helicity of \bar{f} being opposite. The total cross section in terms of the Z^0 width and the partial widths can be written [18]

$$\sigma_0(s) = \frac{s N_c^f}{(s - M_Z^2)^2 + M_Z^2 \Gamma_Z^2} \left[\frac{12\pi \Gamma_e \Gamma_f}{M_Z^2 N_c^f} + \frac{I(s - M_Z^2)}{s} \right] + \frac{4\pi \alpha^2}{3} N_c^f \frac{Q_f^2}{s} \quad (3.4)$$

with

$$I = \pm \frac{4\pi Q_e Q_f \alpha}{\sqrt{N_c^f} M_Z} \left[(\Gamma_e^+)^{\frac{1}{2}} - (\Gamma_e^-)^{\frac{1}{2}} \right] \left[(\Gamma_f^+)^{\frac{1}{2}} - (\Gamma_f^-)^{\frac{1}{2}} \right] \quad (3.5)$$

There is general agreement that the tree level cross section (3.4) has to be corrected for

- electroweak effects to first order (vacuum and vertex loops as described in section 1),
- QED initial bremsstrahlung to second order (α^2),
- QCD effects to first order (α_s).

The electroweak effects can be taken into account

- by replacing α in the tree level formula (3.4) by its running value at the Z^0 , $\alpha(M_Z^2)$;
- by using effective coupling constants when calculating the partial widths;
- by replacing Γ_Z by the s -dependent width $s\Gamma_Z/M_Z^2$, which is the width of a Z^0 with mass \sqrt{s} [30].

The resulting cross section for massless fermions is

$$\sigma(s) = \frac{s}{(s - M_Z^2)^2 + (s\Gamma_Z/M_Z^2)^2} \left[\frac{12\pi \Gamma_e \Gamma_f}{M_Z^2} + \frac{I N_c^f (s - M_Z^2)}{s} \right] + \frac{4\pi \alpha^2(M_Z^2)}{3} N_c^f \frac{Q_f^2}{s}. \quad (3.6)$$

(with I as in eqn. (3.5)). It describes the exact electroweak corrected cross section within 0.2% in the range $(M_Z - \Gamma_Z, M_Z + \Gamma_Z)$ [18]. Introducing the s -dependent width shifts the position of the peak maximum to lower values by ~ 35 MeV. The partial widths calculated in different schemes [27, 28, 29] agree to within 0.1%.

Final state QED and QCD corrections broaden the width by a factor $(1 + \delta_{QED,final})$ or $(1 + \delta_{QCD})$, respectively. Final state QED corrections are small

$$\delta_{QED,final} = \frac{3\alpha}{4\pi} Q_f^2 < 0.17\%. \quad (3.7)$$

The QCD corrections for quark decays are [31]

$$\delta_{QCD} = \frac{\alpha_s}{\pi} + \left(\frac{\alpha_s}{\pi}\right)^2 (1.986 - 0.115n_f) + \left(\frac{\alpha_s}{\pi}\right)^3 (70.985 - 1.2n_f - 0.005n_f^2),$$

where $\alpha_s = \alpha_s(M_Z^2)$, n_f = number of quark flavours.

In view of the error on α_s the second and third term are at present of no importance. The value for δ_{QCD} measured at PEP/PETRA/TRISTAN and extrapolated to the Z^0 mass is [32]

$$\delta_{QCD}((92\text{GeV})^2) = 0.046 \pm 0.005.$$

The error of this correction is in general negligible compared to the measurement errors, except in the case of very heavy top masses, where the QCD correction becomes a sizeable fraction of the top mass correction [33].

Table 3

The total cross section for $e^+e^- \rightarrow \mu^+\mu^-$ and $e^+e^- \rightarrow \text{hadrons}$
for $M_Z = 92$ GeV, $m_H = 100$ GeV and
two values of m_t (all corrections included, values from Zshape).

process	m_t GeV	Γ_Z GeV	σ_{max} nb	$\sqrt{s_{max}}$ GeV	$\sqrt{s_-}$ GeV	$\sqrt{s_+}$ GeV
$e^+e^- \rightarrow \mu^+\mu^-$	90	2.567	1.453	92.094	90.751	93.728
	230	2.607	1.464	92.095	90.732	93.755
$e^+e^- \rightarrow \text{hadrons}$	90	2.567	30.054	92.095	90.770	93.709
	230	2.607	30.238	92.097	90.751	93.736

In Table 3 are listed the position and the values of the maximum of the cross section and the half maxima for two values of the top mass. The dependence of the maximum position $\sqrt{s_{max}}$ on the unknown model parameters m_t , m_H is insignificant ($< 2\text{MeV}$). This is important for the experimental determination of M_Z , which is required to be free of model assumptions. The width is sensitive to the top mass: the resonance becomes broader by 40 MeV going from $m_t = 90$ to $m_t = 230$ GeV; the half-maxima of the cross section are farther apart for muons than for hadrons. This is due to the one-photon exchange, which is proportional to Q_f^2 and hence more significant for muons than for hadrons.

The change of the unpolarized cross section with the top mass is too small to be measurable (0.8%). But polarized cross sections are much more sensitive to the top mass, as is shown in Table 4. The effect of a heavy top mass is measurable absolutely, though the relative measurement with $A_{LR} = (\sigma_L - \sigma_R)/(\sigma_L + \sigma_R)$ will be much more sensitive to m_t .

Table 4
Unpolarized and polarized cross sections for $e^+e^- \rightarrow \mu^+\mu^-$ and $M_Z = 92$ GeV
(all corrections included, values from Expostar)

m_t GeV	σ nb	σ_L nb	σ_R nb	A_{LR}
90	1.468	1.720	1.216	0.172
230	1.468	1.781	1.155	0.213

QED radiative corrections.

QED corrections consist of those diagrams with an extra photon added to the tree level diagrams, either as real bremsstrahlung photon or virtual photon loop. QED corrections depend on experimental cuts and hence on the details of the experiment. The aim will be to understand QED effects sufficiently well and correct the experimental data such that the results can be presented with QED effects removed.

The contributions to QED corrections are initial state radiation, final state radiation and the interference between initial and final state radiation. The final state radiation (3.7) is negligible as long as only loose cuts are applied. The same is true for the interference term. But both contributions can become of order few percent if tight cuts are applied [33]. Initial state radiation lowers the center-of-mass energy and introduces huge corrections. Around the Z^0 peak the radiation is limited by the Z^0 width and therefore dominantly soft. Soft radiation does not change the helicity state of the incoming electrons (or positrons) and has therefore negligible influence on the beam polarization. Although considered not very interesting with respect to the underlying theory, a lot of attention must be given to QED radiative corrections for practical purposes. Three roads have been followed to calculate these corrections:

- exact second order calculations [34],
- structure function approach [35] and
- soft-photon exponentiation [36].

Examples of the corresponding analytic calculations or Monte Carlo generators are ZSHAPE [37], EXPOSTAR [29] and MOE [38], and YFS2 [39], respectively. ZSHAPE has been adopted as *the* analytic calculation to which other analytic calculations and Monte Carlo generators are compared to judge their reliability. The Monte Carlo generator YFS2 is

considered as the potentially best Monte Carlo generator because it produces multiple photon final states. For more extensive reviews of existing programs see [26].

The effect of QED radiative corrections is summarized in Table 5. The main features are a decrease of the peak height by approximately

$$\left(\frac{\Gamma_Z}{M_Z}\right)^\beta (1 - \delta_1^{V+S}),$$

$$\text{with } \beta = \frac{2\alpha}{\pi} \left(\ln \frac{s}{m_e^2} - 1 \right), \quad \delta_1^{V+S} = \frac{\alpha}{s} \left(\frac{3}{2} \ln \frac{s}{m_e^2} + \frac{\pi^2}{3} - 2 \right).$$

a shift of the peak position by

$$\Delta\sqrt{s}_{max} = \frac{\beta\pi}{8} \Gamma_Z.$$

and a shift of the half maxima positions to higher values. An approximate analytic formula for the QED corrections exists that is, to within 0.4%, a good approximation to the line shape in the region $(M_Z - 3\Gamma_Z, M_Z + \Gamma_Z)$ [18].

Table 5
Effect of QED corrections on the line shape

process	decrease of peak height by factor	shift of peak position (MeV)	shift of half maxima	
			$\Delta\sqrt{s}_-$ (MeV)	$\Delta\sqrt{s}_+$ (MeV)
$e^+e^- \rightarrow \mu^+\mu^- (n\gamma)$	0.745	112	50	448
$e^+e^- \rightarrow \text{hadrons} (n\gamma)$	0.740	112	60	432

4. Asymmetries of the Z^0 cross section

4.1. DEFINITION OF ASYMMETRIES

For simplicity we will introduce the asymmetries on the Z pole and at lowest order. The asymmetries are simple combinations of the fermionic coupling constants up to small terms $\approx (\Gamma_Z/M_Z)^2$ coming from pure γ exchange. The ingredients in all expressions are the combinations

$$A_f = \frac{-2c_V^f c_A^f}{(c_V^f)^2 + (c_A^f)^2} = -2 \frac{1 - 4|Q_f| \sin^2 \theta_{eff}}{1 + (2I_3^f - 4Q_f \sin^2 \theta_{eff})^2}$$

A_e is equal to the "natural polarization of the Z^0 " and A_f is the polarization of the final state fermion.

At the Z^0 peak the differential cross section is

$$\frac{d\sigma}{d\Omega} = \frac{\alpha^2}{4} \frac{1}{D(s)} \frac{(c_V^e)^2 + (c_A^e)^2}{\sin^2 2\theta_{eff}^e} \frac{(c_V^f)^2 + (c_A^f)^2}{\sin^2 2\theta_{eff}^f} \times \quad (4.1)$$

$$\left\{ (1 - \mathcal{P}_{e+} \mathcal{P}_{e-}) [2(1 + c^2) + 8cA_e A_f] \right.$$

$$\left. - (\mathcal{P}_{e+} - \mathcal{P}_{e-}) [2(1 + c^2)A_e + 4cA_f] \right\}$$

where $c = \cos\vartheta$ is the angle between the incoming e^- and the outgoing fermion f . \mathcal{P}_{e-} (\mathcal{P}_{e+}) is the longitudinal e^- (e^+) beam polarization.

The first expression in the curly brackets is the unpolarized cross section. Without polarization only the combination of production and decay vertex ($A_e A_f$) can be measured via the forward-backward asymmetry of the differential cross section. The second expression in the curly brackets is present only for longitudinally polarized beams. They give access to the couplings at the production vertex (A_e) and the decay vertex (A_f) separately: the normalized difference of the cross section taken with left- and right- polarized electron beams measures A_e ; the normalized forward-backward difference of the polarized part of the cross section measures A_f .

Table 6
 $Z \rightarrow \bar{f}f$ vertex factors
 $c_A = I^3, \quad c_V = I^3 - 2Q\sin^2\theta_W$

Family	Q	c_A	c_V
$\nu_e, \nu_\mu, \nu_\tau, \dots$	0	$\frac{1}{2}$	$\frac{1}{2}$
$e^-, \mu^-, \tau^-, \dots$	-1	$-\frac{1}{2}$	$-\frac{1}{2} + 2\sin^2\theta_W$
$u, c, t \dots$	$\frac{2}{3}$	$\frac{1}{2}$	$\frac{1}{2} - \frac{4}{3}\sin^2\theta_W$
$d, s, b \dots$	$-\frac{1}{3}$	$-\frac{1}{2}$	$-\frac{1}{2} + \frac{2}{3}\sin^2\theta_W$

Before discussing the asymmetries, we will examine the asymmetry factors A_f in more detail. The vertex factors and their values are listed in Tables 6 and 7. The asymmetry factor A_e is small for the electron family (e, μ, τ) due to the small vector form factor c_V . $|A_f|$ is much larger for the u-family and is close to one for the d-family: going from the e- to u- to d- family the helicity properties become more neutrino-like. This simply reflects the fact that the influence of $\sin^2\theta_W$ decreases with decreasing charge. For the same reason, the e-family is very sensitive to $\sin^2\theta_W$, whereas the d- family is an order of magnitude less sensitive, though its polarization is very large (Table 8). Fig. 6 illustrates the different behaviour of the asymmetry factors.

Table 7
Values of the $Z \rightarrow f\bar{f}$ vertex factors ($\sin^2\theta_W = 0.23$)

Family	vertex factors		helicity factors		asymmetry
	c_A	c_V	c_R	c_L	A_f
ν	$\frac{1}{2}$	$\frac{1}{2}$	0	1	-1
e^-	$-\frac{1}{2}$	-0.04	0.46	-0.54	-0.160
u	$\frac{1}{2}$	0.193	-0.307	0.693	-0.673
d	$-\frac{1}{2}$	-0.347	0.153	-0.847	-0.937

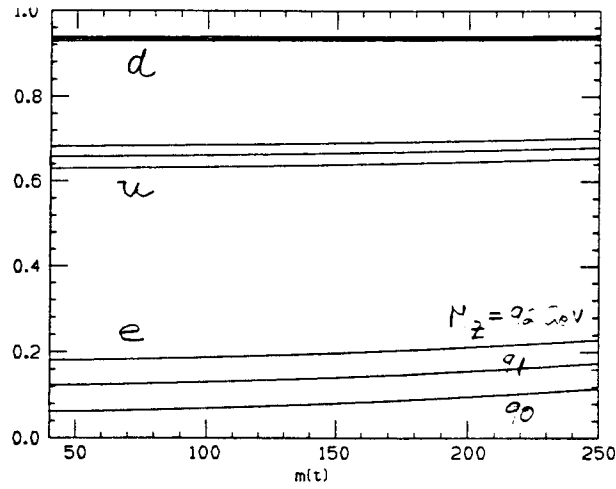


Figure 6. The asymmetry factors for quarks and lepton families e, u, d as function of the top mass and for three different values of the Z^0 mass (from Expostar).

Table 8
Sensitivity of the vertex factors A_f to $\sin^2\theta_W$
 $\sin^2\theta_W = \frac{1}{4}(1 - \delta)$

Family	A_f	$\partial A_f / \partial \sin^2\theta_W$
ν_e	-1	0
e^-	$-\frac{2\delta}{1+\delta^2}$	-8
u	$-\frac{6(1+2\delta)}{9+(1+2\delta)^2}$	-3.7
d	$-\frac{6(2+\delta)}{9+(2+\delta)^2}$	-0.69

Without beam polarization the only asymmetry that can be measured is the forward-backward asymmetry ,

Table 9
Sensitivity of $A_{FB}^f = \frac{3}{4}A_e A_f$ to $\sin^2\theta_W^e$ and $\sin^2\theta_W^f$
 $\partial A_{FB} = \frac{3}{4}[A_f dA_e + A_e dA_f]$ ($\sin^2\theta_W = 0.23$)

Family	sensitivity production vertex	to decay vertex	overall sensitivity
	$A_f \frac{dA_e}{d\sin^2\theta_W^e}$	$A_e \frac{dA_f}{d\sin^2\theta_W^f}$	$\frac{dA_{FB}^f}{d\sin^2\theta_W}$
e^-	1.28	1.28	1.92
u	5.38	0.61	4.49
d	7.49	0.11	5.70

$$A_{FB} = \frac{3}{4}A_e A_f. \quad (4.2)$$

With polarization several additional asymmetries can be explored:
The left-right asymmetry ,

$$A_{LR} = A_e, \quad A_{LR}^{exp} = \mathcal{P} \cdot A_{LR}, \quad \text{with } \mathcal{P} = \frac{\mathcal{P}_{e+} - \mathcal{P}_{e-}}{1 - \mathcal{P}_{e+}\mathcal{P}_{e-}}, \quad (4.3)$$

the forward-backward asymmetry with polarization,

$$A_{FB} = \frac{3}{4}A_Z A_f, \quad \text{with } A_Z = \frac{A_e - \mathcal{P}}{1 - A_e \mathcal{P}}, \quad (4.4)$$

and the forward-backward polarization asymmetry

$$A_{FB}^{Pol} = \frac{3}{4}A_f, \quad A_{FB}^{Pol,exp} = \mathcal{P} \cdot A_{FB}^{Pol}. \quad (4.5)$$

The above equations use the generalized polarization \mathcal{P} and the polarization of the Z^0 boson, A_Z .

4.2. MEASUREMENT ERRORS OF THE ASYMMETRIES

Statistical errors.

The detector geometry and the acceptance of trigger and reconstruction limit the events to a polar angular region $|\cos\vartheta| \leq x$. The number N of accepted events is then, using the cross section (4.1),

$$N(|\cos\vartheta| \leq x) = N_0 \frac{x(3+x^2)}{4}.$$

The variance of the asymmetry measurement A is

$$\text{Variance}(A) = \frac{1}{N}(1 - A^2).$$

Smaller measurement errors can be achieved when the analytic form of the angular distribution is assumed and a moment analysis or log likelihood fit is performed [40].

If the asymmetry A is derived from the experimentally measured asymmetry A^{exp}

$$A^{exp} = kA,$$

$$\text{then } \text{Variance}(A) = \frac{1}{k^2 N}(1 - A^2) + \left(\frac{\delta k}{k}\right)^2 A^2. \quad (4.6)$$

In the list of examples below, k may be a factor due to acceptance, $F(x) = 4x/(3 + x^2)$, or the degree of longitudinal electron beam polarization, $\mathcal{P} = -\mathcal{P}_e$ or the product of both:

$$\begin{aligned} A_{LR}^{exp} &= \mathcal{P} \cdot A_{LR}, \\ A_{FB}^{Pol, exp} &= F(x) \cdot \mathcal{P} A_{FB}^{Pol}, \\ A_{FB}^{exp} &= F(x) \cdot A_{FB}, \\ A_{FB}^{(b), exp} &= F(x) \cdot (1 - 2\chi) \cdot A_{FB}^{(b)}. \end{aligned} \quad (4.7)$$

The effective number of events becomes $k^2 N$. The quantity $k^2/(1 - A^2)$ may be considered as “figure of merit” in the case that A is small. For a large number of events A^{-2} becomes the “figure of merit”. In the case of limited acceptance, the effective number of events for forward–backward asymmetries is $N_{eff} = \frac{4x^3}{3+x^2} N_0$. The error on the acceptance function F , $(\delta F/F)$, enters as well in (4.6), but is less important for a small value of the asymmetry. Typical values for the acceptance function F and the effective number of events are listed in Table 10. They clearly demonstrate the importance of the endcaps. In the case of b -quarks, the effective number of events is in addition reduced by a factor of ~ 2 due to mixing (χ mixing parameter).

Systematic errors of the asymmetries.

Errors due to background processes.

For the measurement of the left-right asymmetry to reach the ultimate accuracy of $\delta A_{LR}/A_{LR} = 1\%$, contributions from production channels other than $e^+e^- \rightarrow Z, \gamma \rightarrow f\bar{f}$ have to be $\leq 1\%$. A moderate cut on the total visible energy (to reject 2-photon processes) and the rejection of Bhabha events should easily achieve this goal.

Backgrounds are more severe for the measurement of the forward–backward asymmetries, where the final state fermion and its charge have to be identified. Backgrounds are of four types:

Table 10
Typical values for the acceptance of SLD

detector	$\cos\vartheta_{max}$	N/N_0	$F(x)$	N_{eff}/N_0
Calorimetry	0.98	0.970	0.990	0.951
Drift chambers				
loose track quality cuts	0.95	0.927	0.974	0.879
tight track quality cuts	0.85	0.791	0.913	0.660
Vertex detector (≥ 2 hits)	0.70	0.611	0.802	0.393
CRID particle identification				
barrel	0.68	0.589	0.786	0.363
barrel + endcap	0.98	0.970	0.990	0.951

same asymmetry, same sign charge;
 same asymmetry, wrong sign charge;
 different asymmetry, same sign charge;
 different asymmetry, wrong sign charge.

Assuming that deviations from the standard model are small, one can calculate the fraction of background that is acceptable for the aimed-at accuracy in the asymmetry measurement. Such an analysis has been performed in [41].

Other error sources.

Errors due to the accuracy of the polar angle measurement should be negligible for μ 's and τ 's. For quarks A_{FB} is modified by QCD effects by $\delta A_{FB}(QCD) \leq 4\%$ (more details below).

For polarized beams, the luminosity difference from bunch to bunch is expected to be, on average, negligible. The correlation between position and energy of the beam particles at the interaction point leads to a correlation between position and beam polarization. Beam polarization changes rapidly with deviation from the nominal energy, $\Delta\mathcal{P}_e \sim \cos(\frac{\Delta E}{E} 50\pi)$. The energy spread within one bunch is expected to be $\Delta E/E = \pm 0.2\%$. Precise head-on collisions of the beams at the interaction point are therefore important to avoid offsets and errors in the polarization, that are not detectable by the Møller and Compton polarimeters.

4.3. MEASUREMENT OF THE ASYMMETRIES AND THEORETICAL UNCERTAINTIES

We discuss now the measurement of the asymmetries in more detail.

The left-right asymmetry .

The jewel among the asymmetries is the left-right asymmetry A_{LR} which is the normalized

difference between the polarized cross sections,

$$A_{LR}^{exp} = \mathcal{P} \frac{\sum_f \int_{-x_f}^{x_f} \frac{d\sigma_f}{d\Omega}(\mathcal{P} = 1)dc - \int_{-x_f}^{x_f} \frac{d\sigma_f}{d\Omega}(\mathcal{P} = -1)dc}{\sum_f \int_{-x_f}^{x_f} \frac{d\sigma_f}{d\Omega}(\mathcal{P} = 1)dc + \int_{-x_f}^{x_f} \frac{d\sigma_f}{d\Omega}(\mathcal{P} = -1)dc}.$$

The measurement of A_{LR} could well lead to the most precise test of the standard model, along with the measurement of M_W . To arrive at a statistical error of $3 \cdot 10^{-3}$ about $4 \cdot 10^5$ events are required.

A few general remarks are relevant, which will be followed by a more detailed discussion. A_{LR} is much larger than A_{FB} and therefore less prone to systematic errors. It is very sensitive to $\sin^2\theta_W$, $\delta A_{LR} \sim -8\delta\sin^2\theta_W$. It is independent of the final state and therefore all the hadronic final states with their large production rate can be used. The energy dependence of A_{LR} is small around the peak, hence the effect of QED radiative corrections is small. For symmetric detector acceptance A_{LR} is independent of the experimental cut $|\cos\vartheta| \leq x$, which can be different for different final state species. The normalization should not introduce any error as the number of electrons per e^- bunch is independent of polarization at SLC. A discussion in more detail follows.

Theoretical uncertainty.

The total cross section is subject to large QED corrections. For the left-right asymmetry the situation is much more favourable. At the peak the dominant Z-exchange term leads to $A_{LR} = A_e$, independent of the final state. The photon exchange term contributes differently to A_{LR} depending on the final state, but this effect amounts to $\mathcal{O}((\Gamma_Z/M_Z)^2)$ and is thus below the planned accuracy.

Initial state radiation smears the effective energy and raises the energy of minimal sensitivity to a slightly higher value $M_Z + 224$ MeV, about 130 MeV higher than the maximum of the cross section ($M_Z + 94$ MeV) [33]. The asymmetry is practically unchanged at the energy of minimal sensitivity as long as only the initial state radiation is taken into account. The addition of the pure s-channel photon contribution changes the asymmetry depending on the final state species. However a sizeable fraction of this effect originates from final states with a very hard photon. This contribution is easily eliminated by a rather loose cut on the photon energy ($k \leq 0.9$) [33]. The difference between different final states is still small enough at the peak such that all channels can be used to measure A_{LR} . The contribution from the $Z - \gamma$ interference cannot be neglected away from the peak and predictions for the asymmetries depend on the final state (Fig. 7).

A potential limit for the interpretation of A_{LR} follows from the uncertainty in the hadronic vacuum polarization. The error $\delta\Delta r$, eqn. (2.3) corresponds to an error $\delta A_{LR} \approx 0.003$. This should be compared with the possible effect of the variation of the Higgs mass from 10 to 1000 GeV, $\delta A_{LR}^{(Higgs)} \sim \pm 0.009$ [9].

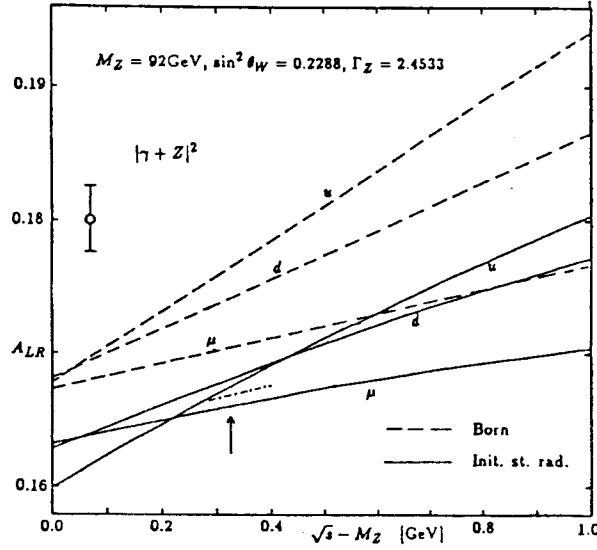


Figure 7. Influence of initial state radiation on A_{LR}^f including the one-photon exchange. The arrow indicates the energy of minimal sensitivity (from [32]).

In conclusion, the dependence of A_{LR} on the final state (or the uncertainty on how to correct for it) is below the measurement accuracy of A_{LR} . The measurement of A_{LR} should be performed about 130 MeV above the peak value of the cross section.

Experimental error.

The experimental error on the left-right asymmetry is (4.6)

$$\delta A_{LR} = \sqrt{\frac{1}{\mathcal{P}^2} \frac{1}{N} + A_{LR}^2 \left(\frac{\delta \mathcal{P}}{\mathcal{P}} \right)^2}.$$

Fig. 8 shows the error as function of the number of detected Z^0 events and for two values of the measurement error of the polarization,

$$\begin{aligned} \frac{\delta \mathcal{P}}{\mathcal{P}} &= 5\% \quad (\text{Møller Polarimeter}) \text{ and} \\ \frac{\delta \mathcal{P}}{\mathcal{P}} &= 1\% \quad (\text{Compton Polarimeter}). \end{aligned}$$

Møller and Compton polarimeters are installed in the electron beam extraction line of SLC. The measurement by the Møller polarimeter, which detects the beam electrons scattered from magnetized iron foils, is limited by background from electron scattering on the iron nucleus ($\Delta P \approx \pm 2\%$) and by the accuracy with which the magnetization of the iron can be determined ($\Delta P \approx \pm 2\%$). Compton polarimetry, for which polarized laser light is scattered on the electron beam, is expected to be limited by the accuracy of the measurement of the laser polarization (1%). The measured asymmetries are much larger for the Compton polarimeter ($\geq 75\%$) than for the Møller polarimeter (2%) [21]. With

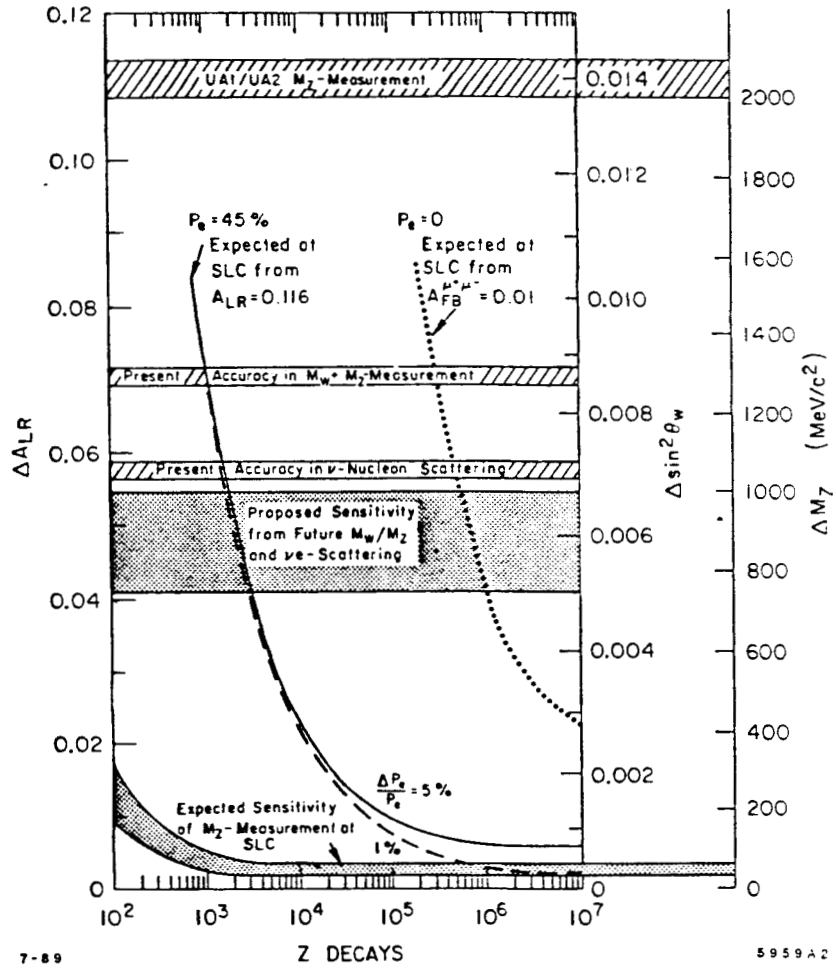


Figure 8. The expected uncertainty of a measurement of A_{LR} as a function of the number of events used. The corresponding uncertainty on $\sin^2\theta_W$ and on the mass of the Z^0 is also shown. The expected precision on $\sin^2\theta_W$ from a measurement of the muonic forward-backward asymmetry with zero polarization is shown for comparison.

2000 Z^0 events the A_{LR} measurement gives a better result than the existing determination of $\sin^2\theta_W$ from νN scattering (R_ν). Once M_Z is precisely measured A_{LR} can be used to put limits on the top mass (Fig. 9a). Similar limits can be extracted from M_W (Fig. 9b). Fig. 10 illustrates the sensitivity of A_{LR} and M_W to the main unknown parameters, m_t and m_H , once M_Z is known. It clearly shows that the information from M_W and A_{LR} are complementary and that the measurement of A_{LR} is not an alternative to the measurement of M_W . A_{LR} is the quantity that may be most sensitive to the Higgs mass, once the top mass is known.

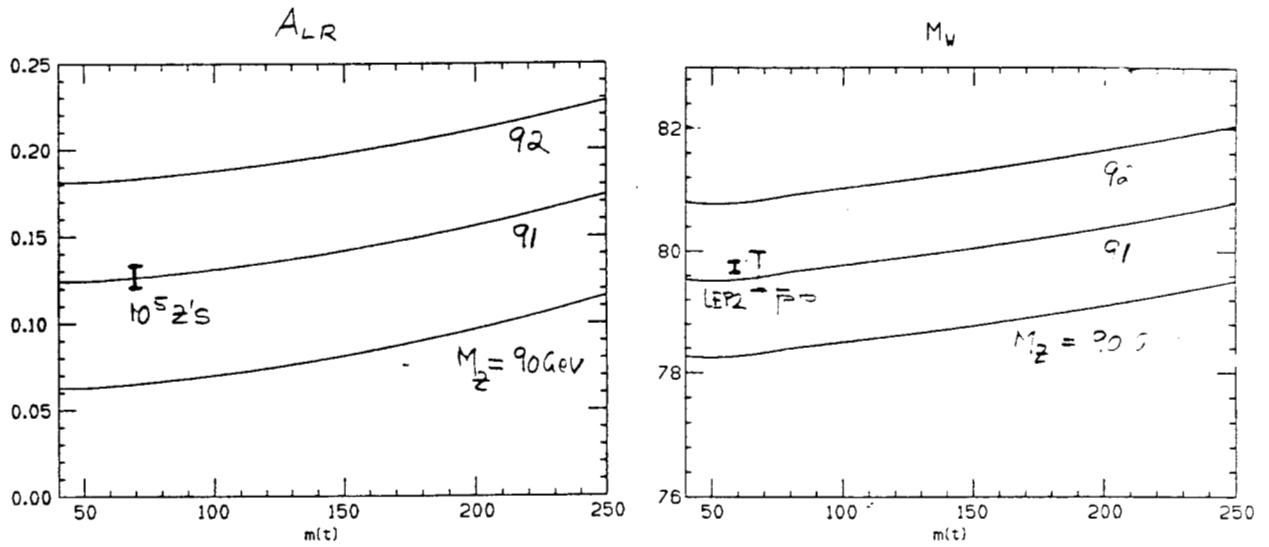


Figure 9. a) The dependence of A_{LR} on the top mass. b) The dependence of M_W on the top mass, for three values of the top mass (from Expostar). The expected accuracy of the corresponding measurements is indicated also. The errors on M_W correspond to a measurement at the $\bar{p}p$ colliders (350 MeV) or LEP2 (100 MeV).

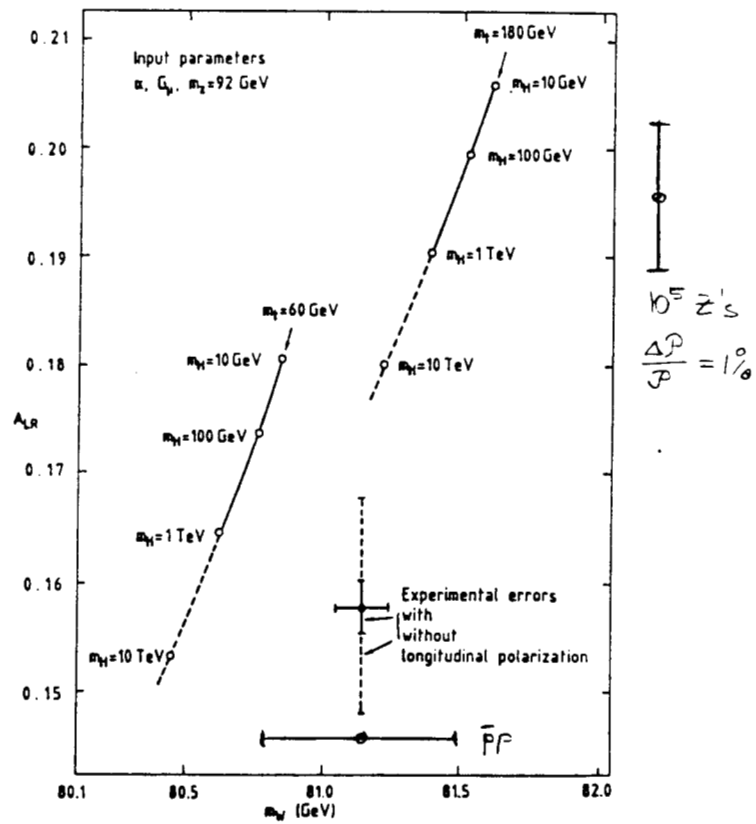


Figure 10. The sensitivity of A_{LR} and M_W to the higgs mass for two values of the top mass (from D. Treille in ref. [4]).

The forward–backward asymmetry A_{FB}

$$A_{FB}^{exp} = \frac{\int_0^x \frac{d\sigma}{d\Omega} dc - \int_{-x}^0 \frac{d\sigma}{d\Omega} dc}{\int_0^x \frac{d\sigma}{d\Omega} dc + \int_{-x}^0 \frac{d\sigma}{d\Omega} dc}.$$

A few general remarks are relevant. The forward–backward asymmetry (also called charge asymmetry) depends on both the electron and the final state fermion couplings, see eqn. (4.2). The asymmetry is small because A_e is a small number.

The experimental value depends on the acceptance. About an equal amount of information comes from the endcap ($\vartheta < 40^\circ$) and the barrel ($\vartheta > 40^\circ$) regions of the detector. The charge of the final state has to be determined, which restricts the number of useful decay channels or dilutes the signal through wrongly tagged channels. A_{FB} is a rapidly varying function of \sqrt{s} and is therefore strongly modified by initial–state QED radiation, the effect of which has therefore to be very accurately determined. The unavoidable uncertainty on M_Z ($\pm 40 \text{ MeV}$) will, for the same reason, limit the accuracy on A_{FB} to 0.25%. Compared with the case of A_{LR} the sensitivity to $\sin^2\theta_W$ is small; for quark final states A_{FB} is mainly sensitive to the electron coupling at the production vertex, see Table 8.

A_{FB} with quarks as final states.

For quarks as final states the quark direction is inferred from the jet axis or the thrust axis. The radiation of gluons changes the original quark axis and dilutes the asymmetry. The QCD corrections are of order α_s/π (plus additional mass terms that are negligible for light quarks) and reduce the asymmetry,

$$A_{FB} = A_{FB}^0 \left(1 - k \frac{\alpha_s}{\pi} + \text{terms of } O\left(\frac{2m}{\sqrt{s}} \frac{\alpha_s}{\pi}\right)\right). \quad (4.8)$$

The factor k reflects the dependence on the algorithm used to determine the jet axis [42].

b quarks are of special interest for two reasons: They can be efficiently tagged and the asymmetry factor A_b has a value close to 1 with small dependence on $\sin^2\theta_W^b$, (see Table 8). This makes the b quark channel an analyzer for the electron vertex. For a tagging efficiency of 20% the rate of accepted b decays is 3% of the total cross section, comparable to the rate of $Z \rightarrow \mu^+\mu^-$, but the measured asymmetry $A_{FB}^b \sim \frac{3}{4} A_e \times 0.93 \sim 0.084$, is much larger than the asymmetry measured with muons, $A_{FB}^\mu = \frac{3}{4} A_e A_\mu = 0.011$. The sensitivity to $\sin^2\theta_W$ is $\delta A_{FB}^b = 5.6 \delta \sin^2\theta_W$. Assuming that b -quarks are tagged through the semi-leptonic decays of B -hadrons, the mixing of neutral B 's reduces the signal to $A_{FB}^{b,exp} = (1 - 2\bar{\chi}) A_{FB}^b$. $\bar{\chi}$ is the averaged mixing parameter, $\bar{\chi} = 0.12 \pm 0.05$ [43]. If we assume that $\bar{\chi}$ is known in future to 10%, then the error contribution from mixing becomes

$$\delta^{(mix)} A_{FB}^{b,exp} = \frac{-2\delta\bar{\chi}}{1 - 2\bar{\chi}} A_{FB}^b = 0.003 \dots 0.005,$$

which is small compared to the expected measurement error. The effective number of events

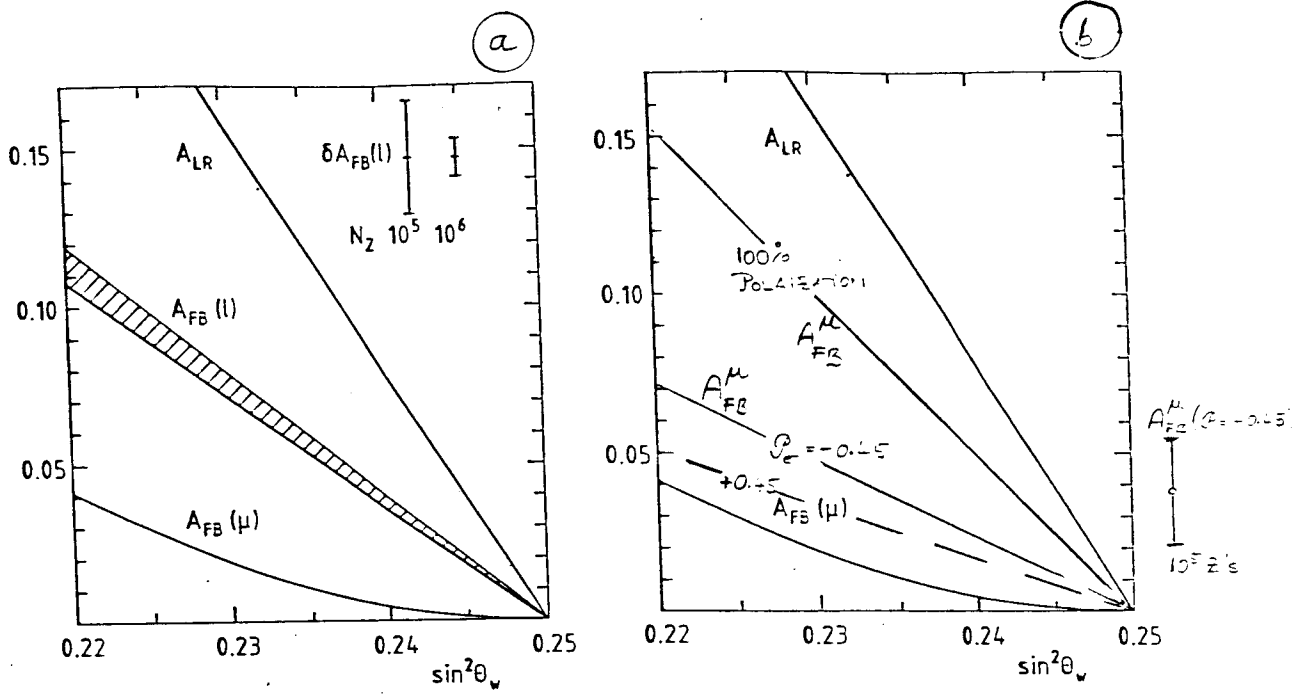


Figure 11. a) Dependence on $\sin^2 \theta_W$ for A_{LR} , A_{FB}^μ and A_{FB}^b (including QCD corrections and mixing). Also shown is the combined uncertainty from QCD and mixing [17]. b) Dependence on $\sin^2 \theta_W$ of A_{FB} measured with polarization ($\mathcal{P}_{e^-} = \pm 0.45$ and ± 1).

is $(1 - 2\bar{\chi})^2 N \sim \frac{1}{2}N$. The importance of A_{FB}^b at machines without polarization has been stressed in [17]. Fig. 11a shows A_{FB}^b and the effect of mixing in comparison with A_{FB}^μ and A_{LR} .

A_{FB} with polarized electron beams

With polarized electron beams the Z^0 polarization is under the control of the experimenter and much larger values of A_{FB} can be achieved (Fig 11b),

$$A_e = 0.11 \longrightarrow A_Z = \frac{A_e + \mathcal{P}_{e^-}}{1 + A_e \mathcal{P}_{e^-}} = -0.53 \quad \text{for } \mathcal{P}_{e^-} = -0.45,$$

$$= 0.33 \quad \text{for } \mathcal{P}_{e^-} = 0.45.$$

With increasing beam polarization the sensitivity to the decay vertex increases, whereas the sensitivity to the production vertex decreases until it vanishes for $\mathcal{P}_{e^-} = \pm 1$. In the realistic case, where $|\mathcal{P}_{e^-}| < 1$, the asymmetry will still depend on both, the initial and final state couplings. It is obvious that A_{FB} becomes a much more powerful tool when polarization is available.

The forward–backward polarization asymmetry A_{FB}^{Pol}

One can simplify the above situation by defining (for every final state species) [44]

$$A_{FB}^{Pol,exp} = \frac{\left[\int_0^x \frac{d\sigma}{d\Omega}(\mathcal{P} = 1)dc - \int_{-x}^0 \frac{d\sigma}{d\Omega}(\mathcal{P} = 1)dc \right] - \left[\int_0^x \frac{d\sigma}{d\Omega}(\mathcal{P} = -1)dc - \int_{-x}^0 \frac{d\sigma}{d\Omega}(\mathcal{P} = -1)dc \right]}{\left[\int_0^x \frac{d\sigma}{d\Omega}(\mathcal{P} = 1)dc + \int_{-x}^0 \frac{d\sigma}{d\Omega}(\mathcal{P} = 1)dc \right] + \left[\int_0^x \frac{d\sigma}{d\Omega}(\mathcal{P} = -1)dc + \int_{-x}^0 \frac{d\sigma}{d\Omega}(\mathcal{P} = -1)dc \right]}.$$

At the Z peak these asymmetries measure the couplings of the final state fermion f to the Z, and are thus complementary to the left–right asymmetry. This indicates a rather unbiased way of testing electron–heavy lepton (μ, τ) universality. In the case of the τ lepton the same information can in principle be obtained from a measurement of the τ polarization; the forward–backward polarization asymmetry, however, makes use of the full statistics of τ pair production and does not require assumptions about the charged current couplings of the τ .

A_{FB}^{Pol} has a very smooth dependence on \sqrt{s} near the Z pole. Similar to A_{LR} , QED effects that result in an effective shift of the center–of–mass energy should be of no relevance. This has been confirmed by [29].

Weak corrections (vertex and oblique) contribute to the renormalization of the final state couplings but do not introduce any dependence on the initial state couplings. The oblique corrections can be simply related at the Z pole to the corresponding oblique corrections of the left–right asymmetry. This leads to expressions [9]

$$\begin{aligned} \delta^{oblique} A_{FB}^{Pol}(\mu, \tau) &= \frac{3}{4} \delta^{oblique} A_{LR} \\ \delta^{oblique} A_{FB}^{Pol}(u, c) &= \frac{9}{25} \delta^{oblique} A_{LR} \\ \delta^{oblique} A_{FB}^{Pol}(d, s, b) &= \frac{1}{15} \delta^{oblique} A_{LR} \end{aligned}$$

showing that in the case of quarks these corrections are relatively much smaller than in the case of leptons. One can redefine asymmetries that are a combination of A_{LR} and A_{FB}^{Pol} , which are independent of oblique corrections and are specially interesting to probe for physics beyond the standard model [45].

The hadronic uncertainty (2.3) due to $\Delta\alpha$ is totally negligible [13],

$$\delta^{(\alpha)} A_{FB}^{Pol,b} \sim 1 \cdot 10^{-4}, \quad \delta^{(\alpha)} A_{FB}^{Pol,c} \sim 1 \cdot 10^{-3}.$$

Strong interaction effects will occur in $A_{FB}^{Pol(f)}$ when f is a quark,

$$A_{FB}^{Pol}(q) \longrightarrow A_{FB}^{Pol}(q) \left(1 - k \frac{\alpha_s}{\pi}\right).$$

The correction is indeed similar to the correction (4.8) of A_{FB} and the same discussion as

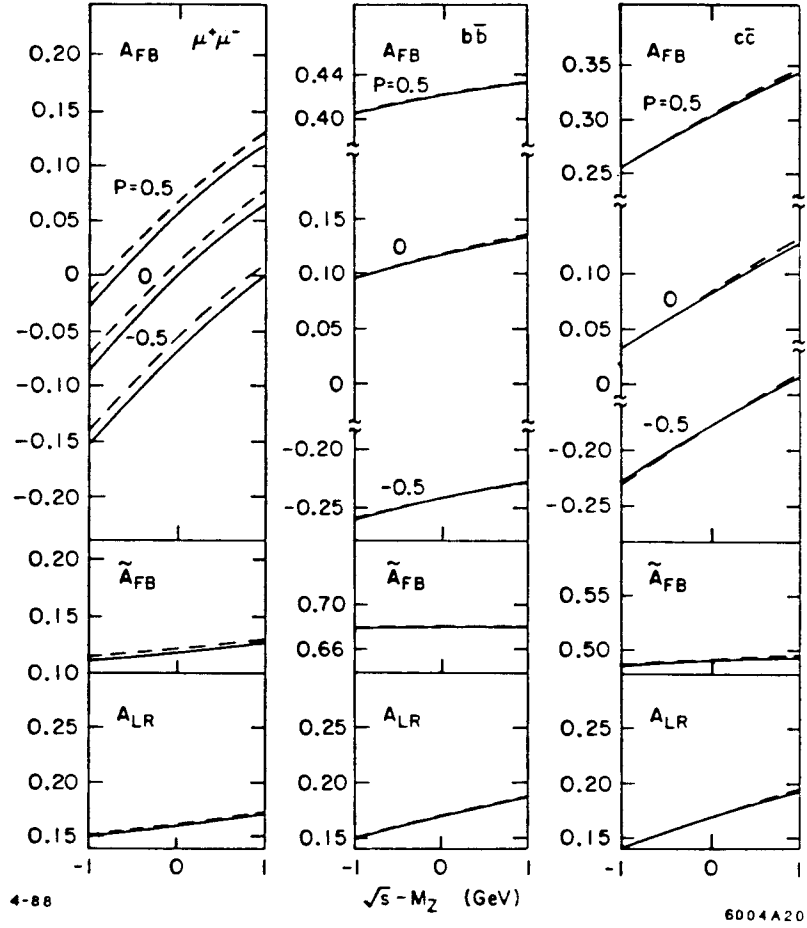


Figure 12. The energy dependence of A_{FB} (polarized and otherwise), A_{FB}^{Pol} , and A_{LR} for several final state fermions. Note that the forward-backward asymmetries are much more sensitive to the center-of-mass energy than the left-right asymmetry and the forward-backward polarization asymmetry.

in reference [42] applies.

Fig. 12 summarizes the main features of the various asymmetries considered: their magnitude, their variation with beam polarization and with energy.

5. τ Polarization

$Z \rightarrow \tau^+ \tau^-$ is the only Z° decay for which the spin polarization of the final state fermion can be measured. For quark final states, even for heavy quarks, the helicity of the original quark is lost in the process of hadronization [46]. The average τ polarization is

$$\mathcal{P}_\tau = A_\tau = \frac{-2c_V^\tau c_A^\tau}{(c_V^\tau)^2 + (c_A^\tau)^2}.$$

The degree of the spin polarization of the τ^- as a function of the polar angle is, at the Z° pole (see eg. [47]),

$$\mathcal{P}_\tau(c) = \frac{A_\tau + \frac{2c}{1+c^2} A_Z}{1 + \frac{2c}{1+c^2} A_\tau A_Z} \approx A_\tau + \frac{2c}{1+c^2} (A_e + \mathcal{P}_{e^-}) \quad (c = \cos\vartheta)$$

(A_Z as in (4.4)). The average τ polarization is due to the coupling of the Z° to the τ and is independent of the beam polarization. The asymmetry of the τ polarization is due to the polarization of the Z° and depends therefore on the beam polarization and the “natural polarization” of the Z° , A_e . The asymmetry of the τ polarization increases significantly with the beam polarization.

The degree of τ polarization can be measured by the momentum distribution of its decay products (see eg. [2]). The normalized energy of a given decay product is defined as

$$u = \frac{E_{decay}}{\sqrt{s}/2}.$$

The average \bar{u} is a linear function of the τ polarization

$$\bar{u}(\mathcal{P}_\tau(c)) \approx u_0 + u_P \mathcal{P}_\tau(c).$$

The best suited decay mode for the measurement of \mathcal{P}_τ is the $\tau \rightarrow \pi \nu$ decay as can be seen from Table 11 that summarizes the values for u_0 and u_P for different decay channels.

A_τ can be extracted from the normalized energies, averaged over $|\cos\vartheta| \leq x$,

$$\langle \bar{u} \rangle = \frac{1}{2x} \int_{-x}^x \bar{u} dc = u_0 + u_P A_\tau. \quad (5.1)$$

The difference of the energies averaged over forward and backward directions measures the Z° polarization A_Z and hence A_e ,

$$\bar{u}_{FB} = \frac{1}{x} \left(\int_0^x \bar{u} dc - \int_{-x}^0 \bar{u} dc \right) = u_P F_\tau(x) A_Z,$$

where $F_\tau(x) < \frac{3}{4}$ is a geometry factor. The τ polarization is low in the backward hemisphere. In the analysis of [48] it was therefore proposed to exclude part of the backward hemisphere

Table 11
Parameters of the average energy distribution
of the τ decay products [(5.1)]

Decay mode	u_0	u_p
e, μ	0.35	-0.05
π, K	0.5	$+\frac{1}{6}$
$V(\rho, K^*, a_1)$	0.5	$+\frac{1}{6} \frac{m_\tau^2 - 2m_V^2}{m_\tau^2 - 2m_V^2}$

($\cos\vartheta < -0.35$). This increases the sensitivity to A_e by about a factor of 2 at the expense of losing 50% of the events.

5.1. QED AND QCD CORRECTIONS

τ polarization changes weakly with the center-of-mass energy. The direct influence of the initial state QED radiation is therefore negligible [48].

Final state QED radiation has also little influence on the τ polarization because it is dominated by soft photon radiation. But both initial and final radiation lower the energy of the τ and therefore soften the τ decay spectrum. Final state radiation from the τ or the decay particle is responsible for the bulk (75%) of the distortion of the energy distribution. To eliminate part of it, the extreme energy values have been removed by cuts in the analysis of [48], which reduces the correction of \mathcal{P}_τ to $\delta\mathcal{P}_\tau = 0.013$.

The $Z \rightarrow \tau^+\tau^-$ decay is potentially a very interesting decay because it allows one to measure A_e , which contains the top mass dependence and A_τ , where this dependence is not present. The τ^- decay contains in addition information on the $W - \tau$ coupling, which is not well known. But $Z \rightarrow \tau^+\tau^-$ suffers from low statistics such that it is difficult to make important improvements in the knowledge of the weak parameters with less than 10^5 produced Z^0 's (Table 12). The situation can be somewhat improved when the τ direction is reconstructed in (1-3)-prong events, using the 3-prong vertex and the precise knowledge of the interaction point [49].

Table 12
Measurement accuracy that can be achieved with 10^4 or 10^5 Z^0 events

quantity	approx. value	accuracy for 10^4 Z^0 events		accuracy for 10^5 Z^0 events		comment
		δ^{meas}	$\delta\sin^2\theta_W$	δ^{meas}	$\delta\sin^2\theta_W$	
M_Z	91 GeV	0.040	0.0003	0.040	0.0003	limited by δE_{beam}
Γ_Z	2.5 GeV	(0.020)		(0.006)		(without δE_{beam} limitation)
		0.060		0.035		limited by δE_{beam}
				(0.019)		(without δE_{beam} limitation)
$A_{LR} (\frac{\Delta P}{P} = 5\%)$	0.16	0.025	0.003	0.014	0.002	
$(\frac{\Delta P}{P} = 1\%)$		0.022	0.003	0.007	0.0009	
A_{FB}^μ	0.026	0.055	0.029	0.017	0.009	
A_{FB}^e	0.15	0.06	0.015	0.025	0.005	20% tagging efficiency
\mathcal{P}_τ (e or μ)	0.16	0.51	0.063	0.16	0.020	
(π)		0.21	0.026	0.066	0.008	
(ρ)		0.35	0.044	0.11	0.14	

6. Conclusions

Longitudinally polarized electron beams will be an extremely valuable tool in measuring the electroweak parameters at the Z^0 . They allow significant measurements with a factor of 5 to 10 less statistics than would be needed for measurements without polarization. They allow a full and precise determination of the fermion couplings without further assumptions about the standard model. Measurements with longitudinally polarized beams are more sensitive and less prone to systematic errors.

10^4 events allow already measurements of $\sin^2\theta_W$ that are better than existing measurements, but the advantages of polarized beams will become significant with statistics of the order of 10^5 Z^0 events (Table 12).

Tagging of quarks will be important, especially tagging of b quark events. The endcap regions of the detector will play an important role for tagging; the larger the polarization of the electron beams, the greater this importance will be.

Acknowledgements: I thank my colleagues of the Electroweak Group for useful discussions. Special thanks go to B. Ward, for his support of our study group. Discussions with H. Kühn, M. Peskin and B. Lynn were very helpful and are appreciated very much. I thank W. Busza for his encouragement to write this note and I thank P. Burrows for careful reading the manuscript.

REFERENCES

1. S. L. Glashow, Nucl. Phys. 22 (1961) 579; A. Salam, in Elementary Particle Theory, ed. N. Svartholm (Almqvist and Wiksell, Stockholm, 1968); S. Weinberg, Phys. Rev. Lett. 19 (1967) 1264
2. SLC Workshop on Experimental use of the SLAC Linear Collider, SLAC-247 (1982).
3. MarkII Workshops on SLC Physics, SLAC-Report-306 (1986) and SLAC-Report-315 (1987).
4. Physics at LEP, Eds. J. Ellis, R. Peccei, CERN 86-02 (1986).
5. Polarization at LEP, Eds. G. Alexander, G. Altarelli, A. Blondel, G. Coignet, E. Keil, D. E. Plane, D. Treille, CERN 88-06 (1988).
6. Radiative Corrections for e^+e^- Collisions, Editor J. H. Kühn, International Workshop at Ringberg Castle, Tegernsee, Bavaria (1989).
7. Radiative Corrections: Results and Perspectives, Editor N. Dombey, Nato Advanced Research Workshop, Brighton, England (1989).
8. W. J. Marciano, A. Sirlin, Nucl. Phys. B 189 (1981) 442.
9. B. W. Lynn, M. E. Peskin, R. G. Stuart in reference 4 p.90, and SLAC-PUB-3725 (1985).
10. M. Veltman, Nucl. Phys. B 123 (1977) 89.
11. W. F. L. Hollik, DESY 88-188 (1988) and references therein.
12. W. Marciano Phys. Rev. D 20 (1979) 274.
13. H. Burkhardt, F. Jegerlehner, G. Penso, C. Verzegnassi, Z. Phys. C 43 (1989) 497.
14. A. Sirlin, Phys. Rev. D 22 (1980) 971.
15. Mark II Collaboration and SLC Group, Phys. Rev. Lett. 63 (1989) 724 and SLAC-PUB-5037 (1989), LBL-27518 (1989); Mark II Collaboration, presented by G. Feldman, Proceedings Lepton-Photon Symposium Stanford, Ca (1989).
16. W. F. L. Hollik in 6 p. 143 and CERN-TH. 5426/89
17. J. H. Kühn in reference 7; A. Djouadi, J. H. Kühn, P. M. Zerwas, MPI-PAE/48/89
18. F. A. Berends (Convenor), D. Bardin, W. Beenakker, M. Bilenky, G. Burgers, W. Hollik, T. Riemann, M. Sachwitz, W. L. van Neerven, S. van der Marck, The Z Line Shape, in reference 7 (1989).
19. M. Swartz, Proc. SLAC Summer Institute, Stanford, CA (1989).
20. Mark II Collaboration and Final Focus Group, Extraction Line Spectrometers for SLC Energy Measurement, SLAC-SLC-PROP-2 (1986).
21. J. Kent, M. King, C. Von Zanthier, S. Watson, M. Levi, F. Rouse, P. Bambade, R. Erickson, C. K. Jung, J. Nash, G. Wormser, Precision measurement of the SLC beam energy, SLAC-PUB-4922 (1989).
22. D. Blockus et al., Proposal for Polarization at SLC, SLAC-PROPOSAL-SLC-01 (1986); K. C. Moffeit, SLAC-PUB-4764 (1988); M. L. Swartz, SLAC-PUB-4689 (1988).

23. If transverse polarization (20%) can be produced at LEP, then the phenomenon of resonant depolarization will permit an absolute energy calibration of 20 MeV.
24. S. C. Berridge et al., OREXP-88-1102 (1988), and J. Brau private communication.
25. M. Böhm, A. Denner, W. Hollik, Nucl. Phys. B 304 (1988) 687; F. A. Berends, W. Hollik, R. Kleiss, Nucl. Phys. B 304 (1988) 712;
26. R. Kleiss, in reference 7 (1989) and reference 6 (1989) and references therein. The Bhabha Monte Carlo generators are: BABAMC, second reference in [25]; BHLUMI by S. Jadach, B. F. L. Ward, unpublished.
27. W. Beenakker, W. Hollik, Z. Phys. C 40 (1988) 141.
28. A. A. Akhundov, D. Y. Bardin, T. Riemann Nucl. Phys. B 276 (1986)
29. D. C. Kennedy, J. M. Im, B. W. Lynn, R. G. Stuart, SLAC-PUB-4128 (1988) and Nucl. Phys. B 321 (1989) 83 (The program Expostar does not yet include the additional vertex corrections for $Z \rightarrow b\bar{b}$ mentioned in section 2)
30. R. N. Cahn, Phys. Rev. D 36 (1987) 2666.
31. S. G. Gorishny, A. L. Kataev, S. A. Larin, JINR E2-88-254.
32. W. de Boer, in reference 6, p.293.
33. B. A. Kniehl, J. H. Kühn, R. G. Stuart, in reference 5, p.158.
34. F. A. Berends, G. J. H. Burgers, W. L. van Neerven, Nucl. Phys. B 297 (1988) 429; Erratum Nucl. Phys. B 304 (1988) 92;
35. E. A. Kuraev, V. S. Fadin, Sov. Journ. Nucl. Phys. 41 (1985) 466; G. Altarelli, G. Martinelli in reference 4, p.47; O. Nicrosini, L. Trentadue, Phys. Lett. 196B (1987) 551.
36. D. R. Yennie, S. C. Frautschi, H. Suura, Annals of Physics 13 (1961) 379; J. Alexander, G. Bonvicini, P. Drell, R. Frey, Phys. Rev. D 37 (1988) 56 and SLAC-PUB-4376 (1987).
37. Program ZBATC: G. Burgers, W. Hollik, in reference 5, p.136. Program ZSHAPE: W. Beenakker, F. A. Berends, S. van der Marck (including results from G. Burgers, W. Hollik).
38. Program MOE: G. Bonvicini, L. Trentadue, UM-HE-88-36; Program DYMU2: J.-E. Campagne, R. Zitoun, LPNHE-88.08.
39. S. Jadach, B.F.L. Ward, SLAC-PUB-4834 and TPJU-15/88.
40. R. Marshall, RAL-84-033 (1984).
41. J. Drees, K. Mönig, H. Staeck, S. Überschar, in reference 5, p. 317.
42. A. Djouadi, Z. Phys. C 39 (1988) 561
43. C. Albajar et al., UA1, Phys. Lett. 186B (1987) 247; ARGUS Collab., Phys. Lett. B 192 (1987) 245; CLEO Collab., R. Fulton et al., invited talk at XXIVth Conf. on HEP (Munich, 1988).
44. A. Blondel, B. W. Lynn, F. M. Renard, C. Verzegnassi, Nucl. Phys. B 304 (1988) 438.
45. M. Cvetič, B. W. Lynn, Phys. Rev. D 35 (1987) 51, C. Verzegnassi in reference 5, p. 204.
46. R. H. Dalitz, G. R. Goldstein, R. Marshall, Z. Phys. C 42 (1989) 441.

- 47. J. H. Kühn, F. Wagner, Nucl. Phys. B 236 (1984) 16.
- 48. S. Jadach, Z. Was, in reference 6, p. 129
- 49. J. Carr, work in progress.

**QED radiative corrections at the Z^0 :
theory versus implementation**

R. BATTISTON, G. BILEI, G. MANTOVANI, M. PAULUZZI, A. SANTOCCHIA
AND L. SERVOLI

*Dipartimento di Fisica and Sezione INFN
I-06100 Perugia, Italy*

Abstract

The role of the QED radiative corrections at the Z^0 energy is briefly reviewed. Although A_{LR} and the other polarization asymmetries are rather insensitive to these corrections, measurements of Z^0 (un)polarized cross section(s), of Bhabha rates in the luminosity monitors and of other asymmetries require a good understanding of QED effects even if polarization is available. We also overview the various Monte Carlos that have been developed in the last few years and are available in order to implement these corrections in the experiments.

Presented by R. Battiston at the SLD Physics Retreat, July 31-August 4, 1989.
Kirkwood, Ca

1. Introduction

When a high energy electron collides with a high energy positron and the two annihilate, both particles, traveling at about the speed of light in the other charge field, undergo a strong acceleration and must emit electromagnetic radiation, i.e. photons. Due to the emitted radiation, the energies of the incoming particles are modified: if the cross section rapidly varies with the c.m. energy, like in the vicinity of a resonance, the effective annihilation cross section will be correspondingly modified and the resonance shape distorted.

These basic facts have important implications on the precision measurements that will be performed at the Z^0 to test the validity of the Standard Model: in order to compare the experimental results with the electroweak predictions one must carefully take into account the QED corrections. It turns out in fact, that these corrections at the Z^0 are much larger, $\sim 30\%$, than the electroweak effects, $O(1\%)$, one is interested to measure. It then follows that accurate QED predictions are badly needed, otherwise it will not be possible to perform precise electroweak measurements at the Z^0 .

The size of these corrections is intrinsically dependent on the experimental characteristics like the acceptance or the cuts applied to remove the background: when detailed predictions are needed, only a Monte Carlo allows one to take into account these effects.

In the last few years, the needs of Z^0 physics have motivated a lot of work on QED radiative corrections (RC): more precise calculations have been made available and implemented in Monte Carlo programs, reaching a much better level of accuracy than before. In this paper we summarize the level of understanding of the RC problem: we will approach QED RC from the experimentalist point of view, briefly discussing their effects on some of the quantities that will be measured at the Z^0 energy, both with and without polarized beams.

2. QED RC at the Z^0 energy

The fact that each annihilating e^+e^- pair radiates before (and after) the collision, translates to the fact that the higher order corrections to the Born -level Feynman diagrams (Figure 1) cannot be of $O(\alpha)$ but must be much larger. For a long time it has been known¹ that their size depends on how stringent is the request to measure the exclusive cross section $e^+e^- \rightarrow f\bar{f}$ without photons in the final state²⁻⁴.

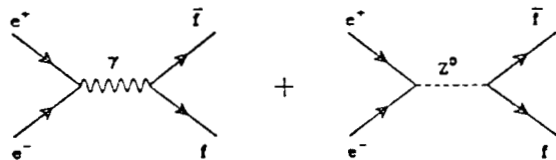


Figure 1. First order Feynman diagrams for the reaction $e^+e^- \rightarrow f\bar{f}$.

In a "gedanken" experiment with infinite energy resolution, these corrections are large enough to cancel exactly the first order result, that is, the strictly exclusive cross-section is zero. However, realistic experiments cannot count photons, in particular soft photons⁵: in fact a given experiment, due to its finite angular and energy resolution and limited acceptance, can only measure the inclusive cross-sections for $e^+e^- \rightarrow f\bar{f} + (\text{unknown number of})\gamma$. Each experiment will then measure a different inclusive reaction and the comparison between the various measurements can only be done using QED calculations that take into account the experimental cuts.

We can write the one loop radiatively corrected result (Figure 2) in term of the maximum photon energy that the experiment cannot (or will not!) resolve:

$$\sigma_1(s) = \sigma_0(1 + \delta_1 + \beta \log \frac{k_{max}}{E_{beam}}) \quad (1)$$

where $\delta_1 = \frac{3}{4}\beta + \frac{\alpha}{\pi}(\frac{\pi^2}{3} - \frac{1}{2})$ arises from effects due to the virtual photon clouds and $\beta = \frac{2\alpha}{\pi}(\log \frac{s}{M_e^2} - 1)$ is the so called "Bond" factor⁶. The logarithmic term takes into account the real radiation: in the case where no cuts are applied this term is equal to zero but can be very large if $k_{max} \ll E_{beam}$ and can even drive σ_1 negative!

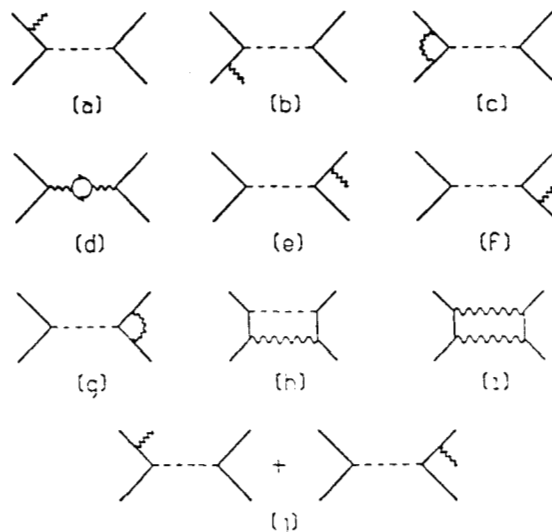


Figure 2. $O(\alpha)$ corrections to the Born cross section.

In addition to effects due to the experimental cuts, at the Z^0 there is an intrinsic cut due to Γ_Z , leading to a large correction $\beta \log \frac{\Gamma_Z}{2E} \sim -38\%$: due to the rapidly falling cross section, it is very unlikely to emit, near the Z^0 , photons having an energy larger than \sim half of the width! At the Z^0 the term $\delta_1 = +8.7\%$, and then the minimal correction (without experimental cuts) that one should apply to the Born term is about -30% .

Higher order corrections are also not negligible if one aims to reach $< 1\%$ experimental accuracy: the second order corrections are still at the level of $+4\%$

mainly due to the real photons' contribution. It has been shown⁴ that, in the limit $k_{max} \ll E_{beam}$ (good approximation in the case of the Z^0), it is possible to take into account the emission of real photons by *exponentiating* their contribution. In fact it is possible to write the total cross section in the form:

$$\sigma = \sigma_0(1+\delta_1+\delta_2)(1+\beta \log \frac{\Gamma}{2E} + \frac{1}{2!}\beta^2 \log^2 \frac{\Gamma}{2E} + \frac{1}{3!}\beta^3 \log^3 \frac{\Gamma}{2E} + \dots) \rightarrow \sigma_0(1+\delta_1+\delta_2)(\frac{\Gamma}{2E})^\beta, \quad (2)$$

where we neglected small terms of order 10^{-4} due to third order virtual contributions. One should note that the resummation done in Eqn. 2 takes care of the disease of the total cross section becoming negative if $k_{max} \ll E_{beam}$: now the total cross section smoothly goes to zero if very stringent cuts on the visible photon energy are applied. Equation 2 takes into account only soft photons and the hard photon contributions (true $O(\alpha^n)$, $n = 1, 2$ terms) must be added through explicit calculation of the relevant Feynman diagrams, as is done in Ref. 7 for the $O(\alpha^2)$ correction to the initial state.

The result of Eqn. 2 has been recently generalized⁸ taking into account the exponentiation of both initial, final and interference contributions, including also collinear hard-photon effects resummed to all orders. Excluding the hard photon emission, the accuracy of this prediction is, in the case of the total and differential cross sections, of the order of 0.5%⁹.

Another approach to exponentiation¹⁰⁻¹² makes use the structure function formalism developed for QCD¹³. With this formalism it is possible to include in the calculation also most of the leading contributions due to hard photon emission; the accuracy of these calculations is very good, at the level of 0.3%¹⁴ and this technique appears well suited for use in a Monte Carlo generator¹⁵. One should note that effects due to interference between initial and final photon emissions are not (yet) taken into account in this approach. In Figure 3 are shown the results of the calculation for the normalized total cross-section made in Reference 12: from the figure the relative size of the various contributions can be appreciated.

A third approach¹⁶ to the RC problem makes use of the (exclusive) exponentiation following the YFS⁴ theory. The result is a very accurate description of RC treating on equal grounds both the soft and the hard part of the photon spectrum: its implementation in a Monte Carlo¹⁷ is particularly effective, and gives the best available simulation of multiple photon effects, including the correct angular and momentum distributions.

The interference between initial and final state photon emission deserves a special comment. There is a general argument suggesting that these effects should be small when running at the peak and without applying strict energy cuts. The finite Z^0 lifetime ($\tau \sim \frac{1}{\Gamma_Z}$) lets the initial and final states be separated in time. Given that interference is a quantum effect governed by the uncertainty principle $\Delta E \Delta t \geq 1$, if the uncertainty on the energy of the intermediate Z^0 state, ΔE , starts to be comparable or smaller than Γ_Z , because of experimental cuts, then the initial and final states are no longer distinguishable and interference effects are important. As we will see in the following, due to the antisymmetric nature of the QED interference correc-

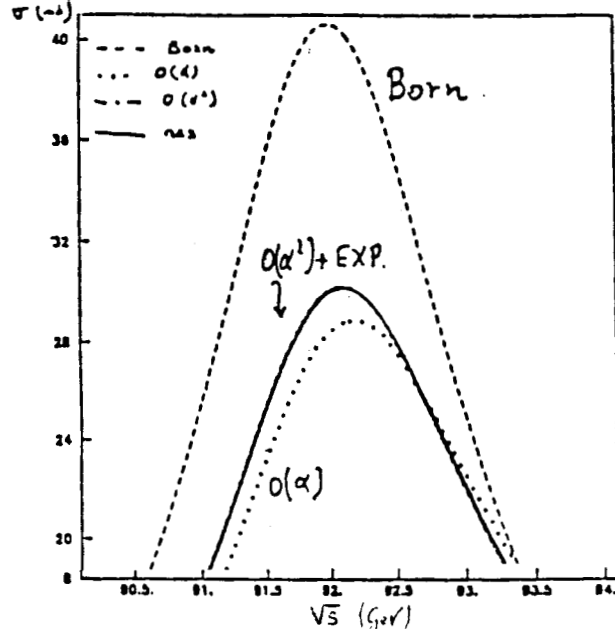


Figure 3. $\sigma(e^+e^- \rightarrow \text{hadrons})$ calculated using the structure function formalism of Ref. 12. Dashes - Born cross section; dots - $O(\alpha)$ corrections; dotdashes - $O(\alpha^2)$; solid - $O(\alpha^2)$ +exponentiation.

tions, this fact has important consequences for the measurement of forward-backward asymmetries (much less in the case of total cross sections), and it is not yet properly taken into account in a Monte Carlo treatment.

The above list of calculations is clearly incomplete, but the bottom line should now be sufficiently clear: a number of accurate calculations on QED RC are available, and their predictions for the total $e^+e^- \rightarrow f\bar{f}$ cross section (even with some experimental cuts) do agree within a fraction of a percent. When calculating differential cross sections, as in the case of the forward-backward asymmetries, the existing predictions are less accurate because of QED interference effects, often not included in the calculations: at the Z^0 peak these effects are small but can become important when the experimental cuts are taken into account.

3. QED versus electroweak RC

In the previous section, we discussed only photonic corrections to the lowest order Feynman diagrams. However, in the unified electroweak theory, all gauge bosons play a similar role and should be treated on equal grounds. For example, corrections to the lowest order coming from diagrams where virtual/real photons are emitted from virtual W 's, should in principle be included in the calculation. Similar diagrams appear in the complete electroweak *two-loop* corrections, but such a calculation does not exist (and probably will not exist for a while, because of its complexity).

It is fortunate that these effects are small at the Z^0 energy (e.w. gauge bosons other than the photon have masses $\simeq M_Z$) and it is possible to neglect them¹⁸! This will not be the case at higher energies.

It then follows, that at the Z^0 it is possible to treat the large photonic corrections

independently from the pure e.w. corrections. This has important consequences on the implementations of RC in the experiments: one can develop QED dresser Monte Carlos to take into account experiment-dependent effects and correct the data for efficiency and acceptance, without bothering to include in the generators the e.w. effects. These may be taken into account in an experiment-independent way at later stages of the analysis; the overall accuracy of the theoretical prediction is expected to be better than 0.5%¹⁹.

4. Experimental implementation of QED RC

In this section we give some examples of the influence of experimental cuts on the size of RC. Cuts are unavoidable in an experiment for two main reasons:

1. limited angular coverage
2. background rejection.

One may be surprised to find that also in the case of simple final states like $e^+e^- \rightarrow Z^0 \rightarrow \mu^+\mu^-$ one should apply cuts to eliminate the background. In Figure 4 we see that in order to eliminate the t - *channel* contamination that is very large at low μ -pair masses, we must apply a cut on $\mu_{\mu\mu}^2$ which will affect the way the RC influence the data. This is illustrated in Table 1 where we list partial widths and cross section changes, as the cut on the dimuon mass is varied from $m_{\mu\mu} \geq 1$ to $\geq 82 \text{ GeV}/c^2$. If very severe cuts are applied, then the $\mu^+\mu^-$ cross section changes by -6%, or about 0.5 ν families; the result of a direct measurement of the width is one order of magnitude less sensitive to this cut. Similar arguments also apply for other cuts like the minimum azimuthal angle cut due to the acceptance of the apparatus or the acollinearity cut between the two particles in the final state.

Due to interference between initial and final states, the influence of cuts on A_{FB}^μ is much more important. Table 2 shows the effect of a cut on E_γ , the radiated energy, on the measured value of A_{FB}^μ : one sees that for low energy thresholds the corrections due to the interference term can be larger than the asymmetry. The results presented in Table 2 were obtained by semianalytical calculations: a satisfactory Monte Carlo approach is not yet available, and it is clearly needed if we want to measure A_{FB}^μ !

Another example of the importance of RC is the case of A_{pol}^τ . It has been shown in Ref. 22 that the corrections to A_{pol}^τ are very small ($\simeq 2.3\%$), as one expects from the fact that $A_{pol}^\tau = A_{LR}$: the only problem is that experiments do not measure directly this quantity, but they extract it from the π^\pm energy distribution. The π 's do radiate photons, and their energy spectrum is modified accordingly; this effect changes the prediction by 22% (no cuts on E_γ), about three times the expected experimental error!

The only way to properly simulate these effects in the experiment is by mean of a Monte Carlo. As we have shown in the second section, various formalisms exist to compute RC to the Born result: it is then not surprising that different algorithms have been developed to perform Monte Carlo simulations.

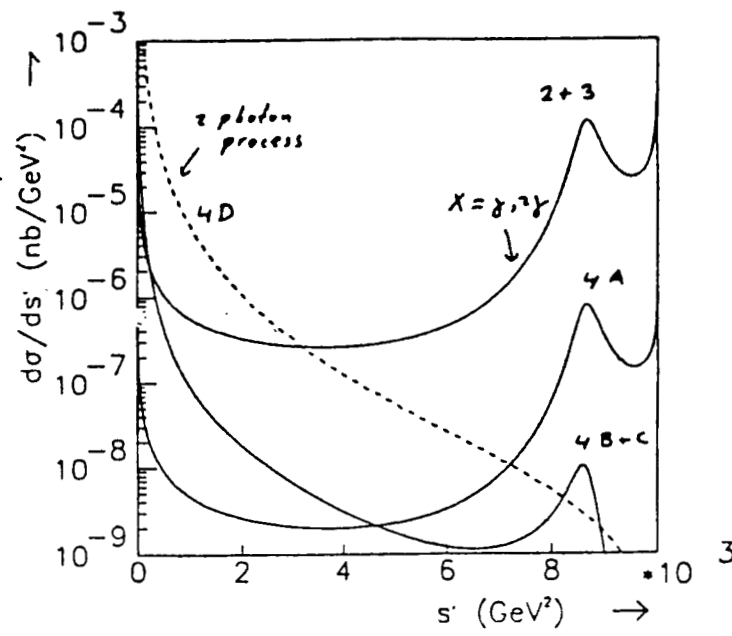


Figure 4. μ pair invariant mass distribution for different contributions to the reaction $e^+e^- \rightarrow \mu^+\mu^- + X$, above the Z^0 ($\sqrt{s} = 100$ GeV). 2+3 and 4A correspond to s -channel contributions (signal), while 4D (t -channel) and 4BC (s - t interference) are spurious contributions²⁰.

Table 1. Influence on the line shape of a cut on $m_{\mu\mu}^2$ ²⁰.

Particle	$m_{\mu\mu}^{min} \frac{GeV}{c^2}$	$\sigma_{peak}(nb)$	\sqrt{s}_{max}	FWHM (GeV)
	1	6.603	92.095	2.930
d -quarks	45	6.596	92.095	2.930
	82	6.549	92.095	2.927
	1	1.453	92.094	2.966
μ	42	1.438	92.094	2.955
	82	1.363	92.097	2.949

Although the goal of these QED dressers is the same, that is to simulate the experiment-dependent effects due to RC, and the agreement between them is increasingly good²³, the strategies that are used in the algorithms are often very different. Examples of two very different approaches are the cases of MOE¹⁵ and YFS2¹⁷ (or KORAL-Z²⁴ that also treats the case of τ pair production). In the first case the formalism of the structure function is used to simulate iteratively the emission of (many) photon(s) from the particles in the initial (final) state, while in the second the rigorous YFS theory is used in the generation algorithm. Both programs are able

Table 2. Initial, final and interference QED corrections to A_{FB}^μ for different photon energy cuts (units 10^{-2})²¹.

<i>Photon</i>	<i>init.</i>	<i>+init.exp.</i>	<i>+fin.</i>	<i>+interf.</i>	<i>all – interf.</i>
<i>no cut QED</i>	0.312	1.086	1.084	1.117	0.033
<i>+EW</i>	-0.134	0.691	0.689	0.723	0.034
<i>10 GeV QED</i>	0.415	1.185	1.047	1.123	0.056
<i>+EW</i>	-0.27	0.794	0.668	0.726	0.058
<i>1 GeV QED</i>	1.574	2.061	1.830	3.192	1.362
<i>+EW</i>	1.209	1.728	1.482	2.949	1.467

to produce multiple real photons, which is important to simulate subtle experimental effects: MOE is the fastest Monte Carlo generator available but YFS2 is more robust from the point of view of its theoretical foundations. However, given their good agreement with the existing analytical calculations (better than 1% for the $\mu^+\mu^-$ total cross section), the choice to use one or the other is probably a matter of taste. Other Monte Carlo like DYMU2²⁵ and FPAIR²⁶ use the available $O(\alpha^2)$ exact calculation in the initial state and are useful for cross checks because one knows exactly which terms are included in the Monte Carlo.

The situation is different in the case of angular distributions. Given the importance of the interference between photon emission in the initial and final states in the case of the asymmetries, one absolutely needs a Monte Carlo including QED interference. A multiphoton Monte Carlo taking into account these effects would then be extremely welcome in the club!

Before leaving this section, we must spend a few words to discuss the situation in the Bhabha sector. A precise knowledge of the Bhabha cross section is needed for at least two reasons:

1. small angle luminosity measurement
2. accurate measurement of $\frac{\Gamma_{ee}}{\Gamma_Z}$ ²⁷.

In the first case one needs $O(1\%)$ accuracy in the very forward direction, where the t – channel dominates, while in the second case one needs a $\simeq 3 \cdot 10^{-3}$ level of accuracy at larger angle where both the t – channel and the s – channel contribute to the cross section.

The studies performed in the case of small angle Bhabhas, show a good agreement ($\simeq 1\%$) between existing $O(\alpha)$ Monte Carlos, in the simplified case where symmetric angular cuts are applied²³. The first order corrections and the effects of exponentiation have in this case a small influence when simulating experimental effects (mainly

edge effects). The situation is less clear if asymmetric cuts are applied. However, in order to calculate the absolute normalization one needs to go above the first order. For these purposes a multiphoton Monte Carlo like BHLUMI²⁸ (YFS algorithm), should be very useful.

Much less work has been done at larger angles where one could measure with high precision $\frac{\Gamma_{ee}}{\Gamma_Z}$ through the Z/Bhabha ratio. The existing $O(\alpha)$ calculation and Monte Carlo²⁹ are not sufficiently accurate. The analytic formulae of Ref. 8 contain the exponentiation of all large contributions including interference effects, both for soft and hard collinear photons: however, a Monte Carlo including these formulae is not yet available. Our group started recently to work on this subject, with the goal of developing a large angle Bhabha Monte Carlo in the next future.

5. QED RC and polarization

When e^- polarized beam are available, QED RC corrections will still be important when measuring the luminosity and polarized cross-sections. However, as shown in Ref. 30, it is possible in this case to define clever observables (polarization asymmetries) that in addition to being very *sensitive* to the EW virtual corrections are also very *insensitive* to QED (and QCD) RC.

The basic reason for that is that photon emission is insensitive to the electron polarization: A_{LR} and other polarization asymmetries are ratios of cross sections where only the electron spin is flipped. In addition, at the peak A_{LR} is independent of the properties of the final state, including photon emission. The effect due to initial state radiation is simply to smear and lower the effective energy of the annihilation as shown in Fig. 5. The presence of the photon propagator (the γZ interference term is zero at the resonance) induces a small flavour dependence of A_{LR} (Figure 6) that can significantly be reduced by suitable cuts on the visible photon energy. Similar arguments also apply for other polarization asymmetries like A_{LR}^f .

It is then very fortunate for SLD that the most important measurements with polarized beams are almost insensitive to QED (and QCD) RC!

6. Conclusions

In this paper we discussed the QED RC to various measurements performed at the Z^0 energy. The understanding of RC has improved dramatically in the last few years, and at least for the cases where initial-final interference is negligible, the agreement between the different predictions and Monte Carlos is now very good.

However, progress needs to be made in at least two areas:

- Monte Carlo implementation of the interference between initial and final states, important for asymmetries other than $A^{(f)}_{LR}$:
- analytical and Monte Carlo development on large angle Bhabhas, important for the measurement of $\frac{\Gamma_{ee}}{\Gamma_Z}$ and (at high statistics) for the overall cross-section normalization.

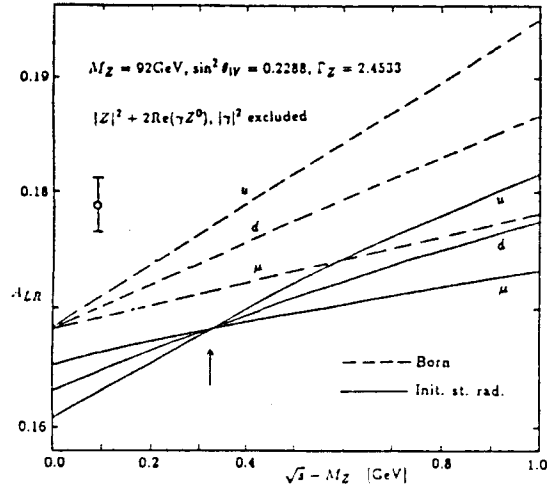


Figure 5. Influence of the initial state radiation on A_{LR} , excluding the contribution of the photon propagator ³¹.

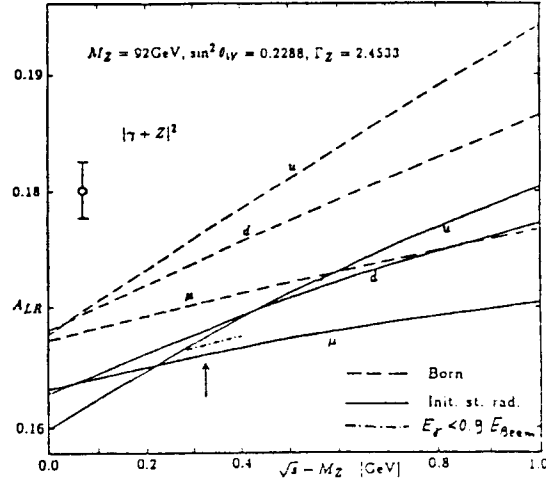


Figure 6. Effect of the photon propagator on A_{LR} ³¹.

We thank all the people who helped, through discussions, presentations and private communications, to improve our understanding of RC. In particular we would like to thank G. Bonvicini, M. Greco, T. Hansl-Kozanecka, O. Nicrosini, P. Rankin, Y. Srivastava, L. Trentadue, B.F.L. Ward and Z. Was.

REFERENCES

1. F. Bloch and A. Nordsieck, Phys. Rev., 52, 54 (1937)
2. J. Schwinger, Phys. Rev., 76, 790 (1949).
3. J.M. Jauch and F. Rohrlich, Hel. Phys. Acta, 27, 613 (1954).
4. D.R. Yennie and H.Suura, Phy. Rev., 105, 1378 (1957); D.R. Yennie, S.C.Frautschi and H. Suura, Ann. of Phys., 13, 379 (1961).
5. E. Etim. G. Pancheri and B. Toushek, Nuovo Cimento, 51B, 276, (1967).
6. M. Greco, G. Pancheri-Srivastava and Y. Srivastava, Phys. Lett., 56B, 367. (1975). The name for the β factor comes from the fact that at ADONE it was equal to 0.07.
7. F.A.Berends, G.J.H. Burgers and W.L. Van Neerven, Phys. Lett., 185B, 395. (1987).
8. M. Greco, Riv. del Nuovo Cimento, 11, 1 (1988).
9. F.Aversa and M.Greco, LNF 89/025 PT, (1989), submitted to Phys. Lett.
10. E.A.Kuraev and V.D. Fadin, SJNP, 41(3), 466, (1985).
11. G. Altarelli and G. Martinelli, CERN/EP 86-02, pag. 47.
12. O. Nicrosini and L. Trentadue, UPRF-86-132; O. Nicrosini and L. Trentadue. CERN-TH-5437/89 (1989); S. Catani and L. Trentadue. UPRF-89/197 (1989).
13. G. Altarelli and G.Parisi. Nucl. Phys., B126, 298. (1977).
14. J. Alexander, G.Bonvicini, P. Drell, R.Frey, Phys. Rev., D37, 56, (1988).
15. J. Alexander, G. Bonvicini, P.Drell and R. Frey, Mark II/SLC-Physics Working Group Note # 1-12, in Proceedings of the Third Mark II Workshop on SLC Physics, SLAC-Report-315 (1987).
G. Bonvicini and L.Trentadue, UM-HE-88-36 (1988).
16. S. Jadach and B.F.L. Ward, Phys. Rev., D38, 2897,(1988); ERRATUM:ibid, 39, 1471, (1989); S. Jadach and B.F.L. Ward, CERN-TH-5399/89, (1989).
17. S. Jadach and B.F.L. Ward, SLAC-PUB-4834, (1988).
18. If high-precision measurement of A_{FB}^b are performed, one should probably take into account higher order electroweak corrections, including photon radiation from virtual W 's. B.F.L. Ward private communication.
19. M. Martinez, talk given at the NATO Advanced Research Workshop on Radiative Corrections: Results and Perspectives, July 10-14, 1989, Brighton.
20. F. Berends, talk given at the NATO Advanced Research Workshop on Radiative Corrections: Results and Perspectives, July 10-14, 1989, Brighton.
21. M. Sachwitz, talk given at the NATO Advanced Research Workshop on Radiative Corrections: Results and Perspectives, July 10-14, 1989, Brighton.
22. Z. Was, talk given at the NATO Advanced Research Workshop on Radiative Corrections: Results and Perspectives, July 10-14, 1989, Brighton.
23. R. Kleiss, summary talk given at the NATO Advanced Research Workshop on Radiative Corrections: Results and Perspectives, July 10-14, 1989, Brighton.
24. S. Jadach, R.G. Stuart. Z. Was and B.F. Ward. KORAL-Z. Long Write-up. preliminary version, (1988).
25. J.E. Campagne, talk given at the NATO Advanced Research Workshop on Radiative Corrections: Results and Perspectives. July 10-14, 1989, Brighton.

26. S. van der Mark, talk given at the NATO Advanced Research Workshop on Radiative Corrections: Results and Perspectives, July 10-14, 1989, Brighton.
27. R. Battiston, M. Pauluzzi, A. Santocchia, L. Servoli, presented by M. Pauluzzi, these Proceedings.
28. S. Jadach and B.F.L. Ward, UTHEP-88-11-01 (1988).
29. M. Böhm, A. Denner and W. Hollik, N.P., B304, 687, (1988); F.A. Berends, R. Kleiss and W. Hollik, N.P., B304, 712, (1988).
30. B.W. Lynn and C. Verzegnassi, Phys. Rev., D35, 3326, (1987).
31. J.H. Kühn, in Proceedings of the Workshop on Polarization at LEP, CERN 9-11 November, 1987.

Precision measurements of electroweak observables
and testing of the Standard Model

R. BATTISTON

*Dipartimento di Fisica and Sezione INFN
I-06100 Perugia, Italy*

Abstract

We discuss to what extent the measurement of various physical observables at the Z^0 peak will test the Standard Model, with two parameters still unknown, M_{top} and M_{Higgs} . In particular we concentrate on the role of A_{LR} and Γ_{ee}/Γ_Z . We show how a precise measurement of Γ_{ee}/Γ_Z corresponds to an accurate test of the Standard Model that is independent of the value of the two unknown masses. This variable is also useful to disentangle $\rho_0 < 1$ from M_{top} .

Presented at the SLD Physics Retreat, July 31- August 4, 1989, Kirkwood, Ca

1. Introduction

One of the most important goals of Z^0 physics is the accurate test of the electroweak part of the Standard Model. A precise measurement of the Z^0 mass ($\delta M_Z/M_Z \simeq 20 \div 40 \text{ MeV}$) will reduce to two the number of unknown quantities still present in the model, M_{top} and M_{Higgs} ; the test will then correspond to the exploration of this two dimensional parameter space. Unless the Higgs is light ($\leq 50 \text{ GeV}/c^2$), we will not be able to produce these particles at the Z^0 , and the measurement of their masses will only be possible through virtual effects affecting the physical observables (electroweak radiative corrections). These corrections are rather small; the more precise the measurements of the physical observables, the deeper will be our understanding of the validity of the Standard Model. It follows that the following question can be addressed: given the expected experimental accuracy, what will be the ultimate precision in the test of the minimal SM with two free parameters?

In this paper we try to answer qualitatively this question. We overview both the sensitivity and the (ultimate) experimental accuracy of many physical observables that will be measured in the next few years and discuss the rather extraordinary role that three of them will play in the high precision test of the SM: A_{LR} , Γ_{ee}/Γ_Z , and M_W (or M_W/M_Z). The consequences for the physics with the SLD detector are also discussed.

2. Electroweak physical observables and the test of the SM

Table 1 lists the main electroweak physical observables that will be accessible to the experimentalists in the next few years. The second column in Table 1 shows the minimal ($\rho_0 = \rho_{tree} = \frac{M_W^2}{M_Z^2 \cos^2 \theta_W} = 1$) SM prediction^{1,2} for $M_Z = 91 \text{ GeV}/c^2$, $M_{top} = 100 \text{ GeV}/c^2$ and $M_{Higgs} = 100 \text{ GeV}$.³⁻¹¹

In order to evaluate the *sensitivity* of each observable X to the two unknown masses (M_{top} and M_{Higgs}) we calculated the theoretical uncertainty, δX_{th} , that is the difference between the extreme values that X takes when M_{top} and M_{Higgs} vary between 60 and 200 GeV/c^2 and between 10 and 1000 GeV/c^2 respectively (column 2 and 3 of the table). Also the corresponding experimental error is reported: column 5 and 6 show the precision already obtained while column 7 and 8 give the best guess about the ultimate accuracy the experiments will reach in the next few years.

The ratio between the experimental error and the theoretical uncertainty gives an idea of the role each variable will play in the test of the SM. That is shown in column 9: a large value of the ratio ($\gg 1$) indicates variables that will have a sufficiently good experimental precision to *measure* M_{top} and/or M_{Higgs} . On the other side, small ratios indicate quantities that will test the SM with a precision of the order of their relative experimental error, independently from the exact value of the unknown masses.

Table 1. Measurement of electroweak observables and the test of the Standard Model: the SM predictions (column 2) correspond to $M_Z = 91 \text{ GeV}$, $M_{top} = 100 \text{ GeV}$, $M_{Higgs} = 100 \text{ GeV}$.

<i>Observable</i>	$X_{SM}^{(1,2)}$	$\delta X_{th}^{(1,2)}$	$\frac{\delta X_{th}}{X}$	$\delta X_{exp}^{(now)}$	$\frac{\delta X_{exp}^{(now)}}{X}$	$\delta X_{exp}^{(ult)}$	$\frac{\delta X_{exp}^{(ult)}}{X}$	$\frac{\delta X_{th}}{\delta X_{exp}^{(ult)}}$
R_ν^0	0.31	0.0115	3.7%	0.035 ⁽³⁾	1%	0.035	1%	3.7
$M_W(\frac{\text{GeV}}{c^2})$	79.96	0.960	1.4%	0.600 ⁽⁴⁾	0.7%	< 0.100 ⁽⁵⁾	$< 0.12\%$	> 11.7
M_W/M_Z	0.877	0.011	1.3%	0.007 ⁽⁴⁾	0.8%	≤ 0.003 ⁽⁶⁾	$\leq 0.3\%$	≥ 4.3
$\Gamma_Z(\text{GeV})$	2.459	0.031	1.3%	0.400 ⁽⁷⁾	15%	~ 0.030	$\sim 1.2\%$	~ 1
$\Gamma_{ee}(\text{MeV})$	82	1.2	1.5%	19 ⁽⁸⁾	25%	~ 1.6	$\sim 2\%$ ⁽⁹⁾	~ 0.75
$\Gamma_{ee}/\Gamma_Z(10^{-2})$	3.364	0.01	0.4%	—	—	0.003 ⁽¹⁰⁾	0.1%	4
$\Gamma_{inv}(\text{MeV})$	496	6.6	1.3%	145 ⁽⁷⁾	30%	~ 40	$\sim 8\%$	~ 0.16
$\Gamma_{bb}(\text{MeV})$	373	3	0.8%	—	—	—	$\sim \text{few}\%$	$<< 1$
A_{FB}^μ	0.012	0.009	60%	—	—	0.0035 ⁽⁶⁾	30%	2
A_{FB}^u	0.063	0.025	40%	—	—	0.010 ⁽¹¹⁾	16%	2.5
A_{FB}^s	0.089	0.034	38%	—	—	0.007 ⁽¹¹⁾	8%	4.7
A_{FB}^c	0.063	0.025	40%	—	—	0.007 ⁽¹¹⁾	11%	3.6
A_{FB}^b	0.089	0.034	38%	—	—	0.005 ⁽¹¹⁾	6%	6.8
A_{LR}	0.13	0.05	40%	—	—	0.0013 ⁽⁶⁾	1%	40
A_{pol}^τ	0.13	0.05	40%	—	—	0.010 ⁽⁶⁾	8%	5

As one can see from the Table, one can classify the observables in two categories, depending on their sensitivity:

1. $\frac{\delta X_{th}}{X} \sim 40 - 60\%$
2. $\frac{\delta X_{th}}{X} \simeq O(1\%)$.

To the first category belong all the asymmetries: their relative *sensitivity* is large. However, in most cases, the experimental accuracy that will be reached (often after many millions of Z^0 's), will not allow one to exploit all the sensitivity available. It follows that these measurements will only represent $O(10\%)$ tests of the SM. This is less true for A_{FB}^b : the experimental error on A_{FB}^b quoted in Table 1 comes from a study of the DELPHI Collaboration ¹¹ and depends on the b -tagging capability of

the experiment. Due to its superior vertex detector and particle identification, SLD could eventually achieve a better result.

The important exception to the general behavior of the asymmetries is represented by A_{LR}^{12} , which exhibit an extraordinary ratio of 40 between its sensitivity and its ultimate experimental accuracy. In addition this ultimate accuracy can be reached with relatively small statistics; in fact after only $\sim 10^5 Z_0$ the statistical error is already dominated by the systematics on the beam polarization. As one can see from a comparison with all the other variables listed in Table 1 A_{LR} is really the "queen" not only of all asymmetries but also of all observables. That is the reason why A_{LR} is the most important measurement of SLD at polarized SLC.

To the second category belong all Z^0 (partial) width(s) and branching ratios and also two other observables included in the table but not measurable at SLC. M_W (M_W/M_Z) and R_ν^0 . Again, most observables in this category will have an error comparable with or larger than, the theoretical uncertainty: their measurements will then correspond to $O(1\%)$ tests of the minimal SM that are independent of M_{top} and M_{Higgs} .

One exception is the case of M_W : in fact, at LEP II it will be possible to measure the W mass with an accuracy about one order of magnitude better than at the colliders (there one will measure with good accuracy M_W/M_Z). If M_W will be measured with this accuracy, its value will be very sensitive to the unknown parameters of the SM. When high precision measurements of both A_{LR} and M_Z are available, they will give the most accurate limits on both M_{top} and M_{Higgs} . Figure 1 shows what this result could eventually look like.

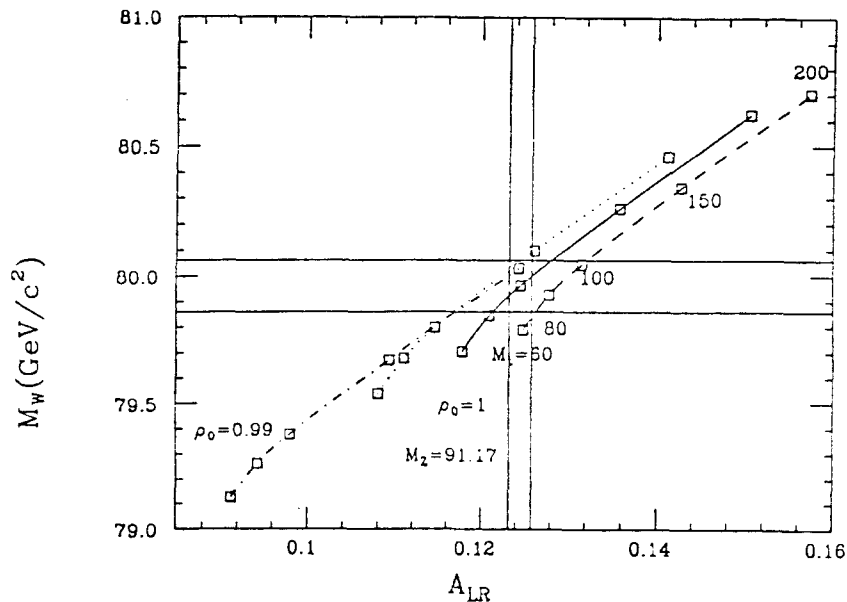


Figure 1. Hypothetical constraints on M_{top} , M_{Higgs} obtained from precise measurements of A_{LR} ($\sigma = \pm 1\%$) and M_W ($\sigma = \pm 0.12\%$). We used $M_Z = 91.17 \text{ GeV}/c^2$, $\rho_0 = 1$ and $M_{Higgs} = 10$ (dots), 100 (full) and 1000 GeV/c^2 (dashes). The case $\rho_0 = 0.99$, $M_{Higgs} = 100 \text{ GeV}/c^2$ is also shown (dotdashes).

The case of Γ_{ee}/Γ_Z deserves particular comment: as we have shown¹⁰, in SLD it will be possible to measure this quantity with an accuracy limited only by the statistics available ($< 1\%$ -or $< 0.15 \nu$ families- with $\sim 2 \cdot 10^5 Z^0$). The ultimate experimental limit is probably in the 10^{-3} range, and it matches the corresponding theoretical uncertainty. It then follows that an accurate measurement of this quantity will allow a test of the SM that is independent of M_{top} and M_{Higgs} , at the 10^{-3} level of precision. This is probably the most accurate parameter-independent test of the SM that will be available in the next few years. Figure 2 illustrates this by showing the hypothetical result of combined high precision measurements of both Γ_{ee}/Γ_Z and of A_{LR} . The figure shows clearly that the e^+e^- branching ratio is very insensitive to the unknown masses, at the 10^{-3} level of accuracy.

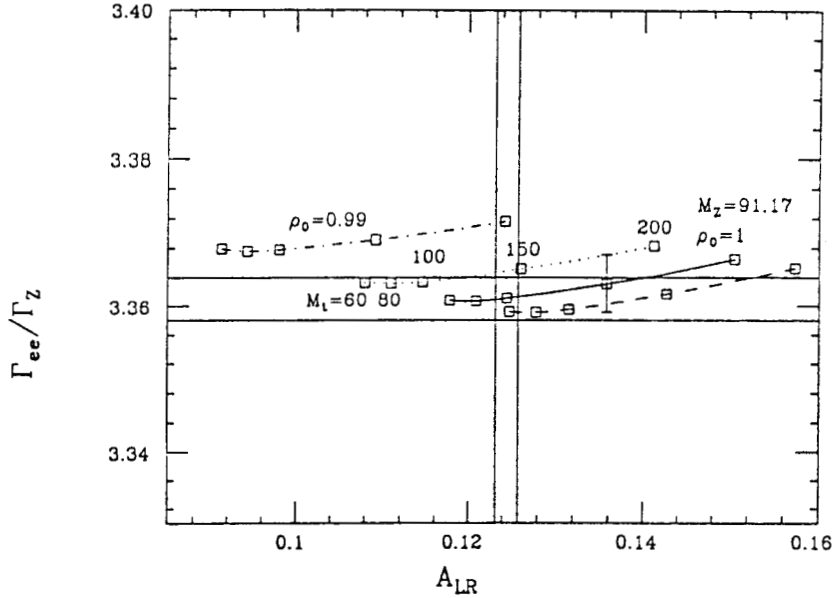


Figure 2. Hypothetical result of the combined precise measurements of A_{LR} ($\sigma = \pm 1\%$) and of Γ_{ee}/Γ_Z ($\sigma = \pm 0.1\%$). We used $M_Z = 91.17 \text{ GeV}/c^2$, $\rho_0 = 1$ and $M_{Higgs} = 10$ (dots), 100 (full) and $1000 \text{ GeV}/c^2$ (dashes). The case $\rho_0 = 0.99$, $M_{Higgs} = 100 \text{ GeV}/c^2$ is also shown (dotdashes). The error bar corresponds to $\delta M_Z = \pm 20 \text{ MeV}/c^2$

From Fig. 1 it appears that, when an asymmetry is combined with M_W (or R_ν^0)² high top masses can counter-balance the effect of deviations from the minimal SM characterized by $\rho_0 < 1$. The use of the e^+e^- branching ratio, which is sensitive to the vertex corrections¹³ to the $b\bar{b}$ decay of the Z^0 , will be extremely useful to disentangle the two effects, as shown in Fig. 2.

As shown in Table 2 the e^+e^- branching ratio is the best physical observable for this purpose: due to larger experimental errors, both Γ_Z , Γ_{bb} and the other branching ratios will be (much) less sensitive to $\rho < 1$.

3. Conclusions

In this paper we have reviewed the role of the various electroweak observables in testing of the SM with two unknown parameter, M_{top} and M_{Higgs} . The most accurate

Table 2. Sensitivity of electroweak observables to ρ_0

<i>Observable</i>	$X_{SM}^{(1,2)}$	$ \delta X_{th} _{\rho_0=0.99}^{(1,2)}$	$\delta X_{exp}^{(ult)}$
R_ν^0	0.31	0.008	0.035 ⁽³⁾
$M_W(\frac{GeV}{c^2})$	79.96	0.580	< 0.100 ⁽⁵⁾
M_W/M_Z	0.877	0.006	0.003 ⁽⁶⁾
$\Gamma_Z(GeV)$	2.459	0.033	~ 0.050
$\Gamma_{ee}(MeV)$	82	1	~ 1.6
$\Gamma_{ee}/\Gamma_Z(10^{-2})$	3.364	0.007	0.003 ⁽¹⁰⁾
$\Gamma_{inv}(MeV)$	496	5	~ 40
$\Gamma_{bb}(MeV)$	373	5	$\sim few\%$
A_{FB}^μ	0.012	0.01	0.0035 ⁽⁶⁾
A_{LR}	0.13	0.03	0.0013 ⁽⁶⁾
A_{pol}^τ	0.13	0.03	0.010 ⁽⁶⁾

constraints on these masses will come by the future measurements of A_{LR} and M_W (LEP II) or M_W/M_Z (SPS,TEVATRON) combined. The measurements of the other asymmetries will in general contribute only marginally to the test. The importance of the role of a measurement of A_{FB}^b will crucially depend on the experimental capability of efficiently tagging $b\bar{b}$ events.

The precise measurement of the e^+e^- branching ratio will allow the most accurate test of the SM that is independent of the values of M_{top} and M_{Higgs} : in addition it will be very important in order to disentangle M_{top} from deviations from the minimal SM with $\rho_0 < 1$.

In conclusion, with $\sim 10^5$ polarized events, SLD will have a unique possibility to contribute in a decisive way to the test of the SM. In addition to the accurate measurement of the "queen" of the electroweak observables, A_{LR} , the good angular coverage of the tracking system will allow a precise measurement of Γ_{ee}/Γ_Z and a correspondingly good parameter-free test of the SM. Finally, using a superior vertex detector and an excellent particle identification system, SLD should also be able to perform a good measurement of A_{FB}^b even with limited statistics.

I thank A. Blondel for a ride from Brighton to Paris, during which I learned a lot about the subtleties involved in the test of a two parameter SM. I thank also B.F.L. Ward for drawing my attention to the plans to improve in the future the measurement of A_{FB}^b at LEP.

REFERENCES

1. D.C. Kennedy, J.M. Im, B.W. Lynn and R.G. Stuart, Slac-Pub 4128 (1988); Computer program Expostar 1.0, version X4. This version include $b\bar{b}$ vertex corrections proposed by G. Burgers partly using code written by W. Hollik for ZBATCH. Courtesy of A. Blondel.
2. A. Blondel, contribution to the LEP Physics Workshop, CERN, 20 february 1989, CERN-EP/89-84 (1989).
3. CDHS Collaboration, H. Abramowicz et al., Phys. Rev. Lett., 57, (1986), 298; also Ref. 2.
CHARM Collaboration, J.V.Allaby et al., Phys. Lett., 177B, (1986), 446; J.V.Allaby et al., Z.Phys., C36, (1987), 611.
4. CDF Collaboration, F. Abe et al., Phys. Rev. Lett., 63, (1989), 721; CDF Collaboration, talk given by M.K. Campbell at the XIV International Symposium on Lepton and Photon Interactions, Stanford, August 6-12, 1989.
5. G.Barbiellini et al., in Physics at LEP, vol II, p.1. edited by J. Ellis and R. Peccei, CERN 86-02 (1986).
6. G. Altarelli, talk given at the XIV International Symposium on Lepton and Photon Interactions, Stanford, August 6-12. 1989.
M. Swartz, Lectures given at the 1989 SLAC Summer Institute, July 10-21. 1989.
7. MARK II Collaboration, talk given by G.Feldman at the XIV International Symposium on Lepton and Photon Interactions, Stanford, August 6-12, 1989.
8. MARK II Collaboration, talk given by A. Weinstein at the XIV International Symposium on Lepton and Photon Interactions, Stanford, August 6-12, 1989.
9. Assuming 2% normalization error.
10. Contribution presented by M. Pauluzzi, these Proceedings.
11. J. Drees in Proceedings of the Workshop on Polarization at LEP, CERN 9-11 November 1987, p. 89; also Ref. 6.
At LEP I and with the present vertex detectors, it does not seem likely that A_{FB}^b will be measured with a sufficiently high precision to compete with A_{LR} : however, given the importance of this measurement. one expects that the improvement of the existing LEP vertex detectors will be one of the first priorities in the experimental upgrades that are expected in the next few years. as it has been discussed in the recent Blois meeting. B.F.L. Ward. private communication.
12. B.W. Lynn and C. Verzegnassi, Phys. Rev., D35, 3326, (1987).
13. W. Beenakker, W. Hollik, Z. Phys., C40, (1988) 141; F.A. Berends, G. Burgers, W. Hollik, W.L. van Neerven, Phys. Lett., 203B, (1988), 177.

High-precision measurement of Γ_Z in SLD using large-angle e^+e^- events

R. BATTISTON, M. PAULUZZI, L. SERVOLI AND A. SANTOCCHIA

*Dipartimento di Fisica and Sezione INFN
I-06100 Perugia, Italy*

Abstract

The accuracy of the measurements of the Z^0 width at SLC will be limited by the error on the normalization from the small-angle luminosity monitors at the level of a few per cent. We show how the measurement of large-angle e^+e^- events produced near to the Z^0 pole will enable a much more accurate measurement of Γ_Z or Γ_{ee}/Γ_Z to be made by SLD, as soon as the integrated luminosity is larger than $\sim 1 \text{ pb}^{-1}$. This measurement is free from most systematic errors affecting the other proposed techniques. Using this method, the expected relative accuracy on Γ_{ee}/Γ_Z after $\sim 2.4 \cdot 10^5 \text{ } Z^0$ is $\sim 1 \cdot 10^{-2}$ ($1.5 \cdot 10^{-1}$ neutrino families), with a systematic limit which is about one order of magnitude smaller.

Presented by Michele Pauluzzi at the SLD Physics Retreat, July 31- August 4, 1989, Kirkwood, Ca

1. Introduction

One important physics goal of SLD is the accurate testing of the validity of the Standard Model of electroweak interactions, looking for the presence of new, unexpected physical effects.

After a precise measurement of the Z^0 mass is available, precise measurements of other physical quantities like the Z^0 width and (un)polarized asymmetries will help the understanding of the particle content of the theory and of the role of $\sin^2\theta_W$. The more precise the measurements of these quantities, the deeper will be our understanding of the validity of the Standard Model: it follows that every effort should be made to reach the best possible accuracy. However it is foreseeable that, in many cases, systematic errors will fairly quickly dominate over statistical errors, thereby setting the limit to the ultimate precision.

The case of the measurement of the Z^0 width is very instructive.

It has been shown¹ that, after $\sim 4 \text{ pb}^{-1}$ the statistical errors on Γ_Z , obtained in the fit of the line shape using dimuons, will be $< 15 \text{ MeV}$, while the corresponding systematic error, mainly due to quadratic terms in the uncertainties on the luminosity measurements across the resonance, is expected to be in the range of a few tens of MeV , thus dominating the overall error. Similarly the measurement of Γ_Z through the determination of $\sigma_{\mu^+\mu^-}$ at the peak will be affected by an error of about 2–3%, again due to the uncertainty on the knowledge of the luminosity measured by the small angle Bhabha detectors. Finally, the measurement of the invisible Z^0 partial width, both at the peak² and above,³ will also reach a similar level of precision.

In this paper we show how, at or close to the peak, the study of the reaction $e^+e^- \rightarrow e^+e^-$ at large angles may give precise information on the Z^0 width. The basic idea is the following: the large angle e^+e^- events are a mixing of $Z^0 \rightarrow e^+e^-$ decays and t –channel large angle Bhabha scattering, plus contributions (small at the Z^0 peak) due to various interference terms. It is easy to show that in a detector like SLD, covering the region above $\theta \simeq 13^\circ$, the Z^0 and the γ contributions are about the same. By choosing suitable variables, it is possible to build luminosity-independent quantities that depend on the Z^0 propagator and then on Γ_Z . As soon as the integrated luminosity is larger than 1 pb^{-1} the statistical accuracy on Γ_Z starts to be better than 2%, the typical systematic limit of other methods using the luminosity measurement.

The variables we use are ratios of e^+e^- rates measured within the same detecting device so that systematics due to detection efficiency tend to cancel. In addition, the error induced by the uncertainty on the absolute scale of the c.m. energy can be made negligible by running at energies very close to the Z^0 peak. To exploit fully the intrinsic accuracy of this method, it is important to understand the size of the QED radiative correction to the variables we introduced: we show how an accuracy on the radiative corrections of a few 10^{-3} should induce an error on Γ_Z smaller than 10^{-3} . In fact, it turns out that Γ_Z or Γ_{ee}/Γ_Z can in principle be measured with an ultimate overall accuracy of one part in 10^{-3} after $\sim 10^7 Z^0$. The accuracy that can be obtained is then one order of magnitude better than with other methods discussed in the literature. A nice feature is that one needs only to run at (or very close to) the

peak: thus, this way of measuring Γ_Z with high precision takes advantage of the total luminosity delivered without affecting other measurements that need the maximum available statistics.

This method can be used at SLC only by SLD, because of the need for accurate electron tracking in the forward regions (above $\simeq 13^\circ$), that is not possible with the MARK II detector.

2. The e^+e^- cross section at the Z^0 peak.

The differential e^+e^- cross section, calculated from the four Feynman diagrams shown in Fig. 1, contains ten contributing amplitudes: due to the presence of the diverging t -channel the total cross section depends strongly on the minimum angle, θ_{min} chosen in the integration. Figure 2 shows the lowest order total cross section together with the ten different contributions for the case $\theta_{min} = 15^\circ$. Unless otherwise specified, we use throughout the paper the following SM parameters. $M_Z = 92 \text{ GeV}/c^2$, $\sin^2\theta_W = 0.2290$, $M_{top} = 65 \text{ GeV}/c^2$, $\Gamma_Z = 2.493 \text{ GeV}$.

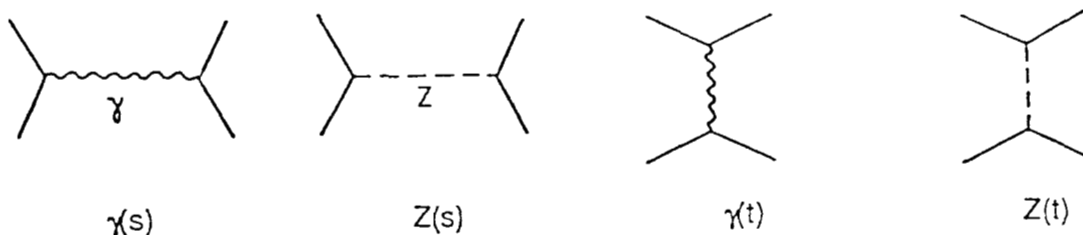


Figure 1. Lowest order Feynman diagrams for the Bhabha scattering. Throughout the paper we number the ten corresponding contributions to the total cross section as follows: #1 $\gamma(s)\gamma(s)$, #2 $\gamma(s)\gamma(t)$, #3 $\gamma(t)\gamma(t)$, #4 $\gamma(s)Z(t)$, #5 $\gamma(t)Z(t)$, #6 $Z(t)Z(t)$, #7 $Z(s)\gamma(s)$, #8 $Z(s)\gamma(t)$, #9 $Z(s)Z(t)$ and #10 $Z(s)Z(s)$.

In Fig. 2 we note that at the peak most of the terms are small or negligible. At the Born level, all interference terms with the $Z(s)$ diagram (#7,8 and 9), vanish because the real part of the Z^0 propagator goes to zero. One should note that these contributions to the total cross section become non-negligible when we move slightly away from the pole. Of the remaining contributions, only three contribute significantly to the total cross section: these are $\gamma(t)\gamma(t)$ (#3), $Z(s)Z(s)$ (#10) and (one order of magnitude smaller) $\gamma(t)\gamma(s)$ (#2). As shown in Fig. 3, at the pole the relative size of the first two terms depends on θ_{min} . At lowest order, they are equal for $\theta_{min} = 13^\circ$: at smaller θ_{min} , $\gamma(t)\gamma(t)$ dominates, while at larger θ_{min} , $Z(s)Z(s)$ is the most important. The $\gamma(t)\gamma(s)$ term is always much smaller.

The total cross section as a function of the energy is shown in Fig. 4 for different values of θ_{min} .

Throughout the paper, we show, where relevant, the radiatively corrected distributions obtained using the analytical formulae discussed in Ref. 4 that include exact

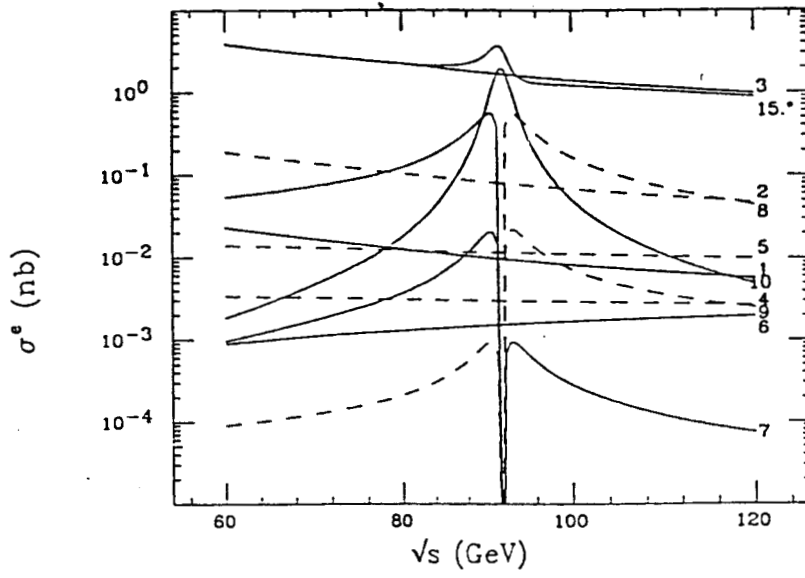


Figure 2. Lowest order total Bhabha cross section (labelled 15°) together with the ten contributions versus the c.m. energy. Dashed lines correspond to negative contributions from interference terms. Minimum angle 15° .

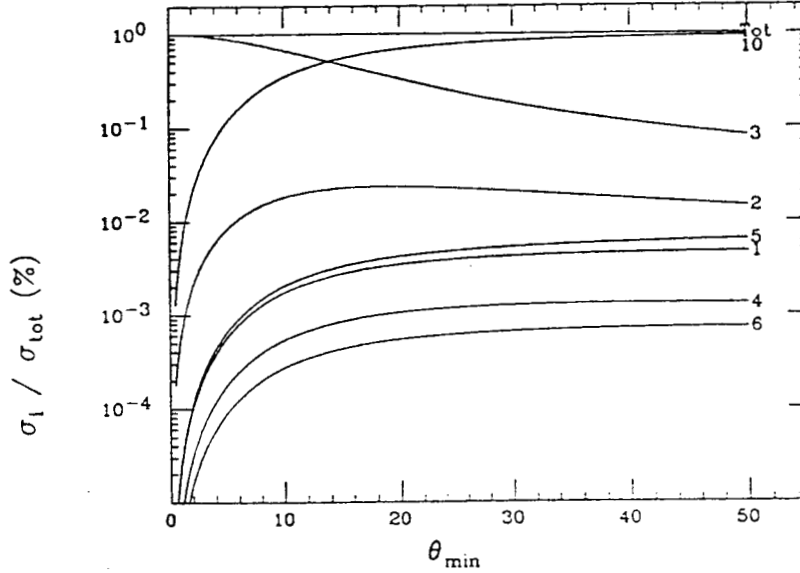


Figure 3. Relative size of the contributing term to the total cross section at the peak versus θ_{min} . Lowest order calculation.

analytical expressions for all one loop diagrams, and soft and collinear hard-photon effects resummed to all orders. We use the following choice of parameters: energy threshold for photon detection $\Delta = \frac{E_\gamma}{E_{beam}} = 10^{-2}$ and angular resolution of the calorimeter $\delta = 1^\circ$. These formulas include all double logarithmic terms of the form $(\frac{\alpha}{\pi}) \ln(\frac{s}{m_e^2}) \ln(\Delta, \frac{\Gamma_Z}{M_Z})$, $(\frac{\alpha}{\pi}) \ln \delta^2 \ln \Delta$, simple logs as $(\frac{\alpha}{\pi}) \ln(\frac{s}{m_e^2})$, $(\frac{\alpha}{\pi}) \ln(\Delta, \frac{\Gamma_Z}{M_Z}, \delta^2)$, resummed to all orders and all finite terms of order $(\frac{\alpha}{\pi})$: they are correct up to $O(1\%)$,

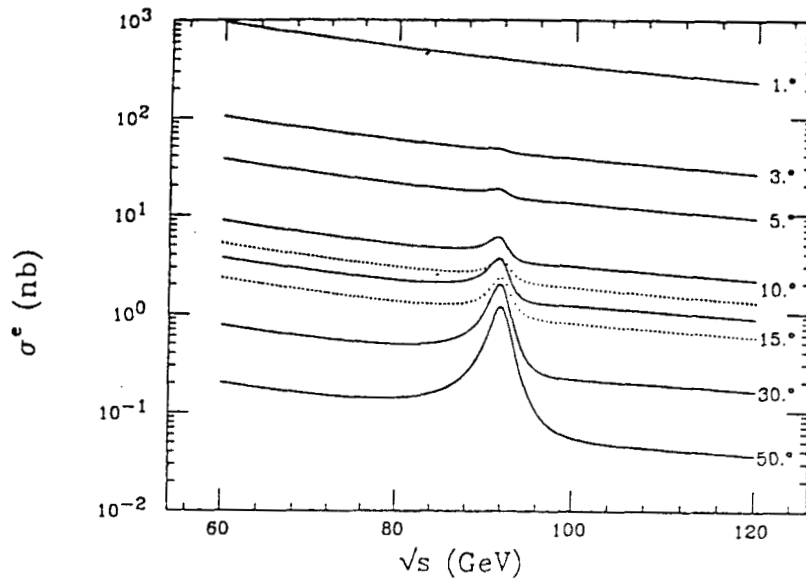


Figure 4. Lowest order Bhabha cross section versus the c.m. energy, for different values of θ_{min} . For two values of θ_{min} the radiatively corrected result is also shown (dotted lines) ⁴

and are then useful for a first comparison with the Born results. In the paper we did not include hard (visible) photon emission to any order, in particular terms of order $(\frac{\alpha}{\pi})(\Delta, \delta)$.

We may build different quantities that are sensitive to the Z^0 cross section, using the fact that t -channel Bhabha's have a different angular distribution than $Z^0 \rightarrow e^+e^-$. We investigated four quantities having the above property ⁵;

$$A_{FB}^e(x_1) = \frac{\int_0^{x_1} (\frac{d\sigma}{dz}) dz - \int_{-x_1}^0 (\frac{d\sigma}{dz}) dz}{\int_{-x_1}^{x_1} (\frac{d\sigma}{dz}) dz} \quad (1)$$

$$R_1(x_1, x_2) = \frac{\int_0^{x_1} (\frac{d\sigma^*}{dz}) dz - \int_{-x_2}^0 (\frac{d\sigma^*}{dz}) dz}{\int_{-x_2}^{x_1} (\frac{d\sigma^*}{dz}) dz} \quad (2)$$

$$R_2(x_1, x_2) = \frac{\int_{-x_2}^{x_2} (\frac{d\sigma^*}{dz}) dz}{\int_{-x_1}^{x_1} (\frac{d\sigma^*}{dz}) dz} \quad (3)$$

$$R_3(x_1, x_2) = \frac{\int_{-x_2}^{x_2} (\frac{d\sigma^*}{dz}) dz}{\int_{x_2}^{x_1} (\frac{d\sigma^*}{dz}) dz + \int_{-x_1}^{-x_2} (\frac{d\sigma^*}{dz}) dz} \quad (4)$$

where $z = \cos\theta$, $\frac{d\sigma}{dz}$ is the e^- differential cross-section while $\frac{d\sigma^*}{dz}$ is the sum of the differential cross-section for e^- and e^+ , and $x_1 = \cos\theta_1 = \cos\theta_{min} > x_2 = \cos\theta_2 > 0$. In this analysis we use $\theta_{min} = 15^\circ$. A_{FB}^e makes use of the charge measurement of the final state electrons while the others rely on the use of an additional angular

cut in the central region. All variables are characterized by the property of having a maximum (minimum) very close to the Z^0 peak; they map the Z^0 shape in a luminosity-independent way. The size of this maximum (minimum) depends on $\theta_1 = \theta_{\min}$, θ_2 and on the ratio $Z^0/t - \text{channel} Bhabha$, while its location depends on the Z^0 mass; both size and location are affected by QED radiative corrections. For a given variable chosen, when running at the energy where it reaches its extreme value, the measurement will be insensitive to the error on the beam energy, another kind of systematic that could affect the measurement of the width.

In the next paragraphs the sensitivity that can be reached by this kind of measurements is discussed in greater detail.

3. Sensitivity to the Z^0 propagator and to the width.

The quantities defined in the previous section, $X_i(x_1, x_2)$, $i = A_{FB}^e, R_1, R_2, R_3$, depend on σ_{Z^0} , the contribution to the cross-section relative to the $Z(s)Z(s)$. At lowest order:

$$\sigma_{Z^0} = \frac{12\pi}{M_Z^2} \frac{s\Gamma_{ee}^2}{(s - M_Z^2)^2 + \frac{s^2\Gamma_Z^2}{M_Z^2}} \longrightarrow \frac{12\pi}{M_Z^2} \left(\frac{\Gamma_{ee}}{\Gamma_Z} \right)^2 \Big|_{s=M^2} \quad (5)$$

If we assume the validity of the minimal SM, apart for electroweak effects depending on M_{top} and M_{Higgs} (the dependence of Γ_Z on these parameters is discussed in another contribution to these proceedings⁶), once M_Z is known with an accuracy of a few tens of MeV , then σ_{Z^0} does not depend on additional parameters (i.e. $\Gamma_{ee} = \Gamma_{ee}(M_Z)$, $\Gamma_Z = \Gamma_Z(M_Z)$ and so on). If instead the minimal SM is not valid then the value of σ_{Z^0} obtained by a measurement of X_i will be different from the prediction. This could be due to deviations for the SM that affect only Γ_Z (like the presence of additional ν 's, light SUSY particles⁷ and so on) or the ratio $\Gamma' = \frac{\Gamma_{ee}}{\Gamma_Z}$ (like unexpected virtual corrections). A precise measurement of X_i will then provide a powerful way to test the SM.

If we call $N(x_1) = L_{tot}\sigma(x_1)$ the number of e^+e^- events seen by a detector covering down to $\cos\theta_{\min} = x_1$ after an integrated luminosity L_{tot} , then the statistical errors on the above quantities turn out to be:

$$\frac{\delta A_{FB}^e(x_1)}{A_{FB}^e} \sim \frac{1}{\sqrt{N(x_1)}} \frac{1}{A_{FB}^e} \sqrt{1 - A_{FB}^e{}^2} \quad (6)$$

$$\frac{\delta R_1(x_1, x_2)}{R_1} \sim \frac{1}{\sqrt{N(x_1)}} \frac{1}{R_1} \sqrt{1 - R_1^2} \quad (7)$$

$$\frac{\delta R_2(x_1, x_2)}{R_2} \sim \frac{1}{\sqrt{N(x_1)}} \sqrt{\frac{1 - R_2^2}{R_2}} \quad (8)$$

$$\frac{\delta R_3(x_1, x_2)}{R_3} \sim \frac{1}{\sqrt{N(x_1)}} \sqrt{\frac{(1 + R_3)(1 + 2R_3)}{R_3}} \quad (9)$$

We note that these statistical errors decrease substantially when we accept events at very small angles where the cross section diverges. However, in that case also the sensitivity to the Z^0 term vanishes due to the dominance of the Bhabha contribution. It is easy to show that the gain in accuracy on the measurement of the Z^0 contribution when θ_{min} is below $\sim 13^\circ$ is marginal; in addition, to exploit this additional accuracy we must be able to control the systematics at the level of the (very small) statistical errors. In other words to perform our normalization we do not need a t -channel cross-section much larger than σ_{Z^0} . If we decide to go to smaller θ_{min} we will at most gain a factor $\sqrt{2}$ in statistics at the expense of being far more sensitive to systematic errors.

The result of our study is that a good compromise for SLD is to use $\theta_{min} \sim 15^\circ$; if θ_{min} is larger than 30° then the sensitivity of this method starts to be uninteresting, because in this way a too small fraction of t -channel cross-section is collected.

We turn now to the sensitivity of X_i to the various parameters (M_Z, Γ_Z and Γ_{ee}) that appear in Eqn. 5. If we run at the energy where the (radiatively corrected) quantity X_i has its extreme value, then $\frac{\partial X_i}{\partial \sqrt{s}}$ is zero. Because of the very similar dependence of Eqn. 5 on M_Z^2 and s it follows that also $\frac{\partial X_i}{\partial M_Z^2}$ will be close to zero, and then we are not sensitive to the error on the value of M_Z when doing this measurement. Assuming the validity of the SM, it then follows that the sensitivity to other parameters like $\sin^2\theta_W$, Γ_{ee} , Γ_Z also vanishes at that energy (i.e. $\frac{\partial X_i}{\partial \Gamma_{ee}} \simeq \frac{\partial X_i}{\partial \Gamma_{Z^0}} \simeq 0$).

On the other hand, if the Γ_{ee} or Γ_Z deviates from the minimal SM predictions, the effects on X_i may be rather large.

Let us discuss the case of the width. After introducing $\delta^*\Gamma_Z = \Gamma_Z^{MSM} - \Gamma_Z^{MSM}$, we note that the sensitivity $\frac{\partial X_i}{\partial \delta^*\Gamma_Z}|_{15^\circ}$ is weakly dependent on Γ_Z^{MSM} when running at energies close to the peak: the radiative corrections change its value by a few %.

In Fig. 5 we show the sensitivity expected for X_i after 1 pb^{-1} integrated luminosity, as a function of θ_2 for fixed $\theta_{min} = 15^\circ$. The following choice of θ_2 optimizes the sensitivity for R_1, R_2 and R_3 : $\theta_2 = 43.7^\circ, 32^\circ$ and 34.2° respectively. From the plot it appears that the most sensitive quantity is $R_2(\delta^*\Gamma_Z/\Gamma_Z|_{(1 \text{ pb}^{-1})} = 2.5 \cdot 10^{-2})$ followed by A_{FB}^e and R_3 ($3.1 \cdot 10^{-2}$). In Fig. 5 we also show the sensitivity to $\delta^*\Gamma_Z$ of

$$R_\mu(x_1) = \frac{\int_{-x_1}^{x_1} (\frac{d\sigma_\mu^*}{dz}) dz}{\int_{-x_1}^{x_1} (\frac{d\sigma_Z^*}{dz}) dz} \quad (10)$$

where we use the ratio of $\mu^+\mu^-$ (or $\tau^+\tau^-$) over e^+e^- cross sections (without measurement of the charge sign) in the same angular region. From a statistical point of

view R_μ is even better than R_2 ($\delta^*\Gamma_Z/\Gamma_Z|_{(1pb^{-1})} = 1.7 \cdot 10^{-2}$) but, because R_μ is the ratio of two different final states, it will be more sensitive to the systematics on the detection efficiencies, ϵ_e and ϵ_μ , to an extent that could possibly limit its use in a very high precision measurement of Γ_Z (see also the next paragraph). In Fig. 6 the statistical accuracy $\delta^*\Gamma_Z/\Gamma_Z$ is plotted versus the total integrated luminosity. In the case of R_2 , after an integrated luminosity larger than $\sim 1 pb^{-1}$ the statistical accuracy is better than 2.5%, the typical systematic error that affects the other measurements of the width. Extrapolating to $L \simeq 3 \cdot 10^2 pb^{-1}$ ($\sim 10^7$ visible Z^0 's) we obtain the ultimate statistical accuracy of this method, $\delta^*\Gamma_Z/\Gamma_Z = \delta^*\Gamma'_Z/\Gamma'_Z \simeq 10^{-3}$, that is equivalent to $\simeq 1.5 \cdot 10^{-2}$ additional neutrino families.

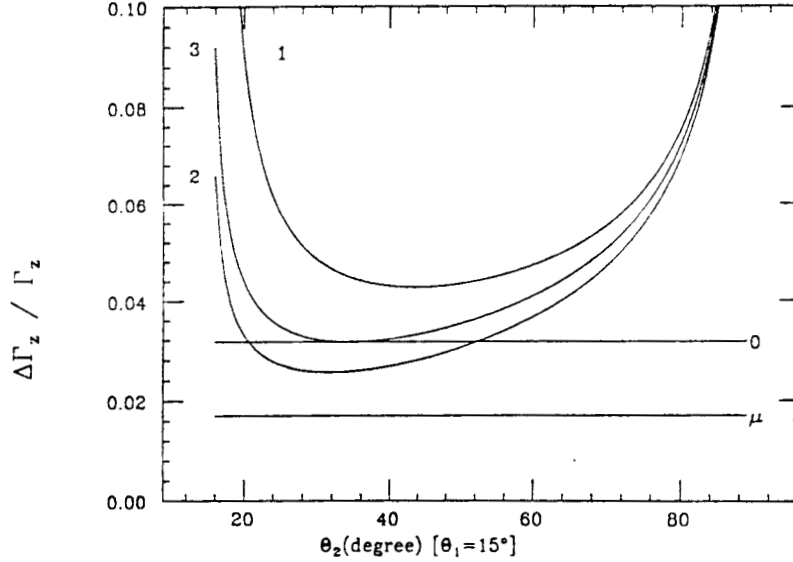


Figure 5. Accuracy on the total width versus θ_2 for the various quantities defined in the text ($\theta_{min} = 15^\circ$): (0) A_{FB}^e , (1) R_1 , (2) R_2 , (3) R_3 and (μ) R_μ .

4. Systematics

The systematics that will affect the measurement of X_i come from three possible sources

- knowledge of the machine parameters,
- understanding of the experiment
- understanding of the theory.

From Eqn. 6 to Eqn. 9 it follows that in order to reach the 10^{-3} level of precision on the total width, we have to keep the systematics on X_i below $\sim 5 \cdot 10^{-4}$.

a) Machine parameters (luminosity, beam energies).

A strong point in favor of the use of the variables we introduced is that, being the ratio of cross sections measured within the same detector, they are luminosity-independent quantities.

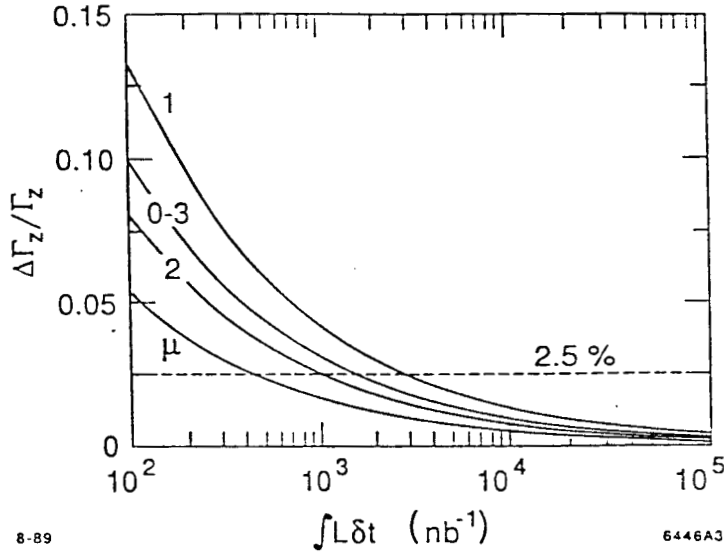


Figure 6. Statistical accuracy on the measurement of the total width as a function of the integrated luminosity with $\theta_{min} = 15^\circ$ and θ_2 as discussed in the text: (0) A_{FB}^e , (1) R_1 , (2) R_2 , (3) R_3 and (μ) R_μ .

The dependence of R_2 on the c.m. energy is shown in Fig. 7. The maximum value of R_2 is very close to the pole for the choice of θ_{min} and θ_2 discussed above. The distance between the maximum and the pole $\Delta E = \sqrt{s} - M_Z$ is 100 MeV at lowest order and becomes 150 MeV after the radiative corrections are applied. When running at that energy, the systematic error on the beam energy, that would otherwise severely limit the accuracy of the width measurement, can be substantially reduced. Recalling that the radiative corrections move the peak of the $\mu^+\mu^-$ cross section by $\simeq 100$ MeV above the Z^0 pole⁸ we note that this requirement does not affect significantly the Z^0 production rate. A simple calculation shows that, when running 150 MeV above the pole, the error induced by a systematic uncertainty $\delta\sqrt{s} = 50$ MeV (25 MeV) is $\delta R_2/R_2 \simeq \delta\Gamma_Z/\Gamma \simeq 1.10^{-3}$ ($2.5 \cdot 10^{-4}$). We would like to stress the importance of running where R_2 (or X_i) takes its extreme value; as soon as we move from this energy by few tens of MeV (the machine energy resolution) the sensitivity to the width is dominated by $\delta\sqrt{s}$. We note that in the case of R_μ this requirement on ΔE has significant consequences on the cross section collected. In this case the radiatively corrected ΔE is much larger $\simeq 600$ MeV: by running at that energy, one would then loose $\simeq 30\%$ of the total cross section.

The above arguments apply for all X_i : they are insensitive to the two main sources of error that affect the direct measurement of the total width, i.e. the systematic error on the luminosity and on the beam energies.

b) Experimental parameters (detection efficiency, charge measurement, θ_{min} , two-photon background)

In order to measure the ratio of two cross sections we must correct the number of

Finally, suitable cuts (for instance on e^+e^- acollinearity or invariant mass) must be studied to reject two photon events where only two electrons are detected in the detector.

The case of R_μ deserves further study: from one side this quantity has the best statistical sensitivity but from the other side the systematics on the detection efficiency do not cancel and could limit the precision on the width measurement.

c) Theory (QED, QCD and electroweak radiative corrections).

As one might expect, QED radiative corrections play an important role in the precise measurement of the width. A detailed knowledge of QED corrections is important in order:

- to build an accurate QED Monte Carlo needed to correct the measured value of $R_2(X_i)$ for experimental effects, (for instance detector acceptance and efficiency effects);
- to obtain the radiatively corrected prediction for $R_2(X_i)$. As we see from Fig. 7, both the location and the size of $Max(R_2(\sqrt{s}))$ are modified with respect to the Born prediction;
- to take into account the effects on $\Gamma_Z(\Gamma'_Z)$ due to final state photon radiation⁹.

Also the electroweak and, more importantly, the QCD corrections to the width⁹, have to be applied before the resulting Γ_Z (Γ') can be compared with the minimal SM prediction. A more accurate measurement of α_s would also improve the ultimate accuracy on the width: in fact the present uncertainty¹⁰ induces an error on Γ_Z of $4.6 \cdot 10^{-3}$.

In order to fully exploit the sensitivity of this measurement, the QED radiative corrections must be precisely known. If we try to extrapolate the results obtained with the analytical formulae of Ref. 4 we obtain that an accuracy of 3 parts in 10^{-3} on the knowledge of the QED radiative corrections should induce a relative error on the width smaller than 10^{-3} . This precision is what one could expect from a complete $O(\alpha)$ calculation including exponentiation of the large soft and collinear logarithms: a Monte Carlo based on such a calculation would then be essential to properly take into account the detector-dependent corrections. We are planning to work on this subject during the coming months.

The above results are in general valid for all quantities we introduced. However the numerical results, for instance the effects of the radiative corrections, clearly depend on the quantity chosen. In Table 1 the main properties of A_{FB}^e , R_2 and R_μ are given, that is the effects of the radiative corrections on the location of $Max(X_i)$ ($Min(X_i)$) with respect to the (uncorrected) Z^0 pole and on its size ($\delta X_i/X_i$), the 1 pb^{-1} statistical accuracy on the width and the sensitivity to θ_{min} . We note that the radiative corrections shift the position of $Max(X_i)$ ($Min(X_i)$) in a different way, depending on the variable: the choice of the variable will then determine at which c.m. energy the experiment should take data. As we have seen in this paper, that is very important in order to minimize the systematic error due to the knowledge of the beam energy. We recall that the formulae used in this paper do not contain $O(\alpha)$

radiative corrections relating to hard photon emission: the results shown in Table 1 must be recalculated using a full $O(\alpha)$ calculation, in order to obtain more reliable values for ΔE_{RC} .

Table 1. Properties of A_{FB}^e, R_2, R_μ

X_i	$\Delta E_{Born}(MeV)$	$\Delta E_{RC}(MeV)$	$\frac{\delta X_i}{X_i} (RC-Born)$	$\frac{\delta \Gamma_Z}{\Gamma_Z} _{1pb^{-1}}$	$\frac{1}{X_i} \frac{\partial X_i}{\partial \theta_{min}} _{15^\circ}$
A_{FB}^e	325	265	$-3.7 \cdot 10^{-2}$	$3.1 \cdot 10^{-2}$	$-7.7 \cdot 10^{-2}$
R_2	100	150	$4.7 \cdot 10^{-2}$	$2.5 \cdot 10^{-2}$	$6.9 \cdot 10^{-2}$
R_μ	500	600	$10.2 \cdot 10^{-2}$	$1.7 \cdot 10^{-2}$	$5.8 \cdot 10^{-2}$

5. Conclusions

In this paper we have shown how it is possible to perform a precise measurement of the Z^0 width in SLD by using e^+e^- produced at large angles. With the statistics expected at SLC in the next few years the sensitivity we can obtain will be much better than what one expects with other methods, reaching already the 1% level after $\sim 6 \cdot pb^{-1}$ of integrated luminosity. This method can be used only if an accurate electron tracking in the forward directions is available as in the case of the forward drift chambers of our detector. We introduced various quantities that can be used and we showed how they are insensitive to many experimental systematic effects. We also discussed the effects of the electromagnetic radiative corrections to intermediate angle Bhabha scattering, and we concluded that a calculation of the Bhabha cross section in this angular region having an accuracy of a few 10^{-3} is needed in order to exploit the accuracy of this method. Due to the importance of a very accurate measurement of the width, any effort to improve the knowledge of the radiative corrections to the Bhabha differential cross section below the 1% level, either analytically or using a Monte Carlo, is then well-motivated.

We thank M.Greco and B.F.L. Ward for stimulating discussions on QED radiative corrections to Bhabha scattering. One of the authors (R.B.) also thanks R.Barbieri for his useful suggestions.

REFERENCES

1. See for instance the contribution of A. Blondel et al. in Physics at LEP, edited by J.Ellis and R.Peccei, CERN 86-02 (1986).
2. G. Feldman, Mark-II/SLC-Physics Working Group Note # 2-24, in Proceedings of the Third Mark-II Workshop on SLC Physics, SLAC-Report-315, July 1987.
3. G. Barbiellini, B. Richter and J. Siegrist, Phys. Lett. B106, 414 (1981)
4. M. Greco, Riv. del Nuovo Cimento, 11, 1 (1988)
5. For a more detailed experimental study of the properties of A_{FB}^e see R.Battiston, M. Pauluzzi, L.Servoli and A.Santocchia, SLD Physics note #2 also in Proceedings of the NATO Workshop on "Radiative Corrections: Results and Perspectives", July 10-14, 1989, Brighton, UK
6. R.Battiston, "Comments on high-precision measurement of Γ_Z ", these Proceedings
7. R. Barbieri, G. Gamberini, F. Giudice and C. Ridolfi, Phys. Lett. B195, 500. (1987); also Nucl. Phys. B296, 75 (1988)
8. F.A.Berends, G. Burgers, W. Hollik and W.L. van Neerven, Phys. Lett. B203, 1771 (1988)
9. W. Hollik, CERN-TH.5426/89 (1989)
10. W. de Boer, SLAC-PUB 4428 (1987); see also G. Altarelli, CERN-TH-5290/89 (1989)

A Test of Electron-Muon Universality Using Polarization Cross Section Asymmetries.

John M. Yamartino

Introduction

One of the most precise determinations of $\sin^2\theta_w$ will come from a measurement of the left-right polarization cross section asymmetry, A_{LR} , to be measured at the SLC^{1,2}. This quantity depends only upon the electron vector and axial-vector coupling constants v_e and a_e .

$$A_{LR} = \frac{-2v_e a_e}{v_e^2 + a_e^2} = \frac{4\sin^2\theta_w - 1}{1 - 4\sin^2\theta_w + 8\sin^4\theta_w} \quad (1)$$

All events (except $e^+e^- \rightarrow e^+e^-$) can be used giving it a great statistical advantage. In addition, A_{LR} is very sensitive to $\sin^2\theta_w$.

$$\Delta A_{LR} \cong 8\Delta\sin^2\theta_w \quad (2)$$

A measurement of a similar quantity,

$$A_\mu = \frac{-2v_\mu a_\mu}{v_\mu^2 + a_\mu^2} = \frac{4\sin^2\theta_w - 1}{1 - 4\sin^2\theta_w + 8\sin^4\theta_w} \quad (3)$$

can be made by a different method (to be described) using only $e^+e^- \rightarrow \mu^+\mu^-$ events². A comparison of A_μ to $A_e=A_{LR}$, or $\sin^2\theta_w$ extracted from A_μ and A_e respectively, is a test of electron-muon universality. (Notation: S_μ^2 and S_e^2 will be used to denote $\sin^2\theta_w$ extracted from A_μ and A_e respectively.)

Differential Cross Section Asymmetries

The (Born level) differential cross section for $e^+e^- \rightarrow \mu^+\mu^-$ at $\sqrt{s} = M_Z$ with longitudinal electron polarization p is:

$$\frac{d\sigma(p)}{d\cos\theta} = 2\sigma_0 \lambda_e \lambda_\mu \left\{ (1+pA_e)(1+\cos^2\theta) + 2A_\mu(p+A_e)\cos\theta \right\} \quad (4)$$

where

$$\sigma_0 = \frac{\pi\alpha^2}{4\Gamma_Z^2} \left(\frac{1}{\sin 2\theta_w} \right)^4, \quad \lambda_e = v_e^2 + a_e^2 \quad \text{and} \quad \lambda_\mu = v_\mu^2 + a_\mu^2$$

This is plotted for various values of p in fig. 1.

The forward-backward asymmetry, A_{FB} , as a function of polarization is given by the following expression.

$$A_{FB}(p) = \frac{\sigma_F(p) - \sigma_B(p)}{\sigma_F(p) + \sigma_B(p)} = \frac{3}{4} A_\mu \left(\frac{p+A_e}{1+pA_e} \right) \quad (5)$$

We see that it depends on both A_μ and A_e . Because this quantity is a product of A_μ and A_e , it is much less sensitive to $\sin^2\theta_w$.

Another quantity, known as the improved forward-backward asymmetry, A_{FB}^p

$$A_{FB}^p = \frac{\sigma_F(p) - \sigma_F(-p) - [\sigma_B(p) - \sigma_B(-p)]}{\sigma_F(p) + \sigma_F(-p) + \sigma_B(p) + \sigma_B(-p)} = \frac{3}{4} p A_\mu \quad (6)$$

is only dependent upon A_μ .

We can now compare A_μ to A_e (A_{LR}). A_e is determined by measuring the polarization cross section asymmetry.

$$A_{LR}^{\text{exp}} = \frac{\sigma_{\text{TOTAL}}(p) - \sigma_{\text{TOTAL}}(-p)}{\sigma_{\text{TOTAL}}(p) + \sigma_{\text{TOTAL}}(-p)} = p A_e \quad (7)$$

Where TOTAL refers to all events (except $e^+e^- \rightarrow e^+e^-$).

The Ratio of A_μ to A_e is then independent of polarization and therefore free of error due to polarization uncertainty. In addition, much of the radiative corrections will cancel. The change in A_μ/A_e due to radiative corrections is less than 1%, well below the expected experimental accuracy in measuring A_μ/A_e . See table 1 of reference 3 for details of radiative corrections to A_μ and A_e

Precision

The precision in measuring A_e and A_μ is shown in fig. 2 and is given by

$$\Delta A_e = \sqrt{A_e^2 \left(\frac{\Delta p}{p}\right)^2 + \frac{1}{p^2} \left(\frac{1}{N_z}\right)} \quad (8)$$

$$\Delta A_\mu = \sqrt{A_\mu^2 \left(\frac{\Delta p}{p}\right)^2 + \left(\frac{4}{3p}\right)^2 \left(\frac{1}{N_{\mu\mu}}\right)} \quad (9)$$

Where Δp is the uncertainty in p , N_z is the total number of observed Z^0 's and $N_{\mu\mu}$ is the total number of observed $Z^0 \rightarrow \mu+\mu^-$ decays ($\approx 4\%$ of N_z). The corresponding precision in measuring S_μ^2 and S_e^2 is shown on the right hand scale. The improved forward-backward assymetry will have a small ($\approx 3\%$) correction due to the SLD muon angular acceptance. The polarization cross section assymetry will not have any acceptance correction (assuming symmetric $\cos\theta$ cuts).

The resulting precision in measuring A_μ/A_e is given by

$$\begin{aligned} \Delta \left(\frac{A_\mu}{A_e} \right) &= \frac{1}{p A_e} \sqrt{\frac{16}{9 N_{\mu\mu}} + \frac{1}{N_z}} \\ &\equiv \frac{1}{p A_e} \left(\frac{20}{3} \right) \frac{1}{\sqrt{N_z}} \end{aligned} \quad (10)$$

This is shown in fig. 3 for relevant values of $\sin^2\theta_w$ (0.004 increments) and $p=\pm 0.45$.

The ratio of A_μ to A_e is very sensitive to the ratio of S_μ^2 to S_e^2 . This is shown in fig. 4 and is given by

$$\Delta\left(\frac{A_\mu}{A_e}\right) \approx (10-20)\Delta\left(\frac{S_\mu^2}{S_e^2}\right) \quad (11)$$

Combining equations (10) and (11) we obtain the expression for the precision in measuring S_μ^2/S_e^2 . This is shown in fig. 5.

$$\Delta\left(\frac{S_\mu^2}{S_e^2}\right) = \frac{25}{48p} \frac{(1-4S_e^2+8S_e^4)^2}{S_e^4(2S_e^2-1)} \frac{1}{\sqrt{N_Z}} \equiv \frac{8}{\sqrt{N_Z}} \quad (12)$$

As is evident from fig. 5 a comparison of $\sin^2\theta_w$ from the electron and muon couplings at the level of a few percent will be achieved with 10^5 Z^0 's and 45 percent polarization. A 1% measurement will be achieved with about 6×10^5 Z^0 's.

References

1. T Hansl-Kozanecka, these proceedings.
2. M. Swartz, Physics With Polarized Electron Beams, SLAC-PUB 4656
3. F. M. Renard et. al., Polarization at LEP, CERN 88-06, p. 197

Figures

1. The (Born level) differential cross section for $e^+e^- \rightarrow \mu^+\mu^-$ at $\sqrt{s} = M_Z$ with longitudinal electron polarization.
2. The precision in measuring A_μ , A_e , S_μ^2 and S_e^2 vs. the number of Z^0 's produced.
3. The precision in measuring the ratio A_μ/A_e for various values of $\sin^2\theta_w$
4. The dependance of S_μ^2/S_e^2 on A_μ/A_e for various values of $\sin^2\theta_w$.
5. The precision in measuring S_μ^2/S_e^2 .

Figure 1

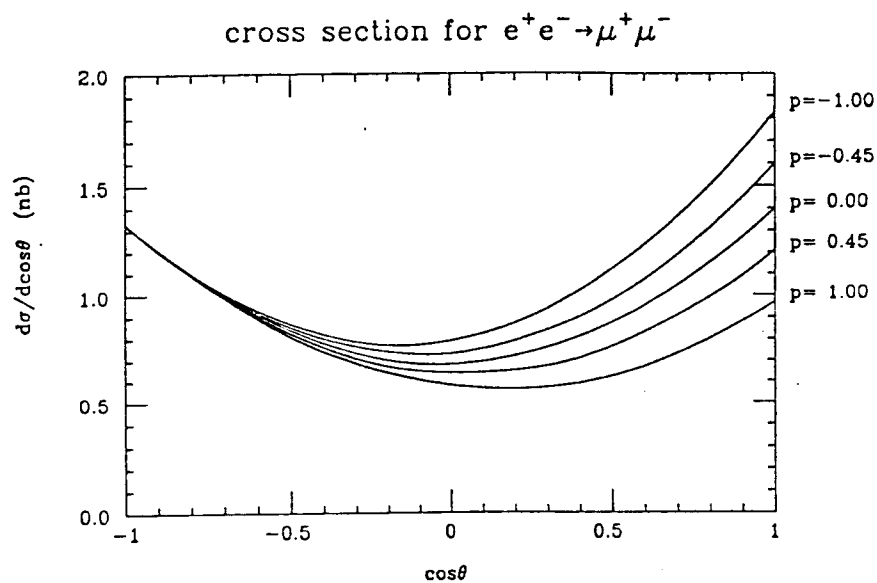


Figure 2

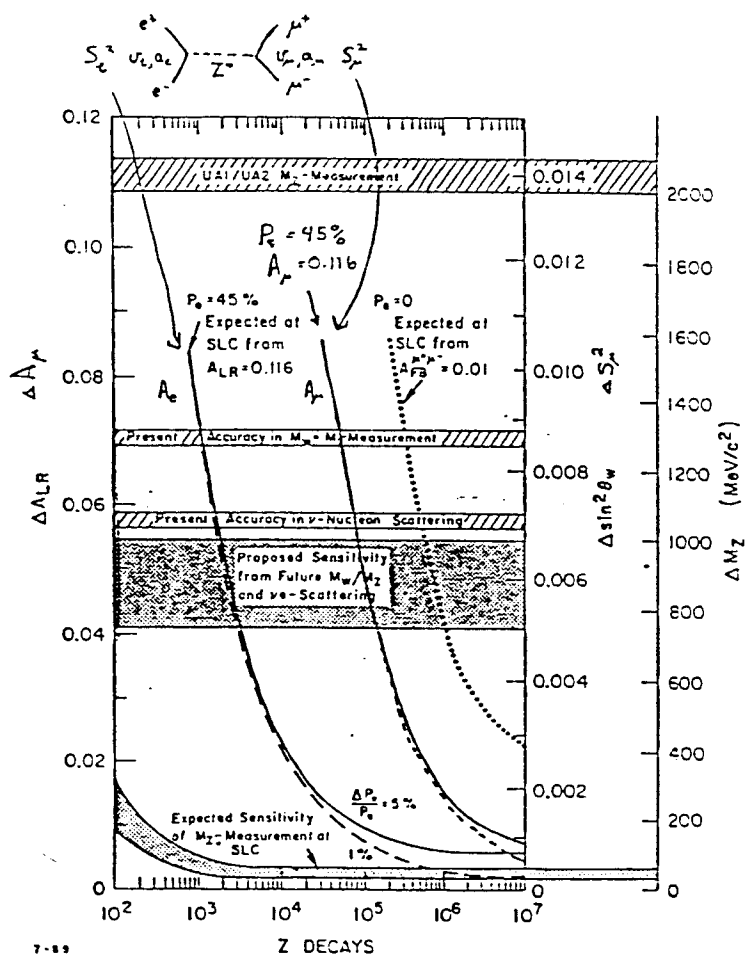


Figure 3

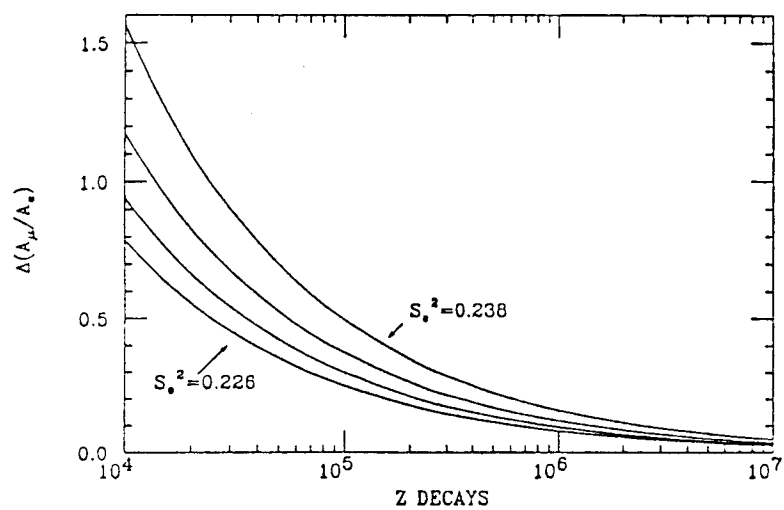


Figure 4

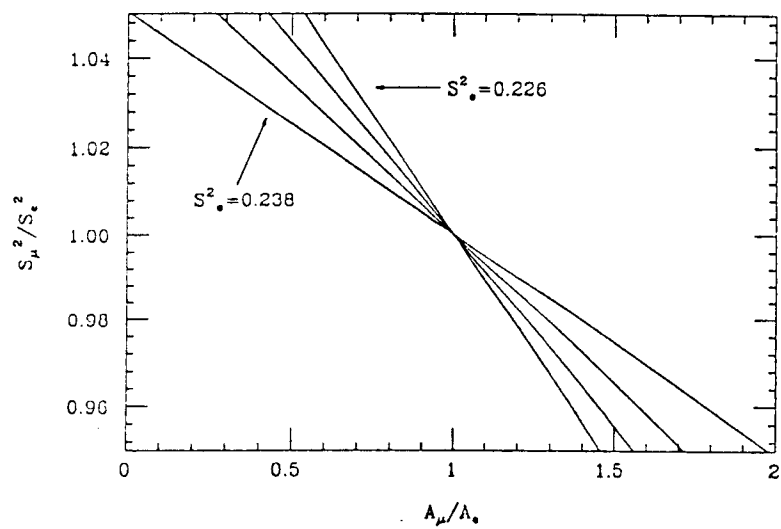
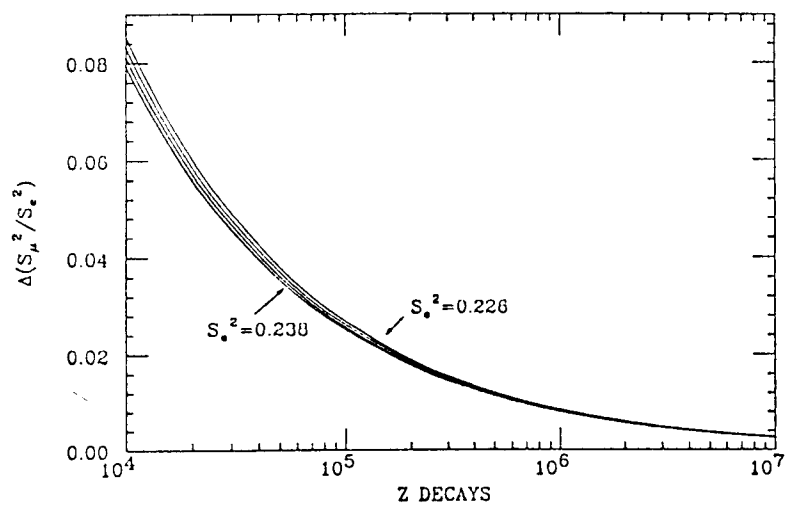


Figure 5



Prospects of Tau Physics with the SLD Detector

U. Schneekloth

Physics topics that can be addressed by studying τ pair events can be divided into the study of τ pair production, e.g. total cross section, partial Z^0 width, differential cross sections and various asymmetries (left-right, forward-backward), and the τ decay, e.g. τ lifetime, τ branching fractions, and Michel parameter. Most importantly, the τ decay products can be used for studying τ production properties, namely, the τ polarization. In this note, we will briefly describe the event signatures and selection criteria for τ events at the Z^0 peak, and look at the τ physics prospects of the SLD detector.

At PETRA and PEP energies it was relatively difficult to obtain τ data samples with high efficiency and low background, due to large Bhabha and two-photon cross sections relative to the τ cross section. The efficiency for selecting τ pair events varied from 6% to 50% for different experiments, while backgrounds were typically about 5%. The most important detector requirements were good charged particle tracking, calorimetry and muon identification over the full solid angle. The signal to noise ratio is greatly improved at the Z^0 peak. The background for τ pairs at the Z^0 peak can be roughly estimated by simply scaling the background at PETRA energies by the ratios of the total cross sections. It is expected to be of the order of 1%. The rate of hadronic Z^0 decays is larger, but due to more distinctive event signatures, higher particle and jet multiplicities and larger jet masses, the resulting hadronic background should be small.

The following selection criteria were applied to τ Monte Carlo events, generated by using the LULEPT program of D. Stoker ^{/1/}, and subjected to the fast simulation program of the SLD:

- 1) The number of charged tracks was required to be at least 2 and less than 10.

- 2) The tracks were combined into 2 jets (at least one track in each jet), and all tracks were required to lie within a cone of 40° opening angle with respect to the jet axis.
- 3) The total visible energy, including tracks and all calorimeter clusters, had to be greater than 0.2 of the center of mass energy.
- 4) The energy measured in the electromagnetic part of the calorimeter was required to be less than 0.8 of the beam energy (E_b), and the energy of the highest electromagnetic shower less than $0.9 E_b$.
- 5) The invariant mass of all tracks and clusters in each hemisphere (jet) had to be smaller than 3 GeV.
- 6) For 2 prong events, the acoplanarity angle was demanded to be greater than 10 mrad.

74% of all τ Monte Carlo events passed these selection criteria, without rejecting ee and $\mu\mu$ events. Applying the same cuts to LUND Monte Carlo events, the reduction factor was 3.5×10^{-4} , resulting in a background of 1%.

It should be straightforward to obtain an almost background free data sample with high efficiency of about 70%. We will therefore be able to do the same physics as with μ pair events with similar statistical errors and slightly different systematic errors. This was covered in the talks by T. Hansl-Kozanecka^{/2/} and J. Yamartino^{/3/}.

Due to its excellent particle identification capabilities, the SLD detector is very well suited for studying the τ decay properties. One of the most important issues is the so-called missing one-prong puzzle^{/4,5/}, which has not yet been resolved. In order to achieve statistical errors comparable to existing e^+e^- experiments, which have data samples corresponding to up to 10^5 produced τ pairs, the required number of produced Z 's is 10^6 to 10^7 events, because of the small $Z^0 \rightarrow \tau^+\tau^-$ branching fraction of about 3%. This will not be considered any further.

The same statistics are needed in order to improve the existing measurements of the charged current coupling of the τ (Michel parameter). The sensitivity can be improved with polarized beams, as has been shown in a LEP study report^{/6/}. The parameter $\kappa = -2g_v g_a / (g_v^2 + g_a^2)$, which is linearly proportional to the Michel parameter $\kappa = \frac{8}{3}\rho - 1$, has been measured by using the electron and muon energy distributions in τ decays. The

present value of κ is 0.95 ± 0.19 ^{/7/}. It has been estimated that experiments at the Z^0 peak can get a statistical error of 0.03 with an integrated luminosity of 100pb^{-1} corresponding to about 10^5 τ pairs. The same statistical error can be achieved with half the data sample (50pb^{-1}) and an electron beam polarization of 50% ^{/6/}.

The τ lifetime has been determined by several experiments either by reconstructing the 3-prong τ decay vertex or by using the impact parameter of all tracks. The most recent world average is $(3.04 \pm 0.09)10^{-13}\text{s}$ ^{/7/}. It is interesting to note that while the decay length ℓ grows with γ (ℓ is 2.3 mm at the Z^0 energy) the error on the decay length $\delta\ell$ also increases proportional to γ , because of the small opening angle between the decay products. Thus, the sensitivity is to first order independent of the center of mass energy, $\delta\ell(\sqrt{s})/\ell(\sqrt{s}) = \text{constant}$. The τ lifetime measurement can only be improved with better vertex resolution, which makes SLD the best detector to do this measurement, or with significantly improved statistics.

τ Monte Carlo events that passed the selection criteria mentioned above were used for the following analysis. Only events were considered where one τ decayed into one and the other τ decayed into three charged particles (1-3 topology). The $\cos\theta$ was required to be less than 0.7 ($|\cos\theta| < 0.7$) to ensure full solid angle coverage of the vertex detector. The 3-prong decay vertex was reconstructed by using the vertex finding program. The reconstructed decay length distribution and the true decay length are shown in figures 1 and 2, respectively. The resolution was estimated by taking the difference of the reconstructed and true decay lengths, see figure 3, since the present version of the vertex finding program does not yet provide the full error matrix. The sigma of the distribution is 0.72 mm, resulting in a relative error of $\delta\ell/\ell = 0.32$. This is considerably better than the errors achieved by present experiments, which have $\delta\ell/\ell$ values from 1.6 to 3.9. Scaling the relative error of the MARK II τ lifetime measurement at PEP by the ratio of the MARK II/PEP ^{/8/} and SLD impact parameter resolutions, the expected error is 0.3, which is in agreement with this analysis.

The statistical precision of the τ lifetime measurement is given by: $P = \frac{1}{\sqrt{N}} \frac{\delta\ell}{\ell}$, where N is the number of reconstructed vertices. The required number of vertices reconstructed in the SLD is 100, in order to make a measurement of the same precision (3%) as the present world average. Taking into account the τ branching ratios, 0.25 for the 1-3 topology, and

the vertex reconstruction and event selection efficiencies, also 0.25, the required number of produced τ events is 1600, corresponding to 50,000 produced Z 's. It should be pointed out that the systematic error is expected to be small compared to the statistical error. One can easily obtain a practically background free data sample and the uncertainty of the beam position and the beam size of the SLC is very much smaller than the vertex resolution, and considerably better than at any e^+e^- storage ring.

The τ polarization and the polarized forward-backward asymmetry are defined as:

$$P^\tau = \frac{\sigma_R^\tau - \sigma_L^\tau}{\sigma_R^\tau + \sigma_L^\tau} = \frac{-2v_\tau a_\tau}{v_\tau^2 + a_\tau^2},$$

$$A_{FB}^{pol} = \frac{1}{2}(P_F^\tau - P_B^\tau),$$

where σ_R^τ and σ_L^τ are the cross sections for right and left handed τ 's. Note that the τ polarization has the same dependence on the coupling constants as the left-right asymmetry (A_{LR}) with beam polarization. Whereas the left-right asymmetry is sensitive only to the electron coupling, the τ polarization is sensitive only to the coupling of the final state, the τ . Since A_{LR} and P^τ have the same sensitivity to $\sin^2 \theta_W$ ($\delta \sin^2 \theta_W = \frac{1}{8} \delta P^\tau = \frac{1}{8} \delta A_{LR}$), the τ polarization measurement offers the best tool for precision measurements of $\sin^2 \theta_W$ at the Z^0 peak, if beam polarization is not available. This has been discussed by several authors. For the most recent review see reference 9.

Experimentally, the τ polarization is studied using the energy distributions of the τ decay products (e, μ, π and ρ) and their forward-backward asymmetries. A study done by the MARK II group ^{/10/} concludes that by combining the four decay modes, a statistical error in $\sin^2 \theta_W$ of 0.009 can be obtained with a data sample of 10^5 produced Z^0 events. The systematic error will be dominated by uncertainties in the detector efficiencies and backgrounds due to particle misidentification. The MARK II analysis shows that it should not be difficult to achieve background levels such that the systematic error will be less than one-third of the statistical error, assuming 10^5 Z^0 's. An analysis using the ALEPH detector simulation Monte Carlo claims ^{/11/} that the expected overall systematic uncertainty in the measurement of the τ polarization is 0.006, leading to a systematic error in the $\sin^2 \theta_W$ determination of 0.0008.

It is very likely that the τ polarization measurement will be limited by systematics. Due to its better particle identification capabilities, the SLD will be able to identify the

decay channels with higher efficiency and lower background than the MARK II detector. This will, however, not give a significant advantage. There is currently work in progress on an improved method by trying to reconstruct the τ direction and using it simultaneously with the energy of the decay products.

References

1. D. Stoker, LULEPT Monte Carlo event generator, MARK II/SLC Note 161 (1986).
2. T. Hansl-Kozanecka, these proceedings.
3. J. Yamartino, these proceedings.
4. F.J. Gilman, S.H. Rhie, Phys.Rev. D31, 1066 (1985)
5. M. Perl, SLAC-PUB 4632 (1989)
6. Z. Was, CERN 88-06 Vol.1 (1988) 250
7. 'Review of Particle Properties', Phys.Lett. B204 (1988)
8. D. Amidei et al., Phys.Rev. D37, 1750 (1988)
9. M. Swartz, 1989 SLAC Summer Institute
10. D. Cords et al., SLAC-Report 315, 172 (1987)
11. F. Boillot and Z. Was, Z.Phys.C43, 109 (1989)

Figure Captions

1. Reconstructed decay length.
2. True decay length.
3. Difference between reconstructed and true decay length.

A GEOMETRIC METHOD OF TAGGING B FLAVOR EVENTS

D. C. WILLIAMS

L. S. OSBORNE

Massachusetts Institute of Technology

Laboratory for Nuclear Science

1. Introduction

The unique, double decay topology of the b-hadron suggests that geometrical reconstruction may pose a powerful method of b tagging. This paper describes how the impact parameter and track distance of closest approach can be used for b tagging, and how they perform in the SLD and in a typical LEP vertex detector.

In a typical $Z^0 \rightarrow b\bar{b}$ event, two b-hadrons are formed and travel some distance before decaying into one or two c-hadrons and other fragments. The c-hadrons then travel further away from the interaction point and decay themselves, releasing more fragments. The result is a collection of particle tracks that originate from several decay vertices. Since the lifetimes of the b and c-hadrons are on the order of 0.04 cm, a good vertex detector can resolve these vertices and identify the flavor of the event.

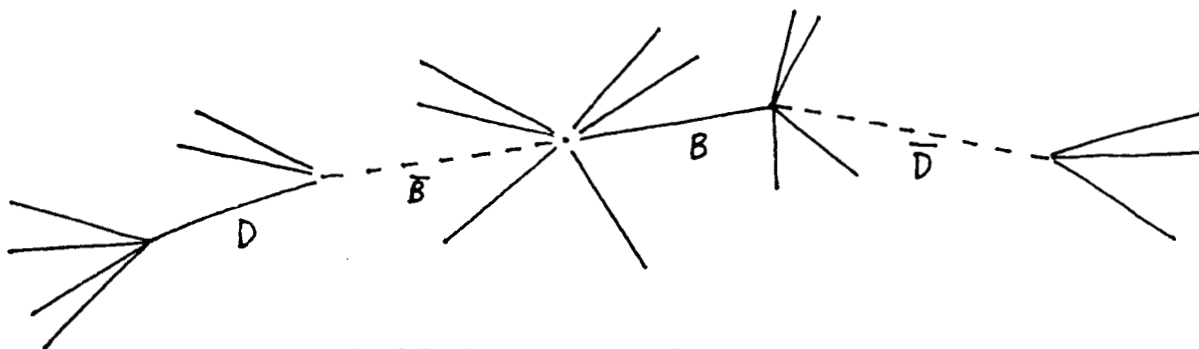


Fig. 1. An example of the double decay topology of a b flavor event.

There are other types of vertices, however, that may pose a potential background. C flavor events produce secondary vertices as their c hadrons decay. Light,

semi-stable hadrons, such as K_S and Λ , created in abundance in any hadronic event during fragmentation, also produce vertices. C events, however, only produce one secondary vertex per jet, and most light hadrons have far longer lifetimes than the c and b. Thus, with care, these backgrounds can be reduced.

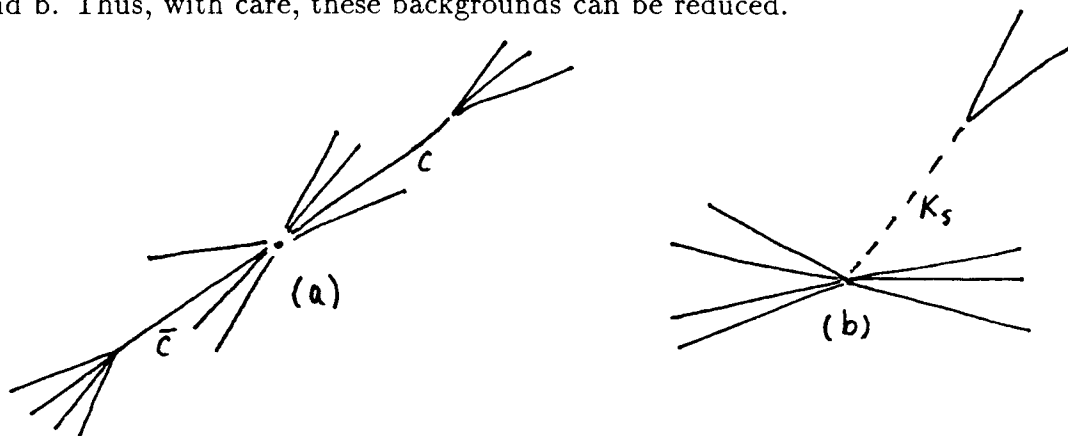


Fig. 2. Background events that appear like a b event. (a) A c flavor event with two secondary vertices and (b) the decay of an ordinary semi-stable meson forming an unrelated vertex.

2. Monte Carlo Used

To develop and test geometric tagging of b events, a simple simulation of the SLD vertex detector was added to LUND 6.3. The primary function of the simulation was to calculate particle tracking errors due to Coulomb multiple scattering and vertex detector resolution. These errors, only now being added to the SLD Monte Carlos, were crucial in calculating the χ^2 distributions and in understanding the vertex detecting resolution of SLD.

The simulation approximates the vertex detector as a thin, finite length cylinder covering a thin cylindrical beam pipe (Fig 3). The relevant parameters of the SLD vertex detector are shown in Table 1. Based on this model, analytic expressions for the multiple scattering errors in the particle tracks were developed. These errors were used to smear the track parameters and to calculate the errors in the quantities needed for geometric b tagging.

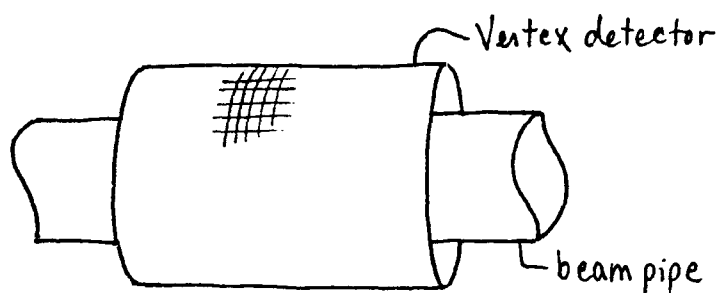


Fig. 3. Geometry used in the simple simulation of the vertex detector. All four layers of the vertex detector are condensed into one thin cylinder.

Table 1. Vertex detector characteristics used for the SLD vertex detector and a typical LEP vertex detector.

	SLD	LEP
<i>beam pipe</i>		
radius	2 cm	8 cm
thickness	1 mm	2 mm
<i>vertex detector</i>		
radius	2.5 cm	8.5 cm
pixel size	22 μm	100 μm
radiation length	.0037	.0037

As a check of the model, samples of several hundred electrons were sent through SLD's GEANT vertex detector simulation, and their deflection due to multiple scattering measured. When these deflections were compared to the vertex detector simulation, they agreed within the statistical errors for track angles as low as 20 degrees from the beam axis.

In order to predict how this method will work at LEP, the approximate parameters of a LEP vertex detector were entered into the simulation (see Table 1). Since these parameters are a rough estimation, the simulation can give only a first approximation of a LEP detector's performance.

3. Tagging Method

The b tagging method involves three steps. First, identify and remove K_S , Λ , and other ordinary decays from the event. Second, tag both c and b events by looking for any secondary vertices. Third, separate b from c events by looking for more than one secondary vertex per jet.

The first step uses standard methods of particle reconstruction, and won't be discussed further. These mesons have lifetimes on the order of several centimeters and should be easy to distinguish.

The second step consists of searching for a track in the event that did not originate from the interaction point as evidence of a b or c hadron decay. This is most efficiently accomplished by checking the error weighted impact parameter. If the impact parameter squared of one or more tracks is greater than some sigma cut, the event is tagged as either a b or c flavor event.

The advantage of using an error weighted cut in the impact parameter cannot be over emphasized. For tracks from the interaction point, the impact parameter distribution has a long tail (see Fig. 4a). Because of this tail, there is no clean place to make a cut in the impact parameter. The weighted impact parameter squared, however, has no tail (see Fig. 4c). Because of the shape of this distribution, tracks of greater than 2σ nearly always originate from a secondary vertex.

If track errors are accurately predicted, the major source of background comes from unidentified K_S and Λ . If, however, track errors are underestimated, tracks from the interaction point will begin to wander outside the sigma cut. Checks for underestimated errors can be made by using a more sophisticated Monte Carlo like GEANT, or by using impact parameter distributions from actual uds flavor events.

The final step involves a search for the extra vertices that characterize a b jet. To begin, it is necessary to obtain a sample of tracks that originate only from one of the b or c decays. To do this, all particle tracks that have a weighted impact parameter squared greater than 2σ are selected and divided into two jets. Those

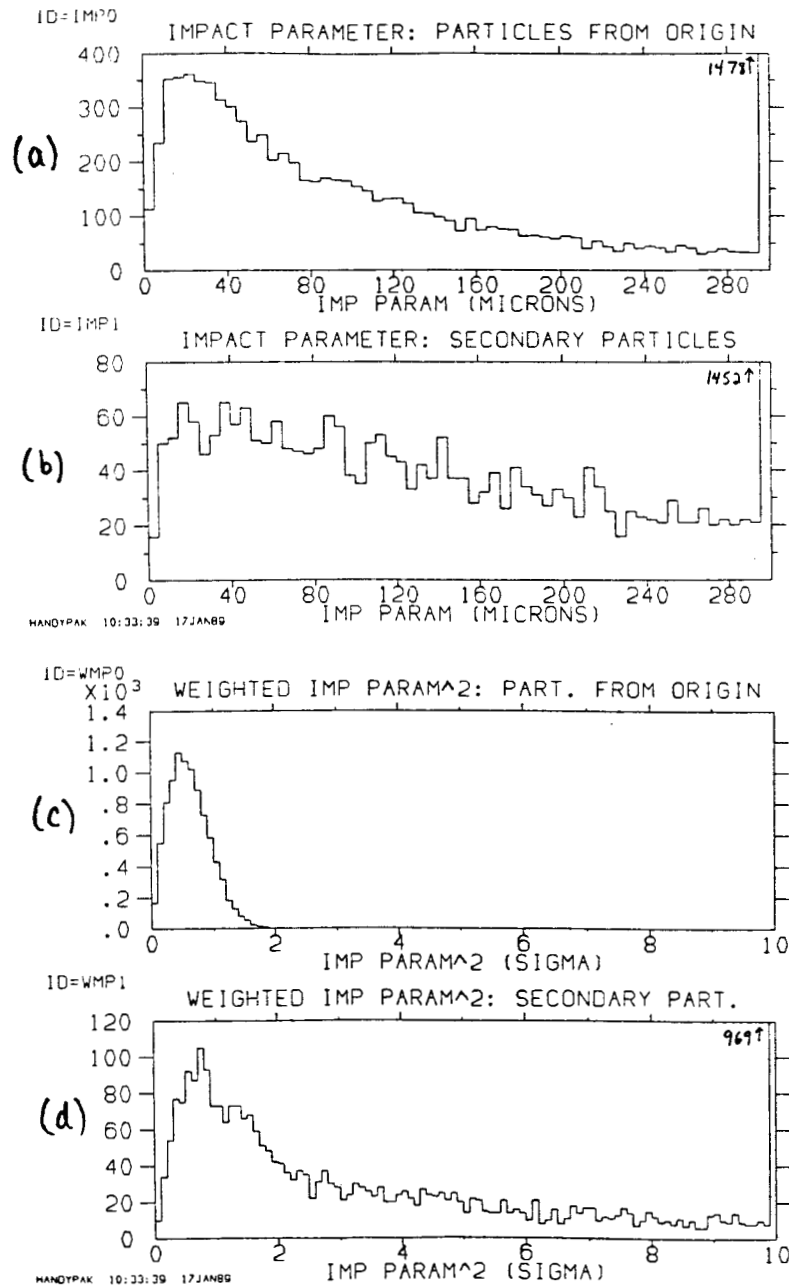


Fig. 4. The impact parameter for b flavor events in microns for (a) tracks from the interaction point and (b) tracks from secondary vertices (b and c-hadron decays). The weighted impact parameter squared in σ for (c) tracks from the interaction point and (d) tracks from secondary vertices. The lack of a tail in the weighted impact parameter allows for cleaner cuts.

tracks that cannot be unambiguously assigned to a jet are discarded. The two sets of tracks left can be checked to see whether they each are consistent with a single

vertex. If they are not, then the event is tagged as a b flavor event.

To determine whether there is more than one vertex, the weighted distance of closest approach (WDCA) is checked for each pair of tracks (see Fig 5). If the WDCA of one or more pairs is greater than some sigma cut, then the two tracks are not consistent with a single vertex, and a b-hadron has been identified. If a b-hadron is identified in *either* jet, then the event is tagged.

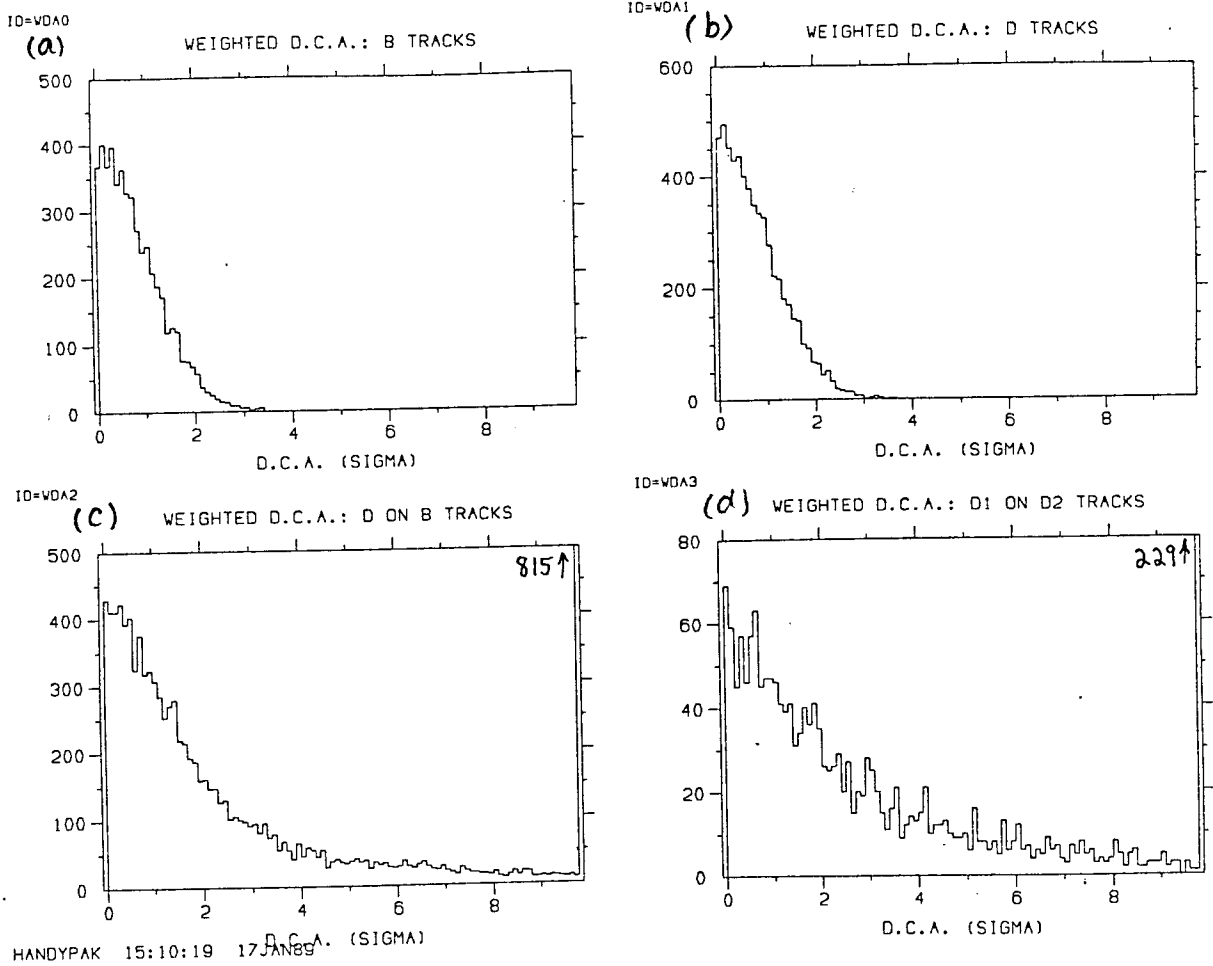


Fig. 5. Weighted distance of closest approach for (a) two tracks from the b decay vertex, (b) two tracks from a c decay vertex, (c) one track from a b vertex and one track from a c vertex, and (d) tracks from different c vertices.

Backgrounds from c events appear when a track not originating from a c-hadron decay gets included in the selected track sample. This rogue track will not

intersect the c decay vertex and will be seen as evidence for the secondary decay of a b-hadron. To reduce this background, more stringent jet cuts can be made or more than one exclusive pair of tracks of large WDCA can be required as a tag. Both methods, of course, decrease the tagging efficiency.

The calculation of the weighted impact parameter squared and the WDCA is too involved to describe here. Those interested are referred to SLD SOFTWARE NOTE 89-3 which describes the method and routines in detail.

4. Results

Table 2. B tagging efficiencies and background. (a) The fraction of b and c events tagged using the weighted impact parameter for the SLD and (b) for a typical LEP detector. The background is due primarily to misidentified K_S and Λ and is not simulated. (c) The fraction and background of b from c separation for SLD and (d) for a typical LEP detector. Because some b and c decay vertices include no charged tracks, there is a limit to the efficiency. (e) An example of b tagging efficiency and background using various cuts.

(a)			(b)		
Weighted Impact para. Cutoff (σ)	Efficiency		Weighted Impact para. Cutoff (σ)	Efficiency	
	1 track > Cutoff	2 tracks > Cutoff		1 track > Cutoff	2 tracks > Cutoff
2.00	0.89	0.79	2.00	0.68	0.51
2.25	0.87	0.77	2.25	0.64	0.48
2.50	0.86	0.75	2.50	0.61	0.44

(c)			(d)		
WDCA Cutoff (σ)	Efficiency, Signal:Noise		WDCA Cutoff (σ)	Efficiency, Signal:Noise	
	1 track > Cutoff	2 tracks > Cutoff		1 track > Cutoff	2 tracks > Cutoff
2.00	0.70, 10:1	0.52, 51:1	2.00	0.33, 13:1	0.16, 33:1
2.25	0.66, 19:1	0.47, 79:1	2.25	0.28, 20:1	0.13, 63:1
2.50	0.63, 37:1	0.42, 141:1	2.50	0.23, 33:1	0.10, 50:1
<i>Best possible efficiency</i>	0.80,	0.72,	<i>Best possible efficiency</i>	0.80,	0.72,

(e)		
Efficiency, Signal:Noise		
SLD	LEP	
.49, 37:1	.12, 33:1	

The efficiencies and background for this method, measured by the simulation, are shown in Table 2, for both SLD and a fictitious LEP detector. The efficiency and signal to noise are found to be 49% and 37:1 for SLD and 12% and 33:1 for LEP. Because of two weaknesses in the Monte Carlo, however, these results should be viewed as only a preliminary measure of the b tagging's performance.

First, identification of K_S , Λ , and other ordinary decaying mesons are not simulated. Thus the backgrounds in the b and c selection step could not be measured. Such backgrounds are expected to be on the order of a few percent.

The second problem is that the Monte Carlo, lacking a proper jet finder, uses privileged information from LUND to separate the event jets. This probably results in optimistic predictions for b from c event separation. Since b jets are generally well collimated, however, the use of a true jet finder is not expected to drastically decrease efficiency.

Despite these problems, there is still optimism about the high performance and low background of this method. A more realistic test of the method will be conducted when the true track error matrices are added to the SLD fast simulator.

CHARGED TRACKING ACCEPTANCE FOR HADRONIC EVENTS

Gregory J. Baranko
Physics Department
University of Colorado

SLD's ability to make charge asymmetry measurements for quarks depends greatly on the charged tracking acceptance. Given a production, σ , and an integrated luminosity, L , the statistical significance of an ideal forward-backward asymmetry measurement is approximately:

$$S = \frac{A_{FB}}{\delta A_{FB}} \approx \sqrt{L\sigma} |A_{FB}| a^{3/2}$$

for an acceptance a . Thus, evaluating the acceptance for a given signature gives a figure of merit for the detector's hardware and reconstruction as applied to this measurement.

It is an advantage of SLD to have charged tracking in the endcap region as well as in the central detector. This extends the acceptance for signatures using only inclusive charged tracking into the small polar angles, where the production and sensitivity are the highest. For example, the endcap drift chambers geometrically cover 20% of 4π , but the acceptance for the approximately $1 + \cos^2\theta$ production is 27% (for perfect efficiency). This added acceptance improves the statistical significance above by 60%. The endcap charged tracking also aids in SLD's lepton and flavor tagging at low angles, and hence increases the acceptance for these types of signatures. Finally, although these advantages in acceptance will yield better statistical errors, the ultimate limit to the measurement's accuracy will come from the systematic errors. The endcap charged tracking will afford smaller uncertainties in estimates of backgrounds to signatures involving lepton and flavor tagging, and thus reduce a large part of the total systematic error as well. We present below a first estimate for the polar angle dependence of the inclusive charged track acceptance in hadronic events.

The acceptance is defined as the average of the total detection efficiency, $\epsilon(\mathbf{x})$, for a given production process. If the production is described by a normalized probability

distribution, $f(\mathbf{x})$, for a set of n physical variables, \mathbf{x} , then the acceptance, a , can be written:^[1]

$$a = \int_{\Omega} \epsilon(\mathbf{x}) f(\mathbf{x}) d^n \mathbf{x} \quad \forall \mathbf{x} \in \Omega.$$

The total detection efficiency can be factored into more specific efficiencies (assuming here that they are uncorrelated):

$$\epsilon(\mathbf{x}) = \epsilon_{tr}(\mathbf{x}) \cdot \epsilon_{es}(\mathbf{x}) \cdot \epsilon_g(\mathbf{x}) \cdot \epsilon_h(\mathbf{x}) \cdot \epsilon_r(\mathbf{x}) \cdot \epsilon_{an}(\mathbf{x})$$

where these are for the trigger, event selection, geometry, hardware, reconstruction, and analysis, respectively.

In our present study, we have only evaluated the acceptance for $\epsilon_g(\mathbf{x}) \cdot \epsilon_r(\mathbf{x})$. Since the tracking Monte Carlo and reconstruction are still under development, the results shown here are only a rough outline of our coverage.

Hadronic events were generated using the LUND Monte Carlo with SLD's present default parameters. The choice of generator for the radiative corrections is not important for the present study. The charged tracks were swum through the detector geometry and the hits were digitized using the expected resolution functions of the drift chambers. The reconstruction was then done starting from the raw data banks as expected for real data. This reconstruction includes the swim-fitting for tracks in the central drift chamber. The fitting efficiency is not included for the endcap tracks, but this is expected to be uniform and high.

The polar angle distribution of the generated tracks is shown in Figure 1, for a sample of 1000 events. The acceptances are calculated bin by bin by dividing the accepted distributions, as functions of the measured angles, by this generated distribution. The acceptances for the inner and outer endcap drift chambers are shown in Figures 2 and 3 respectively. The acceptance of the central drift chamber is shown in Figure 4. Some tracks have segments reconstructed in both the central chamber and the inner endcap chamber. The acceptance for these tracks is shown in Figure 5. It should be noted that the acceptance near the edges of the chambers is a strong function of the track

definitions used there, and the success of the inter-chamber track merging algorithm. This work is still in development.

In conclusion, we have shown the charged tracking acceptance for hadronic events, given the present level of development of the tracking swimmer and reconstruction. These Monte Carlo studies could now be used to evaluate the acceptance for specific signatures in the asymmetry measurements.

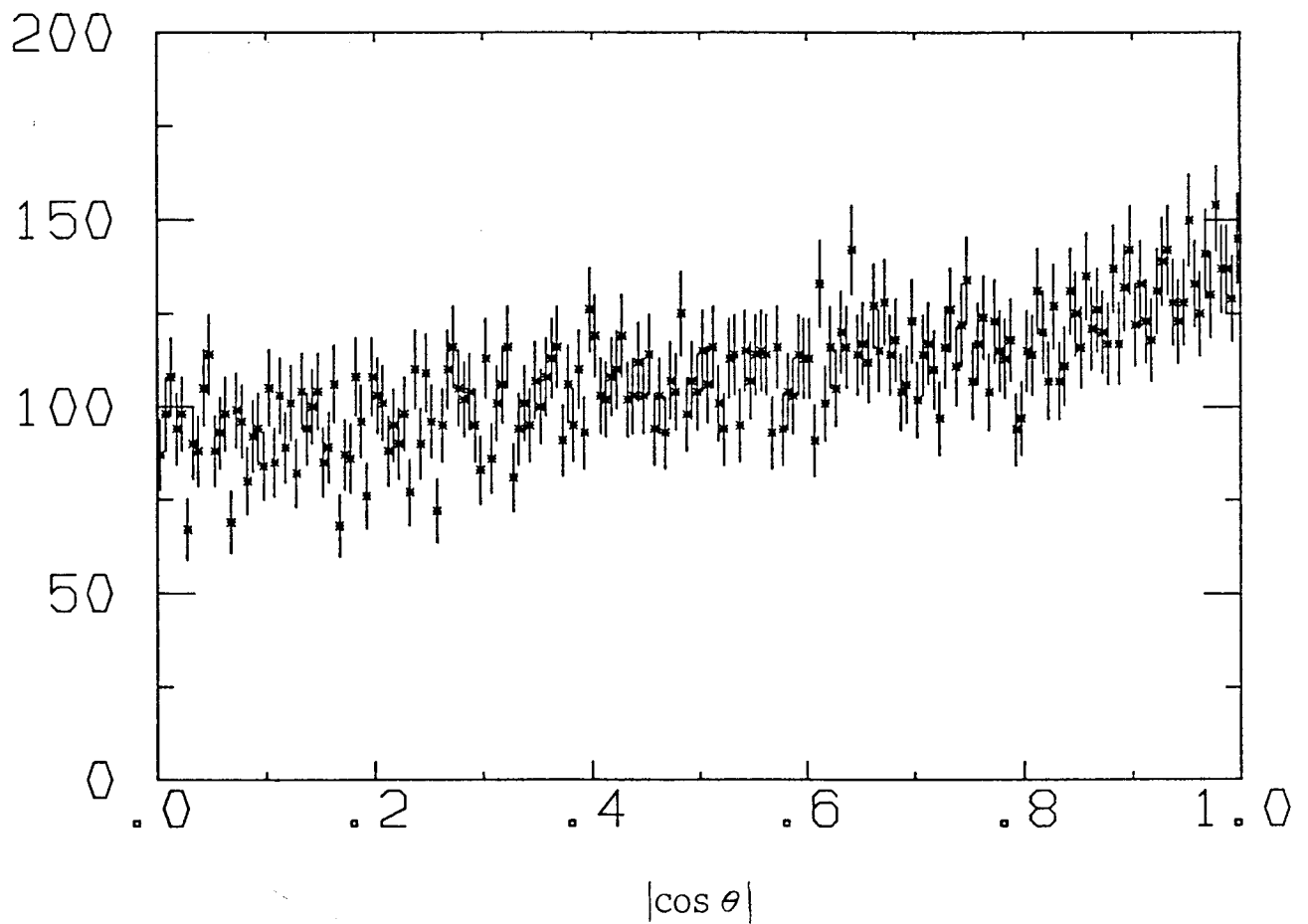


Fig. 1. Generated polar angle distribution

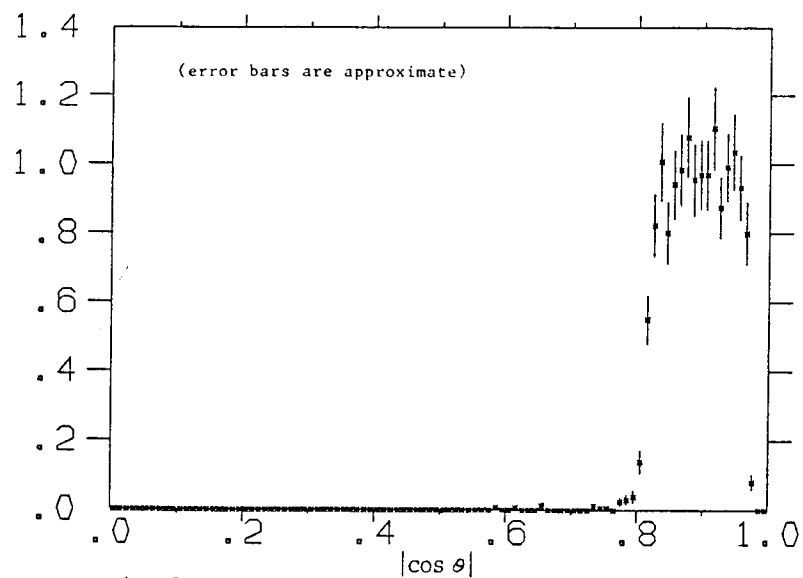


Fig. 2. Inner endcap acceptance vs. polar angle

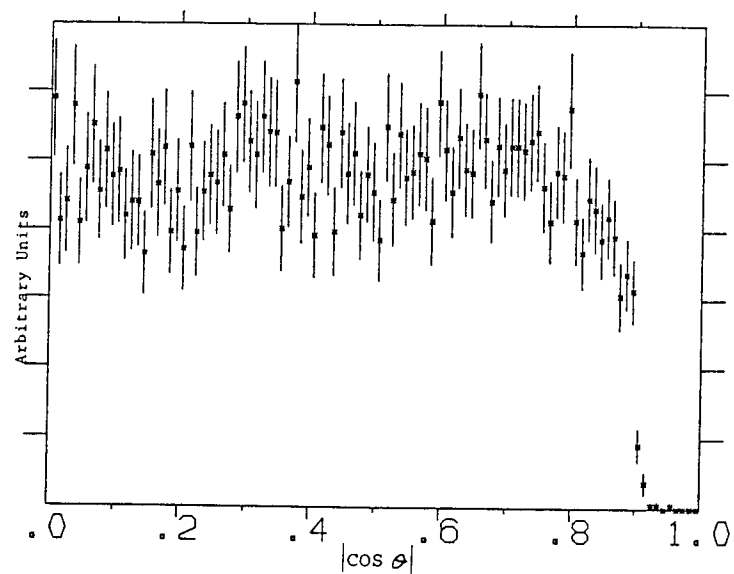


Fig. 4. Central chamber acceptance vs. polar angle

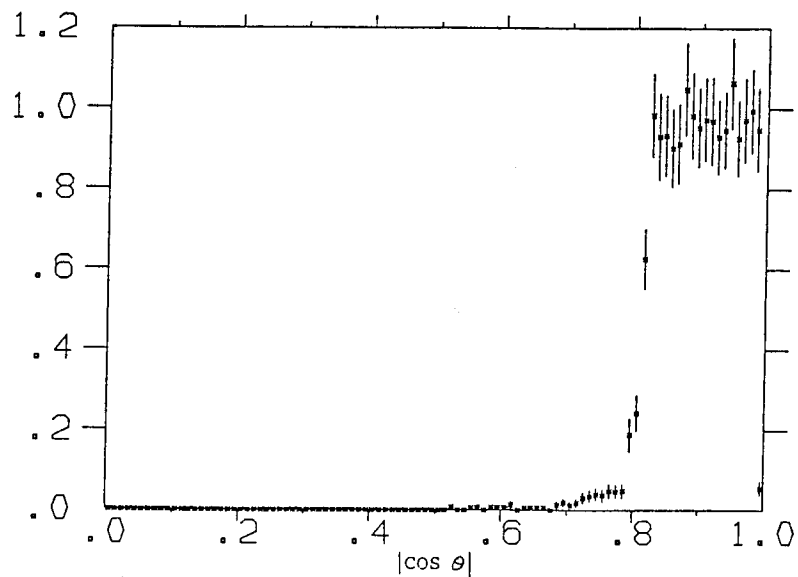


Fig. 3. Outer endcap acceptance vs. polar angle

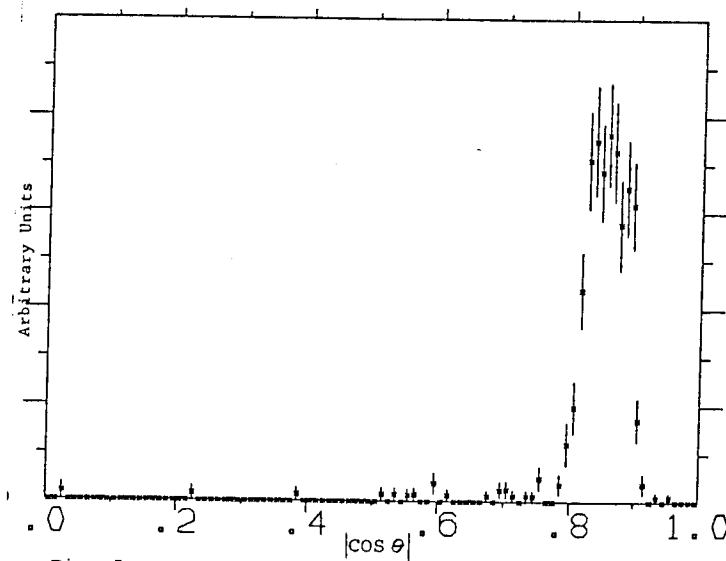


Fig. 5. Inner endcap and central chamber overlap acceptance

REFERENCES

1. R. K. Bock et. al ed. (1984) "Formulae and Methods in Exerimental Data Evaluation", CERN.

QCD at the Z^0

P.N. Burrows

Introduction

I give a brief overview of issues in QCD physics, with particular emphasis on areas which could be studied during running at the Z^0 energy. I choose (arbitrarily) to divide this huge field into the following sections: 1) QCD as a background; 2) fundamental tests of QCD; 3) 'standard' QCD physics. Section 1 gives a brief outline of QCD and fragmentation calculations with examples of how such calculations have been used to search for new particles by looking for deviations from the QCD predictions. The many QCD-inspired Monte Carlo models and their current status are listed. In section 2 I indicate aspects of QCD which remain to be tested or demonstrated conclusively by experiment. There is a review of the experimental search procedures and the current status of the results. This is the most important section in terms of testing the QCD part of the Standard Model. In section 3 I discuss the more standard issues of jet fragmentation, comparison with QCD + fragmentation models and hadronisation. There is a brief summary in Section 4.

1. QCD as a Background and QCD Calculations

1.1 QCD as a Background

For those interested in QCD physics in its own right, this is the least interesting section of this review. However, for those interested in searching for new particles, such as the top and b' quarks, the Higgs boson, sequential heavy leptons, supersymmetric and technicolour particles, this is a very important topic. New physics will stand out as a deviation of the data in some distribution from the predictions of the Standard Model. If the new particle decays hadronically, it will show up as some excess of events/tracks compared with the expectation from production of coloured u,d,s,c,b quarks according to the electroweak theory, and their subsequent fragmentation into observable colourless hadrons according

to Quantum Chromodynamics.

For example, consider the process $e^+e^- \rightarrow t\bar{t}$. If the top quark has a much larger mass than the known five flavours of quarks, it will tend to give rise to more spherical events because its decay products will have large transverse momentum relative to its line of flight. Event shape distributions such as sphericity [1], thrust [2], aplanarity or acoplanarity will then reflect the presence of top by an excess of spherical events compared with the five-flavour expectations. The TRISTAN experiments have all used this technique to set lower mass limits for the production of the top quark [3] and for sequential heavy leptons [4].

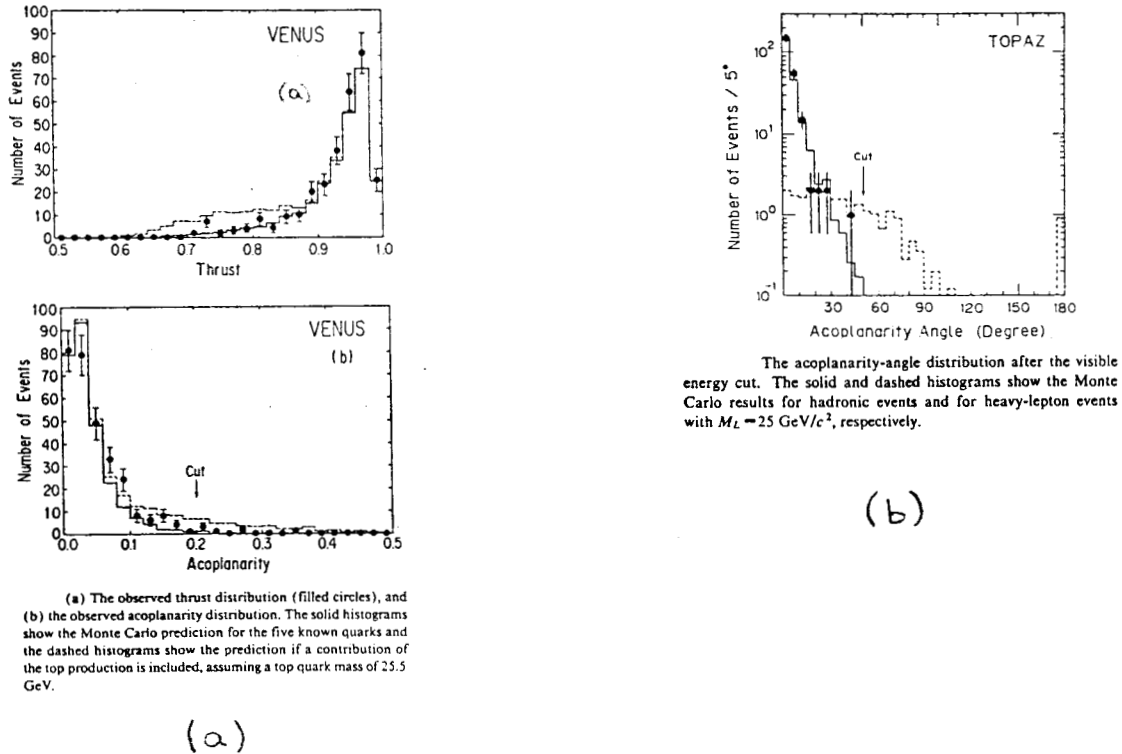


Figure 1.

Fig. 1 (a) shows the first results from VENUS on the top quark search: a top quark of mass $\sim 25 \text{ GeV}$ would give an excess of low thrust events in the range $0.6 \leq T \leq 0.85$ and an excess of events of high acoplanarity $A > 0.1$ (dashed lines); the solid line is the expectation for five-flavour production. The histograms are the results of Monte Carlo calculations comprising an $e^+e^- \rightarrow \text{hadrons}$ event generator and a detailed detector simulation. There is clearly no evidence in the data for production of a new heavy quark.

Shown in Fig. 1 (b) is the result of a search for a sequential heavy lepton by TOPAZ, where the expected signal is an excess of events with high acoplanarity-angle (dashed line; solid line: five-flavour hadronic events). In both of these examples, comparison of the number of observed events in the sensitive region with that expected from the Monte Carlo calculations enables an upper limit to be placed upon the production cross-section

of the new state. The latest results from TRISTAN using these methods were presented recently [5].

Note that such signals are complimentary to searches in other channels, such as the value of R , the ratio of the total hadronic cross-section to the lowest order muon pair cross-section, and depend for their accuracy upon the reliability of the calculations of the ‘standard’ five-flavour hadronic event properties. In practice these calculations are performed using Monte Carlo models incorporating a perturbative QCD calculation of parton-level processes, combined with a phenomenological hadronisation model to represent the non-perturbative transformation of the coloured partons into the colourless hadrons observed experimentally in the final state.

1.2 Perturbative QCD Calculations

These calculations may be loosely divided into two classes: matrix elements and parton showers.

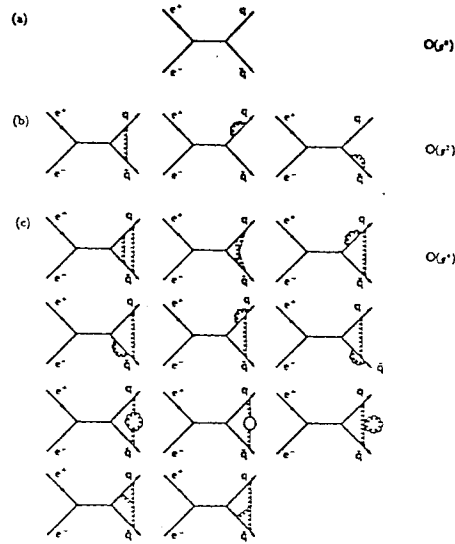
1.2.1 Matrix Elements

To date, parton-level calculations complete to $O(\alpha_s^2)$ have been performed, although the task is complex and difficult: the amplitudes for all the Feynman diagrams shown in Fig. 2 must be summed and squared. There have been several independent calculations in the past decade (Table 1) which have evoked some controversy and disputes, although the differences between the results of the various groups are now understood.

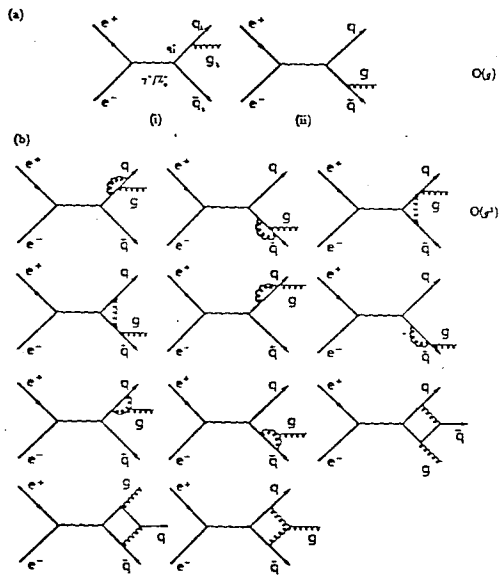
Table 1: Matrix Element Generators

Matrix elements	Comments	event generator
FKSS [6]	mistakes originally	private interface to Lund
GKS [7]	incomplete correction to FKSS	official interface to Lund
GS [8]	almost complete	private interface to Lund
ERT [9]	complete, practical limitations	private interface to Lund
KL [10]	complete	program now available

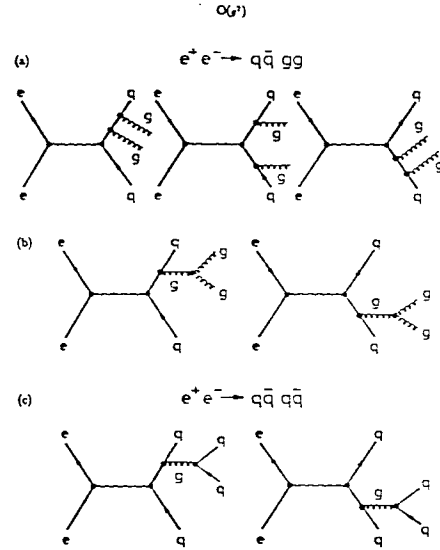
These generators are discussed in more detail in [11]. In summary, there were mistakes in the original FKSS calculations. Some, but not all, of these mistakes were corrected by



Diagrams for $e^+e^- \rightarrow q\bar{q}$: (a) lowest order; (b) radiative correction to order α_s ; And (c) radiative correction to order α_s^2 .



Diagrams for $e^+e^- \rightarrow q\bar{q}$: (a) lowest order; And (b) radiative correction due to the gluon to order α_s .

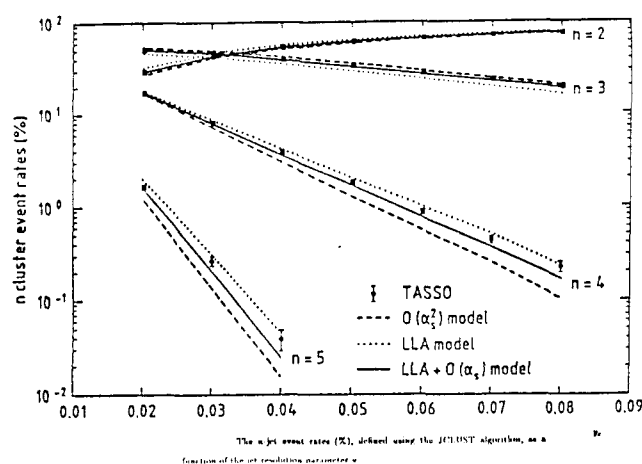


Feynman-diagrams for four-jet events.

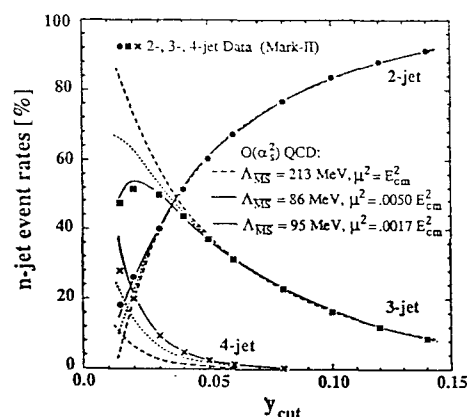
Figure 2. Feynman diagrams to $O(\alpha_s^2)$.

GKS; however, these incomplete GKS calculations are the only matrix elements presently available in the official Lund Monte Carlo package. A later analytic calculation by GS is not quite complete in that not all soft/collinear terms could be integrated analytically, although a working package exists which has been interfaced privately to the Lund Monte Carlo [11]. The ERT calculations are complete, although there are some practical limitations in that only discrete values of the parton resolution cutoffs are allowed; private interfaces to Lund exist. Finally, the KL calculations are complete, but the code is lengthy and complex; the authors have just prepared a more useable program.

Very recently three different groups [12,13] have calculated all tree-level matrix elements contributing to the cross-section for $e^+e^- \rightarrow 5$ partons at $O(\alpha_s^3)$. There is found to be good agreement between the calculations [11] and all three groups have programs available upon request. (This subject will be discussed further in Section 2.6).



(a)



(b)

Figure 3. Rates of multijet events as a function of y_c .

Complete matrix element calculations to $O(\alpha_s^2)$ for $e^+e^- \rightarrow 4$ partons thus exist, and now also do tree-level calculations up to $O(\alpha_s^3)$ for 5 parton production. However, there is already evidence from PETRA [14,15,16,17] that the $O(\alpha_s^2)$ calculations severely underestimate the rate of 4-jet events observed in the data (Fig. 3 (a) [16,17]), and do not reproduce the event shape observables related to gluon emission out of the event plane [17,18,19]. However, calculations based upon the Leading Logarithm Approximation (LLA) in QCD are able to describe well the 4-jet rate (Fig. 3 (a)) and give a better description of the $p_{T_{out}}$ -like observables. A reasonable interpretation of these facts is that higher order corrections beyond $O(\alpha_s^2)$ are needed to describe the data already at PETRA energies around 35 GeV. This implies that the situation for the $O(\alpha_s^2)$ calculations will be even worse at the Z^0 energy, where we expect more gluon radiation to be resolvable experimentally, so that the missing higher order terms will be even more noticeable. The

LLA-inspired calculations are expected to perform better because they include soft and collinear gluon emission in principle to infinite order, although in an approximate way. These calculations will be briefly reviewed in the next section.

A very interesting recent development has been the use of so-called ‘optimised’ perturbation theory, in which the renormalisation scale μ^2 is chosen so as to minimise (in principle) the unknown higher order terms in a perturbative series calculated only up to finite order. In practice this means finding simultaneously μ^2 and $\Lambda_{\overline{MS}}$ values which give the best agreement between the $O(\alpha_s^2)$ matrix elements and the data in terms of the 2,3 and 4-jet rates. Analyses with the Mark II [20] and AMY [21] data have shown that $\Lambda_{\overline{MS}} \sim 100\text{-}200$ MeV and $\mu^2 \sim 0.002 \times s$ are preferred (Fig. 3 (b) [20]), but it should be noted that there is a strong correlation between these two fitted parameters.

The significance of these results is not clear: on one hand the procedure is theoretically respectable (see [22] and references therein); on the other hand, however, the calculation of physical observables should not depend upon the choice of renormalisation scale, it only does so because we have a finite, rather than infinite, number of terms in the perturbative series. One can ask what is the physical significance of the fact that the renormalisation scale turns out to be as low as 1-2 GeV?

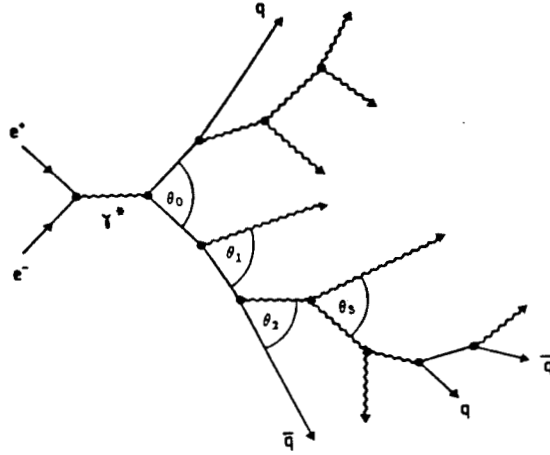
Another concern is that the third (and higher) order terms, as yet uncalculated completely, in the perturbative series for the jet rates may be large relative to the second order terms. Such behaviour has been seen in the recent calculation of R to $O(\alpha_s^3)$ [23]. Writing:

$$R = \sigma_0 + (a_1 + a_2 + a_3) \sigma^{ew}$$

where σ_0 is the quark-parton model electromagnetic cross-section, σ^{ew} represents the electroweak effects, and a_1, a_2, a_3 are the first, second and third order QCD corrections respectively. One finds that $a_1 : a_2 : a_3 = 1 : 0.09 : 0.26$. The fact that a_3 is three times larger than a_2 has raised doubts as to whether the perturbative QCD series converges. One might argue that the third order terms could also be large for the jet rate calculations, and that the results of optimising the theory to second order may not be reliable or meaningful. Until the third order terms are calculated one can only speculate and conjecture. The fact remains that from a phenomenological point of view, $O(\alpha_s^2)$ matrix elements give an excellent description of the 2,3 and 4-jet rates (Fig. 3 (b)) if the renormalisation scale is optimised along with $\Lambda_{\overline{MS}}$.

1.2.2 Parton Shower Calculations

As I have just described, the exact matrix element calculations are difficult and have only been performed completely to second order in α_s , allowing production of up to 4-parton final states. An alternative perturbative treatment is provided by the LLA. In this approach the quarks produced in $e^+e^- \rightarrow q\bar{q}$ may be very much off mass-shell and are allowed to radiate gluons, which may themselves branch into parton pairs. A parton



A typical parton cascade, showing the angular ordering of successive branchings.

Figure 4. Representation of a parton shower or cascade.

shower thereby develops (Fig. 4) until virtualities become small and branching is stopped. The probability for each branching is given by the Altarelli-Parisi equations [24], and the total cross-section for a shower is assumed to be proportional to the product of independent probabilities, one for each branching, namely, no interference between Feynman diagrams for each tree-level branching is taken into account. Formally such showers are therefore iterative classical Markov processes and are amenable to Monte Carlo simulation.

Many parton shower Monte Carlo event generators have been devised; an excellent review and comparison is given in [11]. In Table 2 I give a brief list of the most widely used programs (see [11] for references and details of other programs).

HERWIG (formerly BIGWIG for e^+e^- annihilation) contains an elaborate treatment of azimuthal correlations due to the gluon spin and of the coherent emission of soft gluons. The BIGWIG version has been extensively compared with data by Mark II and TASSO and found to be in generally good agreement. The JETSET parton shower is matched on to the $O(\alpha_s)$ matrix element and gives an excellent description of most features of the data, in particular of the 2,3,4 and 5-jet rates seen at TASSO (Fig. 3 (a)). NLLJET is a relatively young program which is still in development. It has the attractive feature of implementing the next-to-leading order logarithmic calculations of parton emission. Comparison by the authors indicates generally good agreement with data from PEP, PETRA and TRISTAN. ARIADNE provides an alternative approach to perturbative QCD cascades in that it is formulated in terms of colour dipoles rather than explicit quarks and gluons. Soft gluon coherence and correlations are automatically included in a natural way. The authors show good agreement with Mark II data. Finally, the Caltech-II model was shown by Mark II to describe the data poorly compared with BIGWIG and JETSET.

Table 2: Parton Shower Generators

Program	Features	Hadronisation	Comparison with Data
HERWIG	azimuthal correlations	clusters	Mark II [18], TASSO [17,19]
JETSET	$O(\alpha_s)$ matrix element	Lund string	Mark II [18], TASSO [17,19]
NLLJET	next-to-leading LLA	Lund string	authors [25]
ARIADNE	colour dipoles	Lund string	authors [26]
Caltech-II	elaborate hadronisation	string + cluster	Mark II [18,27]

Although parton shower models have been around for almost a decade and have reached a level of high sophistication, some outstanding theoretical uncertainties remain. Firstly, values must be assigned to the arbitrary parameters. There are two of these common to all cascades: the QCD scale in the LLA, Λ_{LLA} , and the virtuality cutoff used to stop the parton branching, Q_0 . Other uncertainties include: the Q^2 -scale is not well-defined, the physical significance of the QCD scale Λ_{LLA} is unclear, and there are various options for handling the kinematics of the parton branchings and choosing the splitting variable in the Altarelli-Parisi kernels. Each program author chooses a particular solution to the problems, which adds another layer of difficulty to the comparison of the results between different models, since the choice of solution influences the results [28].

1.2.3 Hadronisation Models

An excellent review of this subject was published recently [29], so only very brief details are given here. Once partons have been produced by a perturbative QCD event generator, either matrix element- or parton shower-based, they must be fragmented into colourless hadrons so that the calculations can be compared with the data. It is generally accepted that hadronisation occurs at a Q^2 scale of around 1 GeV^2 , where the strong coupling is so large that perturbation theory breaks down and we are unable to do QCD calculations. Phenomenological schemes are therefore by necessity invoked to transform the partons into observable hadrons. These have been implicitly assumed in the preceding sections.

A widely used hadronisation model (see Table 2) is the Lund string [30]. Basically, a colour triplet string is stretched between quark and antiquark, the gluons being momentum-carrying kinks on the string. More than one piece of string can occur if a gluon converts into a $q\bar{q}$ pair (analogous to e^+e^- pair production by a photon in QED). The string is then fragmented according to a particular recipe to give final state hadrons. Heavy flavour and baryon production is controlled by a large set of parameters, although such particles play a relatively minor role in the global properties of the final state. The parameters which have the greatest influence are a, b in the symmetric Lund fragmentation

function:

$$f(z) = \frac{1}{z} (1 - z)^a \exp\left(-\frac{bm_T^2}{z}\right)$$

which control the longitudinal momentum distribution of particles in jets, and σ , which controls the transverse momentum distribution.

In HERWIG [31], at the termination of the parton cascade colourless clusters are formed from nearest neighbour partons in colour index. Large mass clusters are split into two by a string-like mechanism, then clusters are decayed according to phase space, via resonances, to produce the known spectrum of stable particles. The only parameter is in principle the cluster-splitting mass M_c .

Caltech-II employs a hybrid scheme [32], whereby the multiparton system is broken up into smaller mass colourless subsystems by a string mechanism. These clusters are then decayed according to a parametrisation of low energy data. A large number of parameters is involved, although it is claimed that many of these are either redundant or constrained by the low energy data.

Other hadronisation models, such as independent jet fragmentation, are less popular today as they cannot reproduce important features of the data such as the string effect [33], although they are important historically. These issues are covered in detail in the review of Sjöstrand [29].

Suitable values for the model arbitrary parameters are obtained by comparison with experiment (see *eg.* [17,18,19]). Results quoted using the models will normally indicate the parameter values used; in addition, the influence of varying the parameter values should be investigated before drawing firm conclusions.

1.2.4 Summary

Some indication of the current status of these perturbative QCD + fragmentation models, when confronted with the data, is given in Table 3, where total χ^2 values are given by Mark II and TASSO for a wide spectrum of event shape observables and single track quantities. The χ^2 value for ARIADNE was calculated by the authors themselves.

Table 3: χ^2 values for comparison of QCD models with data

	Mark II	TASSO
c.m. energy (GeV)	29	35
# data points	450	245
Program		
HERWIG	2870	942
JETSET shower	960	367
ARIADNE	1200	-
CALTECH-II	6830	-
JETSET $O(\alpha_s^2)$	1230	658

It cannot be emphasised too strongly that these numbers are not absolute values with precise statistical meaning, in that they depend upon which observables were fitted and do not take into account the correlations between these observables. In other words, if a model describes one observable badly, it will probably automatically fail to describe the many other observables which are correlated with that one. Nevertheless, the χ^2 values do indicate qualitatively the trend of the agreement between models and data. Two

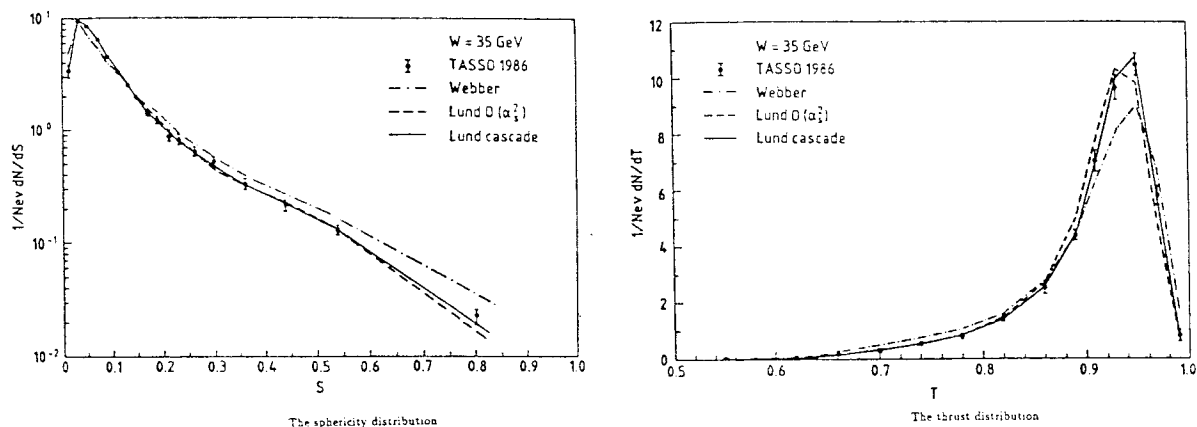


Figure 5. Sphericity and thrust distributions from TASSO comparing the data with three QCD + fragmentation models.

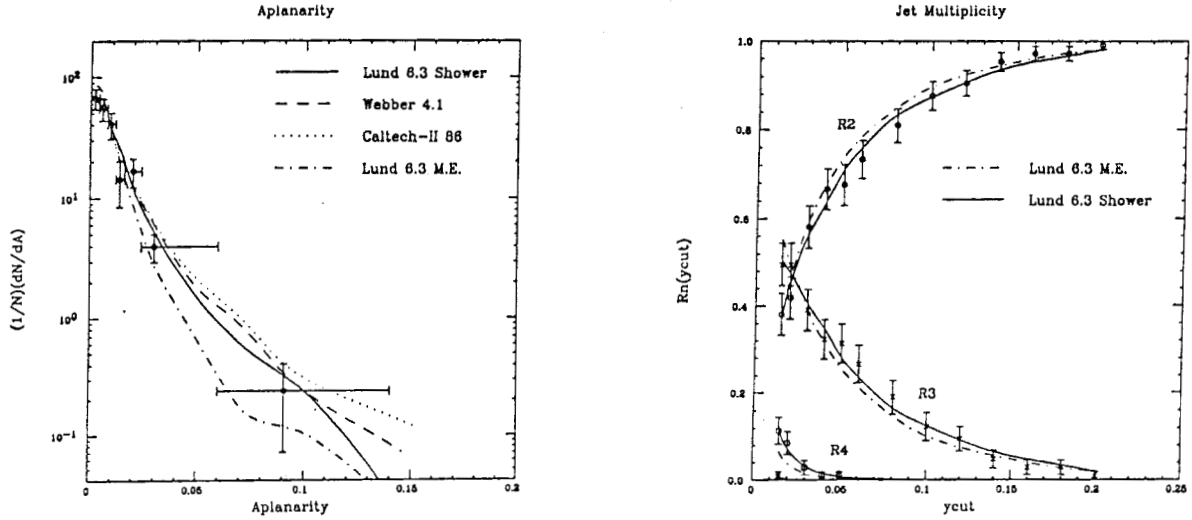


Figure 6. Aplanarity and jet multiplicity distributions from Mark II at the SLC comparing the data with QCD + fragmentation models.

sample distributions are shown in Fig. 5 [17,19], where three models are compared with the high statistics data sample collected by TASSO in 1986 (31176 hadronic events). To a good approximation all models describe the data well, although one can discern some discrepancies in the fine details. Some very latest results from Mark II at the SLC [34] are shown in Fig. 6, where the models, with the parameters optimised at $W = 29$ GeV, describe the data well within the limited statistics collected so far (184 hadronic events).

One can only reiterate the importance of having sound QCD-based models which are in good agreement with the PEP/PETRA data, for new physics at the Z^0 will manifest itself as deviations from the model predictions beyond the variations which can be produced by different choices of the parameter values.

2. Fundamental Tests of QCD

2.1 Introduction

The essential features of QCD may be summarised [35] as:

- (i) quarks with spin $1/2$ exist as colour triplets
- (ii) gluons with spin 1 exist as colour octets
- (iii) the coupling $q\bar{q}g$ exists

- (iv) *the couplings ggg and gggg exist*
- (v) *the above couplings are equal*
- (vi) *the coupling strength decreases like $\ln Q^2$*

where the items in italics are those features which have yet to be convincingly demonstrated experimentally. Clearly QCD needs to be tested more rigorously to put these features on a firm experimental footing. In my opinion it is unfortunate that ‘testing the Standard Model’ has come to mean testing the *electroweak* sector by precision measurements; **QCD is a vital component of the Standard Model and needs to be tested too!** I shall briefly mention the experimental evidence for the non-italicised items, and then review in detail the status of the attempts to verify the other features, with indications of the measurements which need to be made.

The first direct evidence for the existence of quarks came from the observations at SLAC in the late 1960’s that in electron-nucleon scattering experiments, at high momentum transfers the electron scatters from quasi-free pointlike particles carrying roughly one third of the nucleon mass. These particles were identified with the quarks which had been postulated by Gell-Mann and Zweig in 1964 as a calculational device to explain the spectra of mesons and baryons in terms of bound $q\bar{q}$ and qqq (or $\bar{q}\bar{q}\bar{q}$) states respectively [36]. If the quarks are assigned spin 1/2, possess the flavour quantum number ($f = u, d, s, c, b$) and are triplets in terms of the colour quantum number ($c = r, b, g$) then a consistent picture of the existence and quantum numbers of virtually all known hadrons can be created, (the only exceptions being a few resonances which may be candidates for glueball states). The colour quantum number is required to explain the existence of states such as Δ^{++} ($=u\uparrow u\uparrow u\uparrow$) or Ω^- ($=s\uparrow s\uparrow s\uparrow$), which otherwise should not exist as they contain three quarks in identical quantum states, thereby violating the principles of Fermi-Dirac statistics.

To explain the measured charges of the hadrons the quarks are assigned fractional charges: $u(2/3)$, $d(-1/3)$, $s(-1/3)$, $c(2/3)$, $b(-1/3)$ in units of the electron charge. Note that alternative models with integer charged quarks have been proposed [37] and have not yet been totally excluded experimentally (see [38] and references therein) although as this is not really a QCD feature of the quarks I shall not discuss it further here.

The number of colours N_c can be determined experimentally, for the decay width of the reaction $\pi^0 \rightarrow \gamma\gamma$ should be proportional to N_c^2 within the quark model, and measurements yield $N_c = 3$ [39]. $N_c = 3$ is also needed to explain the measured value of R .

The assignment of spin 1/2 to the quarks, in addition to providing a consistent explanation of all known hadron spins, has been verified experimentally in terms of the distribution of the angle θ between the jet axis and the e^+e^- beam axis in two-jet hadronic events. For single photon production of two massless spin-1/2 particles, neglecting electroweak interference effects, the distribution of the jet axis is predicted [40] to be proportional to $(1 + \cos^2\theta)$, and has been measured to be so [41]. Feature (i) is thus established experimentally beyond any reasonable doubt.

Evidence for the existence of massless electrically neutral particles within the nucleon

first came from the discovery that in the electron-nucleon scattering experiments mentioned earlier, only about 50% of the nucleon momentum was carried by the charged quarks. The remaining momentum can therefore be assigned to the gluons which mediate the strong interactions between the quarks. More direct evidence came from the observation of three-jet events in e^+e^- annihilation, which are understood in terms of the radiation of a hard gluon by either the produced quark or antiquark [42]. Gluon jets have also been observed in high energy proton-antiproton collisions [43]. The existence of the gluon and its coupling to quarks are thus beyond reasonable doubt. Measurements of the topologies of three-jet events have also demonstrated [44] that the gluon is a spin-1 particle.

The fact that gluons exist as colour octets (part of feature (ii)), and features (iv) - (vi), have yet to be directly demonstrated from an experimental point-of-view. Of course the fact that QCD calculations including these features do describe the data, and that alternative possibilities beyond the theory which we have are difficult to imagine from a theoretical viewpoint, lend indirect support to QCD as it is formulated. The features which remain to be verified are mainly related to the non-Abelian nature of the theory, in other words that the gluons themselves carry colour charge and interact strongly (feature (iv)), that the charge is of a certain magnitude and different from the quark colour charge (features (ii),(v)) and that this leads to a coupling strength which increases as the separation between partons increases (feature (vi)). It is possible to construct an Abelian form of QCD, but not so easy to rule it out experimentally, as we shall now see.

In the remainder of this section I shall discuss the Q^2 -dependence of α_s , the ggg coupling, the flavour-blindness of α_s , the colour charge of the gluon and perturbative calculations of multijet cross-sections.

2.2 The Q^2 -dependence of α_s

There have been many measurements of α_s in the last decade from hadron-hadron, lepton-hadron and e^+e^- interactions; see [45] for a recent review. In particular the measurements from e^+e^- experiments have been controversial; large systematic differences are seen in the measured values according to which matrix elements (see Section 1.2.1), which fragmentation scheme (see section 1.2.3) and which observables were used in the determination. These results are summarised in Fig. 7 [46], which I shall not discuss as it is by now a familiar diagram.

The expected decrease in the value of α_s as W increases is small compared with the systematic errors in these measurements. For example, using the first order formula [47] as an illustration:

$$\alpha_s^{(1)}(Q^2) = \frac{12\pi}{(33 - 2N_f) \ln(\frac{Q^2}{\Lambda^2})}$$

and taking $\Lambda = 150$ MeV as a reasonable value [45]:

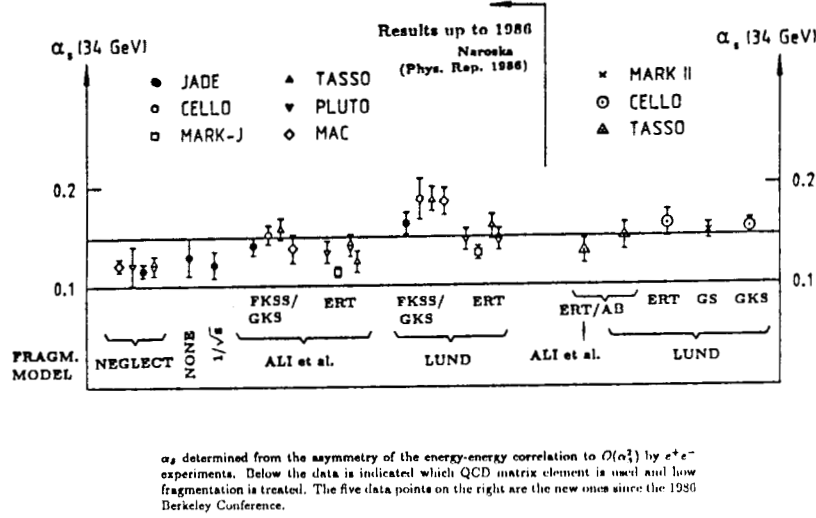


Figure 7. Compendium of α_s measurements in e^+e^- annihilation scaled to $W = 34$ GeV.

$$\alpha_s^{(1)}(14^2)/\alpha_s^{(1)}(44^2) \sim 1.3$$

where $14 \leq W \leq 44$ GeV spans the PETRA energy region. However from Fig. 7, there are systematic shifts by a factor of roughly 1.5 between measurements at the *same* energy (34 GeV).

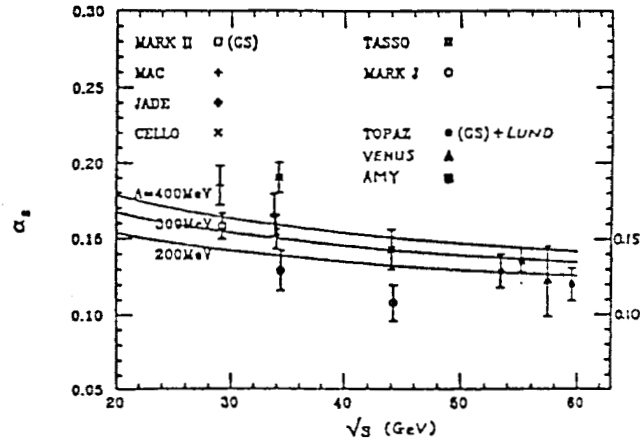


Figure 8. Compendium of α_s measurements in e^+e^- annihilation as a function of W .

This is reinforced in Fig. 8, [48], where a compendium of measurements of α_s using the asymmetry of the energy-energy correlation [49] at PETRA, PEP and TRISTAN shows

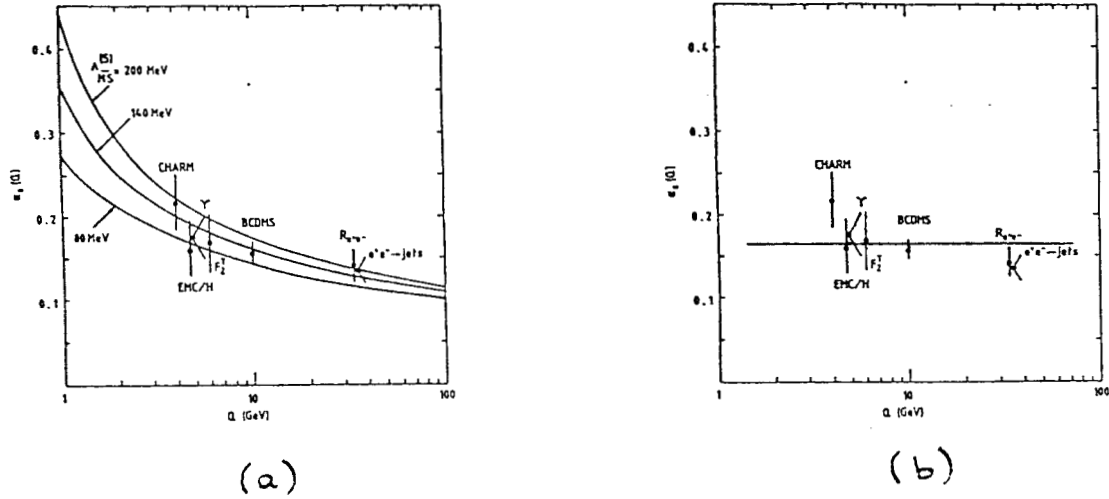


Figure 9. Compendium of α_s measurements as a function of W .

the magnitude of the systematic uncertainties. Any attempt to see α_s running by direct measurement seems therefore hopeless.

The experimental situation is summarised in Fig. 9 (a), compiled by Altarelli [45]. The theoretical curves of $\alpha_s^{(2)}$ for different values of $\Lambda_{\overline{MS}}$ indicate that the data are in agreement with a coupling which decreases with Q^2 . The same data are shown in Fig. 9 (b) with the suggestive theoretical curves removed and a flat line drawn by eye so as to pass through as many data points as possible. From these measurements there is clearly no evidence for an energy-dependent coupling strength as opposed to a constant one.

A few years ago a method of measuring the *running* of α_s without being concerned with measuring the actual *value* at a given energy was proposed [15]. To $O(\alpha_s^2)$ the rate of three-jet events is calculated in perturbative QCD to be

$$R_3 = C_1 \alpha_s + C_2 \alpha_s^2$$

where C_1, C_2 are independent of s . Studying the energy-dependence of R_3 is thus effectively studying the energy-dependence of α_s . A complication arises in that C_1 and C_2 do depend upon the jet resolution criteria. Using the well-known JADE cluster algorithm [14], all jet pairs i, j are required to have invariant masses which satisfy:

$$m_{ij}^2 > y_c s$$

where y_c is a dimensionless jet resolution parameter. Provided y_c is chosen large enough that the ratio of R_3 's at different energies does not depend upon y_c , no variation in R_3 as a function of s is introduced by the jet algorithm. In detailed studies [15,16,17] $y_c \geq 0.08$

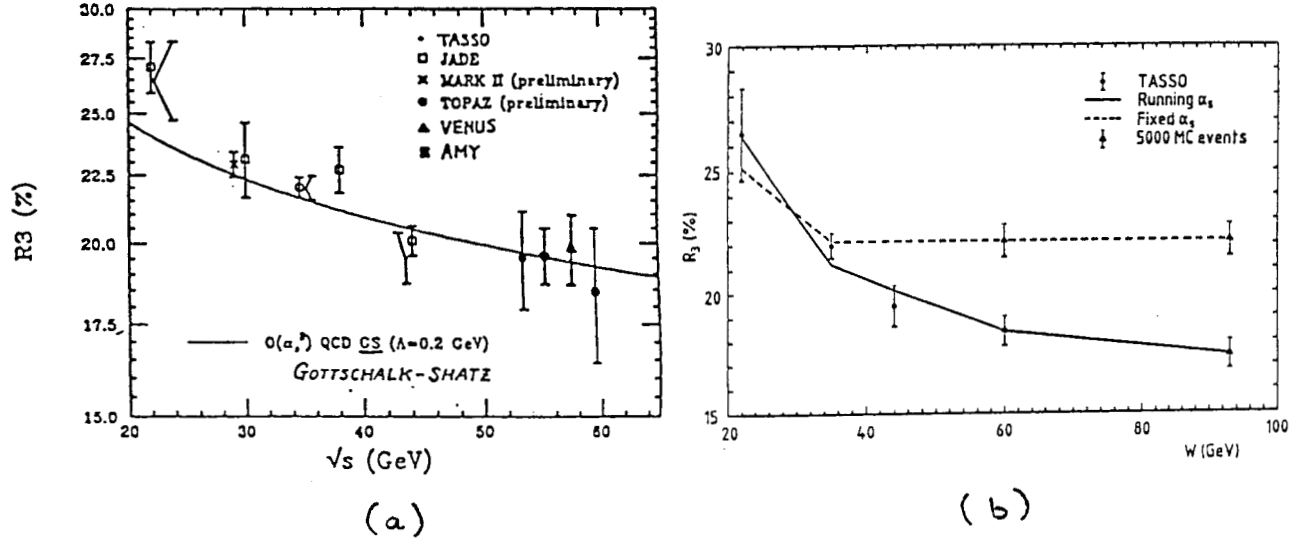


Figure 10. The three-jet rate as a function of W , defined using the JADE cluster algorithm with $y_c = 0.08$.

was found to be a suitable range at PETRA energies, corresponding to a jet-pair mass resolution of $\geq 10 \text{ GeV}/c^2$ at $W = 35 \text{ GeV}$.

Several analyses have been performed at PETRA [15,16,17,50], PEP [20] and TRISTAN [5]; results for $y_c = 0.08$ are compiled in Fig. 10 (a) [48]. At first sight the data give a strong indication of R_3 decreasing with increasing W , in good agreement with the $O(\alpha_s^2)$ prediction of Gottschalk and Shatz. Some caution is necessary however. Firstly, the TASSO study showed [16,17], by using the Lund parton shower model, that a decrease in R_3 between 22 and 35 GeV is evident also for the case where α_s is fixed (Fig. 10 (b)), presumably because of fluctuations in the hadronisation process at this relatively low energy. The TASSO and JADE data points at 22 GeV in Fig. 10 (a) should thus be ignored. In addition, the large errors (due to low statistics) on the TRISTAN data points between 50 and 60 GeV do not give much of a lever arm. The case thus rests on the high-statistics data points from JADE, TASSO and Mark II in the range $29 \leq W \leq 44 \text{ GeV}$. These data are clearly consistent with an energy-dependent strong coupling, but the case is hardly conclusive, and a constant coupling strength cannot be excluded.

There is hence a pressing need for high-statistics data points from TRISTAN and SLC/LEP. In this case, high-statistics in fact means only a few thousand events. Shown in Fig. 10 (b) are error bars at 60 GeV and around the Z^0 mass, indicating the statistical precision which could be obtained from a sample of only 5000 hadronic events. Clearly real measurements at those energies with such a modest number of events would demonstrate, or otherwise, the energy dependence of α_s with a significance of many standard deviations relative to the fixed α_s case. In view of the continuing accumulation of events at TRISTAN, and the successful operation of SLC and LEP, one can look forward to those measurements in the near future.

2.3 The Triple Gluon Vertex

The gluon self-coupling is a manifestation of the non-Abelian nature of QCD. Methods to verify its existence have been proposed and involve studying the Q^2 evolution of the longitudinal structure function in lepton-hadron collisions and the k_T spectrum of back-to-back jets in hadron-hadron collisions. The theoretical and experimental uncertainties are unfortunately larger than the effects being investigated [51]. An ideal place to look would be the hadronic decay of a heavy quarkonium resonance into three gluon jets. Unfortunately the only known system is the Υ , which is too light to produce narrow, well-separated jets. The remaining search-ground is thus at high energy e^+e^- colliders.

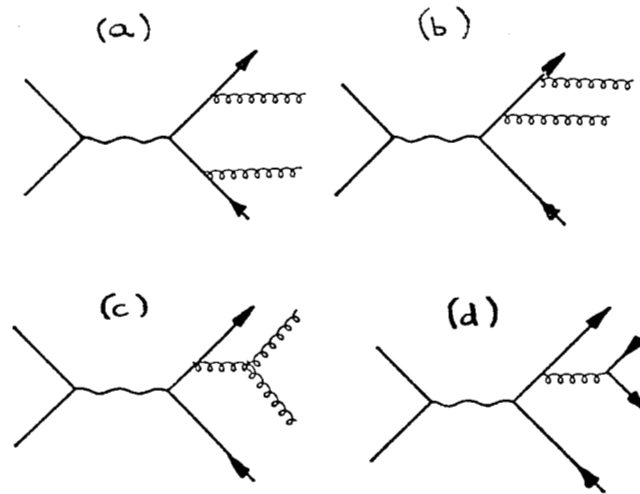


Figure 11. Feynman diagrams for production of four partons in second order perturbation theory.

Feynman diagrams for production of four partons at $O(\alpha_s^2)$ are shown in Fig. 11. The gluon self-coupling appears for the first time in these second order diagrams. It is clear that tests of the three gluon vertex will involve four-jet events. The task is to find a property of the so-called 'QCD-like' events (Fig. 11 (c)), containing the $g \rightarrow gg$ coupling, which distinguishes them from events involving two-gluon emission by the quarks (Fig. 11 (a,b)) or gluon conversion into a $q\bar{q}$ pair (Fig. 11 (d)), the so-called 'QED-like events'.

An Abelian form of QCD can be constructed in which three coloured quarks interact via colour singlet vector gluons, with a coupling constant $\alpha^* = \frac{4}{3} \alpha_s$. The colour factors are also different and enhance the probability for $g \rightarrow q\bar{q}$ by a factor of about eight [52], so that $g \rightarrow gg$ in the non-Abelian model is effectively replaced by $g \rightarrow q\bar{q}$ in the Abelian model. Searches for the ggg vertex are thus based upon the different jet angular distributions which result when a gluon splits into two spin-1 bosons (gluons) as opposed to two spin-1/2 fermions (quarks).

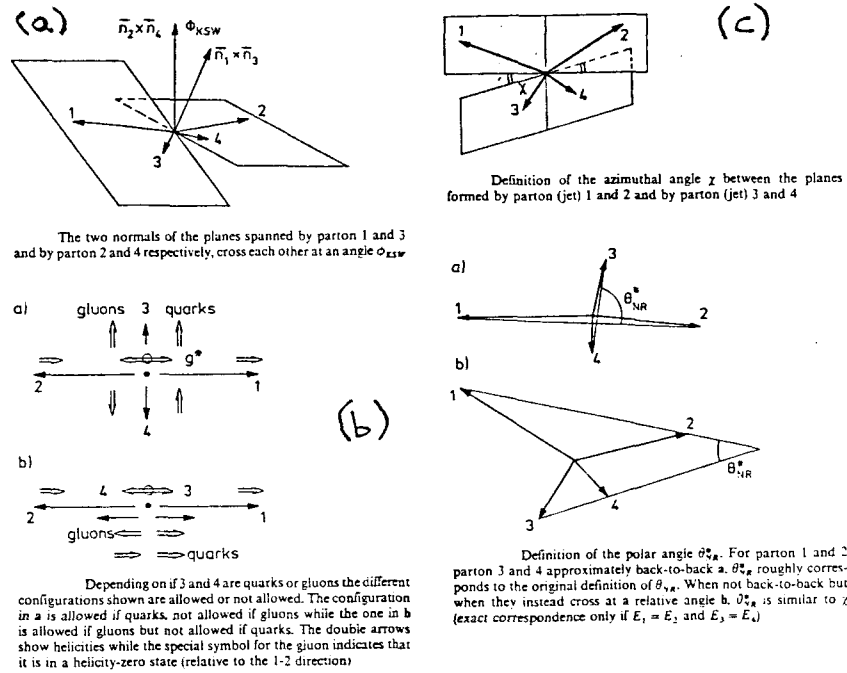


Figure 12. Definitions of measures proposed for searching for the triple gluon vertex in 4-jet events.

Three different measures have been proposed based upon the jet topologies in 4-jet events [53]. These measures are detailed in the original papers and compared in the review by Bengtsson [52]. I shall briefly explain the observables, using the notation that the jets be ordered 1,2,3,4 in order of decreasing energy, jet 1 being the highest energy jet in the event. The Körner, Schierholz, Willrodt angle, ϕ_{KSW} , is defined in Fig. 12 (a) [52] as the angle between the normals to the planes containing jets 1,3 and jets 2,4. Gluon alignment in the splitting process $g \rightarrow gg$ tends to force these two planes to be parallel, whereas $g \rightarrow q\bar{q}$ prefers the planes to be orthogonal. The Nachtmann-Reiter angle, θ_{NR}^* (Fig. 12 (b)), is that between the momentum vector sums of jets 1,2 and jets 3,4. Using helicity arguments, NR showed that $\theta_{NR}^* \sim 0$ is favoured by $g \rightarrow gg$ and $\theta_{NR}^* \sim 90^\circ$ is favoured by $g \rightarrow q\bar{q}$. Finally Bengtsson and Zerwas define the angle χ (or θ_{BZ}) as that between the planes containing jets 1,2 and jets 3,4 (Fig. 12 (c)). Linear polarisation of the gluon in $e^+e^- \rightarrow q\bar{q}g$ results in quite different distributions of χ for Abelian and non-Abelian QCD.

Results of Monte Carlo studies [52] of these three measures are summarised in Fig. 13, where large differences between non-Abelian and Abelian models remain after hadronisation according to the Lund string model. The current status of experimental measurements is given in Fig. 14. JADE results [15] at $W = 44$ GeV (Fig. 14 (a,b)) show no power to discriminate between Abelian and non-Abelian models; some indication that the data prefer QCD is given in a very recent AMY study [5] (Fig. 14 (c,d)), although the significance is only at the level of a few standard deviations and the Abelian model is clearly not ruled out. The latter results, based on a few thousand hadronic events, are very promising

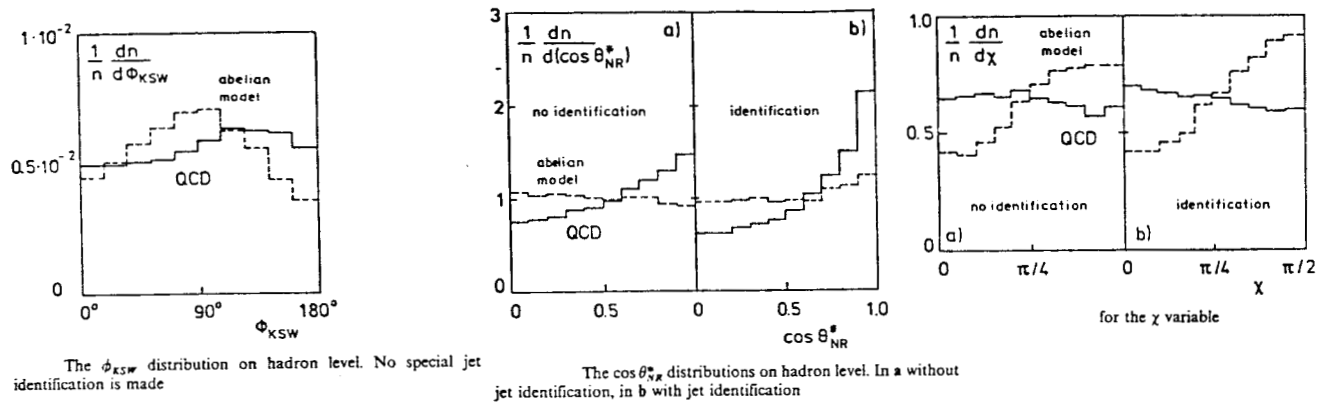


Figure 13. Differences between Abelian and non-Abelian QCD at the hadron level for the three proposed measures, at the Z^0 energy.

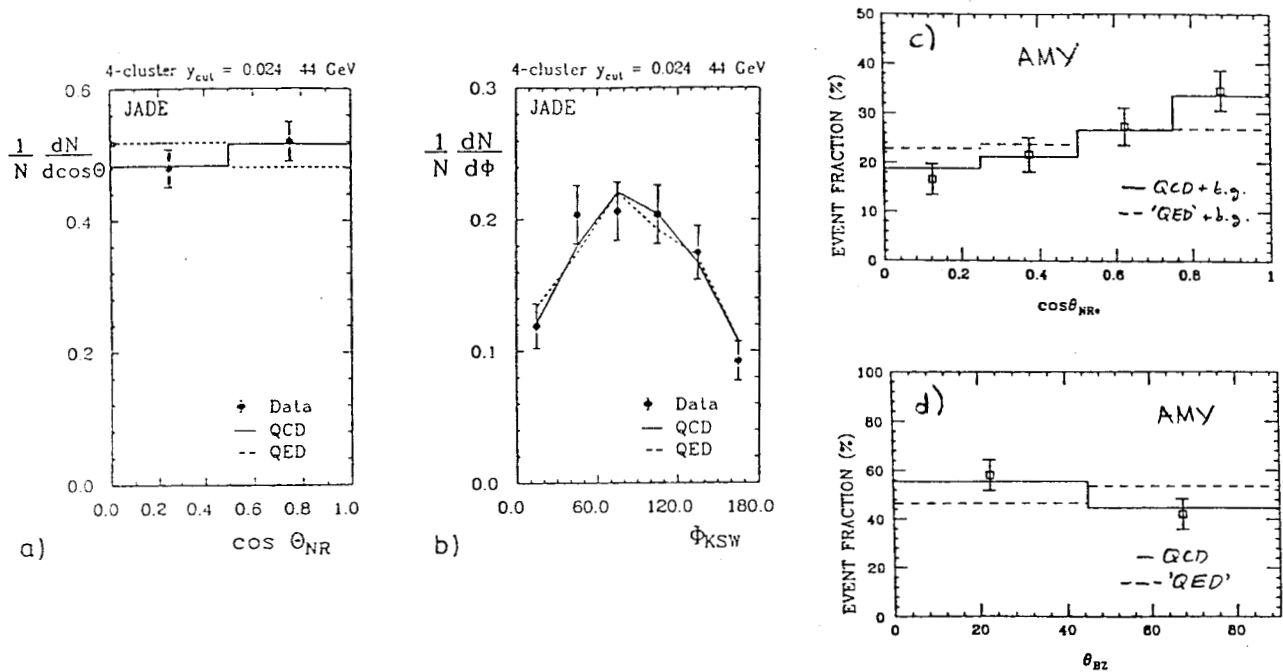


Figure 14. Experimental results from JADE and AMY on testing the non-Abelian Nature of QCD.

in that they indicate that a precise test should be straightforward with the large event samples expected at SLC/LEP.

2.4 The Flavour-Independence of the Strong Coupling

The idea that the strong interaction between quarks does not depend upon the quark flavour is so implicit in the foundations of QCD that it is not usually even mentioned, and the thought that this may not be so would be considered outrageous by theoreticians. Nevertheless, a skeptical experimentalist may ask if there is any hard evidence to support this notion. What little evidence there is is summarised in this section. Of course a theorist might argue that the fact that QCD, as it is formulated, describes data well indicates that our assumptions are correct, but in my opinion such arguments are not compelling.

TASSO has measured the ratio: $\alpha_s(f)/\alpha_s(all)$, where the numerator is for a data sample enriched with heavy quark events of flavour f and the denominator is for all flavours, for the cases $f = \text{charm}$ [54] and $f = \text{bottom}$ [55], using the same technique in both cases. Firstly, $\alpha_s(all)$ was determined by fitting the AEEC distribution with an $O(\alpha_s^2)$ matrix element + hadronisation Monte Carlo model, allowing α_s to vary to obtain the best fit. The very high statistics data sample above $W = 30$ GeV (around 60000 hadronic events) gave a small statistical error. Samples of events enriched with b-quarks or c-quarks were obtained in separate analyses using tagging procedures [54,55]. The percentages of the enriched flavour events and the remaining flavour events were estimated from Monte Carlo calculations. $\alpha_s(f)$ was allowed to vary in fits to the AEEC distributions of the enriched

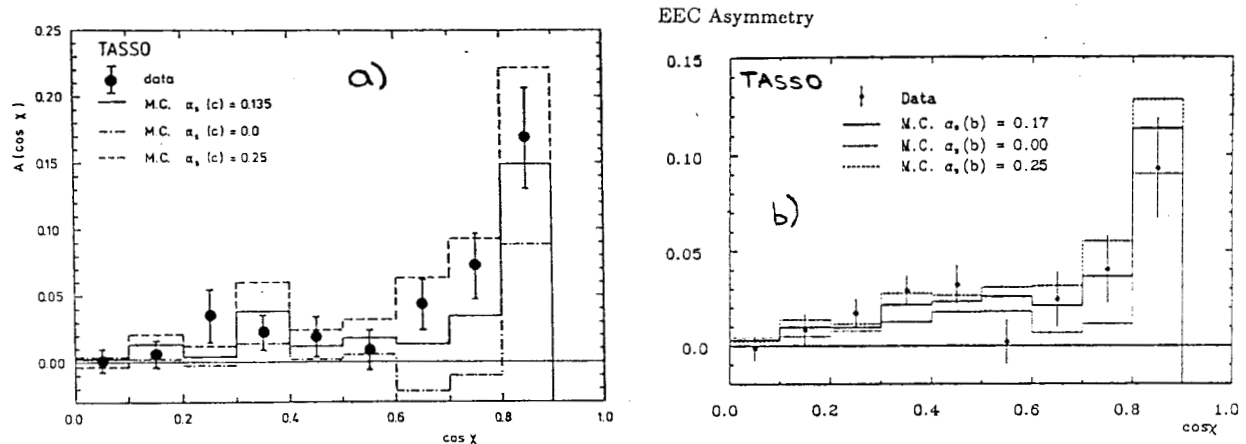


Figure 15. TASSO Fits to the AEEC distribution for enriched samples of charm (a) and bottom (b) events to determine α_s for the heavy flavour events separately.

samples (Fig. 15), with α_s for the background events being fixed to $\alpha_s(all)$. The statistical errors on these values were much larger because of the relatively small number of tagged events. By taking the ratio $\alpha_s(f)/\alpha_s(all)$, many of the systematic effects discussed in Section 2.2 cancel out and the measurement is less biased. The results are:

$$\frac{\alpha_s(c)}{\alpha_s(all)} = 0.98 \pm 0.38 \pm 0.15 \qquad \frac{\alpha_s(b)}{\alpha_s(all)} = 1.17 \pm 0.50 \pm 0.28$$

indicating no flavour dependence within the (large) errors.

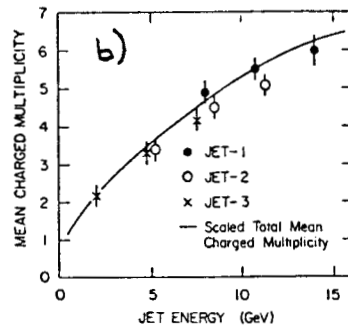
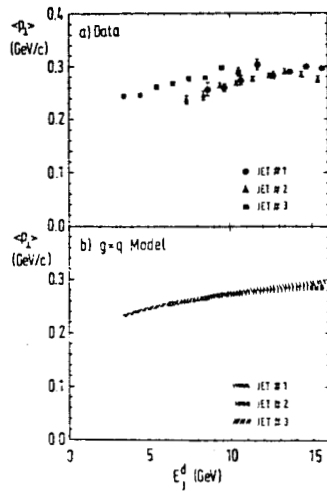
Many of the experiments at SLC/LEP will have high-precision vertex detectors, allowing the potential for tagging heavy flavour events with a higher efficiency than was possible at TASSO, aided by the fact that at the Z^0 energy the decay lengths of charmed and bottom hadrons are much longer than at PETRA energies because of the Lorentz boost. Given the expected high luminosities, there is a tremendous opportunity to make high-precision tests of the flavour-independence of the strong coupling.

2.5 The Colour Charge of the Gluon

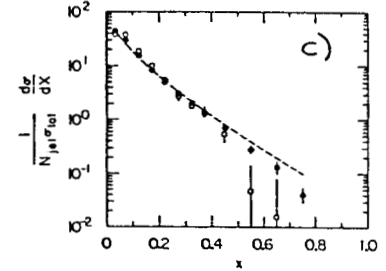
It was pointed out many years ago [56] that the strong coupling constant of the gluon to separating colour octets is 9/4 times the coupling constant to separating 3 and $\bar{3}$. Loosely speaking, one may rephrase this statement as that the colour charge of the gluon is 9/4 times the colour charge of the quark. A leading logarithm bremsstrahlung-type calculation predicts [56] that in the asymptotic limit $s \rightarrow \infty$, the multiplicity of soft gluons in a gluon-initiated jet is 9/4 times the multiplicity in a quark-initiated jet. Assuming proportionality between gluon multiplicity and the ensuing hadron multiplicity leads to the prediction that the particle multiplicity in gluon jets should be $r = 9/4$ times that in quark jets, and hence that the former will be softer by roughly the same factor. Using the same arguments, it was also shown [57] that the angular widths of gluon and quark jets are related by: $\delta_g = \delta_q^{4/9}$ (δ in radians, < 1 by construction), *i.e.* that gluon jets should be wider than quark jets.

Many experimental searches for these effects have been made; I give a brief summary below. However, it is worth noting first that there are several caveats to the above arguments which tend to dilute the factor r . First and foremost the searches at PETRA and PEP were at energies a little short of ∞ , in fact around 30 GeV. Finite energy corrections up to second order in α_s reduce r from 9/4 to ~ 2 (see [58] and references therein). Heavy quark and fragmentation effects further reduce r to around 1.3 [58]. The differences in particle multiplicity, width and hardness of fragmentation may thus be less apparent than naively expected.

Experimental investigations of these effects are usually based upon obtaining a sample of symmetric three-jet events, interpreted as quark, antiquark and gluon jets of roughly equal energy. The least energetic jet (jet 3) is found to be most probable to originate from the gluon. JADE reported [59] that particles coming from the lowest energy jet tend to have larger transverse momentum w.r.t. the jet axis: averaging over jet energies between 6 and 10 GeV (Fig. 16 (a)) they found $\langle p_T \rangle_3 / \langle p_T \rangle_2 = 1.16 \pm 0.02$, indicating



Mean charged particle multiplicity for the data of fig. 1a as a function of jet energy. The line shows the variation of the single jet multiplicity for $e^+e^- \rightarrow \text{hadrons}$ as a function of the jet energy ($\sqrt{s}/2$).



The detector-corrected inclusive charged-particle distribution for threefold-symmetric three-jet events at $E_{\text{cm}} = 29$ GeV (filled circles) in comparison with the inclusive charged-particle cross section of hadronic events at $E_{\text{cm}} = 19.3$ GeV, extrapolated from the fitted curves in Fig. 2 (dashed curve). The inclusive charged-particle distribution of a gluon jet of $E_j = 9$ GeV, with the assumption of the subtraction discussed in the text, is shown by the open symbols.

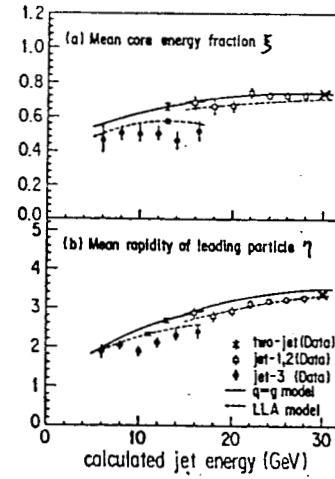
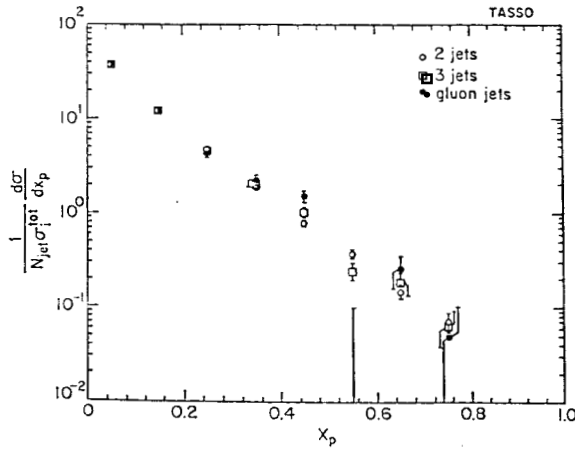


Figure 16. Searches for differences between quark and gluon jets by PETRA, PEP and TRISTAN experiments.

wider gluon jets. HRS found [60] essentially no differences in particle multiplicity between quark and gluon jets within experimental errors (Fig. 16 (b)): $\langle n \rangle_g / \langle n \rangle_q = 1.29^{+0.21}_{-0.41} \pm 0.20$. Mark II found [61] some evidence for a softer fragmentation of inclusive charged particles in gluon jets (Fig. 16 (c)), although their analysis involved extrapolating lower energy data from other experiments, with the possibility that there may be some systematic bias. Other preliminary results from TPC and CELLO show no differences [58].

Recent results from TASSO [58] also show no evidence for a difference in the fragmentation spectra of inclusive charged particles in quark and gluon jets (Fig. 16 (d)) and suggest an explanation of the Mark II results in terms of the selection cuts applied to the jet samples. The latest contribution to this subject is provided by AMY at TRISTAN [62], which claims to observe effects in the variables 'mean core energy fraction' and 'mean rapidity of leading particle' (Fig. 16 (e)). Note that quark and gluon jets must be compared

at the same energy, as particle multiplicities and flows within jets change with energy. In Fig. 16 (e) there is only one data point in each distribution where the quark and gluon jets overlap in energy. For that particular jet energy the gluon jets appear to be wider and have a softer fragmentation function. A greater overlap in sample energies would be needed to make a more conclusive statement.

In summary, the experimental situation concerning the different fragmentation properties of quark and gluon jets, reflecting the different colour charges of quarks and gluons, is confused. Some experiments claim to see an effect, whilst others do not. It is certainly true that any effect is much smaller than the $9/4$ factor expected in the naive QCD limit. The field is therefore wide open for definitive measurements to be made at SLC/LEP. A problem which must, however, be addressed if differences between quark and gluon jet fragmentation are observed, is whether the different properties arise from the perturbative QCD processes of multiple soft gluon bremsstrahlung, or whether they may be explained by non-perturbative hadronisation models. For example, it is well-known that the Lund string hadronisation model alters the particle flow and multiplicity around the directions of the parton parents of hadron jets. In particular, a hard gluon, represented as a kink on the string stretched between quark and antiquark, may be expected on average to fragment into a softer, higher multiplicity jet because two string-sections are associated with the energy-carrying kink, compared with one section for the quark and antiquark. The untangling of these effects will require careful, systematic study of high-statistics data samples.

2.6 Tests of Higher Order QCD: Multijet Cross-Sections

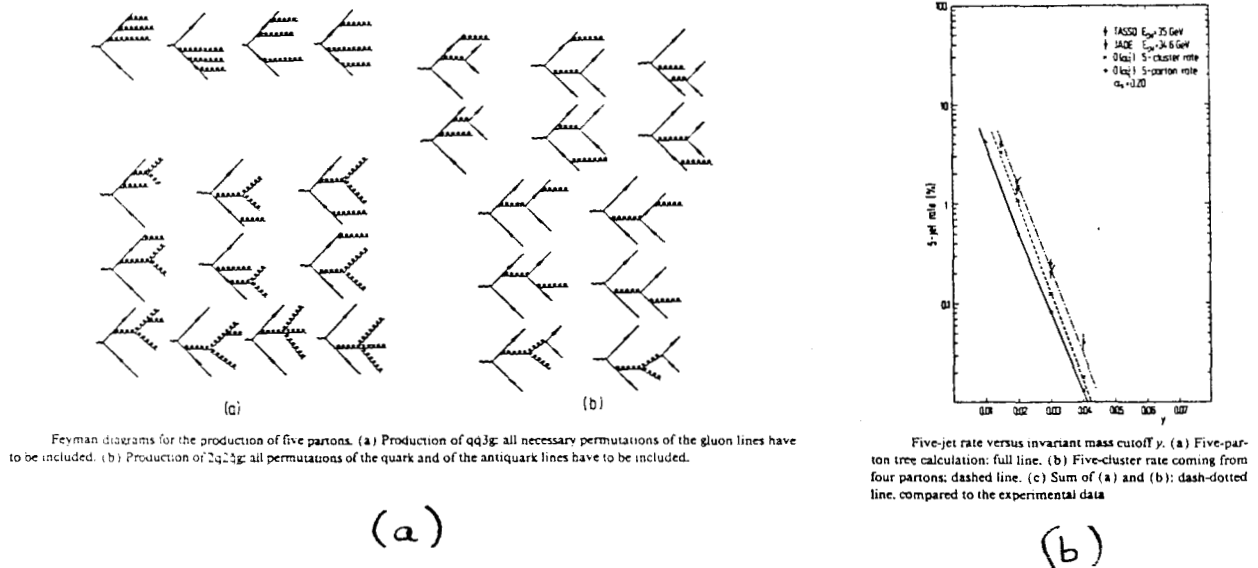


Figure 17.

As mentioned in section 1.2, tree-level matrix element calculations of five parton production to order α_s^3 in perturbation theory have recently been performed [12,13]. The relevant set of Feynman diagrams is shown in Fig. 17 (a) [13]. In Fig. 17 (b) the 5-jet calculations of [13] are compared with the JADE and TASSO data at 35 GeV and found to be in good agreement.

Note that just as the ggg vertex first appeared at second order, now the gggg vertex appears at third order, so that to test the existence of the four-gluon coupling one would need to study 5-jet events. Very low rates of such events were observed at PETRA [14,15,16,17], but resolvable multiple gluon emission should be more observable at SLC/LEP in the form of multijet events.

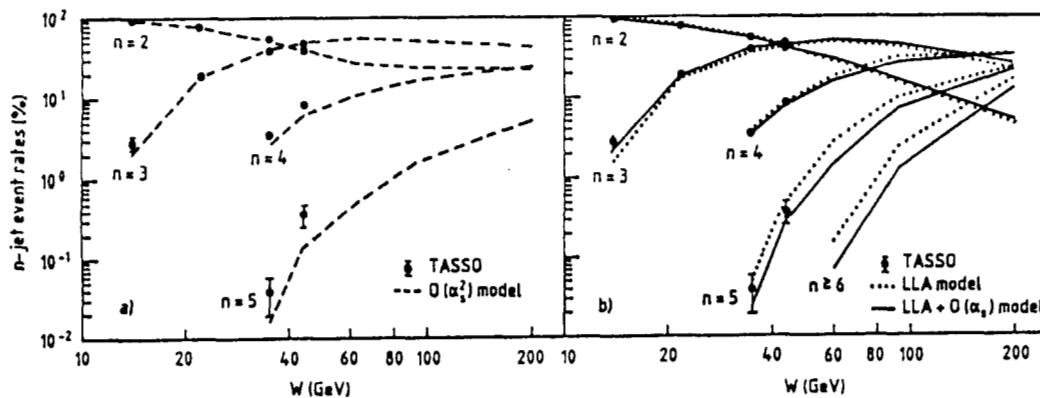


Figure 18.

For example, shown in Fig. 18 [17,63] are the rates of n -jet events, defined using the JADE algorithm with m_{ij} fixed at 7 GeV/ c^2 , as a function of W . The TASSO data lie between 14 and 44 GeV, but the QCD model calculations are extended up to 200 GeV. The $O(\alpha_s^2)$ model (GKS in JETSET) curves tend to saturate at high W , indicating that the jet structure is more-or-less fully resolved in these finite order predictions. The LLA model (BIGWIG) and LLA + $O(\alpha_s)$ model (JETSET shower) calculations show a much richer jet structure however, with 2- and 3-jet rates which decrease at large W as 4,5 and 6-jet rates 'switch on'. In other words, as W increases, even though α_s decreases, more gluon bremsstrahlung is resolved as separate jets. From Fig. 18, parton shower models predict rates of 5 and ≥ 6 -jet events of 7% and 1% respectively at the Z^0 energy, though of course these numbers depend upon the choice of jet-jet mass resolution.

The observation of such multijet final states at SLC/LEP will thus provide both qualitative and quantitative tests of higher order QCD.

3. 'Standard' QCD Physics

In this section I have arbitrarily collected topics which, though still interesting and important, do not represent 'fundamental' tests of QCD in the same sense as those discussed in Section 2. I shall mention general features of jet fragmentation expected at the Z^0 , with emphasis on the fragmentation properties of the bottom quark; as these comprise about 20% of all hadronic events at the Z^0 , SLC and LEP will effectively be 'b-factories'. Other subjects briefly outlined are QCD coherence effects, intermittency and local parton-hadron duality.

3.1 Jet Fragmentation

In the last decade a wealth of information has been collected at PETRA, PEP and TRISTAN on hadron production in high energy e^+e^- annihilation. The data have been studied in terms of observables such as sphericity, thrust, aplanarity, $\langle\langle p_{T_{in}}^2 \rangle\rangle$, $\langle\langle p_{T_{out}}^2 \rangle\rangle$, $p_{T_{in}}$, $p_{T_{out}}$, x_p , n_{ch} , rapidity, M_h^2 , M_l^2 , $M_h^2 - M_l^2$, energy-energy correlations and so on. Exclusive studies of strange, charmed, vector and tensor meson production and baryon production, rapidity correlations and Bose-Einstein correlations have all shed considerable light on the processes by which hadrons are produced. Much has also been learned by interpreting the observations in terms of the family of perturbative QCD + hadronisation models. For an overall review see [64]. Hadronisation is (presumably) a manifestation of QCD, but in the low-energy regime where perturbative calculations break down. Just because we do not yet have a respectable theory of such non-perturbative processes does not mean that the physics issues should be neglected: hadronisation is probably the least-understood part of the strong interaction sector of the Standard Model.

All of the above-mentioned topics can be studied further at SLC/LEP. Initial studies will check that the general features of hadronic events are as expected from the energy evolution of the low energy data. QCD model predictions of event topologies have been made by Mark II [18] for the Z energy, and by Burrows [63] for W up to 200 GeV. Just four examples from [63] are shown in Fig. 19. $\langle\langle p_{T_{in}}^2 \rangle\rangle$ and $\langle\langle p_{T_{out}}^2 \rangle\rangle$ are shown (Fig. 19 (a)) as a function of W between 12 and 200 GeV for three fragmentation models, compared with a compilation of PETRA/PEP data spanning energies up to about 42 GeV. A similar plot is shown (Fig. 19 (b)) for the mean charged particle multiplicity in hadronic events, $\langle n_{ch} \rangle$. The first thing to note is that the models describe the data well, using parameter sets optimised at 35 GeV [17,19]. However, at the Z^0 energy and beyond, large differences begin to open up between the two shower models and the $O(\alpha_s^2)$ model: the shower models show higher $\langle\langle p_{T_{out}}^2 \rangle\rangle$ but lower $\langle\langle p_{T_{in}}^2 \rangle\rangle$, reflecting multiple gluon emission out of the event plane and the softer nature of the radiation in the plane than that calculated to $O(\alpha_s^2)$. The shower models also predict higher multiplicities by 3 units at the Z^0 and about 7 units at $W = 200$ GeV, in qualitative agreement with what one would expect if there is some proportionality between the number of soft gluons in an event and the resulting hadron multiplicity.

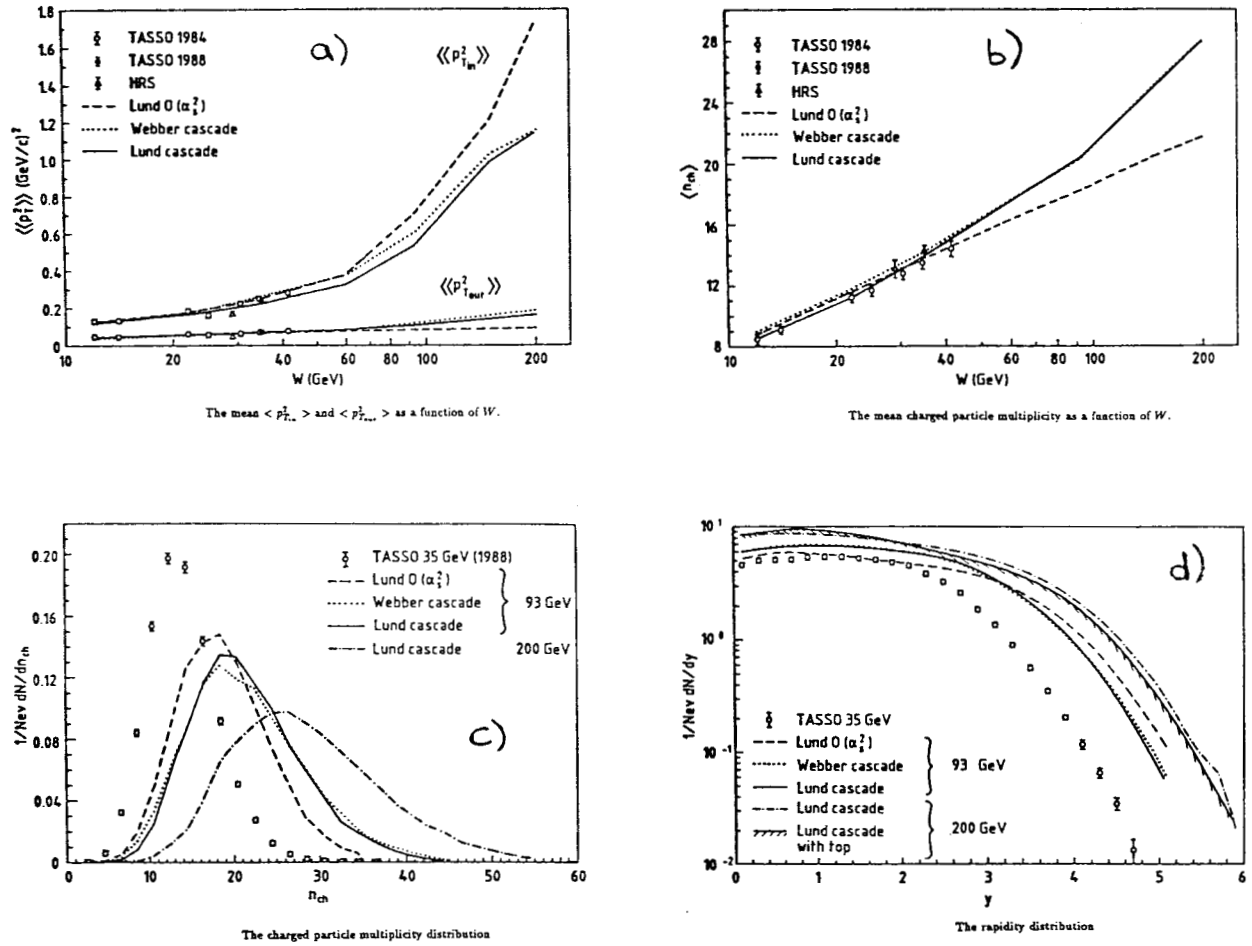


Figure 19.

The differential multiplicity and rapidity distributions are shown in Figs. 19 (c,d) respectively. The lower $O(\alpha_s^2)$ model multiplicity is reflected in a smaller peak value (Fig. 19 (c)) and a lower rapidity plateau (Fig. 19 (d)). Note also that the shower models show a larger dispersion (width) of the multiplicity distribution (Fig. 19 (c)).

Such differences between models, which will be almost impossible to tune away whilst still preserving agreement with the PETRA/PEP data, present the possibility for great discriminating power with high statistics data at the Z^0 energy, and even greater power at $W = 200$ GeV. An estimate of this power of discernment can be made by noting that the error bars on the TASSO data derive from a sample comprising 31176 hadronic events with a mean charged multiplicity of 13.6 at 35 GeV. In addition to the models already tested extensively at PETRA, PEP and TRISTAN, the newcomers NLLJET and ARIADNE can be confronted with the Z^0 data to shed new light on the jet fragmentation process.

3.2 b-jet Physics

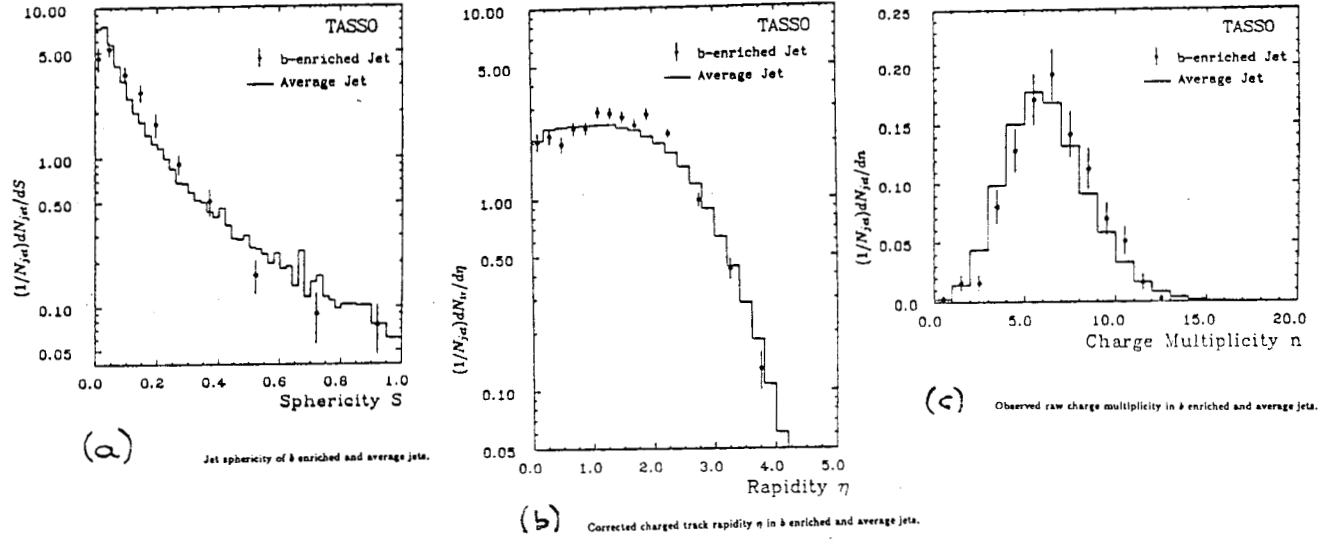


Figure 20.

The fragmentation properties of jets initiated by b quarks were studied recently by TASSO [55] and are summarised in Fig. 20, where samples of jets enriched with b events by a tagging procedure are compared with average jets of all flavours. TASSO used a sample of roughly 400 tagged jets, with a b purity of 68%.

Due to its large mass relative to the c.m. energy studied (35 GeV) and its hard fragmentation function [65], the b quark is expected to have somewhat different fragmentation properties compared with those of the light quark flavours. The majority of the particles in a $b\bar{b}$ event come from the decay of the initial B hadrons, which each takes roughly 70% of the beam energy [65], leaving only a small phase space for additional fragmentation particles. The large B hadron mass ensures that its decay products will typically have large transverse momentum relative to its line of flight, so that b jets will tend to be fatter, *i.e.* the events are more spherical in nature (Fig. 20 (a)). The hard fragmentation of the B , combined with the high p_T of its decay products, produces a depletion of particles at low rapidities (Fig. 20 (b)). The high decay multiplicity of B hadrons, about 5.5 charged tracks per decay [66], gives higher overall particle multiplicity in b events than in light flavour-initiated events (Fig. 20 (c)).

Further studies of these properties at the Z^0 will be extremely useful. As mentioned in Section 2.4, the SLC/LEP experiments will have high-resolution vertex detectors

which should be very efficient at tagging b-jets compared with what was achieved at PETRA/PEP. Given high luminosity delivered by the colliders, large samples of tagged b-jets may be expected to yield precision measurements of their properties. For one thing, it will be interesting to discover whether these fragmentation differences persist at high energies, or whether at the scale of 91 GeV the b of mass about 5 GeV becomes like a ‘light’ quark.

3.3 Miscellaneous Topics

In this section I shall not even attempt to do justice to several topics which are very worthy of detailed study at SLC/LEP, but mention them briefly for the sake of completeness.

Intermittency is a relatively new subject which is difficult to explain briefly. Essentially, large density fluctuations have been observed in (pseudo)-rapidity distributions in cosmic ray events [67], hadron-hadron [68], hadron-nucleus, nucleus-nucleus [69] and e^+e^- collisions [70,71]. These fluctuations are significant beyond purely statistical variations and are analysed in terms of quantities known as ‘scaled factorial moments’ [72]. The moments exhibit an inverse power law dependence upon the size of the rapidity bins used in the distribution, and it is this property which is known as ‘intermittency’.

The two most interesting features of the intermittent behaviour are that it occurs in all of the reaction channels mentioned above, in particular its appearance in e^+e^- annihilation excludes certain proposed explanations based upon hadron reaction mechanisms, and that it is not reproduced well by any of the current perturbative QCD + fragmentation models [71], even though these models describe the vast majority of the other known features of hadronic events. It is therefore possible that we may have to modify somewhat our present picture of parton hadronisation to take into account the intermittency effects.

Two further related topics worthy of study are local parton-hadron duality (LPHD) and colour coherence effects (see [73] and references therein). The former concept states that the distribution of final state hadrons follows rather closely the distribution of the initial partons, with non-perturbative effects being absorbed into a normalisation constant relating the hadronic and partonic amplitudes. The coherence effects refer to the patterns of inter- and intra-jet gluon radiation which are a direct manifestation of quantum effects in colour fields. For both of these topics, observables and theoretical predictions have been proposed [73] which can be tested against the experimental evidence. In particular, the inter-jet coherence has been suggested as a perturbative QCD explanation of the string effect [33], although it is well known that this effect can also be well-explained at PETRA/PEP energies by an $O(\alpha_s)$ matrix element calculation + string hadronisation [74]. This may no longer be true at SLC/LEP energies [11], providing a strong test of the idea of colour coherence, which up until now has been considered elegant from a theoretical point-of-view, but almost irrelevant phenomenologically [28,75].

4. Summary

By way of summary I list in Table 4 the experimental tests of QCD covered in this survey. As it is considered of some interest by experimental collaborations, I have also listed two numbers of events for each observable, representing my *estimate* of the number of events needed at the Z^0 to make a 'poor' and a 'good' measurement. These estimates are clearly highly subjective, and depend upon one's definition of 'poor' and 'good'. By 'poor' I mean a measurement of comparable precision to what has already been achieved to date, and by 'good' I mean a much better measurement than already exists or a conclusive demonstration of the existence of the phenomenon. The 'good' measurements invariably require a factor 10 more statistics than the 'poor' ones. The actual numbers themselves are based upon my own experience of analysis at TASSO and on the quality of measurements which have been made at the PETRA, PEP, TRISTAN and SLC experiments to date, with appropriate extrapolations to attain a 'good' measurement at the Z^0 .

Table 4: Estimated numbers of hadronic events at the Z^0 for testing aspects of QCD

Observable	Poor meas.	Good meas.
Running of α_s	1000	5000
Gluon self-coupling	5000	50000
Flavour-independence of α_s	400 b-jets	4000 b-jets
Colour charge of gluon	10000	100000
Multijet states	5000	50000
Standard jet fragmentation	1000	50000

I reiterate that these numbers are personal estimates and should be regarded in that light. The only thing which is certain is that the more events collected, the better the analysis will be.

References

- [1] J.D. Bjorken, S.J. Brodsky, Phys. Rev. **D1** (1970) 1416.
- [2] S. Brandt *et al*, Phys. Lett. **12** (1964) 57.
E. Farhi, Phys. Rev. Lett. **39** (1977) 1587.
- [3] VENUS Collab.: H. Yoshida *et al*, Phys. Lett. **B198** (1987) 570.
AMY Collab.: H. Sagawa *et al*, Phys. Rev. Lett. **60** (1988) 93.
TOPAZ Collab.: I. Adachi *et al*, Phys. Rev. Lett. **60** (1988) 97.
- [4] VENUS Collab.: H. Yoshida *et al*, Phys. Rev. Lett. **59** (1987) 2915.
TOPAZ Collab.: I. Adachi *et al*, Phys. Rev. **D37** (1988) 1339.
- [5] A. Maki, presentation at the XIV International Symposium on Lepton and Photon Interactions, Stanford, August 6-12 1989.
- [6] K. Fabricius *et al*, Phys. Lett. **B97** (1980) 431; Z. Phys. **C11** (1982) 315.
- [7] F. Gutbrod, G. Kramer, G. Schierholz, Z. Phys. **C21** (1984) 235.
- [8] T.D. Gottschalk, M.P. Shatz, Phys. Lett. **B150** (1985) 451; Z. Phys. **C34** (1987) 497.
- [9] R.K. Ellis, D.A. Ross, A.E. Terrano, Phys. Rev. Lett. **45** (1980) 1226; Nucl. Phys. **B178** (1981) 421.
- [10] G. Kramer, B. Lampe, Z. Phys. **C39** (1988) 101; Fortschr. Phys. **37** (1989) 161.
- [11] B. Bambah *et al*, CERN-TH.5466/89 (1989).
- [12] K. Hagiwara, D. Zeppenfeld, Nucl. Phys. **B313** (1989) 560.
F.A. Berends, W.T. Giele, H. Kuijf, to appear in Nucl. Phys. B.
- [13] N.K. Falck, D. Graudenz, G. Kramer, Phys. Lett. **B220** (1989) 299; DESY 89-046 (1989).
- [14] JADE Collab., W. Bartel *et al*, Z. Phys. **C33** (1986) 23.
- [15] S. Bethke, Habilitationsschrift, University of Heidelberg (1987) (unpublished).
- [16] TASSO Collab., W. Braunschweig *et al*, Phys. Lett. **B214** (1988) 286.
- [17] P.N. Burrows, Oxford D.Phil. Thesis, RAL-T-071 (1988).
- [18] Mark II Collab., A. Petersen *et al*, Phys. Rev. **D37** (1988) 1.
- [19] TASSO Collab., W. Braunschweig *et al*, Z. Phys. **C41** (1988) 359.
- [20] S. Bethke, Z. Phys. **C43** (1989) 331.
- [21] AMY Collab., paper submitted to the XIV International Symposium on Lepton and Photon Interactions, Stanford, August 6-12 1989.

- [22] S. Komamiya, paper submitted to the XIV International Symposium on Lepton and Photon Interactions, Stanford, August 6-12 1989.
- [23] S.G. Gorishny, A.L. Kataev, S.A. Larin, Phys. Lett. **B212** (1988) 238.
- [24] G. Altarelli, G. Parisi, Nucl. Phys. **B126** (1977) 298.
- [25] T. Kamae, Proceedings of the 24th Int. Conf. on High Energy Physics, Munich 1988, 156.
- [26] G. Gustafson, U. Pettersson, Nucl. Phys. **B306** (1988) 746.
- [27] H. Stone, Ph.D. Thesis, Calif. Inst. Tech. (1988).
- [28] M. Bengtsson, T. Sjöstrand, Nucl. Phys. **B289** (1987) 810.
- [29] T. Sjöstrand, Int. J. Mod. Phys. **A3** (1988) 751.
- [30] B. Andersson *et al*, Phys. Rep. **97** (1983) 33.
- [31] G. Marchesini, B.R. Webber, Nucl. Phys. **B310** (1988) 461.
- [32] T.D. Gottschalk, D.A. Morris, Nucl. Phys. **B288** (1987) 729.
- [33] B. Andersson, G. Gustafson, T. Sjöstrand, Phys. Lett. **94B** (1980) 211,
- [34] A. Weinstein, talk presented at the XIV International Symposium on Lepton and Photon Interactions, Stanford, August 6-12 1989.
- [35] G. Kramer, Theory of Jets in Electron Positron Annihilation, Springer Tracts of Modern Physics, Vol. **102**, Springer (1984).
- [36] See *eg.* M. Gell-Mann, Y. Ne'eman, The Eightfold Way, Benjamin, New York (1972).
- [37] M.Y. Han, Y. Nambu, Phys. Rev. **139B** (1965) 1006.
- [38] TASSO Collab., W. Braunschweig *et al*, Z. Phys. **C41** (1988) 385.
- [39] E. Reya, Phys. Rep. **69** (1981) 195.
- [40] See *eg.* R. Gatto, Proceedings of the International Symposium on Electron and Photon Interactions at High Energies, Hamburg 1965, 106.
- [41] G. Hanson *et al*, Phys. Rev. Lett. **35** (1975) 1609.
TASSO Collab., M. Althoff *et al*, Z. Phys. **C22** (1984) 307.
- [42] See *eg.* R.J. Cashmore, Sci. Prog., Oxf. **71** (1987) 305.
- [43] UA1 Collab., G. Arnison *et al*, Phys. Lett. **158B** (1985) 494.
UA2 Collab., J. Appel *et al*, Z. Phys. **C30** (1986) 341.
AFS Collab., T. Åkesson *et al*, Z. Phys. **C32** (1986) 317.
- [44] TASSO Collab., R. Brandelik *et al*, Phys. Lett. **97B** (1980) 453.
- [45] G. Altarelli, CERN-TH.5290/89 (1989).
- [46] S.L. Wu, proceedings of the International Symposium on Lepton and Photon Interactions at High Energies, Hamburg 1987, 39.

- [47] T. Appelquist, H. Georgi, Phys. Rev. **D8** (1973) 4000.
A. Zee, Phys. Rev. **D8** (1973) 4038.
- [48] S. Uno, presentation at the 1989 SLAC Summer Institute, Stanford, July 10-21.
- [49] For a recent review see W.J. Stirling, M.R. Whalley, RAL-87-107 (1987).
- [50] JADE Collab., S. Bethke *et al*, Phys. Lett. **B213** (1988) 235.
- [51] UA2 Collab., P. Bagnaia *et al*, Phys. Lett. **144B** (1984) 283.
- [52] M. Bengtsson, Z. Phys. **C42** (1989) 75.
- [53] J.G. Körner, G. Schierholz, J. Willrodt, Nucl. Phys. **B185** (1981) 365.
O. Nachtmann, A. Reiter, Z. Phys. **C16** (1982) 45.
M. Bengtsson, P.M. Zerwas, Phys. Lett. **208** (1988) 306.
- [54] TASSO Collab., W. Braunschweig *et al*, DESY 89-053 (1989).
- [55] TASSO Collab., W. Braunschweig *et al*, Z. Phys. **C42** (1989) 17.
- [56] S.J. Brodsky, J.F. Gunion, Phys. Rev. Lett. **37** (1976) 402.
- [57] K. Shizuya, S. Tye, Phys. Rev. Lett. **41** (1978) 787.
M.B. Einhorn, B.G. Weeks, Nucl. Phys. **B146** (1978) 445.
- [58] TASSO Collab., W. Braunschweig *et al*, DESY 89-032 (1989).
- [59] JADE Collab., W. Bartel *et al*, Phys. Lett. **123B** (1983) 460.
- [60] HRS Collab., M. Derrick *et al*, Phys. Lett. **165B** (1985) 449.
- [61] Mark II Collab., A. Petersen *et al*, Phys. Rev. Lett. **55** (1985) 1954.
- [62] AMY Collab., paper submitted to the XIV International Symposium on Lepton and Photon Interactions, Stanford, August 6-12 1989.
- [63] P.N. Burrows, Z. Phys. **C41** (1988) 375.
- [64] D.H. Saxon, High Energy Electron-Positron Physics, ed. A. Ali, P. Söding, World Scientific, (1988) 540.
- [65] R.J. Cashmore, Oxford Nuclear Physics 96/87 (1987).
- [66] CLEO Collab., R. Giles *et al*, Phys. Rev. **D30** (1984) 2279.
- [67] JACEE Collab., T.H. Burnett *et al*, Phys. Rev. Lett. **50** (1983) 2062.
- [68] UA5 Collab., G.J. Alner *et al*, Phys. Rep. **154** (1987) 247.
NA22 Collab., M. Adamus *et al*, Phys. Lett. **B185** (1987) 200.
- [69] EMU-01 Collab., M.I. Adamovich *et al*, Phys. Lett. **B201** (1988) 397.
- [70] B. Buschbeck, P.Lipa, R. Peschanski, Phys. Lett. **B215** (1988) 788.
- [71] TASSO Collab., W. Braunschweig *et al*, paper submitted to the XIV International Symposium on Lepton and Photon Interactions, Stanford, August 6-12 1989.

[72] A. Bialas, R. Peschanski, Nucl. Phys. **B273** (1986) 703, *ibid.* **B308** (1988) 857.

[73] V.A. Khoze, Proceedings of the 24th Int. Conf. on High Energy Physics, Munich 1988, 1048.

V.A. Khoze, presentation at the XIV International Symposium on Lepton and Photon Interactions, Stanford, August 6-12 1989.

[74] JADE Collab., W. Bartel *et al*, Phys. Lett. **157B** (1985) 340.

TASSO Collab., M. Althoff *et al*, Z. Phys. **C29** (1985) 29.

[75] R. Odorico, Z. Phys. **C30** (1986) 257.

B DECAYS AND SPECTROSCOPY

I. Peruzzi, M. Witherell, P. Antilogus, T. Browder, S. Dasu,
G. Eigen, G. Gladding, D. Hitlin, M. Kelsey, J. Labs, L. Mathys,
J. McGowan, S. McHugh, L. Osborne, R. Panvini, J. Richman,
C. Simopoulos, P. De Simone, M. Strauss, D. Williams, and G. Word

(The SLD B Spectroscopy Group)

Introduction

The goal of each of the SLD physics groups is to identify compelling physics issues which SLD is well suited to study. For B physics, the advantages of the detector are clear: a powerful vertex detector with small beam pipe, and good particle identification with the CRID. In this area of physics there is obvious competition from CLEO in the next few years. There are some physics topics for which SLD does have unique advantages, but they all require a reasonable number of Z 's.

The strategy of our group has therefore been to identify the subset of physics topics which require the lowest integrated luminosity. We then have tried to make an honest estimate of how many Z 's it will take to make an important measurement. These estimates are based on the present status of the detector simulation in the fast Monte Carlo, and should improve as the simulation matures.

Present Experimental Status

The largest sample of $B\bar{B}$ events is from CLEO, which has $3 \cdot 10^5$ events now. They should collect about 10^6 events with the upgraded CLEO II detector in 1990. They have no precise vertex information, and modest particle identification, but will have a very large sample of B^+ and B_d decays. It will take special runs to study the B_s , and there are no plans to go above threshold for the Λ_b .

The major experimental results on B decays come from CLEO, ARGUS, and the continuum experiments at PEP and PETRA.¹ The mixing measurement is $r(B_d^0) = 0.20 \pm 0.07$, where r is the fraction of mesons created as a B which decay as a \bar{B} . The lifetime, for the continuum mixture of B^+ , B_d , and B_s , is $(11.8 \pm 1.4) \cdot 10^{-13}$ s. The ratio of lifetimes has been measured from the ratio of semileptonic decays, and the average of CLEO and ARGUS measurements is $\tau^+/\tau^0 = 0.9 \pm 0.2$. The inclusive semileptonic decay rate is fairly well measured, $B(B \rightarrow X\ell\nu) = (10.9 \pm 0.6)\%$, but the individual exclusive rates are

only measured to about 30–40%. Finally, the ratio of K-M matrix elements, V_{ub}/V_{cb} , has an upper limit of 0.13. There is a recent 2 standard deviation excess from CLEO at the endpoint of the electron spectrum, which can be interpreted as first signs of charmless decays, with $V_{ub}/V_{cb} = 0.04 - 0.12$.

One can identify fairly easily the important results which will be sought in the near future: 1) Mixing, especially B_s ; 2) Lifetimes for B_d , B^+ , B_s , and Λ_b ; 3) V_{cb} , measured in $B \rightarrow D e \nu$ and $D^* e \nu$; 4) V_{ub} measured in $B \rightarrow \rho e \nu$; 5) hadronic decays, especially decays such as $B \rightarrow \pi\pi$, $K\pi$, and ψK_s , which are important for probing where to look for CP violation; 6) rare decays, starting with the benchmark mode $B \rightarrow K\mu\bar{\mu}$; and 7) spectroscopy, including properties of the B_s and Λ_b . Of these, all but rare decays offer some opportunities for SLD, because of the advantage from the vertex detector with small beam pipe and Čerenkov identification of hadrons. The crucial question is how many Z's are required to do the physics in each case.

Charm Identification for B Decay Physics

The rates for observing B decays using conventional techniques are at first discouraging. With 100,000 produced Z's (75,000 visible Z's), there are 14,000 $b\bar{b}$ events, which include 11,000 B_u (and \bar{B}_u) decays and a similar number of B_d decays. This gives a total of 1500 $\bar{B}_d \rightarrow D^{*+} \ell^- \bar{\nu}$ decays. Putting in the branching ratios, $B(D^{*+} \rightarrow \pi^+ D^0) = 0.5$ and $B(D^0 \rightarrow K^- \pi^+) = 0.04$, and an efficiency times acceptance of 20%, one expects 6 observed events. The lesson from this exercise is that we must be very efficient in reconstructing charm, and use more than the single mode $D^0 \rightarrow K^- \pi^+$. In addition, we cannot afford the usually high cuts on minimum momenta for the D and the lepton. Our studies tell us that it will be possible to satisfy these requirements because of the VXD and CRID performance.

Figure 1 shows the mass spectra for the decay $D^0 \rightarrow K^- \pi^+$ in $b\bar{b}$ events. These are unremarkable in appearance, showing clear signals with signal-to-background ratios of about 1.5 or so. What is unusual is the relatively large efficiency achieved, because only minimal kinematic cuts were applied. With good particle identification from the CRID and good vertex separation with the VXD, there is no need to do more than exclude tracks with $P < 0.5$ GeV/c. An efficiency of 40% is obtainable in the $D^0 \rightarrow K^- \pi^+$ mode, as an example.

The goal is to assemble a reconstructed charm list, containing the largest fraction of D^0 , D^+ , D_s^+ , and $D^{*+} \rightarrow \pi^+ D^0$ possible. The modes used for D^0 will be $K^- \pi^+$, $K^- \pi^+ \pi^- \pi^+$,

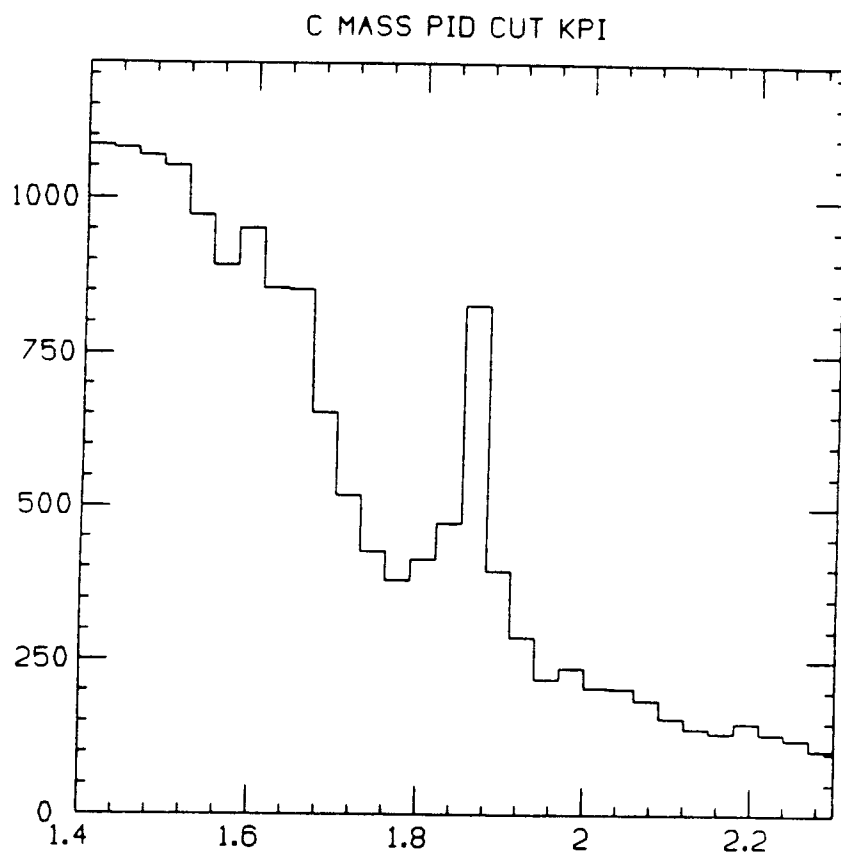


Fig. 1. The mass spectrum for $K^-\pi^+$ combinations in the region of the D^0 , from a Monte Carlo simulation of $Z^0 \rightarrow b\bar{b}$ events. The vertex cuts are very loose to achieve high efficiency. The large collection of events with mass less than 1.72 GeV is due to the decay $D^0 \rightarrow K^-\pi^+\pi^0$, which is also useful for B decay studies.

$K^-\pi^+\pi^0$, and $K_s^0\pi^+\pi^-$, with a total branching ratio of about 30%. We should be able to reconstruct about 30% of these, for a total D^0 efficiency of about 9%, with somewhat smaller numbers for D^+ and D_s^+ , and larger for $D^{*+} \rightarrow \pi^+D^0$. These numbers are about $5\times$ the usual charm efficiencies, because of the lack of kinematic cuts and the use of more modes. In a related paper from Strauss, McHugh and Browder, the status of the charm reconstruction is detailed.

Physics Example 1: B Lifetimes

Some of the most important measurements needed to study the weak decays of the B mesons are the lifetimes of individual particles. In particular, the ratio $\tau^+/\tau^0 = \tau(B^+)/\tau(B_d)$ is important for three reasons: 1) to measure the size of the correction to the simple spectator model (recall $\tau(D^+)/\tau(D^0) \simeq 2.5!$); 2) to measure $B(B^+ \rightarrow Xe^+\nu)/B(B^0 \rightarrow Xe^+\nu) = \tau^+/\tau^0$, which is necessary for mixing measurements; and 3) to measure relative exclusive decay rates for B^0 and B^+ decays modes, so as to compare with existing models.

Recent measurements of τ^+/τ^0 using the semileptonic branching ratios are $0.85^{+0.30}_{-0.26}$ from CLEO² and 1.00 ± 0.27 from ARGUS.³ Thus, the ratio is consistent with 1, but also with 0.5 or 1.5. We expect deviations from 1 at the level of 20% or less, so there is little help from the experimental results. Moreover, the systematic errors are about 20%, and are probably not reducible to the 10% level with existing experiments.

We need to measure the lifetimes to an accuracy of 10%. The error in lifetime is given by the rule $\sigma_\tau = \tau/\sqrt{N}$ in the limit that the resolution in decay time is much less than the lifetime and the background is small. Thus 100 events are required for a 10% measurement. Keeping the systematic errors to 5% is a formidable problem, however. This requires obtaining clean signals without severe cuts on the B vertex separation, which might be difficult to model. The systematic problems in the lifetime ratio are less severe than those in the ratio of semileptonic rates, however.

There are many methods available to measure the lifetimes. In an inclusive approach, one can resolve the five vertices typical of $b\bar{b}$ events, and separate the three B mesons by charge and strangeness.⁴ This may be difficult, because the efficiency is small for completely separating all vertices. In addition, the effect of such vertex cuts on the time-dependence of the efficiency is very sensitive to Monte Carlo models of the underlying event.

We have concentrated on using exclusive decays, in particular the semileptonics, which

have large branching ratios and are easy to identify. In addition, the species of charmed meson tags the B meson type. The major decay modes are:

$$B^- \rightarrow (D^0, D^{*0}) \ell^- \bar{\nu}$$

$$\bar{B}_d \rightarrow (D^+, D^{*+}) \ell^- \bar{\nu}$$

$$\bar{B}_s \rightarrow (D_s^+, D_s^{*+}) \ell^- \bar{\nu}.$$

Separating B^- from \bar{B}_d requires simply tagging the charge of the D meson. Of course, we can check the lifetime ratio by measuring the ratio of exclusive branching ratios.

The rates for exclusive semileptonic decays are acceptable, even for a total of 100,000 Z^0 's produced. In that case there are about 2400 $B^- \rightarrow X\ell\bar{\nu}$ decays, and an equal number of \bar{B}_d decays. Assuming a 9% efficiency for detecting charm and a 50% efficiency for detecting the lepton and B vertex cuts, the expected number of observed semileptonic decays is 110 for each meson. Figure 2 shows the $D^*\ell\bar{\nu}$ signal and background from the Monte Carlo simulation, with cuts appropriate to lifetime studies. This represents 10% measurement of each lifetime, and 14% measurement of the ratio. A measurement of the lifetime ratio with comparable statistical accuracy is possible using the ratio of branching ratios.

The use of exclusive D decays makes the separation by charge relatively easy. The D^{*0} always decays to a D^0 with accompanying neutral; the D^{*+} decays about 1/2 to $D^0 + \pi^+$ and 1/2 to $D^0 + \pi^0$ or γ . Thus if one can tag the $D^{*+} \rightarrow \pi^+ D^0$ decay with good efficiency, and correct for the pions not seen, one can separate the decays reliably. It will also be possible to measure the small contribution from $D^{**}\ell\bar{\nu}$ decays.

The sources of possible systematic error for the lifetime measurement are fairly straightforward. One must correct for the D^0 decays that come from D^{*+} , as discussed already. One must measure the relativistic factor $\gamma\beta = P/M$ to about $\pm 15\%$ ($d = \gamma\beta ct$). There are two independent sources for this measurement. Figure 3 shows the momentum spectrum of the B mesons, which is peaked near 37 GeV/c and represents a measurement of about $\pm 25\%$. One can also use the momentum and mass of the $D\ell$ (or $D^*\ell$) system to measure the B momentum to better than $\pm 20\%$, for a combined error of about $\pm 15\%$. Reconstruction of the missing neutrino will only improve this result.

The other issue in measuring lifetimes is to study the efficiency as a function of time. It is important to obtain clean signals using minimal vertex cuts. The present studies show that the $D^*\ell\bar{\nu}$ signals are very clean with almost no cut on the B decay time. Similarly clean signals should be attainable for $D\ell\bar{\nu}$, since clean D signals are used.

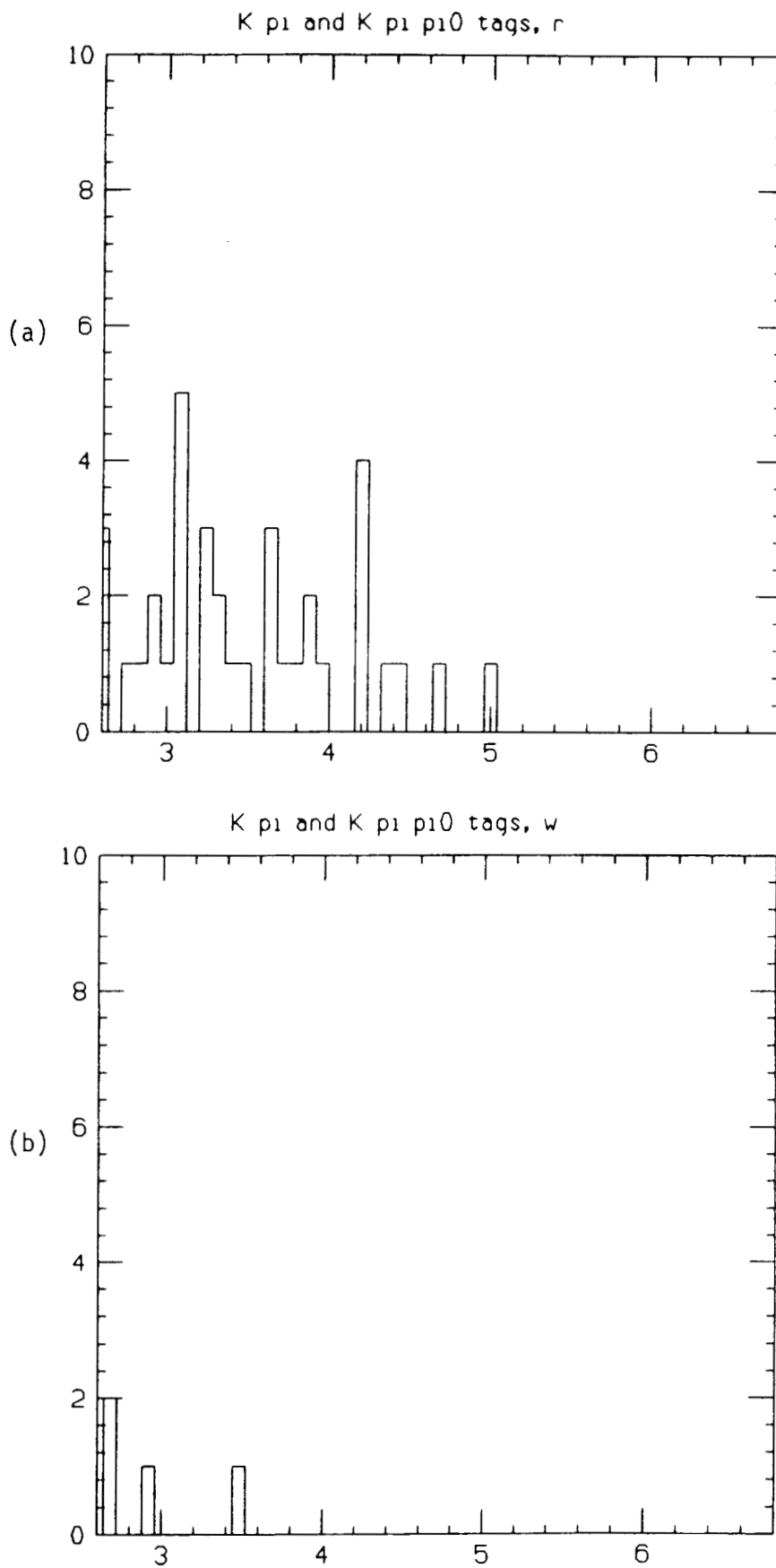


Fig. 2. The (a) $D^{*+}e^-$ and (b) $D^{*+}e^+$ mass spectrum for $M(D^*e) > 2.6$ GeV. The differences between the two plots is entirely due to $B \rightarrow D^{*+}e^-\bar{\nu}$ decay.

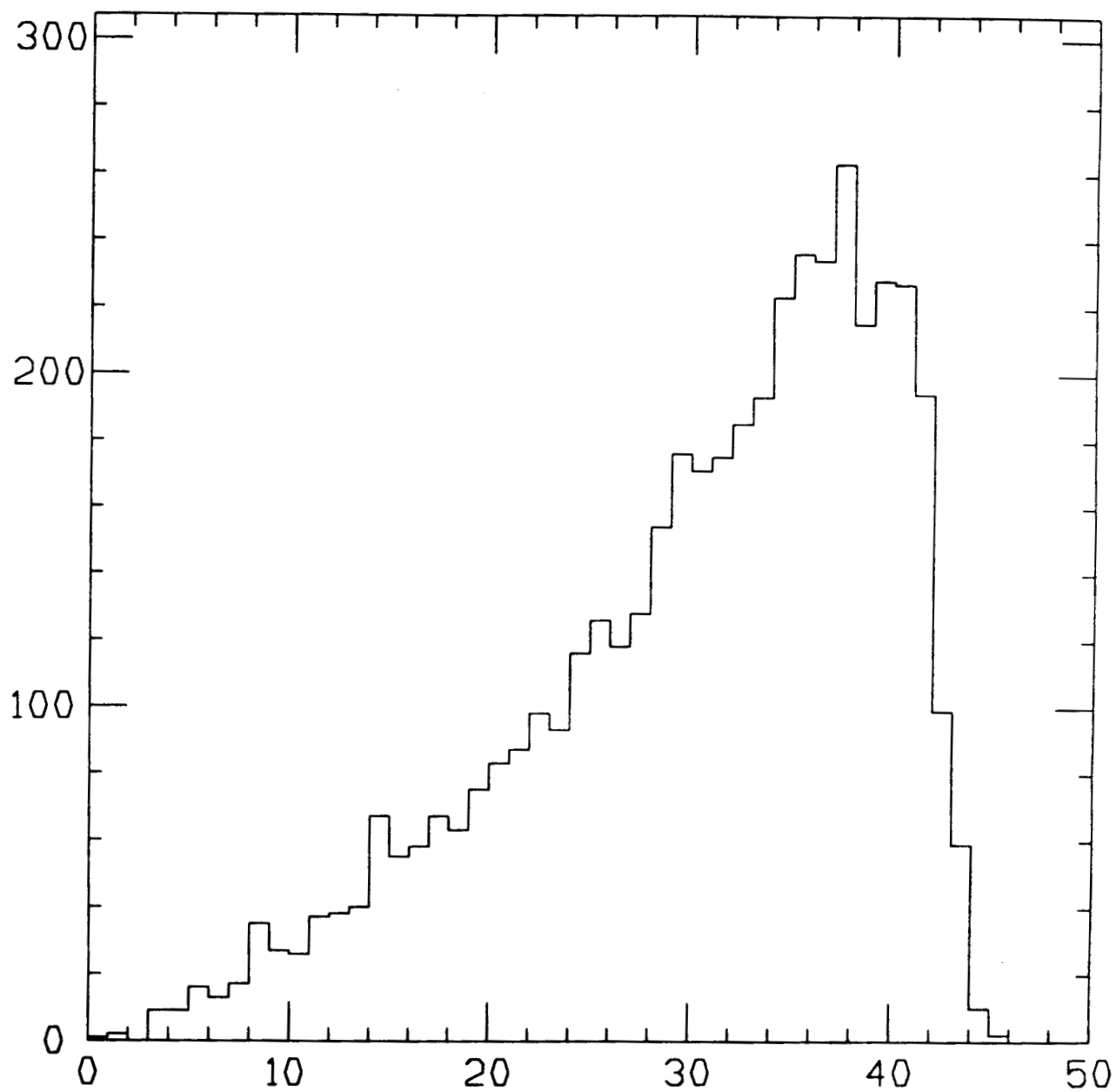


Fig. 3. The momentum spectrum of B mesons resulting from Z^0 decay.

The studies on measuring the lifetimes using semileptonic decays have been carried out by Tom Browder. A separate paper in this volume gives details and results.

Other B Physics Topics

The most important source of information on the weak decays of the b quark is semileptonic decay. The Kobayashi-Maskawa matrix elements V_{cb} and V_{ub} are two of the fundamental parameters in the Standard Model still not well measured, which can only be done in exclusive semileptonic decays. These elements are also crucial in determining the expected level for CP violation in B decays.

There is also important information on the hadronic structure of mesons that come from exclusive semileptonic decays. The weak current serves as a point-like probe of the meson wave function, similar to electroproduction in the case of nucleons. There is a great amount of theoretical work, using both analytical and lattice gauge techniques, on models of these form factors. Such models are needed to reliably extract V_{cb} and V_{ub} from the measurements.

The problem in determining V_{cb} is fairly straightforward. The decay $B \rightarrow D^* \ell \nu$ is relatively easy to measure, but hard to interpret, because of three form factors that contribute. The decay $B \rightarrow D \ell \nu$ is easier to interpret, but much harder to measure, because the D signals are not as clean as the D^{*+} . The decay $B \rightarrow \rho \ell \nu$ needed to measure V_{ub} is both hard to measure and very hard to interpret. The most important lesson in this area is this: *The entire kinematic range must be measured to determine the form factors accurately.*

Of course, CLEO and ARGUS have already measured $B \rightarrow D \ell \nu$, for example. ARGUS sees 120 $D^+ \ell^- \nu$ events on 200 background,⁵ of which about 1/2 are from $D^{*+} \ell \nu$ with an undetected neutral. CLEO sees 58 ± 10 $D^0 \ell^- \nu$ events, after subtracting about 150 $D^+ \ell \nu$ events.⁶ In both cases, the results suffer from large background and large contamination from $D^* \ell \nu$. Because there are severe cuts on P_D and P_e in the B rest frame, it is difficult to use the different kinematic dependence of the D^* decays to separate them from the D decays. Finally, the limiting systematic uncertainty is an unknown amount of $D^{**} \ell \nu$ decay, since it is impossible to observe the low momentum pion from the D^{**} often enough to measure its rate well.

The SLD environment has many advantages for this problem. The VXD and CRID make it possible to obtain a high charm efficiency and thus reasonable semileptonic rates,

as pointed out above. Because the signal is clean without severe kinematic cuts, especially if one cuts on the vertex, full coverage of the Dalitz plot is possible. This is necessary for determining the form factors and useful for separating the D^* contamination to the D signal. Finally, there is good sensitivity to $D^{**}\ell\nu$ decay, because one can easily identify an extra charged pion from the B decay vertex.

In the area of B_s and Λ_b physics, there is presently no experimental information. Starting with 300,000 Z^0 's, there also are 2500 produced $\bar{B}_s \rightarrow (\gamma)D_s^+\ell^-\nu$ decays, of which 60 or so should be observed. This would be enough to measure the B_s lifetime to about 20% and to compare the semileptonic decay with those of the B^- and \bar{B}_d . One should gain first evidence of B_s decays with as few as 100,000 Z^0 's, along with a rough lifetime measurement. The first work on observing the D_s decays modes is reported in Gerald Eigen's talk.

There are a number of hadronic decays of B mesons for which the detailed vertex information of SLD is useful. Ida Peruzzi reports on a first look at studying $B \rightarrow \psi X$ decays. In that case it is possible to locate the charged tracks attached to the $\psi \rightarrow \mu^+\mu^-$ decay vertex quite cleanly, but the expected rate is low. High multiplicity decays are also much cleaner using precise vertex information, but this case has not yet been studied. Lou Osborne discusses the prospects for tagging B decays with high efficiency using the vertex information.

Analysis Tools

The preliminary physics studies summarized here are at the end of a long program of developing Monte Carlo and analysis programs which give a reasonable description of the real environment. Much additional work is needed to improve the simulation and the analyses.

The two detectors which are particularly crucial for B physics are the CRID and the VXD. A small subgroup of the CRID analysis effort conducted a pre-Kirkwood study of the fast and slow Monte Carlos, which is reported in the paper of Pierre Antilogus. Much work has been done on the proper description of vertex errors and on developing useful vertexing algorithms. Gary Gladding reports on the vertexing status in his paper for the B mixing group, and Jeff Richman's paper describes a fast program to calculate error matrices.

The existing Lund description of D and B decays is not satisfactory, even for present planning purposes. A number of people, especially Jon Lats, Peter Kim, and Tom Browder

developed the model of D and B decays used. It is very detailed and realistic for D decays, but needs more work for B's. Jon Labs describes the present status and Gerald Eigen a new version for B decay modes, which is not yet complete.

All of this development of analysis and Monte Carlo programs was done in cooperation with the B mixing group. In particular, Rafe Schindler and Gary Gladding led the push in the few weeks before Kirkwood to pull the many pieces of software together and make it possible to achieve the preliminary results that exist.

Summary

One of the first topics for SLD in B physics will be the lifetime measurements. The sources of possible competition are the Fermilab fixed target program, LEP, and CLEO II (for the ratio only). It is probable that the fixed target experiments will not collect clean samples of 100's of B's before the 1992 run. The LEP experiments will have large samples of B's, but the beampipe and vertex detectors for the early runs are not adequate for a precise lifetime measurement. The CLEO II experiment will improve their measurement of the ratio of semileptonic branching ratios, but it is unclear whether the systematics can be reduced much below the level of 25%.

Similar comments apply for the study of the semileptonic decay matrix elements. The main question is whether CLEO II can do much better in studying $B \rightarrow D\ell\nu$ than the past experiments. This will require relaxing the kinematic cuts that they now use, without increasing the already large background contamination.

With 10^5 Z^0 's, it will be possible for SLD to study lifetime ratios either directly or through the ratio of semileptonic branching ratios, with clean samples of 100's of events. The same sample can be used to study the form factors and extract V_{cb} more reliably than it is now known. The first observation of B_s decays will also be possible, with a rough lifetime measurement.

With more running, to about $3 \cdot 10^5$ Z^0 's, other physics opens up. Accurate lifetime measurements for B_s and A_b would be possible, along with mass measurements. Other physics that would be accessible at this level are measurement of complicated hadronic decays, and determination of V_{ub} , if it is not too small.

REFERENCES

1. K. Schubert, review talk at the International Symposium on Heavy Quarks (Ithaca, 1989). Very similar results were presented at the Lepton-Photon Symposium (Stanford, 1989) by D. Kreinick (CLEO) and M. Danilov (ARGUS).
2. J. Alexander *et al.*, (CLEO Collaboration), paper submitted to the Lepton-Photon Symposium (SLAC, 1989).
3. H. Albrecht *et al.*, (ARGUS Collaboration), paper submitted to the Lepton-Photon Symposium (SLAC, 1989).
4. W.B. Atwood, SLAC-PUB-5047, 1989.
5. H. Albrecht *et al.*, (ARGUS Collaboration), paper submitted to the Lepton-Photon Symposium (SLAC, 1989).
6. J. Alexander *et al.*, (CLEO Collaboration), paper submitted to the Lepton-Photon Symposium (SLAC, 1989).

SEMILEPTONIC DECAYS AND MEASUREMENT OF THE B-MESON LIFETIMES

T.E. Browder

Stanford Linear Accelerator Center

M.S. Witherell

University of California, Santa Barbara

Introduction

The most fundamental measurements in understanding the weak decays of the B mesons are the lifetimes and the semileptonic branching ratios. It is from these measurements that one extracts the value of V_{cb} , which is not yet very precise. The present experimental information consists of an average B lifetime, for a continuum mixture of B^+ , B_d , and B_s , of $(11.8 \pm 1.4) \times 10^{-13}$ s, and a semileptonic decay rate of $(10.9 \pm 0.6)\%$,¹ averaged over the mix of B^+ and B_d at the $\Upsilon(4s)$.

The next step in measuring lifetimes is, of course, to measure the lifetimes of the B^+ , B_d , and B_s individually. In the simplest spectator quark picture, the three lifetimes are expected to be equal, because the light antiquark has no effect. In the charm system, the lifetimes violate this picture very badly ($\tau(D^+)/\tau(D^0) = 2.5$), primarily due to interference effects in the D^+ . Simple scaling of this picture leads to the expectation that $1 \leq \tau(B^+)/\tau(B^0) \leq 1.2$.

It is important to measure the lifetime ratio with sufficient precision to observe an effect of 10–20%. This precision will be needed to measure V_{cb} precisely and to compare the strong interaction corrections to the existing models of the weak decay. The derived ratio $\lambda \equiv B(B^+ \rightarrow X e^+ \nu)/B(B^0 \rightarrow X e^+ \nu)$ is equal to τ^+/τ^0 , and this ratio must be known well to extract the mixing rate from the measurement of the rate of wrong-sign dileptons. All present mixing experiments assume $\lambda = 1$.

The other important measurements in determining the K-M matrix element are the semileptonic decay branching ratios. Because of the limits of theoretical models for the inclusive decay, this requires precise measurement of the exclusive decays, which are not yet available. In addition, the best sources of information on the hadronic structure of mesons are the form factors measured in semileptonic decay.

Fortunately, the best way to measure the lifetimes is to use semileptonic decays, because of the large branching ratio and relative ease of separating B^+ , B_d , and B_s . Thus we

will be able to use the same sample, with slightly different cuts, to measure $\tau(B^0)$ and $B(\bar{B}^0 \rightarrow D^+ e^- \bar{\nu})$.

Lifetimes

The ratio $r_\tau = \tau(B^+)/\tau(B^0)$ can be measured indirectly by CLEO and ARGUS, using the relationship $r_\tau = \lambda$. The present results are $r_\tau = .85 \pm 0.20^{+0.22}_{-0.16}$ for CLEO,² and $r_\tau = 1.00 \pm 0.23 \pm 0.14$ for ARGUS.³ Thus the results are consistent with $r_\tau = 1$, but the errors are about 30%. The systematic errors are large, and are not likely to improve quickly, as can be seen by looking at the data from which these numbers are extracted.

Figure 1 shows the CLEO sample of decays $\bar{B} \rightarrow D^0 \ell^- \bar{\nu}$. The (missing mass)² is calculated of the unseen particle(s) other than the D^0 and ℓ^- , and should be zero for $D^0 \ell^- \bar{\nu}$. The resolution is about 0.4 GeV^2 , coming from the $0.3 \text{ GeV}/c$ momentum of the B at the $\Upsilon(4s)$, in an unknown direction. The data points shown result after a continuum subtraction, the size of which can be estimated by the errors on the points. There is a large peak due to semileptonic decay, but it is centered at $MM^2 = 0.3 \text{ GeV}^2$, because the hadronic component is a mixture of D^0 , D^{*0} , and D^{*+} . From a fit to this spectrum the component which is $(D^{*0} + D^{*+})$ is determined, from which the D^{*+} is subtracted. The ratio $B(B^- \rightarrow D^{*0} \ell^- \bar{\nu})/B(\bar{B}^0 \rightarrow D^{*+} \ell^- \bar{\nu})$ is then used to measure r_τ , with relatively large statistical error. There is a significant systematic error from the $D^{*+} \ell \nu$ decays which might contribute as much as 20% of the signal.

At SLD the lifetime ratio can be measured in two ways using the semileptonic decay sample. The lifetimes can be measured directly, using the precise vertex information from the VXD. Also, the semileptonic branching ratios can be measured for B^+ and B^0 separately. The vertex information can be used to cleanly separate pions that come from $D^{*+} \rightarrow D^+ \pi$ decay, and to measure the bachelor pion from D^{*+} decay with high efficiency.

The observed event rates for the semileptonic decays in SLD can be estimated from the completed Monte Carlo studies. In 100,000 produced Z^0 events, there are 14,000 $b\bar{b}$ events, which provide 11,000 B_u and \bar{B}_u decays, with a similar number of B_d and \bar{B}_d . The inclusive semileptonic decay rate is 10.9%. (Although the sum of the measured exclusive rates is less than this, the errors are much larger.) This gives about 2400 $B^- \rightarrow X \ell^- \bar{\nu}$ decays, about 60% D^* , 30% D , and 10% D^{*+} . The efficiency for detecting the charmed meson in one of the few exclusive modes should be about 9% on average, and the lepton can be detected with a good vertex about 50% of the time. Thus the number of detected semileptonic decays is about 110 for each of the B^- and \bar{B}_d .

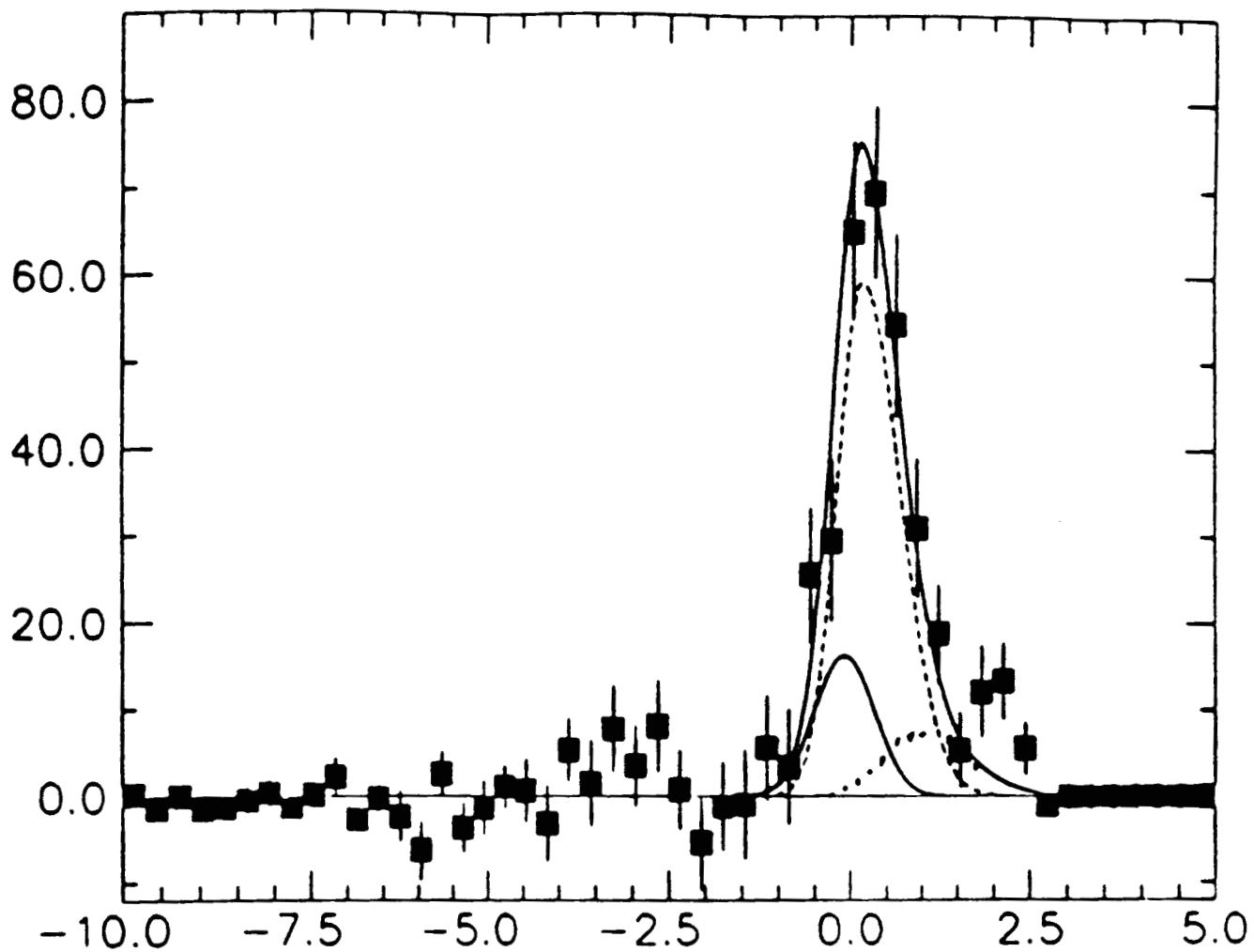


Fig. 1. Missing mass squared distribution for $D^0 e^-$ events from CLEO, with continuum subtracted. The dashed line is $D^{*0} e^- \bar{\nu}$ and $D^{*+} e^- \bar{\nu}$, the shorter solid is $D^0 e^- \bar{\nu}$, and the dotted line is $D^{*+} e^- \bar{\nu}$.

The statistical error on the lifetime, for a signal with low background, is $\delta\tau = [\tau^2 + (\delta t)^2]^{1/2}/N^{1/2}$, where $\delta\tau$ is the error on the lifetime and δt is the error on proper time for each event. If the resolution is good, $\delta\tau \ll \tau$, and $\delta\tau = \tau/N^{1/2}$. Thus 10% measurements of each lifetime, and a 14% measurement of the ratio, is possible with $10^5 Z^0$'s.

The error on proper decay time comes from two sources, the measurement of decay length and the measurement of B momentum. Monte Carlo simulations show that δL , the error in decay length L , is about $200 \mu\text{m}$, while $L = 2.3 \text{ mm}$, so $\delta L/L \simeq 0.09$, which is small. The proper decay time is $t = L/\gamma\beta c$, where $\gamma\beta = P/M$, and the error on the momentum will dominate.

The difficulty with using semileptonic decays is that the missing neutrino momentum is not measured. It is clear that one does not do too badly estimating the B momentum, however, simply by looking at the B momentum spectrum (Fig. 2). The peaking near $37 \text{ GeV}/c$ due to the hard fragmentation of the b quark corresponds to a momentum measurement of about $\pm 25\%$. One can do better by using the formula $\gamma_B = E_D/E_0$ where E_D is the total energy of the D (or D^*) and electron, and E_0 is the energy of the same system in the B center of mass: $E_0 = (M_B^2 + M_D^2)/(2 \times M_B)$. Figure 3 shows the ratio of gamma calculated this way to the true gamma as a function of M_D . It gives an estimate of $\gamma\beta$ with 19% error, which is even better for high M_D . The resolution on $\gamma\beta$ can be improved further by using the measured B direction to solve for the neutrino momentum.

Monte Carlo Study of $B \rightarrow D^{*+}e^-\bar{\nu}$

As an example of an exclusive semileptonic decay, we studied $B \rightarrow D^{*+}e^-\bar{\nu}$ extensively. The decay mode $D^0 \rightarrow K^-\pi^+$ was used to start; we can do equally well with a number of D^0 decay modes, but with tighter cuts and lower efficiency.⁵ With basic requirements on particle identification, and requiring each track to have $P > 0.5 \text{ GeV}/c$, one gets the $D^0 \rightarrow K^-\pi^+$ signal shown in Fig. 4. The efficiency is very high, because the cuts used are very open, but the background is quite low. The collection of events with mass less than 1.72 GeV is not background, but $D^0 \rightarrow K^-\pi^+\pi^0$ events, which are also usable for D^{*+} studies. If we now add these D^0 's to pions, and calculate $Q = M(D^0\pi^+) - M(D^0) - M(\pi^+)$, we get the spectrum shown in Fig. 5, with a very clean D^* signal.

Finally, we combine these D^{*+} candidates with electrons, both right sign ($D^{*+}e^-$ and c.c.) and wrong sign ($D^{*+}e^+$ and c.c.). The electron is identified with very good efficiency for $P > 2 \text{ GeV}/c$ and partially identified down to $0.5 \text{ GeV}/c$. We should do comparably well with muon efficiency. We also require the electron and the bachelor pion from the

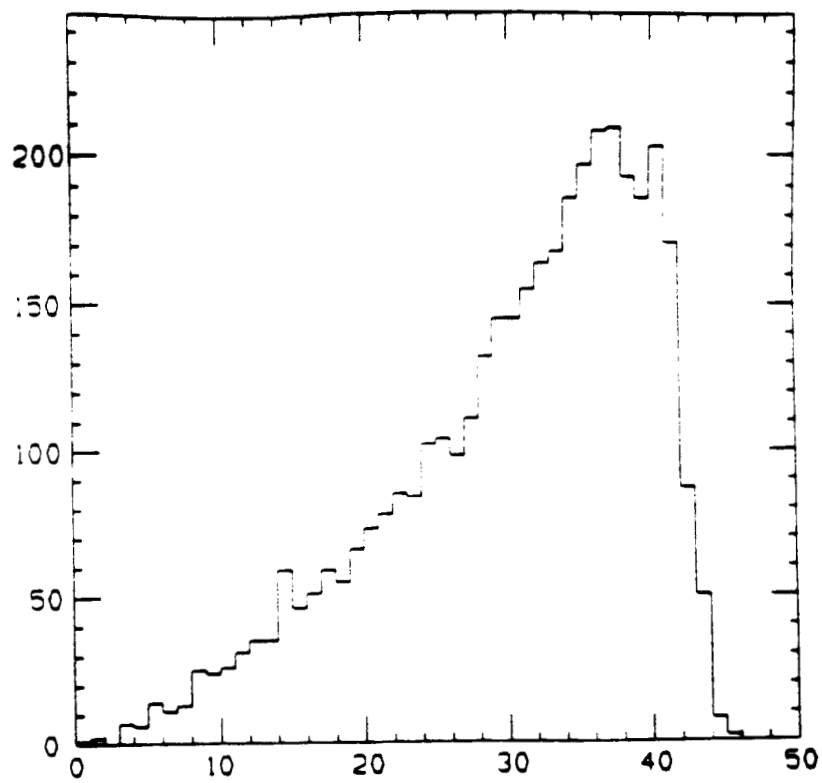


Fig. 2. Momentum spectrum of B's from Z^0 decays.

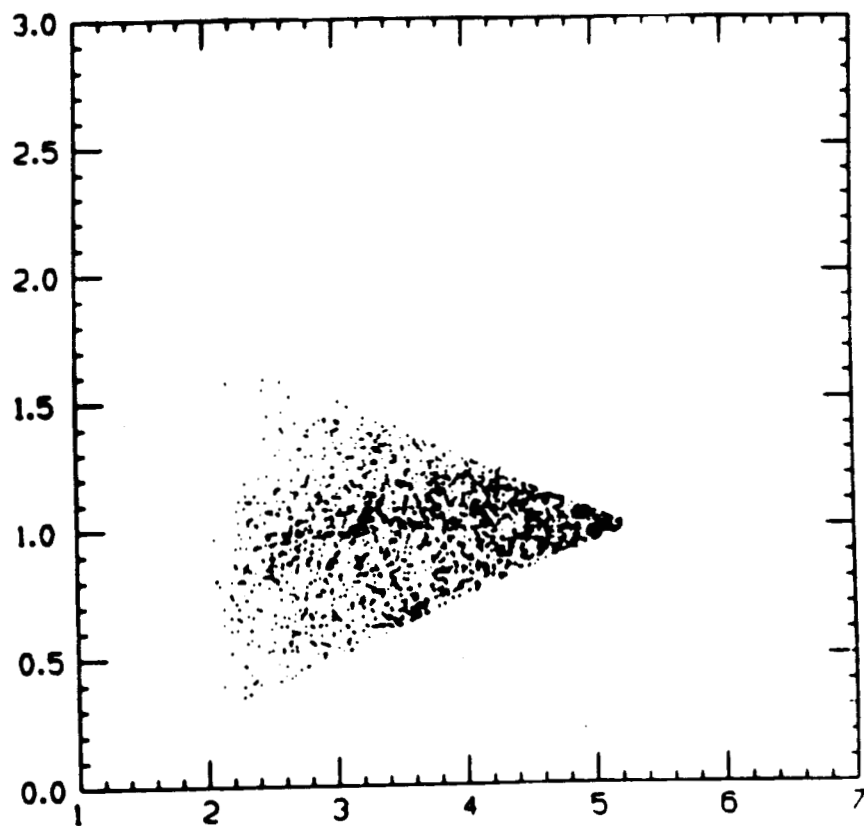


Fig. 3. Scatterplot of $\gamma_{\text{meas}}/\gamma$ vs. γ for B semileptonic decays.

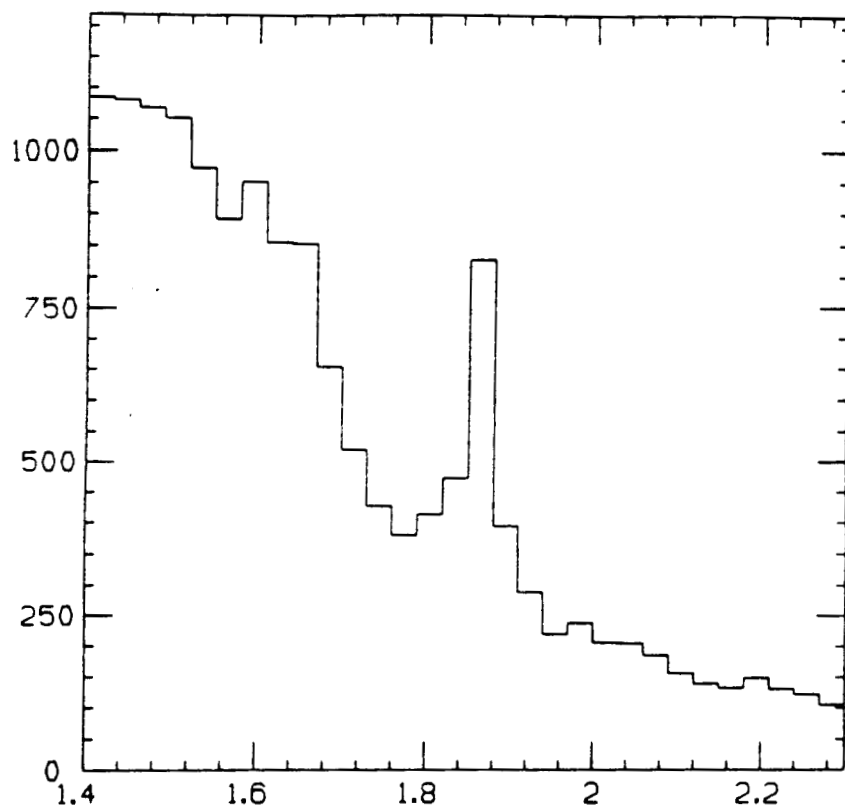


Fig. 4. The $K^-\pi^+$ mass spectrum from $b\bar{b}$ events.

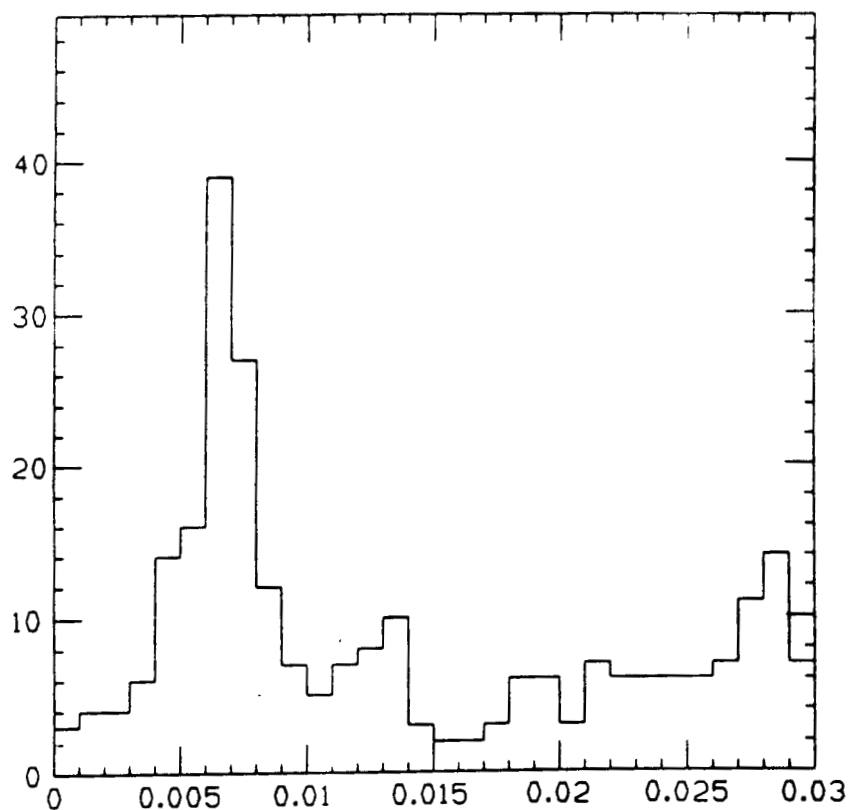


Fig. 5. The Q-value [$Q = M(D\pi) - M(\pi) - M(D)$] in GeV for the D^0 candidates from Figure 4. The D^+ peak is seen clearly at $Q = .006$ MeV.

D^{*+} decay to form a good vertex, closer to the primary than the $D \rightarrow K\pi$ vertex.

The D^*e mass spectrum gives a good indication of the signal. The spectra for right sign and wrong sign samples are shown in Fig. 6, for 50,000 $Z^0 \rightarrow b\bar{b}$ events. For this plot, with a lower cut at $M(D^*e) = 2.6$ GeV, the signal is 32 events and the background is 4, which probably indicates the cuts are tighter than they need to be. The full efficiency for this mode is about 50%.

The systematic error on the lifetime measurement should be quite small. One problem in lifetime measurements is the difficulty in measuring the production point, and in modeling this process with the Monte Carlo. The small beam spot at SLC reduces this problem significantly. A second problem is the effect of vertex cuts used to clean up the signal on the time spectrum. Figure 7 shows the proper time spectrum for a large sample of accepted D^*e events. (Actually the plotted variable is ct , in units of centimeters.) Even uncorrected, the time spectrum follows the exponential decay law well after about 0.02 cm. Following the procedure developed in measuring charm decays, we will define a minimum decay time t_{\min} , which is outside the region of partial vertexing efficiency. One can then fit the time evolution with $\exp[(t - t_{\min})/\tau]$ and need only minor corrections for efficiency.

We have completed this study using the mode which is simplest to study, but we should be able to obtain similar results summing over many charm channels. The backgrounds should be comparable in the D^*e or De spectrum, as long as the charm signal is larger than background before being combined with the electrons. Other studies show this is possible for a wide range of modes. The individual particle lifetimes will be calculated from three samples: $D^{*+}e^-$, D^0e^- , and D^+e^- . The \bar{B}_d lifetime will be measured using the D^{*+} and D^+ samples. The B^- lifetime will use the D^0e^- sample, with a correction for the $D^{*+} \rightarrow \pi^+D^0$ decays in which the bachelor pion is missed, which is unlikely.

An independent measurement of the lifetime ratio, $\tau(B^+)/\tau(B^0)$, is possible using the ratio of semileptonic decays. Here one uses the number of events in the three samples, corrected for efficiency:

$$\frac{\tau(B^+)}{\tau(B^0)} = \frac{N(D^0e^-) - f N(D^{*+}e^-)}{N(D^+e^-) + N(D^{*+}e^-)}$$

where N for each channel represent the observed number of events divided by the efficiency, and f represents the fraction of D^{*+} events in which the bachelor pion is missed. There is an additional correction for possible $D^{*+}e^- \bar{\nu}$ decays since the various D^{*+} mesons decay with equal probability to D^{*+} and D^{*0} , or D^+ and D^0 . These contributions will be measured directly quite well in SLD, because the only extra charged pions coming from a semileptonic

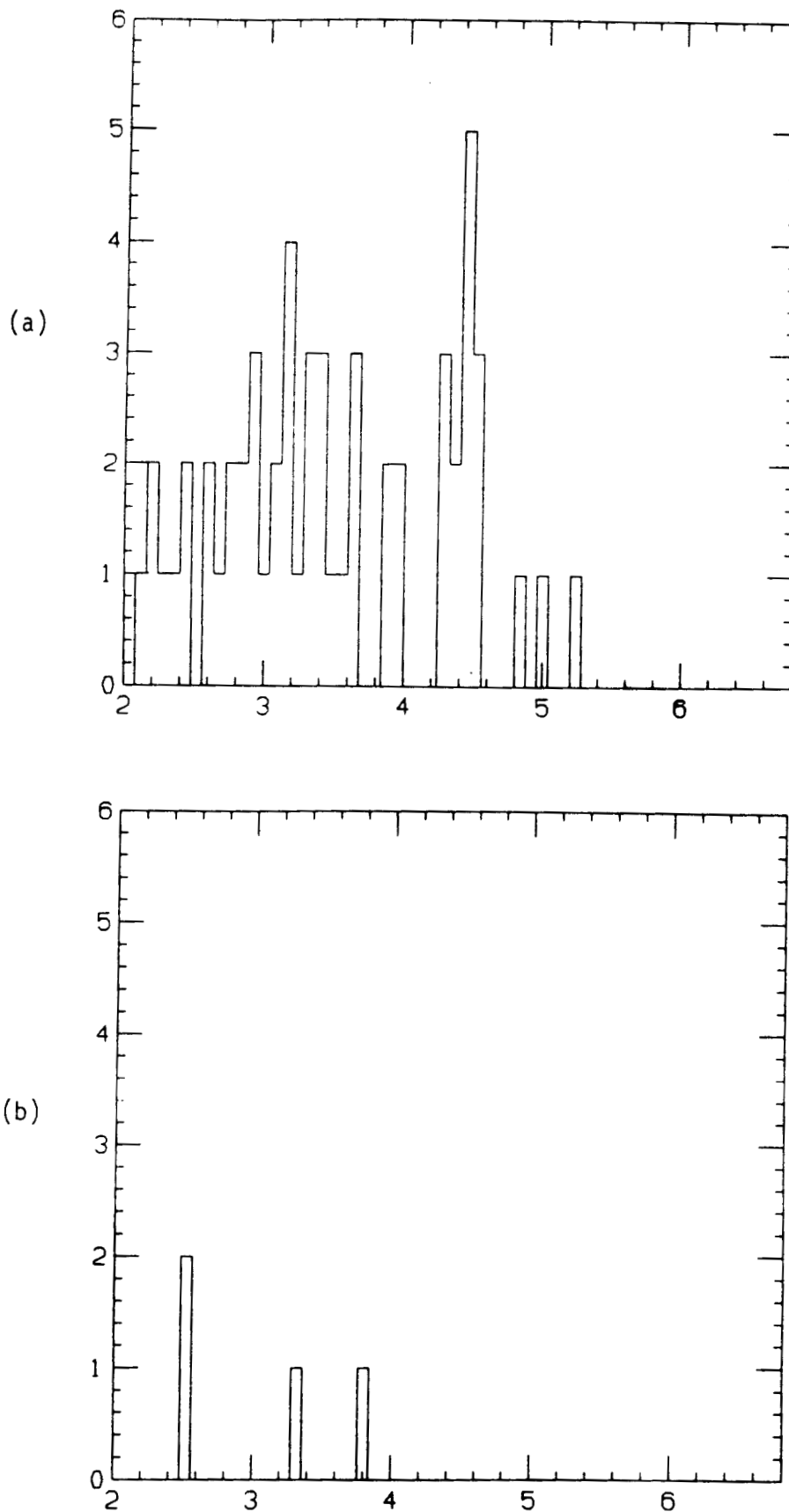


Fig. 6. The D^*e mass spectrum in GeV, for (a) $D^{*+}e^-$ and charge conjugate and (b) $D^{*+}e^+$ and c.c.

decay vertex will be from this source. If the systematic errors can be reduced sufficiently, this method will give a second measurement of the lifetime ratio with about 14% accuracy.

Semileptonic Decay Studies

The same sample of exclusive semileptonic decays used for the lifetime sample can be used for studying the semileptonic decay process. There is great interest in measuring the K-M matrix elements V_{cb} and V_{ub} precisely, since they are two of the fundamental parameters in the Standard Model which are not very well known. This will be useful in checking whether CP violation can be described as a product of the mixing angles.

To extract the matrix elements reliably, however, it is necessary to understand the form factors of semileptonic B decays. In the semileptonic decay, the weak current serves as a point-like probe of the meson wave function. The form factor measurements are therefore important in their own right. There is presently a great deal of theoretical effort in calculating the form factors, using both conventional and lattice gauge techniques.

Figure 8 shows the electron momentum spectrum in the endpoint region from CLEO. There has already been a continuum subtraction, which leads to the large statistical errors on the data points, even where there is no B decay signal. The spectrum in this region, especially 2.30–2.60 GeV, is used to find the contribution from $b \rightarrow ue^- \bar{\nu}$ decays. On the basis of this data, they reported the first significant excess of charmless B decays. The plot demonstrates the importance of understanding the form factors and relative rates for $D\bar{\nu}$ and $D^*e\nu$ decays. It also shows how difficult it is to obtain precise results in inclusive measurements.

In our picture of semileptonic B decays, the b quark decays primarily to $ce^- \bar{\nu}$, and the c quark combines with the light antiquark to form the hadronic decay products. By isospin, $\Gamma(B^- \rightarrow D^0 e^- \bar{\nu}) = \Gamma(\bar{B}^0 \rightarrow D^+ e^- \bar{\nu})$, and a similar relation holds for D^* and D^{**} hadronic states. All strong interaction effects are contained in the form factors that describe the hadronization process for the $c\bar{q}$ meson. One critical issue is to what extent D and D^* mesons saturate the inclusive rates, since some models depend on this hypothesis. In the ISGW model, the rates are 60% D^* , 30% D, and 10% D^{**} . Another issue is the dependence of the form factors on $q^2 = M_{e\nu}^2$. For the $D^*e\nu$, which is the one most accessible experimentally, there are three separate form factors, which contribute different amounts in different regions of the Dalitz plot. Measurement of the complete kinematic region is needed to discriminate between models.

The present situation can be summarized in two statements. The $B \rightarrow D^*e\nu$ channel

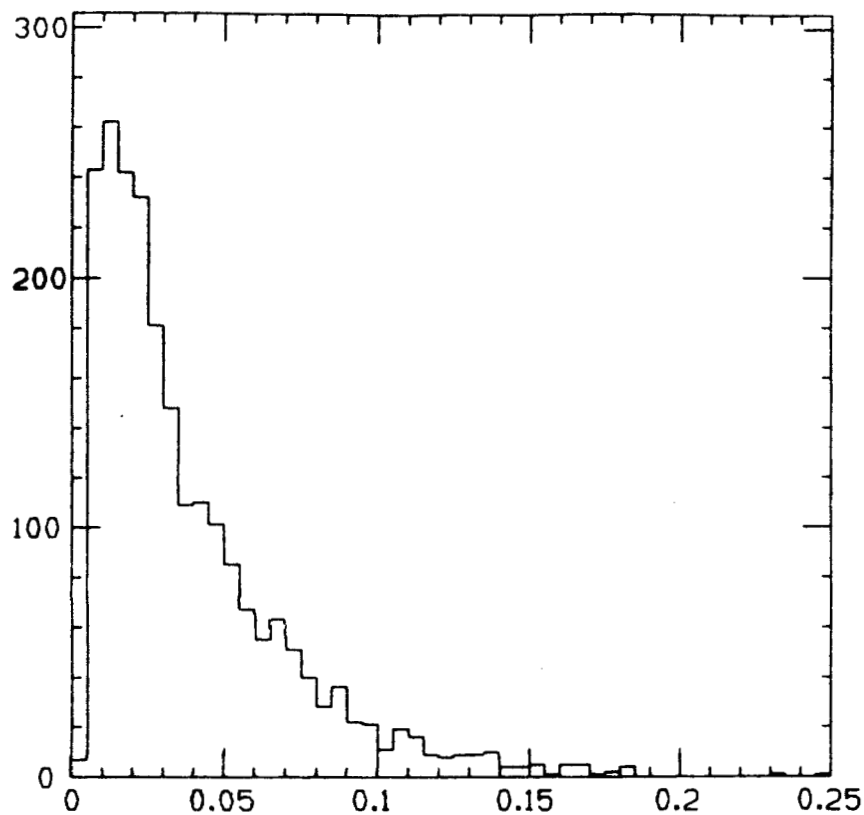


Fig. 7. The spectrum of ct , where t is the proper decay time of the B, in centimeters.

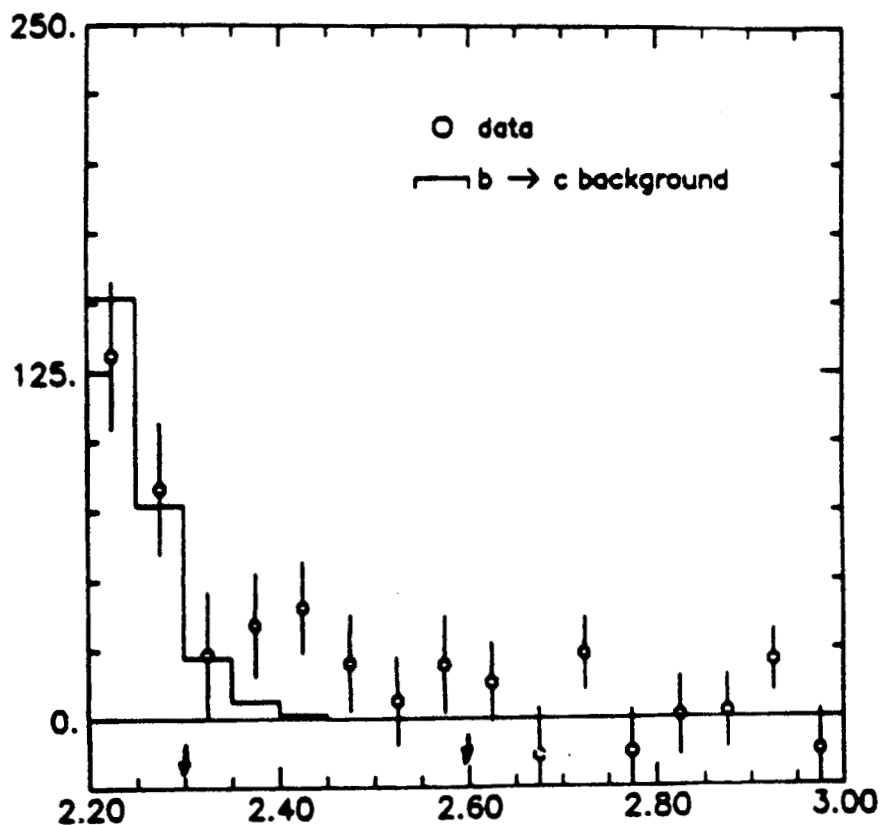


Fig. 8. The electron momentum spectrum from CLEO, in GeV, with continuum subtracted. The endpoint spectrum for $D \rightarrow ue^- \bar{\nu}$ decays is at 2.6 GeV. The histogram shows the contribution from $b \rightarrow ce^- \bar{\nu}$ decays.

is easy to measure, but hard to interpret; the $B \rightarrow D e \nu$ channel is easier to interpret but hard to measure. The $D^{*+} e^- \nu$ signal is easy to observe at CLEO and ARGUS, but they need to measure the polarization and rate over the entire Dalitz plot to determine the three form factors, in order to extract V_{cb} . Figure 9 shows a Dalitz plot for this process. The experimental information is very weak at low electron energy because the backgrounds are very severe there.

Figure 1 shows the $D^0 e^- \bar{\nu}$ signal seen by CLEO. After sideband subtraction there are 330 ± 30 events above background, which is equivalent to 100 clean events. These 330 consist of 58 D^0 , 133 D^{*0} , 70 D^{*+} , and 70 background events, according to their fit. This is why the statistical error of the $D^0 e^- \bar{\nu}$ component is $\pm 35\%$, equivalent to 8 clean events. It should be possible to separate D from D^* more reliably because the Dalitz plots for the two decays are rather different, but the cuts on electron momentum and D momentum necessary to see even this signal leave only about 1/4 of the Dalitz plot to work with.

The advantages for SLD come primarily from the vertex detector and the fact that the laboratory momenta of the decay products are not directly related to the kinematic region in the B center-of-mass. As we have shown, there is good efficiency for detecting charm, by using many modes with vertex cuts. Thus this measurement will become feasible with relatively few produced B mesons. The low backgrounds for $D^0 e \nu$ and $D^+ e \nu$ samples further improve the effective statistics.

More importantly, for the purpose of disentangling the form factors and the relative amounts of D and D^* , the acceptance covers the entire Dalitz plot. Figure 10 shows the accepted electron spectrum in the B c.m.s. which looks very much like the generated spectrum down to about $P_e^* = 0.1$ GeV/c. Typically studies are done with cuts on this variable of 1.0–1.4 GeV/c. There is a similarly good acceptance for P_D^* , since cuts in the laboratory frame are smeared in the B c.m.s.

The rates from 100,000 produced Z^0 's are quite good, as we show above. One would get samples of about 120 $D^0 e^-$ events, 70 $D^+ e^-$, and 50 $D^{*+} e^-$. For comparison, the CLEO sample is statistically equivalent to 40 clean events, and they have shown no $D^+ e^-$ signal. CLEO does have statistics in their $D^{*+} e^-$ sample comparable to those obtained in such an SLD sample.

In summary, SLD could have better statistics in the $D^0 e^- \bar{\nu}$ and $D^+ e^- \bar{\nu}$ samples than existing experiments. The acceptance over the entire kinematics range will make it possible to measure the form factors for $D e \nu$ and $D^* e \nu$ decay directly. The analysis of the

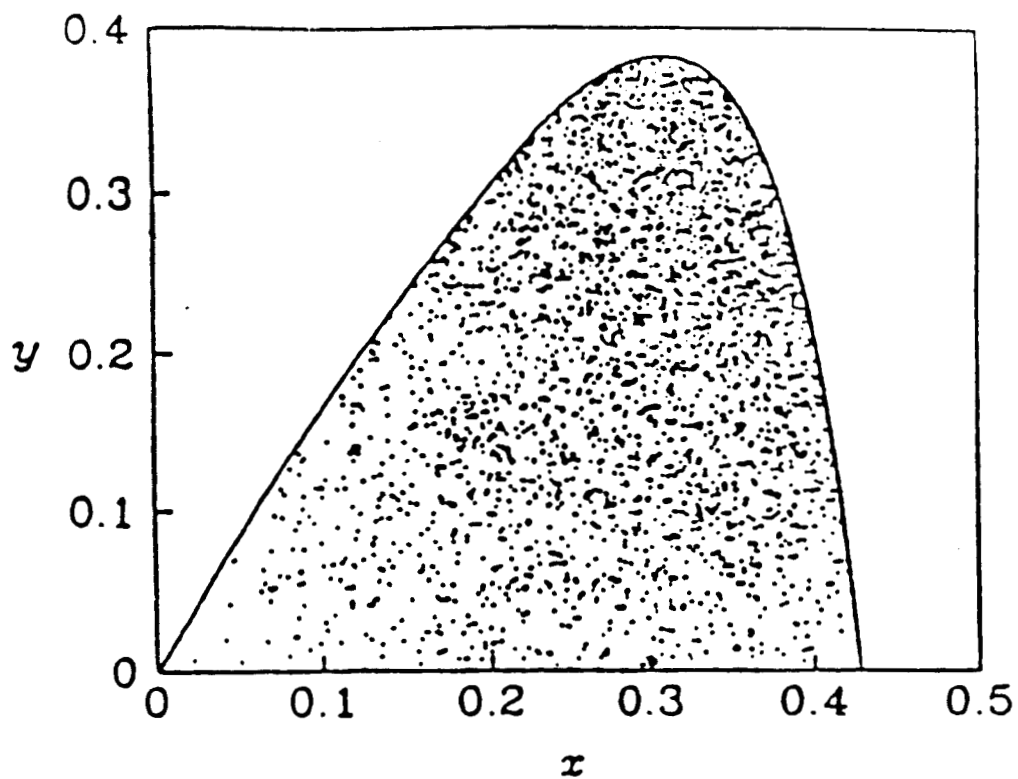


Fig. 9. The expected Dalitz plot for $B \rightarrow D^* e \nu$. ($x = q^2/M_B^2$ and $y = E_e/M_B$, where E_e is the electron momentum in the B center of mass.

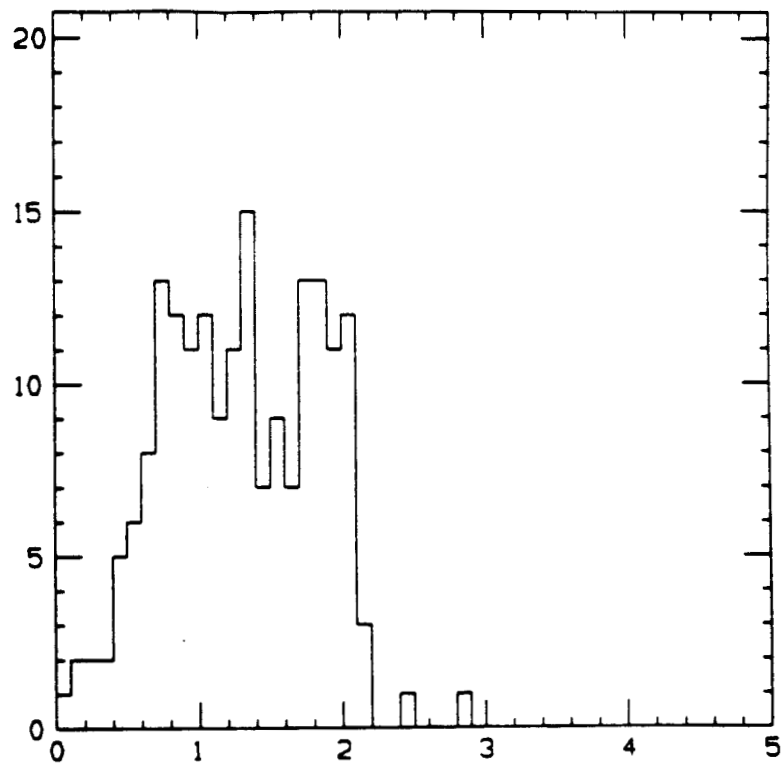


Fig. 10. The spectrum of E_e , for accepted events.

theoretically preferred $De\nu$ channel depends critically on separating the true $De\nu$ events from the larger $D^*e\nu$ contribution, and an unknown contamination of $D^{**}e\nu$. We would be able to use good signals in the three samples to disentangle D and D^* : the fractions of $De\nu$ in each sample are about 50% (D^+), 35% (D^0), and 100% (D^{*+}). In addition, the different kinematic dependence of the D 's from $D^* \rightarrow \pi D$ decay would make it easier to measure.

The ultimate goal in semileptonic decays is to measure $B^- \rightarrow \rho^0 e^- \bar{\nu}$, to extract a reliable number for V_{ub} . This shares the problems of $B \rightarrow De\nu$ and $B \rightarrow D^*e\nu$: it is hard to measure and hard to interpret. $B \rightarrow \rho e\nu$ is an extreme example of dependence on theoretical models, with differences of factors of 4 or more at different points in the Dalitz plot. Thus one cannot measure V_{ub} reliably with stringent kinematic cuts, which is the only way it could be done operating at $\Upsilon(4s)$ with no vertex information. On the other hand, it will take at least 300,000 Z^0 's to obtain measurable signals in this channel. This is a good example of important physics which takes a good vertex detector operating at the Z^0 to do well.

Conclusions

To understand the weak decay process in B mesons, precise measurements of the individual lifetimes and the rates and spectra for semileptonic decay modes are needed. These goals can both be reached using the exclusive semileptonic decays, $B \rightarrow D\ell\nu$ and $B \rightarrow D^*\ell\nu$. Present estimates show that with about 100,000 Z^0 's produced it will be possible to obtain clean signals of about 240 exclusive semileptonic decays. This will enable us to measure the individual B^+ and B_d lifetimes to 10% each. In addition, we will be able to measure the lifetime ratio independently with comparable accuracy and different systematics by measuring the ratio of semileptonic branching fractions.

These same events can be used to measure precisely the relative branching ratios into $(D, D^*, D^{**})e\nu$. The good acceptance and low background over the entire Dalitz plot will make it possible to measure the form factors for $De\nu$ and $D^*e\nu$ decay. These will be used to refine the form factor models and to extract V_{cb} with good precision.

All of this physics can be done with about 100,000 Z^0 's. With about 300,000, one could do comparably well with B_s meson, observed in $\bar{B}_s \rightarrow D_s(D_s^*)e\nu$. It would also be enough to measure V_{ub} in the decay $B \rightarrow \rho\ell\nu$, if the present indications of the approximate range for V_{ub} hold up.

These physics topics demand a powerful vertex detector. Using only $R\text{-}\phi$ measure-

ment in the vertex detector decreases the efficiency for measuring exclusive charm decays by a large factor, and costs an additional factor due to the requirement that the B decay products form a good vertex which is well separated from the primary interaction point. Comparable losses are expected using a beam pipe of large radius, even if a three-dimensional vertex detector is used, because tracks from one vertex are consistent with passing through the other more often.

REFERENCES

1. K. Schubert, review talk at the International Symposium on Heavy Quarks (Ithaca, 1989).
2. J. Alexander *et al.* (CLEO collaboration), paper submitted to the Lepton-Photon Symposium (SLAC, 1989).
3. H. Albrecht *et al.* (ARGUS collaboration), DESY preprint 89/117 (1989).

STUDY OF THE $B \longrightarrow J/\psi$ DECAYS WITH THE SLD

A. Calcaterra, R. De Sangro, P. De Simone, I. Peruzzi[†], M. Piccolo

Laboratori Nazionali di Frascati dell'INFN - Frascati, Italy

[†] *also Dipartimento di Fisica, Università di Perugia, Italy*

INTRODUCTION

The B decays into a J/ψ have been measured by both the CLEO^[1] and the ARGUS^[2] collaboration; although the inclusive branching ratio is roughly of only 1%, these channels provide a rather large fraction of the completely reconstructed B mesons. The J/ψ is identified through its decay into an electron or a muon pair (combined Br is 14 %), has a rather hard momentum distribution, compatible with mostly two-body production, and is usually accompanied by a strange meson, K or K^* ; the final state is therefore quite easy to identify.

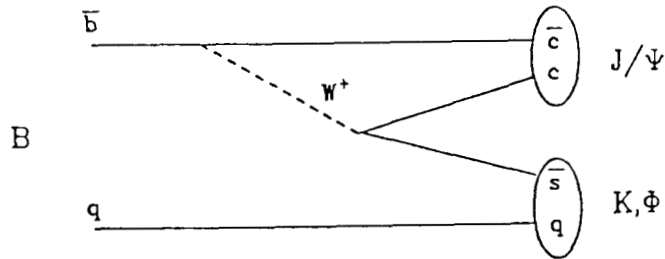
B studies usually start with D or D^* tagging and the presence of a tertiary vertex from the D decay considerably complicates the analysis; the complete decay chain can be reconstructed in a very small number of cases. The $B \longrightarrow J/\psi$ decays lead instead to final states where all B decay products originate at the same point; the B charge is determined by simply counting the vertex prongs; its momentum is well approximated by summing over the charged tracks in the vertex.

At the Z^0 energy, these channels provide a powerful B tag, since a J/ψ in a secondary vertex can only be produced by a b -particle, and the leptons from the J/ψ decay can be easily identified because their momentum is typically several GeV/c. The excellent vertex detection and particle identification capabilities of the SLD detector, together with the small size of the SLC vacuum pipe, will allow an almost background free identification of these decays.

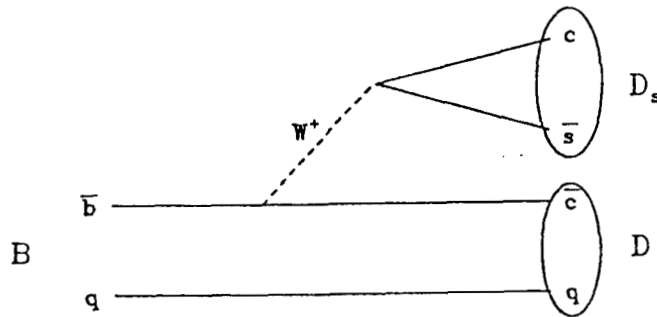
The aim of this study is to evaluate the acceptance and the background level for measuring these channels with the SLD , and to assess which physics topics can be addressed in the first year or two of running, when the collected data sample is expected to be of the order of 100,000 Z^0 's.

1. THE $B \rightarrow J/\psi X$ DECAYS

The B meson decays into a J/ψ proceed through the *color matched* diagrams:



the *color* of the \bar{c} quark from the W decay has to match the color of the c quark from the b decay; the amplitude is therefore 3 times smaller than the the DD_s corresponding modes:



In the naive spectator model the branching ratio suppression is therefore of a factor 9 ; when comparing the Br's for the actual particles, the QCD effects due to gluon radiation and to final state interaction between the quarks should be taken into account; theoretical prediction vary by large factors and accurate measurements of several final states would be necessary in order to shed some light on the mechanism of color suppression. The b system is the most suitable for these studies, since contributions from non-spectator diagrams should be small.

The final state also contains at least one kaon, due to the presence of a s quark in the W decay; in the B_s decay an additional s quark is present. A J/ψ in a *detached* vertex together with two opposite sign kaons, from a Φ decay or non resonant, would be a clean signature for a B_s decay, and even few events should be enough to measure the mass of this yet unidentified particle. For this experiment to be possible, both vertex detection and particle identification up to high momenta and over a large solid angle are essential features required to the detector.

Once a J/ψ has been identified away from the interaction point, the multiplicity of the tracks in the vertex determines the charge of the decaying B particle; given enough events, the lifetime for the different B species could be measured. The ratio τ_b^+/τ_b^0 has been measured from the B semileptonic branching ratios at the $\Upsilon(4S)$, assuming that the semileptonic widths are the same for charged and neutral B mesons. The ARGUS measurement^[3] $(1.00 \pm 0.23 \pm 0.14)$, is presently the most accurate, and doesn't exclude a difference of 20 % or more; the theoretical prejudice is that the two lifetimes should differ by 20% at most. A precise measurement of the separate lifetimes is one of the outstanding topics in B Physics; the SLD at the SLC is ideally suited for this difficult experiment; the number of events required is however large, and it will be useful to exploit as many decay channels as possible.

2. THE MC ANALYSIS

We have generated a sample of 1000 $b\bar{b}$ events in which one B meson was forced to decay into a J/ψ and all J/ψ 's were only allowed to decay into lepton pairs. The Fast Montecarlo simulation of the SLD detector was then used to smear the parameters of the produced particles and to simulate, at least at a crude level, the detector effects. Such a sample was used to study the kinematics and the vertex topology of the *signal* events and to test the vertex finding algorithm presently available in the Fast Montecarlo. Large samples of $b\bar{b}$ and $c\bar{c}$ Z^0 events were then used to study the background level for different analysis strategies.

The tracking efficiency in the fast Montecarlo is practically 100 %, so that all particles produced within the geometric acceptance are found in the detector; the identification efficiency is very high for both electrons and muons with momentum above 1 GeV/c as shown in figure 1. In our sample of 1000 produced leptons pairs, 720 are tracked and correctly identified; even if this simulation is rather crude and many effects which are likely to worsen the efficiency are not taken into account, this result is probably only slightly optimistic: a pair of high momentum leptons in the same jet can hardly be missed in the SLD for reasons other than the geometric acceptance.

Once the lepton pairs are identified, their invariant mass can be calculated: a fit to the distribution for the *signal* events gives a r.m.s. of 26 Mev/c² ; 660 events lie between 3.0 and 3.2 GeV/c², which will be used in the following as the J/ψ region.

The production point of the J/ψ is distinct from the primary vertex and this provides a powerful tool for separating this process from the background; the algorithm now available in the Fast Montecarlo allows vertex identification for tracks with momentum above 500 Mev/c and distance of at least 500 μ m from the interaction point. Applying this algorithm we find that 438 lepton pairs out of 720 are found in a secondary vertex; figure 2 shows the decay path distribution for all of the the B 's and for the events where the lepton pair is identified in the detector and assigned to a secondary vertex: the efficiency is zero for decay paths below 500 μ m and rises to \approx 80 % at 2 mm.

The distribution of the differences between the coordinates of the *produced* and the *measured* vertices are shown in figure 3; the r.m.s. of these distributions are 60-70 μ m. It seems therefore possible to reduce the cut on the minimum distance of the vertex from the IP to 200-300 μ m, thus increasing the efficiency for shorter decay paths.

The charged tracks multiplicity in the B vertex is quite low, and in 76% of the $B \rightarrow J/\psi$ decays all the charged particles produced were found in the detector;

the fraction of cases where the correct charge would be assigned to the parent B is $\approx 80\%$, higher because in few cases two tracks are lost. These decay modes are therefore very suitable for measuring the parent B 's charge, even for partial B reconstruction.

A complete B reconstruction even for few events would be very important in order to measure the yet unknown B_s mass and to measure lifetime with no bias; a large fraction of these decays ($\approx 60\%$ for B_u and B_d , 83% for B_s) lead to final states which contain only charged prongs or charged prongs plus K_s 's, a large fraction of which can be detected through the $\pi^+\pi^-$ decays.

In summary, 40% of the $B \rightarrow J/\psi \rightarrow l^+l^-$ events will have the J/ψ identified and assigned to a secondary vertex and in approximately half of the cases the B meson will be fully reconstructed.

3. THE LIFETIME MEASUREMENTS

The B meson lifetime, averaged over the produced species, can be evaluated from the momentum and the vertex distance of the J/ψ 's. A correction is needed because the detection efficiency varies with the B decay path, as previously pointed out, and the J/ψ 's $\gamma\beta$ factor is not the same as for the parent B ; this measurement, however, would have a smaller systematic uncertainty than yielded by the impact parameter method which must rely on the MC modeling of B production and decay. The SLD vertex resolution is much smaller than the average B decay path ($\approx 2\text{mm}$), so a good lifetime measurement can be done with even a relatively small sample of events, the statistical error scaling as $1/\sqrt{N_{\text{events}}}$.

In order to evaluate the separate lifetimes for neutral and charged B mesons, a further step is needed in the vertexing algorithm: given the pair of lepton tracks from the J/ψ decay, one should be able to identify which, if any, additional tracks originate at the same point. These events do not have a tertiary (charm) vertex in the same hemisphere, so this assignment will be more reliable than for channels

containing a D meson, where it's more difficult to correctly assign the right tracks to each vertex.

The B charge assignement will be correct if all the tracks from the B decays are found in the same vertex together with the lepton pair, or if two of them are missing; it will be wrong if one track is missing. Using the current Fast Montecarlo, 66 % of the J/ψ in a secondary vertex have all the remaining charged tracks from the B decay identified as belonging to the same vertex; we don't have yet a tool to discriminate among various vertices hypotheses on the basis of maximum likelihood, so that the best guess for the J/ψ vertex multiplicity can be determined. We should however be able to identify the correct charge in ≈ 70 % of the cases.

4. BACKGROUND STUDIES

Since no physical process other than b -particles decays can produce J/ψ 's in a secondary vertex, the possible background sources are limited to :

- a)– events where the B and the D in the same jet both decay semileptonically in a muon or an electron.
- b)– one of the tracks is a lepton from a heavy quark semileptonic decay while the other is a misidentified hadron.
- c)– events with two opposite charge hadrons identified as a muon or an electron pair.

Events of the type a) have to be $b\bar{b}$: the second category includes both $b\bar{b}$ and $c\bar{c}$ events, while for the third case also light quark events can contribute. Light quark events can be quite easily separated from $b\bar{b}$ and $c\bar{c}$ using vertex and/or impact parameter tagging techniques, so the only significant background will come from heavy quark events.

We have run our analysis program using MC events where the initial quark flavor, $b\bar{b}$ or $c\bar{c}$, was known; we used a sample of 90,500 $b\bar{b}$ events where 231 $B \rightarrow$

$J/\psi \rightarrow l^+l^-$ events were present and a sample of 36,500 $c\bar{c}$ events. In the invariant mass distribution of the lepton pairs a J/ψ signal is barely visible in the $b\bar{b}$ events and it practically disappears when the $c\bar{c}$ events are added. The J/ψ peak stands out clearly when the lepton pair is required to belong to a secondary vertex. The separate distributions are shown in figure 4, the shaded area under the J/ψ peak is the contribution of the background.

In the $b\bar{b}$ sample we find 120 lepton pairs in a secondary vertex having invariant mass between 3.0 and 3.2 GeV/c² , 92 of these are genuine events, while 28 are background. In the $c\bar{c}$ events we find 2 events satisfying our cuts; in both cases the *lepton* tracks are misidentified hadrons. The signal in this MC sample is ≈ 80 % of what we would expect on the basis of the CLEO and ARGUS measurements, since a total branching ratio of 1 % was assigned to $c\bar{c}$ decays of the B mesons, which include, other than the J/ψ , the χ states, the η_c etc.

5. SUMMARY

In a sample of 100,000 hadronic Z events , ≈ 70 events of the type $B \rightarrow J\psi \rightarrow l^+l^-$, will be present, according to the $\text{Br}(B \rightarrow J/\psi \text{ X})$ measured by CLEO and Argus. SLD will be able to find ≈ 28 of these lepton pairs in a separate vertex, plus approximately 7-8 background events. without using any kinematical cuts. We expect in this sample: $\approx 13 B_d$, $\approx 12 B_u$, $\approx 3 B_s$. More work on the vertexing algorithm could lead to a substantial improvement in the signal to background ratio, since in most cases the tracks which fake the signal don't have the same origin. In at least 70 % of the cases we should be able to correctly assign the mass of the B meson produced. and about half of the time the B particle will be completely reconstructed.

With some luck the B_s could be identified even in such a relatively small size sample of events; in 2-3 years running time, the analysis of these channels will allow us to:

- Measure the B_s mass

- Measure the B lifetime
- Have a first shot at the $\tau_b^0 - \tau_b^+$ separate lifetime measurements.

In view of the crucial importance of the vertex detector in this analysis, we will study a more specialized vertex algorithm to increase the efficiency of vertex finding and improve the track assignement to each vertex; we also plan to study the improvement that could be obtained if a smaller beam pipe (1.6 cm radius) is used.

REFERENCES

1. CLEO Collab. M.S. Alam et al. Phys. Rev. D 34 (1986) 3279
2. ARGUS Collab. H. Albrecht et al. Phys. Lett. 162B (1985) 395
3. M. V. Danilov, Invited talk to the XIV Int. Symposium on Lepton and Photon Interactions, Stanford 1989

FIGURE CAPTIONS

- 1) Momentum distribution of a) electrons , b) muons from the J/ψ decay ; the shaded areas refer to the tracks correctly identified according to the Fast MC.
- 2) Distance from the I.P. of the lepton vertices for all J/ψ 's; and for the lepton pairs in a measured secondary vertex (shaded area)
- 3) Distribution of the differences between the coordinates of the *produced* and the *measured* vertices
- 4) Lepton pair invariant mass distributions for $b\bar{b}$ (left) and $c\bar{c}$ (right) events.
 - a) All pairs; b) pairs in a secondary vertex

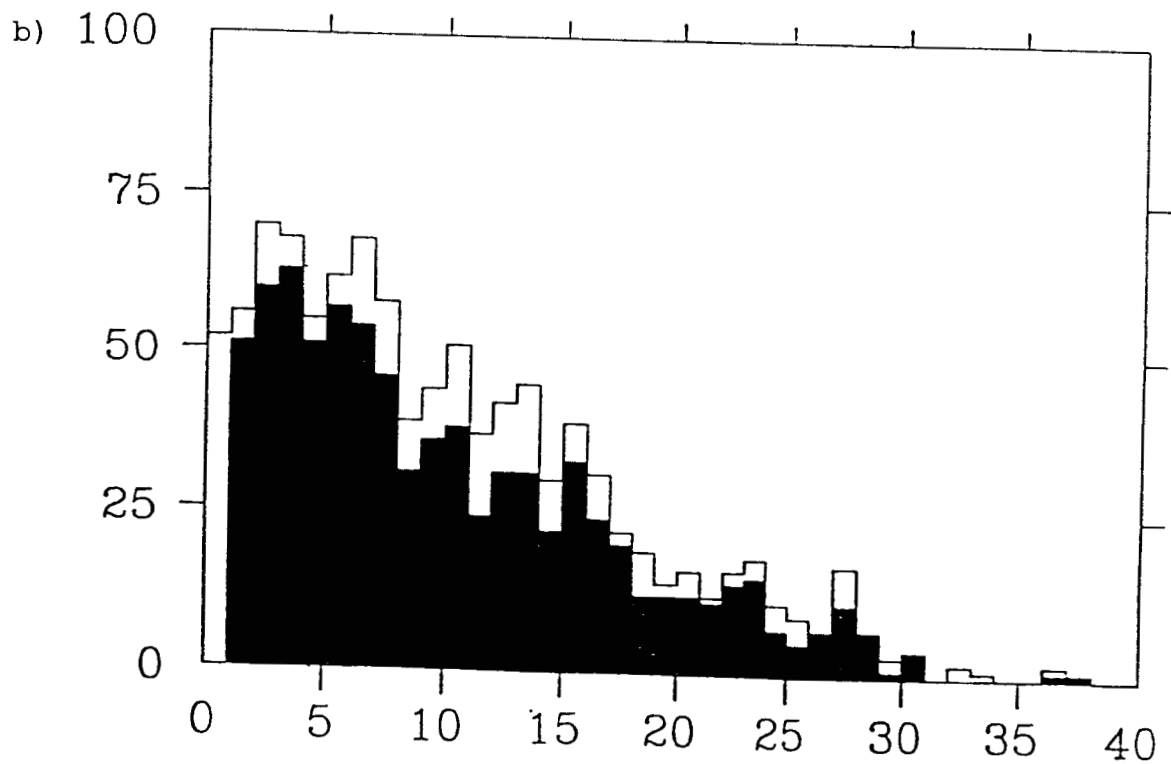
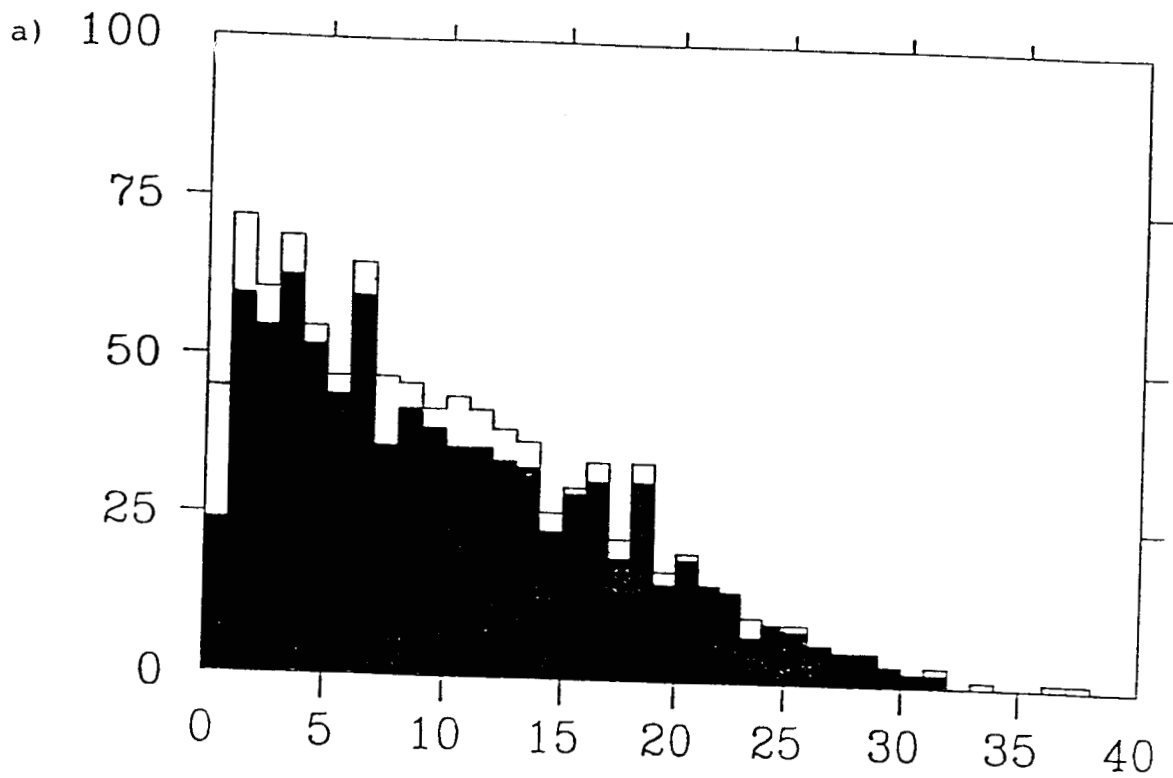


Figure 1

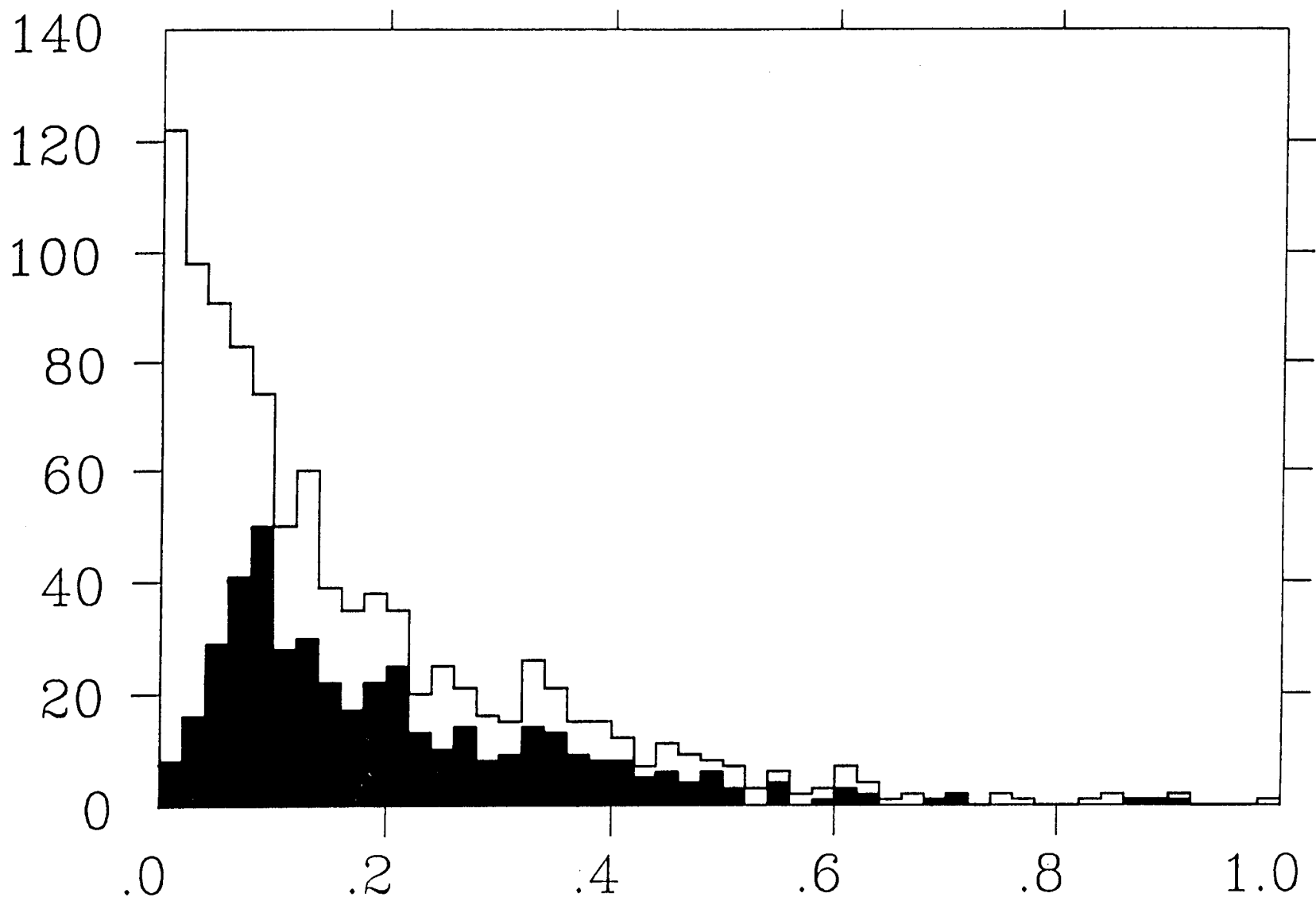


Figure 2

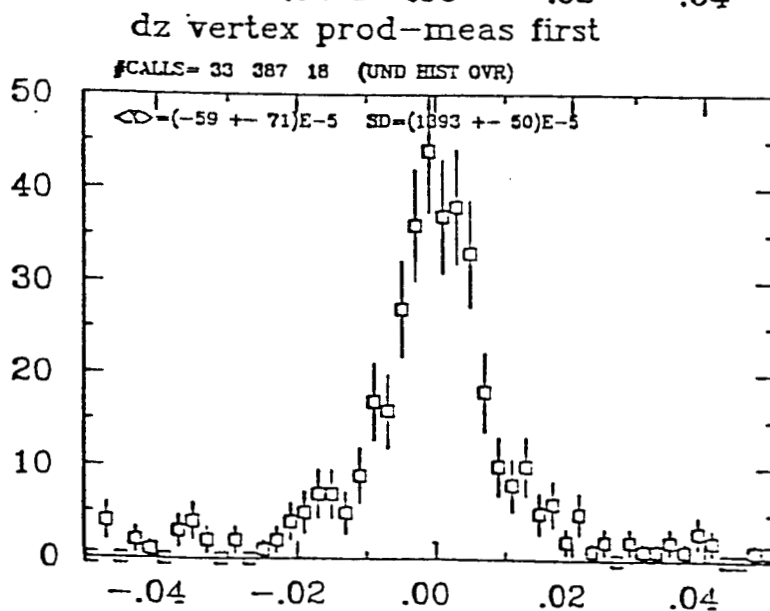
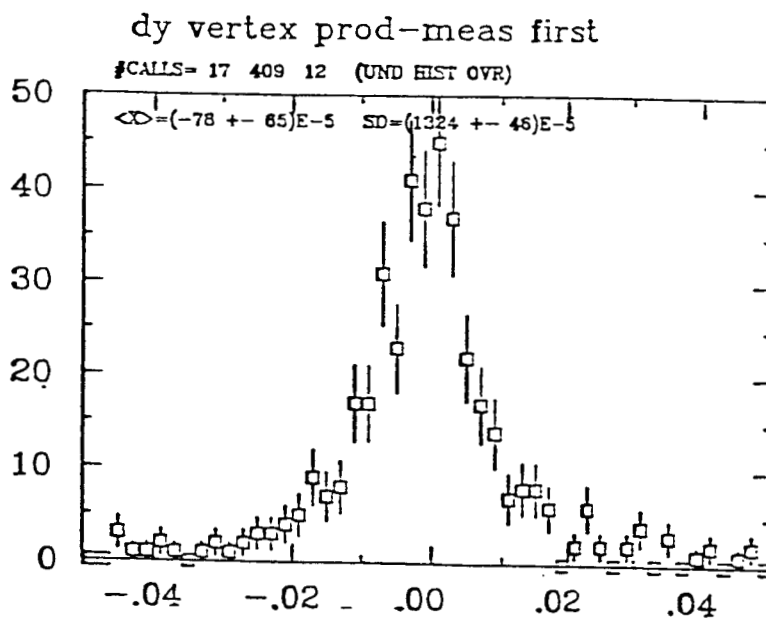
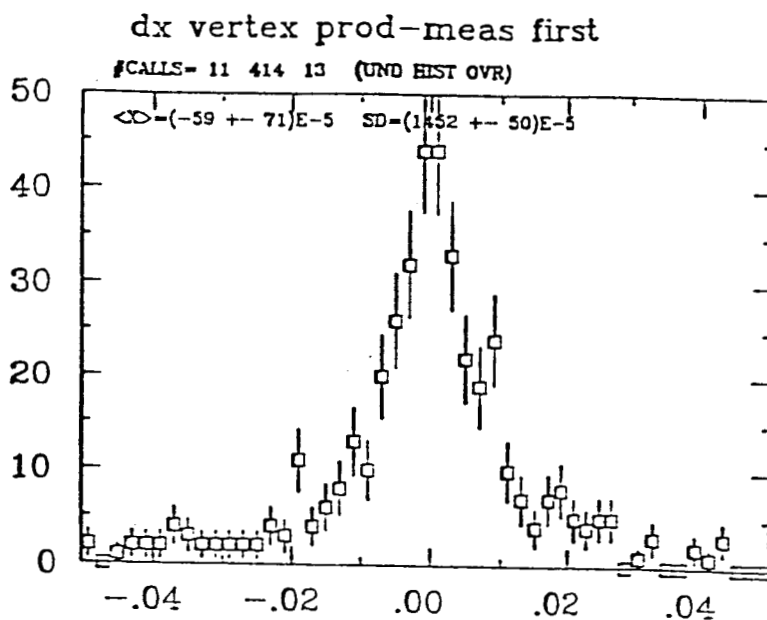


Figure 3

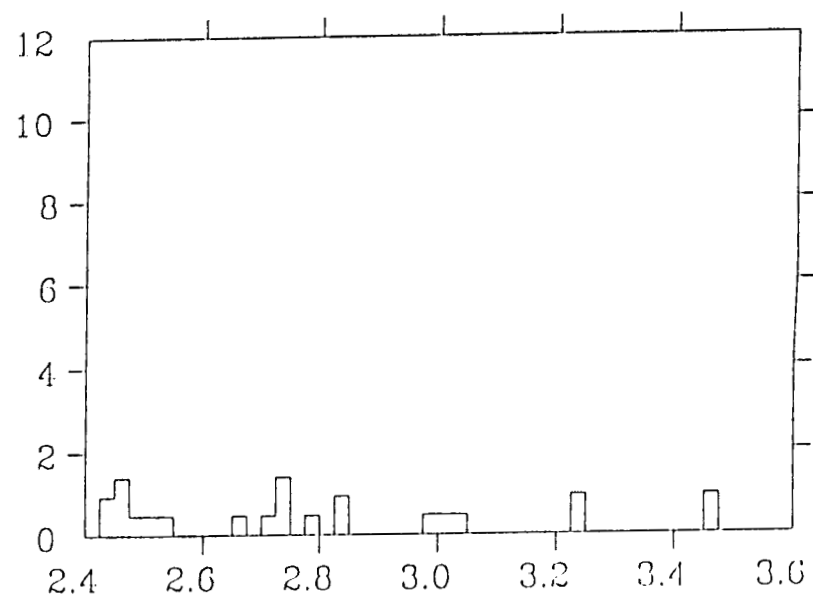
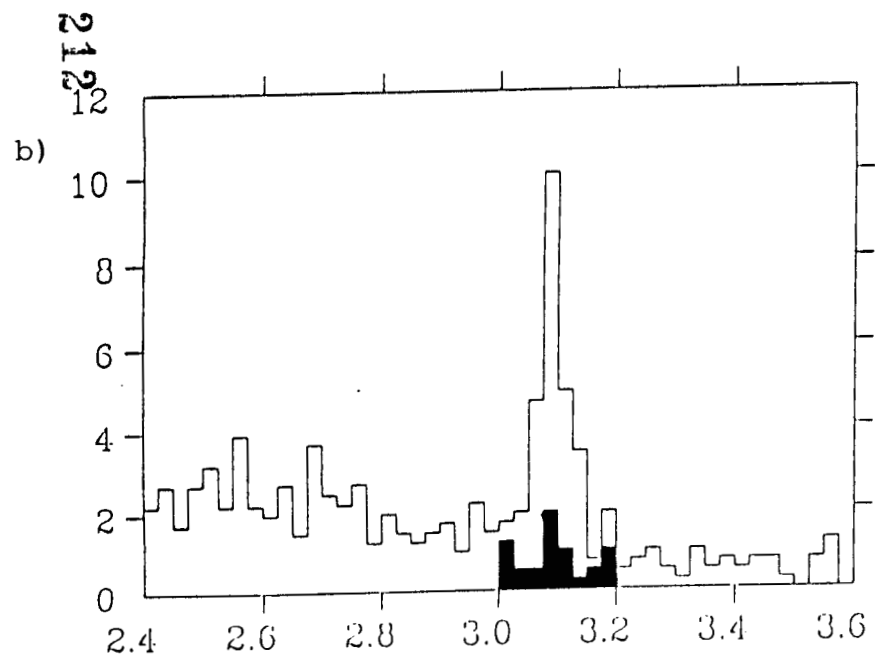
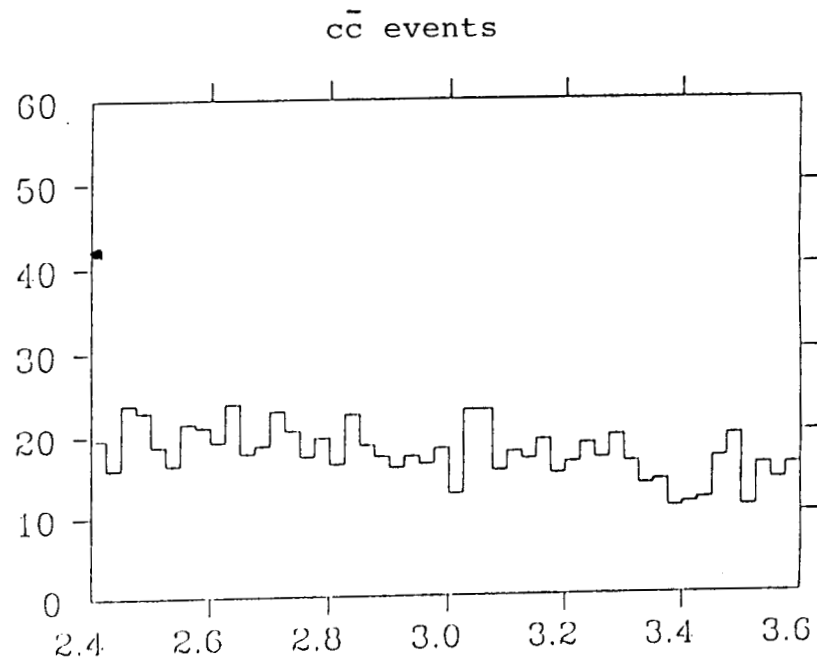
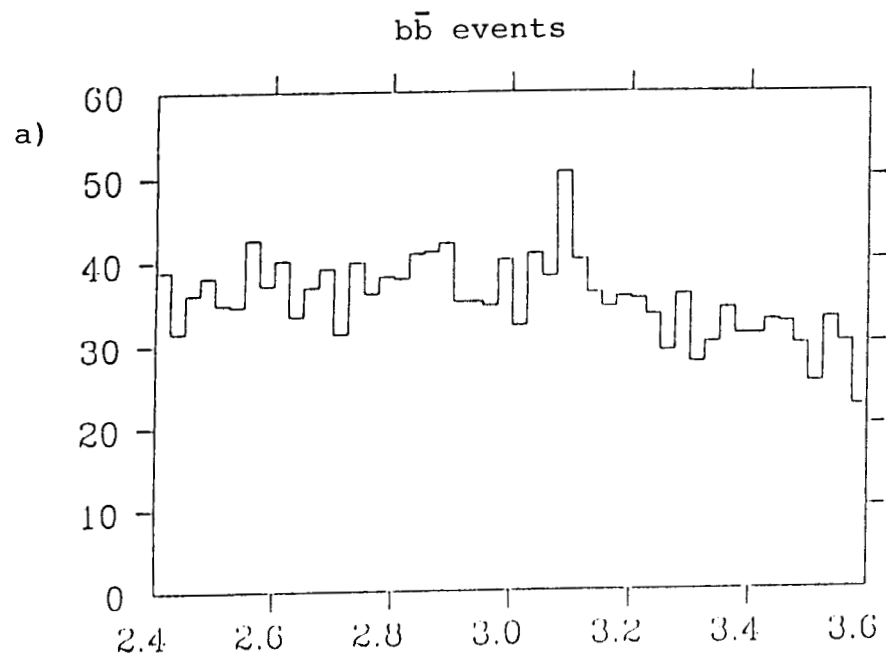


Figure 4

Tagging D_s Mesons in $b\bar{b}$ Events Produced in Z^0 Decays^{*}

GERALD EIGEN AND MICHAEL H. KELSEY

*California Institute of Technology
Pasadena, California 91126*

ABSTRACT

A study of tagging D_s mesons from B decays in the all-charged hadronic final states $K^+K^-\pi^+$, $K^+\pi^+\pi^-$, and $\pi^+\pi^-\pi^+$ is presented, using samples of $\sim 68,000$ $Z^0 \rightarrow b\bar{b}$ Monte Carlo events for the first two topologies and 153,000 for the latter. For three final states, reconstruction efficiencies of about 14%, 41%, and 14%, with tagging efficiencies ($\epsilon \cdot B$) of about 0.6%, 0.5%, and 0.1% are found, respectively. Background levels are reasonable, except for the $\pi^+\pi^-\pi^+$ topology.

^{*} Presented at the SLD Physics Retreat, Kirkwood, CA, July 31–August 4, 1989

1. Introduction

The tagging of D_s mesons is an important tool for the study of B_s mesons which originate from Z^0 decays. Since the B_s has not been detected in current experiments, an initial goal is its observation and the measurement of its mass. The next step is to perform a detailed study of B_s decay modes in order to test the predictions made by different models of heavy flavored meson decay.^[1-3] This study requires a large B_s sample. D_s tagging plays a major role since $\sim 80\%$ of all B_s mesons decay to D_s , whereas $\sim 15\%$ of the B^0 and B^- mesons decay to D_s . Although the study of exclusive B_s decays may be preferred, it may not be practical due to small B_s and D_s branching fractions and low detection efficiencies for individual channels. The solution may lie in a semi-exclusive method. But in any case it is important to identify many D_s decays with high detection efficiency.

In the present study we have focussed on D_s decays which contain only charged particles. Modes which contain π^0 's, η 's or γ 's will be studied later. Table 1 gives a detailed list of all modes studied including branching fractions, final states and final "visible" branching ratios — the product of the D_s decay mode branching fraction and the branching fractions of the resonance decays into the particular final state. For this study 67,870 $Z^0 \rightarrow b\bar{b}$ Monte Carlo events have been analyzed, which contained a total of 56,221 D_s mesons. This sample corresponds to (with $Z^0 \rightarrow b\bar{b} \sim 14\%$) about 485,000 produced Z^0 's. These events were generated using the Lund Monte Carlo^[4] together with a heavy meson decay program written for SLD.^[5] The branching ratio $B(D_s \rightarrow \phi\pi)$ is assumed to be 3%; all other D_s branching fractions are scaled to this value.

For background estimates, 33,942 $Z^0 \rightarrow c\bar{c}$ events were generated using the same software package. Background is expected from $c\bar{c}$ events which contain a D_s , from D_s mesons originating from B decays containing 3 charged particles plus photons, from D^+ or D^0 decays containing photons, or from u , d , or s jet events, where the first two sources are probably the major ones.

One must remember that this study is based on a specific D_s decay model.

Since few D_s decay modes have been observed, many surprises may await us.

Table 1. D_s^+ Decay Modes Studied

Decay Mode $D_s^+ \rightarrow$	B [%]	Observed Final State	Visible B [%]
$\phi(1020)\pi^+$	3.00	$K^+K^-\pi^+$	1.48
$\overline{K}^{*0}K^+$	2.90	$K^+K^-\pi^+$	1.94
$(K^+K^-\pi^+)_{NR}$	0.89	$K^+K^-\pi^+$	0.89
Total $K^+K^-\pi^+$			4.31
\overline{K}^0K^+	2.93	$K^+\pi^+\pi^-$	1.01
$K^{*0}\pi^+$	0.16	$K^+\pi^+\pi^-$	0.11
Total $K^+\pi^+\pi^-$			1.12
$f_0(975)\pi^+$	1.51	$\pi^+\pi^-\pi^+$	0.79
Total $\pi^+\pi^-\pi^+$			0.79

2. Analysis of D_s Decay Modes

In our present study, we have selected events using a common prescription for all studied final states. First, all tracks in a candidate final state must extrapolate to a single secondary vertex which is separated from the primary vertex (interaction point) by at least $500\mu\text{m}$. Second, each of the three tracks must have momenta exceeding $500\text{ MeV}/c$ (except for the $\pi^+\pi^-\pi^+$ final state, see below). Finally, for the final states involving one or more kaons the track must be identified as a K^\pm , which imposes a polar angle cut of $|\cos\theta| < 0.75$ since the SLD detector, for this exercise, does not have particle identification in the endcap regions. With these requirements we find a total of 2,762 candidate vertices in all final states.

For the decay modes involving resonances, we compute the mass of the two-body final state of each resonance, and require that it fall within 3σ of the peak, where σ is the width of the resonance, fit to a Gaussian. We fit the background in the two-body mass distributions to a polynomial. The results of this exercise, the measured peaks, widths, and identification mass cuts, for the resonances we studied are shown in Table 2. The mass distributions are shown in the sections on each final state. We have made no attempt to model the various backgrounds in any systematic way, since this is only a preliminary analysis.

Table 2. Reconstructed Resonance Parameters

Two body Resonance	Final State	Fit Parameters (MeV/ c^2)		Mass Cut ($Peak \pm 3\sigma$)
		Peak	Width(σ)	
$\phi(1020)$	K^+K^-	1019.0 ± 0.2	3.9 ± 0.19	1005 – 1035
$K^{*0}(896)$	$K^\pm\pi^\mp$	898.4 ± 3.8	22.9 ± 5.1	820 – 970
K_S^0	$\pi^+\pi^-$	497.3 ± 0.2	4.4 ± 0.19	480 – 520
$f_0(975)$	$\pi^+\pi^-$	999.6 ± 2.5	20.2 ± 2.4	940 – 1060

For the “non-resonant” three-body decay modes marked NR in Table 1, we accept all candidate vertices with two-body masses outside the resonance regions for that final state. For example, in the $K^+K^-\pi^+$ final state, the non-resonant candidates are all those in which $m(K^+K^-) \neq m(\phi)$ and $m(K^-\pi^+) \neq m(K^{*0})$.

Finally, we present a brief summary of the same analysis for a sample of 33,942 $Z^0 \rightarrow c\bar{c}$ events. In order to measure the background from these events in our analysis package, the same cuts on resonance masses and on the D_s vertex mass are used as for the $b\bar{b}$ events. In each section below, we present only the D_s vertex mass distributions from this background sample, for comparison with the $b\bar{b}$ “signal” events.

2.1. THE $K^+K^-\pi^+$ FINAL STATE

The D_s decay model used in our Monte Carlo contains three decay modes which can lead to the final state $K^+K^-\pi^+$, listed in Table 1 above. The plots below show the three-body mass and two-body submasses for all candidates of this final state obtained from the $b\bar{b}$ Monte Carlo sample. The D_s signal stands out clearly, with a mass of $1971.5 \pm 0.9 \text{ MeV}/c^2$ and a peak width of $24.5 \pm 2.0 \text{ MeV}/c^2$. The resonances $\phi(1020)$ from K^+K^- and $K^{*0}(896)$ from $K^-\pi^+$ also show up well above background in the submass plots; comparing the $K^-\pi^+$ plot to the $K^+\pi^+$ plot shows the shape of the $K\pi$ background clearly.

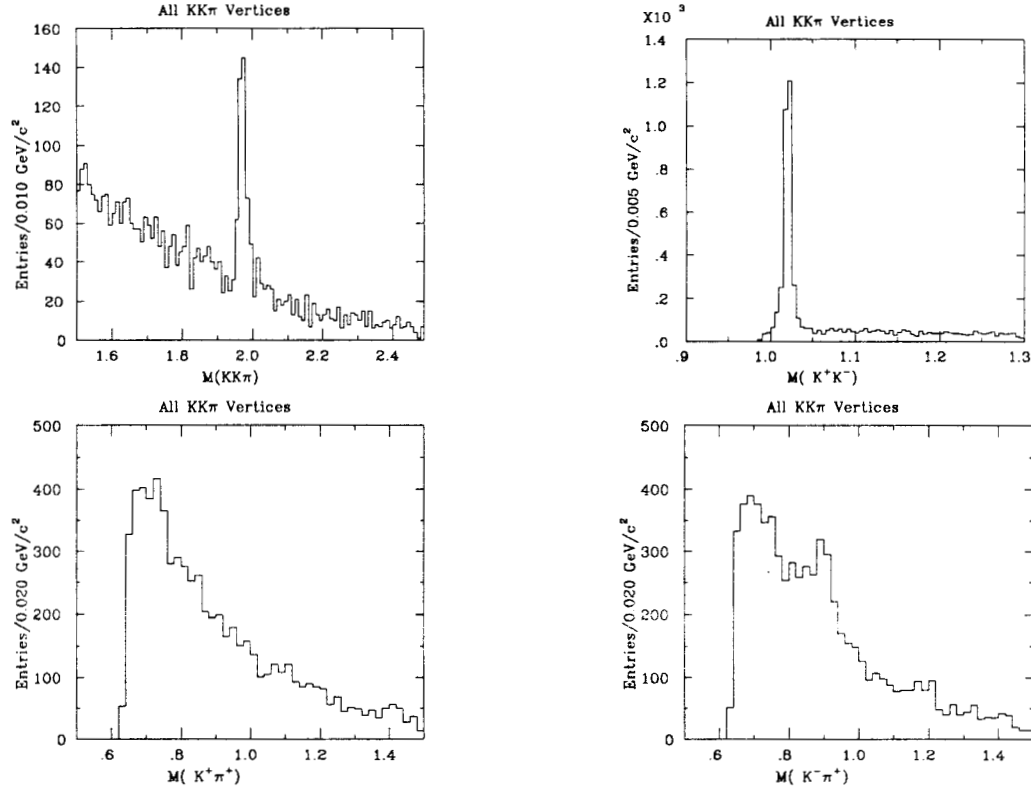


Figure 1. Mass Plots of $K^+K^-\pi^+$ Candidates.

To identify a candidate vertex as a D_s we require that its invariant mass fall within roughly 3σ of the peak value; specifically, we cut on the mass range 1935–

2000 MeV/c^2 . Using this criterion and fitting the D_s mass plot to a Gaussian peak plus a cubic background, we find a total of 504 vertices, of which 143 are estimated to be background. The efficiency for finding $D_s \rightarrow K^+ K^- \pi^+$ (after subtracting background) is 14.9%. The ratio of signal-to-background is 2.0 : 1.

Below we show the two-body invariant masses for those candidates which satisfy the D_s mass cut. A prominent $\phi(1020)$ signal as well as a prominent K^{*0} signal are visible. The two strong peaks in the $m(K^- \pi^+)$ and $m(K^+ \pi^+)$ plots are kinematic reflections of the $\phi(1020)$.

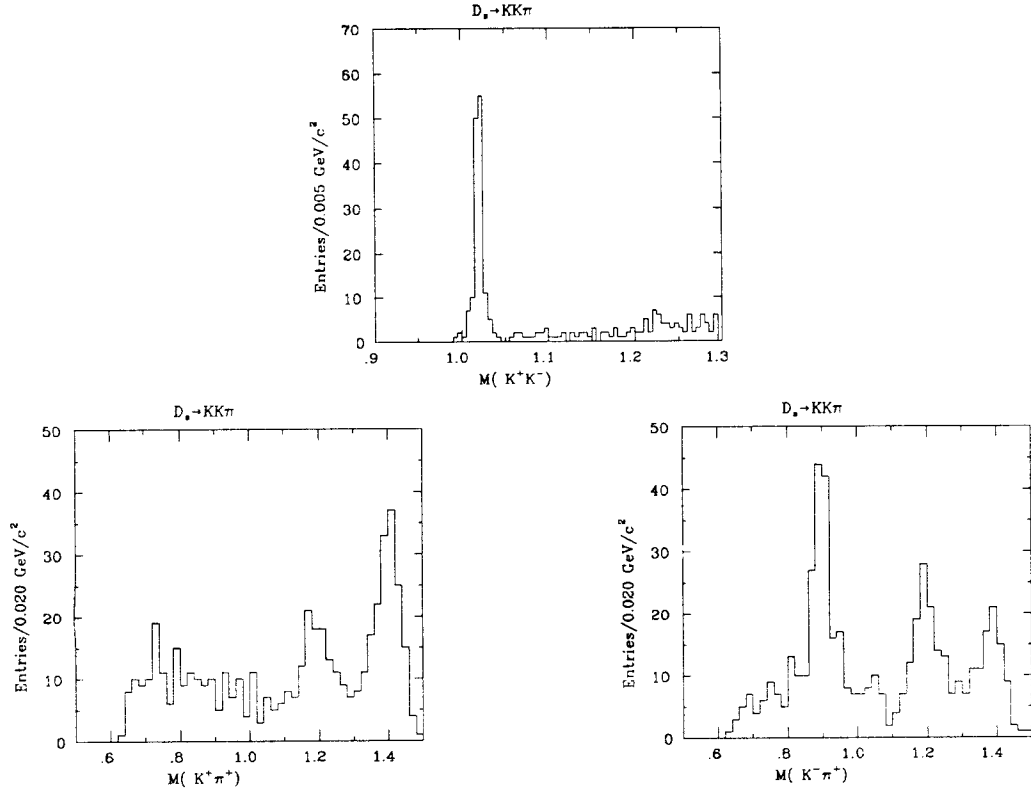


Figure 2. *Two-Body Masses of $K^+ K^- \pi^+$ Vertices (after D_s cut).*

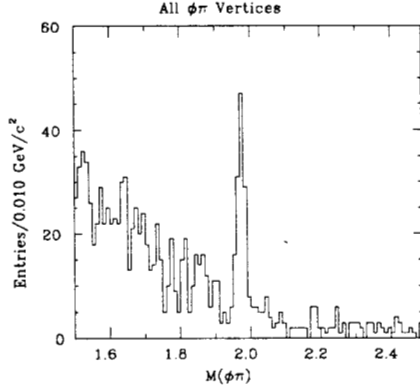


Figure 3. Mass Plot of $\phi(1020)\pi^+$ Candidates.

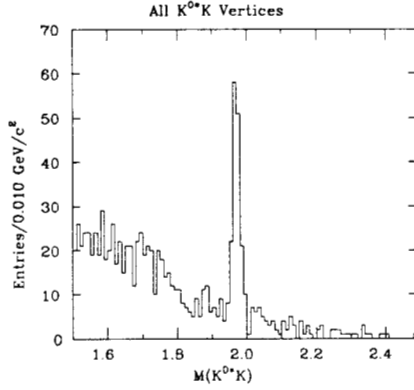


Figure 4. Mass Plot of $\bar{K}^{*0}K^+$ Candidates.

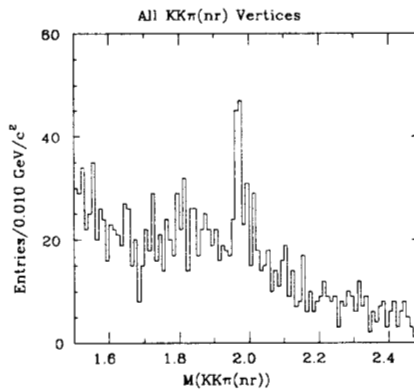


Figure 5. Mass Plot of $K^+K^-\pi^+$ Non-Resonant Candidates.

For the decay mode $D_s \rightarrow \phi\pi$, we require that the mass of the K^+K^- pair fall within the mass range of the $\phi(1020)$ shown in Table 2. The distribution of vertex masses is shown at left; the background is significantly reduced. Fitting this plot as above, we find that the efficiency for reconstructing $D_s \rightarrow \phi\pi$ (after subtracting background) is 13.5% and the ratio of signal-to-background is 4.3 : 1.

For the decay mode $D_s \rightarrow \bar{K}^{*0}K^+$ we require that the $K^-\pi^+$ mass fall within the acceptance range of the K^{*0} shown in Table 2. The distribution of vertex masses in this decay mode is shown at left; as with the $\phi\pi$ mode, the background is significantly reduced over that of all $K^+K^-\pi^+$ candidates. The fit to

this plot gives an efficiency of 13.0% and a signal-to-background ratio of 4.7 : 1.

Finally, we collect all the remaining candidate vertices, those in which neither two-body mass meets the appropriate resonance cut, into the $K^+K^-\pi^+$ Non-Resonant mode. Because this mode certainly contains candidates from the tails of resonances (especially K^{*0}) it has a somewhat higher efficiency, and a much lower signal-to-background ra-

tio that might be expected. The fit indicates that the efficiency (corrected for background) is 21.5% and the signal-to-background ratio is only 1.2 : 1. The slightly higher efficiency for the $K^+K^-\pi^+$ channel is due to two facts: first events from the tails in the $\phi\pi$ and $K^{*0}K$ channels feed into the non-resonant mode (Gaussian versus Breit-Wigner distributions); second due to kaon decays, events are lost in the two-body decays which partly end up in the non-resonant $K^+K^-\pi^+$ sample.

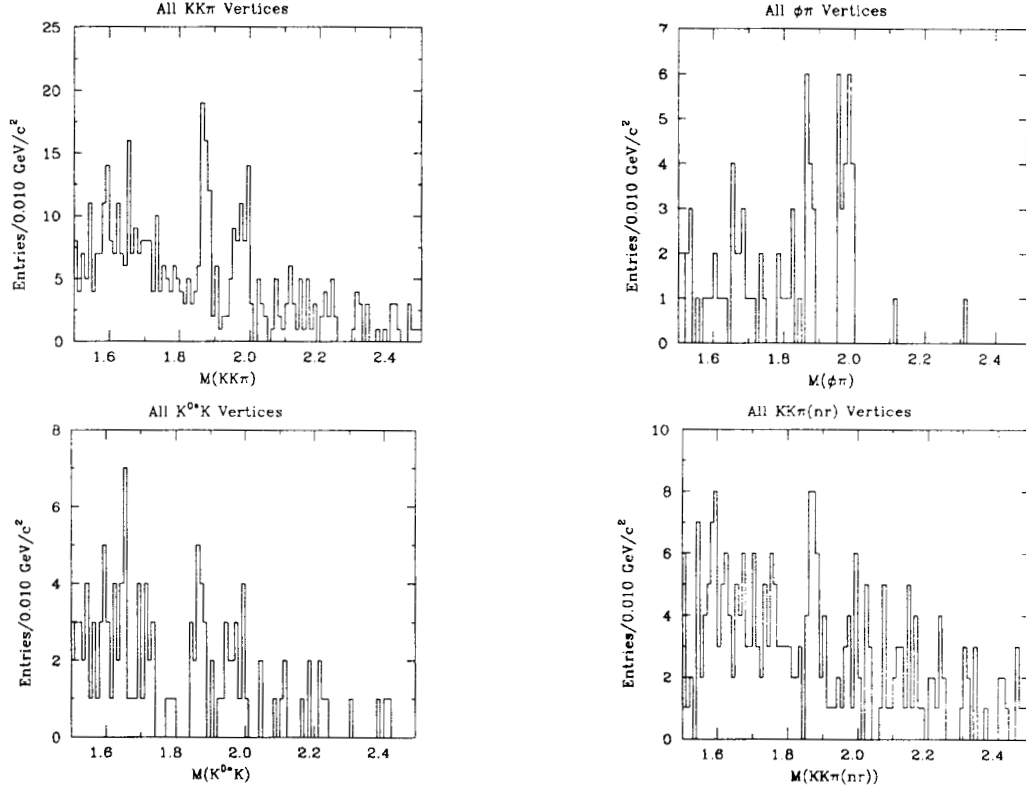


Figure 6. Mass Plots of $K^+K^-\pi^+$ From $c\bar{c}$ Events.

The first section of Table 3 summarizes our analysis of the $K^+K^-\pi^+$ final state candidates in $b\bar{b}$ events. We compute the number of *expected* vertices in each decay mode using the visible branching ratio (D_s decay fraction multiplied by *resonance* \rightarrow *final state* fraction) for that mode, as listed in Table 2. The total number of D_s mesons generated in our sample is 56,221. As noted above, we estimate the

background by fitting each mass plot with a cubic polynomial outside the D_s peak region, and integrating that polynomial over the range of the mass cut used for the D_s .

In Figure 6 we show the mass distributions for the $K^+K^-\pi^+$ final state and each of the exclusive decays we studied for our sample of 34,000 $Z^0 \rightarrow c\bar{c}$ events. In this final state, the dominant source of candidates is clearly the decay $D^+ \rightarrow K^+K^-\pi^+$, which contributes strongly in all three exclusive modes. However, the D^+ peak, at ~ 1870 MeV/ c^2 , is well outside our D_s identification cut and does not contribute to background. We find that in the $K^+K^-\pi^+$ final state from $c\bar{c}$ events, the reconstruction efficiency is roughly comparable to that for $b\bar{b}$, and the signal-to-background ratio is significantly higher, being 17.4% and 10.5 : 1 for the $\phi\pi$ mode and 8.2% and 6.5 : 1 for $\overline{K^{*0}}K$. The background analysis is summarized in the first section of Table 4.

2.2. THE $K^+\pi^+\pi^-$ FINAL STATE

In analyzing the final state $K^+\pi^+\pi^-$, we select the two exclusive two-body decay modes $K_S^0K^+$ and $K^{*0}\pi^+$. We neglect several other modes which could lead to the $K^+\pi^+\pi^-$ final state, because the branching ratios imply that less than 10 decays in each mode would be present, and with the average reconstruction efficiency we have, we would be unlikely to find any of them. The three-body mass distributions and the two-body submasses are shown in Figure 7 for all candidate vertices.

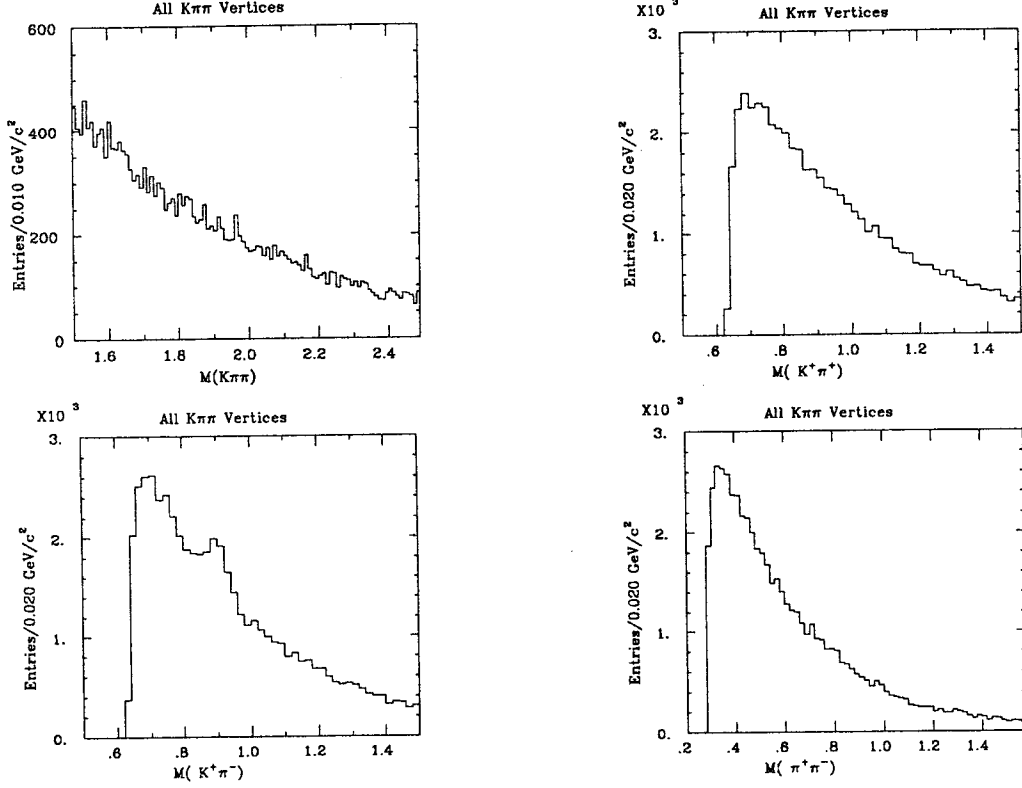


Figure 7. Mass Plots of $K^+\pi^+\pi^-$ Candidates.

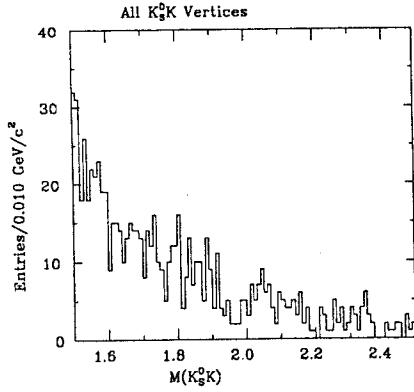


Figure 8. Mass Plot of $K_S^0 K$ ($K^+\pi^+\pi^-$) Candidates.

($R(K_S) > 5\text{cm}$). We then pair each candidate K_S^0 with every K^\pm track in the event. Requiring that the K - K_S opening angle have $|\cos\theta| > 0.5$ to help reject combinatoric background, we find 494 candidates, as shown below. Fitting this

We find a total of 518 vertices in the decay mode $K_S^0 K^+$. Of these 24 are three-prong vertices reconstructed according to the prescription described earlier, using $K^+\pi^+\pi^-$ particle identification, and are shown in Figure 8. We reconstruct the remaining vertices using a software package^[6] optimized for finding K_S^0 vertices far from the primary vertex

plot to a Gaussian plus polynomial background (as described above) we estimate that 276 of the candidates are background. Combining these plots, we find a total of 518 candidate vertices of which about 300 are background. The efficiency for the $K_S^0 K^+$ decay mode is 38.6%, and the signal-to-background ratio is 0.73 : 1.

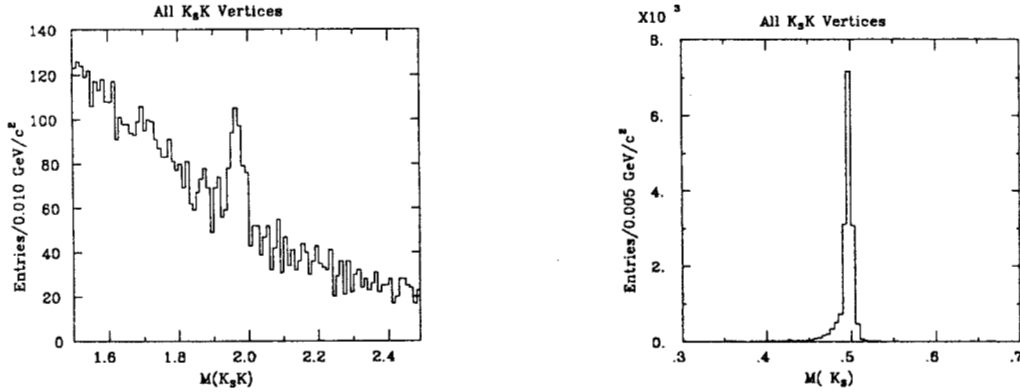


Figure 9. Mass Plots of $K_S^0 K$ (VEEFIX) Candidates.

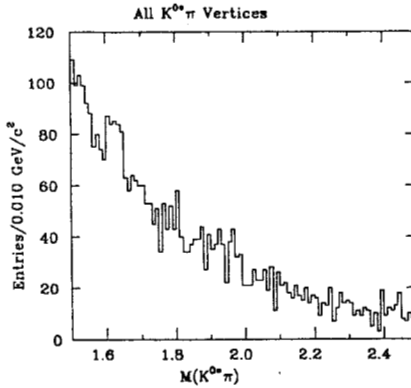


Figure 10. Mass Plot of $K^{*0} \pi^+$ Candidates.

For the decay mode $K^{*0} \pi^+$ we require that the mass of the $K^+ \pi^-$ pair fall within the acceptance range of the K^{*0} shown in Table 2. With this cut, we find a total of 204 candidate vertices (only 59 would be expected, if we had 100% efficiency and no background), of which we estimate that 164 are background

(left). This decay mode has an efficiency (after correcting for the background) of 67.8% but a signal-to-background ratio of only 0.24 : 1.

The second section of Table 3 summarizes our analysis of the $K^+ \pi^+ \pi^-$ final state, and shows that we have an overall reconstruction efficiency (including both methods of finding the $D_s \rightarrow K_S^0 K$ decay mode) of 48%, and a signal-to-background ratio of 0.23 : 1.

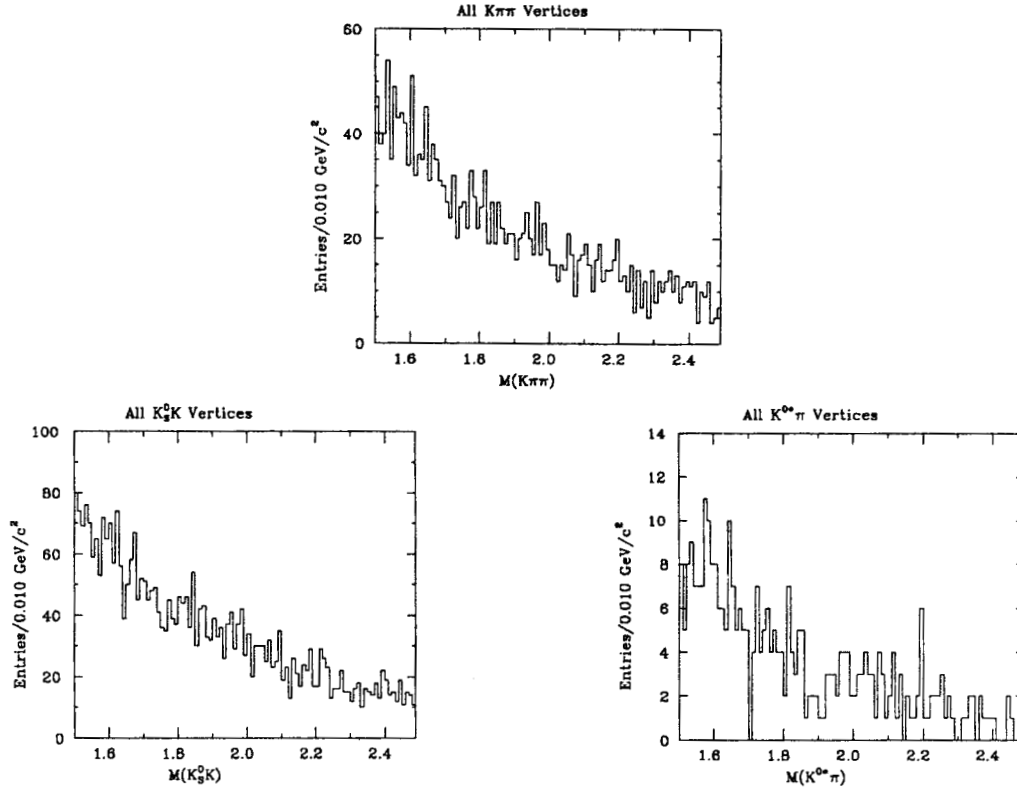


Figure 11. Mass Plots of $K^+\pi^+\pi^-$ From $c\bar{c}$ Events.

In Figure 11 we show the mass distributions for the $K^+\pi^+\pi^-$ final state and its exclusive decay modes, from our $Z^0 \rightarrow c\bar{c}$ sample. For this plot, we have added the two $K_S^0 K$ histograms to produce the single plot shown. This final state has little contribution from $c\bar{c}$ events, because of the small branching ratios for the various decay modes combined with the small production rate of D_s mesons. Neither of the exclusive modes shows any clear D_s signal. Our results for this background of the $K^+\pi^+\pi^-$ final state are summarized in the second section of Table 4.

2.3. THE $\pi^+\pi^-\pi^+$ FINAL STATE

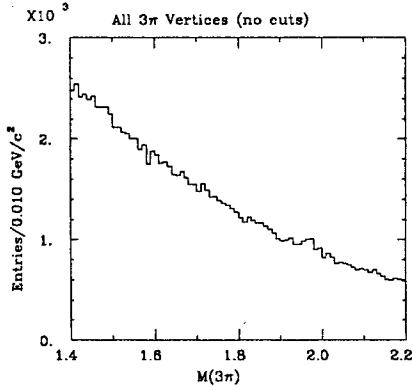


Figure 12. Mass Plot of All $\pi^+\pi^-\pi^+$ Candidates (no cuts).

Our analysis of the $\pi^+\pi^-\pi^+$ final state involves a larger event sample than for the two final states discussed previously. We analyzed 152,856 $Z^0 \rightarrow b\bar{b}$ events containing a total of 126,776 produced D_s mesons. The initial distribution of candidate $\pi^+\pi^-\pi^+$ vertex masses from this data set is shown in Figure 12. The combinatoric back-

ground which results without particle ID cuts is extreme and *must* be reduced if we are to make any use of this final state.

We expect that the major contribution to this channel is from the decay $D_s \rightarrow f_0(975)\pi^+$ whose branching ratio (in the model used) is 1.51%. The $f_0(975)$ decay to $\pi^+\pi^-$ is 78%. In order to reduce the background, both from combinatorics and from other decays, we restrict the momenta of the three pions to be greater than 2 GeV/c. This cut is included in all of the analysis (and the plots shown) below. In our analysis of the $\pi^+\pi^-\pi^+$ final state we have not looked at the non-resonant three-body decay, where background cannot be suppressed by use of the $\pi^+\pi^-$ resonance requirement.

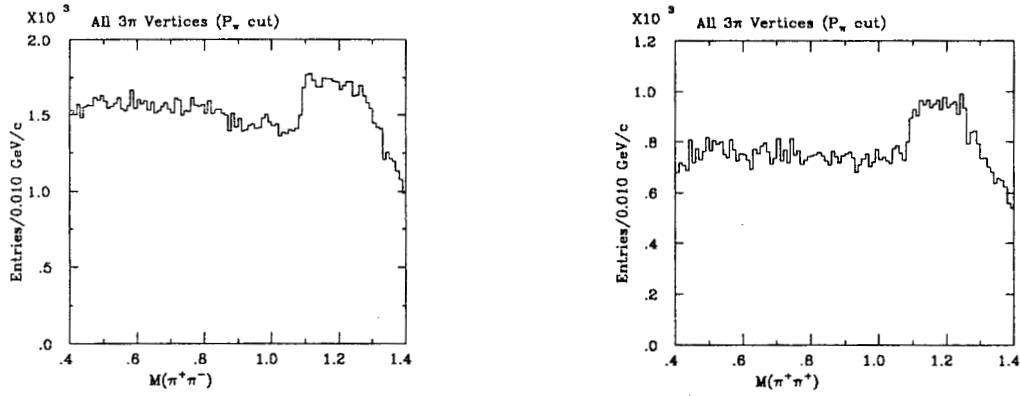


Figure 13. Mass Plots of $\pi\pi$ Pairs From $\pi^+\pi^-\pi^+$ Candidates.

After restricting the pion momenta as discussed above, the distribution of two-pion masses (both $\pi^+\pi^-$ and $\pi^+\pi^+$) from $\pi^+\pi^-\pi^+$ candidates in Figure 13 does not indicate any structure near the $f_0(975)$ peak ($0.975 \text{ GeV}/c^2$). In Figure 12 there is a slight excess in the D_s mass region (just below $2.0 \text{ GeV}/c^2$), and when we plot two-pion masses from candidates in this mass region ($1.93 \leq m(D_s) \leq 2.00 \text{ GeV}/c^2$), we find that a reasonable $f_0(975)$ signal appears around $1.0 \text{ GeV}/c^2$, as the plots below indicate (we have not studied the additional structures in these plots in any detail).

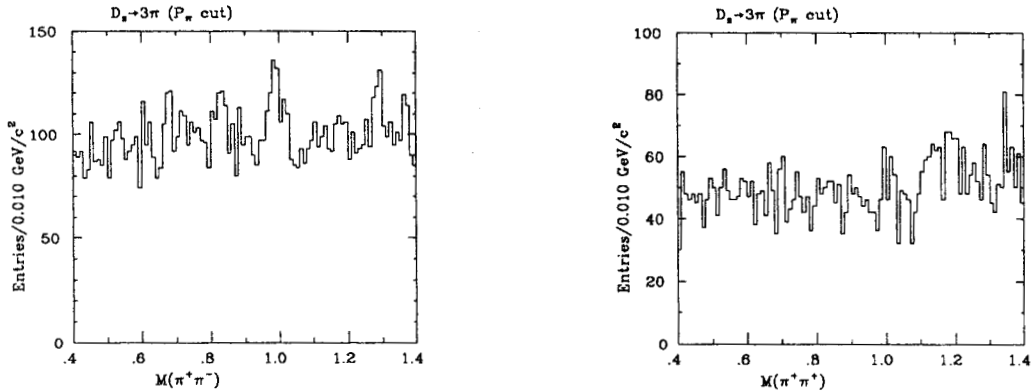


Figure 14. Mass Plots of $\pi\pi$ Pairs From $\pi^+\pi^-\pi^+$ Candidates (after P_π and D_s cut).

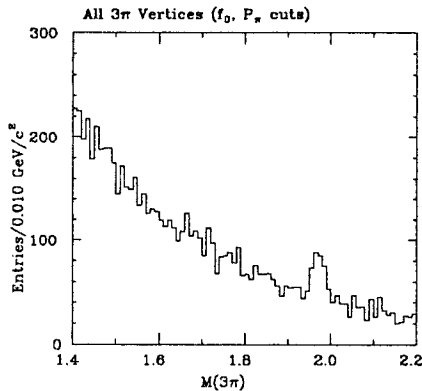


Figure 15. Mass Plot of $\pi^+\pi^-\pi^+$ Candidates ($f_0(975)$ ID, $|p_\pi| > 2$ GeV/c).

pion momentum are shown in Figure 15. A D_s signal is now clearly visible, and the background has been significantly reduced. Using the same fit as before (Gaussian peak plus polynomial background) we find that the D_s mass in this final state is 1972.0 ± 2.2 MeV/ c^2 , and the width of the peak is 31.9 ± 5.1 MeV/ c^2 . The reconstruction efficiency is 14.4%, and the signal-to-background ratio is 0.48 : 1. The third section of Table 3 summarizes our analysis of the $\pi^+\pi^-\pi^+$ final state candidates in $b\bar{b}$ events.

2.4. SUMMARY OF D_s RECONSTRUCTION STATISTICS

Table 3 summarizes our results on D_s exclusive decay modes in the all charged hadronic decay modes $K^+K^-\pi^+$, $K^+\pi^+\pi^-$, and $\pi^+\pi^-\pi^+$ for the $Z^0 \rightarrow b\bar{b}$ Monte Carlo sample. Table 4 shows our preliminary results of $Z^0 \rightarrow c\bar{c}$ background, which has only been performed in $K^+K^-\pi^+$. The number of vertices expected in each mode are computed using the known number of D_s mesons produced in the Monte Carlo sample and the net branching ratio to produce the final state from that mode. Background is estimated in each mode and for the total final state by fitting the vertex mass plots with a cubic polynomial plus a Gaussian centered on the D_s mass. For this fit, the mass region of the D^+ meson is excluded to minimize distortions of the background polynomial. Besides the reconstruction efficiencies we also quote the tagging efficiencies for each individual mode as well as for the

By fitting a Gaussian to the presumed $f_0(975)$ peak in the $\pi^+\pi^-$ mass plot, we find a mass of 999.6 ± 2.5 MeV/ c^2 and a width of 20.2 ± 2.4 MeV/ c^2 . As Table 2 indicates, we identify an f_0 candidate by restricting the $\pi^+\pi^-$ mass to the region 940–1060 MeV/ c^2 . The masses of $\pi^+\pi^-\pi^+$ candidates using both f_0 identification and restricting the

entire final state. The signal-to-background ratio for each decay mode and the significance of the signal, are shown in the last two columns of each table. and $K^+\pi^+\pi^-$ final states.

Table 3. Reconstruction of D_s Decay Modes.

Decay Mode $D_s^+ \rightarrow$	Expected Vertices	Observed Vertices	Estimated Background	Signal (Obs-Bkg)	Efficiency (ϵ) [%]	$\epsilon \cdot B$ [%]	$\frac{\text{Signal}}{\text{Bkg}}$	Significance (Sig/ $\sqrt{\text{Bkg}}$)
$\star K^+ K^- \pi^+$ $m(D_s) = 1971.5 \pm 0.9 \text{ MeV}/c^2$, $\sigma = 24.5 \pm 2.0 \text{ MeV}/c^2$								
$\phi(1020)\pi^+$	831	138	26	112	13.5	0.200	4.31	21.97
$\overline{K}^{*0} K^+$	1088	171	30	141	13.0	0.252	4.70	25.74
$(K^+ K^- \pi^+)_{NR}$	502	195	87	108	21.5	0.191	1.24	11.58
All $K^+ K^- \pi^+$	2421	504	143	361	14.9	0.644	2.52	30.19
$\star K^+ \pi^+ \pi^-$ $m(D_s) = 1968.0 \pm 2.1 \text{ MeV}/c^2$, $\sigma = 36.9 \pm 5.0 \text{ MeV}/c^2$								
$K_S^0 K$	565	518	300	218	38.6	0.390	0.73	12.59
$K^{*0} \pi^+$	59	204	164	40	67.8	0.075	0.24	3.12
All $K^+ \pi^+ \pi^-$	624	722	464	258	41.3	0.465	0.56	11.98
$\dagger \pi^+ \pi^- \pi^+$ $m(D_s) = 1972.0 \pm 2.2 \text{ MeV}/c^2$, $\sigma = 31.9 \pm 5.1 \text{ MeV}/c^2$								
$f_0(975)\pi^+$	1002	447	303	144	14.4	0.114	0.48	8.27
All $\pi^+ \pi^- \pi^+$	1002	447	303	144	14.4	0.114	0.48	8.27

\star Sample contains 67,870 $Z^0 \rightarrow b\bar{b}$ events, 56,221 D_s mesons.

\dagger Sample contains 152,856 $Z^0 \rightarrow b\bar{b}$ events, 126,776 D_s mesons.

• The summed tagging efficiency $\sum \epsilon_i \cdot B_i$ is 1.2%.

Table 4. Background From $c\bar{c} \rightarrow D_s X$.

Decay Mode $D_s^+ \rightarrow$	Expected Vertices	Observed Vertices	Estimated Background	Signal (Obs-Bkg)	Efficiency (ϵ) [%]	Signal Bkg	Significance (Sig/ $\sqrt{\text{Bkg}}$)
$\star K^+ K^- \pi^+$ $m(D_s) = 1974.6 \pm 4.5 \text{ MeV}/c^2$, FWHM = $34.5 \pm 9.6 \text{ MeV}/c^2$							
$\phi(1020)\pi^+$	121	23	2	21	17.4	10.50	14.84
$\overline{K}^{*0} K^+$	159	15	2	13	8.2	6.50	9.19
$(K^+ K^- \pi^+)_{NR}$	73	18	18	0	—	—	—
All $K^+ K^- \pi^+$	353	56	22	34	9.6	1.50	7.25
$\star K^+ \pi^+ \pi^-$ $m(D_s) = 1946.3 \pm 15.1 \text{ MeV}/c^2$, FWHM = $68.8 \pm 12.3 \text{ MeV}/c^2$							
$K_S^0 K$	82	184	143	41	50.0	0.29	3.43
$K^{*0} \pi^+$	8	19	13	6	75.0	0.46	1.38
All $K^+ \pi^+ \pi^-$	90	203	156	47	52.2	0.30	3.76

\star Sample contains 33,942 $Z^0 \rightarrow c\bar{c}$ events, 8,228 D_s mesons.

3. Conclusions and Outlook

In this report we have discussed the reconstruction of D_s mesons in the all-charged hadronic final states $K^+ K^- \pi^+$, $K^+ \pi^+ \pi^-$, and $\pi^+ \pi^- \pi^+$, using a sample of 68,000 $Z^0 \rightarrow b\bar{b}$ Monte Carlo events for the first two topologies and 153,000 events for the third. In particular, we have determined reconstruction efficiencies, tagging efficiencies ($\epsilon \cdot B$), and signal-to-background ratios for the exclusive two-body decay modes $\phi\pi$, $K^{*0}K$, K^0K , and $f_0\pi$ as summarized in Table 3.

The $K^+ K^- \pi^+$ final state is best suited to tag D_s mesons. Even though the reconstruction efficiency (14%) is lower than for $K^+ \pi^+ \pi^-$ (41%), which is mainly a consequence of requiring two identified kaons ($\sim 50\%$) and tight selection criteria on the three-prong vertex, our analysis yields the largest value for $\epsilon \cdot B$ (0.64%) and the highest signal-to-background ratio in this final state. In particular, for the

two-body decays $\phi\pi$ and $K^{*0}K$ the background levels are rather small. This, in turn, will help to minimize the number of falsely reconstructed B_s mesons.

For the $K^+\pi^+\pi^-$ final state the highest reconstruction efficiency (41%) is obtained, which compared to $K^+K^-\pi^+$, is due to two facts: first, this final state contains only one kaon which enhances the efficiency by a factor of ~ 1.5 ; second, this final state consists of two consecutive two-particle vertices which are reconstructed with high efficiencies, thus gaining another factor of ~ 1.5 . However, the resulting tagging efficiencies (0.47%) are lower than for the $K^+K^-\pi^+$ final state; in addition, the background levels are considerably higher.

The three-pion final state is the least promising channel: high combinatoric background greatly suppresses the signal, and the low resolution of the $f_0(975)$ makes it difficult to separate the background. The efficiency for the $f_0(975)\pi$ channel (14%) is comparable to the value for $K^+K^-\pi^+$, but without the f_0 mass cut, a D_s peak is barely observable. The tagging efficiency is only 0.11%.

Our analysis clearly shows that ideally one would like to use the $K^+K^-\pi^+$ final states for D_s tagging. However, for B_s selection this will be not sufficient because of a small B_s production cross section in Z^0 decays, small B_s decay branching fractions, and the low value of $\epsilon \cdot B$ for the $K^+K^-\pi^+$ final state. Even a combination of the three final states discussed above, which yield $\sum \epsilon_i B_i \sim 1.2\%$, will not suffice to do the job: a sample of 10^6 Z^0 's contains approximately 140K $b\bar{b}$ decays, which in turn would produce ~ 40 K B_s or \bar{B}_s events if both a B_s and a \bar{B}_s were always produced (if decays patterns such as $B_s B^- K^+$ dominate, the number of produced B_s events is closer to 20K); assuming a branching fraction of $B(B_s \rightarrow D_s X) \sim 80\%$ we would optimistically obtain 32K D_s mesons, of which only ~ 380 could be reconstructed in the three final states. Since the predicted branching fractions for exclusive B_s decays are at the few percent level, only a handful of events can be expected in any exclusive B_s decay mode. Therefore it is absolutely necessary to increase the D_s tag sample significantly, which requires an improved three-prong vertex reconstruction for the all charged decay modes as well as studies of further

decay modes containing π^0 's and η 's, as e.g. $K^{*+}K_S^0$, $\eta\pi$, and $\eta'\pi$.

Another important issue concerns the background sources feeding into the tag sample. Backgrounds originating from $b\bar{b}$ events are included in our analysis (see Table 3). To estimate the contribution from $c\bar{c}$ events, the $K^+K^-\pi^+$ and $K^+\pi^+\pi^-$ final states have been analyzed, using 34,000 $Z^0 \rightarrow c\bar{c}$ Monte Carlo events. The background resulting from this sample is only slightly higher than that from $b\bar{b}$ events. This is due to a requirement that the secondary vertex is at least 500 μm separated from the interaction point. By requiring both a secondary (B_s) and tertiary (D_s) vertex we expect to considerably reduce the $c\bar{c}$ background, although we have not performed a detailed study, nor have we studied the background contributions from u , d , or s jets. However, we expect that the 500 μm cut and requirements on secondary and tertiary vertices will reduce these background sources considerably.

The analysis discussed is the first step in studying B_s decays. However, many more studies are needed to complete the job. The next steps will consist of:

- detailed background studies from u , d , s , decays as well as $c\bar{c}$ events for all final states;
- analyses of final states containing neutrals, such as π^0 's, η 's and K_L^0 's;
- reconstructions of B_s mesons by pairing D_s candidates with separate π^\pm tracks and π^0 's;

In the long run we also plan to study other B_s decay modes such as semileptonic decays and $B_s \rightarrow \psi X$.

ACKNOWLEDGEMENTS

We would like to thank David Hitlin, Bill Wisniewski, and Mike Witherell for several fruitful discussions of our analysis and for their constructive criticism in revising the manuscript for this paper.

REFERENCES

1. M. Bauer, B. Stech, and M. Wirbel, *Z. Phys. C* **29** (1985), 637
2. M. Bauer, B. Stech, and M. Wirbel, *Z. Phys. C* **34** (1987), 103
3. M. Savage and M. Wise, *Phys. Rev. D* **39** (1989), 3346
4. T. Sjöstrand and M. Bengtsson, *Comput. Phys. Commun.* **43** (1987), 367
5. J. Labs, *NHDK Heavy Meson Decay Package* (1989)
6. G. Gladding, *VEEFIX K_S and Λ Finder* (1989)

Particle identification with the CRID

Kirkwood, August 3rd 1989

by Pierre Antilogus.

We present here the kind of particle identification that you can obtain using the CRID.

We underline also the basic points that the user has to know if he wants to reproduce these results with the CRID MonteCarlo [‡].

[‡] *from a work done inside the CRID pre-Kirkwood group by:*

Pierre Antilogus, Sridhara Dasu, Dave Muller.

1. Outline of the Slow and the Fast CRID MonteCarlo.

1.1. THE SLOW MONTECARLO.

The Slow CRID MonteCarlo produces a full simulation of the Cherenkov photons and performs the reconstruction of the Cherenkov rings.

Detector simulation: The simulation of the CRID detector ^[1] can be divided into the following steps :

- (a) Cherenkov photons are generated along the path of each charged track which goes through the liquid and/or the gas radiators (cf fig. 1).
- (b) All the Cherenkov photons are tracked. In this way the full geometry of the detector is taken into account (cf fig. 1).

- (c) The point of production of each photo-electron is calculated (cf fig. 2).
- (d) The electrons are smeared from their production point to the TPC wire plane (cf fig. 2).
- (e) As an option, the digitization of the signal (electronic noise , pulse de-convolution...) is simulated.

At the end of this simulation we have a reconstructed production point for each photo-electron (Raw Data X,Y,Z).

Event reconstruction. The main ideas of the reconstruction are :

- (a) By using the informations from the drift chamber, each track is extrapolated into the CRID.
- (b) For each photo-electron a Cherenkov angle is calculated.
- (c) A likelihood is calculated [2] for each hypothesis (e, μ, π, K, p) using the Cherenkov angles.

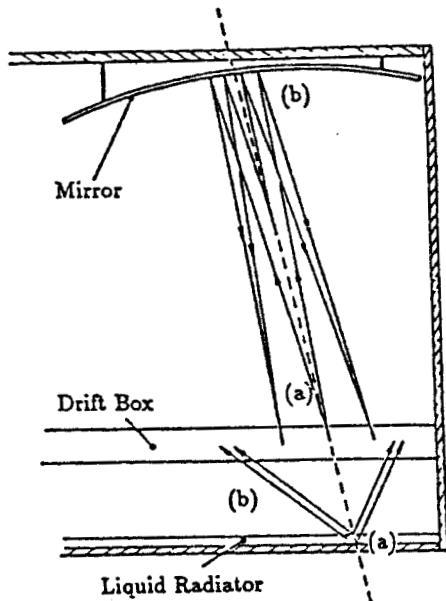


Figure 1: Production by a charged track of the Cherenkov photons inside the CRID (cf text).

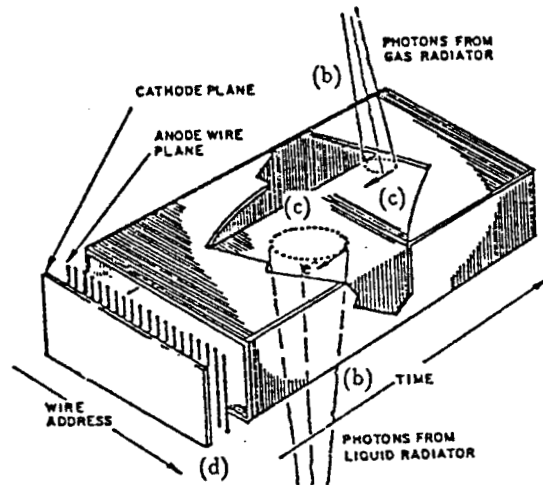


Figure 2: Production and detection of the photo-electrons (cf text).

1.2. THE FAST MONTECARLO.

The Fast CRID MonteCarlo uses a simplified simulation and reconstruction of CRID events:

- (a) As for the Slow MonteCarlo, the number of Cherenkov photons expected ($n_{\gamma exp}$) and the Cherenkov angle expected ($\theta_{\gamma exp}$) are calculated for each charged track.
- (b) $n_{\gamma exp}$ is corrected to take into account the geometrical effects.
- (c) To take into account the problems due to the overlap of the gas Cherenkov rings, the region of intersection of two rings is ignored (=reduction of $n_{\gamma exp}$, this version ^[3] is not in production yet).
- (d) From $n_{\gamma exp}$ and $\theta_{\gamma exp}$, the observed quantities are generated :
 - (i) Poisson distribution ($n_{\gamma exp}$) $\rightarrow n_\gamma$
 - (ii) Gaussian distribution ($\sigma, \theta_{\gamma exp}$) $\rightarrow \theta_\gamma^i$ for $i = 1 \rightarrow n_\gamma$.
- (e) The likelihoods are calculated with these θ_γ^i and the $\theta_{\gamma exp}^0$ of the extrapolated track from the drift chamber for the five hypotheses (e, μ, π, K, p).

Using this method (which supresses for example the tracking of each Cherenkov photon), the Fast MC is faster by a factor ~ 15 than the Slow MC.

2. What the User has to know.

2.1. A FEW NUMBERS.

To understand the variation of the CRID information as a function of the momentum for a given particle, you have to know the different Cherenkov thresholds.

	μ	π	K	p	
Liquid	0.1	0.2	0.6	1.2	GeV
Gas	1.8	2.4	8.4	16.0	GeV

2.2. THE PHCRID BANK.

The CRID information can be found in the PHCRID bank. This bank exist for each track seen by the CRID (if the track is not seen, the bank doesn't exist → check for a 0 pointer !). Sometimes the analysis of the track can't be done (e.g ,a geometrical reason) , in this case the content of the PHCRID bank must not to be used ! This situation is flagged by the return code PHCRID%RC , if this return code is negative , DON'T use the content of the PHCRID bank.

The useful information for the particle identification can be found in PHCRID%LLIK ($= \log(\text{likelihood})$) for the five hypotheses (e, μ, π, K, p). Those numbers are the combined information from the liquid and the gas radiators. In the next chapter you can find out how to use this information for the particle identification.

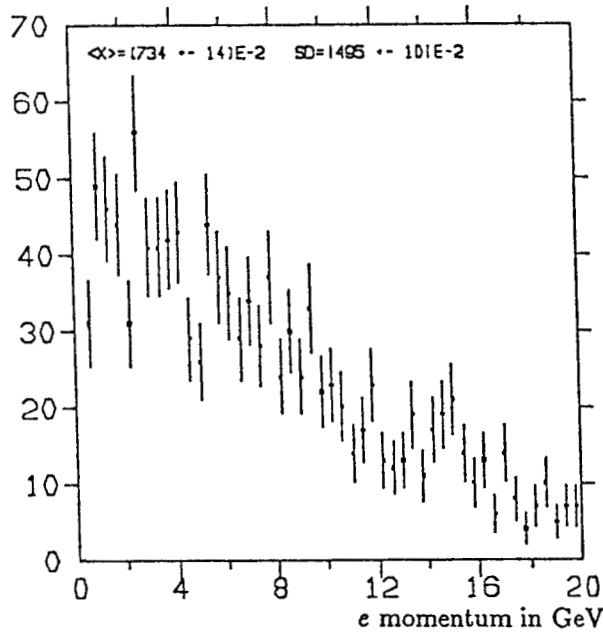


Figure 3: Momentum distribution of electrons produced by the process $B \rightarrow e + \nu + D$.

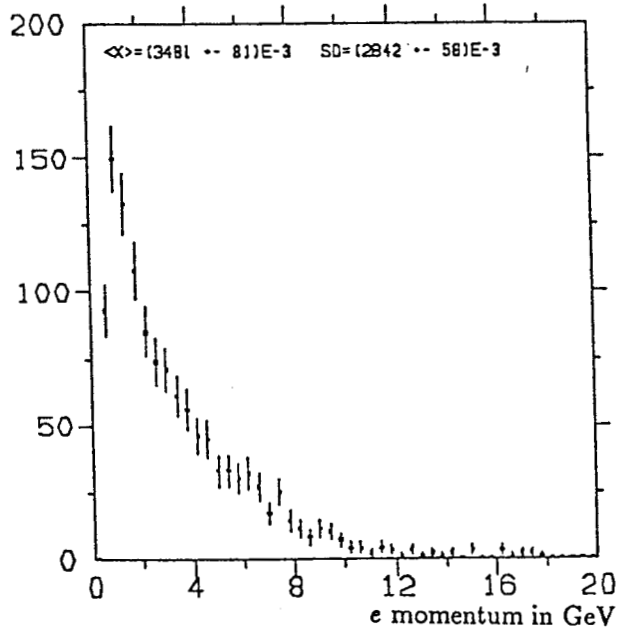


Figure 4: Momentum distribution of electrons produced by the process $B \rightarrow D \rightarrow e + X$.

3. Particle ID with the CRID .

3.1. AN EXAMPLE : e/π SEPARATION.

Lund events : In $b\bar{b}$ events, the leptons can be used both to separate the b and c quarks and to give the sign of the quark which has produced this lepton. In such a study, electron identification is fundamental. The momentum spectrum of the electrons in $b\bar{b}$ events show that for

$$B \rightarrow e + \nu + D$$

$\sim 40\%$ of the electrons have a momentum lower than 5 GeV (cf fig. 3) and for

$$B \rightarrow D \rightarrow e + X$$

$\sim 80\%$ of the electrons have a momentum lower than 5 GeV (cf fig. 4).

As you will see in figure 7 the CRID in this momentum region has good e/π separation.

Study of $\log(\text{likelihood}_\pi) - \log(\text{likelihood}_e)$: After those physical motivations, we give here more detail on the identification itself.

For the study of the e/π separation with the CRID, we have generated 10000 single e^- and 10000 single π^- with the Fast MonteCarlo in the barrel in the momentum range 0.4 GeV to 10 GeV.

The probability to be an electron, for a given track, is proportional to likelihood_e and the probability to be a π is proportionnal to likelihood_π . Therefore the difference $\log(\text{likelihood}_\pi) - \log(\text{likelihood}_e)$ (cf fig. 5) is simply the logarithm of the ratio of those probabilities. In fact, due to some non Gaussian error in the Cherenkov angle measurement, this is only true in first approximation.

The way to perform the e/π separation, is to make a cut on $\log(\text{likelihood}_\pi) - \log(\text{likelihood}_e)$. This cut has to suppress the common events between the $\log(\text{likelihood}_\pi) - \log(\text{likelihood}_e)$ distributions for e generated and the $\log(\text{likelihood}_\pi) - \log(\text{likelihood}_e)$ distributions for π generated (cf fig. 5).

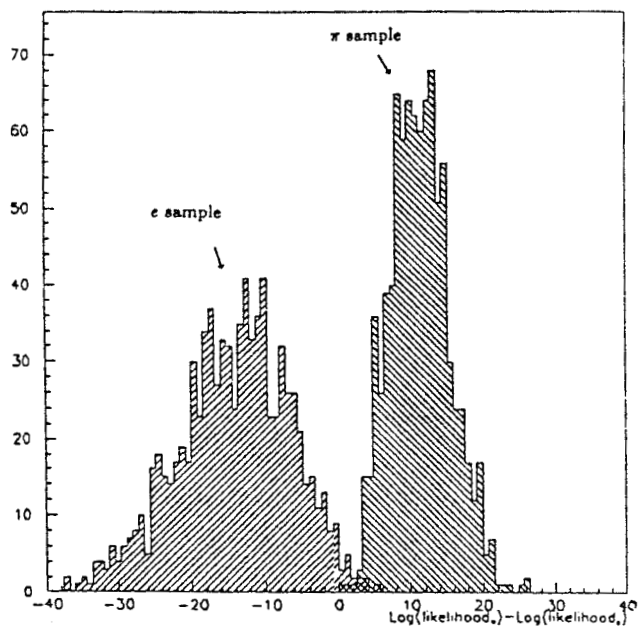


Figure 5: $\log(\text{likelihood}_\pi) - \log(\text{likelihood}_e)$ distribution for $3 \text{ GeV} \leq P \leq 4 \text{ GeV}$. For this momentum the sample of e and the sample of π are clearly separated.

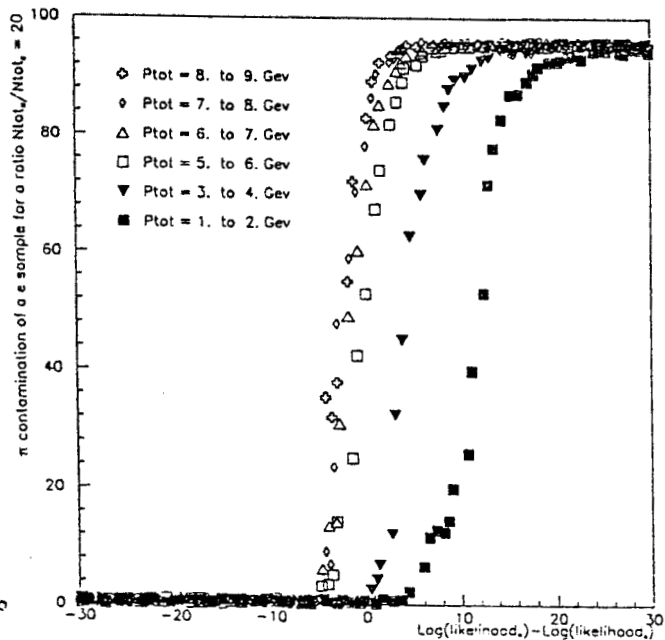


Figure 6: The π contamination in % of a sample of e as a function of the cut on $\log(\text{likelihood}_\pi) - \log(\text{likelihood}_e)$. To give a realistic meaning to this contamination we have taken a sample of π 20 time larger than the sample of e (contamination = number of π / (number of e + number of π)).

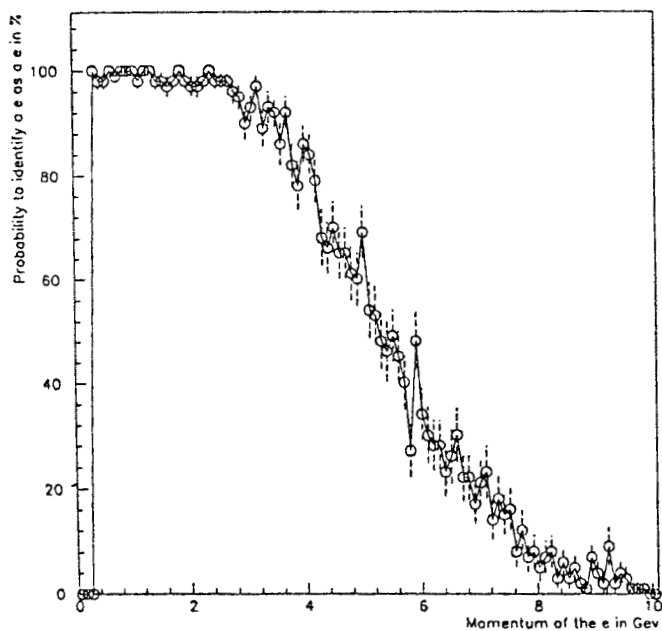


Figure 7: Probability to identify an e as an e as a function of the momentum. We test only the e/π hypothesis with the cut : $\log(\text{likelihood}_\pi) - \log(\text{likelihood}_e) \leq -5$.

Cut on $\log(\text{likelihood}_\pi) - \log(\text{likelihood}_e)$: In figure 6 you can see that if you ask for

$$\log(\text{likelihood}_\pi) - \log(\text{likelihood}_e) \leq -5.$$

you reduce the contamination of a e sample by π to practically zero .

As figure 6 shows, for higher values of $\log(\text{likelihood}_\pi) - \log(\text{likelihood}_e)$, the contamination increases quickly . In the region of quick variation, estimation of the π contamination is difficult . It is better to do a "clear" cut on $\log(\text{likelihood}_\pi) - \log(\text{likelihood}_e)$.

This remark is related in fact to one of the interesting proprieties of the particle identification with the CRID : when you are able to do an identification, it is in general related to a strong rejection of the contamination .

Conclusion : With the cut $\log(\text{likelihood}_\pi) - \log(\text{likelihood}_e) \leq -5.$, we obtain for the electron identification with the Fast MC (cf fig. 7) :

- (a) below 3 Gev a full efficiency,
- (b) at 5 GeV an efficiency ~ 50 %,
- (c) on 10000 π with $P \leq 10$ GeV , only one is identified as an electron.

Since the the LAC e/π separation becomes efficient at around 3 Gev, SLD will be able to perform e/π separation for the full electron spectrum.

3.2. μ, π, K, p IDENTIFICATION

We present here the separation obtained between different hypotheses using the CRID. To obtain these curves, we have generated 10000 single track events in the barrel for each kind of particle, using the Fast MonteCarlo.

μ/π separation : The CRID can contribute to the identification of low momentum μ . As you can see in figure 8 , we can perform the μ identification using the same cut,

$$\log(\text{likelihood}_\pi) - \log(\text{likelihood}_\mu) \leq -5.,$$

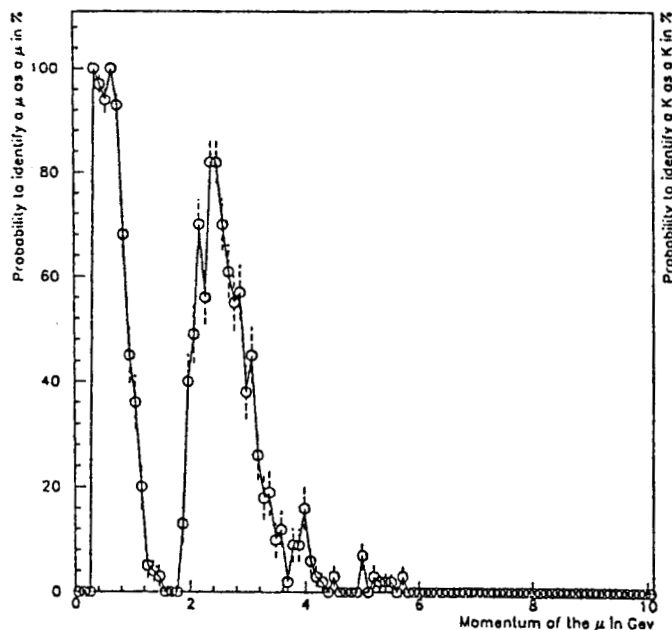


Figure 8: Probability to identify a μ as a μ as a function of the momentum. We test only the μ/π hypothesis with the cut $\log(\text{likelihood}_\pi) - \log(\text{likelihood}_\mu) \leq -5$.

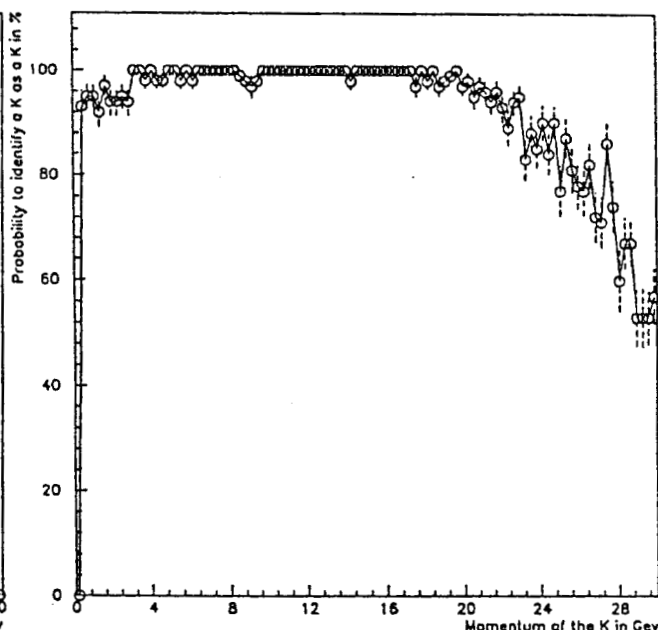


Figure 9: Probability to identify a K as a K as a function of the momentum. We test only the K/π hypothesis with the cut : $\log(\text{likelihood}_\pi) - \log(\text{likelihood}_K) \leq -5$.

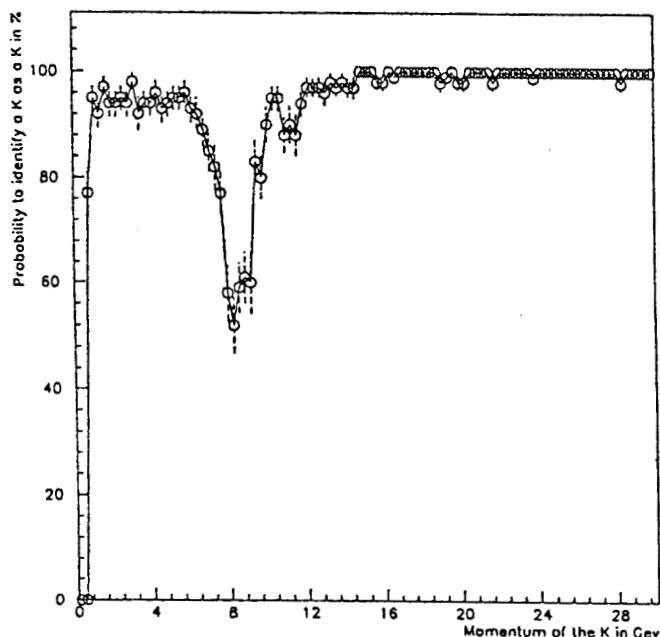


Figure 10: Probability to identify a K as a K as a function of the momentum. We test only the K/p hypothesis with the cut : $\log(\text{likelihood}_p) - \log(\text{likelihood}_K) \leq -5$.

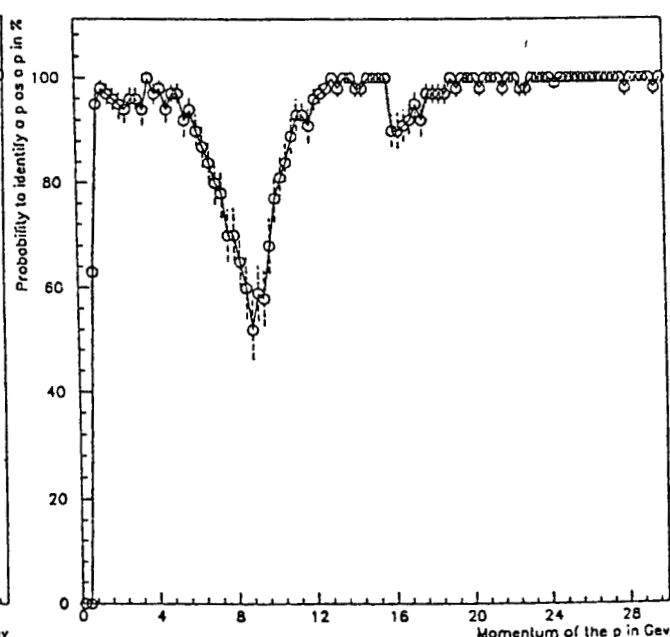


Figure 11: Probability to identify a p as a p as a function of the momentum. We test only the p/K hypothesis with the cut : $\log(\text{likelihood}_K) - \log(\text{likelihood}_p) \leq -5$.

with an efficiency higher than 50% below 1.4 GeV using the liquid radiators and between 2.2 and 3. GeV using the gas radiators. In those region the pion contamination stays at a low level ($\sim 10^{-3}$). This CRID contribution can complete the WIC information wich becomes fully efficient for tracks with a $P_{\perp} > 2$ GeV in the barrel.

π/K separation : One of the nicest possibilities of the CRID is its capacity to perform the K identification. In figure 9 you can see that the π/K separation is fully efficient below 20 GeV and stays higher than 50% up to 30 GeV. For 10000 π generated between .4 and 30 GeV only one has been identified as a K .

K/p separation : To perform the K identification we have to add the K/p separation. As you can see in figure 10 this separation works to a high momentum, in fact the efficiency decreases to 50% only around 50 GeV. But for this separation and in the p/K separation as well (cf figure 11) you can observe a hole in the efficiency around 8 GeV due to a non complete overlap between the liquid and the gas identification. On the other hand, the efficiency in this region stays higher than 50%.

4. Conclusion.

The CRID MonteCarlo continues to be under developement, but we are actually testing the "secondary type effect", which means that the MonteCarlo already produces realistic outputs.

We have presented here the status of what kind of particle identification you can obtain using the Fast CRID MonteCarlo. It's clear that it's not enough to take the best CRID hypothesis (actual content of the PHPART bank), you have to perform a cut on the probability connected to this hypothesis to really use the CRID identification.

We have underlined here the CRID contribution to the electron identification. The CRID has for the e/π separation an efficiency higher than 50% below 5 GeV

with an extremely low contamination specific to all CRID identification ($\leq 10^{-3}$).

Using the different contributions to the e, μ, π separations, the SLD detector has an unique possibility to perform the e identification in the full momentum range.

REFERENCES

1. D.Aston, CRID Simulation Walkthrough , Analysis and Techniques August 11th 1989.
2. S.Yellin, CRID hypothesis testing , Analysis and Techniques October 7th 1988.
3. A.Bukin, Improvement of the CRID Fast MC, Analysis and Techniques May 5th 1989.

CALCULATION OF TRACK-ERROR MATRICES FOR THE SLD FAST MONTE CARLO

Jeffrey D. Richman and Laurent Mathys

Department of Physics

University of California

Santa Barbara, CA 93106

1. Introduction

The SLD physics program relies heavily on the charged-particle tracking information that will be provided by the CCD Vertex Detector. The tracks used to find vertices will each have two or three vertex-detector hits; these will be linked with the corresponding central-drift-chamber track, and the information will then be combined in an overall fit. To use the resulting information, it is essential to know both the uncertainties ("errors") in all track parameters and the correlations between these errors. For example, large impact-parameter tracks are best tagged using b/σ_b , where the impact-parameter error σ_b is calculated from the error matrix of the track parameters.

The track-error matrices are normally computed during the combined vertex-detector and central-drift-chamber track fit. In the fast Monte Carlo, however, a short cut is taken: track parameters and their error matrices are simulated directly from the generated four-vectors. That is, without generating any raw data or performing any track fits, we must compute the error matrix and fluctuate the track parameters so that they reflect the errors and correlations contained in the error matrix. The error matrix must include all multiple-scattering contributions and correlations induced by different types of measurements, such as those from stereo-angle wires.

We have written new software to compute the error matrices as a function of track angle and momentum. The following sections briefly describe the algorithm and various tests that we have performed. It should be emphasized that these programs are quite general and can be used to compute error matrices for most collider tracking systems given a description of the detector.

2. Definition of the Track-Error Matrix

The track-error matrix is defined by

$$V_{\mu\nu} [\vec{\alpha} (R_{ref})] = \langle (\alpha_\mu - \langle \alpha_\mu \rangle) (\alpha_\nu - \langle \alpha_\nu \rangle) \rangle \quad , \quad (1)$$

where $\alpha_\mu(R_{ref})$, $\mu = 1, \dots, 5$ are the helix parameters. In SLD the convention is to specify the set $\vec{\alpha} = \left\{ \phi_x, z, \phi_p, \lambda, \frac{Q}{p_t} \right\}$ on a reference cylinder of radius R_{ref} in the xy plane. The azimuthal angles ϕ_x and ϕ_p are the angles between the x -axis and the xy projections of \vec{r} and \vec{p} at the point where the track intersects the reference cylinder. The dip angle λ is measured with respect to the xy plane, so that $\tan \lambda = p_z/p_t$. The charge of the particle in the last helix parameter, Q/p_t , has the effect that none of the error matrix elements change sign when Q does.

3. Calculation of the Track-Error Matrix

The main idea for the error-matrix computation comes from P. Billoir[1]. Suppose that measurements are performed at radii r_1, \dots, r_n , and consider first the subset of measurements at radii r_i, \dots, r_n . This subset of measurements leads to an inverse error matrix, or weight matrix, on the helix parameters at radius r_i , which we temporarily assume is known. We use the notation

$$W_{\mu\nu} [\vec{\alpha}(r_i)|r_i, \dots, r_n] \equiv V_{\mu\nu}^{-1} [\vec{\alpha}(r_i)|r_i, \dots, r_n] \quad , \quad (2)$$

where the reference cylinder now has radius r_i and the radii of the measurements so far incorporated are explicitly shown.

We then transport $W_{\mu\nu}$ inward to the radius r_{i-1} . (Multiple scattering will be considered later.) The transport is done using the derivatives

$$T_{\mu\nu}(r_i; r_{i-1}) = \frac{\partial \alpha_\mu(r_i)}{\partial \alpha_\nu(r_{i-1})} \quad , \quad (3)$$

which can be determined using simple geometrical methods. The transported $W_{\mu\nu}$ is

$$W_{\mu\nu} [\vec{\alpha}(r_{i-1})|r_i, \dots, r_n] = T^\top(r_i; r_{i-1}) W_{\mu\nu} [\vec{\alpha}(r_i)|r_i, \dots, r_n] T(r_i; r_{i-1}) \quad , \quad (4)$$

which is the weight matrix on $\vec{\alpha}(r_{i-1})$ resulting only from the measurements at r_i, \dots, r_n .

The essential point is that there are now two independent sources of information about $\vec{\alpha}(r_{i-1})$: the local measurement at r_{i-1} and the transported parameters and errors from measurements at r_i, \dots, r_n . If the locally measured quantities are C_k , the corresponding local contribution to the weight matrix is

$$W_{\mu\nu} [\vec{\alpha}(r_{i-1})|r_{i-1}] = \sum_{k,l} \frac{\partial C_k(r_{i-1})}{\partial \alpha_\mu(r_{i-1})} V_{kl}^{-1} \left[\vec{C}(r_{i-1}) \right] \frac{\partial C_l(r_{i-1})}{\partial \alpha_\nu(r_{i-1})} \quad . \quad (5)$$

In the simplest case, the measurements $C_k(r)$ directly provide one or more of the helix parameters at that radius, such as $r\phi_x$ or z . A drift-chamber axial wire measures $r\phi_x$, charge division provides z , and a stereo-angle wire measures a linear combination of z and $r\phi_x$. The vertex detector provides uncorrelated measurements of $r\phi_x$ and z at one radius. It is important to note that the weight matrix exists even before there are enough measurements for $V[\vec{\alpha}]$ to exist, since the absence of information—about, say, the track curvature—corresponds to a zero weight but an infinite error.

The total weight matrix at r_{i-1} is given by

$$W_{\mu\nu} [\vec{\alpha}(r_{i-1})|r_{i-1}, \dots, r_n] = W_{\mu\nu} [\vec{\alpha}(r_{i-1})|r_i, \dots, r_n] + W_{\mu\nu} [\vec{\alpha}(r_{i-1})|r_{i-1}] \quad . \quad (6)$$

This simple additivity of the weight matrices is the generalization of the result that when two independent measurements with Gaussian errors σ_1 and σ_2 are combined, the error is

$$\begin{aligned} \frac{1}{\sigma^2} &= \frac{1}{\sigma_1^2} + \frac{1}{\sigma_2^2} \quad , \\ \text{or} \\ w &= w_1 + w_2 \quad . \end{aligned} \quad (7)$$

We have discussed how the weight matrix is transported and how the information from additional measurements is included. In contrast to measurements, which give an additive contribution to the local *weight* matrix, multiple scattering gives an additive contribution to the local *error* matrix. We treat multiple scattering with the following procedure:

1. Transport the weight matrix to the radius r_{MCS} of the multiple scattering layer, which is assumed to be a thin cylinder (or a surface approximately tangent to the local radius vector). This calculation yields $W_{\mu\nu}[\vec{\alpha}(r_{MCS})|r_i > r_{MCS}]$.
2. Invert the weight matrix to obtain the local error matrix, which we denote by $V_{\mu\nu}[\vec{\alpha}(r_{MCS})|r_i > r_{MCS}]$.
3. Calculate a local multiple-scattering matrix reflecting the errors induced in the local track-direction angles. We denote this matrix by $\delta V_{\mu\nu}[\vec{\alpha}(r_{MCS})|MCS]$.
4. Sum the results from steps (2) and (3),

$$V_{\mu\nu}[\vec{\alpha}(r_{MCS})|r_i > r_{MCS}; MCS \text{ at } r_{MCS}] = V_{\mu\nu}[\vec{\alpha}(r_{MCS})|r_i > r_{MCS}] + \delta V_{\mu\nu}[\vec{\alpha}(r_{MCS})|MCS] \quad . \quad (8)$$

5. Invert $V_{\mu\nu}[\vec{\alpha}(r_{MCS})|r_i > r_{MCS}; MCS \text{ at } r_{MCS}]$ to obtain the weight matrix at r_{MCS} including multiple scattering. (If there is a measurement at r_{MCS} as well, a weight matrix contribution as defined by Eq. (5) must be added.)
6. Transport the resulting weight matrix inwards to the next measurement or multiple-scattering layer.

4. Tests of the Track-Error-Matrix Calculation

The error-matrix calculation was tested by comparing it with results obtained by running the Geant Monte Carlo with full track reconstruction and fitting. Two methods were used.

First, we studied the error-matrix elements without multiple scattering. This procedure tests the measurement contribution to the weight matrix and can be regarded as the high-momentum limit. Table 1 lists the square roots of the error-matrix diagonal elements (i.e., the sigmas) for a $p = 10 \text{ GeV}/c$, $\lambda = 0$ track. The predicted values agree quite well with the values obtained from the CDC track fit. The worst disagreement is 12% for ϕ_p , but other values agree to better than about 1%. In Table 2 we compare the off-diagonal terms, first dividing each element by $\sigma(\alpha_\mu)\sigma(\alpha_\nu)$ in order to obtain the correlation terms normalized

Table 1. CDC Track Errors: $p = 10 \text{ GeV}/c$, $\lambda = 0$, no MCS (from error matrix at $R_{ref} = 4.16 \text{ cm}$)		
α_μ	$\sigma(\alpha_\mu)$ Geant MC + CDC fit	$\sigma(\alpha_\mu)$ Predicted Value
ϕ_x	1.54 mr	1.53 mr
z	898 μm	888 μm
ϕ_p	0.25 mr	0.22 mr
λ	1.53 mr	1.53 mr
$\frac{Q}{p_t}$	$2.41 \times 10^{-3} \frac{1}{\text{GeV}/c}$	$2.43 \times 10^{-3} \frac{1}{\text{GeV}/c}$

Table 2. CDC Track Error Correlations: $p = 10 \text{ GeV}/c$, $\lambda = 0$, no MCS (from error matrix at $R_{ref} = 4.16 \text{ cm}$)		
α_μ, α_ν	$\frac{\langle \delta\alpha_\mu \delta\alpha_\nu \rangle}{\sigma(\alpha_\mu)\sigma(\alpha_\nu)}$ Geant MC + CDC fit	$\frac{\langle \delta\alpha_\mu \delta\alpha_\nu \rangle}{\sigma(\alpha_\mu)\sigma(\alpha_\nu)}$ Predicted Value
ϕ_x, z	0.222	0.216
ϕ_x, ϕ_p	-0.965	-0.959
ϕ_x, λ	-0.218	-0.212
$\phi_x, \frac{Q}{p_t}$	-0.918	-0.916
z, ϕ_p	-0.207	-0.200
z, λ	-0.953	-0.950
$z, \frac{Q}{p_t}$	-0.202	-0.198
ϕ_p, λ	0.211	0.203
$\phi_p, \frac{Q}{p_t}$	0.983	0.989
$\lambda, \frac{Q}{p_t}$	0.213	0.209

from -1 to 1 . As expected, large correlations are present between ϕ_x and ϕ_p , ϕ_x and $\frac{Q}{p_t}$, z and λ , and ϕ_p and $\frac{Q}{p_t}$.

The comparisons presented thus far have not tested the multiple-coulomb-scattering contribution to the error matrix. The natural method would simply be to compare predicted and CDC-fit error matrices with multiple scattering, but at the time of this paper the CDC track fit did not include multiple-scattering errors. We therefore use a different approach.

Because the Geant Monte Carlo correctly multiple scatters the tracks, we can perform Monte Carlo “experiments” to generate distributions of (measured minus true) track parameters and fit them to Gaussians. Specifically, tracks measured in the CDC are extrapolated back to the outer layer of the vertex detector. We then compute the difference between the coordinate obtained by extrapolation and the true coordinate at the vertex detector. This difference has contributions both from the CDC measurement error and from the multiple scattering between the vertex detector and the CDC. Figure 1 shows the difference distributions for the z and $r\phi_x$ coordinates ($p = 1 \text{ GeV}/c$, $\lambda = 0$). These differences are particularly interesting since they determine the initial search area when CDC tracks are linked to vertex-detector hits.

Similar distributions are obtained for higher momentum tracks, and the resulting $\sigma(r\phi_x)$ and $\sigma(z)$ are obtained for each momentum (at $\lambda = 0$) by fitting to a Gaussian. Figure 2 shows $\sigma(r\phi_x)$ and $\sigma(z)$ as a function of track momentum in comparison with the predicted values (curve). (These plots assume an $80 \mu\text{m}$ CDC resolution, which is the average over a drift cell.) Figure 3 shows the variation of $r\phi_x$ and z errors with the dip angle λ , at constant momentum $p = 1 \text{ GeV}/c$. The agreement between the Monte Carlo points and the predictions (curves) is quite good as a function of both p and λ .

We see that at $p = 1 \text{ GeV}/c$ and $\lambda = 0$, a 3σ error ellipse at layer 4 of the vertex detector has an area of $\pi(3.972 \mu\text{m})(3.355 \mu\text{m}) \approx 10 \text{ mm}^2$, which corresponds to about 20 k pixels. After the CDC track is linked to a candidate hit in an outer vertex-detector layer, a further extrapolation is performed to an inner layer of the vertex detector. The error ellipse from this secondary extrapolation has an area covering only 40 pixels (at $p = 1 \text{ GeV}/c$, $\lambda = 0$).

GEANT MC : CDC track extrapolated to VXD L4

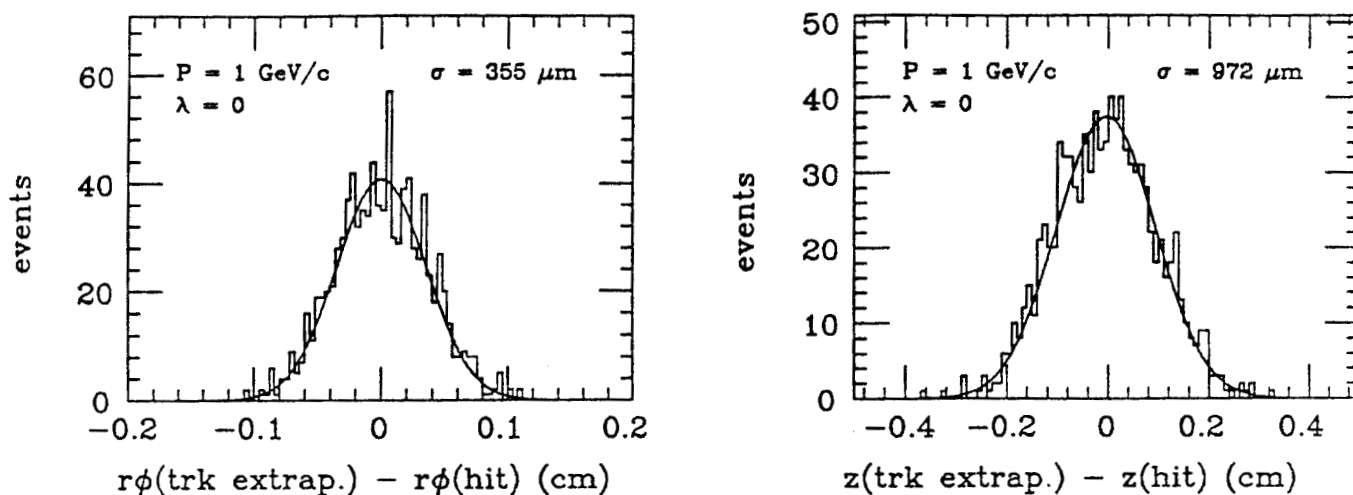


Figure 1.

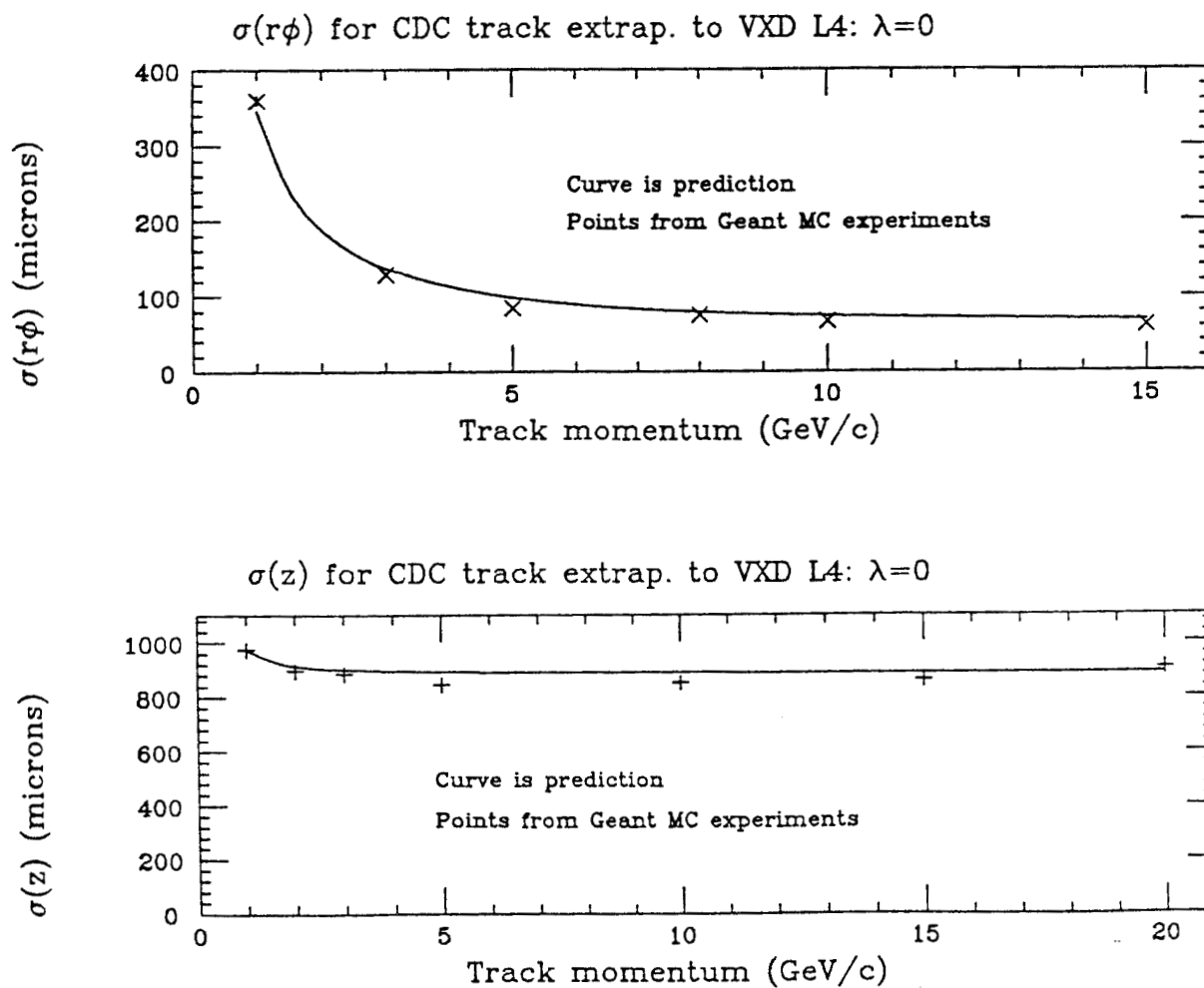


Figure 2.

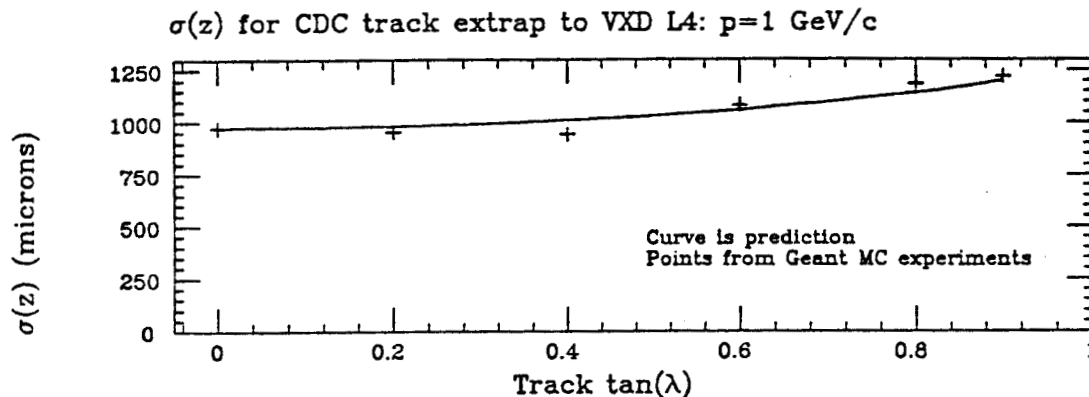
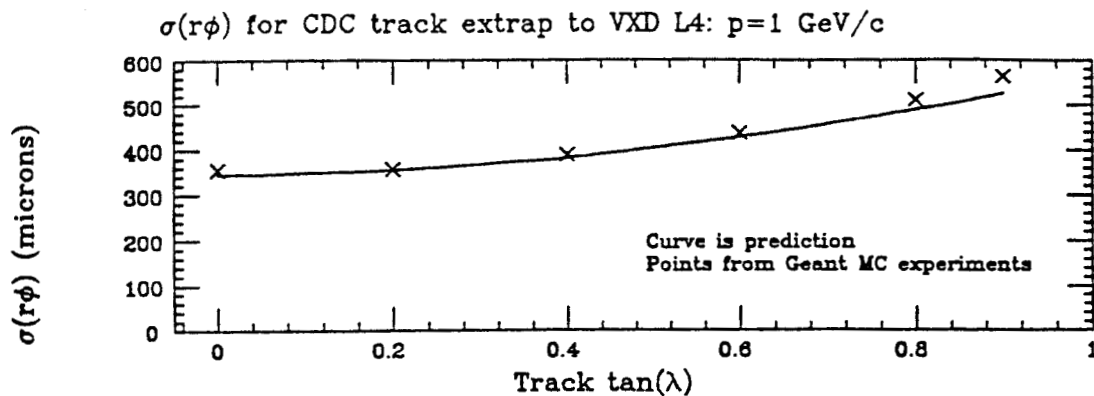


Figure 3.

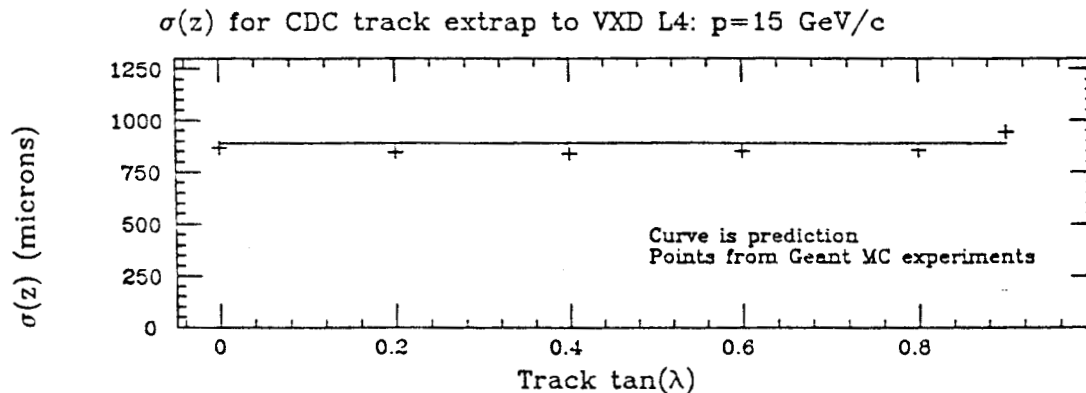
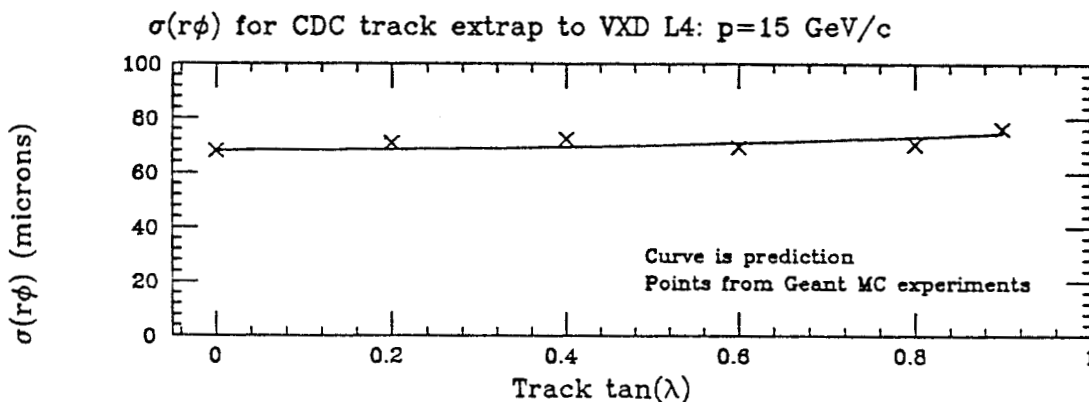


Figure 4.

Figure 4 also shows the variation of $r\phi_x$ and z errors with λ , but this time at $p = 15 \text{ GeV}/c$. The $r\phi_x$ error is substantially smaller than at low momentum (Fig. 2), where it is dominated by multiple scattering. The z error is roughly ten times worse than the $r\phi_x$ error at high momentum, and it is only slightly better than the low-momentum z error.

5. Conclusions

We have developed and tested software to provide simulation of SLD tracking error matrices that agree with Geant results to better than 10%. We plan additional tests and implementation in the fast Monte Carlo in the near future.

Reference

1. P. Billoir, *Nucl. Inst. Meth.* **225** (1984): 352.

B-Meson Reconstruction

L. Osborne (reporting) and D. Williams
Massachusetts Institute of Technology
Laboratory for Nuclear Science
and
Physics Department

I. Purpose

It is clearly desirable to be able to extract as much information as possible out of each Z^0 decay event. This starts with measuring the momentum and identity of each stable final product but also determining the parentage of each particle whether it be from a fast decay ($\pi^0, \eta^0, J/\psi$, etc.) or a "slow" decay (B, D, K_s^0 , etc.). This noble goal is frustrated by the large number of stable particles in the final state and the many particle combinations that may be formed. Typically the final state will contain about 25 stable particles. For a $b\bar{b}$ event the final state (according to LUND) will have about 5 π 's in each charge category, 1 K in each, 1 charged lepton and 1 neutrino. A rough guide to the source of these particles is that 1/3 come from each of the B and \bar{B} decays and the remaining 1/3 from the residual di-jet hadronization. Reconstructing ideally is out of the question yet much can be done given the power of the SLD as a detector with its high precision momentum measuring capability, particle identification,

and vertex detection. This paper aims to evaluate what might be done using all this artillery with particular reference to reconstructing B-mesons.

We list below some specific physics results obtained by B reconstruction:

- A. Event Identification i.e. separation of b from c from u, d, s quark events. B identification is possible by other methods, such as use of high p_T leptons, ^{1,2}. Below, we consider vertex finding as another technique not requiring reconstruction.
- B. Separation of B from \bar{B} and D from \bar{D} jets to get angular distributions and through this the Z^0 to quark coupling. Again reconstruction is not necessary.
- C. Separation of charged from neutral B and D mesons and measuring their lifetime differences. This sheds light on the decay mechanisms.
- D. Separation of B_d and B_s mesons. Again full reconstruction is not necessary (see Attwood ³).
- E. Study of the Mechanism of Weak Decay. The prime candidate for the elementary quark decay is shown in Figure 1(a). It is the counterpart of μ -decay and the quark kinematics are predictable. However, the resulting quarks must then

hadronize somewhat as shown in the figure. The "annihilation" diagram (Fig. 1b) is disfavored, unlike D-decay, at the higher energies of the B-meson mass. The pairing of the quarks as shown to form jets is favored over crossed pairing since the color match is automatic. However, one can certainly not rule out more complex jet-jet or quark-quark interactions. Reconstructed B-decays will shed light on the true mechanisms.

- F. Measurement of the K-M matrix element, V_{ub} . Though semi-leptonic decays to a strangeness zero state is cleaner in interpretation, decays to a pure hadronic state will be more plentiful.
- G. C P non-invariance. Measuring the difference in Γ between $B \rightarrow f$ and $\bar{B} \rightarrow \bar{f}$ is cleanest for 2 particle final states; one can guess the quark diagrams and compare with expected differences⁴. However, such states have small branching ratios. One might see CP non-invariance in more complex and more plentiful final states.

We allude to other methods for performing the same tasks in A-E above; this is so but B-meson reconstruction, when possible, certainly leads to a cleaner interpretation and may be statistically more powerful.

II. The Tools

A. Vertex Finding

The use of the impact parameter to find particles as candidates for B-meson products is well explored. We wish to restate the more useful concept of the "normalized" impact parameter which is fundamentally the χ^2 for a particle trajectory being associated with the main production vertex. The expected error is computed from the expected multiple scattering in beam tube and vertex detector and the measuring error in the vertex detector. The methodology is discussed by D.C. Williams⁵. A plot of this χ^2 from events generated by a LUND Monte Carlo is shown in Figure 2. We use this method to extract B-decay particle candidates. This method is also used to find the presence of a second "long" lived particle (the D meson) thus separating b and d events from u, d, s events. Included in this analysis is the finite coverage of the vertex detector. We have assumed it to be located at a radius of 2.5 cm. and extending ± 5.5 cm. in z.

B. Secondary Vertex Finding

We also examine track pairs from the candidates found in A and calculate the distance of closest approach (DCA). This

is the length of the line with direction $\bar{a}_1 \times \bar{a}_2$; (a_1 and a_2 are the direction vectors of the 2 tracks) and passing through lines \bar{a}_1 and \bar{a}_2 ; it, in turn, is divided by its expected error.

The results of this analysis are shown in Figure (or Table)

3. One may pick the χ^2 cut and the number of tracks that do not intersect within this χ^2 and so tune the percentage of double vertices found and degree of contamination. Note that one need only find a double vertex in either B or \bar{B} jet to identify a b-quark event.

C. Rapidity Cuts

It is well known that heavy meson production from $e^+e^- \rightarrow$ heavy quarks results in mesons with large X_F and, therefore, high rapidity. When these mesons decay the products occur centered about this high rapidity. A rapidity plot of particles from a $b\bar{b}$ event is shown in Figure 4. We have, then, a further means of selecting B-decay particle candidates. This is the only selection tool we can use for neutral particles.

III. Results

We use the criteria above to select candidate particles as B-meson decay products. The Monte Carlos were done under the following conditions:

- 1) χ^2 cut in impact parameter of 2.0 or
- 2) Charged particle rapidity cut > 2.0 .
- 3) Neutral particle rapidity cut > 1.7 .
- 4) Gluon radiation turned off. This is a temporary convenience obviating removal of low sphericity events and/or adjustment of the rapidity cut on an event by event basis.
- 5) Perfect K- π separation.
- 6) Jets with charged leptons and therefore neutrinos were included. This source of background is easily excluded by removing jets with charged leptons.
- 7) Perfect momentum measurement. This was done initially so that the correct B-mesons would give the identically correct mass. We add measuring error later.
- 8) K_L^0 's detected by the calorimeter.
- 9) The cuts in 1) - 3) have been varied to optimize the results.

The results of this analysis are shown in Figure 5. By virtue of 7) correct identification is demonstrated by the spike at the correct mass. One finds that one has correctly reconstructed 11% of the B-mesons and a comparable number for \bar{B} -mesons.

With this amount of success one may then consider whether an even more detailed reconstruction were possible. For example, the debris from the secondary D-mesons must all be included among the candidate particles. Again, it might seem trivial to locate these but one still faces a large number of combinations to find these correctly. As a quick perfunctory test we examine those events where a charged K was included in the B debris and assume it marks the D-decay vertex; we lose half of our events thereby. We then use the χ^2 test for the DCA to find charged particles which do not fit that particular vertex. We add to these one or two π^0 's reconstructed from the high rapidity gamma rays. We use all these to reconstruct a D-meson. If we get a D-meson (or F-meson) mass we again examine the reconstructed B-mass. The results are shown in Figure 6. Our percentage of reconstructed B-masses is now down to 4% but the background has been reduced by a greater factor.

One cannot legitimately quote a signal to background number from the plots in Figure 5 and 6. When momentum measuring errors are

included the spike of true B's will spread over more than one bin and will give the true signal to background ratio on a per bin basis. This is illustrated in Figure 7 where we have redone the analysis but including a smear in momentum measurements given by⁶:

$$\sigma/p = .002 \text{ p (Gev/c)} \quad \text{for charged particles}$$

$$\sigma(E) = .08 \sqrt{E(\text{Gev})} \quad \text{for gammas}$$

$$\sigma(E) = 0.5 \sqrt{E(\text{Gev})} \quad \text{for } K_L^0$$

Finally it is worth noting to what degree the vertex detector was a help in this reconstruction. We have redone the Monte Carlo using only rapidity cuts for charged particles. The results are shown in Figure 8. The reconstruction efficiency decreases to 6.5% from 11%. The equivalent of finding the D-meson cannot be done however; the vertex detector was needed to separate tracks of the D-decay point from the B-decay point.

IV. Conclusions

This analysis shows the potential strength of the SLD using all its features in reconstructing B-mesons. To be sure, a Monte Carlo such as this without all the real factors (noise, efficiencies, etc.) gives a rosier picture than reality. Nevertheless the study suggests that we can make a significant contribution to the understanding of B physics and weak interactions in general.

Also to be noted -- a B factory near $B\text{-}\bar{B}$ threshold will lose the reconstruction capability obtained by rapidity separation as used here.

This work supported in part by the US Department of Energy contract DE-AC02-76-ER03069.

REFERENCES

1. S. Wagner, et al., Proceedings of the Second Mark II Workshop on SLC Physics, SLAC-Report-306, November 1986.
2. W.T. Ford, *ibid*
3. W. Atwood, "B Meson Physics with Polarized e^- Beams at the SLC", SLAC-Pub. 4668, September 1989.
4. For example -- I. Dunietz and L. Rosner, Phys. Rev. D 34, 1404 (1986). The appendix points to one (of other) problems for more than 2 body final states for measuring CP non-unvariance.
5. D.C. Williams, SLD Software Note 89-3
6. SLD Design Report -- SLAC-Report-273, May 1984.

Figure Captions

- Figure 1 A simple diagram for B-meson decay (a). The "annihilation" diagram (b) is less favored.
- Figure 2 A plot of the distribution in normalized impact parameters (χ^2 distribution) for tracks from a $B\bar{B}$ event.
- Figure 3 A table of correct/incorrect separations of b-quark from c-quark events by measuring whether an extra vertex (from D-meson decay) is found from a B-meson decay. This efficiency is shown as a function of the number of extra tracks (lines) desired and the χ^2 cut-off.
- Figure 4 A rapidity plot for tracks from b-quark events. The "horns" at high rapidity come from B-meson decay tracks.
- Figure 5 A plot of reconstructed B-meson masses. The spike at the correct B mass indicates the number of true-reconstructions.
- Figure 6 A plot of reconstructed B-masses where a D-mass is also reconstructed successfully. See text for details.
- Figure 7 A redo of Figure 5 with measurement error included. See text for details.
- Figure 8 As in Fig. 6 but without use of vertex information.

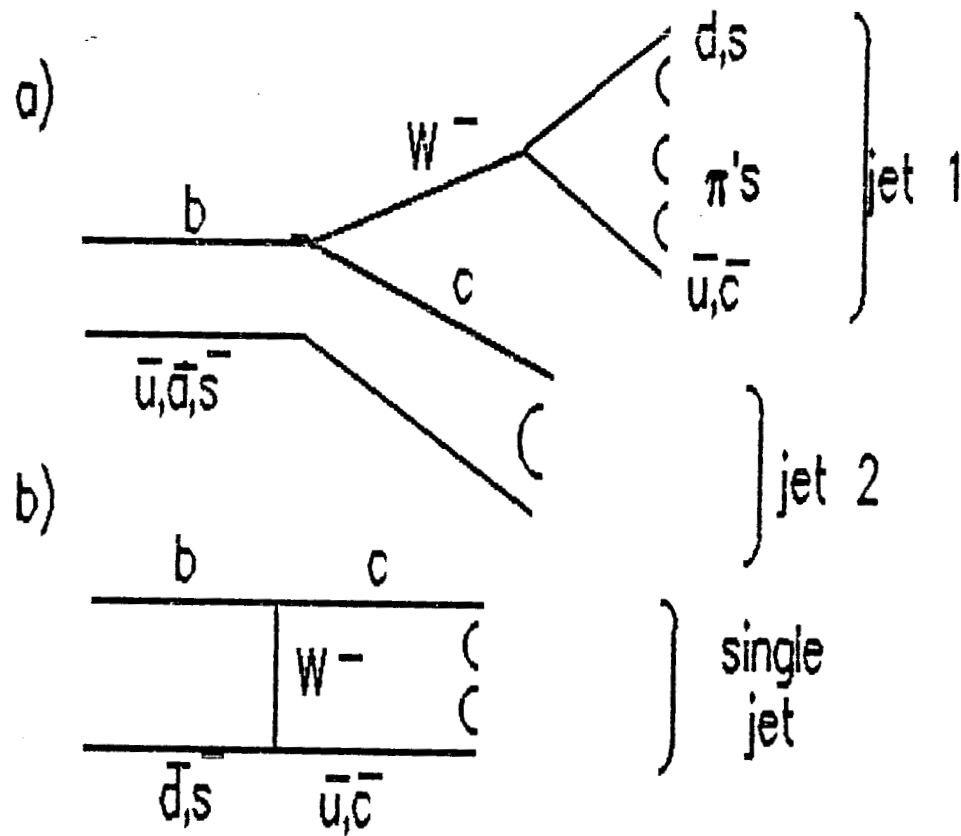


Figure 1 A simple diagram for B-meson decay (a). The "annihilation" diagram (b) is less favored.

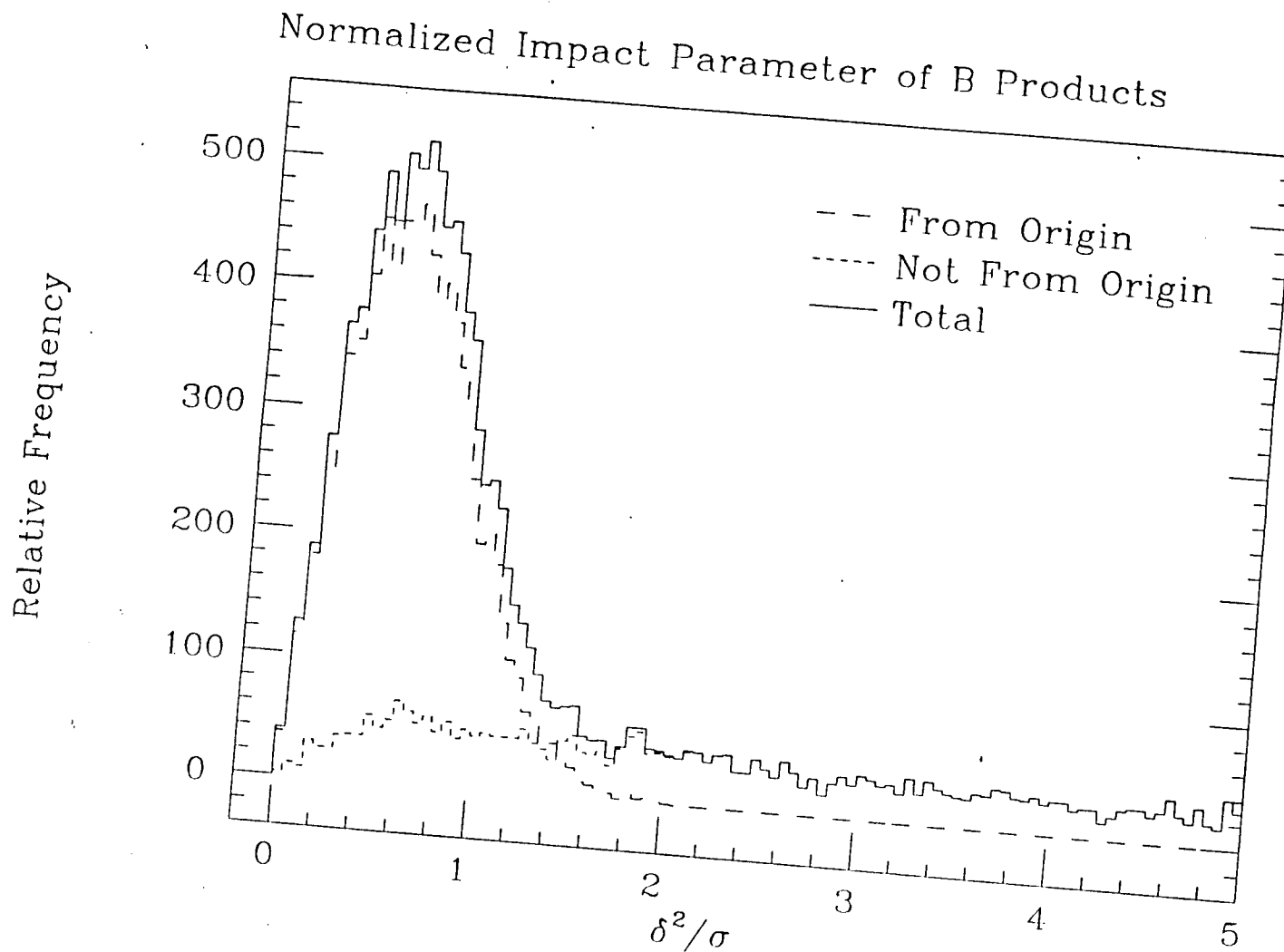


Figure 2 A plot of the distribution in normalized impact parameters (χ^2 distribution) for tracks from a $B\bar{B}$ event.

Table of efficiency of b from c flavor event selection
Output from BDSEP ver 2.1 made: 13-JAN-89 with 1000 b and 1000 c events

Method: If N different pairs of tracks have a weighted distance of closest approach (d.c.a.) greater than the cutoff in EITHER jet, than the event is identified as a b flavor event.

Each entry: (fraction correct), (fraction background)

CutOff	Number lines above cutoff			
	1	2	3	4
1.250	0.788, 0.2220	0.647, 0.0590	0.507, 0.0210	0.389, 0.0060
1.500	0.756, 0.1470	0.575, 0.0280	0.439, 0.0130	0.329, 0.0020
1.750	0.712, 0.0930	0.537, 0.0150	0.380, 0.0050	0.273, 0.0020
2.000	0.670, 0.0470	0.475, 0.0090	0.330, 0.0040	0.219, 0.0010
2.250	0.625, 0.0250	0.440, 0.0050	0.277, 0.0020	0.182, 0.0000
2.500	0.588, 0.0140	0.404, 0.0030	0.254, 0.0010	0.159, 0.0000
2.750	0.561, 0.0060	0.379, 0.0010	0.220, 0.0010	0.140, 0.0000
3.000	0.536, 0.0020	0.354, 0.0010	0.200, 0.0010	0.131, 0.0000
3.250	0.510, 0.0020	0.321, 0.0010	0.186, 0.0010	0.124, 0.0000

Figure 3 A table of correct/incorrect separations of b-quark from c-quark events by measuring whether an extra vertex (from D-meson decay) is found from a B-meson decay. This efficiency is shown as a function of the number of extra tracks (lines) desired and the χ^2 cut-off.

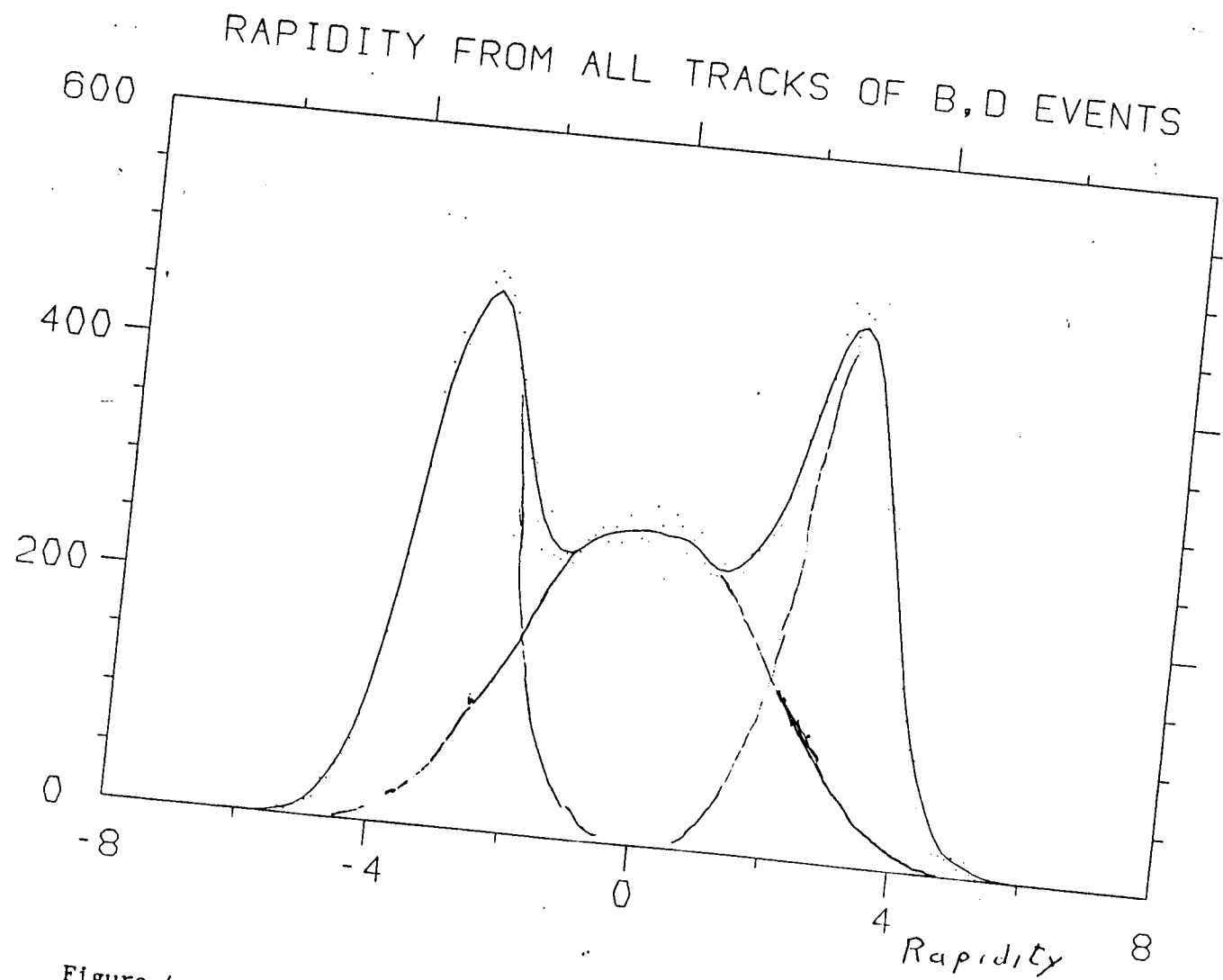


Figure 4 A rapidity plot for tracks from b-quark events. The "horns" at high rapidity come from B-meson decay tracks.

268

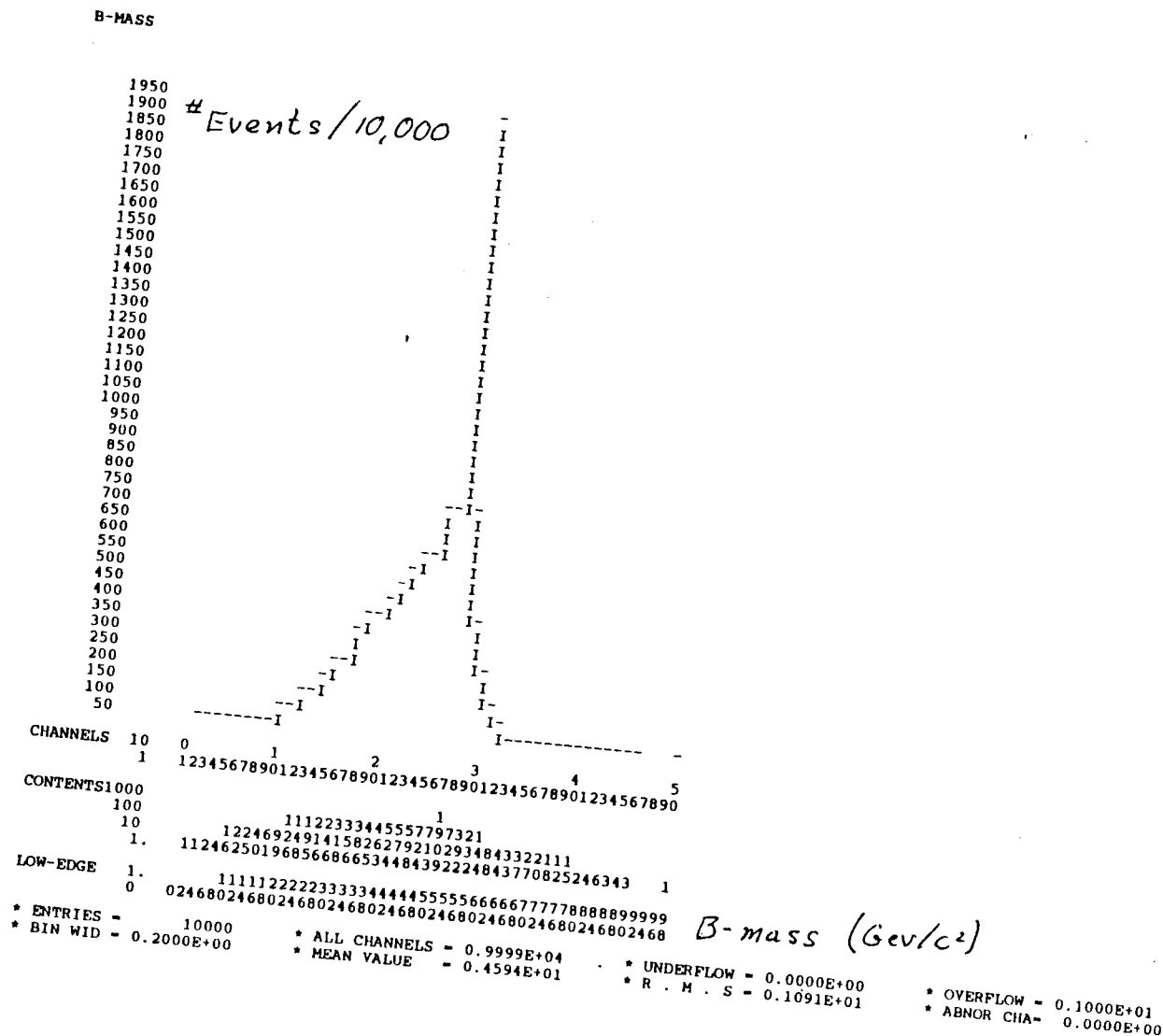


Figure 5 A plot of reconstructed B-meson masses. The spike at the correct B mass indicates the number of true-reconstructions.

B-MASS

269

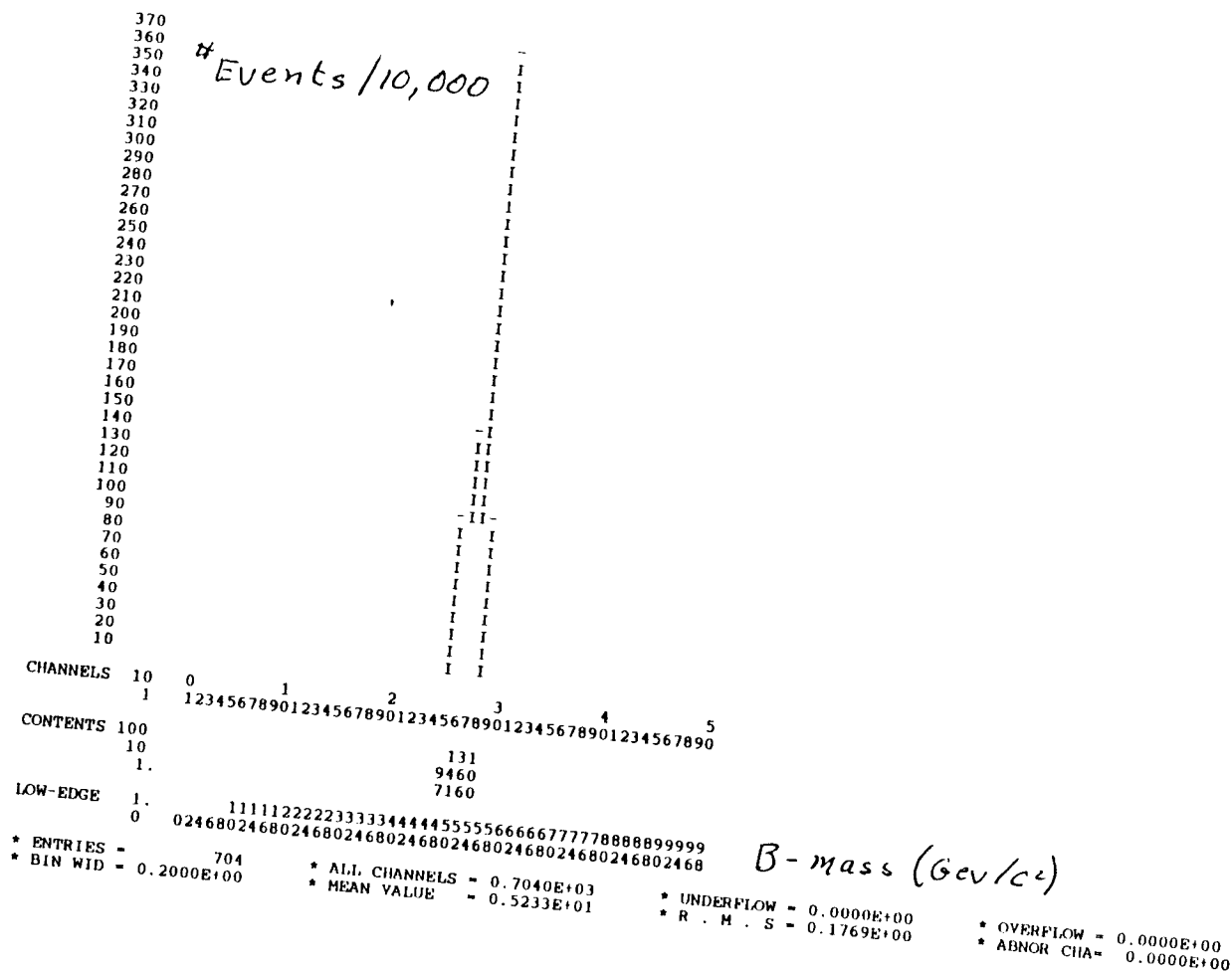


Figure 6 A plot of reconstructed B-masses where a D-mass is also reconstructed successfully. See text for details.

270

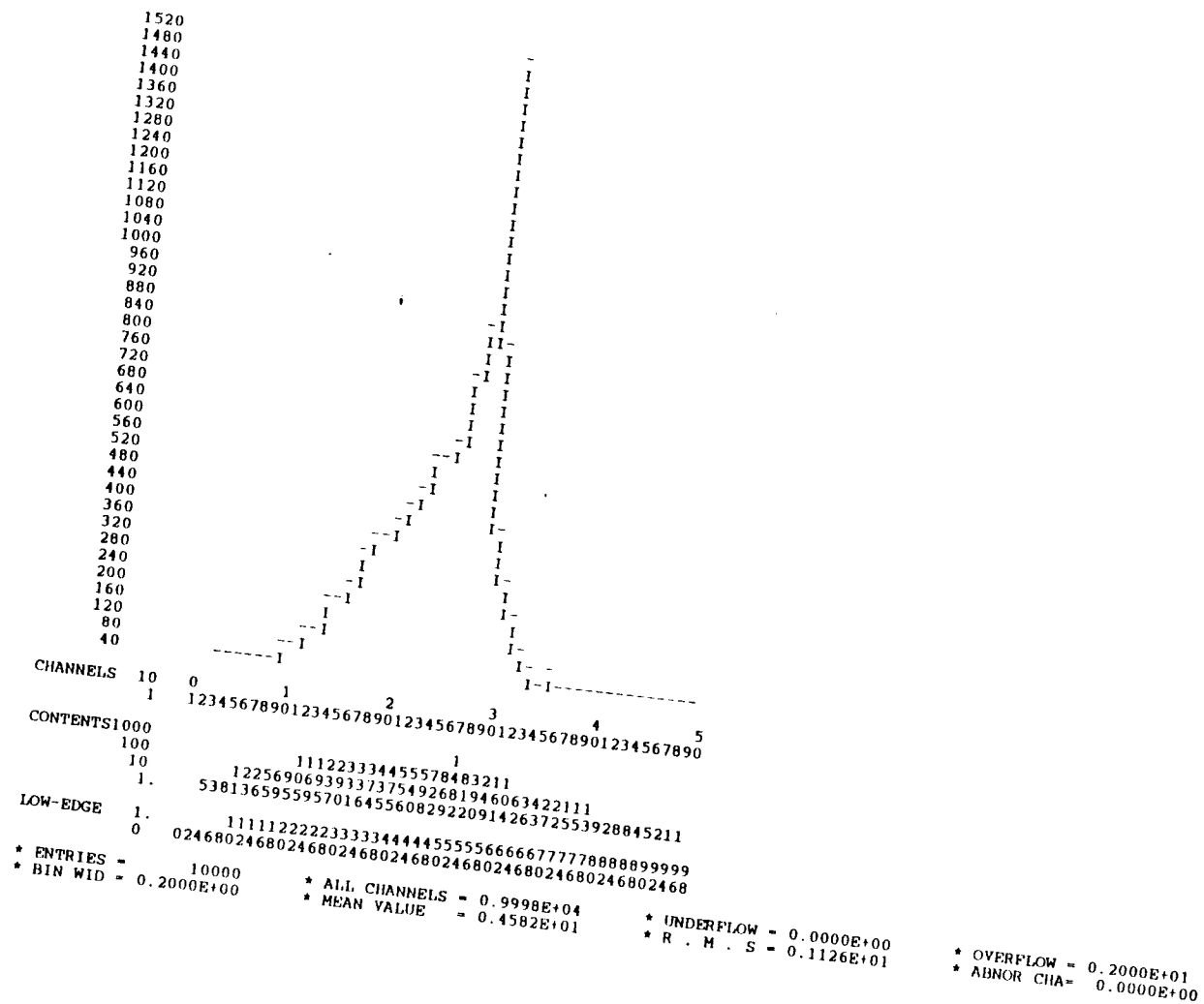


Figure 7 A redo of Figure 5 with measurement error included. See text for details.

271

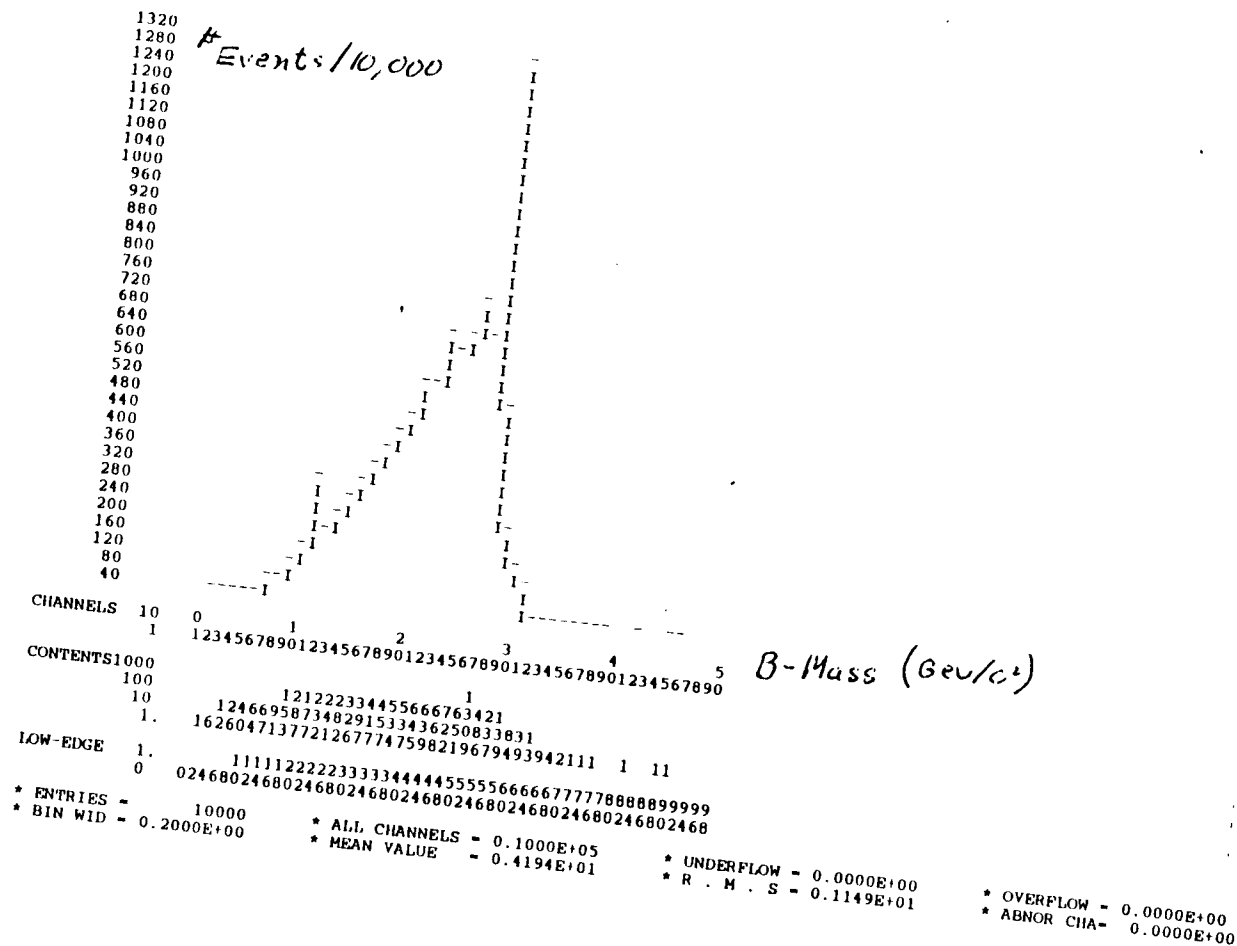


Figure 8 As in Fig. 6 but without use of vertex information.

IDENTIFICATION OF D^0 , D^+ , AND D^* MESONS
WITH THE SLD

by

Mike Strauss
Tom Browder
Sean McHugh

August 1989

272

Introduction

The SLD detector will be a valuable tool to study b-quark physics due to its high resolution vertex detector and its ability to identify particle types using the CRID. In the first year of operation, we hope to produce 10^5 Z^0 particles which will decay to about 14,000 $b\bar{b}$ events. In order to effectively compete with the detectors at LEP, it is essential that we reconstruct as many B mesons and baryons as possible. Since most non-leptonic decays of B mesons produce D mesons, one way to increase our reconstruction efficiency is to reconstruct as many D decay modes as possible. In this paper, we will investigate our efficiency for reconstructing various exclusive D decay modes.

The data for this paper was produced using the LUND Monte Carlo, and the standard SLD Fast Monte Carlo. We have used 15,000 $b\bar{b}$ events, 11,000 $c\bar{c}$ events, and a total of 42,000 $u\bar{u}$, $d\bar{d}$, and $s\bar{s}$ events for background studies. We have studied efficiency for reconstructing the following decay modes, (including their charge conjugates), as well as signal to background ratios as a function of D momentum:

$$\begin{aligned}
 D^0 &\rightarrow K^- \pi^+ \\
 D^0 &\rightarrow K^- \pi^- \pi^+ \pi^+ \\
 D^+ &\rightarrow K^- \pi^+ \pi^+ \\
 D^{*+} &\rightarrow D^0 \pi^+ & (D^0 \rightarrow K^- \pi^+) \\
 D^{*+} &\rightarrow D^0 \pi^+ & (D^0 \rightarrow K^- \pi^+ \pi^+ \pi^-) \\
 D^0 &\rightarrow K_s^0 \pi^+ \pi^- & (K_s^0 \rightarrow \pi^+ \pi^-) \\
 D^0 &\rightarrow K^* \pi & (K^* \rightarrow K_s^0 \pi) \\
 D^+ &\rightarrow K_s^0 \pi^+ \pi^+ \pi^- & (K_s^0 \rightarrow \pi^+ \pi^-)
 \end{aligned}$$

where the D^0 to $K^* \pi$ mode is a subset of the D^0 to $K_s^0 \pi^+ \pi^-$ mode.

Charged track vertices were found using the standard vertexing routines developed by Bill Atwood and modified by Gary Gladding and Tom Browder. Since this vertexing package is still under development, it is important to realize that the results of this paper have been obtained using the package as it existed at the end of July, 1989. The only exception to this is that we have also used the new K_s^0 finding routine which had not been implemented as the default package as of August 1, 1989. Geometric vertices are reconstructed using all combinations of charged tracks which come from any common vertex. Various cuts are made in order to define these common vertices. First, each charged track must have a momentum greater than 500 MeV/c. Second the reconstructed vertex must be

greater than 500 microns from the primary interaction point. Finally, the reconstructed vertex must satisfy a χ^2 test. The χ^2 value for a two prong vertex is defined by,

$$\chi^2 = \frac{(\vec{x}_1 - \vec{x}_v)^2}{\sigma_1^2} + \frac{(\vec{x}_2 - \vec{x}_v)^2}{\sigma_2^2}$$

where \vec{x}_v is the position of the reconstructed vertex, \vec{x}_1 and \vec{x}_2 are the positions of the two tracks at their closest approach to \vec{x}_v , and σ_1 and σ_2 are the error on the track position at \vec{x}_v .

For a two prong vertex $\chi^2 < 1.6$. Similar expressions for χ^2 are defined for multipronged vertices.

For each D decay mode we have tried to optimize efficiencies and signal to background ratios using $b\bar{b}$ events then apply those cuts to $c\bar{c}$ and light quark events. Figures 1a and 1b show the momentum distribution of D mesons coming from a subset of the $b\bar{b}$ and $c\bar{c}$ events, respectively. Throughout this paper, backgrounds are quoted in a region of ± 35 MeV/c² around the D mass peak. The total number of D mesons produced by the Monte Carlo were approximately 30,000 D^0 's, 16,000 D^\pm 's and 12,000 $D^{*\pm}$'s.

Analysis and Results

For each decay mode we have determined the reconstruction efficiency as a function of D momentum for $b\bar{b}$ and $c\bar{c}$ events separately. The results, as well as invariant mass plots, are shown in Figures 2 through 4. Figure 2 shows the reconstruction efficiency as a function of D momentum for D decays to charged tracks. For each of these modes we have required that one charged track be identified as a kaon from the CRID particle identification, as reported in PHPART. For Figure 2b and 2c we have also required that $b/\sigma_b > 3$ where b is the distance from the reconstructed vertex to the next closest charged track, and σ_b is the error on the track position at the distance of closest approach. Finally, for Figure 2c we have also required that each track have a momentum greater than 1 GeV/c.

Figure 3 shows the results from our reconstruction of the D^* meson. We look for the D^* decaying into a D^0 and a charged π . Figure 3a shows our D^* results when the D^0 decays to a $K\pi$ combination, and Figure 3b shows our results when the D^0 decays to one charged K and three charged pions. The D^* is interesting since it can be reconstructed with a minimal number of cuts. For D^* reconstruction, we have not used vertexing, but have made only two cuts. First, one track must be identified as a kaon by the CRID. Second,

we plot the value of Q against the invariant mass of the $D\pi$ combination, with Q defined as,

$$Q = M_{D^*} - M_{D^0} - M_{\pi^+},$$

where M_x is the mass of the various particles. A clustering occurs at the mass of the D^* in a region of $0.004 < Q < 0.010$. Signal to noise ratios for D^* reconstruction are actually determined by making a cut on the mass of the D^* and projecting on the Q axis since this gives a cleaner signal.

Figure 4 shows the results of our D reconstruction when the D decays to a neutral K_s^0 and charged pions. We reconstruct the K_s^0 by combining two charged pions, and requiring that the reconstructed vertex is more than 5 mm from the primary vertex. Figure 5 shows our K_s^0 signal. The K_s^0 is reconstructed with an efficiency of 48%. Next, we extrapolate the K_s^0 back to another charged track vertex (see Figure 6). The distance of closest approach between the K_s^0 direction and that vertex (b_v) must be less than some value which has been tuned for different D decay modes. Other cuts are made on the distance between the reconstructed vertex and the interaction point (d), the distance between the extrapolated momentum vector (p_v) of the charged track vertex and the interaction point (b'), and the ratio of b/σ_b , as defined in the charged D decay modes. Figure 4a shows the results for the D^0 to $K_s^0 \pi^+ \pi^-$ decay. Cuts used for these histograms are $b_v < 0.1$ cm, $p_K > 2.5$ GeV/c, $p_v > 2.0$ GeV/c, $d > 0.05$ cm, $b/\sigma_b > 2.0$, and $p_D > 5.0$ GeV/c, where p_K is the magnitude of the K_s^0 momentum, p_v is the magnitude of the vector momentum of the charged track vertex, and p_D is the magnitude of the D momentum. Since many of the D^0 to $K_s^0 \pi^+ \pi^-$ decays occur via a K^* decay, we have tried to improve the signal shown in Figure 5a by cutting on the K^* mass. We require that the invariant mass of the K_s^0 and one charge pion be between 0.84 and 0.94 GeV/c². We also change the above cuts slightly requiring $b_v < 0.125$ cm, and $b/\sigma_b > 2.5$. With these constraints the signal to noise ratio is significantly increased, as can be seen by the results in Figure 4b. Figure 4c shows our results in reconstructing the D^+ to $K_s^0 \pi^+ \pi^+ \pi^-$ decay. Cuts used for this mode are $b_v < 0.1$ cm, $p_K > 2.0$ GeV/c, $p_v > 4.0$ GeV/c, $d > 0.1$ cm, $b/\sigma_b > 4.0$, $p_D > 5.0$ GeV/c, and $b' > 0.005$ cm. A small peak of about 2 standard deviations above background appears in the invariant mass plot.

Summary and Conclusions

We have investigated the ability of the SLD to reconstruct decay modes of the D meson as a precursor to doing B physics. A summary of our results for all $b\bar{b}$ and $c\bar{c}$

events is shown in Table 1. In Table 1, we list efficiencies, total branching fractions, signal to background ratios, and the number of decays reconstructed for 100,000 Z's. We are able to reconstruct a number of different decay modes with reasonable efficiencies and signal to background ratios. In order to optimize our D finding algorithms, there is still work to be done. First, we must add D decays involving neutral π mesons to our list, as well as investigate other charged decay modes, particularly multiple prong decays. Second, we must further investigate background from $u\bar{u}$, $d\bar{d}$, and $s\bar{s}$ events. Initial results show that backgrounds from light quarks contribute about 20% more background than reported in this paper. Using geometric cuts, as well as cuts on the total number of vertices in the event, these backgrounds should be able to be minimized. Next, we plan on writing these found D decays to a bank in the DST. This will allow anyone interested in doing B or D physics to access a generic list of optimized D decays. Finally, we intend to repeat and verify this analysis as the SLD vertexing package is further refined and improved.

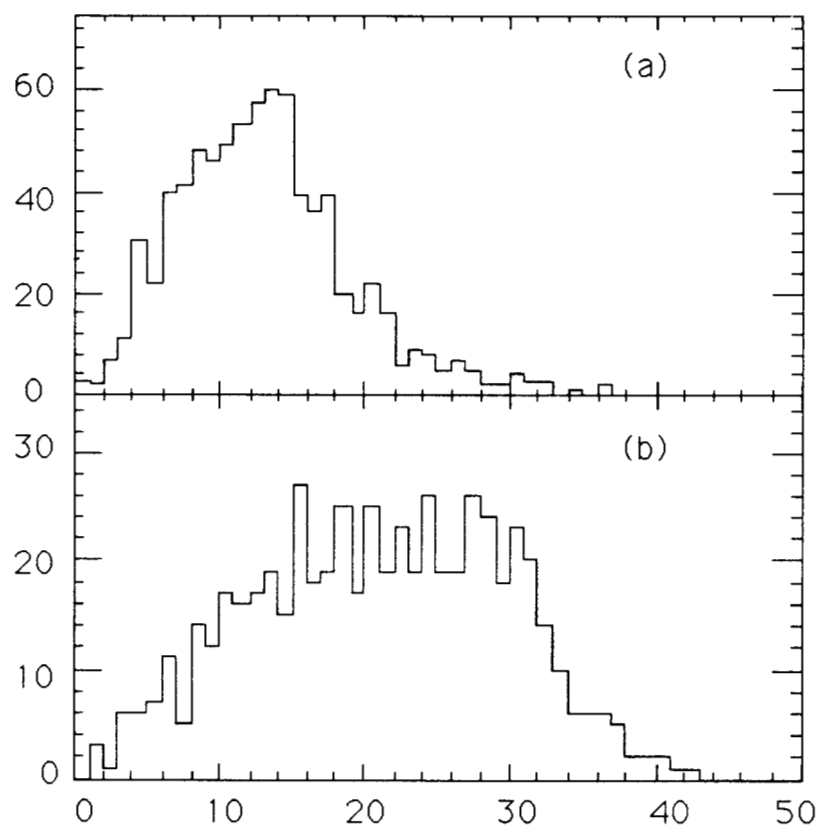


Figure 1: Momentum of D Mesons from
a) $b\bar{b}$ events, and b) $c\bar{c}$ events

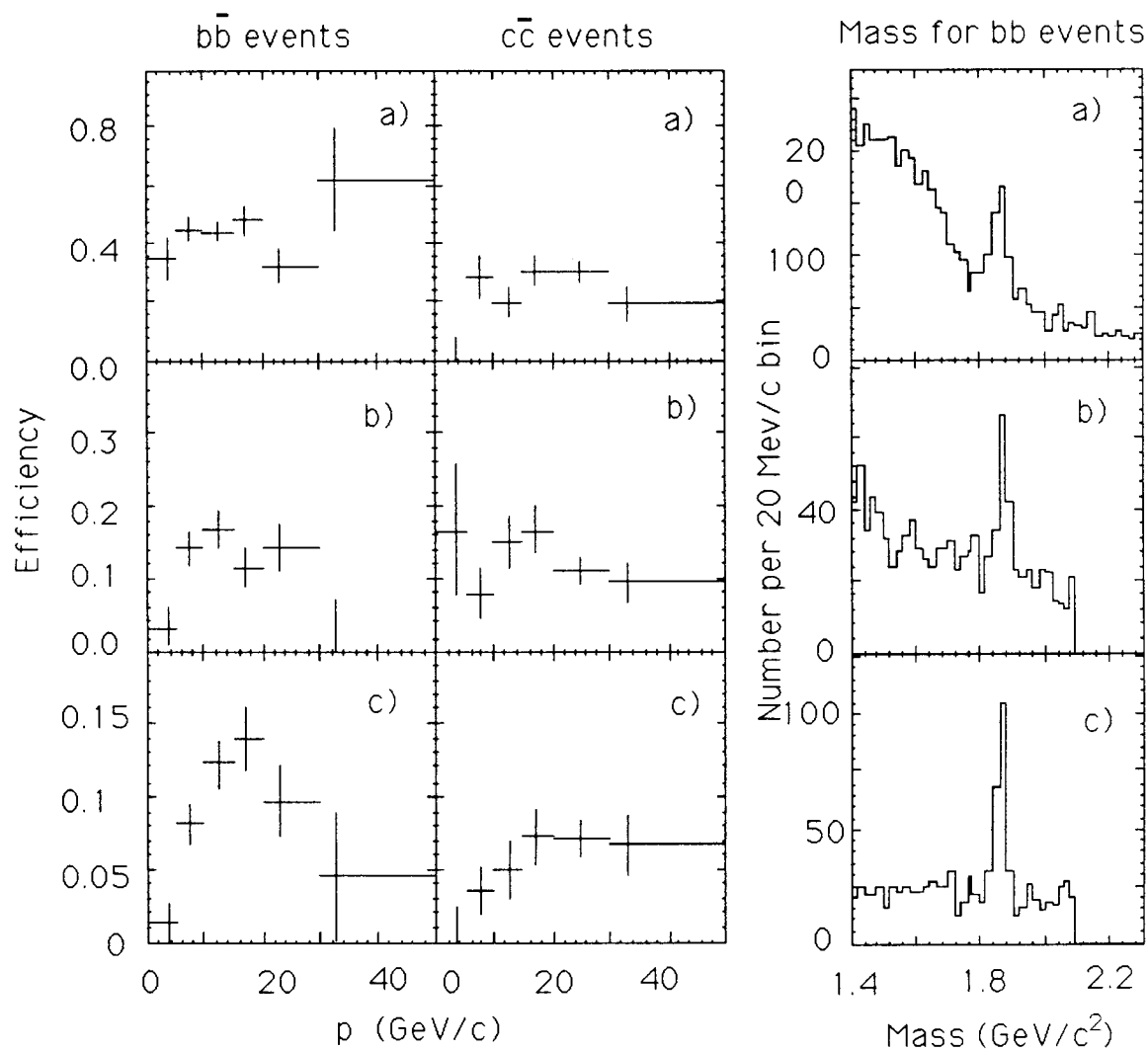


Figure 2: Efficiency vs Momentum and mass plots for
a) $D^0 \rightarrow K^- \pi^+$ b) $D^+ \rightarrow K^- \pi^+ \pi^+$
c) $D^0 \rightarrow K^- \pi^- \pi^+ \pi^+$

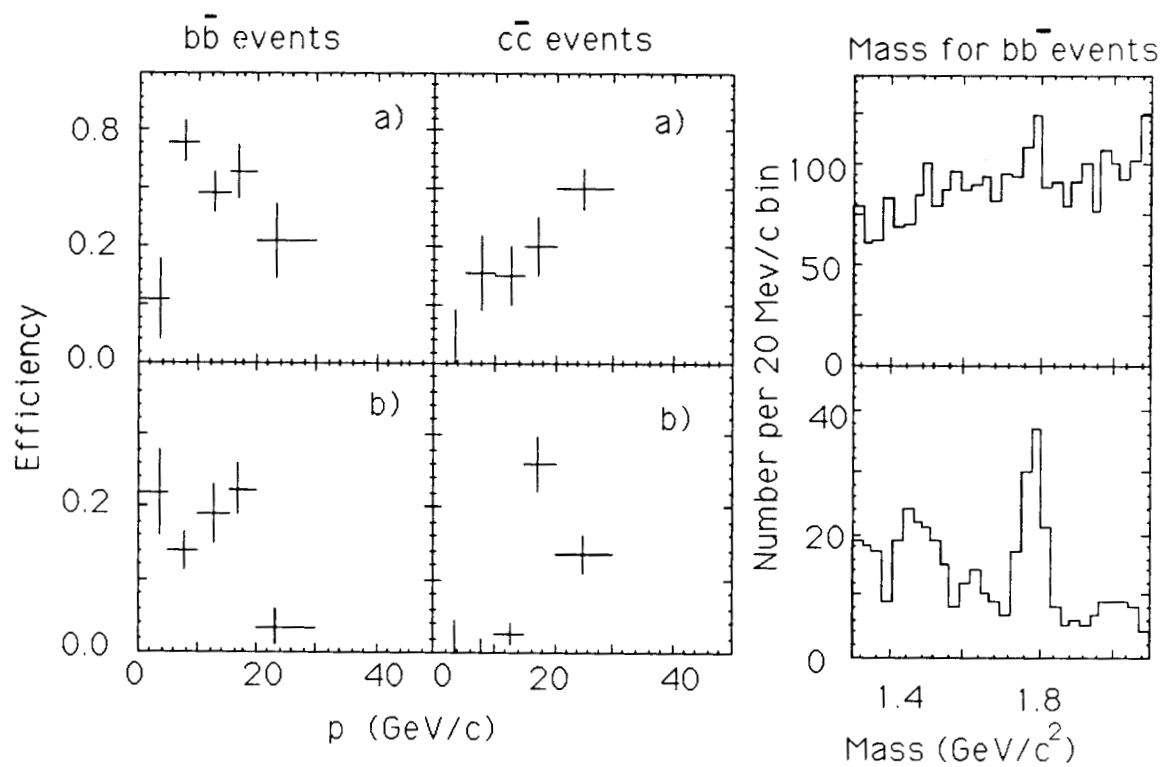


Figure 3: Efficiency vs Momentum and Invariant Mass for

a) $D^{*+} \rightarrow D^0 \pi^+$ b) $D^{*+} \rightarrow D^0 \pi^+$

$\rightarrow K^- \pi^+$

$\rightarrow K^- \pi^+ \pi^+ \pi^+$

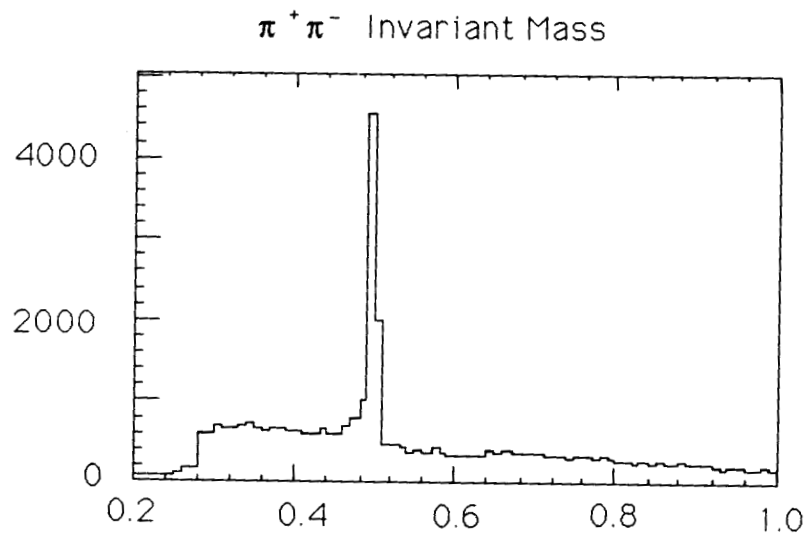


Figure 5: K short signal for $b\bar{b}$ events

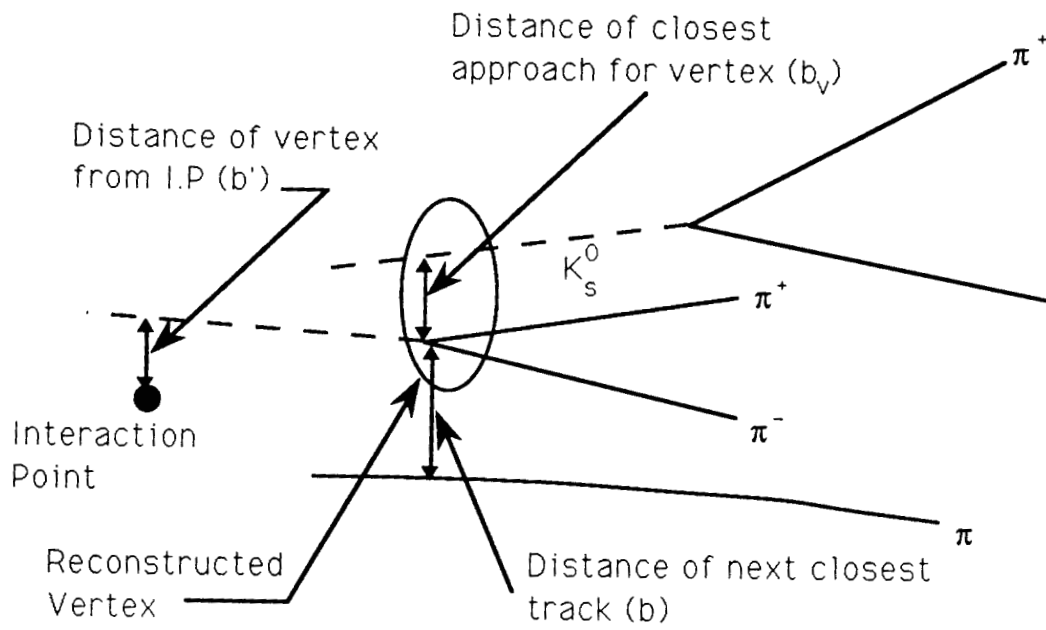


Figure 6: Reconstruction of a $D \rightarrow K_s^0 + X$ decay

Decay Mode	Efficiency %	B.F.	$S/\sqrt{S+B}$	S / B	No. Found
$D^0 \rightarrow K^- \pi^+$	36.4	3.77	14.5	1.3	372
$D^0 \rightarrow K^- \pi^+ \pi^+ \pi^+$	8.5	7.9	11.2	1.8	195
$D^+ \rightarrow K^- \pi^+ \pi^+$	12.8	7.8	10.7	2.0	183
$D^{*+} \rightarrow D^0 \pi^+$ ($D^0 \rightarrow K^- \pi^+$)	53.0	1.8	9.9	4.0	123
$D^{*+} \rightarrow D^0 \pi^+$ ($D^0 \rightarrow K^- \pi^+ \pi^+ \pi^-$)	29.5	3.9	8.0	1.2	142
$D^0 \rightarrow K_s^0 \pi^+ \pi^-$ ($K_s^0 \rightarrow \pi^+ \pi^-$)	9.6	2.8	4.7	0.6	62
$D^0 \rightarrow K^* \pi$ ($K^* \rightarrow K_s^0 \pi$) [†]	8.2	2.3	5.0	0.9	53
$D^+ \rightarrow K_s^0 \pi^+ \pi^+ \pi^-$ ($K_s^0 \rightarrow \pi^+ \pi^-$)	8.0	3.5	3.0	0.7	23

[†] This is a subset of the $D^0 \rightarrow K_s^0 \pi^+ \pi^-$ mode

Table 1: Summary of Decay modes for both $b\bar{b}$ and $c\bar{c}$ events

Reconstruction of D's, F's, and Neutrals with the SLD Detector.

Joseph M. Izen

University of Illinois at Urbana/Champaign

Urbana, Illinois 61801

Presented at the Kirkwood Physics Retreat

Kirkwood, California. July 31-August 4, 1989

Abstract

A Monte Carlo study of the reconstruction of D and F mesons in $B\bar{B}$ events is presented. Charmed mesons are reconstructed exclusively in charged modes and in modes with a single π^0 . CRID information is used to distinguish F and D^+ vertices with missing neutrals. The decay distance of a charmed meson from its parent B can be reconstructed for around 50% of correctly reconstructed charm mesons.

Neutral B_d and B_s mesons are expected to mix with their own antiparticles. CLEO and ARGUS have detected B mixing by observing the signs of leptons and charm mesons in decays of the $\Upsilon(4S)$. They observe only B_d mixing since the $\Upsilon(4S)$ lies below $B_s\bar{B}_s$ threshold. In decays of the Z^0 , both B_d and B_s mesons are present which makes distinguishing $B_s\bar{B}_s$ from $B_d\bar{B}_d$ mixing a challenge. Complete reconstruction of B_d or B_s would be ideal, but small branching ratios and reconstruction efficiencies make this unrealistic at SLC luminosities. Partial reconstruction using a secondary B vertex and either a D or F meson is more promising. The B_s meson decays predominantly to states containing an F meson. Spectator decays of the B_d meson contain an F only if the W mediating the decay couples to a $(c\bar{s})$ as in figure 1. Hence, an F meson among the daughters of a B meson with no other accompanying charmed particle can be used to tag a B_s decay.

It is possible to distinguish D^+ from F^+ decays by the number of charged kaons coming from the decay vertex. Figure 2 shows bar graphs of the charged kaon multiplicity for D^+ and F^+ decay. The D^+ prefers states with an odd number of charged kaons, and the F^+ prefers states with an even number. It is the three and five prong decays which are most important for this analysis since they can be reconstructed as a secondary vertex with a reasonably high efficiency. The lifetimes of D^+ and F^+ mesons are 10.7×10^{-13} and 4.4×10^{-13} respectively. The distribution of decay times according to these values are shown in figure 3. If the proper decay length of a secondary vertex is measured, then a cut at one or two F^+ lifetimes selects F^+ decays while rejecting D^+ decays.

In addition to its charged prongs, a charm vertex may have one or more reconstructable neutrals associated with it. Figure 4 shows bar graphs of the number of π^0 s in D^+ and F^+ decays. Approximately two thirds of the decays contain at least one π^0 . The ability to use both π^0 s and charged tracks when reconstructing F^+ s would increase the F^+ full-reconstruction tagging efficiency. This is made clearer by figure 5 which shows the relative numbers of π/K only and $\pi/K + \text{one } \pi^0$ decays. In addition, there are the reconstructable decays $F^+ \rightarrow \eta' + n\pi$, $\eta' \rightarrow \rho^0\gamma$, $\rho^0 \rightarrow \pi\pi$ which contain charged pions plus one photon. A short look into use π^0 s for reconstructing heavy mesons is appropriate.

Photons are detected in SLD using the LAC calorimeter. Figure 6 shows the invariant mass of pairs of photons from the Kirkwood $B\bar{B}$ tapes. All photons with $E_\gamma > 100\text{MeV}$ are used. A clear $\pi^0 \rightarrow \gamma\gamma$ signal is present. A search for $\eta \rightarrow \gamma\gamma$ is made. First, photons which belong to a pair with mass in the π^0 region of figure 6 are removed, and then the invariant mass of the remaining photon pairs are formed as shown in figure 7. The η signal is lost in a large combinatorial background. A benchmark for π^0 reconstruction is the $D^0 \rightarrow K^-\pi^+\pi^0$ decay. Combinations of a two prong $K^-\pi^+$ vertex (with CCD and CRID information, $\text{VTX\%DCARMS} < 2$) and a reconstructed π^0 ($E_\gamma > 100\text{MeV}$, $100\text{MeV} < M_{\gamma\gamma} < 165\text{MeV}$) are formed. Combinatorial backgrounds are reduced with two sets of cuts. First, use is made of the resonant structure of the $K^-\pi^+\pi^0$ decay by removing

events from the nonresonant central region of the Dalitz plot (cut events with either $1.4\text{GeV} < M_{K\pi^0}^2 < 2.0\text{GeV}$ or $0.8\text{GeV} < M_{\pi\pi^0}^2 < 1.4\text{GeV}$). Much of the remaining background comes from soft π^0 s from the fragmentation process. These are suppressed with a cut on the cosine of the angle between the π^0 and the D^0 direction as calculated in the D^0 rest frame ($\cos\theta_{D^0-\pi^0} > -0.5$). The invariant mass of these combinations (figure 8a) shows a clear enhancement at the D^0 mass. The two body $D^0 \rightarrow K^-\pi^+$ signal (figure 8b) is shown for comparison. As expected, the $D^{*+} \rightarrow D^0\pi^+$ signals formed from these D^0 samples (figures 8c and 8d) are quite clean.

Next, three prong vertices from the Kirkwood $B\bar{B}$ tapes are used to reconstruct D^+ and F^+ decays. The same CCD, CRID and vertexing requirements used for the D^0 study were used. All vertices in VTX banks are at least $500\ \mu$ from the origin, but no further cut is used. The invariant mass of $K^-\pi^+\pi^+$ vertices are shown in figure 9. The correctly reconstructed (solid) D^+ vertices have a small background from Cabbibo suppressed F^+ decays (hatched), but the dominant background is coming from incorrect vertex combinations. The situation is better for $F^+ \rightarrow K^-K^+\pi^+$ reconstruction (figure 10). A small improvement in the vertexing algorithm, perhaps with resonance cuts on the ϕ and K^* will permit inclusive F^+ tagging with $K^-\pi^+\pi^+$ vertices. Exclusive reconstruction of $F^+ \rightarrow K^-K^+\pi^+\pi^0$, even with the current vertexing scheme (figure 11). Three pion $\pi^-\pi^+\pi^+$ vertices (figure 12) do not look promising; the background from incorrect vertices is very large.

Five prong vertices are quite promising. Backgrounds are very low for $K^-K^+\pi^+\pi^+\pi^-$ vertices (figure 13) and exclusive $F^+ \rightarrow K^-K^+\pi^+\pi^+\pi^-\pi^0$ decays (figure 14). All-pion five prong vertices (figure 15) have a large background from incorrect vertices but may be useable with improved vertexing techniques. The vertices are clean enough that they can be used to produce a substantial $F^+ \rightarrow \pi^+\pi^-\pi^+\pi^+\pi^-\pi^0$ signal (figure 16).

This survey demonstrates that SLD will be able to supplement completely re-

constructed $F^+ \rightarrow K^- K^+ \pi$ decays with five prong tags and with modes containing a π^0 . Decays of D^+ mesons are not a serious background to F^+ tags; incorrect vertices are the main challenge. Our vertexing algorithms can bear some improvement. All-pion vertices have the worst backgrounds, and it may require a 1.5 cm beam pipe with the original SLD vertex detector design if we are to make use of $\pi^+ \pi^+ \pi^-$ vertices as an F^+ tag.

Once an F^+ decay has been tagged, the question of whether it can be associated with a B vertex arises. In the following exercise, correctly reconstructed D^+ or F^+ vertices from the Kirkwood $B\bar{B}$ tapes are used. Vertices in the same hemisphere as the tagged decay are considered. Two alignment cuts are designed to reject fake B vertices. The most troublesome are $B \rightarrow DF + X$ decays where the second charmed meson produces a genuine vertex which can fake a B . The cosine of the angle between the (origin \rightarrow “ B ” vertex) and the (“ B ” vertex \rightarrow “charm vertex”) vectors must be greater than 0.8 and the perpendicular distance of the “ B ” vertex from the flight path of the tagged charm meson must be less than 0.6 mm. If more than one “ B ” candidate is found, a decision among them is made based on the least reliable track in the vertex. The reconstructed and true decay lengths (laboratory frame) obtained by following this procedure are shown in figure 17. A “ B ” vertex is found for about half of the tags; when no “ B ” vertex is found, the measured decay length is entered as zero. When the “ B ” vertex is located, the decay length is correctly measured.

Figure Captions

Figure 1. The decay $B_d \rightarrow D^- F^+$

Figure 2. Charge kaon multiplicity for D^+ (a) and F^+ (b) mesons.

Figure 3. Proper decay time ($c\tau$ in cm) for D^+ (a) and F^+ (b) mesons.

Figure 4. Multiplicity of π^0 s in D^+ (a) and F^+ (b) decay.

Figure 5. Frequency of all-charged final states for D^+ (a) and F^+ (b) mesons and one π^0 final states for D^+ (c) and F^+ (d) mesons

Figure 6. Invariant mass of $\gamma\gamma$ pairs in the π^0 region. The background consists of photons pairs that do not originate from the same π^0 .

Figure 7. Invariant mass of $\gamma\gamma$ pairs in the η region. Photons forming a pair in the π^0 region have been removed. The background consists of photons pairs that do not originate from the same η .

Figure 8a. $K^-\pi^+\pi^0$ invariant mass.

Figure 8b. $K^-\pi^+$ invariant mass.

Figure 8c. $M_{D^0\pi^+} - M_{D^0}$ for D^0 s formed from $K^-\pi^+\pi^0$.

Figure 8d. $M_{D^0\pi^+} - M_{D^0}$ for D^0 s formed from $K^-\pi^+\pi^0$.

Figure 9. Invariant mass of $K^-\pi^+\pi^+$ vertices. The solid histogram are reconstructed D^+ s. The hatched histogram are reconstructed F^+ s.

Figure 10. Invariant mass of $K^-K^+\pi^+$ vertices. The solid histogram are reconstructed F^+ s. The hatched histogram are reconstructed D^+ s.

Figure 11. $K^+K^-\pi^+\pi^0$ invariant mass.

Figure 12. Invariant mass of $\pi^+\pi^-\pi^+$ vertices. The solid histogram are reconstructed F^+ s. The hatched histogram are reconstructed D^+ s.

Figure 13. Invariant mass of $K^-K^+\pi^+\pi^-\pi^+$ vertices. The solid histogram are reconstructed F^+ s. The hatched histogram are reconstructed D^+ s.

Figure 14. $K^+K^-\pi^+\pi^-\pi^+\pi^0$ invariant mass.

Figure 15. Invariant mass of $\pi^+\pi^-\pi^+\pi^-\pi^+$ vertices. The solid histogram are reconstructed F^+ s. The hatched histogram are reconstructed D^+ s.

Figure 16. $K^+K^-\pi^+\pi^-\pi^+\pi^0$ invariant mass.

Figure 17. True vs measured decay lengths (cm) for for D^+ (a) and F^+ (b) mesons

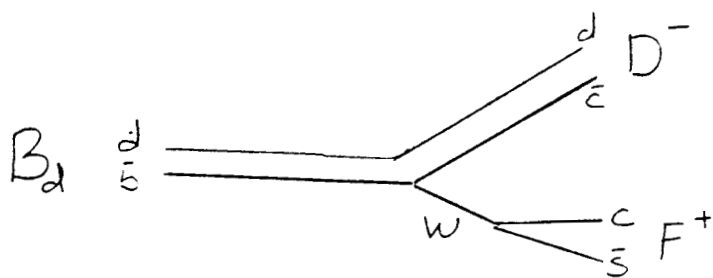


Fig. 1

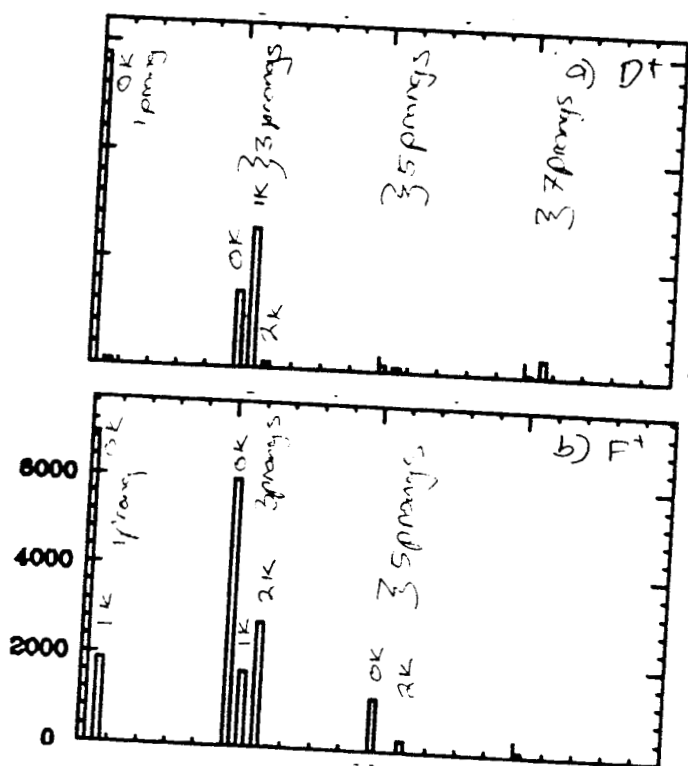


Figure 2

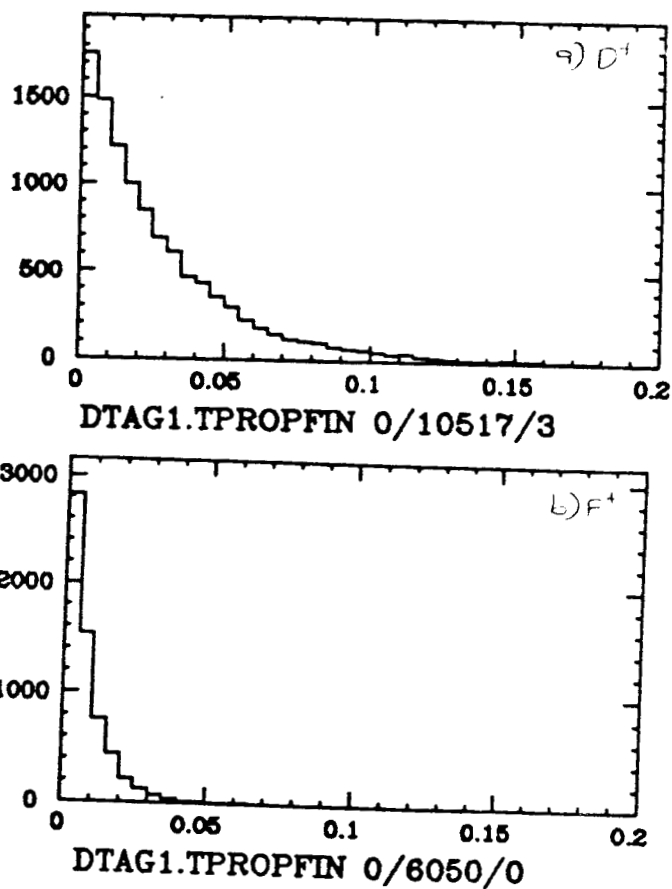


Figure 3

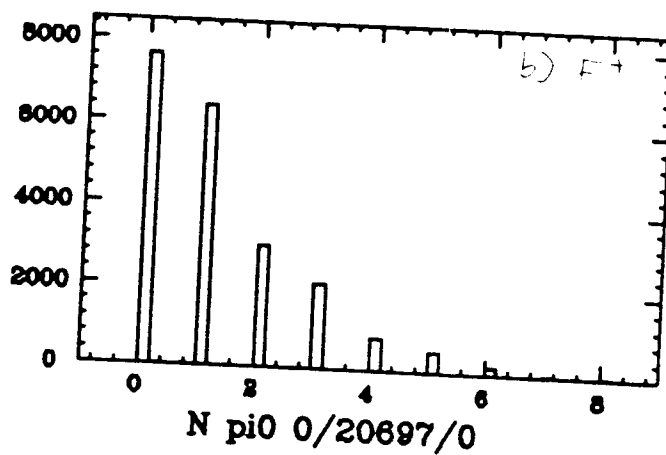
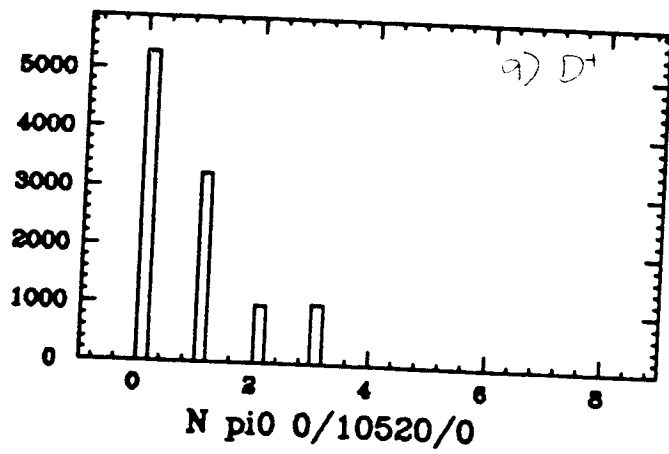


Figure 4

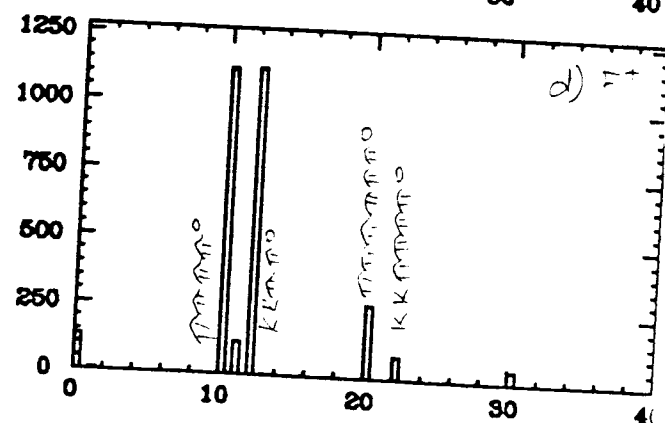
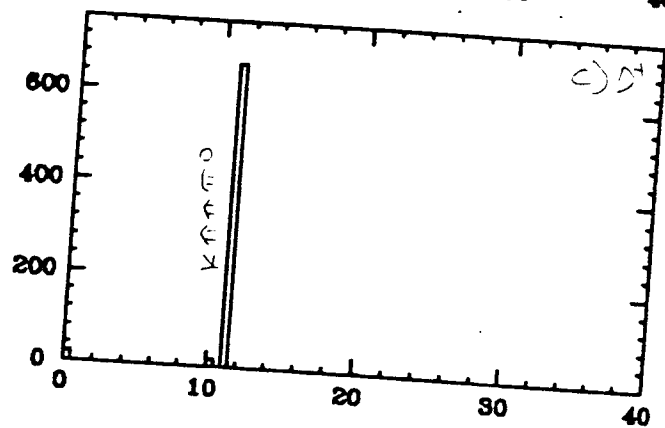
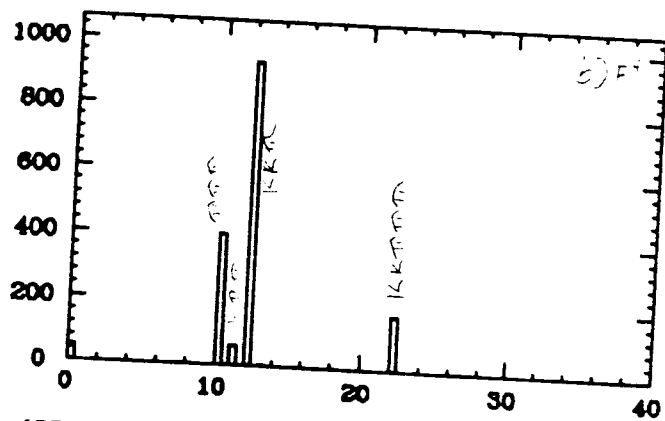
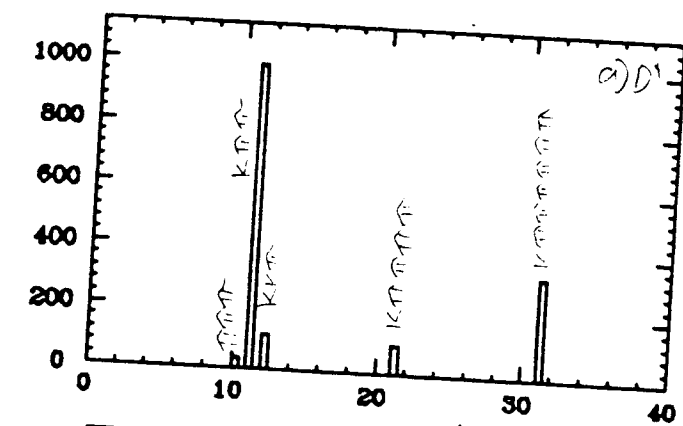


Figure 5

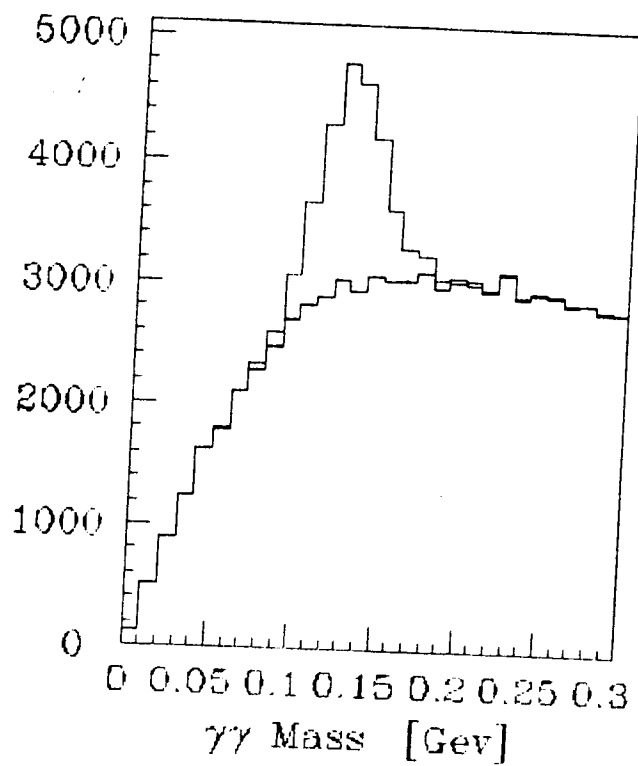


Figure 6.

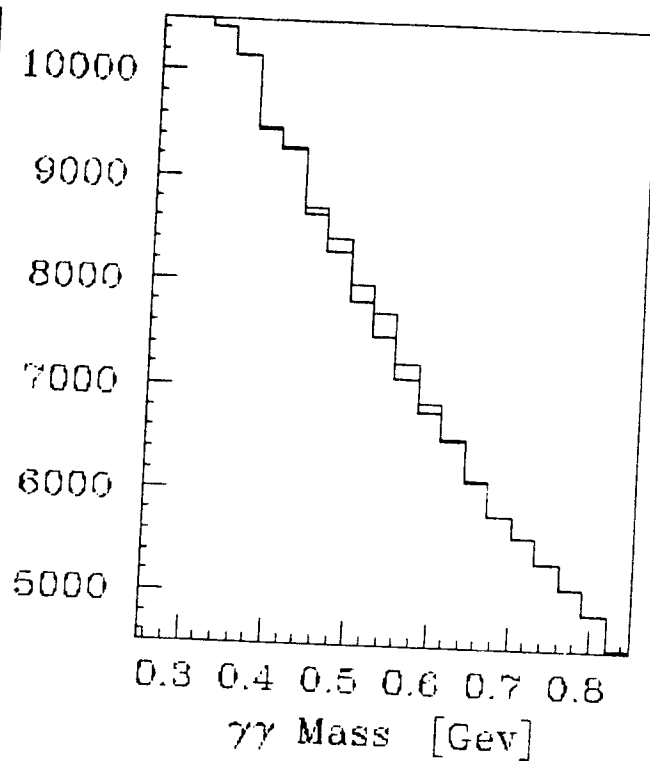


Figure 7.

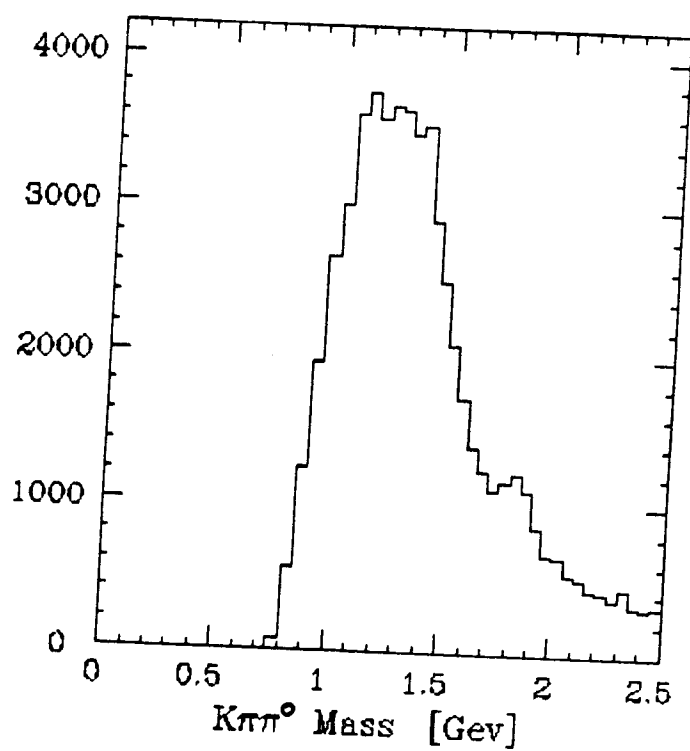


Figure 8a

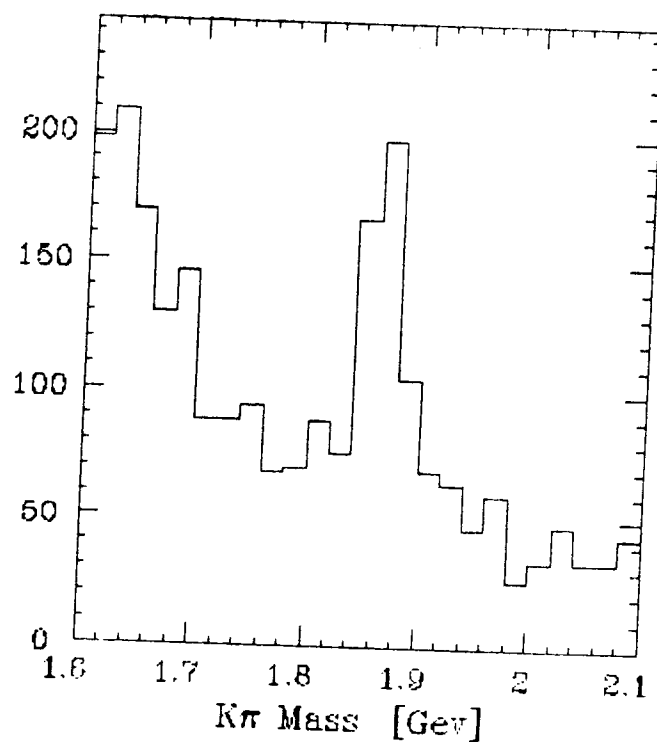


Figure 8b

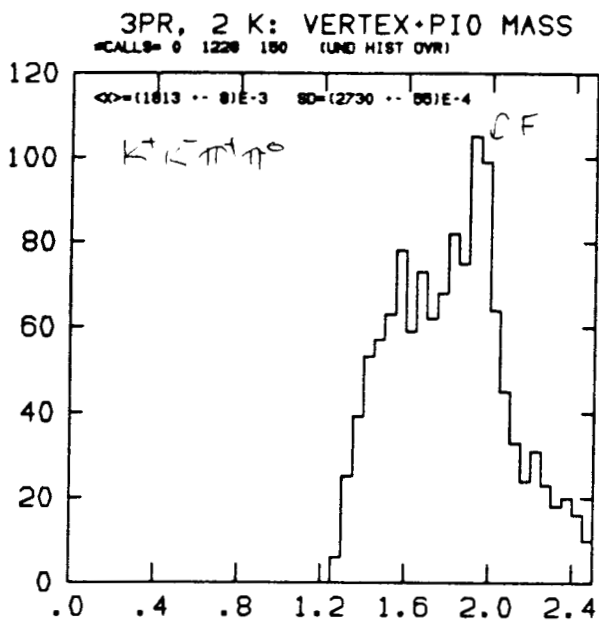


Figure 11

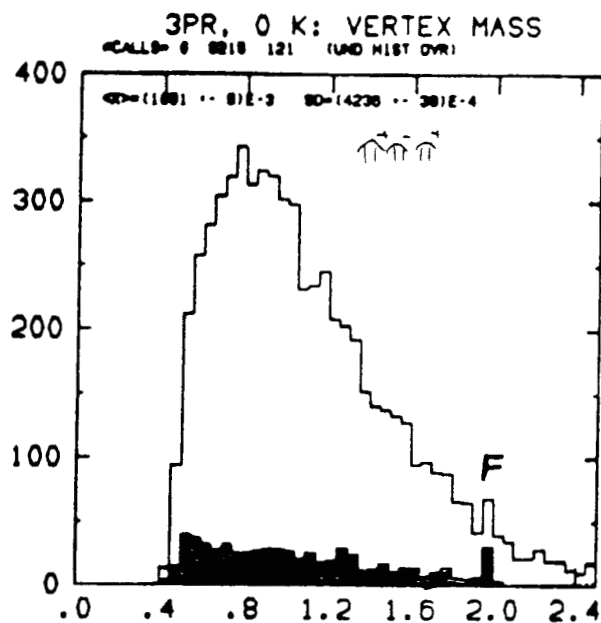


Figure 12

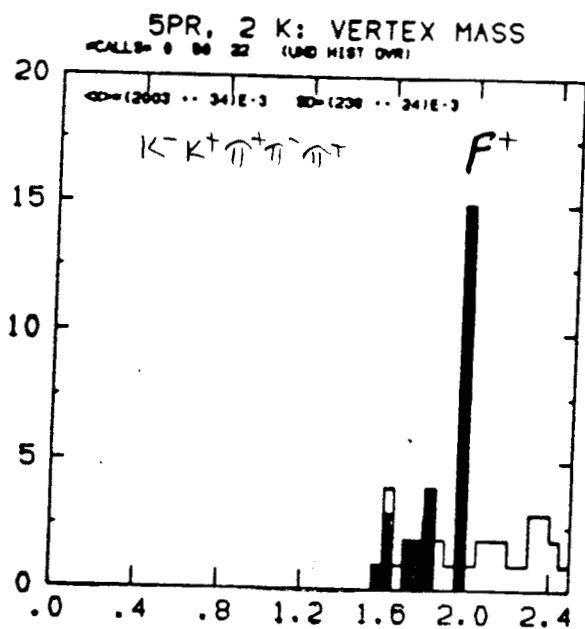


Figure 13

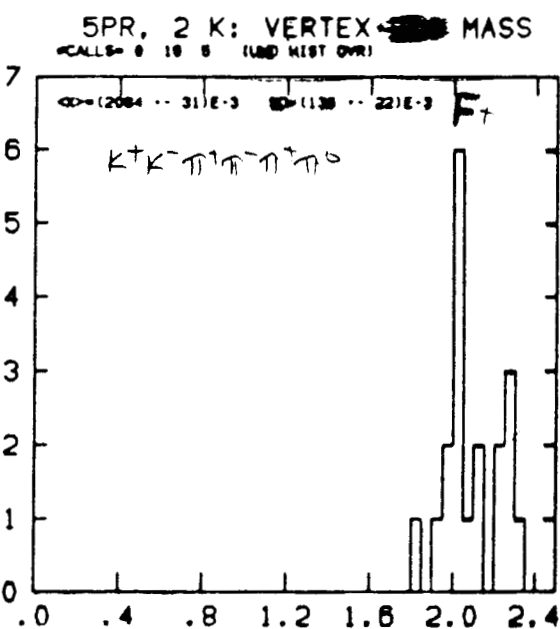
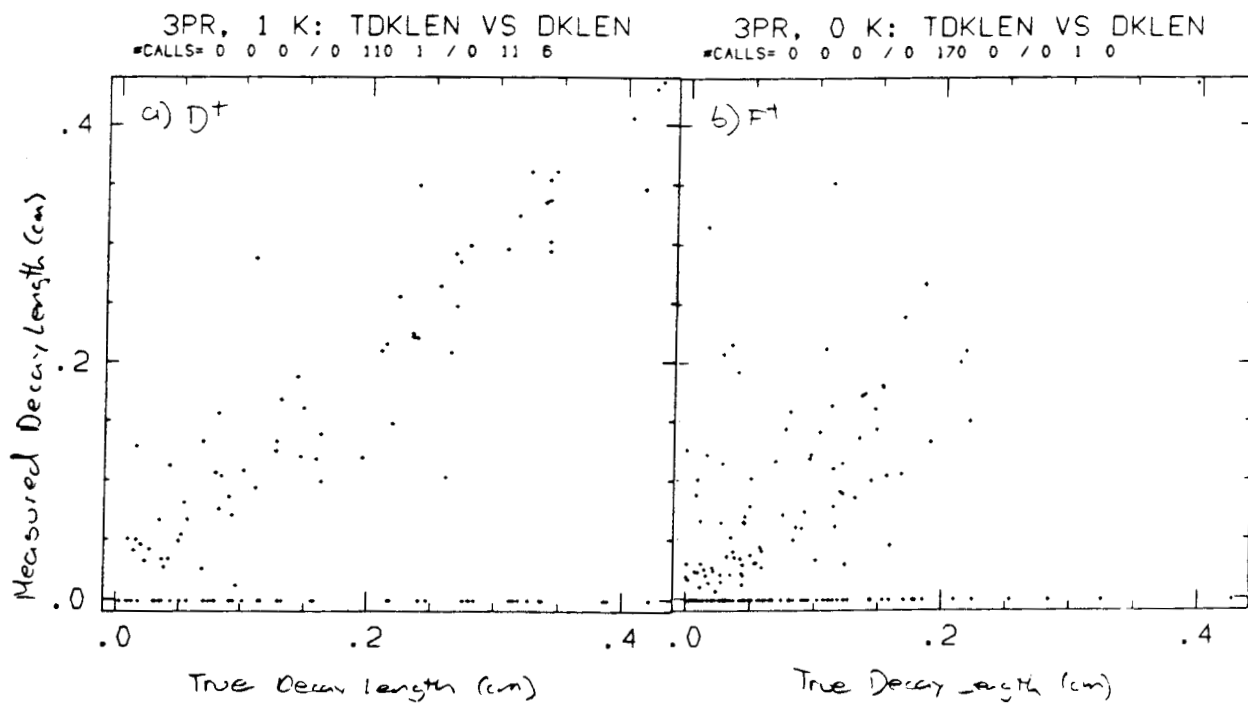
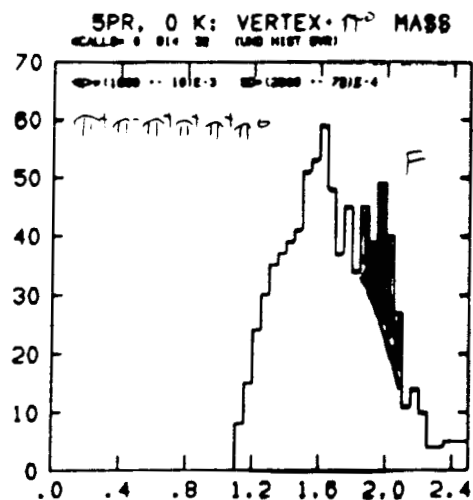
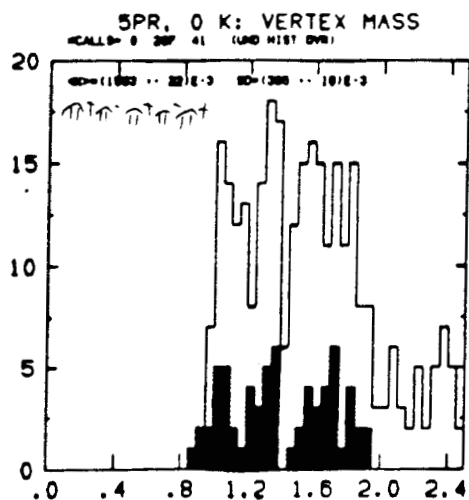


Figure 14



PRELIMINARY REPORT OF THE $B\bar{B}$ MIXING AND CP VIOLATION GROUP

T. Browder, G. Eigen, G. Gladding, J. Izen, P. Kim
J. Labs, R. Schindler, C. Simopoulos

$B^0\bar{B}^0$ MIXING PHENOMENOLOGY

A neutral strong-interaction (flavor) eigenstate will oscillate between particle and anti-particle reflecting the fact that it is not a definite weak-interaction eigenstate - the process by which it decays. Examples are of course the $K^0\bar{K}^0$ system, the $D^0\bar{D}^0$ system, and the $B^0\bar{B}^0$ system.

Formally, the time evolution is given by:

$$i\frac{d}{dt} \begin{bmatrix} B^0 \\ \bar{B}^0 \end{bmatrix} = \begin{bmatrix} M - i\Gamma/2 & M_{12} - i\Gamma_{12}/2 \\ M_{12} - i\Gamma_{12}/2 & M - i\Gamma/2 \end{bmatrix} \begin{bmatrix} B^0 \\ \bar{B}^0 \end{bmatrix}$$

Assuming CPT and T invariance,^[1] the matrix has four real parameters Γ, Γ_{12}, M , and M_{12} . Diagonalizing the matrix and solving for the eigenvalues and eigenvectors (the states B_1 and B_2 , of definite mass and lifetime) one finds:

$$B_1(t) = \frac{1}{\sqrt{2}} [B^0(t) + \bar{B}^0(t)]$$

$$B_2(t) = \frac{1}{\sqrt{2}} [B^0(t) - \bar{B}^0(t)]$$

$$M_1 = M - M_{12} \quad \Gamma_1 = \Gamma - \Gamma_{12}$$

$$M_2 = M + M_{12} \quad \Gamma_2 = \Gamma + \Gamma_{12}$$

$$\Delta M = M_2 - M_1 = 2M_{12} \quad \Delta\Gamma = \Gamma_2 - \Gamma_1 = 2\Gamma_{12}$$

If a pure B^0 state is produced at $t = 0$, the resulting time evolution is given by:

$$I(B^0(t)) = \frac{1}{4}(e^{-\Gamma_1 t} + e^{-\Gamma_2 t} + 2e^{-\Gamma t} \cos \Delta M t)$$

$$I(\bar{B}^0(t)) = \frac{1}{4}(e^{-\Gamma_1 t} + e^{-\Gamma_2 t} - 2e^{-\Gamma t} \cos \Delta M t)$$

Oscillations are thus induced by $\Delta\Gamma$ from differences in the real decay widths, or from ΔM from the mass matrix itself. For experiments that do not measure time evolution, one integrates the expressions for intensity over time, yielding:

$$I(B^0) = \int I(t) dt = \frac{1}{4} \left\{ \frac{1}{\Gamma_1} + \frac{1}{\Gamma_2} + \frac{2\Gamma}{\Gamma^2 + (\Delta M)^2} \right\}$$

$$I(\bar{B}^0) = \int \bar{I}(t) dt = \frac{1}{4} \left\{ \frac{1}{\Gamma_1} + \frac{1}{\Gamma_2} - \frac{2\Gamma}{\Gamma^2 + (\Delta M)^2} \right\}$$

Then, the mixing probability χ is defined:

$$\chi = \frac{I(\bar{B}^0)}{I(B^0) + I(\bar{B}^0)} = \frac{\text{mixed}}{\text{unmixed} + \text{mixed}} = \frac{(\Delta M)^2 + (\frac{\Delta\Gamma}{2})^2}{2(\Delta\Gamma^2 + (\Delta M)^2)}$$

Defining $x = \Delta M/\Gamma$ and $y = \Delta\Gamma/2\Gamma$ then

$$\chi = \frac{x^2 + y^2}{2(x^2 + 1)}$$

Often, the variable r is used in place of χ :

$$r = \frac{I(\bar{B}^0)}{I(B^0)} = \frac{\text{mixed}}{\text{unmixed}} = \frac{x^2 + y^2}{2 + x^2 - y^2}$$

The variable χ ranges from 0 to 1/2 and r ranges from 0 to 1.

THEORETICAL UNDERPINNINGS - THE IMPORTANCE OF $B^0\bar{B}^0$ MIXING

The importance of the measurement of $B_d\bar{B}_d$ and $B_s\bar{B}_s$ mixing lies in the fact that mixing probes the effect of heavier quarks in the 2^{nd} order weak interaction - box graphs, that couple to the b-quark, as shown in Figure 1.

Using the Maiani representation of the CKM matrix to order λ^3 , we define

$$V_{ij} = \begin{bmatrix} V_{ud} & V_{us} & V_{ub} \\ V_{cd} & V_{cs} & V_{cb} \\ V_{td} & V_{ts} & V_{tb} \end{bmatrix} = \begin{bmatrix} 1 - \lambda^2/2 & \lambda & A\lambda^3\rho e^{i\phi} \\ -\lambda & 1 - \lambda^2/2 & A\lambda^2 \\ A\lambda^3(1 - \rho)e^{-i\phi} & -A\lambda^2 & 1 \end{bmatrix},$$

where $\lambda = \sin \theta_c \approx 0.22$.

Mixing directly probes V_{td} , V_{ts} and M_t . Strange, charm and beauty decays provide information on other elements of the matrix. The upper left corner is probed by charm and strange decays and give us $\lambda \approx 0.22$ to about 15% precision. By combining the average B lifetime ($\tau_B \approx 1.11 \pm 0.15$ ps) with the average B semimuonic branching ratio ($\sim 0.10 \pm 0.01$) and a guess at the mass of the b-quark, the value of $A\lambda^2$ is accessible; by dividing by λ^2 , we obtain $A = 1.05 \pm 0.17$. Finally, the limits from CLEO and ARGUS on charmless B decays ($\frac{|V_{bu}|}{|V_{bc}|} \leq 0.13$) give $\lambda\rho$ which then imply $\rho \leq 0.6$. The recent observation of excess events in the endpoint spectrum of semileptonic B decays from CLEO and ARGUS suggest that $\frac{|V_{bu}|}{|V_{bc}|} \sim 0.1 \pm 0.03$. This implies a value of $\rho \sim 0.45 \pm 0.15$. We will return shortly to the implications of these values for mixing of B_d and B_s mesons.

EXPECTATIONS FOR MIXING

For mixing arising from the mass matrix (ΔM), the twelve box diagrams of Figure 1 must be evaluated for B_d and B_s . The result may be expressed^[2] for the mixing of the B_q^0 meson ($q=d$ or s) as:

$$\frac{\Delta M_q}{\Gamma_q} = \frac{G_F^2 M_t^2}{6\pi^2} \tau_{B_q} B_{B_q} f_{B_q}^2 M_{B_q} \left[|V_{tb} V_{tq}^*|^2 \frac{A(\zeta)}{\zeta} \eta_{QCD} + Q \right]$$

The terms in the expression above have the following origins and uncertainties for B_s and B_d :

- 1) The species lifetimes, τ_{B_d} and τ_{B_s} , probably deviate less than about 20% from the average B lifetime of about 1.11 ps since the spectator picture of heavy quark decay probably is more accurate a representation of B decay, than D decay. The values of the lifetimes will be independently measured by SLD and perhaps by LEP, by the time a B_s mixing measurement is made. The value of the relative B_d and B_u lifetimes will be known from CLEO, through their relative semileptonic branching ratios, probably within 1.5 years. This will already help to assess how large a difference in B_d and B_s lifetimes, to expect.
- 2) The masses of the species (M_{B_q}) will be accurately determined either by CLEO, SLD or LEP. This factor of mass comes from the evaluation of the second order weak matrix element (see item (3), below).
- 3) The quantity $B_{B_q} f_{B_q}^2$ [.....] comes from the evaluation of the second order hadronic weak matrix element (the matrix element of the product of two hadronic currents J_μ) under the vacuum insertion approximation:

$$\langle B_q^0 | J_\mu J^\mu | \bar{B}_q^0 \rangle = |\langle B_q^0 | J_\mu | 0 \rangle|^2 B_{B_q} = \frac{4}{3} M_{B_q} f_{B_q}^2 B_{B_q}$$

The B parameter, B_{B_q} , is just the ratio of the true matrix element to the matrix element evaluated under the vacuum insertion approximation. The B parameter effectively represents the internal QCD corrections in the box-diagrams. The vacuum insertion approximation leaves us with the square of the axial vector current of the meson to the vacuum; this is evaluated from the Van Royen - Weisskopf definition of the weak decay constant f_M of a meson M_q appearing in the pure leptonic decay of the meson. The pure leptonic decays of heavy mesons will thus ultimately provide us with information on the f_M .

No pure leptonic decays of any heavy meson have yet been experimentally measured in spite of their great theoretical interest. The partial width for these decays is proportional to the product of the weak hadronic current (J_{had}) and the leptonic current (J_l). The axial vector current J_{had} is fully defined by the Van Royen - Weisskopf equation for the D^+ , for example by $\langle 0 | J_{had}^\alpha | D^+ \rangle = i V_{cd} P^\alpha f_D$ in terms of the weak decay constant f_D . The weak decay constant f_D is thus a fundamental constant characterizing the overlap of the c and d(s) quarks in the $D^+(D_s)$ and contains

the QCD corrections which modify the decay vertex. In potential models it is easy to write f_D in terms of the wavefunctions of the heavy and light quarks and the meson mass:

$$f_D^2 = \frac{|\Psi(0)|^2}{M_D}.$$

Precision measurements of the leptonic decays of the D^+ and D_s are most likely to be made earliest, and will allow the unambiguous determination of f_D or f_{D_s} :^[3]

$$B(D^+ \rightarrow \mu^+ \nu) = \frac{G_F^2}{8\pi} f_D^2 \tau_D M_D m_\mu^2 |V_{cd}|^2 \left(1 - \frac{m_\mu^2}{M_D^2}\right)^2$$

where M_D is the meson mass, m_μ the muon mass, V_{cd} the KM matrix element, G_F the Fermi constant, and τ_D the lifetime of the D^+ . Naively, the decay constants scale like the square root of the inverse of the heavy quark mass (the $1/M_D$ term) times the reduced mass (μ_{cd}) to a power between one and two, ($\Psi(0)$ term). This $1/M_D$ dependence already appears to be reproduced in Lattice calculations for the D mesons.^[4] Thus, by measuring two distinct decay constants to adequate precision, say f_D and f_{D_s} , it will be possible to distinguish among models and reliably extrapolate to the B system for which precise measurements are probably unobtainable because of the small value of V_{bu} that leads to branching fractions of less than 10^{-5} . The same Lattice calculations for B mesons are considerably more difficult than for D mesons, (see Figure 2) making the early comparison of precise charm measurements of *both* f_D and f_{D_s} important benchmark tests in the development of Lattice QCD. Table I summarizes the theoretical ranges for decay constants.^[5]

Most recent estimates of the B – *parameter* for D and B mesons place it close to unity, unlike the Kaon system where values close to 0.5 are expected. Thus we take, $B_{B_d} \sim 1.0$. For the purpose of our estimates, we take $B_{B_d} f_{B_d}^2 \sim (140 \pm 40)^2 \text{ MeV}^2$, and assume that the decay constant of the B_s will be slightly larger, in analogy to the predictions for D_s and D^+ .

- 4) The term $\frac{A(\zeta)}{\zeta}$, where $\zeta = (\frac{M_t}{M_w})^2$ comes from the calculation of the box diagram, and is a slow function of the top quark mass (M_t). The function is shown in Figure 3, and can be estimated to be 0.65 ± 0.10 for $85 < M_t < 200 \text{ GeV}$.

Table I. Theoretical Estimates of Weak Decay Constants

Author	Year	Type	f_D	f_{Ds}	f_{Bd}	f_B/f_D
Mathur and Yamawaki	(81)	QCD SUM RULE	192	232	241	1.3
Aliev and Eletsii	(83)	QCD SUM RULE	170	-	132	0.8
Shifman	(87)	QCD SUM RULE	170	-	110/130	0.7/0.8
Narison	(87)	QCD SUM RULE	173	-	187	1.1
Dominguez and Paver	(87)	QCD SUM RULE	220	270	140/210	0.6/1.0
Reinders	(88)	QCD SUM RULE	170	-	132	0.8
Kraseman	(80)	POTENTIAL	150	210	125	0.8
Suzuki	(85)	POTENTIAL	138	-	89	0.6
Godfrey and Isgur	(85-86)	POTENTIAL	234	391	191	0.8
Bernard	(88)	LATTICE	174	234	105	0.6
DeGrand and Loft	(88)	LATTICE	134	157	-	-
Golowich	(80)	BAG	147	166	-	-

- 5) The term η_{QCD} contains the lowest order short distance corrections to the weak hamiltonian. Formally, η_{QCD} can be written for $M_b < M_t < M_W$:

$$\eta_{QCD} = \left[\frac{\alpha_s(b)}{\alpha_s(t)} \right]^{-6/23} \times \left[\frac{3}{2} \left(\frac{\alpha_s(t)}{\alpha_s(W)} \right)^{-4/7} - \left(\frac{\alpha_s(t)}{\alpha_s(W)} \right)^{2/7} + \frac{1}{2} \left(\frac{\alpha_s(t)}{\alpha_s(W)} \right)^{8/7} \right]$$

The value of η_{QCD} is about 0.83 ± 0.03 over most of the plausible range of M_t . For $M_t > M_W$, both η and $\frac{A(\zeta)}{\zeta}$ appear smooth functions and we expect that the product of $\frac{A(\zeta)}{\zeta} \times \eta_{QCD}$ will thus remain correct (see ref. 2).

- 7) The remaining terms are the CKM parameter products. The leading terms $V_{tb}V_{ts}^*$ or $V_{tb}V_{td}^*$ go like λ^4 and λ^6 , respectively. The other coefficients, already discussed are of order unity. Q represents the sum of nonleading contributions:

$$Q = [|V_{cb}V_{cq}^*|^2 U_1 \eta_1 + 2 |V_{cb}V_{cq}^* V_{tb}V_{tq}^*| U_3 \eta_3] \zeta$$

which take on values of about $10^{-3} \times \lambda^4$ for $q = s$ and $10^{-3} \times \lambda^6$ for $q = d$. The Q term can therefore be dropped without loss of experimental generality.

Thus, mixing from the mass matrix can be written:

$$\begin{bmatrix} \frac{\Delta M}{\Gamma}(B_s) \\ \frac{\Delta M}{\Gamma}(B_d) \end{bmatrix} \propto \tau_{B_q} M_t^2 M_{B_q} f_{B_q}^2 \begin{bmatrix} A\lambda^4 \\ A^2\lambda^6(1 - \rho e^{-i\phi}) \end{bmatrix}$$

The contribution from the width $\Delta\Gamma$, is suppressed:

$$\begin{bmatrix} \frac{\Delta\Gamma}{\Gamma}(B_s) \\ \frac{\Delta\Gamma}{\Gamma}(B_d) \end{bmatrix} \propto M_b^2 \begin{bmatrix} \lambda^4 \\ \lambda^6 \end{bmatrix}$$

and thus, can usually be ignored.

Thus, by taking the ratio of $\frac{\Delta M}{\Gamma}$ for B_d and B_s mixing, we achieve a simplification:

$$\left[\frac{\frac{\Delta M}{\Gamma}(B_s)}{\frac{\Delta M}{\Gamma}(B_d)} \right] = \frac{x_d}{x_s} = \left(\frac{f_{B_d}}{f_{B_s}} \right)^2 \left(\frac{B_{B_d}}{B_{B_s}} \right) \left(\frac{\tau_{B_d}}{\tau_{B_s}} \right) \left(\frac{M_{B_d}}{M_{B_s}} \right) \left| \frac{V_{td}}{V_{ts}} \right|^2$$

Substituting where possible for $f_B \sim 1/\sqrt{(M)}$, and expected deviations in lifetimes, etc. we obtain:

$$\left[\frac{\frac{\Delta M}{\Gamma}(B_s)}{\frac{\Delta M}{\Gamma}(B_d)} \right] = (1.0 \pm 0.20) \left| \frac{V_{td}}{V_{ts}} \right|^2$$

Thus the remaining uncertainties (largely SU(3) breaking) are about 20%.

Substituting from the Maiani representation for the CKM parameters and taking the extreme value for $\cos \phi = -1$

$$|V_{td}|^2 = |A\lambda^3(1 - \rho e^{-i\phi})|^2 = A^2\lambda^6(1 + \rho^2 - 2\rho \cos \phi) \leq A^2\lambda^6(1 + \rho)^2$$

$$|V_{ts}|^2 = |-A\lambda^2|^2 = A^2\lambda^4$$

This gives us:

$$\left[\frac{\frac{\Delta M}{\Gamma}(B_s)}{\frac{\Delta M}{\Gamma}(B_d)} \right] = \frac{x_d}{x_s} \leq 0.12$$

ARGUS and CLEO have measured mixing in the B_d system, with a value presently of $r = 0.21 \pm 0.06$.^[6] Using the conversion for r to get x_d , assuming $y_d \ll x_d$, we obtain

$x_d = 0.73 \pm 0.10$, hence:

$$x_s \geq \frac{x_d}{0.12} = 5.9$$

Figure 4 shows a plot of $\frac{\Delta M}{\Gamma}(B_s)$ versus $\cos \phi$ for contours of ρ . With no restriction on $\cos \phi$ we see the lower limit of 5.9 at $\cos \phi = -1$. If $\rho \sim 0.45$ as suggested by the recent CLEO and ARGUS results on V_{bu} , then the lower limit is raised to about $x_s > 7$.

What about a constraint on the upper end? From the box diagram for B_d we can get a limit taking the safe extreme values $M_t = 200$ GeV and $B_{B_d} f_{B_d}^2 = (240)^2$ MeV². Using

$$x_d = 0.15 \left(\frac{\tau_{B_d} |V_{td}|^2}{3.3 \times 10^{-16}} \right) \left(\frac{M_t}{40} \right)^2 \left(\frac{B_{B_d} f_{B_d}^2}{(140)^2} \right)$$

and taking $x_d = 0.73 \pm 0.10$, we then obtain $|V_{td}| \geq 0.0046$. Furthermore, since $|V_{bc}| = |V_{ts}| = A\lambda^2 = 1.05 * (0.22)^2$

$$x_s = x_d \left| \frac{V_{ts}}{V_{td}} \right|^2 = x_d \left| \frac{V_{bc}}{V_{td}} \right|^2 \leq 100 \quad \text{at } 90\% C.L.$$

Another way to constrain the upper limit is by use of the K decay measurement of $|\epsilon| = (2.3 \pm 0.02) \times 10^{-3}$. Using this value of ϵ , and the central value of $A=1.05$, one can plot the value of $\cos \phi$ as a function of the top quark mass, and ρ . This is shown in Figure 5 (from G. Altarelli *et al.*) where we see that for $\rho = 0.45$, the value from recent V_{bu} measurements, one obtains some constraint on $\cos \phi$, away from the extremes of ± 1 . We note however that as the top quark mass increases, the constraint on $\cos \phi$ away from the extremes diminishes.

In conclusion, measuring mixing in the B_s system will provide direct information on the CKM matrix element V_{ts} . Information on this matrix element could also be obtained from the Penguin class of decays of the B meson ($b \rightarrow (g \text{ or } \gamma) + s$). These decays have considerably larger theoretical uncertainties, since they are generally subject to large QCD corrections, as well as to the presence of identical amplitudes occurring through rescattering processes. To evaluate the matrix element through measurements of Penguin decays would probably require concurrent measurements in the charm sector, to establish in detail an understanding of the rescattering and QCD corrections. Such a measurement could only be done at a Tau-Charm factory. The constraints from current measurements of x_d , suggest

that the value of x_s is greater than ~ 6 . It is only loosely bounded from above to a value of between 60 and 100.

THE EXPERIMENTAL CONFRONTATION WITH B_s MIXING

Two classic techniques are used experimentally to observe mixing oscillations:

- 1) **double arm correlations:** Flavor tag both B mesons in an event, and compare the expectation for mixing versus no-mixing.
- 2) **single arm correlations:** Flavor tag one B meson in an event, and use some additional piece of information such as polarization to establish the initial state. Flavor tagging can take on several forms such as leptons at high (p, p_T) from the B-jet axis (from $b \rightarrow l^- + X$), or the reconstruction (or partial reconstruction) of charm from the B meson decay cascade ($b \rightarrow c + X$).

As we will show, in the limit of full mixing, the measurement of r or χ will not be able to determine $\frac{\Delta M}{\Gamma}$. Only time evolution information coupled with flavor tagging that gives $x = \frac{\Delta M}{\Gamma}$ directly, will be sensitive to values of x greater than about 2.

The first attempt to measure $B\bar{B}$ mixing in the e^+e^- continuum, at $\sqrt{s} = 30$ GeV was by JADE^[7] They looked for the *dilution of the forward-backward asymmetry* (A_{FB}) of leptons from B decay. Briefly, the existence of $A_{FB} \neq 0$ due to interference of the photon and Z^0 propagators can be used to look for mixing, because the presence of mixing reduces the observed asymmetry. It is trivial to show^[8] that $A_{FB}(\text{observed}) = (1 - 2\chi)A_{FB}(\text{produced})$. Thus in the limit of complete mixing ($\chi = 0.5$), any produced asymmetry is reduced to an observed asymmetry of zero.

On the Z^0 resonance the differential fermion anti-fermion cross section can be written:

$$\frac{d\sigma_{f\bar{f}}}{d\cos(\theta)} \propto 1 + \cos(\theta)^2 + \frac{8}{3}A_{FB}^0 \cos(\theta)$$

This cross section is shown in Figure 6 for different values of A_{FB}^0 . The term in $\cos(\theta)$ introduces a forward backward production asymmetry whose magnitude can be written in terms of the product of the left-right asymmetries for quarks and leptons:

$$A_{FB}^0 = \frac{3}{4}A_{LR}^f A_{LR}^e$$

Note that the maximum forward backward asymmetry is 0.75, for left-right asymmetries of

unity. Figure 7 shows the left - right asymmetry for quarks and leptons versus $\sin^2(\theta_W)$. Typical values are 0.13 for leptons and 0.95 for charge 1/3 quarks, yielding a small natural $A_{FB} \sim 0.09$. If the electron beam is longitudinally polarized to a polarization $\langle \mathbf{P} \rangle$, then the left-right asymmetry of the electron is enhanced to:

$$A_{LR}^e = \frac{\langle P \rangle + A_{LR}^e}{1 + \langle P \rangle A_{LR}^e} \approx \langle P \rangle$$

Figure 8 shows what the resulting values A_{FB} are for a $q=1/3$ quark versus $\sin^2(\theta_W)$ for different values of $\langle \mathbf{P} \rangle$. For $\sin^2(\theta_W)=0.233$, Table II shows the values of A_{FB} obtainable (no radiative corrections).

Table II. A_{FB}^0 versus Polarization
(for $\sin^2(\theta_W)=0.233$)

$\langle \mathbf{P} \rangle$	A_{FB}^0
0.0	0.09
0.25	0.25
0.45	0.40
0.65	0.51
0.90	0.65

Values of polarization of 0.45 are expected to be obtained in the SLC, implying reasonably large forward-backward asymmetries.

One can think of the forward-backward asymmetry as a way of automatically tagging B^0 meson parentage, with some known error rate or purity. Figure 9 shows the signal to background ratio R , defined below, for a detector that could tag B^0 mesons within a certain (polar) solid angle $|\cos(\theta)|$. The ratio R is defined as the differential cross section integrated from 0 to $\cos(\theta)$ divided by the cross section integrated from $-\cos(\theta)$ to 0. In essence, it is the direct B^0 signal in one hemisphere, divided by the leakage signal of \bar{B}^0 mesons from the other hemisphere. In SLD, with vertexing extending to $|\cos(\theta)| < 0.75$, the value of $R \approx 2$ for 45% polarization.

Since asymmetry dilution measurements are in principle the *easiest* measurements to make, we examine the requirements on the error in χ or r to determine $x \equiv \frac{\Delta M}{\Gamma}$ to a certain

precision. Since χ and x are related, we can write

$$\chi = \frac{r}{1+r} \quad r = \frac{x^2}{2+x^2} \quad \text{hence} \quad \chi = \frac{x^2}{2(1+x^2)}$$

Figure 10 shows the consequence of this conversion from χ to x . Once x is above about 2, the error in χ must be very small, to get reasonable errors in x . Since $x_s \geq 5$ or 6, $\chi \geq 0.48$ is expected. Figure 11 shows the relationship quantitatively, where the fractional error on x is plotted as a function of χ , in contours of the fractional error in χ .

To ascertain whether dilution type measurements can be used to measure x a simple Monte Carlo is run to see how many events are required to achieve a certain error in χ for a fixed value of χ and a fixed polarization (A_{FB}). Figure 12a and 12b show two of these plots. Figure 13 attempts to summarize the information for the two cases of 45 % polarization versus no polarization at two values of χ , ($\chi_d = 0.2$ and $\chi_s = 0.4$). One concludes that if χ_s is as small as 0.4, (we believe that $0.47 - 0.48 \leq \chi_s \leq 0.50$), then with polarized e^- beams at 45%, we could *observe* an asymmetry with fewer than 100 events. Without polarization, it would require about 1000 events, to *observe* an asymmetry. Here we have defined *observe* as a 2.5 standard deviation effect, or about a 40% error. Similarly, to make a 5 standard deviation effect (20%) error, would require fewer than 300 events with polarization and about 4000 events without. **Thus 45% polarization gives about a factor of ten improvement in establishing asymmetries.** If χ is as large as 0.5, then somewhat fewer events are required (only about 200 with 45% polarization yield an error of 20%) to establish a signal.

ESTIMATES FOR DIRECTLY ESTABLISHING B_s MIXING

Several techniques will be discussed in this section, and where available, the present status of our work will be reviewed. First we will look at the double and single arm measurements that may be used to establish the presence of B_s mixing, in the presence of smaller B_d mixing. As we have shown, this will not *measure* mixing if χ is close to saturation, but it can directly establish the presence of a large mixing signal from B_s , which has hitherto not been done.

Then we will look at the question of whether time-evolution measurements are possible in SLD, to directly measure the value of $\frac{\Delta M}{\Gamma}$. The errors leading to the measurement will

be addressed in detail, as will factors leading to uncertainties in the result.

For the purpose of our studies we have used (see Table III) the following picture of Z^0 decay based on the assumption of 100K Z^0 produced.

We see that there are 2800 B_s mesons and 11200 B_d mesons in the sample, suitable for B mixing studies, if a *single - arm* technique can be utilized.

**Table III. Assumptions of Z^0 and B Fragmentation
Scaled to 100 K $Z^0 \rightarrow \text{all Events}$**

Channel	Fraction	Events
$Z^0 \rightarrow b\bar{b}$	0.14	14000
$Z^0 \rightarrow c\bar{c}$	0.11	11000
$b \rightarrow B_u$	0.40	11200
$b \rightarrow B_d$	0.40	11200
$b \rightarrow B_s$	0.10	2800
$b \rightarrow B_p$	0.10	2800
$Z^0 \rightarrow B_u \bar{B}_u + X$	0.16	2240
$Z^0 \rightarrow B_d \bar{B}_d + X$	0.16	2240
$Z^0 \rightarrow B_u \bar{B}_d + X$	0.32	4480
$Z^0 \rightarrow B_u \bar{B}_s + X$	0.08	1120
$Z^0 \rightarrow B_d \bar{B}_s + X$	0.08	1120
$Z^0 \rightarrow B_s \bar{B}_s + X$	0.01	140
$Z^0 \rightarrow B_u \bar{B}_p + X$	0.08	1120
$Z^0 \rightarrow B_d \bar{B}_p + X$	0.08	1120
$Z^0 \rightarrow B_s \bar{B}_p + X$	0.02	280
$Z^0 \rightarrow B_p \bar{B}_p + X$	0.01	140

A) Double-Arm Measurements: Double-arm measurements provide the benchmark for understanding all aspects of the detector. To overcome the problem of acceptance, the most inclusive measurement possible for B decays must be examined. The first technique we discuss is the benchmark di-lepton measurement. We look for lepton pairs originating from the B semileptonic decay, which tag the parentage of the decay (B^0 or \bar{B}^0). The rate for

$l^\pm l^\mp$ is compared with $l^\pm l^\pm$ to establish mixing. For incoherent production the dilepton ratio measured, is trivially related to the measured mixing probability χ_M as follows:

$$\frac{N(l^+l^+) + N(l^-l^-)}{N(l^+l^-)} = \frac{2\chi_M(1 - \chi_M)}{\chi_M^2 + (1 - \chi_M)(1 - \chi_M)}$$

This expression is not entirely correct because dilepton sources such as $Z^0 \rightarrow B^0 B^+ + X$ and $Z^0 \rightarrow B^- B^+ + X$ are not included. In practice, since these events cannot be separated, and we observe (with the obvious notation) a weighted sum

$$\frac{N(l^+l^+) + N(l^-l^-)}{N(l^+l^-)} = \frac{f_{00} \cdot 2\chi_M(1 - \chi_M) + f_{+0} \cdot \chi_M + f_{+-} \cdot (0)}{f_{+0} \cdot (1 - \chi_M) + f_{00} \cdot (\chi_M^2 + (1 - \chi_M)(1 - \chi_M)) + f_{+-} \cdot (1)}$$

The complications begin when one looks at what the measured mixing probability (χ_M) really is. A dilepton signature can come from either B_d or B_s mixing, or from backgrounds from light quark (u,d,s,c) jets and misidentification. Ignoring the experimental sources, we see that χ_M can be written:

$$\chi_M = f(B_d)\chi_d \frac{\langle B_d \rangle_{SL}}{\langle B \rangle_{SL}} + f(B_s)\chi_s \frac{\langle B_s \rangle_{SL}}{\langle B \rangle_{SL}} + \dots O(0) \text{ from unmixed } (\chi = 0) \text{ sources}$$

Here, $f(B_q)$ is the fraction of B_q mesons produced at the Z^0 , the ratio $\frac{\langle B_q \rangle_{SL}}{\langle B \rangle_{SL}}$, is the ratio of semileptonic branching fractions of the B_q meson, to the average semileptonic branching fraction, and χ_q is the usual mixing probability. In principle, $f(B_q)$ is measured by reconstructing a few discreet final states of B_s^0, B_d^0 and B^+ . The value of $\chi_d = 0.17 \pm 0.03$ will become better and better known as CLEO-II comes up. The ratio of lifetimes of specific final states of B_s^0, B_d^0 and B^+ will provide the ratios of semileptonic branching fractions. These will be done at SLD, or directly at CLEO-II and perhaps even at LEP.

If we assume the fractions from Table III, then $\chi_M = (0.4 \times 0.17 \times 1) + (0.1 \times \chi_s \times 1) = 0.07 + 0.1\chi_s$. How many events do we expect? The dilepton rate is the product:

$$N_{l^\pm l^\mp} + N_{l^\pm l^\pm} + N_{l^\mp l^\mp} = 0.14 \times N_{Z^0} \times Br(b \rightarrow l + X)^2 \times \epsilon_{SL}^2 \times \epsilon_{c\bar{c}}^2 \approx 10^{-3} N_{Z^0}$$

where we have assumed $Br(b \rightarrow l + X) = 0.21$, $\epsilon_{SL} = 0.8$, and the loss due to cuts rejecting secondary and primary charm, $\epsilon_{c\bar{c}} = 0.5$.

Table IV summarizes the expectations for dilepton measurements:

Table IV. Dilepton Measurements

χ_s	χ_M	$\delta\chi_M$ from $10^5 Z^0$	$\delta\chi_M$ from $10^6 Z^0$
0.5	0.12	± 0.03	± 0.010
0.4	0.11	± 0.03	± 0.010
0.3	0.10	± 0.02	± 0.007
0.2	0.09	± 0.02	± 0.007
0.0	0.07		

If the signal to background is about 1:1 as is the case typically in CLEO and ARGUS, then we see that to establish the presence of B_s mixing at the $3 - 3.5\sigma$ level, if $\chi_s = 0.5$ by the method of seeking deviations of χ_M from 0.07, would require a minimum of $10^6 Z^0$. This is not an *easy* measurement for SLD or LEP.

B) Single-Arm Measurements Exploiting Polarization: Here we use the inclusive lepton signature from $b \rightarrow l + X$ to again gain efficiency, but do not use a second lepton to tag it. Instead, we use polarization to tell if it should have arose from a B or \bar{B} meson. We measure the dilution of the forward backward asymmetry in the presence of $B\bar{B}$ mixing. Again, χ_M comes from the admixture:

$$\chi_M = f(B_d)\chi_d \frac{\langle B_d \rangle_{SL}}{\langle B \rangle_{SL}} + f(B_s)\chi_s \frac{\langle B_s \rangle_{SL}}{\langle B \rangle_{SL}} + \dots O(0) \text{ from unmixed } (\chi = 0) \text{ sources}$$

and $\chi_M \approx 0.07 + 0.1\chi_s$. The single lepton rate is given:

$$N_{l\pm} = 0.14 \times N_{Z^0} \times 2 \times Br(b \rightarrow l + X) \times \epsilon_{SL} \times \epsilon_{c\bar{c}} \approx 0.025 \times N_{Z^0}$$

Thus, one obtains about 2500 events in $10^5 Z^0$. It may be possible to improve the signal to background here by use of further vertexing on the hadron tracks, to enrich the B meson content of the events, in addition to the vetoing of charm events by p and p_t cuts. One could even try to enrich the B_s content by additional flavor requirements on the hadrons. In general, this is in the realm of B -tagging as opposed to B -vertexing, our ultimate goal.

Table V summarizes the expectations for single lepton measurements:

Table V. Single Lepton Measurements

N_{evt}	χ_s	χ_M	$A_{FB}^{observed}$ ($\langle P \rangle = 0.$)	$A_{FB}^{observed}$ ($\langle P \rangle = 0.45$)
2×10^3	0.5	0.12	0.084 ± 0.023	0.306 ± 0.0211
	0.4	0.11	0.087 ± 0.022	0.314 ± 0.0214
	0.3	0.10	0.088 ± 0.022	0.322 ± 0.0211
	0.2	0.09	0.092 ± 0.022	0.330 ± 0.0210
	0.1	0.08	0.093 ± 0.022	0.337 ± 0.0207
	0.0	0.07	0.095 ± 0.023	0.346 ± 0.0207
1×10^4	0.5	0.12	0.084 ± 0.010	0.306 ± 0.0097
	0.4	0.11	0.086 ± 0.010	0.314 ± 0.0094
	0.3	0.10	0.088 ± 0.010	0.322 ± 0.0095
	0.2	0.09	0.091 ± 0.010	0.330 ± 0.0095
	0.1	0.08	0.093 ± 0.010	0.337 ± 0.0093
	0.0	0.07	0.095 ± 0.010	0.346 ± 0.0094

The change from $\chi_s = 0 \rightarrow 0.5$ represents a 12% change in the observed forward backward asymmetry. Without polarization, even 10^4 leptons (a few $\times 10^6$ Z^0) fails to establish a signal at 1σ , while for the 45% polarization case, only two thousand events are required to establish a 2σ level effect; these can be obtained from a sample of about 10^5 Z^0 . With 10K events and polarization, one can establish a $3-4\sigma$ effect. Thus, the single arm measurement with polarization should provide an unambiguous signature of B_s mixing with a few $\times 10^5$ Z^0 .

C) Exclusive Single Arm Measurements: In the general dilepton and single lepton case, there is always the problem of admixtures. That is, leptons come from mixing and non-mixing sources. One way to address this is to tag with a lepton on one side, and a D or D_s on the other. Again we would look at the ratio of like sign to unlike sign, but now take advantage of the fact that B_d , B_s and B_u go to specific final states, preferentially as shown in Table VI: Table VI should be considered as lying on the optimistic side, since more sophisticated models (see later sections) would predict that internal quark loops will create a more uniform blend of D^+ and D^0 than is indicated for B_d decays. In particular,

$B_s \rightarrow D_s + X$ may be as small as 55%.

Table VI. Estimates For Tagging B Decays Through Charm

Channel	Branching Ratio (%)
$B_d \rightarrow D^- + X$	63%
$B_d \rightarrow D^0 + X$	37%
$B_s \rightarrow D_s + X$	dominant
$B_u \rightarrow D^0 + X$	80%

The measured parameters are:

$$R_s = \chi_M(1 - \chi_s) + \chi_s(1 - \chi_M)$$

$$R_d = \chi_M(1 - \chi_d) + \chi_d(1 - \chi_M),$$

where χ_M has the usual definition used in sections (A) and (B).

To estimate the rates we again assume that $0.025 \times N_{Z^0}$ leptons can be reconstructed from the Z^0 . We assume that

$$D^0 \rightarrow K^- \pi^+, K^- \pi^+ (\pi^0), K^- \pi^+ \pi^+ \pi^- (\pi^0), \bar{K}^0 \pi^+ \pi^- \approx (30\%) \times \bar{\epsilon} \approx 10\%$$

$$D^+ \rightarrow \bar{K}^0 \pi^+, K^- \pi^+ \pi^+, K^0 \pi^+ (\pi^0), K^0 \pi^+ \pi^+ \pi^- \approx (17\%) \times \bar{\epsilon} \approx 6\%$$

$$D_s \rightarrow \phi \pi^+, K^* K^+, K^0 K^+, S^* \pi^+ \approx (7\%) \times \bar{\epsilon} \approx 2\%$$

Using the values in Table III for production of different B_q , we obtain:

$$N(D_s + l) = (2.5 \times 10^4) \times (0.02) \times (0.1) = 50 \text{ events}/(10^6 Z^0)$$

$$N(D^- + l) = (2.5 \times 10^4) \times (0.06) \times (0.4) = 600 \text{ events}/(10^6 Z^0)$$

In passing, we note that given these efficiencies, one might consider B tagging using charmed particles, in conjunction with the polarization to look for dilution of the forward backward

asymmetry of the B . If the D^- is used to tag B_d and the D_s to tag B_s then we would expect in 10^6 Z^0 decays:

$$B_d \rightarrow (D^- + X)_{\text{tagged}} \approx 4250 \quad (1340 \text{ background from } B_u)$$

$$B_s \rightarrow (D_s + X)_{\text{tagged}} \approx 560 \quad (\text{equal background from } B_u, B_d)$$

Note that the D_s background will be *wrong-sign*, and assumes 10% for B_u or $B_d \rightarrow D_s$.

D) Conclusion of Exclusive and Semi-Inclusive Techniques:

The results of the past sections lead us to several conclusions. First, only the most inclusive analysis, namely the single lepton with polarization can establish a signal for B_s mixing of more than 3 standard deviations significance, with about 10^5 Z^0 . Without polarization, all of these techniques require in excess of 10^6 Z^0 to get to the same significance, however it is likely that with poorer vertexing and calorimetry, the number will in fact be somewhat greater than 10^6 .

THE GENERALIZATION: TOPOLOGICAL TAGGING TECHNIQUES

The conclusions of the previous section lead us to believe that in order to increase statistics, a more general technique is required that allows both the tagging of parentage by polarization, *and* a higher reconstruction efficiency for the B vertex itself. Such a technique must isolate the B vertex, to get the decay length, and the charm vertex to tag the B flavor. It is clear that such a technique must not specialize on semi-leptonic events, but must try to partially-reconstruct the B vertex with charged tracks (and perhaps some neutrals). The first experiment to apply partial reconstruction techniques to B decay was CLEO^[9]. Figure 14 shows in detail the various patterns of B decay and the finite number of cases that one must consider. Figure 15 abstracts this, and Table VII summarizes the 5 possible cases of interest.

If we specialize on the B_s exclusively, then it is easy to make a naive estimate of the required vertexing efficiency to obtain ~ 100 B_s events in 10^5 Z^0 . We see that:

$$100 = \frac{2800 B_s}{(10^5 Z^0)} \times \epsilon_{D_s} \times \epsilon_{B_s}$$

Here, the ϵ_{D_s} is the charm vertexing efficiency times the tagging efficiency for D_s . The most likely applicable tag for a D_s is a multi-kaon requirement, which preliminary data suggest occurs in less than one quarter of the D_s decays. Thus, $\epsilon_{D_s} \approx 0.25\epsilon_V$, where ϵ_V is the vertexing efficiency for a D_s , assuming the B is vertexed. The average multiplicity of B decays is 5.8 charged tracks. The average multiplicity of D_s decays is 2.5, thus leaving an average of 3.3 tracks at the B_s vertex. We can take about 20% for the number of $B_s \rightarrow D_s + \text{one prong}$, leaving $\epsilon_{B_s} \approx 0.8\epsilon_V$. Thus very roughly, we need ϵ_V , the single vertex geometric efficiency (for two or more tracks) to be $\geq \sqrt{(100/2800/0.8/0.25)} \approx 0.42$. Requiring all tracks from a D or B decay to pass through the vertex detector places an upper limit of 65-70% on ϵ_V . Since cuts will no doubt be required to improve signal to background and to separate B and D_s vertices, it is more likely that efficiencies of about one half those required above, will be obtained. That means that to achieve a signal of about 100 events, we will require a single vertex efficiency of about 0.2-0.30 and realistically about $2.5 \times 10^5 Z^0$ events.

Table VII. Reaction Summary For $B \rightarrow D$ Cascades

FOR THE PRIMARY REACTIONS				
Meson Species	Charge at B Vertex	Charge at D Vertex	Flavor Tag X	Flavor Tag Y
B_u^+	$Q_B = +1$	$Q_c = 0$		
B_d^0	$Q_B = +1$	$Q_c = -1$	$X = D^-$	
B_s^0	$Q_B = +1$	$Q_c = -1$	$X = D_s^-$	
FOR THE SECONDARY REACTIONS				
B_u^+	$Q_B = +2$	$Q_c = -1$		
B_d^0	$Q_B = 0$	$Q_c = 0$	$X = \bar{D}^0$	$Y = \text{non-strange}$
B_s^0	$Q_B = 0$	$Q_c = 0$	$X = \bar{D}^0$	$Y = \text{non-strange}$

In the next sections we examine the current status of our understanding of the problem of multi-vertexing, and the sources of error that lead to our ultimate sensitivity in $\frac{\Delta M}{\Gamma}$.

There are (at least) seven elements contributing ultimately to the uncertainty in measuring the decay length in SLD:

- i.* Measuring error in the starting point of the B flight path.
- ii.* Measuring error in the decay point of the B .
- iii.* Measuring error in returning to proper time.
- iv.* Pattern recognition of primary, B and charm vertices.
- v.* Uncertainty from model dependence.
- vi.* Error in the assignment of \mathbf{X} and \mathbf{Y} .
- vii.* Background from erroneous assignment of parentage (B_d background, and polarization limited to 45%).

Let us consider these items in turn, starting with the flight path errors. Recall that the proper decay length of the B meson is about $360 \pm 72 \mu m$, the central value from the average species lifetime and the 20% error owing to uncertainties in the lifetime of any particular species, which, however, should become better measured in the future.

Measuring error in the starting point.

The average $b\bar{b}$ event at the Z^0 produces about 12 charged tracks in the hadronization process accompanying the b - quarks. The distribution of non- B meson tracks is shown in Figure 16a. These tracks have a momentum distribution shown in Figure 16b (a mean of about 1.2 GeV), and on average, 3.6 of these tracks have momentum greater than 1 GeV, in each event (see Figure 16c). At PEP and PETRA (and LEP) the production point of the B mesons is somewhere in the beam envelope (about $100 \times 400 \mu m$). In SLC, the spot size of less than $5 \times 5 \mu m$ implies an error on the starting point which contributes to the error in the proper flight path of less than about $1 \mu m$. In fact, the event to event jitter in the beam position determination dominates. If that number is $30 \mu m$, then since $\gamma\beta \approx 7.4$ (more on this shortly), the error is still reduced in proper length to less than $5 \mu m$.

If as in LEP, the spot size is large, then the primary vertex on an event to event basis should have an error of $\delta_V^{proper} \approx \delta_{dca} \times f / \sqrt{3.6}/7.4$ where f is a fudge factor accommodating the fact that the error along the track is worse than the error orthogonal to the track

by some factor ($f \sim 5$ in SLD). Thus, if the error on distance of closest approach (δ_{dca}) is about $50 \mu m$ at 1 GeV, the contribution to the proper flight path error is still less than about $10\text{--}15 \mu m$. For the purpose of estimates, we take the SLD error from the primary vertex to be $\delta_{pri}(c\tau) = 10 \mu m$.

Measuring error in the decay points of D and B .

The fragmentation of the B mesons is hard, with $x = p_B/(M_{Z^0}/2)$ peaking at about 0.8 (see Figure 17a). For $x=0.8$, the boost factor for B mesons is thus $\gamma\beta = 7.4$. Taking the proper lifetime of 1.2 ps, we thus expect a decay length in the laboratory of 2.7 mm (Figure 17b). While the boost factor is large compared say to an asymmetric B factory ($\gamma\beta \leq 1$), one still has the problem of an equal number of hadronization tracks as B meson tracks, and the jettiness of the events making all the vertices (and tracks) line up.

The average multiplicity of charged tracks in B mesons is 5.8 ± 0.3 (see Figures 18a-c). When the charmed particle vertex of average charged multiplicity 2.5 is removed, that leaves on average 3.3 charged tracks at the B vertex. If both vertices charmed and B vertices are required, then the charm by itself must reduce the overall efficiency because of the prong counts: D^0 0-prongs account for 10%, while D^+ or D_s have about 40% of their tracks in 1-prongs.

The D and D_s from B decay have a softer x distribution (see Figure 19), with an average $x=0.3$. Since the mass is lower, this 13.8 GeV average momentum corresponds to a $\gamma\beta = 7.3$, very similar to the B meson. The D^+ is then expected to separate from the B by 2.2 mm (for a lifetime of 1.07 ps), the D^0 by 0.95 mm, (for a lifetime of 0.43 ps) and the D_s by 1.02 mm, (for a lifetime of .47 ps).

Figure 20 shows the longitudinal error on reconstructing the B meson vertex as a function of the B meson vertex multiplicity. The errors are summarized in Table VIII.

Three features are apparent in these numbers; first, the non-gaussian tails on the low multiplicity vertices are larger. Second, the errors diminish roughly as the $\frac{430 \mu m}{\sqrt{N}}$ as might naively be expected. Third, the longitudinal error should be compared with the transverse errors on individual tracks ($\sim \frac{57 \mu m}{p}$).^[10] Since these tracks average greater than 1 GeV, we see that the effective longitudinal error is about 8-10 times larger than the transverse error. For the purpose of discussion, We will use a B vertex error of $200 \mu m$ since the average

Table VIII. Longitudinal Error in B Meson Vertex

Multiplicity of Vertex	σ_L μm
2	310
3	240
4	200
5	166

multiplicity is about 4 when unusable 0 and one prong vertices are removed. For the D and D_s meson, the proper value is about $250\mu m$.

If the average value of $200\mu m$ is taken for the error in the flight path in the lab, then we can divide this by $\gamma\beta = 7.4$ to obtain an error on $\delta_{fp}(c\tau) = 27\mu m$.

Measuring error in the boost ($\gamma\beta$) of the B .

For B mesons produced at the Z^0 , the kinematic limit on momentum implies a maximum boost of about $\gamma\beta \approx 8$. The distribution is shown in Figure 21 for the true (produced) boost. While the average value is 5.8, an x cut on B mesons raises the average to about 7.4. In the cascade vertex reconstruction, we have not associated neutrals to the B meson. If the neutrals are not accounted for, the measured boost from the charged tracks deviates from the true boost, leading to an error $\delta_{\gamma\beta}(c\tau)$. The simplest method to estimate $\gamma\beta$ is to use the total momentum that is visible in the charged tracks, divided by the visible mass in the charged tracks. The reason this works is shown in Figure 22a-b, where one sees that the x carried by the visible tracks is about 0.65 times the true x , while the reconstructed mass is about .61 times the true mass. The ratio is close to unity.

The measuring error in the boost is most dramatically shown in Figure 21b, where the measured boost is plotted against the true value. The residual is shown in Figure 21c, and is seen to have a FWHM of about 0.5-0.6 which for a mean boost of 6 gives an average fractional uncertainty of 8 – 9%.

The most naive correction one can make to $\gamma\beta$ is to set all events having values greater than the kinematic limit, to a value of the kinematic limit. This reduces the tail somewhat (see Figure 22), and improves the resolution somewhat. Figure 23 shows the residuals in

bins of $\gamma\beta$. Table IX summarizes the preliminary fractional error in the boost.

Table IX. Fractional Error in $\gamma\beta$ (Preliminary)

$\gamma\beta$ Range	Fractional Error From FWHM (%)
0-2	13.0
2-4	10.6
4-6	11.0
6-7	9.7
7-8	8.5

Because of the long tails, we will take 10% as the average fractional error on $\gamma\beta$. This means that *at one proper lifetime*, the error on $\gamma\beta$ will contribute $\sim 36\mu m$ to the proper decay length. As a fractional error, it means that the smearing introduced by the $\gamma\beta$ error will be larger at longer decay lengths, hence making the early decay events most important for measuring the frequency of oscillations. To properly model this in fits, the production x distribution should be included.

The error in the boost is probably the area where we can make some improvements. For example, if a B meson were fully reconstructed, then this error would vanish. Alternately, we can try to constrain parts of the cascade sequence:

- 1.) Evaluate the quadratic ambiguity for the entire B meson. We have tried to use the B-jet direction (\hat{P}_B) as an estimator of the true B direction and the momentum vector of the tracks assigned to the B (\vec{P}_B^{obs}) to calculate a missing longitudinal momentum (\vec{P}_L) component. We conserve B mass and transverse momentum of the B meson to the jet axis, and calculate a new longitudinal momentum (\vec{P}_L). This requires an *assumption* about the missing mass, and then results in a quadratic ambiguity. If the event were a semileptonic decay, then the missing mass could be set to zero, and the fast solution chosen most of the time. Figure 24 shows this from an earlier study. We find however that for hadronic B decays, the resulting missing mass is large (typically 1-1.5 GeV) and has a broad distribution, making the selection of the solution unreliable. Presumably the B-jet direction as an estimator of the B direction is in part to blame.

- 2.) Constrain the charm vertex tracks to the D or D_s mass. This has not been tried yet, but may improve the $\gamma\beta$ error. It may also be possible to include direction information, by tying the B and D vertices together to get further improvement.

Pattern recognition of primary, B and D Cascade vertices.

The single most important feature of this technique is the requirement that the three vertices be reliably separated, and track confusions be reduced to a minimum. With the previous vertex chamber geometry (16 mm radius) and more optimistic errors^[11] it was possible to separate primary, secondary and tertiary vertices. This allowed about $2\times$ better separation power in the detector than we are now obtaining because of the recent decision to move the vertex chamber out to 25 mm. In addition, a more realistic assessment of material in the detector is incorporated in the Monte Carlo. These changes are still under study by the group and we do not want to draw final conclusions at this time. We point out the following issues however:

The primary vertex lies 2.4 mm from the B and is separated by about 10σ in laboratory vertex errors with the current vertex chamber configuration. The jettiness of the events and the large multiplicity, tends to mix the primary tracks and the B meson tracks. However, a cut on the two-dimensional normalized impact parameter^[12] can eliminate 95% of the tracks from the primary vertex while removing only 35% of the tracks from secondary vertices. We find that 46% of the B vertices have at least two tracks which pass through the vertex detector and which also pass the above requirement on the two-dimensional normalized impact parameter. The hope then is to first find these vertices and then try to assign the previously cut tracks to these vertices to make the identification of the B complete. Unfortunately, the main difficulty with this plan is that tracks from the B vertex and the daughter D vertex often make (false) vertices of good quality. In particular, we find that an algorithm which retains 90% of the true two-particle pairings from the B and D decays also creates false pairs at a rate of $1.5 \times$ that of the true pairs. Furthermore, unlike the primary/ secondary separation, we do not know the position of the B vertex; therefore, we cannot simply require tracks from the D vertex to be well separated from the B vertex. Disentangling the B and D vertices is a challenging problem for SLD (and an impossible? one for LEP). The final report will detail the SLD capabilities for both the 25mm and 16mm beampipe options, since the differences could be quite significant (corresponding to $\approx 3\sigma \rightarrow$

5σ in the secondary/ tertiary vertex separation, respectively).

We are planning the following strategy to understand the sources of problems:

- 1.) Restore original geometry at 16 mm and repeat old analysis.
 - a.) compare with the 25 mm geometry currently in place.
 - b.) try to decouple changes in material, modeling and geometry (increased radius), to understand differences.
- 2.) Rewrite pattern recognition and incorporate a vertex fitting program.
 - a.) fit primary vertex and establish candidate list of primary tracks
 - b.) remove all pairs of secondary vertices forming long lived K^0 and Λ .
 - c.) form all pairs of secondary vertices that are distinct from the primary, and fit their positions.
 - d.) combine and fit all possible multiprong geometric vertices
 - e.) make an ordered list (in χ^2 order) of mutually exclusive event hypotheses using the geometric vertex fits, demanding a cascade vertex topology constraint.
 - e.) impose physics cuts on this list to select B_s and B_d cascades, following ideas already in place.

This program of detailed analysis of the vertexing is now underway.

Uncertainty from model dependence.

While our current understanding of D^0 and D^+ decays is adequate for predicting the reconstruction rates of B_d and B_u , we have little knowledge of the D_s decays and hence the ultimate efficiency for reconstructing or partially tagging B_s . Table X summarizes the current knowledge of D_s branching fractions *relative* to $D_s \rightarrow \phi\pi^+$. We also anticipate that the semileptonic branching fraction of the D_s is about 8% for electrons and 8% for muons inclusively, based on the assumption that the partial leptonic width of the D_s is the same as the D^+ or D^0 , and the lifetimes are taken from the E691 measurements. Thus, *less than 50% of the D_s decays can be accounted for.*

Table X. D_s Branching Ratios Relative to $\phi\pi$

Decay Mode	Experiment	Result or Limit
$D_s \rightarrow \bar{K}^0 K^+$	MKIII	$0.92 \pm 0.32 \pm 0.20$
	CLEO	$0.99 \pm 0.17 \pm 0.06$
$D_s \rightarrow K^{*-} K^0$	CLEO	$1.2 \pm 0.21 \pm 0.07$
$D_s \rightarrow K^{*0} K^+$	E691	$0.87 \pm 0.13 \pm 0.05$
	ARGUS	1.44 ± 0.37
	MKIII	$0.84 \pm 0.30 \pm 0.22$
	CLEO	$1.05 \pm 0.17 \pm 0.06$
$D_s \rightarrow \rho\pi^+$	E691	< 0.08 at 90% CL
$D_s \rightarrow S^* \pi^+$	E691	$0.28 \pm 0.1 \pm .03$
$D_s \rightarrow \eta\pi^+$	E691	< 1.5 at 90 % CL
	MarkII	3.0 ± 1.1
$D_s \rightarrow \eta' \pi^+$	MarkII	4.8 ± 2.1
	NA14	5.7 ± 1.5
$D_s \rightarrow \omega\pi^+$	E691	< 0.5 at 90 CL%
$D_s \rightarrow K^{*0} K^{*+}$	NA32	2.3 ± 1.2
$D_s \rightarrow \phi\pi\pi^0$	E691	$2.4 \pm 1.0 \pm 0.5$
	NA14	< 2.6 at 90% CL
$D_s \rightarrow (K^- K^+ \pi^+)_{NR}$	E691	$0.25 \pm .07 \pm .05$
	NA32	0.96 ± 0.32
$D_s \rightarrow (\pi^- \pi^+ \pi^+)_{NR}$	E691	$0.29 \pm .09 \pm .03$
$D_s \rightarrow (\pi^- \pi^+ \pi^+ \pi^- \pi^+)_{NR}$	E691	< 0.29 at 90% CL
$D_s \rightarrow \phi\pi^- \pi^+ \pi^+$	E691	$0.42 \pm 0.13 \pm .07$
	NA32	0.39 ± 0.17
	ARGUS	$0.41 \pm 0.13 \pm 0.11$
$D_s \rightarrow (K^- K^+ \pi^+ \pi^0)_{NR}$	E691	< 2.4 at 90% CL
$D_s \rightarrow (K^- K^+ \pi^- \pi^+ \pi^+)_{NR}$	E691	< 0.32 at 90% CL
	NA32	0.11 ± 0.07

Very preliminary inclusive measurements from MARKIII suggest that the visible multiplicity of D_s decays is about one third one-prong, one half three-prong, and the balance to five-prongs. Surprisingly, the D_s decays *only* 20 – 25% of the time to one or two charged kaons. This is not unlike the D^+ , which also has a small charged kaon fraction.

In any partial reconstruction technique, we will have to separate the **X** vertex going to D_s from D^+ in order to separate the B_s from B_d , respectively. The separation of cascade

vertices (**X**) for D^+ and D_s will be complicated by the fact that the preliminary data of MarkIII suggest similarities in inclusive D^+ and D_s . The only options that we would retain to separate them are:

1. full reconstruction of D^+ or D_s - resulting in too low an efficiency.
2. requiring two opposite sign kaons (for D_s) - resulting in the loss of $\sim 70\%$ of the D_s .
3. requiring one and only one kaon of correct charge - eliminating only $\sim 75\%$ of the D^+ .
4. requiring short decay length to reduce D^+ contamination.

The results from trying each of these options will be presented in final report of the group.

To account for the effects of these observations, we have constructed a model for D^+ , D^0 and D_s decay. For the B physics groups, the new exclusive models of the D^0 , D^+ and D_s were inserted into the Lund Monte Carlo generator, version 6.3. Each model was adjusted such that the charged track multiplicity distributions and total momentum distributions which were generated complied with the distributions observed from real data sets.

In the last ten years the D^0 and D^+ mesons have been well studied; for both particles the modes that have been observed account for approximately 90% of the total branching ratio. These measurements have been incorporated into the D^0 and D^+ models. The D^0 model contains 78 exclusive final states, while the D^+ model contains 55. Figures 25a-f show the charged multiplicity and total momentum distributions for the D^0 .

For the D_s meson, the world data is still rather limited; the observed modes account for less than half of the total D_s branching ratio. Consequently the D_s model is more theoretical. The following procedure was used to construct the model:

- 1) Assuming $\Gamma(sl)$ to be the same for D^0 , D^+ and D_s , the inclusive branching ratio for the D_s semileptonic modes was constrained to 16%.
- 2) The inclusive branching ratio for the D_s leptonic modes was constrained to 2%.
- 3) The hadronic branching ratios were set relative to $\text{BR}(D_s \rightarrow \phi\pi^+)$, $\text{BR}(D_s \rightarrow \phi\pi^+)$ becoming an adjustable parameter.
- 4) Branching ratios for all two body modes, which include $D_s \rightarrow \text{Pseudoscalar} + \text{Pseudoscalar}$, $D_s \rightarrow \text{Pseudoscalar} + \text{Vector}$, $D_s \rightarrow \text{Vector} + \text{Vector}$, were obtained from

a phenomenological model by Bauer, Stech and Wirbel^[13]. The BSW model contains two quantities, a_1 and a_2 , which are treated as free parameters. For the Monte Carlo model, a_2/a_1 was determined from measurements of relative branching ratios for $D_s \rightarrow K^0 K^+$ and $D_s \rightarrow K^{*0} K^+$, while a_1 is determined by the value given for $\text{BR}(D_s \rightarrow \phi \pi^+)$.

- 5) Three body modes for $D_s \rightarrow \text{PPP}$ and $D_s \rightarrow \text{VPP}$ were selected from the quark diagrams for spectator and annihilation decays. The relative branching ratios were set proportional to phase space. Cabibbo suppressed modes were reduced by $\tan^2 \theta_c$. VPP modes were enhanced by a factor of three.
- 6) The branching ratio for $D_s \rightarrow \phi \pi^+$ was set to 3.0%.

To adjust the model essentially three parameters were used: *VVFACT*, *3BOD*, and *4BOD*. *VVFACT* is a suppression factor for the decay modes $D_s \rightarrow VV$, for which the BSW model predictions and real measurements disagree. *3BOD* and *4BOD* are scaling factors which were used to scale the sum of the branching ratios to 100%. Figures 26a-d show the effect of adjusting the *VVFACT* parameter on charged multiplicity distribution. Figures 27a-e show the charged track and momentum distributions for the D_s . The D_s modes inserted into the model, along with their branching ratios and the parameters used to determine the values, are listed in the Appendix. After correction, the true branching ratios for the modes that have been measured were inserted.

The B model we have chosen was revamped after Kirkwood to accurately reflect all our current knowledge of B meson decays. Again it is based on the philosophy of a dictionary of exclusive final states, chosen to reproduce the measured inclusive fractions, $\text{Br}(B \rightarrow D^0 + X)=48.3\%$, $\text{Br}(B \rightarrow D^+ + X)=22.1\%$, $\text{Br}(B \rightarrow D_s + X)=17.5\%$, $\text{Br}(B \rightarrow \Lambda_c + X)=7.8\%$, $\text{Br}(B \rightarrow \psi + X)=2.0\%$, and the average charged multiplicity of about 5.8 tracks. The D and D_s decays are handled by their respective models. The properties that are conserved are shown in Table XII:

Table XII. B Decay Model

Channel	Property	Value in Model
B_u	multiplicity	5.2
B_u	$\rightarrow D^0$	66%
B_u	$\rightarrow D^+$	18%
B_u	$\rightarrow D_s$	16%
B_u	$\rightarrow baryon$	8%
B_d	multiplicity	5.1
B_d	$\rightarrow D^0$	41%
B_d	$\rightarrow D^+$	39%
B_d	$\rightarrow D_s$	18%
B_d	$\rightarrow baryon$	10%
B_s	multiplicity	5.0
B_s	$\rightarrow D^0$	28 %
B_s	$\rightarrow D^+$	13 %
B_s	$\rightarrow D_s$	55 %
B_s	$\rightarrow baryon$	8.5%

Error in the assignment of X and Y. This area has not been covered yet by the group.

Background from erroneous assignment of parentage (B_d background, and polarization limited to 45%). This area has not been covered yet by the group. Some of the effects are discussed in the paper by T.W.Reeves *etal.* in these proceedings, when the errors are introduced into the unfolding procedure for the oscillation frequency.

Summary of vertexing errors. In Table XIII, we summarize the expectations for the vertex error contributions as we presently understand them.

We note that while the errors in LEP detectors having silicon two or three dimensional vertexing may ultimately reach the high end of the total error in Table XIII, (when smaller beam pipes are employed), the error associated with Pattern Recognition will remain significantly worse^[14]

Table XIII. Summary of Errors Contributing to $c\tau$

Assume $\langle \gamma\beta \rangle = 7.4$, $c\tau(B_s) = 360\mu m$

Quantity	Error in Lab	Error in $c\tau$
Event Origin	$30\mu m$	$4\mu m$
Secondary (B) Vertex	$150 \rightarrow$ $200\mu m$	$20 \rightarrow$ $27\mu m$
Boost $\gamma\beta$	10%	$36\mu m$ at 1τ
Pattern Recognition	?	?
Total Error		$45\mu m$ at 1τ $77\mu m$ at 2τ

PRELIMINARY CONCLUSIONS

In the accompanying papers by T. Reeves *et al.*, several techniques are explored to extract the oscillation frequency from a finite number of tagged events (of any origin). A detailed discussion of backgrounds is included in that report, however all detector effects and analysis cuts are not yet considered.

We have also looked at the question of fitting in a way that allows *full* utilization of the information in the event, namely the assumed polarization, the measured $c\tau$ of the B vertex, the observed beauty (B_s^0 or \bar{B}_s^0) and the polar angle of the B . For a given polarization (or A_{FB}^0), we fit the two two-dimensional plots of $\cos(\theta)$ versus $c\tau$:

$$N_{B^0} = \frac{d\sigma}{d\Omega_{B^0}} \times \cos^2\left(\frac{\Delta M}{\Gamma} \frac{t}{\tau}\right) + \frac{d\sigma}{d\Omega_{B^0}} \times \sin^2\left(\frac{\Delta M}{\Gamma} \frac{t}{\tau}\right)$$

$$N_{\bar{B}^0} = \frac{d\sigma}{d\Omega_{\bar{B}^0}} \times \cos^2\left(\frac{\Delta M}{\Gamma} \frac{t}{\tau}\right) + \frac{d\sigma}{d\Omega_{\bar{B}^0}} \times \sin^2\left(\frac{\Delta M}{\Gamma} \frac{t}{\tau}\right)$$

An example of the distribution is shown in Figure 27 for $\frac{\Delta M}{\Gamma} = 5$, and the projections in Figure 28. Any real detector will have acceptance losses both in proper lifetime, ($\tau = 500\mu m/\gamma\beta \leq 70\mu m$), and in polar angle, ($\cos\theta \leq 0.75$).

Figure 29 shows the effect of smearing in $c\tau$ as described in Table XI, and the cut at $500\mu m$ in the lab for $\frac{\Delta M}{\Gamma} = 0.7, 5, 10$, and 15 . For small values of $\frac{\Delta M}{\Gamma}$, the resolution is obviously not very important; the polarization provides the separation of forward and backward B making an extraction of an oscillation possible. For about 100 detected events and $\frac{\Delta M}{\Gamma} = 5$ we can use this technique to obtain an error of about 5-10% on the oscillation frequency. An example fit is shown in Figure 30. To obtain a similar error for $\frac{\Delta M}{\Gamma} = 10$ will require considerably more statistics and is considerably less certain, because resolution effects and background levels start to become more important, as can be seen in Figure 29.

In conclusion then, we believe we can establish a non-zero χ_s using a single arm technique with 45% beam polarization from a sample of 10^5 Z^0 's. Without polarization, more than 10^6 Z^0 's would be required. It is quite possible, though, that CLEO-II will make this measurement before we run. However, a measurement of χ_s does not automatically translate into the theoretically important $x_s \equiv (\frac{\Delta M}{\Gamma})_s$ if $\chi_s \approx 0.5$, as expected. In this case, x_s can only be determined from a direct time evolution measurement. The small beam size, the beam polarization, and the excellent resolution of the SLD vertex detector all combine to give SLD a significant advantage in this measurement. Pattern recognition problems (the confusion of tracks from the B and D vertices) are severe and must be addressed quantitatively to determine whether the measurement is possible, independent of luminosity considerations. Further, the vertex resolution effectively limits the value of x_s which can be probed. We estimate our resolution limit to be on the order of $x_s \approx 15$. At this limit, several thousand observed events would be required, while if $x_s \approx 5$, a few hundred observed events will be needed to determine x_s .

REFERENCES

1. The case of CP violation in the Standard Model is treated separately by S. Manly, in these proceedings.
2. G. Altarelli, **Particle Physics**, ed. Maurice Levy *et al.*, Cargese (1987).
3. E. D. Commins and P. H. Bucksbaum, *Weak Interactions of Leptons and Quarks*, (Cambridge University Press, Cambridge, UK, 1983), pp. 155-156.
4. A. Soni, private communication and
C. Bernard *et al.*, Phys.Rev. D38 (1988) 3540.
5. H. Krasemann, Phys. Lett 96B (1980) 397.
E. Golowich, Phys. Lett. 91B (1980) 271.
V. Mathur *et al.*, Phys. Lett. 107B (1981) 127.
T. Aliev *et al.*, Sov. J. Nucl.Phys. 38 (1983) 6.
M. Suzuki, Phys.Lett. 142B (1984) 207.
S. Godfrey *et al.*, Phys. Rev. D32 (1985) 189.
S. Godfrey, Phys. Rev. D33 (1986) 1391.
C. Dominguez *et al.*, Phys. Lett. 197B (1987) 423.
L. Reinders, Phys. Rev. D38 (1988) 947.
C. Bernard *et al.*, Phys. Rev. D38 (1988) 3540.
T. DeGrand *et al.*, Phys. Rev. D38 (1988) 954.
6. M. Danilov, Talk presented at the International Symposium on Lepton Photon Physics, Stanford CA, August (1989).
7. Jade Collaboration, Phys. Lett. 146B, 437 (1984).
8. R.H.Schindler, Talk presented at the SLD Physics Retreat, Kirkwood, CA (1989).
9. CLEO used partial reconstruction to look for $B \rightarrow D\rho$ and other two-body and quasi two-body decay modes.
10. J. Richman, these proceedings.

11. W. Atwood, SLAC-PUB-5047 (1989).
W. Atwood, SLAC-PUB-4827 (1988).
W. Atwood, SLAC-PUB-4668 (1988).
12. G. Gladding, Talk presented at the at the SLD Physics Retreat, Kirkwood, CA (1989).
13. Bauer, Stech and Wirbel, Z. Phys. C 34, 103 (1987).
14. P. Roudeau, Preprint LAL89-21, May 1989.

APPENDIX

D_s Decay Model

Parameters in D_s Model:

```
-----
a2/a1: -0.550
PhiPiBR: 3.000
vvfact: 0.200
3bod1: .204E-2
3bod2: .840E-3
4bod: 1.200
tan2th: 0.052
vpp: 3.000
```

Ds Mode	Calc. BR	Meas. BR	Parameters Used
-----	-----	-----	-----
PP Modes:			
1 ETA PI+	4.500	4.500*	PhiPiBR
2 ETA' PI+	4.500	16.200	PhiPiBR
3 KO PI+	0.288	0.630*	PhiPiBR
4 K+ KOBAR	2.441	2.760	PhiPiBR a2/a1
5 K+ PIO	0.044		PhiPiBR a2/a1
6 ETA K+	0.022		PhiPiBR a2/a1

sum = 11.795

PV Modes:			
17 ETA RHO+	5.880		PhiPiBR
18 ETA' RHO+	1.688		PhiPiBR
19 PHI PI+	3.000		PhiPiBR
20 KO RHO+	0.555		PhiPiBR
21 KO* PI+	0.159		PhiPiBR
22 K+ KOB*	2.908	2.790	PhiPiBR a2/a1
23 K+* KOBAR	1.118		PhiPiBR a2/a1
24 K+ OMEGA	0.076		PhiPiBR a2/a1
25 K+* PIO	0.026		PhiPiBR a2/a1
26 ETA K+*	0.075		PhiPiBR a2/a1
27 ETA' K+*	0.088		PhiPiBR a2/a1
28 PHI K+	0.001		PhiPiBR a2/a1

sum = 15.573

PA Modes:

40 F0975 PI+	1.512	0.840	PhiPiBR
50 ETA A1+	1.428		PhiPiBR
51 KO A1+	0.203		PhiPiBR
52 K+ A10	0.029		PhiPiBR a2/a1

sum = 3.173

VV Modes:

55 PHI RHO+	3.780		PhiPiBR vvfact
56 KO* RHO+	0.216		PhiPiBR vvfact
57 K++ KOB*	1.246		PhiPiBR a2/a1 vvfact
58 K++ RHOO	0.032		PhiPiBR a2/a1 vvfact
59 K++ OMEGA	0.031		PhiPiBR a2/a1 vvfact
60 PHI K++	0.024		PhiPiBR a2/a1 vvfact

sum = 5.328

SL Modes:

70 ETA E+ NU	1.880		
71 ETA' E+ NU	1.920		
72 PHI E+ NU	3.800		
73 KO E+ NU	0.200		
74 KO* E+ NU	0.200		
75 ETA MU+ NU	1.070		
76 ETA' MU+ NU	2.740		
77 PHI MU+ NU	3.800		
78 KO MU+ NU	0.200		
79 KO* MU+ NU	0.200		

sum = 16.010

L Modes:

sum = 2.000

PPPCA Modes:

90 PI+ K+ K-	0.924	0.960*	PhiPiBR 3bod1
91 PI+ KO KOBAR	0.907		PhiPiBR 3bod1
92 PIO KOBAR K+	0.921		PhiPiBR 3bod1
93 ETA K+ KOBAR	0.298		PhiPiBR 3bod1

sum = 3.050

PPPCS Modes:		
103 KO PI+ PIO	0.084	PhiPiBR 3bod1 tan2th
104 K+ PI+ PI-	0.085	PhiPiBR 3bod1 tan2th
105 K+ PIO PIO	0.085	PhiPiBR 3bod1 tan2th
106 K+ KO KOBAR	0.019	PhiPiBR 3bod1 tan2th
107 K+ K- K+	0.020	PhiPiBR 3bod1 tan2th

sum = 0.293

PPPAN Modes:		
110 PI+ PIO PIO	1.022	PhiPiBR 3bod2
111 PI+ PI+ PI-	1.016	0.870 PhiPiBR 3bod2

sum = 2.038

VPPCA Modes:		
120 PHI PI+ PIO	1.434	PhiPiBR 3bod1 vpp
121 K-* K+ PI+	0.758	PhiPiBR 3bod1 vpp
122 K+* K- PI+	0.758	PhiPiBR 3bod1 vpp
123 RHO+ KO KOBAR	0.210	PhiPiBR 3bod1 vpp
124 RHO+ K+ K-	0.226	PhiPiBR 3bod1 vpp
125 KO* KOBAR PI+	0.745	PhiPiBR 3bod1 vpp
126 KOB* KO PI+	0.745	PhiPiBR 3bod1 vpp
127 RHO0 KOBAR K+	0.218	PhiPiBR 3bod1 vpp
128 OMEGA KOBAR K+	0.193	PhiPiBR 3bod1 vpp
129 KOB* K+ PIO	0.769	PhiPiBR 3bod1 vpp
130 K+* KOBAR PIO	0.755	PhiPiBR 3bod1 vpp

sum = 6.810

VPPCS Modes:		
131 RHO0 PI+ KO	0.064	PhiPiBR 3bod1 vpp tan2th
132 RHO0 K+ PIO	0.066	PhiPiBR 3bod1 vpp tan2th
133 RHO+ KO PIO	0.065	PhiPiBR 3bod1 vpp tan2th
134 RHO+ K+ PI-	0.064	PhiPiBR 3bod1 vpp tan2th
135 RHO- K+ PI+	0.064	PhiPiBR 3bod1 vpp tan2th
136 OMEGA K+ PIO	0.063	PhiPiBR 3bod1 vpp tan2th
137 OMEGA KO PI+	0.062	PhiPiBR 3bod1 vpp tan2th
138 PHI KO PI+	0.019	PhiPiBR 3bod1 vpp tan2th
139 PHI K+ PIO	0.020	PhiPiBR 3bod1 vpp tan2th
140 K+* PI+ PI-	0.109	PhiPiBR 3bod1 vpp tan2th

141 K+* PIO PIO	0.110	PhiPiBR 3bod1 vpp tan2th
142 K+* KO KOBAR	0.002	PhiPiBR 3bod1 vpp tan2th
143 K+* K+ K-	0.002	PhiPiBR 3bod1 vpp tan2th
144 KO* PI+ PIO	0.110	PhiPiBR 3bod1 vpp tan2th
145 KO* K+ KOBAR	0.002	PhiPiBR 3bod1 vpp tan2th
146 KOB* K+ KO	0.002	PhiPiBR 3bod1 vpp tan2th
147 K-* K+ K+	0.002	PhiPiBR 3bod1 vpp tan2th

sum = 0.826

VPPAN Modes:

150 RHO+ PIO PIO	1.188	PhiPiBR 3bod2 vpp
151 OMEGA PI+ PIO	1.147	PhiPiBR 3bod2 vpp
152 RHO0 PI+ PIO	1.181	PhiPiBR 3bod2 vpp
153 RHO+ PI+ PI-	1.174	PhiPiBR 3bod2 vpp
154 RHO- PI+ PI+	1.174	PhiPiBR 3bod2 vpp

sum = 5.864

MB Modes:

200 PHI PI+ PI- PI+	1.512	1.230* PhiPiBR 4bod
201 ETA PI+ PI- PI+	2.232	PhiPiBR 4bod
202 ETA' PI+ PI- PI+	2.232	PhiPiBR 4bod
203 PHI PI+ PIO PIO	2.232	PhiPiBR 4bod
204 ETA PI+ PIO PIO	2.232	PhiPiBR 4bod
205 ETA' PI+ PIO PIO	2.232	PhiPiBR 4bod
206 K+ KOBAR PI+ PI-	1.224	PhiPiBR 4bod
207 K+ KOBAR PIO PIO	1.224	PhiPiBR 4bod
208 PHI PI+ PI- PI+ PIO	0.756	PhiPiBR 4bod
209 ETA PI+ PI- PI+ PIO	1.116	PhiPiBR 4bod
210 ETA' PI+ PI- PI+ PIO	1.116	PhiPiBR 4bod
211 PHI PI+ PIO PIO PIO	0.756	PhiPiBR 4bod
212 ETA PI+ PIO PIO PIO	1.116	PhiPiBR 4bod
213 ETA' PI+ PIO PIO PIO	1.116	PhiPiBR 4bod
214 K+ KOBAR PI+ PI- PIO	0.612	PhiPiBR 4bod
215 K+ KOBAR PIO PIO PIO	0.612	PhiPiBR 4bod

sum = 22.320

Total Multiplicity = 2.436
Total Branching Ratio = 95.079

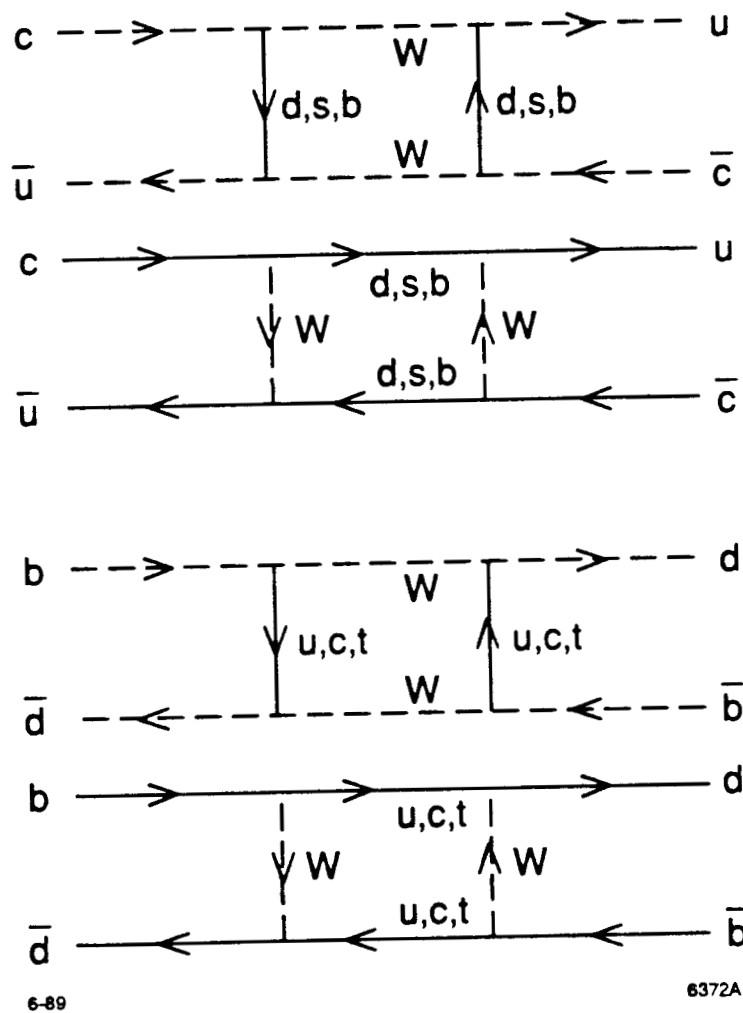


Figure 1. Box diagrams for $B^0\bar{B}^0$ and $D^0\bar{D}^0$ mixing.

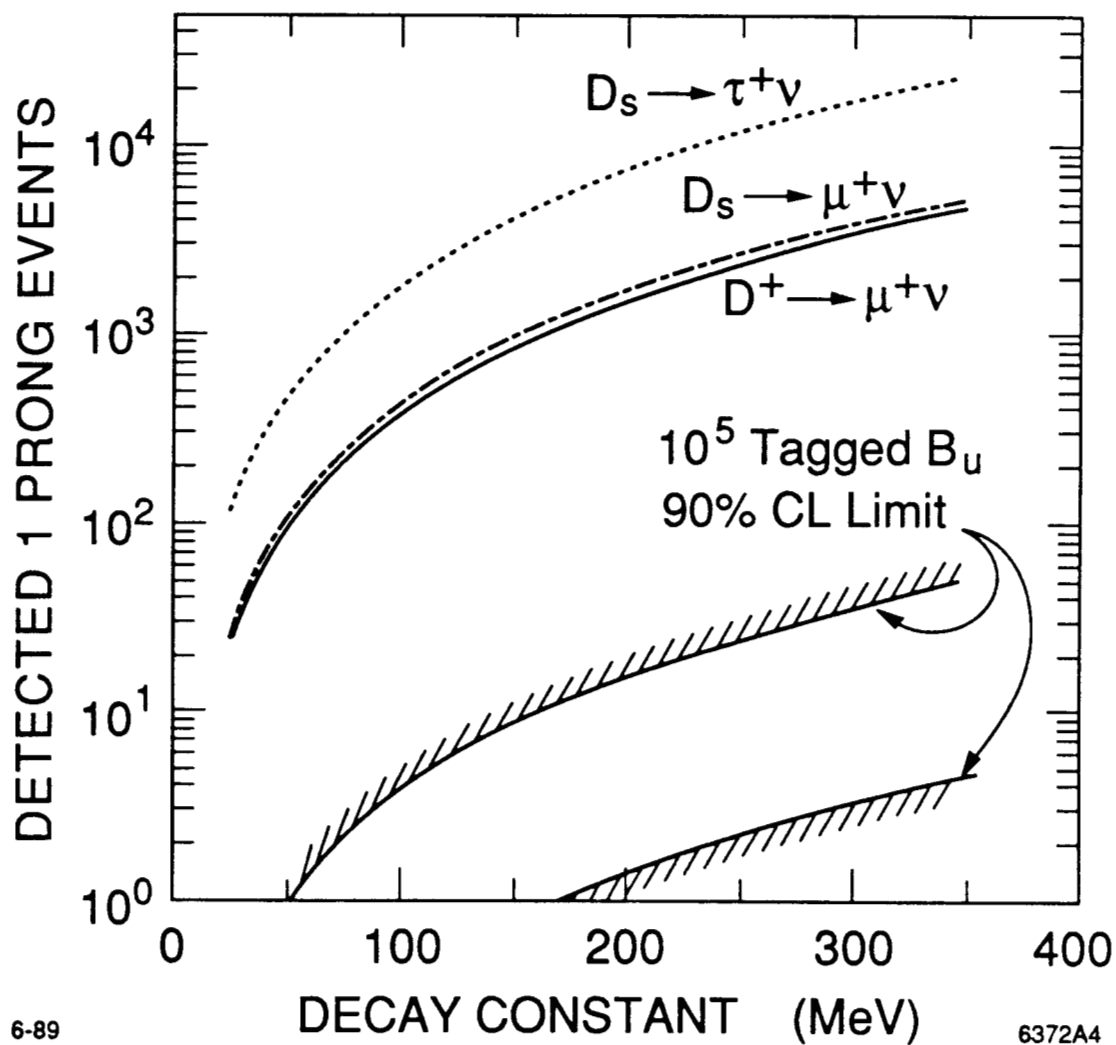


Figure 2. Lower curves represent 90% limits on the number of detected events for $B_u \rightarrow \tau \nu$ as a function of the value of f_B .

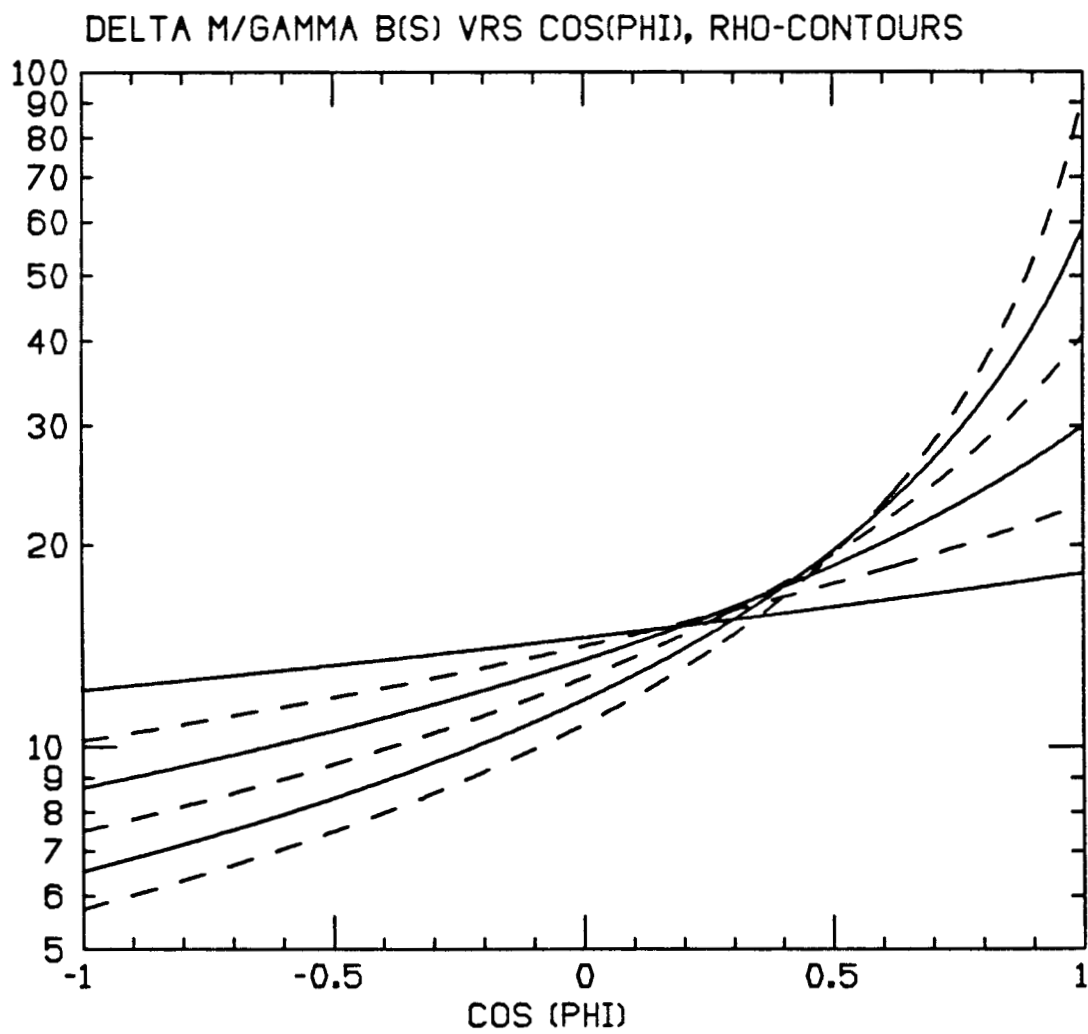


Figure 4. $\frac{\Delta M}{\Gamma}$ versus $\cos(\phi)$ in contours of ρ . The lowest curve corresponds to $\rho = 0.6$, and moves upward to $\rho = 0.1$ in steps of 0.1.

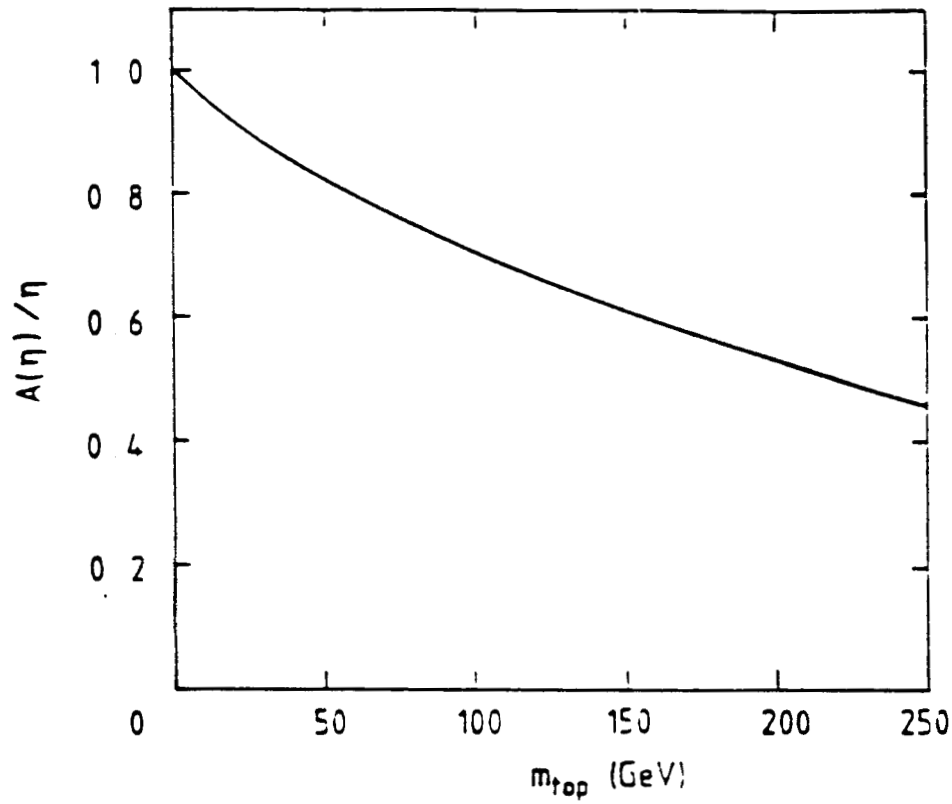


Figure 3. $\frac{A(\zeta)}{\zeta}$ versus the top-quark mass.

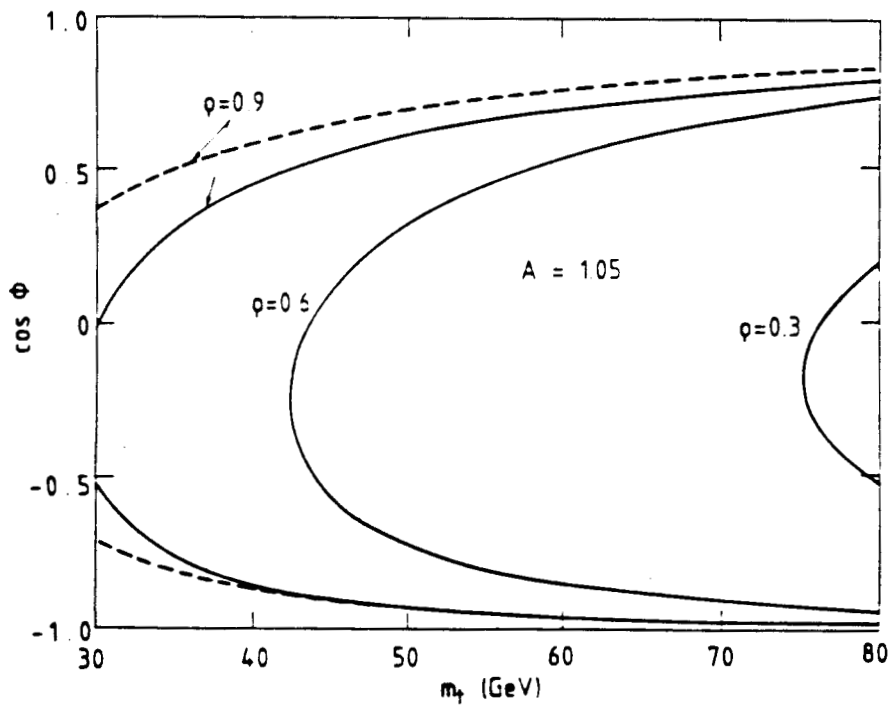


Figure 5. $\cos(\phi)$ versus the mass of the top-quark; contours of ρ for $A=1.05$, (from the measurement of ϵ in K decays, see Altarelli *et al*).

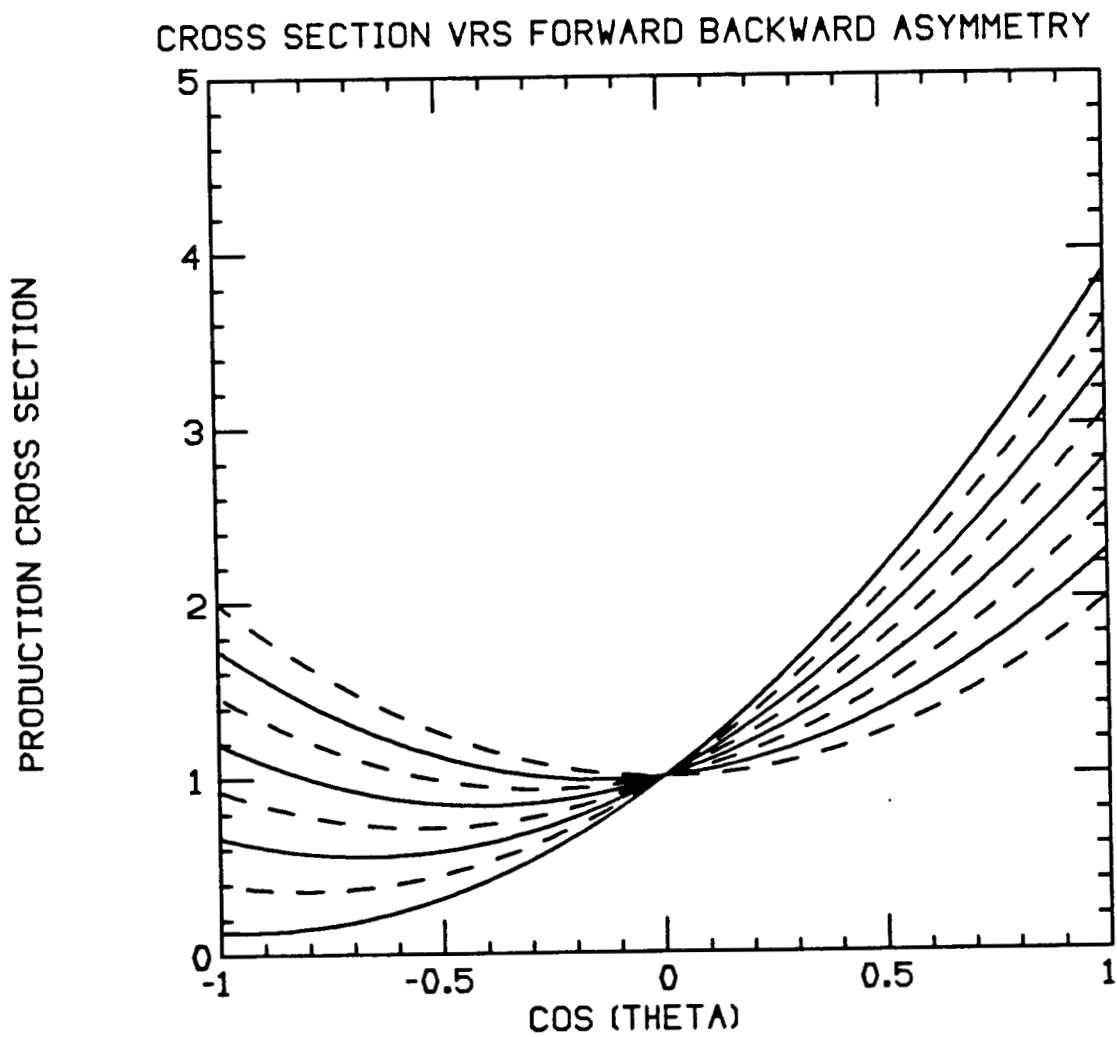


Figure 6. The differential cross section for fermion pair production versus $\cos(\theta)$. Contours of A_{FB} from $0.0 \rightarrow 0.7$ in steps of 0.1.

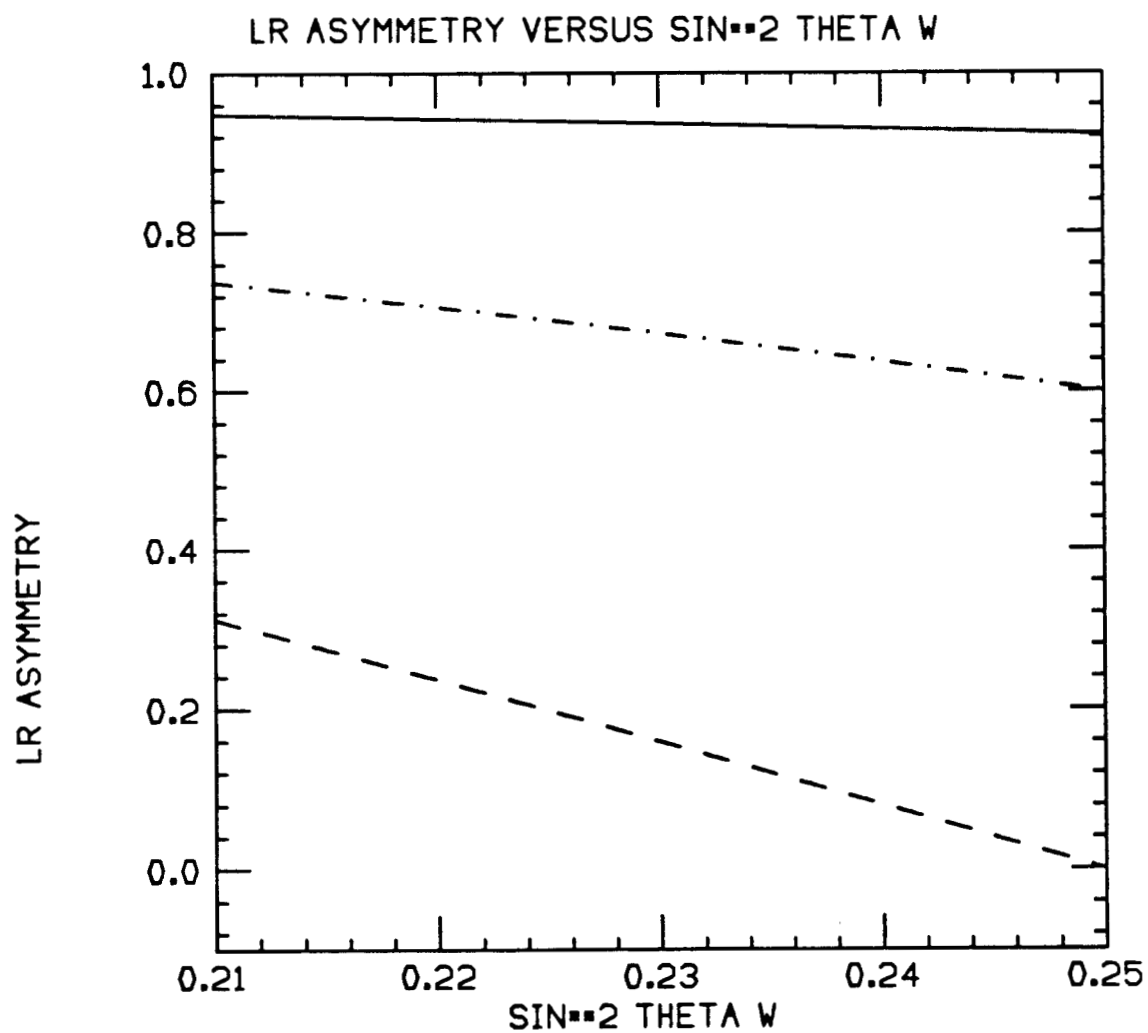


Figure 7. A_{LR} for $q=1/3$ (solid), $q=2/3$ (dotdash) and leptons (dashed) versus $\sin^2(\theta_W)$

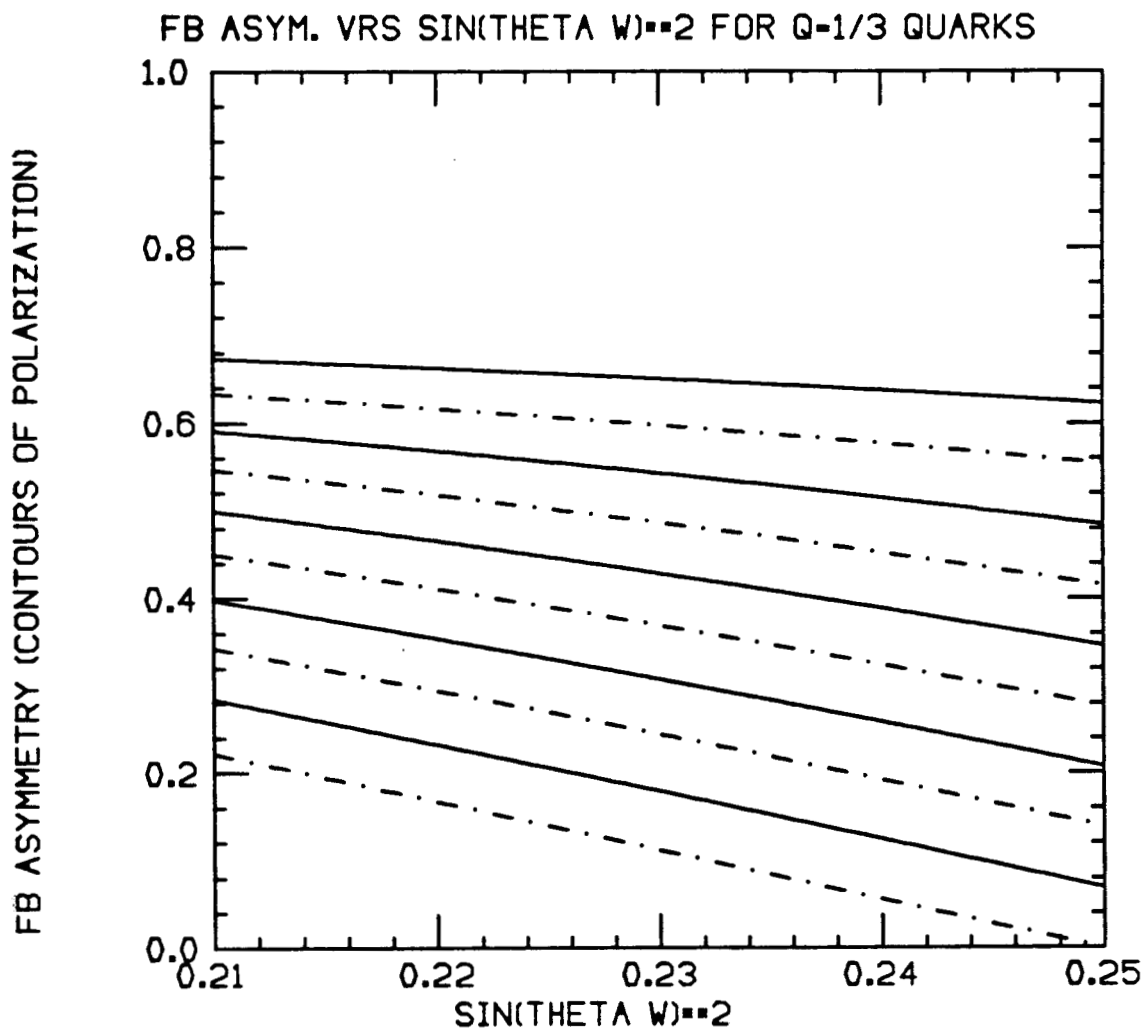


Figure 8. A_{FB} versus $\sin^2(\theta_W)$ for $q=1/3$ quarks; contours of polarization from $P=0$ (bottom curve) to $P=1$ (top curve).

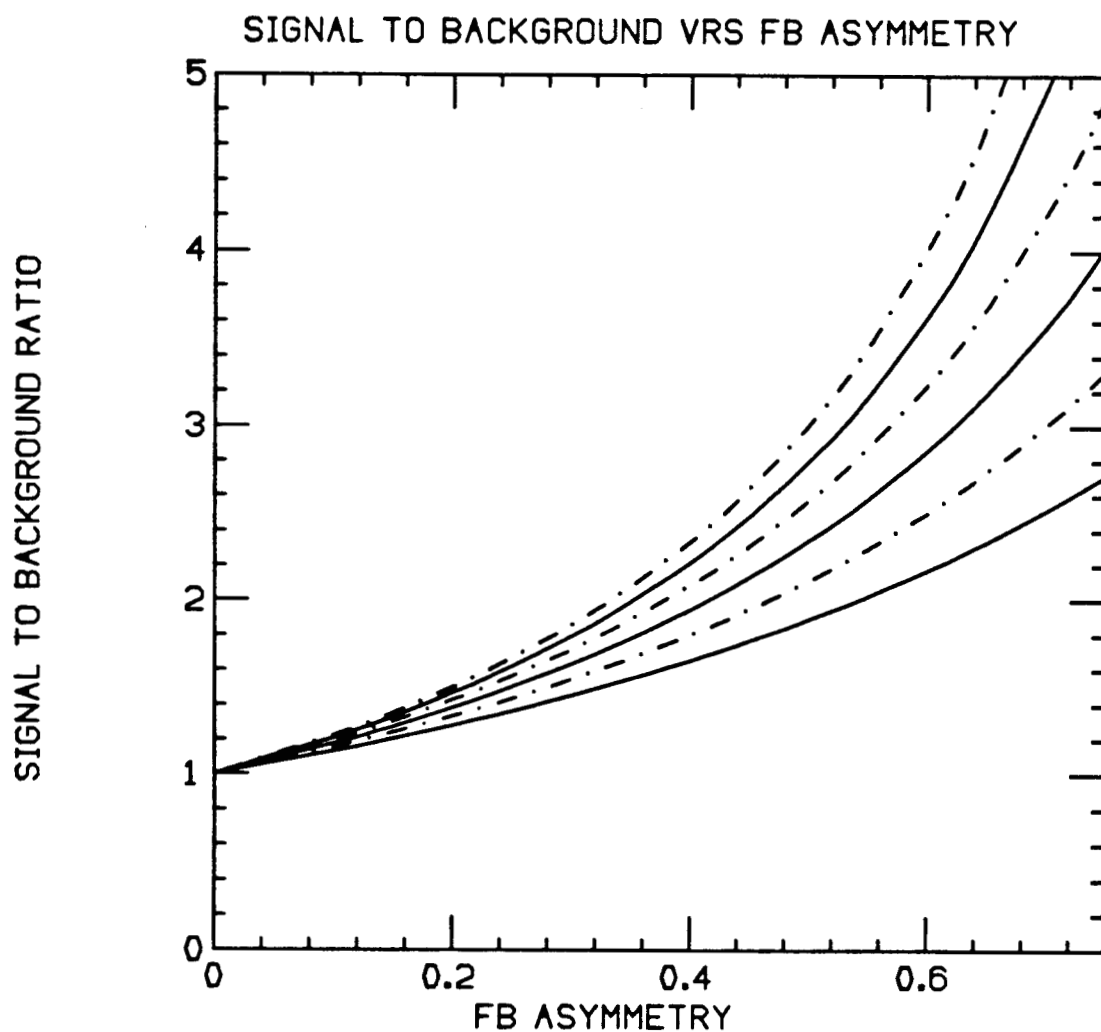


Figure 9. Signal to background ratio (see text) versus A_{FB} ; contours of acceptance in $|\cos(\theta)|$ from 0.5 (bottom curve) to 1.0 (top curve).

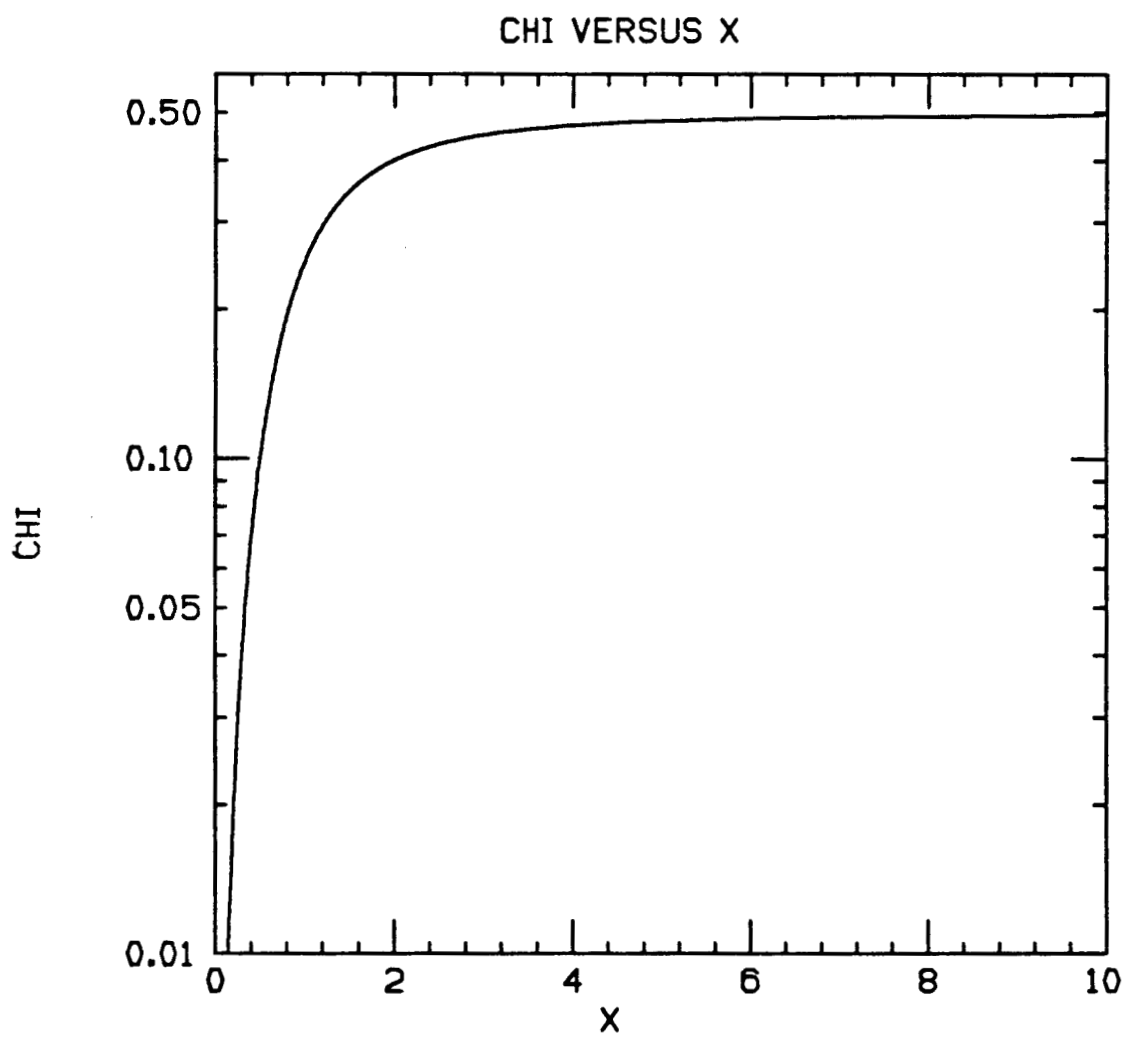


Figure 10. χ versus x_s . Note the log scale.

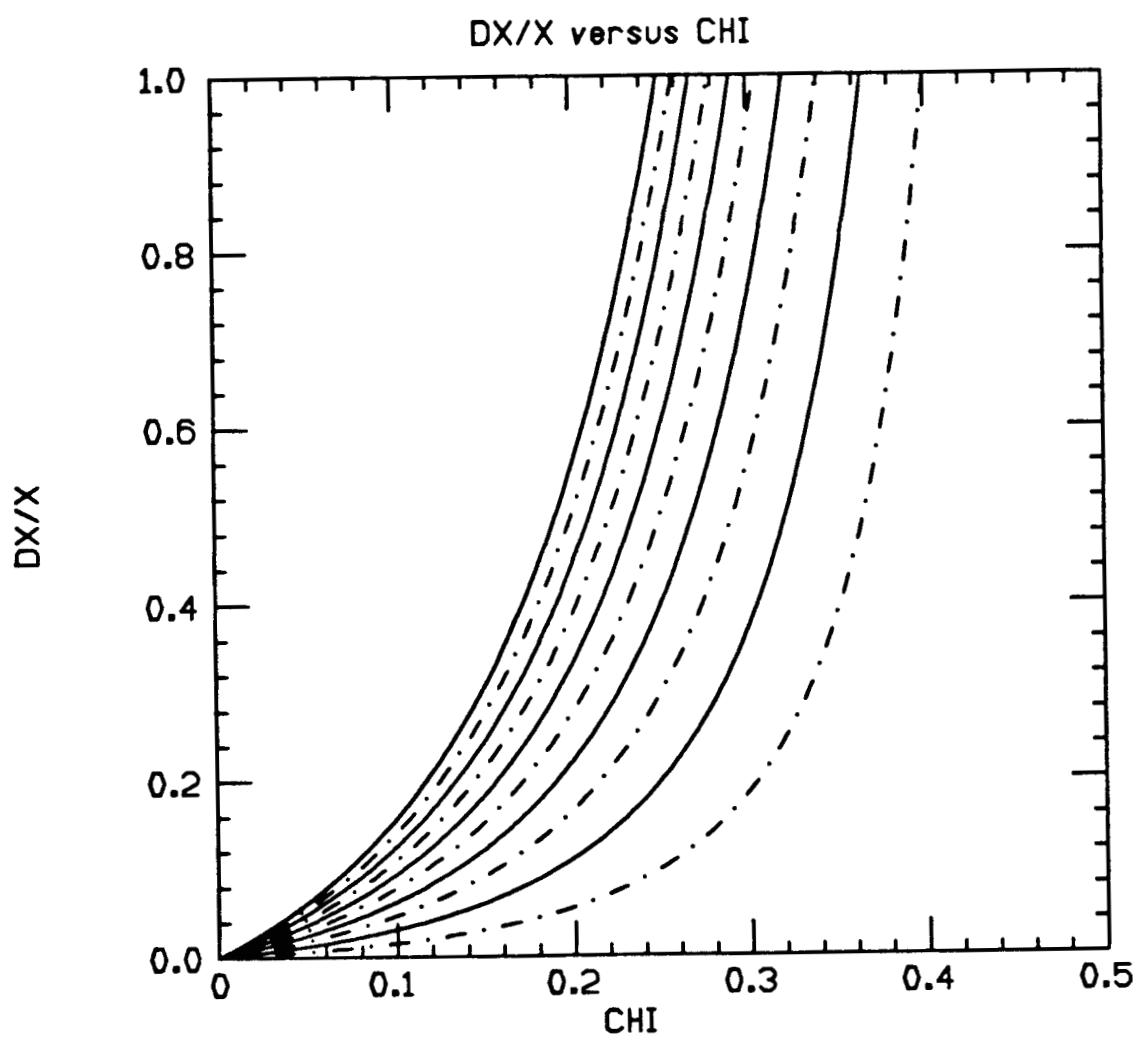


Figure 11. The fractional error in x , $(\frac{\Delta x}{x})$, versus χ ; contours of fractional error in χ , $(\frac{\Delta \chi}{\chi})$

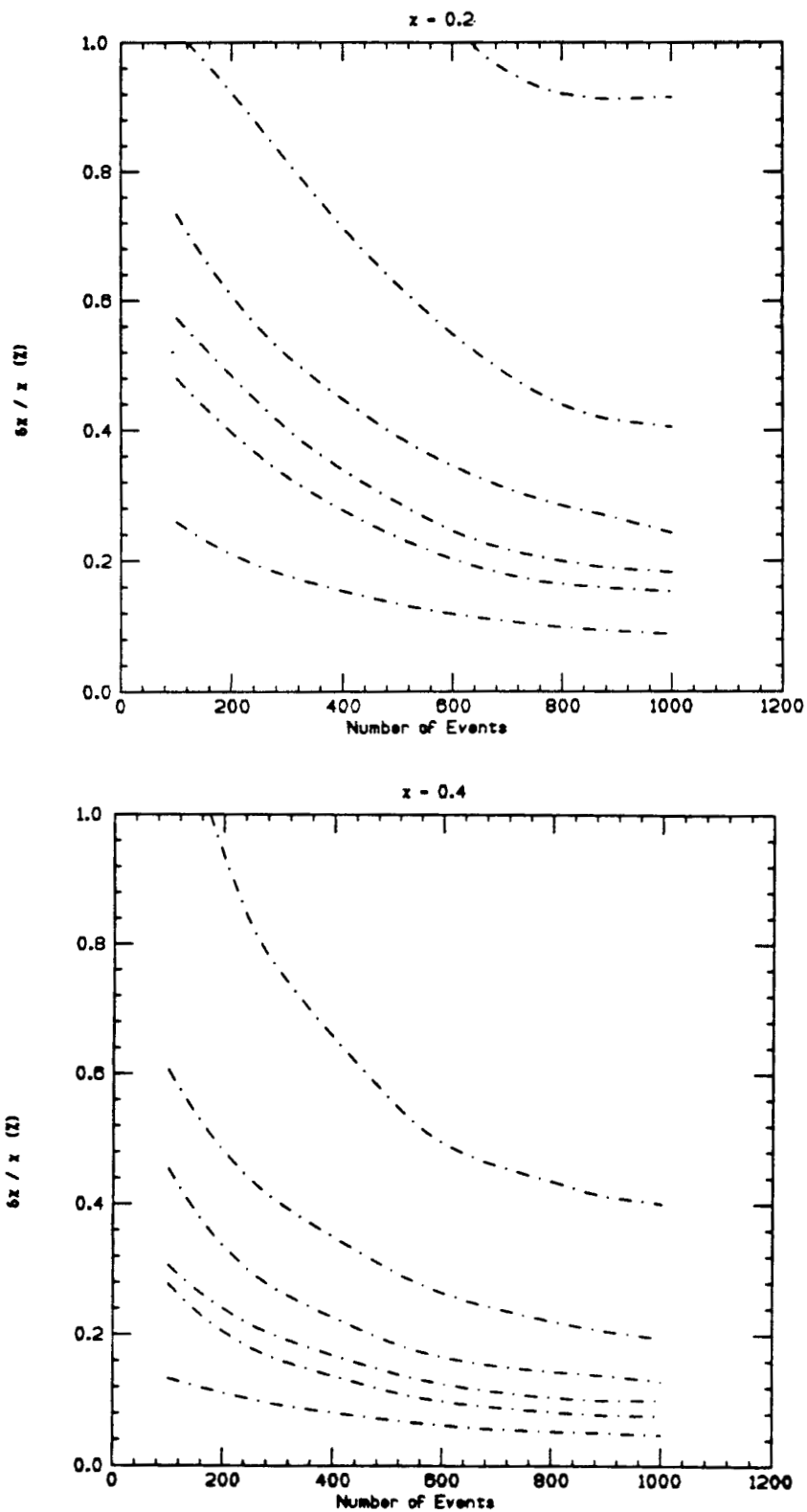


Figure 12. The fractional error in χ versus the number of events for (a) $\chi = 0.2$, and (b) $\chi = 0.4$; Contours of $A_{FB}=0.1, 0.2, 0.3, 0.4, 0.5, 0.75$ (from top to bottom).

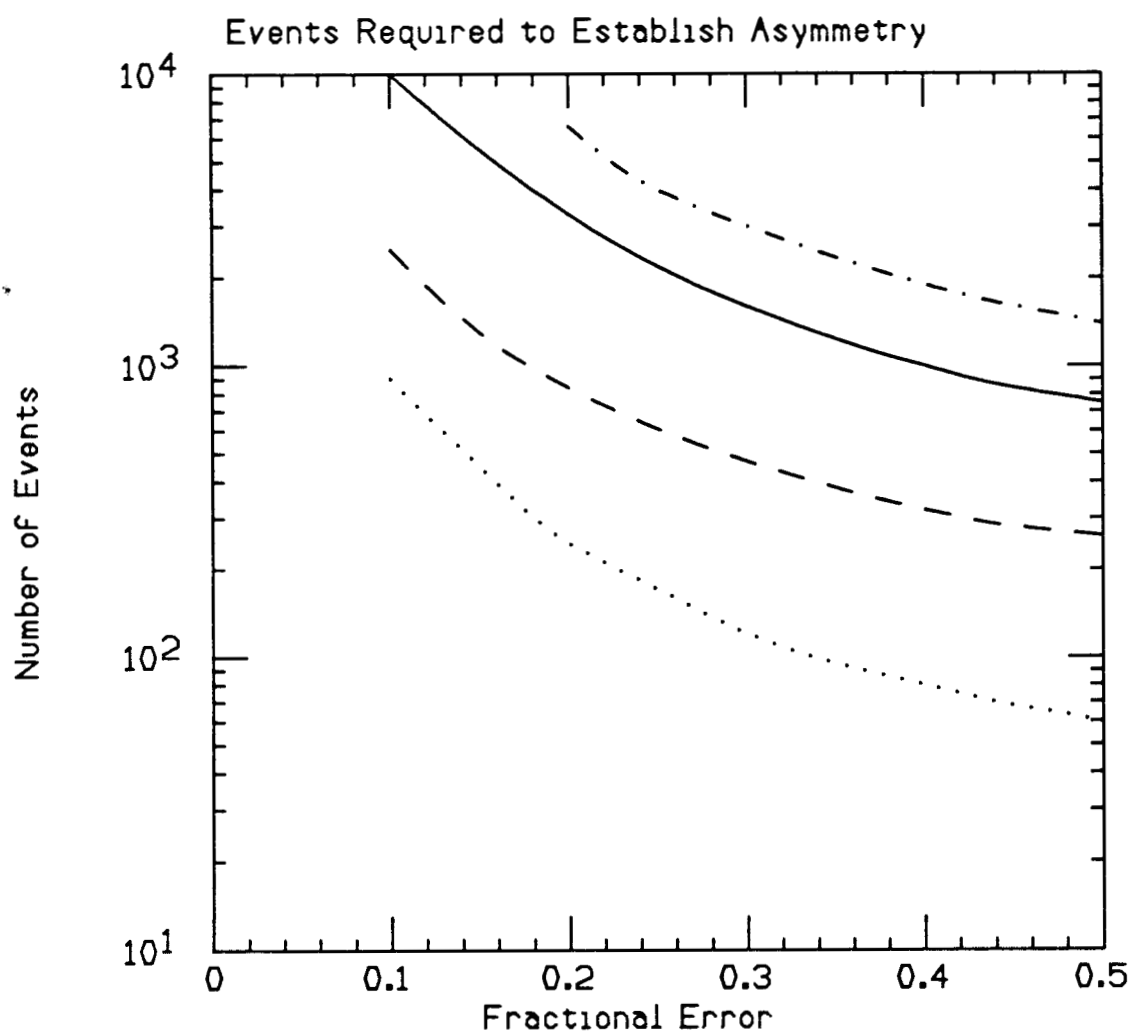


Figure 13. Events required to achieve a fractional error on χ . $A_{FB} = 0.1, \chi = 0.2$ (dotdash), $A_{FB} = 0.1, \chi = 0.4$ (solid), $A_{FB} = 0.4, \chi = 0.2$ (dashed), $A_{FB} = 0.4, \chi = 0.4$ (dotted).

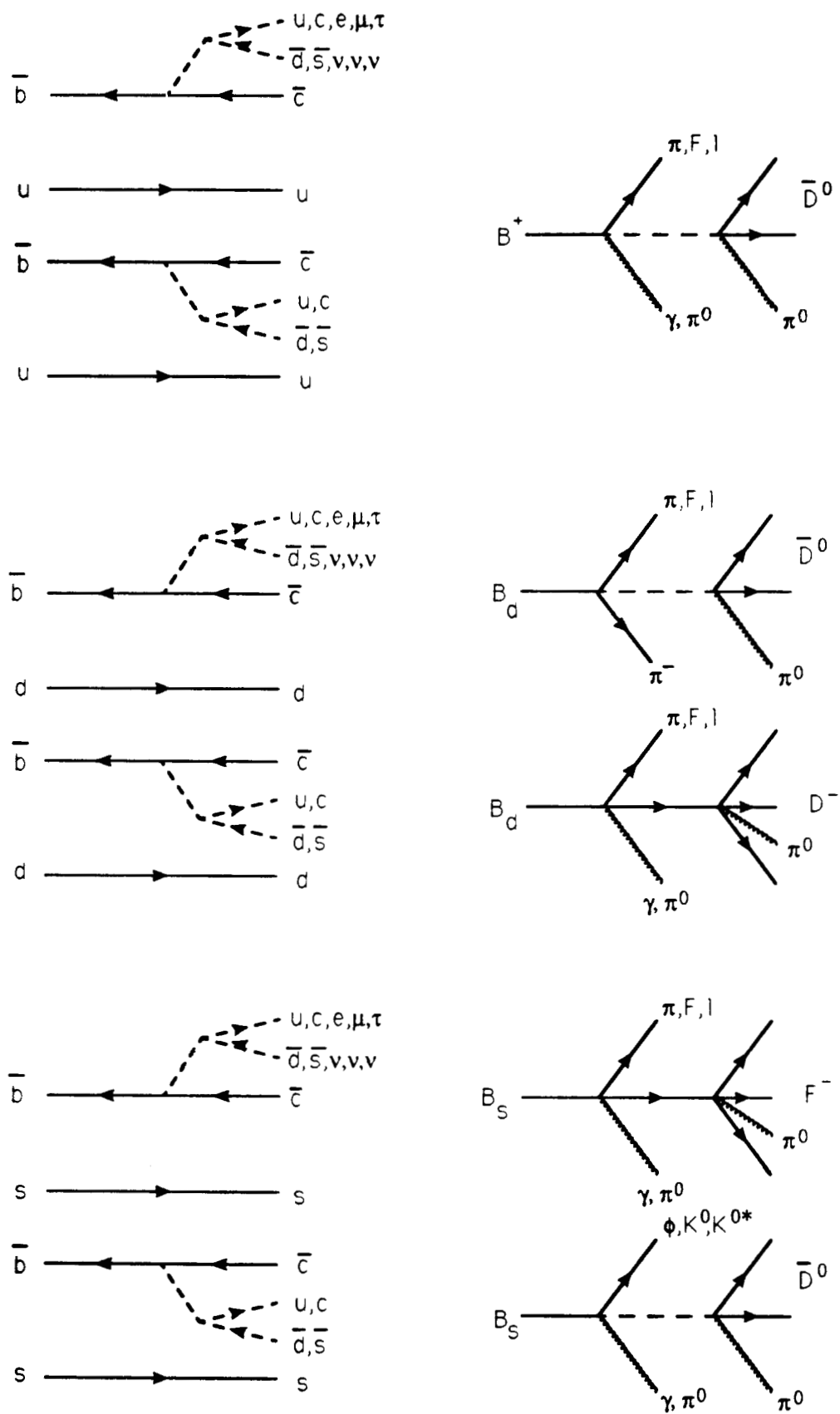


Figure 14. B_u , B_d and B_s primary decays and their topological signatures.

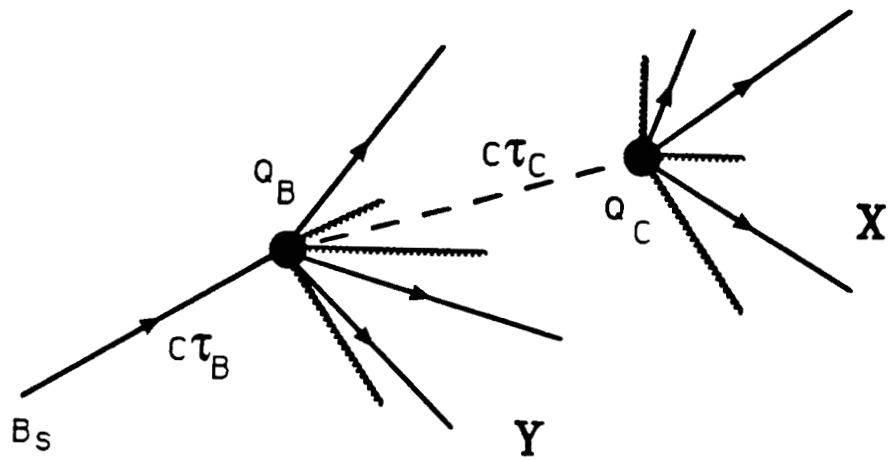


Figure 15. Schematic of the cascade vertex problem.

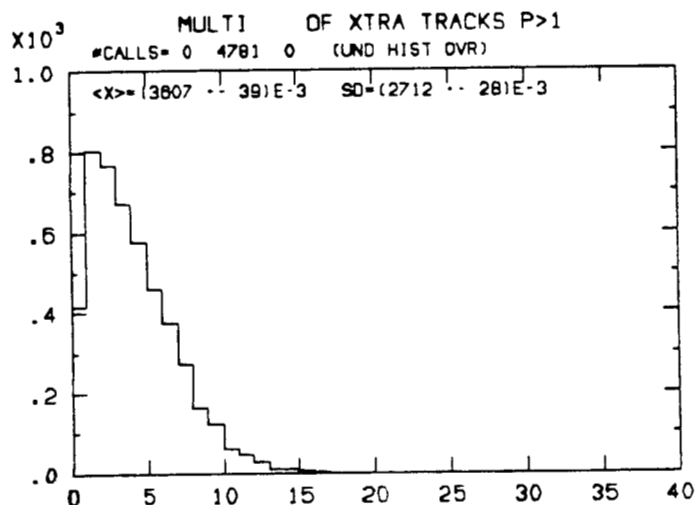
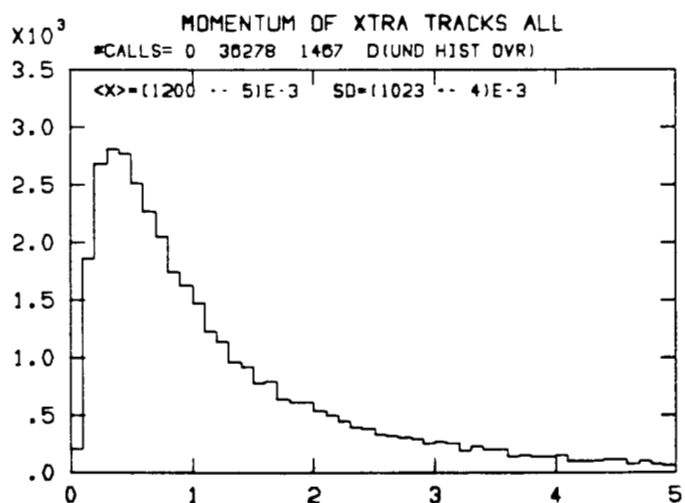
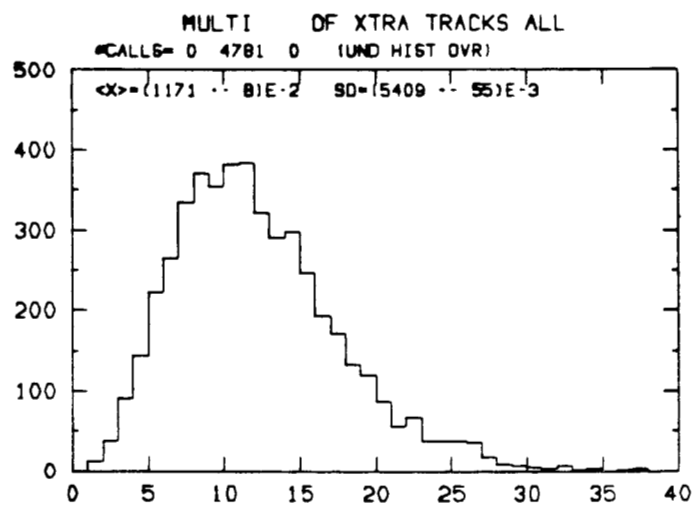


Figure 16.

(a) Multiplicity of non-B meson tracks in $B\bar{B}$

(b) Momentum of non-B meson tracks.

(c) Multiplicity of non-B meson tracks with $p \geq 1$ GeV.

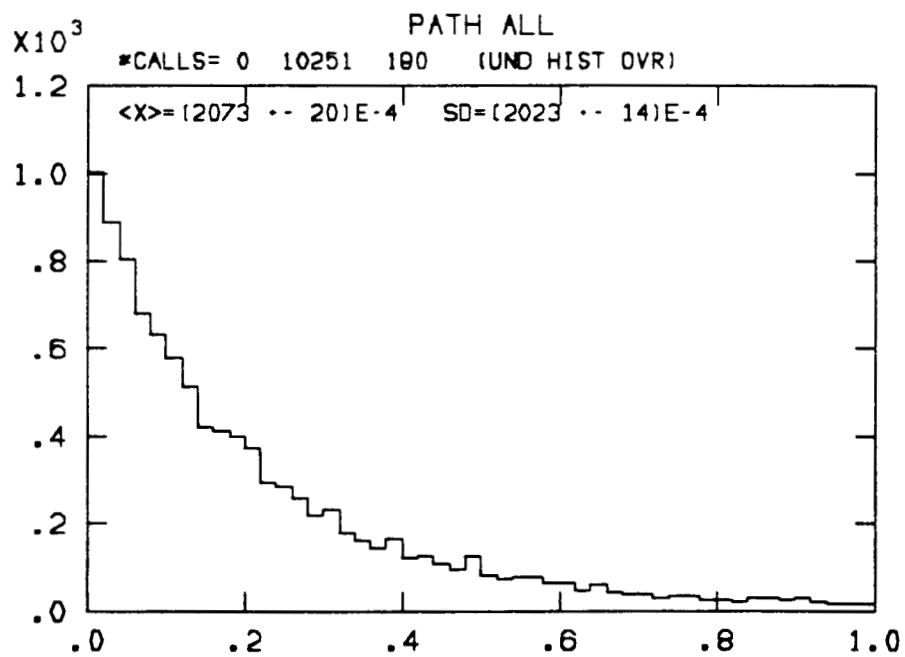
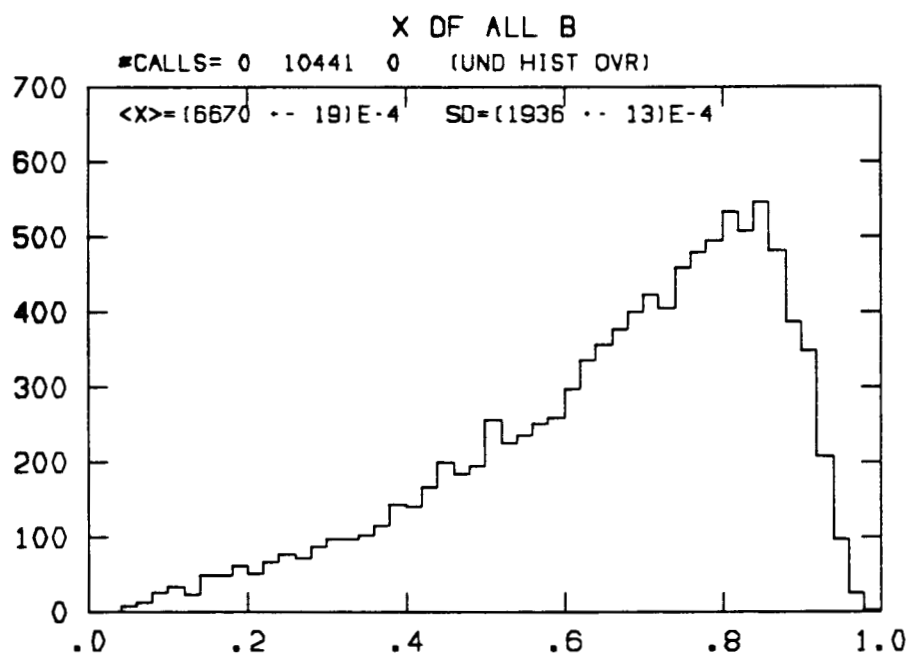
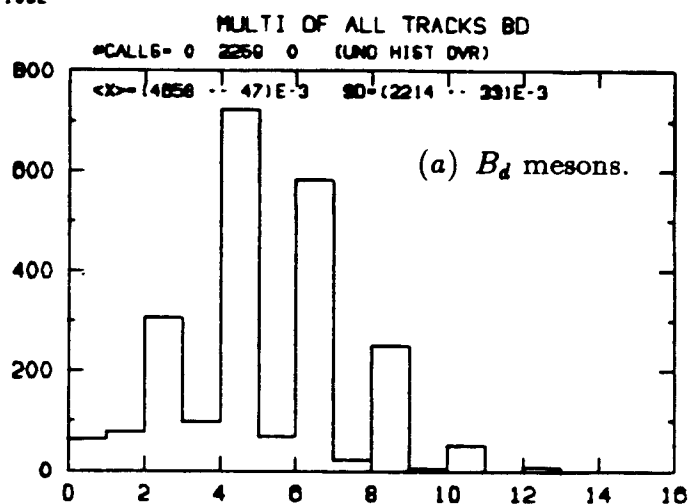


Figure 17.

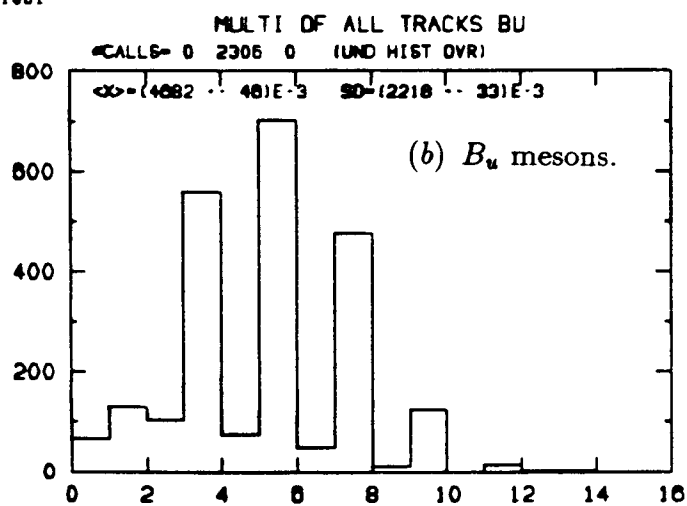
(a) X distribution of B mesons.

(b) Decay length of B mesons in the lab (cm).

10-1002



10-1001



RHS015 31AUG89

10-1003

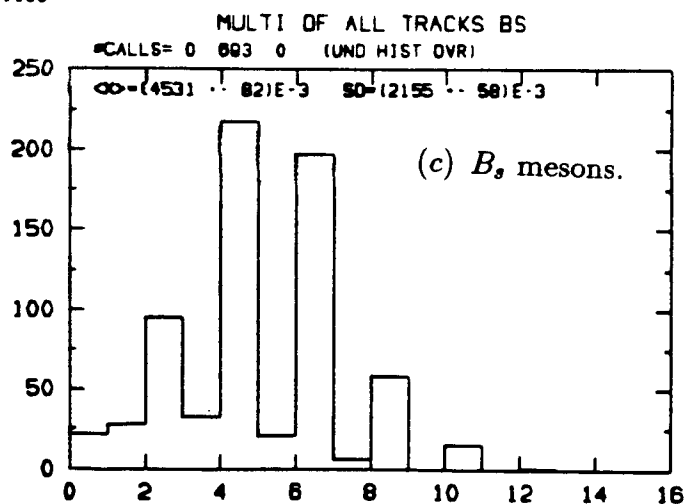
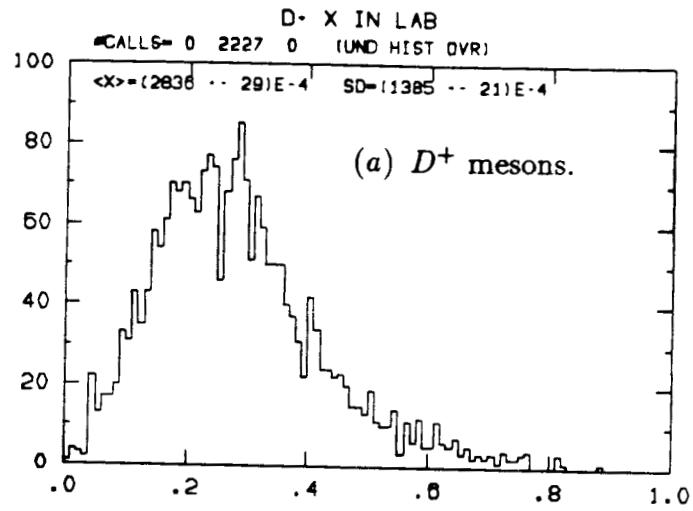
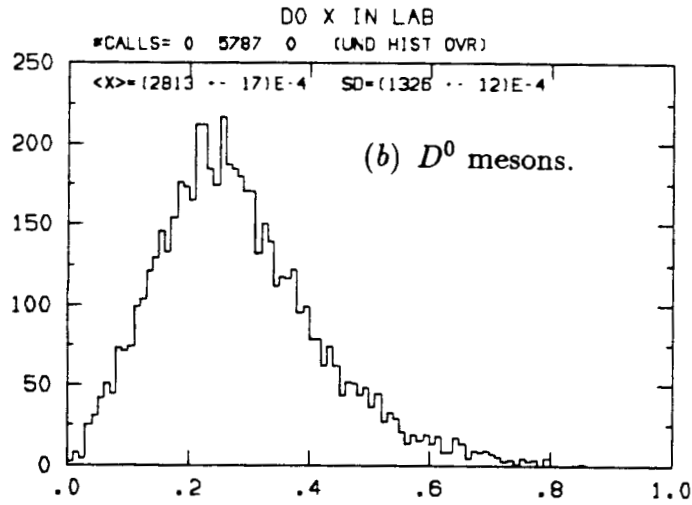


Figure 18. Detected charged multiplicity

ID=4011



ID=4010



ID=4012

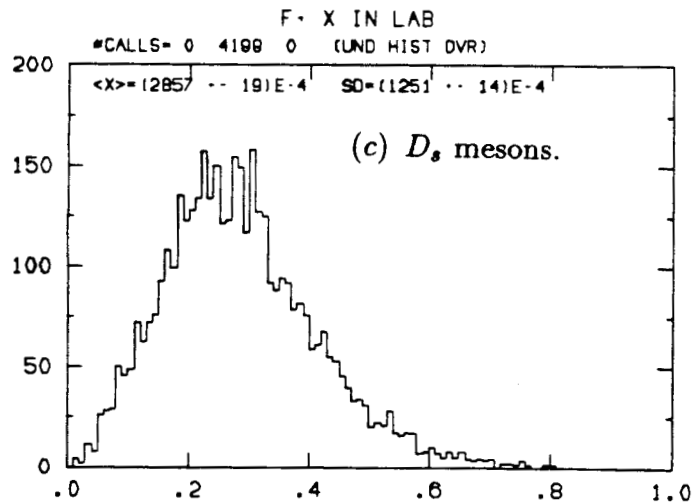


Figure 19. X distribution

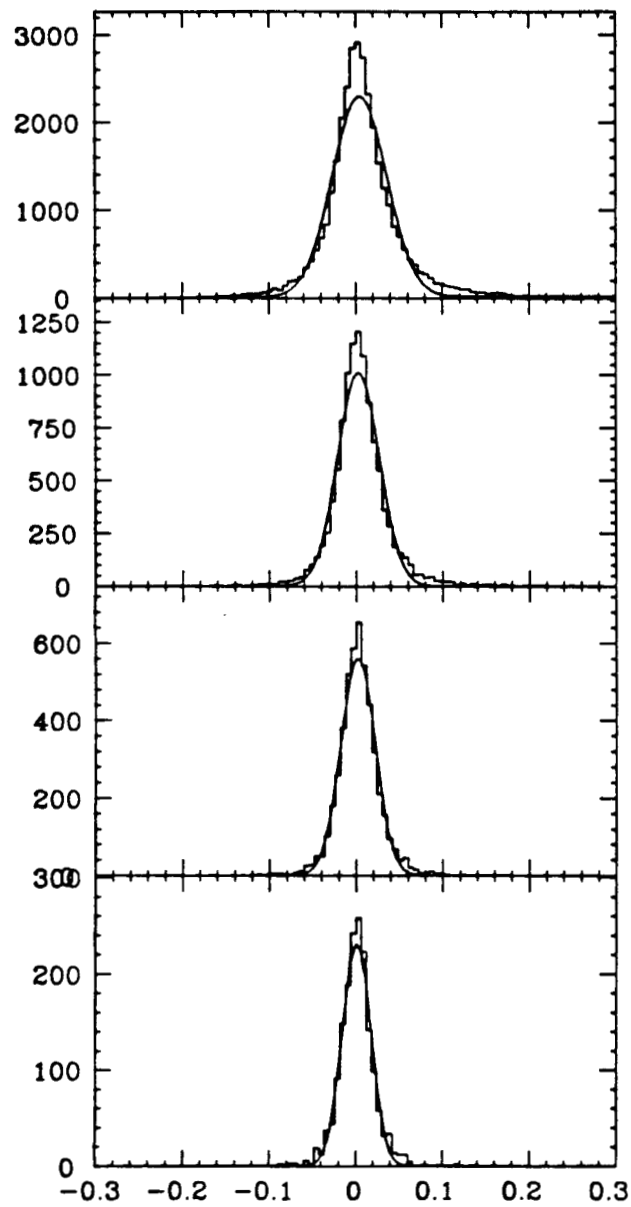


Figure 20. Longitudinal residuals of B meson vertices for:

(a) 2 prongs.

(b) 3 prongs.

(c) 4 prongs.

(d) 5 prongs.

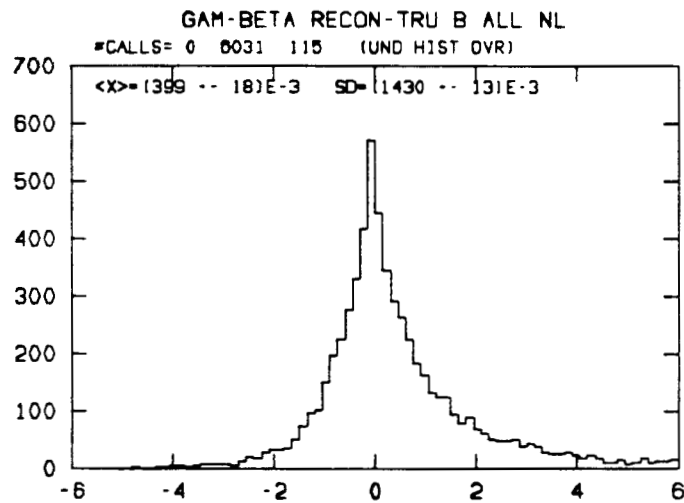
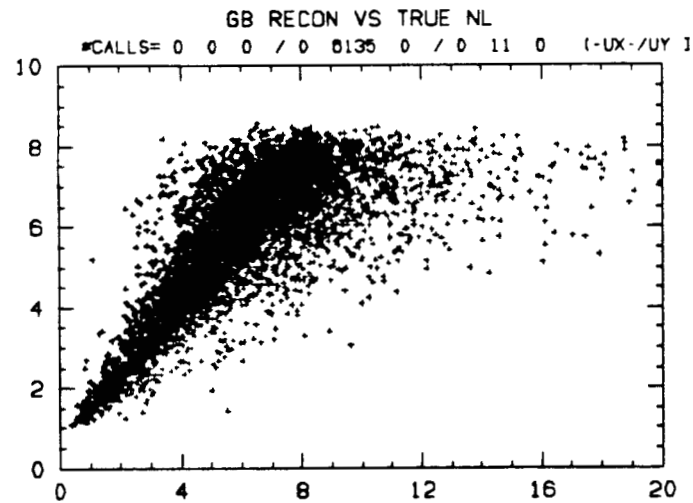
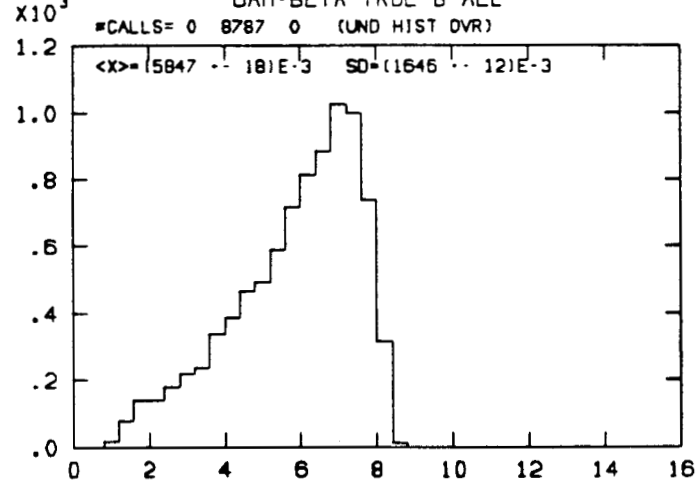
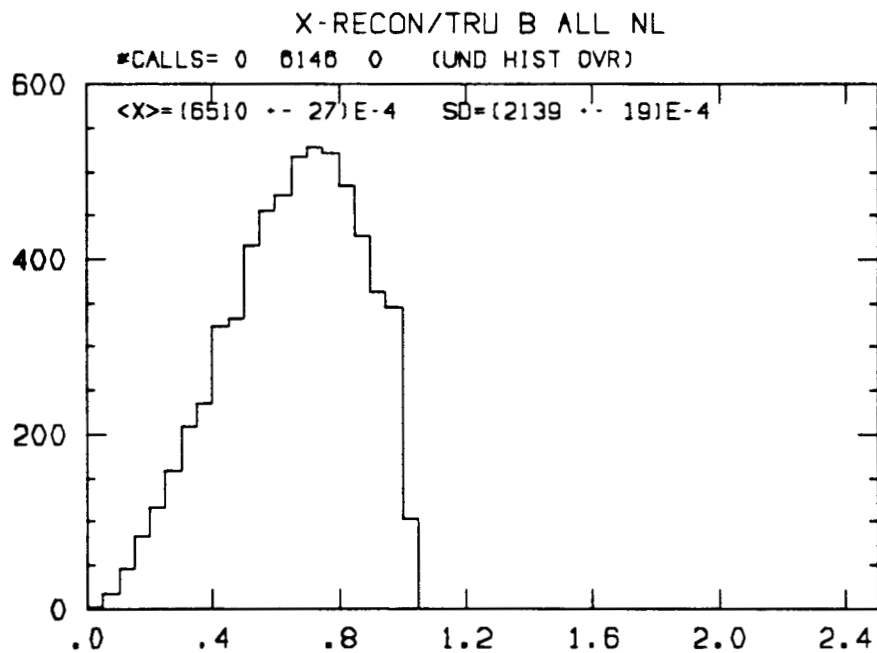


Figure 21.

(a) Produced $\gamma\beta$ for B mesons.

(b) Produced $\gamma\beta$ versus reconstructed $\gamma\beta$.

349 (c) Residual for $\gamma\beta$.



ID=2082

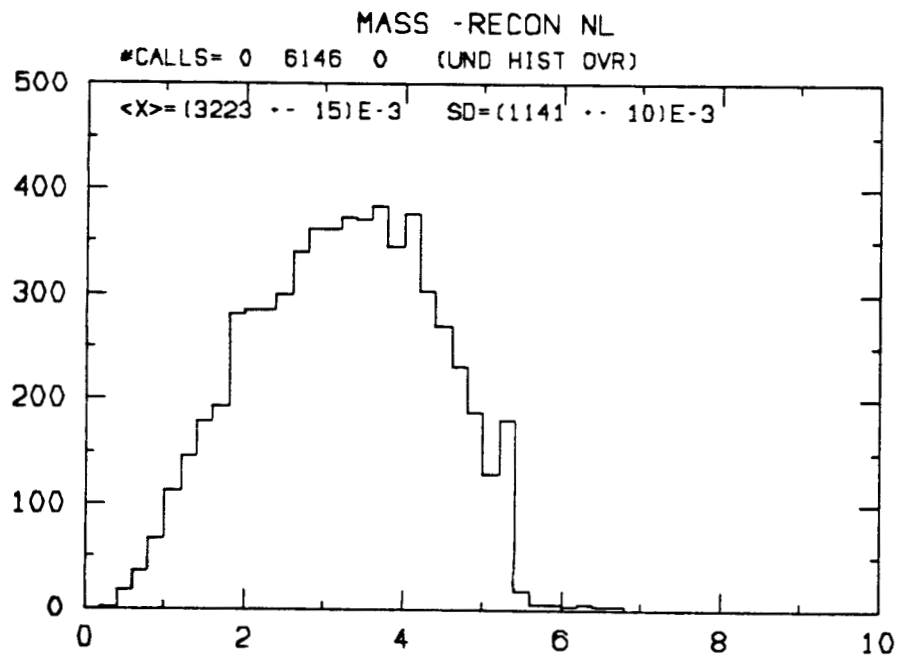


Figure 22.

(a) Ratio of $x(\text{reconstructed})$ to $x(\text{produced})$ for B mesons.

(b) Visible mass in charged tracks for B mesons.

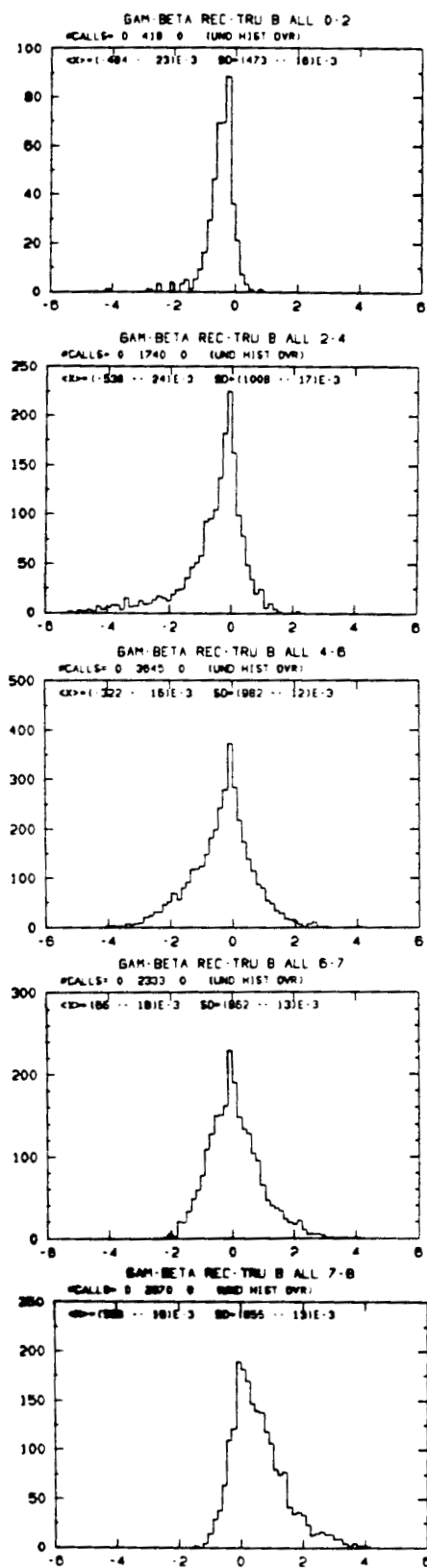


Figure 23. Residuals for $\gamma\beta$ in bins of $\gamma\beta$ (a) 0-2, (b) 2-4, (c) 4-6, (d) 6-7, (e) 7-8.

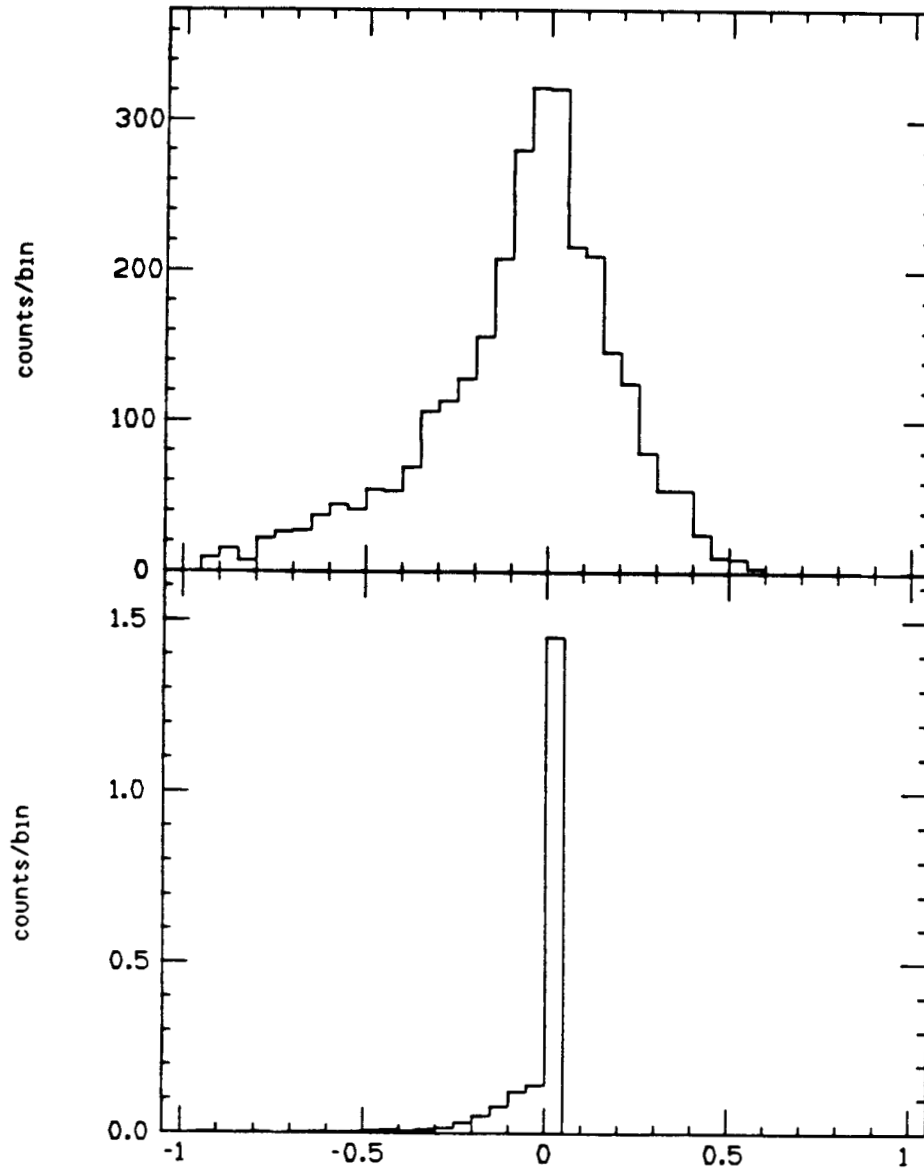
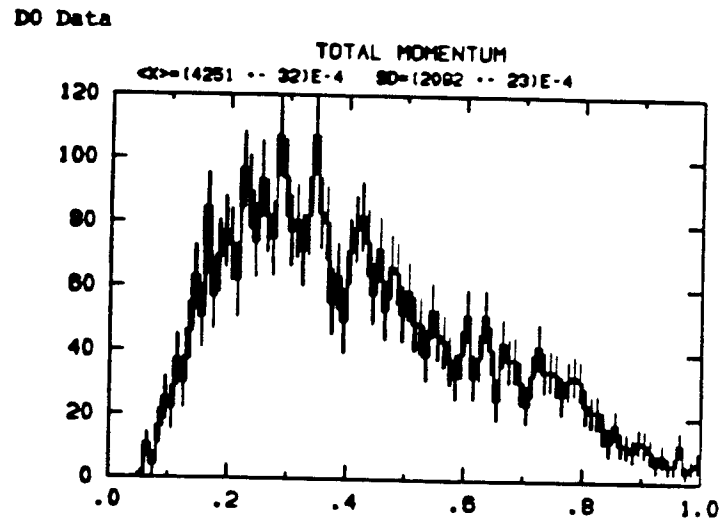
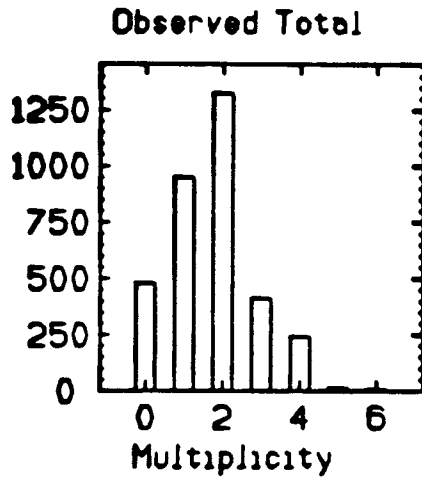


Figure 24. Illustration of improvements to $\gamma\beta$ possible in semileptonic decays. Fractional error in $\gamma\beta$ for semileptonic decays (a) with no correction for the missing ν , and (b) after solving the quadratic ambiguity, and selecting the faster solution. This Monte Carlo calculation does not include resolution smearing or efficiencies of SLD.

D0 Data



D0 MC

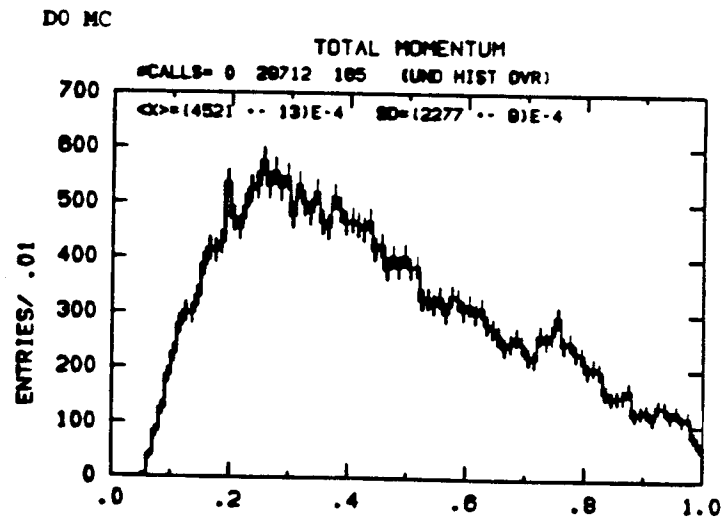
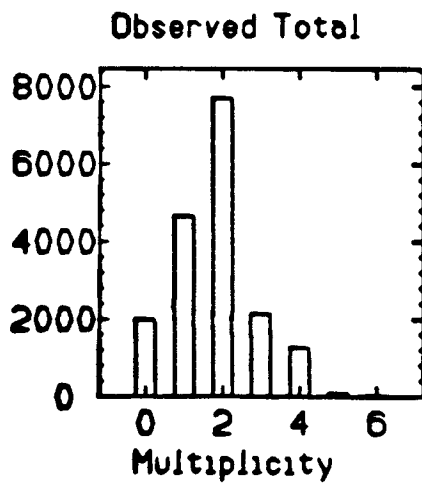


Figure 25. Illustrative comparison of the D^0 Monte Carlo model against data in (a-b) the multiplicity distributions and (c-d) the daughter track momentum distributions.

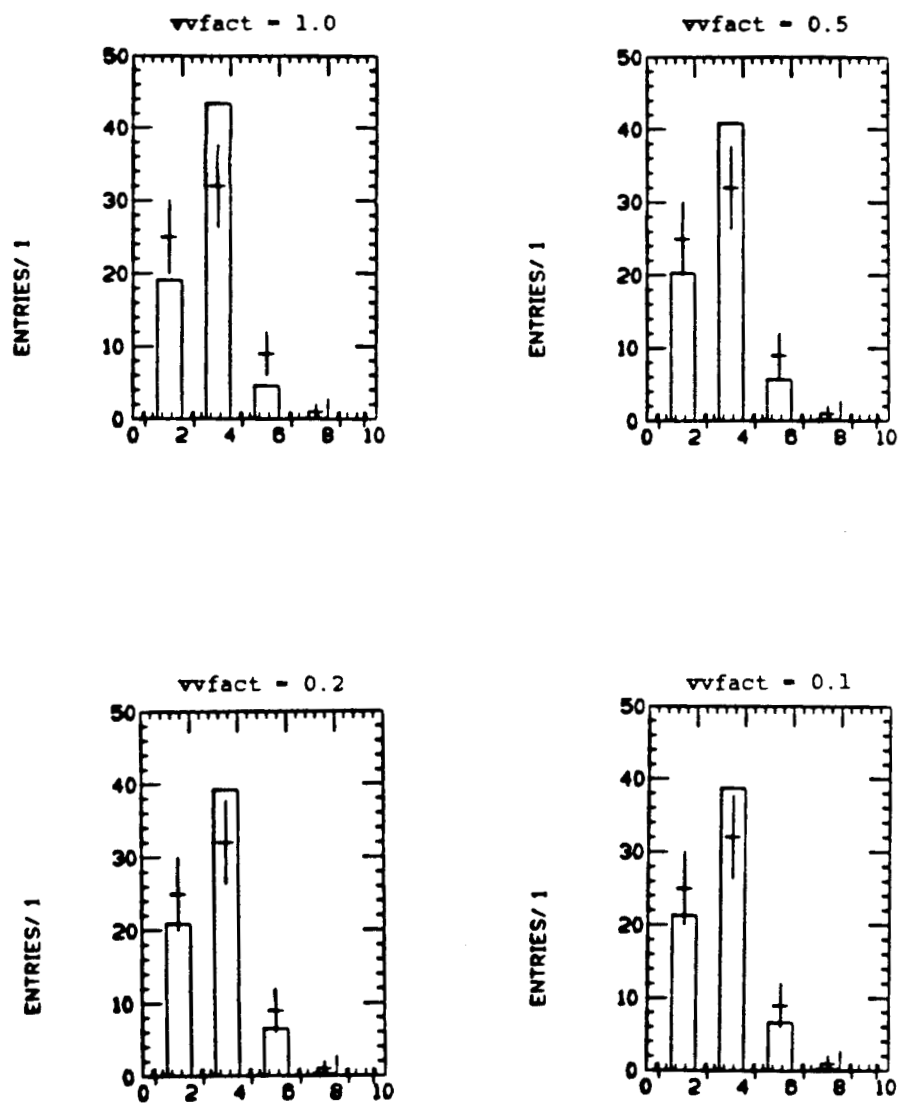


Figure 26. Illustrative comparison of the D_s Monte Carlo model against data with variation of the strength of the vector-vector component in the model.

ID=1000

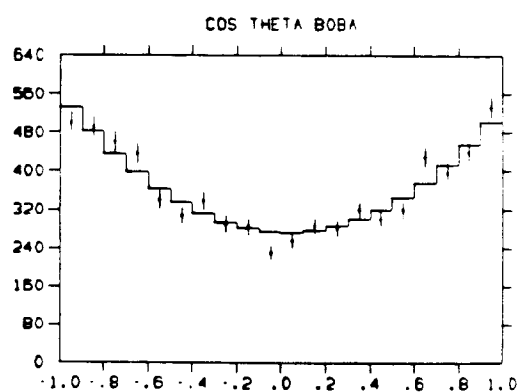
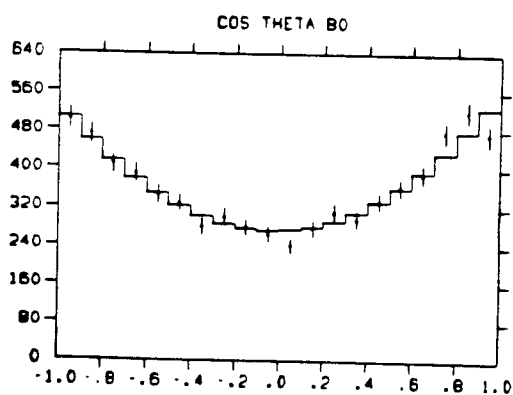
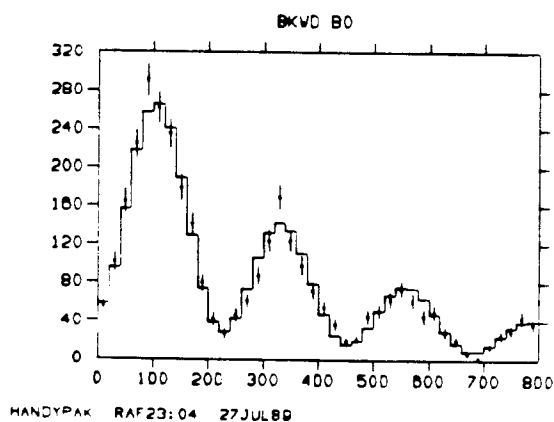
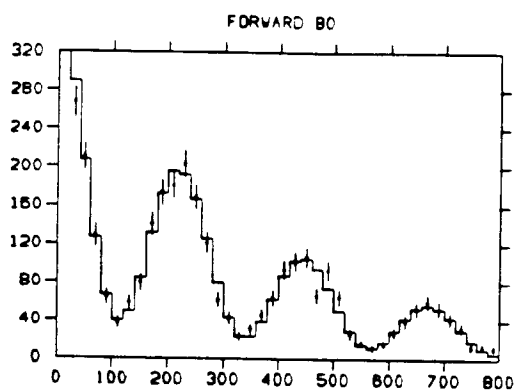
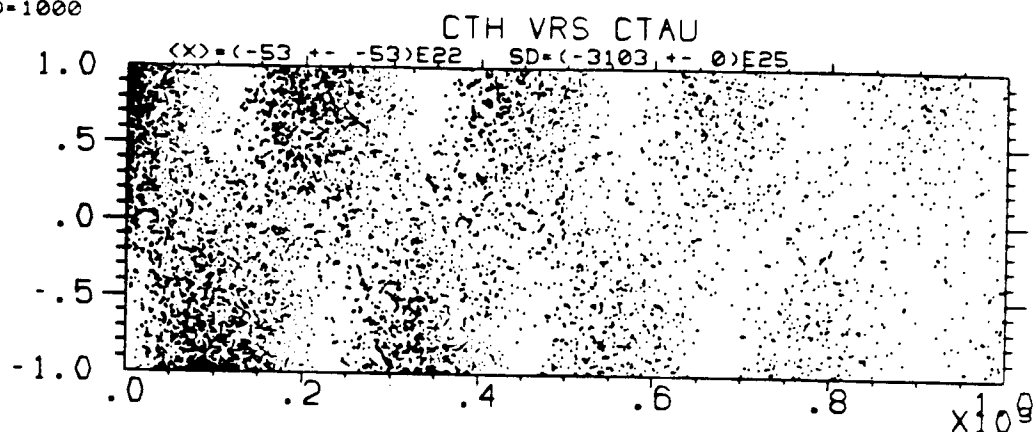


Figure 27. Scatterplot of the production ($\cos \theta$) and evolution ($c\tau$) of a B_s meson with full polarization, and $\frac{\Delta M}{\Gamma} = 5$.

Figure 28. Projections of the scatterplot of Figure 27.

Forward B_s Produced and Detected with $s=50$ micron

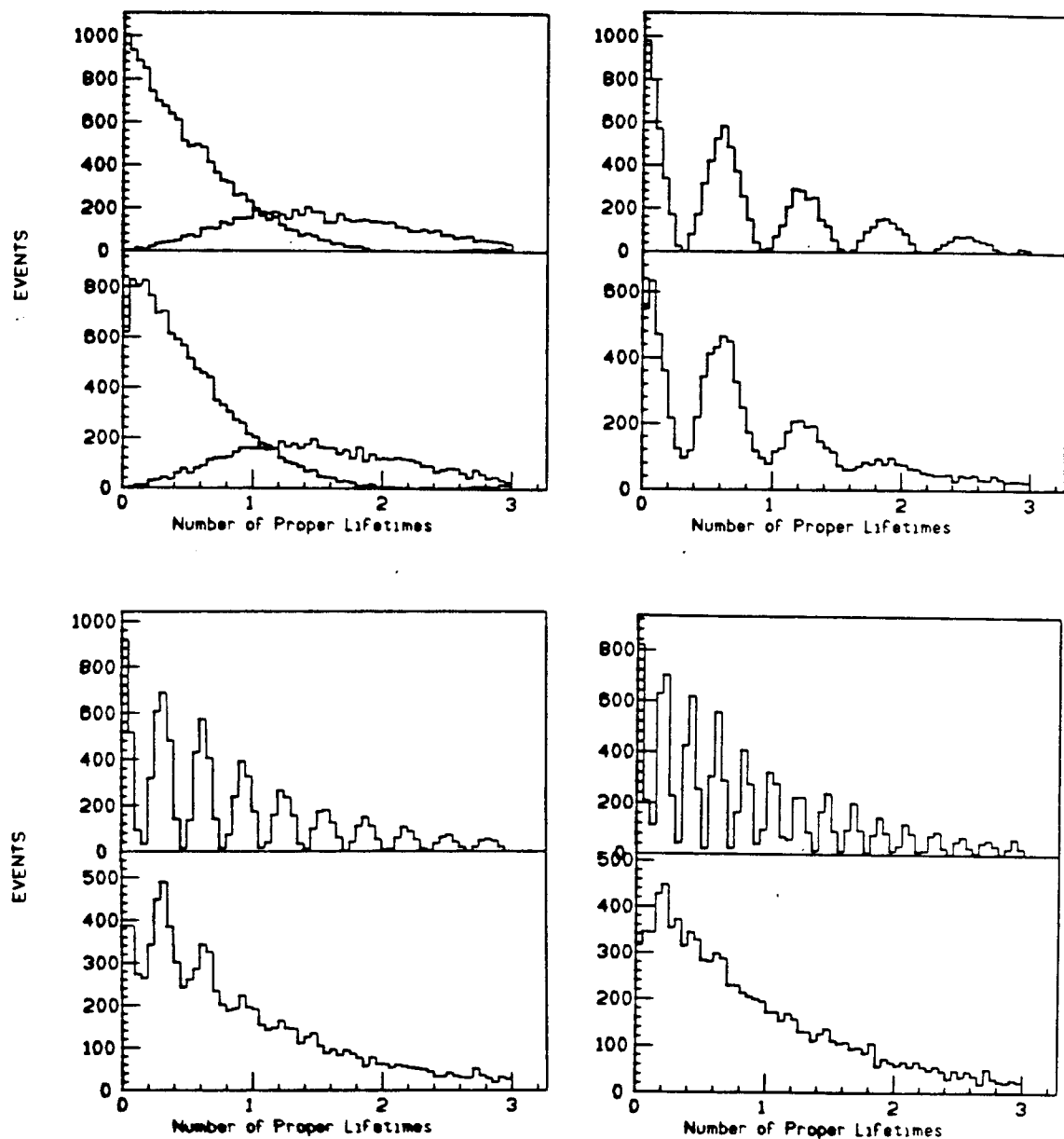


Figure 29. The top curve(s) are the σ of forward going B_s mesons, as produced. The bottom curve contains the corresponding distribution, smeared by detector resolution and cut at $500\mu m$ in the lab.

- (a) $\frac{\Delta M}{\Gamma} = 0.7$ The anti-particle curve is also shown.
- (b) $\frac{\Delta M}{\Gamma} = 5.0$
- (c) $\frac{\Delta M}{\Gamma} = 10.0$
- (d) $\frac{\Delta M}{\Gamma} = 15.0$

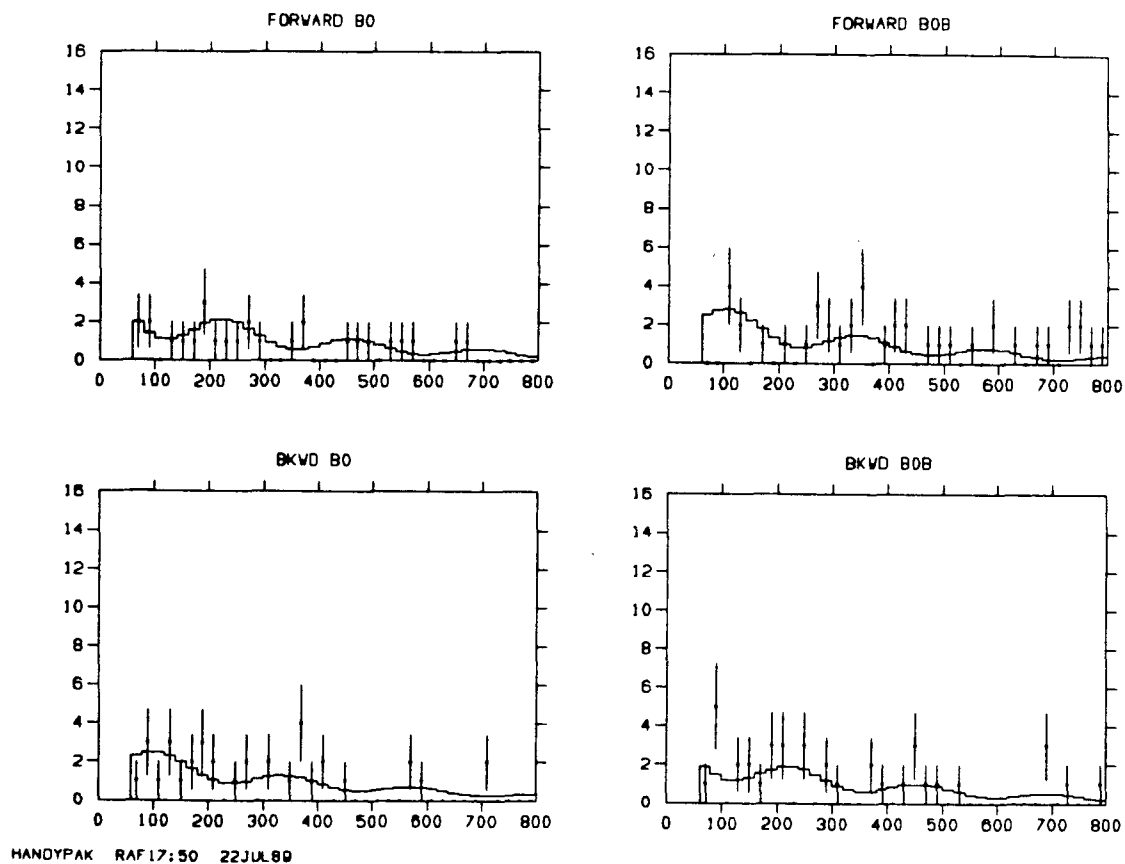


Figure 30. Example of the $c\tau$ projections of a two-dimensional likelihood fit with 100 $B\bar{B}$ events detected, $\frac{\Delta M}{\Gamma} = 5$, $A_{FB} = 0.4$, but no cut on $\cos(\theta)$. The fit yields $\frac{\Delta M}{\Gamma} = 4.8$.

$\overline{B}_s B_s$ Oscillations Seen from $e^+e^- \rightarrow Z^0 \rightarrow \bar{b}b$ with the *SLD* at the *SLC*[†]

T.W. Reeves, R.S. Panvini, G.B. Word
Vanderbilt University, Nashville, Tennessee 37235

ABSTRACT

We present results from a study of simulated $\overline{B}_s B_s$ oscillations as might be expected in the reaction $e^+e^- \rightarrow Z^0 \rightarrow \bar{b}b$, where the \bar{b} -quark jet contains a B_s meson. The ability to measure the oscillation parameter x_s is studied as a function of the average detector resolution, the number of events, background levels, and the frequency of the oscillations.

[†] *Work supported by the National Science Foundation.*

1. Introduction

We estimate the likelihood of measuring the $\overline{B}_s B_s$ mixing parameter, x_s , over an interesting range of values. Maximal $\overline{B}_s B_s$ mixing is expected in the standard model, since $\overline{B}_d B_d$ mixing has already been found to be large, $x_d = 0.66 \pm 0.17$.^[1] The results of our study are based entirely on simulated measurements. We assume the anticipated measuring capability of the *SLD* detector at the *SLC* with precision vertex detection, charged particle identification over a wide range of momenta, near 4π calorimeter coverage, and high resolution momentum measurement.^[2] The B_s (or \overline{B}_s) mesons that are simulated in this study originate from the $\bar{b}(b)$ -quark jets in the reaction $e^+e^- \rightarrow Z^0 \rightarrow \bar{b}b$.

The frequency of B_s mixing oscillations is determined by the parameter x_s and the lifetime τ_s . The value of x_s is determined from a "box diagram" calculation that leads to the expression

$$x_s = \frac{G_F^2}{6\pi^2} m_t^2 \tau_B f_B^2 B_B m_B |V_{tb} V_{ts}^*|^2 g \left(\frac{m_t}{M_W} \right) \eta_{QCD},$$

where f_B is a decay constant, B_B is a bag factor, g is a factor that depends on the t -quark mass ($g = 1$ for $m_t \ll M_W$ and about 0.6 for $m_t = 2M_W$), and η_{QCD} is a QCD correction factor of about 0.85. From this expression we see that a measurement of x_s leads to a determination of the KM matrix element $|V_{ts}|$. (We assume $|V_{tb}| \approx 1$.) A similar expression for x_d —obtained from $\overline{B}_d B_d$ mixing—allows the determination of $|V_{td}|$. The value of x_d is already indirectly measured from the *CLEO* and *ARGUS* measurements^[1] of r_d . The parameter r_d is defined as follows:

$$r_d = \frac{\overline{B}_d^0 \rightarrow B_d^0 \rightarrow X l^+ \nu}{\overline{B}_d^0 \rightarrow X l^- \nu},$$

with a similar expression for r_s . The parameters r_q and x_q are related by the expression $r_q = x_q^2 / (2 + x_q^2)$.

Because of uncertainty in the top mass and in the QCD correction factors in the above equation for x_s (and in the corresponding expression for x_d) the determination of $|V_{ts}|$ from the equation for x_s is in doubt. On the other hand, we may reasonably assume these uncertain factors will cancel if we measure both x_d and x_s so that the ratio will be given by $x_s/x_d \approx |V_{ts}|^2/|V_{td}|^2$. In the standard model with three generations, this ratio is predicted to be much greater than one. However, for four generations this ratio can range from values between 10^{-3} to 10^3 . The possibility that the ratio is less than one is unique to the fourth generation: supersymmetry, charged Higgs bosons and left-right symmetric models all give values greater than unity for this ratio.^[3]

The goal of this simulation study is to consider all the parameters that affect the measurement of x_s and to observe the sensitivity of this measurement to variations in the values of the key

parameters. We determine typical values of these parameters from simulations of the reaction $e^+e^- \rightarrow Z^0 \rightarrow \bar{b}b$ with the *LUND*^[4] (version 6.3) event generator together with the *SLD* parametric Monte Carlo. A separate computer code, controlled solely by these parameters, is used to simulate many samples of $\bar{B}_s B_s$ oscillation data. The input parameters are varied about the expected values to anticipate results obtained with better or worse detector performance.

The next chapter of this paper includes all the basic ideas of this study. Results of the data analysis are discussed in Chapter 3 and we summarize and conclude in Chapter 4.

2. Simulation and Analysis Methods

We begin with a discussion of the basic concepts of an oscillation measurement. This is followed by a discussion of tagging—i.e., how B_s decays are found from among the tracks in a jet and how we determine the particle/antiparticle identity at time $t = 0$. We then discuss the factors which limit the resolution for measuring the proper time of the decay. The chapter concludes with a description of the procedure for simulating the $\bar{B}_s B_s$ oscillation data and of the subsequent analysis of this data for the determination of x_s .

2.1. BASIC CONCEPTS OF OBSERVING $\bar{B}_s B_s$ OSCILLATIONS

Two complementary methods are used for observing oscillations in B_s decays. The first employs a maximum likelihood fit and will henceforth be referred to as the Maximum Likelihood Method. The second method employs an asymmetry calculation and will be referred to as called the Asymmetry Method. For simplicity, these methods are first illustrated for the ideal case where there are no background distributions and the measuring resolution is perfect. The affect of more realistic conditions are discussed in the subsequent sections.

Maximum Likelihood Method

To illustrate this method, we assume that at time $t = 0$ we have a pure sample of B_s mesons—i.e., no \bar{B}_s at $t = 0$. The proper time evolution of B_s will have the form^[5]

$$I(B_s(t)) \propto e^{-t/\tau_s} \cos^2 \left(\frac{x_s t}{2\tau_s} \right), \quad (1a)$$

where τ_s is the B_s lifetime. Likewise,

$$I(\bar{B}_s(t)) \propto e^{-t/\tau_s} \sin^2 \left(\frac{x_s t}{2\tau_s} \right). \quad (1b)$$

We can then perform a maximum likelihood fit for x_s with the probability functions 1a and 1b and a set of proper time measurements $\{t_i\}$. We shall see from discussions below that modified versions of the above two equations are needed for non-ideal data.

Asymmetry Method

We may also define an asymmetry between the cosine-squared and the sine-squared distributions given in equations 1a and 1b.

$$A_{cs} = \frac{I(B_s(t)) - I(\overline{B}_s(t))}{I(B_s(t)) + I(\overline{B}_s(t))}$$

Note that this is the forward-backward asymmetry, A_{FB}^b , if the direction of the e^- beam is used to statistically tag the particle/anti-particle nature at $t = 0$. A straight-forward calculation shows that

$$A_{cs} = \cos\left(\frac{x_s t}{\tau_s}\right). \quad (2)$$

2.2. TAGGING B_s

There are two aspects of B_s tagging that we need to consider for our studies. One of these is due to the requirement that the particle/antiparticle identity of the B_s be determined at time $t = 0$. The other results from B_u and B_d decays which are improperly identified as B_s decays. We discuss in this section various tagging methods and we estimate their effectiveness. What will emerge from this discussion are two of the key parameters which are used for simulating the sample of data for the x_s measurement.

$t = 0$ particle/antiparticle tagging methods

An important feature of the reaction $e^+e^- \rightarrow Z^0 \rightarrow \bar{b}b$ is that the particle-antiparticle identity at time $t = 0$ can be correlated with the polarization of the Z^0 —which, in turn, may be enhanced by using a polarized beam.^[6] The electron polarization method has the highest efficiency for retaining good events since the polarization direction will be known on an event-by-event basis. However, the effectiveness of this tag is limited by the fact that a practical goal for electron polarization at the *SLC* will be 49%, and the *SLD* vertex detector will not cover the small-angle forward-backward direction. With these restrictions, the expected number of correct to incorrect $t = 0$ tags is about 2 : 1.

Another method for tagging the identity of a $B_s(\overline{B}_s)$ at $t = 0$ is to find a $K^+(K^-)$ that emerges in the same jet. More explicitly, the fragmentation process is such that when a B_s is produced from a \bar{b} - and an s -quark, the s -quark will be produced along with a \bar{s} -quark which will often combine with a u -quark to form a K^+ . (This also includes K^+ mesons that come from K^* decay.) This establishes the B_s identity at $t = 0$. The same is, of course, true for the \overline{B}_s — K^- correlation at $t = 0$. The goal is to look for the K^\pm that is consistent with having come from the same part of the fragmentation chain as did the B_s . From Monte Carlo studies, we find that these kaons associated with the production of B_s mesons tend to have a larger momentum and to

be travelling more nearly in the same direction as the B meson than fragmentation kaons which come from other parts of the fragmentation chain.^[7]

This K -tag method requires the good particle identification capability of the SLD detector. It also relies heavily on excellent vertex detection to separate fragmentation kaons from those produced in the decay cascade of B mesons since these kaons have kinematic characteristics that are similar to the fragmentation kaons associated with the production of B_s mesons. With these constraints we find that this tag gives a ratio of better than 5 : 1 for the correct/incorrect identity. The price that must be paid for this good tagging ratio is that by requiring a charged kaon (rather than a neutral) and by requiring other minimal cuts on the kaon, less than one half of the potential B_s events survive.

A third method for tagging at $t = 0$ requires simultaneously tagging the opposite jet for a B_u meson. Since B_u and \bar{B}_u do not mix, establishing the sign of the charge of the B_u also establishes the particle/antiparticle identity of the B_s at $t = 0$. However, estimates of the fraction of events that can be positively identified as a charged B meson are at the level of a few percent at most.^[6] Since statistics is crucial, this method is not as good as the previous two.

Tagging the decay of a B_s

To measure the B_s decay point and to estimate the B_s momentum, it is necessary to find as many of the final state particles as possible. The chief background is from B_u and B_d mesons which together are produced about ten times more often than B_s . A clean tag, in general, for B mesons is via their semileptonic decays. Moreover, a B_s is expected to decay most often into a D_s meson, which subsequently will decay often into $\bar{s}s$ mesons—including ϕ 's and η 's. Unfortunately, D mesons from B_u and B_d decays also decay into ϕ 's and η 's often enough to produce a significant background. Hence, tagging the B_s decay cleanly is very difficult. It requires reconstruction of as much of the final state as possible.

We have made a number of studies of B_s decay and find that the semileptonic modes are particularly useful. In particular, we have studied $B_s \rightarrow D_s^- l^+ \nu$ (and the charge conjugate), with $D_s^- \rightarrow \phi X^-$ and $\phi \rightarrow K^+ K^-$. The details of this study will be discussed elsewhere.^[8] A tentative conclusion is that $O(10^5)$ $\bar{B}B$ or $O(10^6)$ Z^0 events are needed to produce about 100 correctly identified B_s decays with a signal-to-background of about 3 : 1. By extending the number of final states included, it should be possible to increase the correctly identified B_s decays to two or three times this number.

2.3. PROPER TIME MEASURING RESOLUTION

Two factors limit the accuracy of the proper time measurement: the uncertainty in the B_s decay length and the uncertainty in the momentum of the B_s ,—which limits the precision in the

determination of $\gamma\beta$ needed to compute the Lorentz boost between the laboratory frame and the B_s meson frame for the proper time calculation.

Although the absolute uncertainty in the proper time measurement increases with increasing decay length, we use the average value in this study. We estimate that this is not a problem if one does not require a minimum decay length to tag B_s candidates. But if one uses a tagging method which does require a minimum decay length for the B_s candidates, the average measured error will increase. (We estimate that σ_{ct} will increase by about 15% if a minimum decay length of $500\mu\text{m}$ is required.) For large x_s , this effect can be significant.

At *SLD*, the decay length will be determined from track measurements made with a precision vertex detector and from the narrow beam location as provided by the *SLC*. An estimate^[9] of the uncertainty in the decay length for the *SLD* detector at the *SLC* is about $170\mu\text{m}$. This translates into an uncertainty in $\langle ct_{\text{proper}} \rangle$ of $170/\langle \gamma\beta \rangle$, or about $25\mu\text{m}$, since the average $\gamma\beta$ for a B meson from Z^0 decay is expected to be about 7.

Most B_s decays will have some unmeasured final state particles. In the case of semileptonic decay, it will be impossible to measure the momentum accurately due to the missing neutrino(s). This contribution to the proper time uncertainty depends crucially on the final state analyzed. We estimate^[9] that an uncertainty in the measured value of $\gamma\beta$ of about 1.3 can be obtained. This contributes an uncertainty in $\langle ct_{\text{proper}} \rangle$ of about $40\mu\text{m}$.

The total uncertainty in $\langle ct_{\text{proper}} \rangle$ resulting from both of the above contributions is estimated by taking the two in quadrature. Hence, we estimate that the total average error in the measurement of the B_s proper time when using the *SLD* detector should be about $45\mu\text{m}$.

2.4. SIMULATION TECHNIQUE

Our goal is to determine the range of x_s values which can be measured for a given set of measurement conditions. The method used is to simulate B_s mixing data with a short (two page) FORTRAN program which has seven input numbers. These are:

- x_d , the known B_d mixing parameter;
- x_s , an assumed value for the B_s mixing parameter (varied);
- $c\tau$, the average b -hadron lifetime (0.03cm);
- σ_{ct} , the proper time resolution ($50\mu\text{m}$ for $x_s = 1$ and $x_s = 5$; $35\mu\text{m}$ for $x_s = 10$);
- $N_{B_s}/N_{B_u+B_d}$, the ratio of the number of tagged B_s mesons to the number of B_u and B_d mesons incorrectly tagged as B_s mesons (varied);
- Cor./Incor., the ratio of correct to incorrect $t = 0$ tags—(varied);
- $N_{\text{Cor.}}$, the number of “correctly tagged” B_s events ($N_{\text{Cor.}} = 100$ for $x_s = 1$ and $x_s = 5$; $N_{\text{Cor.}} = 400$ for $x_s = 10$).

Finally, from x_s , we compute r_s and apportion the relative numbers of particle vs antiparticle generated accordingly.

The ideal proper time measurements are then generated according to Eqns. 1a and 1b. The measured proper time is then computed by smearing each ideal value according to a gaussian probability distribution with $\sigma = 50\mu\text{m}$. (Note that although we estimated $\sigma = 45\mu\text{m}$ in the studies discussed above, we use $\sigma = 50\mu\text{m}$ to be conservative.)

The net effect of imposing factors which simulate real conditions is to change the form of the expected proper time distributions from those in Eqns. 1a,b to the following:

$$I(B_s(t)) \propto e^{-t/\tau_s} \left[\cos^2 \left(\frac{x_s t}{2\tau_s} \right) + \alpha \right], \quad (3a)$$

and

$$I(\bar{B}_s(t)) \propto e^{-t/\tau_s} \left[\sin^2 \left(\frac{x_s t}{2\tau_s} \right) + \alpha \right]. \quad (3b)$$

The added exponential term with the coefficient α accounts for the misidentified B_s backgrounds, incorrect $t = 0$ tags, and finite measuring resolution. (For simplicity, we have made the approximation that the lifetime of the backgrounds are the same as for B_s decay.)^[10] Note that the worst background will come from those cases where the particle/antiparticle at $t = 0$ is improperly identified. In these cases a sine-squared variation cancels a cosine-squared variation thereby reducing the visible cosine-squared amplitude.

In determining A_{cs} from equations 3, the effect of these backgrounds is to decrease the amplitude of the oscillations. Also note that misidentifying B_d as B_s will yield two superimposed oscillations of the form

$$A_{cs} = A_d \cos\left(\frac{x_d t}{\tau_d}\right) + A_s \cos\left(\frac{x_s t}{\tau_s}\right). \quad (4)$$

The generated data samples are then used as input to the two fitting techniques. The first uses MINUIT to obtain a maximum likelihood (MLH) fit to the parameters τ_s , x_s , and α in equations 3a, b. Note that in this case no choice of binning is required since only the individual measurements are used. The second technique requires a choice of binning in order to subtract the cosine-squared and sine-squared histograms to produce a histogram of the quantity A_{cs} to which a minimum χ^2 fit with equation 4 is made. We choose for simplicity to fix $\tau_s = \tau_B$, where the latter is the average B lifetime. Also, we input and fix the measured value of x_d obtained from *CLEO* and *ARGUS* measurements.

3. Results

A realistic example is one based on the possibility of achieving the kind of measurements discussed above in the section on tagging. The simulated data sample size is 100 correctly tagged B_s mesons. Also, we must include the effects of finite resolution (taken here as $50\mu\text{m}$), the ratio of correct to incorrect $t = 0$ particle/antiparticle identity tagging is $2.5 : 1$, and the assumed signal-to-background of B_s to B_d or B_u is $3 : 1$. The input value of x_s is set equal to 5. The expected distributions are of the form indicated in Equations 3 for the first method and Equation 4 for the second method. The simulated data and the fits for the two methods are shown in Figures 1 and 2, respectively. The fitted values of x_s are compatible with the input value of $x_s = 5$, as indicated in Table 1b for the parameters corresponding to Figures 1 and 2.

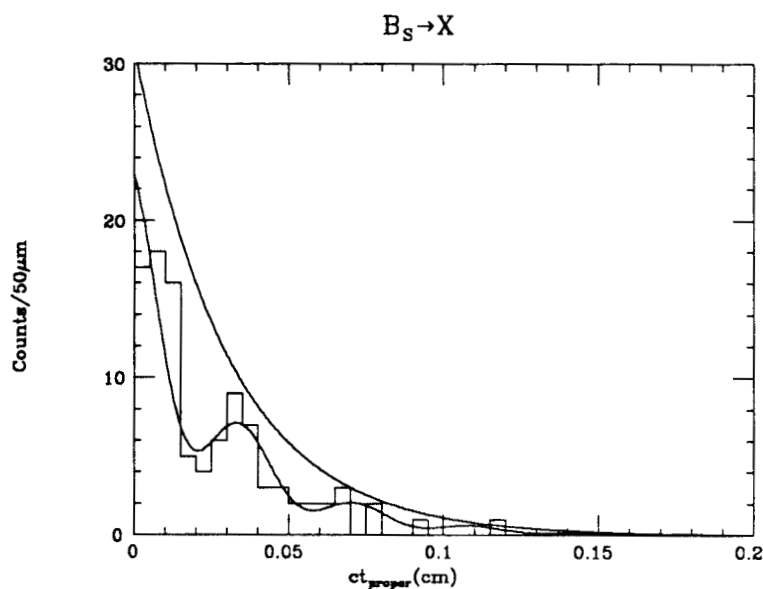


Figure 1a. Histogram of $I(B_s(t))$ for a sample of 100 correctly tagged B_s mesons with $x_s = 5$, $\sigma_{ct} = 50\mu\text{m}$, $B_s/(B_u + B_d) = 3$, and Correct to Incorrect $t = 0$ tag is $2.5 : 1$. The values from the fit are $c\tau = 0.031 \pm 0.003\text{cm}$, $x_s = 5.1 + 0.6 - 0.5$, and $\alpha = 0.81 + 0.81 - 0.35$.

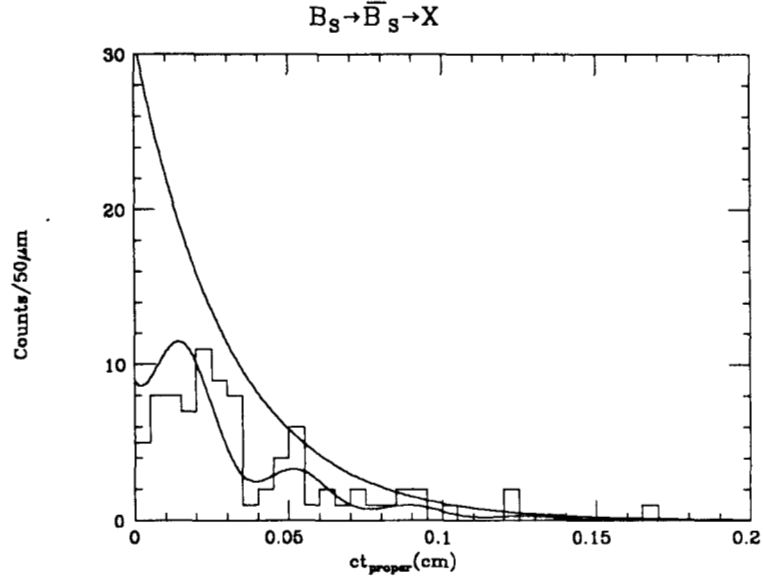


Figure 1b. Histogram of $I(\overline{B}_s(t))$ for a sample of 100 correctly tagged B_s mesons with $x_s = 5$, $\sigma_{ct} = 50\mu\text{m}$, $B_s/(B_u + B_d) = 3$, and Correct $t = 0$ tag to Incorrect $t = 0$ tag is 2.5 : 1. The values from the fit are $c\tau = 0.031 \pm 0.003\text{cm}$, $x_s = 5.1 + 0.6 - 0.5$, and $\alpha = 0.81 + 0.81 - 0.35$.

ID=ACS

ACS FOR BS

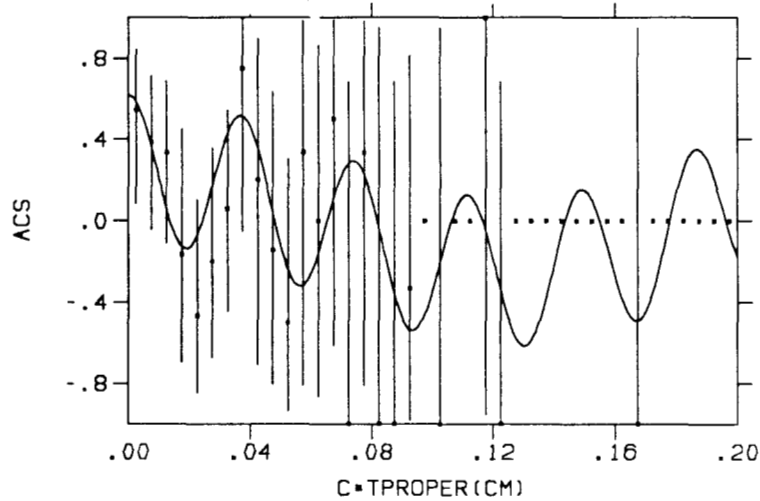


Figure 2. Histogram of A_{cs} for a sample of 100 correctly tagged B_s mesons with $x_s = 5$, $\sigma_{ct} = 50\mu\text{m}$, $B_s/(B_u + B_d) = 3$, and Correct $t = 0$ tag to Incorrect $t = 0$ tag is 2.5 : 1. The values from the fit are $x_s = 5.1 \pm 0.4$, $A_s = 0.36 \pm 0.33$, and $A_d = 0.25 \pm 0.33$.

Tables 1 and 2 include the results of fits for various other values of the assumed conditions—some more and some less favorable than the cases shown in the Figures. Table 1 gives examples

where the number of correctly tagged B_s events is 100 and σ_{ct} , the proper time resolution, is $50\mu\text{m}$, while Table 2 is for 400 such events with $\sigma_{ct} = 35\mu\text{m}$. The table entries are broken down further into levels of tagging effectiveness. We consider the possibility of improving the correct to incorrect $t = 0$ tag from 2.5 : 1 to 5 : 1. This improvement could be achieved at *SLC* if the electron polarization were increased significantly above 49%. We also vary the ratio of correct to incorrect B_s tags for three cases: 1 : 1, 3 : 1, and 5 : 1. Fitted values of x_s are given for both methods.

Table 1a. Fitted values of x_s under the following conditions: $x_s = 1$, $\sigma_{ct} = 50\mu\text{m}$, and 100 correctly tagged B_s mesons.

Cor./Incor.	$B_s : (B_d + B_u)$	x_s from MLH fit	x_s from χ^2 fit
5	5	$1.0^{+0.3}_{-0.2}$	1.1 ± 0.3
5	3	$1.0^{+0.3}_{-0.5}$	1.1 ± 0.3
5	1	1.1 ± 0.2	1.2 ± 0.5
2.5	5	1.1 ± 0.4	1.1 ± 0.6
2.5	3	1.0 ± 0.3	0.98 ± 0.48
2.5	1	1.0 ± 0.3	0.40 ± 0.40

Table 1b. Fitted values of x_s under the following conditions: $x_s = 5$, $\sigma_{ct} = 50\mu\text{m}$, and 100 correctly tagged B_s mesons.

Cor./Incor.	$B_s : (B_d + B_u)$	x_s from MLH fit	x_s from χ^2 fit
5	5	$4.8^{+0.7}_{-0.6}$	4.9 ± 0.4
5	3	$4.9^{+0.6}_{-0.5}$	5.0 ± 0.4
5	1	$5.1^{+0.6}_{-0.7}$	4.6 ± 0.4
2.5	5	5.0 ± 0.6	5.2 ± 0.3
2.5	3	$5.1^{+0.6}_{-0.5}$	5.1 ± 0.4
2.5	1	$5.1^{+0.6}_{-0.3}$	5.3 ± 0.4

Table 2. Fitted values of x_s under the following conditions: $x_s = 10$, $\sigma_{ct} = 35\mu\text{m}$, and 400 correctly tagged B_s mesons.

Cor./Incor.	$B_s : (B_d + B_u)$	x_s from MLH fit	x_s from χ^2 fit
5	5	$10.0^{+0.7}_{-0.6}$	9.9 ± 0.6
5	3	9.7 ± 0.6	9.7 ± 0.5
5	1	9.4 ± 0.5	9.2 ± 0.5
2.5	5	9.9 ± 0.6	9.5 ± 0.6
2.5	3	$9.9^{+0.6}_{-0.5}$	9.6 ± 0.4
2.5	1	$9.7^{+0.6}_{-0.5}$	12.1 ± 1.2

4. Discussion and Conclusions

The results of this study depend on a number of plausible assumptions for studying $\overline{B}_s B_s$ oscillations. They are based on assuming the *SLD* detector at the *SLC*, with some variation in the assumed level of performance. We have used two complementary methods for determining the oscillation parameter x_s . A summary of some observations follow:

- With 100 correctly tagged B_s decays, if $x_s = 1.0$ the maximum likelihood fit to the cosine-squared and sine-squared distributions reliably estimates the correct value while the asymmetry method (A_{cs}) often fails. (However, if x_s were to be this small, comparable to x_d , one could also resort to a time-integrated measurement to extract r_s from which x_s could also be determined.)
- When the maximum likelihood fit converges (or when the χ^2 fit is acceptable), the statistical errors on the x_s values are relatively insensitive to the background levels.
- Obtaining a reliable determination of x_s if it is 10 or larger will require either substantially more than 100 tagged B_s decays, greatly improved resolution, or some combination of the two. We find that $N_{\text{Cor.}} = 400$ events with $\sigma_{ct} = 35\mu\text{m}$ would suffice for all cases within our range of assumptions.
- We use an average value for the proper time resolution in this study. Although we do not expect the results presented in this paper to change, using a simulation of the proper time resolution that depends upon the decay length is an important effect for large x_s when the tagging method requires a minimum decay length for the B_s candidates. This effect will be included in a subsequent study.

REFERENCES

1. See, for example, results reported by *ARGUS* and *CLEO* groups at the 1989 SLAC Summer Institute.
2. See the *SLD* Design Report, SLAC-Report-273, 1984, and updates.
3. V. Barger, *Search for the Fourth Generation: Present and Future Prospects*, University of Wisconsin Preprint, MAD/PH/500, June 1989.
4. Torbjorn Sjostrand, Muts Bengtsson (Lund University), *Comput. Phys. Commun.* **43** (1987) 367.
5. For flavor oscillations, see, for example, E.D. Commins and P.H. Bucksbaum, "Weak Interactions of Leptons and Quarks," (Cambridge: Cambridge Univ. Press, 1983), ch. 7.
6. W.B. Atwood, *B Meson Physics With Polarized Electron Beams at the SLC*, SLAC-PUB-4668, Sept. 1988; also, W.B. Atwood, I. Dunietz, and P. Grosse-Wiesmann, *CP Violation at the Z^0 with Polarized Beams*, SLAC-PUB-4544, April 1988.
7. T.W. Reeves and R.S. Panvini, *On the Use of Charged Fragmentation Kaons for Tagging B_s Mesons*, these proceedings. See also A. Ali and F. Barreiro; The Final States $l^\mp K^\pm K^\pm X$ in Jets as Signatures of B_s^0 — \bar{B}_s^0 Mixings; *Z. Phys. C-Particles and Fields* **30**, 635-642(1986).
8. T.W. Reeves, PhD. thesis, Vanderbilt University, in preparation.
9. The measuring resolution of the *SLD* detector has been simulated with a parametric Monte Carlo that incorporates the expected performance of all parts of the detector. The LUND (version 6.3) generator is used to create a meaningful momentum spectrum of tracks from which these determinations are made.
10. Not only may the B_u and B_d lifetimes differ from the B_s lifetime, but different components of the background may also have different effective lifetimes due to missing final state tracks.

On the Use of Charged Fragmentation Kaons for Tagging B_s Mesons

T.W. Reeves, R.S. Panvini

Vanderbilt University, Nashville, Tennessee 37235

ABSTRACT

We present a study of the utility of using charged kaons produced in the fragmentation process of $Z^0 \rightarrow \bar{b}b$ decay to tag B_s mesons. We find it is possible to obtain a good signal-to-noise ratio with a high efficiency if one assumes that charged kaons from the decay cascade of b -hadrons can be separated from fragmentation kaons originating at the e^+e^- interaction point.

1. Introduction

Measuring $\bar{B}_s B_s$ mixing oscillations is arguably one of the most important measurements that could be done with the *SLD* detector at the *SLC*.^[1] To make this measurement, it is paramount that a method of cleanly tagging B_s mesons be determined. Two aspects^[2] of B_s tagging that strongly influence one's ability to measure $\bar{B}_s B_s$ mixing are: the requirement that the particle/antiparticle identity of the B_s be determined at time $t = 0$, and the requirement that B_u and B_d decays not be identified as B_s decays. It is the purpose of this study to examine the feasibility of a tagging technique that involves looking for charged kaons that are produced along with B_s mesons in the fragmentation process of $Z^0 \rightarrow \bar{b}b$.^[3]

We begin first by describing the fragmentation kaon that is associated with the production of the B_s meson. Next, we describe the method by which we select these associated kaons. Finally, we examine the results of a Monte Carlo study of the performance of this technique. In an example, we show how this technique might improve one's ability to tag not only the decay of the B_s meson, but also its particle/antiparticle identity at time $t = 0$.

2. The Associated Kaon

This method of tagging B_s mesons is to find a $K^+(K^-)$ that emerges in the same jet as the $B_s(\bar{B}_s)$ meson. The momentum and angle of the fragmentation K^\pm relative to the B_s should be consistent with its having coming from the same part of the fragmentation chain as did the B_s . More explicitly, the fragmentation process is such that when a B_s is produced from a \bar{b} -quark and an s -quark, the s -quark will be produced along with a \bar{s} -quark which will often combine with a u -quark to form a K^+ . (This includes K^+ mesons from K^* decay.) This establishes the particle/antiparticle identity of the B_s meson when it is created. The same is, of course, true for the \bar{B}_s — K^- correlation. We will hereafter refer to these fragmentation kaons associated with the production of $B_s(\bar{B}_s)$ mesons as the associated kaons.

3. Method

We use *LUND* 6.3^[4] to generate a sample of $Z^0 \rightarrow \bar{b}b$. We do not study light quark events since we expect to use this technique in conjunction with other techniques that will already have removed these events.^[5] Furthermore, we do not simulate the detector response as the *SLD* is expected to have excellent momentum resolution and to be able to cleanly identify kaons.^[6] We do, however, require that the momentum of the K^\pm be greater than 1 GeV/ c since the *CRID* system will not be able to effectively identify these very slow kaons.

Given the location of the associated kaon in the fragmentation chain, we expect that it will, on the average, follow the direction of the B_s meson and have a higher momentum than other fragmentation kaons. Therefore, we search for these associated kaons by first finding the fragmentation K^\pm in the same hemisphere as the B meson (assumed to have already been tagged as a B_s) with the highest momentum. We then require that the angle between the momentum vector of this associated kaon and the momentum vector of the B meson be below some maximum value.

For this study, we assume that kaons from the decay cascade of B mesons have already been identified and will not be a source of noise. If this requirement cannot be met, the effectiveness of this kaon tag will diminish substantially.

4. Results

If we compare the momenta of the associated kaons with the momenta of other fragmentation kaons, we find that the average momentum of these kaons is 3.5 GeV/ c ; whereas the average momentum for all fragmentation kaons in the same jet as a B_s meson is 3.1 GeV/ c . For B_u and B_d mesons, the average is 2.4 GeV/ c . As expected, the average momentum of the associated kaons is higher than that of fragmentation kaons from other sources.

One can then select the fragmentation kaon in the jet with the highest momentum. We show in Figure 1 a plot of the fraction of events kept versus the maximum angle between the fragmentation kaon and the B meson in the jet. This plot indicates that associated kaons are, as expected, produced at a smaller angle relative to the B meson than other fragmentation kaons. If one sets a maximum angle between the highest momentum kaon and the B meson of 30 degrees, 80% of the B_s mesons will be retained, but only 60% of B_u and B_d events will be retained.

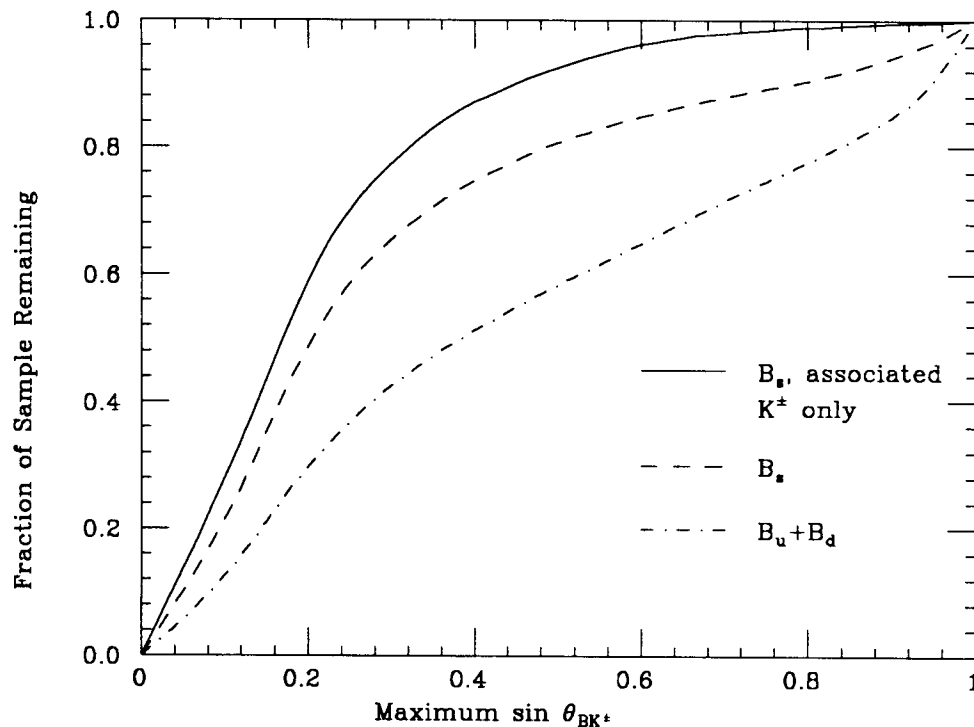


Figure 1. Fraction of events kept versus the maximum angle between the highest momentum fragmentation kaon and the B meson in the jet, kaons are required to have at least 1 GeV/c in order to be identifiable by the CRID system

We illustrate the potential power of this tagging method with a simple example. Suppose that one has already applied a B_s tagging technique that results in a sample of 1000 B_s mesons and 1000 B_u/B_d mesons. Assume further that this technique does not give one any information on the particle/antiparticle nature of the B_s mesons at the time of their creation. The results after applying the kaon tag are summarized in Table 1. The "Correct $t = 0$ tag" and "Incorrect $t = 0$ tag" entries refer to the number of times that the charge of the fragmentation kaon correctly

or incorrectly determines the particle/antiparticle identity of the B_s meson at time $t = 0$. After applying this associated kaon tag to the sample of 2000 B mesons, we find that the ability to tag the particle/antiparticle nature of the B_s at its production is now $345/49 = 7.0$. The ability to reject B_u and B_d is now $394/142 = 2.8$.

Table 1. Summary of results after applying fragmentation K^\pm technique

Cut Applied	B_s			$B_u + B_d$
	Correct $t = 0$ tag	Incorrect $t = 0$ tag	Total	Total
No K^\pm Tag	500	500	1000	1000
Highest Momentum K^\pm	412	83	495	242
$\sin \theta_{BK^\pm} < 0.5$	345	49	394	142

5. Summary

This K -tag method will require the good particle identification capability of the SLD detector. It will also rely heavily on excellent vertex detection to separate fragmentation kaons from those produced in the decay cascade of B mesons since these kaons have kinematic characteristics that are similar to the associated kaons.

If one can ensure that kaons originating in the fragmentation process of $e^+e^- \rightarrow Z^0 \rightarrow \bar{b}b$ can be separated from kaons originating from B meson decay, this technique will provide a ratio of better than 5 : 1 for the correct/incorrect identity. This is to be compared to a correct/incorrect ratio of 2 : 1 provided by using the intrinsic $\bar{b}b$ asymmetry that results when the electron beam has 49% polarization.^[2] The price that must be paid for this good tagging ratio is that less than one half of the B_s meson sample will survive this technique.

REFERENCES

1. L-P Chen, R.S. Panvini, T.W. Reeves, G.B. Word; Aspects of B Physics from $e^+e^- \rightarrow Z^0 \rightarrow \bar{b}b$; these proceedings.
2. For a better understanding of how these aspects affect one's ability to measure mixing, see T.W. Reeves, R.S. Panvini, G.B. Word; $\bar{B}_s B_s$ Oscillations Seen from $e^+e^- \rightarrow Z^0 \rightarrow \bar{b}b$ with the SLD at the SLC ; these proceedings.
3. This idea of using these kaons to measure $\bar{B}_s B_s$ mixing oscillations has previously been suggested by A. Ali and F. Barreiro; The Final States $l^\mp K^\pm K^\pm X$ in Jets as Signatures of $B_s^0 - \bar{B}_s^0$ Mixings; Z. Phys. C-Particles and Fields 30, 635-642(1986).
4. Torbjorn Sjostrand, Muts Bengtsson (Lund University), Comput. Phys. Commun. **43** (1987) 367.
5. Experience in other Monte Carlo studies has shown that tagging $Z^0 \rightarrow \bar{b}b$ events is relatively easy compared to tagging the decay of a specific B meson.
6. SLD Design Report, SLAC-Report-273, 1984, and updates.

Aspects of B Physics from $e^+e^- \rightarrow Z^0 \rightarrow \bar{b}b$ [†]

L-P Chen, R.S. Panvini, T.W. Reeves, G.B. Word
Vanderbilt University, Nashville, Tennessee 37235

ABSTRACT

The study of “ B Physics” from the process $e^+e^- \rightarrow Z^0 \rightarrow \bar{b}b$ has several important features. These include: a large cross-section for $\bar{b}b$ production relative to the $\Upsilon(4S)$; high momentum production of B mesons in jets leading to clear secondary and tertiary vertices; accessibility to high-mass b -flavor states; and the ability to produce polarized Z^0 bosons. As a specific example of an important physics measurement that requires the full power of the SLD detector and a polarized electron beam from SLC , we discuss $\bar{B}_s B_s$ mixing as determined from observing b -flavor oscillations. We conclude that some of the most important measurements in B physics can only be made with the features that are peculiar to B ’s that are produced from Z ’s. In addition, the B physics accessible from Z decays will complement studies at lower energies. This report is not meant to be a comprehensive study of B decays, but rather a subjective overview of the subject with references to the literature and comments relative to what may be achieved with the SLD detector at the SLC .

[†] Prepared for *SLD Physics Week*, Kirkwood, CA, July 31–August 4, 1989. Work supported by the National Science Foundation.

1. Introduction

The importance of physics of the b -quark as a prime testing ground of aspects of the standard model—and of “new physics” beyond the standard model—is reflected in the large number of papers on this subject.^[1] Our purpose here is to gain a perspective on those aspects of B physics which can be done particularly well when studying B mesons resulting from electron-positron interactions at the Z^0 pole with the resulting Z^0 decaying subsequently into $\bar{b}b$ jets.

“ B Physics” is a phrase we use to describe all physics that derives from studies involving the b -quark. There are two main categories: the properties of mesons and baryons that contain a b -quark, and b -hadron tagging as a signature for processes that involve the b -quark—such as Higgs decays, fourth generation (e.g., b' -quark) decays, and couplings of $\bar{b}b$ pairs to the Z^0 .

Both SLC and LEP should be able to make major contributions in the area of B physics. LEP has the potential to achieve sufficiently high luminosities to produce as many or more B 's than will be produced at the $\Upsilon(4S)$ by the upgraded $CESR$ at Cornell—and therefore to have special value for rare processes. Note that the cross section for $\bar{b}b$ production is 1.2 nb at the $\Upsilon(4S)$ and is 6.3 nb from Z^0 decay.

SLC , together with SLD , provides two features of special importance: one is the ability to polarize the electron beam, the other is the small beam size combined with a short duty cycle which allows instrumentation of a high precision vertex detector. B mesons can be cleanly isolated from other flavors by their secondary, and sometimes tertiary, vertices. When studying $\bar{B}^0 B^0$ mixing it is obviously important to know whether the B^0 meson was originally a particle or an anti-particle. By polarizing the electron beam, large forward-backward asymmetries can be produced which allow the experimenter to make a statistical statement about the probability that the original B^0 meson was a particle or anti-particle.^[2] A forward-backward asymmetry can also be used in the study of the $\bar{b}b$ quark couplings to the Z^0 which can be used to test the neutral current couplings in the Standard Model.

We use the Standard Model (SM) as a guide for addressing the most important B physics issues which can only be resolved with additional experimental data. The charged current couplings in the weak sector of the SM are described by the Kobayashi-Maskawa (KM) mixing matrix. We discuss below which matrix elements need to be determined and how measurements involving B mesons (b -quarks) are particularly important.

The neutral current couplings in the standard model include $Z^0 \rightarrow \bar{b}b$. The branching ratios into specific fermion/antifermion pairs depend on the value of the Weinberg angle— $\sin^2 \theta_W$. The fact that the left- and right-handed couplings of fermions to the Z^0 are different causes the Z^0 to be polarized. The asymmetry in the total cross section measured at the Z^0 pole, obtained by changing the longitudinal polarization of the electron beam, will most likely give the best value

of $\sin^2 \theta_W$. However, a rigid testing of the *SM* will also require measuring the forward-backward asymmetry of each fermion-antifermion pair, (A'_{FB}), including $\bar{b}b$.

There are other aspects of *B* physics that should be best studied with Z^0 decays. While studies at the $\Upsilon(4S)$ and $5S$ states will provide the best mass resolution for a wide variety of exclusive decays, the Z^0 is of special value for studies of states too massive to be produced in Υ decays.

We discuss potential *B* physics topics in more detail in Chapter 2, assorted *B* decays in Chapter 3, states requiring a *B* tag in Chapter 4, and we discuss in some detail the subject of $\bar{B}_s B_s$ mixing as determined by *b*-flavor oscillations in Chapter 5. The oscillations measurement is a particularly interesting example of important physics that requires the full capability of the *SLD* detector combined with special features of *SLC*—electron beam polarization and a small beam pipe. In chapter 6 we include a summary of existing and future e^+e^- accelerators capable of doing *B* physics and summarize the present status of various *B* physics measurements as well as the future goals for these measurements.

2. Electroweak Aspects of *B* Physics

Decays of *B* mesons yield essential information on electroweak parameters in the context of the standard model. Extracting these parameters is obscured by the fact that the strong interactions between the quarks are not well understood and they mask the interesting electroweak effects. We summarize some of the key issues in “*B* physics” in this chapter.

2.1. KM PARADIGM—THE STANDARD MODEL FOR THE WEAK CHARGED COUPLINGS

The “KM Paradigm” is the six quark, or three generation, extension by Kobayashi and Maskawa (KM) of Cabibbo’s original mixing hypothesis. The KM formulation includes *CP*-violation in weak decays as a natural consequence of a non-trivial phase angle that appears in this matrix. The phase angle must be a non-integral multiple of π for *CP* violation to occur. The challenge for experimentalists is to measure each of the matrix elements of the 3×3 KM matrix, which must be unitary if the SM is correct. There are several conventional formulations of this matrix, but for three generations and the unitary constraint, a common feature is that there will be a total of four independent parameters—three angles and the *CP* violating phase angle.

Unitarity applied to the first and third column of the KM matrix give the following approximate relationship:

$$V_{ub}^* - s_{12}V_{cb}^* + V_{td} = 0.$$

This relationship can be expressed in terms of a triangle in the complex plane with two sides being the matrix elements V_{ub}^* and V_{td} , and an internal angle which is the *CP*-violating phase

(see Ref. 1). The area of this triangle is a measure of the size of the CP violating effects—in the context of the standard model. Failure to close the sides of this triangle will be a sure indicator of “new physics.”

The two matrix elements in the KM matrix that will be most important for closing the triangle are V_{td} and V_{ub} . These two matrix elements are the ones furthest from the diagonal of the matrix and are expected to be the smallest in magnitude.

The quest for CP violation in B decay

The observation of CP -violation in other than neutral kaon decay remains a central challenge in particle physics. Unfortunately, while the standard model predicts the level at which CP violation should be observed in B meson decays, estimates have shown that the order of 10^8 $B\bar{B}$ pairs are needed for such a measurement. The enthusiasm for B -Factories that would be capable of producing sufficient B 's for this purpose is to a large extent motivated by the desire to observe CP violating effects in B decays.^[3] Short of measuring CP violation in the b -quark sector, it will be highly informative to know whether the standard model for the charged current sector of the weak interactions is correctly described by the KM paradigm—which conveniently carries with it the CP violating phase angle.

Mixing between particle and antiparticle states for B_d and B_s

The *ARGUS* and *CLEO* measurements show strong mixing in the decays of B_d mesons.^[4] Mixing can be measured by observing the fraction of produced neutral $\bar{B}B$ pairs which are observed to decay as $\bar{B}B$ or BB . In particular, one can measure the relative numbers of like sign to unlike sign leptons.

A convenient measure of mixing is a parameter r which is defined as

$$r = \frac{\bar{B}^0 \rightarrow B^0 \rightarrow Xl^+\nu}{\bar{B}^0 \rightarrow Xl^-\nu}. \quad (1)$$

The value of r_d obtained by averaging measurements from the *ARGUS* and *CLEO* collaborations is 0.18 ± 0.05 .

The intensity of oscillations—assuming a B_s meson at $t = 0$ and ignoring CP violation—will be given by the expressions

$$I(B_s) = e^{-t/\tau_s} \cos^2 \left(\frac{x_s t}{2\tau_s} \right), \quad (2)$$

and

$$I(\bar{B}_s) = e^{-t/\tau_s} \sin^2 \left(\frac{x_s t}{2\tau_s} \right), \quad (3)$$

where $x_s = \tau_s \times \Delta m_s$ and Δm_s is the mass difference between the two B_s mass-eigenstates.

Note that the key to observing oscillations is that x_s is large compared to one. This ensures that the period of the oscillations is significantly smaller than the mean lifetime of the B_s . If the opposite is true, the particle decays before it has a chance to be seen to oscillate.

The x_s mixing parameter is given by

$$x_s = \frac{G_F^2}{6\pi^2} m_t^2 \tau_B f_B^2 B_B m_B |V_{tb} V_{ts}^*|^2 g \left(\frac{m_t}{M_W} \right) \eta_{QCD}, \quad (4)$$

where f_B is a decay constant, B_B is the bag factor for B mesons, g is a factor that depends on the t -quark mass ($g = 1$ for $m_t \ll M_W$, $g \approx 0.6$ for $m_t = 2M_W$) and η_{QCD} is a QCD correction factor of about 0.85.

Because of uncertainties in the constants and QCD correction factors in Eqn. 4, a determination of x_s alone will likely be insufficient to determine $|V_{ts}|$ accurately. The same is true for $|V_{td}|$ since it would be determined from a similar expression for x_d . On the other hand, we may reasonably assume these uncertain factors will cancel if we measure both x_d and x_s , so that the ratio will be given approximately by

$$\frac{x_s}{x_d} \approx \frac{|V_{ts}|^2}{|V_{td}|^2}.$$

This ratio is expected to be greater than one with three generations in the standard model. However for four generations this ratio can range from values between 10^{-3} to 10^3 . The possibility that x_d/x_s may be less than one is unique to the fourth generation. Supersymmetry, charged Higgs bosons and left-right symmetric models all give values greater than unity for this ratio.^[5]

These two mixing parameters, r and x , are related by the expression

$$r = \frac{x^2}{x^2 + 2}. \quad (5)$$

The value of x_d is therefore determined from the measured value of r_d and is $x_d = 0.66 \pm 0.17$.

Theoretical considerations, based on box-diagram calculations, predict that mixing in B_s should be maximal, meaning that r_s will be close to one and that b -flavor oscillations could be observable for B_s decays.^[6] Furthermore, with r_s expected to be close to unity, the value of x_s will be large and poorly determined from the value of r_s as determined from Eqn. 5. Thus, the direct measurement of x_s from b -flavor oscillations may be the only way to determine x_s .

$b \rightarrow u / b \rightarrow c$

An estimate of $b \rightarrow u / b \rightarrow c$ has been determined from model dependent studies of the lepton momentum spectrum in semileptonic B decay at the $\Upsilon(4S)$ by *CLEO* and *ARGUS*. They quote the ratio $|V_{ub}|/|V_{cb}| = 0.10 \pm 0.03$ (see Ref. 4). Because the limits placed by studying the

lepton spectrum are very model dependent and are subject to a sensitive background subtraction, the best measurement may ultimately be obtained from the studies of charmless semileptonic B decays, e.g., $B \rightarrow \rho l \nu$ and $B \rightarrow \pi l \nu$. A positive identification of these simple final states would be a sure indicator of a non-zero $b \rightarrow u$ transition. By contrast, non-leptonic charmless decays are not necessarily indicators of $b \rightarrow u$ transitions since diagrams with internal loops ("Penguin diagrams") that contain $b \rightarrow c$ transitions are possible.

The decay $B \rightarrow \tau \nu$ would also be excellent, provided that the branching ratio is not too small to measure.⁶ The expression for the branching ratio is

$$Br(B^+ \rightarrow \tau^+ \nu_\tau) = (1.3 \times 10^{-4}) \left(\frac{f_B}{100 \text{ MeV}} \right)^2 \left(\frac{|V_{ub}|}{0.01} \right)^2, \quad (6)$$

where estimates of the decay constant f_B , unfortunately, have ranged from 75 to 480 MeV (see Ref 6)—though it may be argued that most estimates give a value near 100 MeV.

The detection of the τ from this decay mode could only be made using a decay mode of the τ into at least three charged particles. This inclusive branching ratio is about 13%. The reconstruction efficiency^[7] for a three-prong τ decay from the decay $Z^0 \rightarrow \tau^+ \tau^-$ is expected to be about 25%. Since the τ fermions from two-body B decay will be accompanied by many other particles from the Z decay, the reconstruction efficiency will certainly decrease in attempts to reduce the backgrounds. If the branching ratio is on the order of 10^{-4} , then at least 10^7 B mesons will be needed to measure this branching ratio.

$|V_{cb}|$ and $|V_{ub}|$

The KM matrix elements $|V_{cb}|$ and $|V_{ub}|$ are determined from the B lifetime from the expression

$$\Gamma(B \rightarrow l \nu X) = \frac{G_F^2 m_B^5}{192 \pi^3} \eta (f_c |V_{cb}|^2 + f_u |V_{ub}|^2), \quad (7)$$

where f_q is a phase space factor depending on the quark mass and η is a QCD correction factor estimated to be 0.87 ± 0.05 .^[8] Since $|V_{ub}|$ is much smaller than $|V_{cb}|$, this method serves primarily to determine the latter quantity.

The matrix element in this formula is similar to the one that applies for muon decay, and it depends on knowing the mass of the b -quark raised to the fifth power. Since the free quark model is an over simplification of B decays, it is necessary to rely on models which account for strong interaction effects. Many papers have been written recently on this subject.^[9] These studies suggest how best to measure the relevant KM matrix elements in view of the strong interaction uncertainties.

The decay that can be analyzed most cleanly from an experimental viewpoint is $\overline{B}_d^0 \rightarrow D^{*+} l \nu$. Four independent variables are needed to completely describe this process and there are

also four form factors to be specified (see Ref 9). Three of the four form factors are reasonably well understood, but the fourth is not. However, this undetermined form factor can be parametrized by studying the decay correlations—in particular, the relative amounts of longitudinal and transverse polarization in the D^* decay as a function of the lepton momentum or some other equivalent variable.^[10]

On the other hand, semileptonic decays with a D rather than a D^* are better understood theoretically since there is only one form factor that has a well defined dependence on the variables. However, it is difficult to unravel final states with only a D from those which have a D^* that subsequently decays into a D and an undetected π^0 or γ . There may also be D^{**} states that further complicate matters, although it is thought that the contribution of such states is not more than at the 10% level. Hence there is much work that is needed to understand these decays from both a theoretical and experimental viewpoint—and in particular, there will be some advantage to having B decays with identifiable secondary and tertiary vertices.

2.2. THE STANDARD MODEL FOR THE WEAK NEUTRAL COUPLINGS

Right- and left-handed fermions couple differently to the Z^0 . Though a measurement of the asymmetry between the total cross section with left- and right-handed polarized electrons, A_{LR} , will be the most sensitive asymmetry measurement for determining the Weinberg angle in the SM, measurements of the various forward-backward asymmetry, A_{FB}^f , associated with each possible outgoing fermion, f , (both leptons and quarks) is essential for checking the SM thoroughly. If we assume that a B meson can be used to stand in place of its constituent b -quark, then A_{FB}^b can be determined from a measurement of the asymmetry of final state B (or \bar{B}) hadrons.

With an unpolarized beam, the SM predicts $A_{FB}^b = 0.167$. A polarized electron beam will enhance the asymmetry.^[11] For example, with an electron beam that is 45% polarized the asymmetry will be increased^[2] to 0.34. This amount of polarization is expected to be achieved at the *SLC*.

Various methods of measuring the forward-backward asymmetry for each of the principal kinds of B mesons (B_u , B_d , and B_s) have been studied. These studies include the effect of mixing for the neutral states and include measuring the mixing parameters. With only 5×10^4 $b\bar{b}$ pairs produced with a 45% polarized electron beam and a B_u tagging efficiency of 7.4%, *SLD* should be able to measure^[2] A_{FB}^b to within ± 0.03 .

Measurements of the branching ratios of the Z^0 into the various possible fermion-antifermion pairs will be an important consistency check of the SM. In particular, $b\bar{b}$ jets will be the next easiest to measure after lepton pairs. The standard model predictions for the branching ratios of the Z^0 into various quark pairs and lepton pairs (assuming $\sin^2 \theta_W = 0.226$ and $m_t = 40$ GeV) is as follows:^[12]

Branching Ratios for $Z \rightarrow f\bar{f}$ Based on Standard Model

Fermion type	$\Gamma(\text{GeV})$	Branching ratio (%)
e, μ, τ	0.087	3.3
ν_e, ν_μ, ν_τ	0.172	6.5
u, c	0.298	11.2
d, s	0.383	14.4
b	0.379	14.3
t	0.060	2.3
$\Sigma_i q_i \bar{q}_i g$	0.072	2.7
Total	2.65	100

Note that since the partial width contributed by a 40 GeV t -quark is so small (2% of the total), the exclusion of the t -quark from the calculation of the total width will not significantly change the branching ratio of the Z^0 into $b\bar{b}$ quark pairs. The existence of a fourth generation, however, could appreciably change these branching ratios if the mass of any member of the fourth family is less than $M_Z/2$. While a heavy fourth generation electron-type lepton will not have a significant effect, we note that a fourth generation neutrino would add another 0.172 GeV to the total width and that a fourth generation d -type quark of, say, 40 GeV would add 0.162 GeV. If either of the later two is produced in Z^0 decay, then $B(Z^0 \rightarrow b\bar{b})$ will be reduced by about 1%. Since the efficiency for tagging b -quark jets is expected to be greater than 10%, a sample of about 10^4 Z_0 decays should be sufficient to reach this level.

3. Assorted B Decay Studies

3.1. B_s MIXING VIA FLAVOR OSCILLATIONS

This section summarizes a study of what could plausibly be expected from the SLD detector after a large sample of Z^0 decays is accumulated—and the data is analyzed for observing B_s oscillations. This study is a good model to explore the potential of B physics from Z decays because it requires all of the features of a powerful detector, a polarized electron beam, and good statistics. We summarize in this chapter results discussed in detail elsewhere.^[13]

Basic Concepts

To illustrate this procedure, assume a pure sample of B_s at time $t = 0$. The proper time evolution of B_s will have the form given by Eqn. 2 and the form of the time evolution of \bar{B}_s will be given by Eqn. 3. A maximum likelihood method can be used to simultaneously fit these

two distributions for the parameter x_s . In practice, the data is more complicated because of backgrounds.

The net effect of simulating real conditions is to change the form of the expected proper time distributions from those in Eqns. 2 and 3 to the following:

$$I(B_s(t)) = e^{-\Gamma_s t} (\alpha + \cos^2 \frac{\Gamma_s x_s t}{2}), \quad (8)$$

and

$$I(B_s(t)) = e^{-\Gamma_s t} (\alpha + \sin^2 \frac{\Gamma_s x_s t}{2}). \quad (9)$$

The added exponential term with the coefficient α accounts for misidentified B_s backgrounds, incorrect $t = 0$ tags, and finite measuring resolution.

Tagging B_s

Two methods are found to be most useful for particle/antiparticle tagging at time $t = 0$. One method is to use the forward-backward asymmetry that can be enhanced with a polarized electron beam. The other method is to use a charged kaon that is produced in the jet along with the B_s meson. (Note that the B_s uses an s -quark popped from the vacuum. Its \bar{s} -quark partner often makes a K^+ by combining with a u -quark. This correlation tags the B_s identity at $t = 0$.) For more details, see Ref. 13.

To measure the B_s decay length and to estimate its momentum, it is necessary to find as many of the final state particles as possible. The chief background is from B_u and B_d mesons which together are produced about ten times more often than B_s . A clean tag, in general, for B mesons is via their semileptonic decays. Moreover, a B_s will decay most often into a D_s meson, which subsequently decays often into $\bar{s}s$ mesons—including ϕ 's and η 's. Unfortunately, D mesons, which are copiously produced in B_u and B_d decay, also decay into ϕ and η mesons often enough to provide a significant background. Hence, tagging the B_s decay cleanly is very difficult. It requires reconstruction of as much of the final state as possible. Work on improving our ability to tag B_s mesons is in progress.

Measuring Resolution

Two factors limit the accuracy of the proper time measurement: the uncertainty in the B_s decay point relative to the Z^0 decay point, and the uncertainty in the momentum of the B_s —which limits the precision in the determination of $\gamma\beta$ to compute the Lorentz boost for the proper time calculation.

Although the absolute uncertainty in the proper time measurement increases with increasing decay length, we use the average value. This is valid if a minimum decay length to tag B_s

candidates is not required. If, however, the tagging method requires a minimum decay length for the B_s candidates, the average measured error will increase. We estimate that $\sigma(ct_{\text{proper}})$ will increase by about 15% if a minimum decay length of $500\mu\text{m}$ is required. For large x_s , this effect can be significant.

The total average error in the B_s proper time measurements for the *SLD* detector is estimated to be about $50\mu\text{m}$.

Simulation of Data

B_s mixing data is simulated with a short (two page) FORTRAN program which has seven input numbers. These are: the mixing parameter x_d (determined from r_d measurement of *ARGUS* and *CLEO*); an assumed value for the B_s mixing parameter, x_s ; the (generic) B meson lifetime; the proper time resolution; the ratio $N_{B_s}/(N_{B_u} + N_{B_d})$; the ratio $\frac{N_{\text{correct}}}{N_{\text{incorrect}}} t = 0$ tag; and the number which controls the statistical accuracy of the sample—we fix the number of “correctly tagged” B_s events. From x_s we compute the expected value of r_s and accordingly apportion the relative numbers of particle vs antiparticle generated. The generated data samples are then used as input to two fitting methods.

Conclusions from B_s Simulation Study

A more complete discussion along with plots of fits and tables of results is included in a separate paper on this subject (see Ref. 13). We summarize key points here.

Our studies were made with values of x_s equal to one, five and ten. (The best guess for x_s within the context of the standard model is about five, although it could also be much larger and still be consistent with the standard model.^[14]) With $10^5 \bar{B}B$ pairs, we should be able to find about 100 B_s decays and measure x_s to an accuracy of about 15%, with $x_s = 5$. However, for x_s equal to ten or larger, we find that a measurement error of about $50\mu\text{m}$ in ct will be unacceptable. Of course, with sufficient additional statistics, the oscillations will become statistically significant again.

3.2. LIFETIMES FOR SEPARATE B SPECIES

The B lifetime normally quoted is determined by averaging over all species of b mesons and baryons. For charmed hadrons the lifetimes differ by at least a factor of two over the various species. One would expect the lifetimes to be equal for each kind of charmed particle decay if the spectator model were unmodified by strong interactions—i.e., QCD effects. The first direct measurement^[15] of the B_d lifetime (as distinct from an average B lifetime) has been made recently by the MarkII collaboration, based on B 's produced in the continuum at *PEP* energies. The result, $\tau_{B^0} = 1.21^{+0.55+0.18}_{-0.38-0.16}$, suggests that the lifetimes are probably not too different. Improved

lifetime measurements by the same or similar techniques will apply for the high momentum B 's which emerge from Z decays.

CLEO and *ARGUS* are beginning to provide measurements that are complementary to comparative lifetime measurements. They measure the relative branching ratios of neutral to charged semileptonic B branching ratios at the $\Upsilon(4S)$ which they find to be $1.00 \pm 0.23 \pm 0.14$. (See Ref. 4.) Hence, it does not appear that there will be any surprises in this area.

3.3. BEAUTY BARYONS

Beauty baryons should be produced relatively copiously—a few percent of the rate for producing B mesons.^[16] Semileptonic decays of b -baryons should be relatively easy to find if one can correlate a baryon of the correct particle/antiparticle type with an identified lepton—while the two are consistent with coming from the same vertex and are also kinematically consistent with having come from a b -baryon parent. The available energy should permit production of b -baryons in various combinations: buu , bud , bdd , bsu , bsd , bss , etc. The final states may be difficult to reconstruct because of undetected decay products, but they should be characterized by copious proton and Λ production. Vertex detection and good particle identification should be of particular value in isolating such decay modes.

3.4. B_c —PROSPECTS AND POSSIBILITIES

The B_c meson is interesting from several points of view. It is a heavy $b\bar{c}$ (or charge conjugate) system that can be treated in non-relativistic models like $b\bar{b}$ and $c\bar{c}$ systems. The weak decays should be interesting because either the b - or the c -quark will decay. The relative amounts of one type versus the other will be influenced by the way the quarks interact. One particularly interesting decay mode for tagging purposes involves a $b \rightarrow c$ transition: $B_c \rightarrow \Psi l \nu$. Another interesting final state occurs when the b - and \bar{c} -quarks mutually annihilate and yield a virtual W . A distinctive decay of this kind would be $B_c \rightarrow \tau \bar{\nu}_\tau$.

While there are as yet no published calculations for $B(Z^0 \rightarrow B_c X)$, the rate has been estimated^[17] by extrapolating a calculation^[18] of the total rate for the process $e^+e^- \rightarrow B_c X$, while taking into account the differences between γ and Z couplings to quarks. The branching ratio estimate is $B(Z^0 \rightarrow B_c^{(*)} X) = 5 \times 10^{-5 \pm 1}$ of the total Z^0 width, where $B_c^{(*)}$ is meant to indicate all possible radially excited states and spin states.

The inclusive rate $B(B_c \rightarrow \Psi X)$ has been estimated^[19] by scaling the rate from B_d decay, with the result $B(B_c \rightarrow \Psi X) \approx 2\%$. As is the case for lighter B meson decay to J/Ψ , the remaining hadronic state is predicted to be of low multiplicity with the dominant $J/\Psi X$ final states of B_c decay expected to be $J/\Psi\pi$, $J/\Psi\rho$, and $J/\Psi a_1$, resulting in signatures for B_c decay

being a J/Ψ with one, two or three pions. While the B_c would be able to be fully reconstructed through these decay modes, we expect that combinatoric backgrounds will probably be prohibitive without superior vertex resolution.

Preliminary calculations^[20] have been made of semileptonic B_c meson decay using the quark potential model.^[21] Some of the results are shown in the following table, where the KM matrix element values $|V_{cb}| = 0.045$ and $|V_{cs}| = 0.974$ have been used.

Estimated B_c Branching Ratios	
Process	$\Gamma(10^{10}\text{s}^{-1})$
$c \rightarrow Xe^+\nu_e$	7.11
$b \rightarrow Xe^+\nu_e$	5.60
$B_c^+ \rightarrow Xe^+\nu_e$	12.71
$B_c^+ \rightarrow \eta_c e^+\nu_e$	0.65
$B_c^+ \rightarrow J/\Psi e^+\nu_e$	3.30
$B_c^+ \rightarrow B_s^0 e^+\nu_e$	1.70
$B_c^+ \rightarrow B_s^{*0} e^+\nu_e$	4.92

For the case that the c quark decays semileptonically, calculations of additional radially excited states and other spin states appear to converge quickly with the two lowest states accounting for about 98% of the semileptonic decays to B_s . The calculations of the states possible when the b quark decays semileptonically does not converge at the $2S$ level, however, and calculations at the $3S$ level are in order.

Note that these results suggest that the semileptonic decay rates for the b and c quark are nearly equal.

Probably the most interesting result of these preliminary calculations is that the B_s production is comparable to the Ψ production. While it may turn out that cleanest signature of a semileptonic B_c decay will be a Ψe or $\Psi \mu$ vertex, another possibility will be the decay $B_c \rightarrow B_s \ell \nu$ followed by the decay $B_s \rightarrow D_s \ell \nu$. In order to approximate the number of Z^0 decays required to produce even of a few of this decay chain, we need to estimate the B_c semileptonic branching ratio. As in lighter B meson decay, we estimate that the semileptonic branching ratio is about a quarter for the e and μ channels. Using the measured branching ratios $B(J/\Psi \rightarrow e^+e^-) + B(J/\Psi \rightarrow \mu^+\mu^-) \approx 14\%$ and the above estimate for the B_c production rate, we estimate that on the order of 5×10^6 Z^0 decays will be required. As pointed out by Weiler, however, non-perturbative effects would be more likely to increase than decrease the rate.

3.5. RARE B DECAYS: TESTING STANDARD MODEL OR NEW PHYSICS

The most interesting rare decays are those which are "signatures of new physics." For example, a branching ratio that is too large to be explained in terms of conventional particle exchange could be an indication of a fourth generation or of a supersymmetric particle exchange within a loop diagram. We discussed $\bar{B}B$ mixing which is explained in terms of a box diagram—which contains a loop—and may be modified by non-conventional particle exchanges, although this process could not be classified as a rare decay. Rare decays are typically those that do not decay into final states with charmed particles—since the prominent weak transition is $b \rightarrow c$.

Any charmless decay of B mesons or baryons will be of considerable interest. *CLEO* and *ARGUS* have placed upper limits for a variety of decays that would be expected by Penguin diagrams—these give final states where a $b \rightarrow s$ transition occurs, through the emission and reabsorption of a W . (See Ref. 4.) The experimental upper limits are on the order of 10^{-3} for penguin decays of the form $b \rightarrow s\gamma$, and 10^{-4} for decays of the form $b \rightarrow sg^*$. These limits are now getting close to the experimental predictions.^[22]

Although rare decays must be studied with the largest possible statistics, there will be some problems unraveling rare final states from decays produced at the $\Upsilon(4S)$. Such decays produced at high momentum will not suffer from the combinatoric backgrounds associated with B 's produced at rest. Excellent particle identification and good vertex finding can be extremely important for this application. Since there are many decay channels that could be expected, a sample of the order of 10^5 B 's which can be cleanly isolated can provide some interesting limits if not a few examples of these rare decays.

4. Survey of Existing and Future B Physics Experiments

Here we attempt to summarize in tabular form the current status of B physics and the goals for the future. The table below summarizes the B meson count starting with the current numbers accumulated at *CESR* and *DORIS* and projecting the numbers expected through the mid-'90's at *CESR* and *DORIS* with guesses for *LEP* and *SLC*. We also include a B -Factory entry without prejudging what kind of machine it will be. A B -Factory is assumed to be a machine designed to have sufficient luminosity to observe CP violation in the context of the standard model.

Estimates of B Yields from Current and Future e^+e^- Accelerators

Accelerator	Present, 1989	Early 1990's	Late 1990's
CESR	0.7×10^6	$10^6 - 10^7$	—
DORIS	0.3×10^6	$\approx 10^6$?	—
LEP	—	$> 10^6$	LHC era ?
SLC	—	$> 10^5$?	?
B -Factory	—	—	$>> 10^7$?

The next table includes most of the important B physics topics with a summary of current numbers and with estimates of needed improvements in the measurements. Brief comments are made to indicate where, for example, high momentum B 's with separated vertices would be essential for a certain measurement.

B Physics Topics—Present Status and Future Goals

Topic	Present Status	Goal	Minimum Requirements
CP violation	Not seen	Meas. A_{CP}	$10^8 B_d$
Electroweak Parameters: A_{FB}	—	A_{FB} to ± 0.03	$5 \times 10^4 Z^0$ with $P(e^-) = 45\%$
$Br(Z^0 \rightarrow b\bar{b})$	—	Br to ± 0.01	$10^4 Z^0$
KM Parameters: V_{td} : $B_d \bar{B}_d$ mixing V_{ts} : $B_s \bar{B}_s$ mixing V_{ub} : End-point of p_t $B_u \rightarrow \rho \ell \nu$ $B_u \rightarrow \tau \nu$ $B \rightarrow \bar{p} p \pi(\pi)$ V_{cb} : $B_d \rightarrow D^+ \ell \nu$ $B_d \rightarrow D^{*+} \ell \nu$ <i>b</i> -Spectroscopy: Exclusive Final States $M_{B_u} - M_{B_d}$ (MeV) $R = \frac{Br(B_u \rightarrow \ell \nu X)}{Br(B_d \rightarrow \ell \nu Y)}$ Separate $\tau_{B_{u,d}}$ (10^{-12} s) B_s <i>b</i> -baryons B_c	$r_d = 0.20 \pm 0.08$ — $\frac{ V_{ub} }{ V_{cb} } = 0.1 \pm 0.03^\dagger$ Not seen Not seen $Br < 10^{-4}$ $ V_{cb} = 0.046 \pm 0.008$ $ V_{cb} = 0.048 \pm 0.010$ Account for $\approx 20\%$ $\Delta M = 0.4 \pm 0.6$ $R = 1.0 \pm 0.4$ $\tau_B = 1.15 \pm 0.14$ — — —	r_d to $\pm 0.02^\dagger$ x_s to $\pm 15\%$ Meas. Br Meas. Br Meas. Br $ V_{cb} $ to ± 0.002 $ V_{cb} $ to ± 0.002 $> 50\%^\dagger$ ΔM to $\pm 0.1^\dagger$ R to ± 0.1 τ_{B_u}, τ_{B_d} to ± 0.05 Meas. m, τ_{B_s} , and Br 's Meas. m 's & Br 's Meas. m	$10^6 Z^0$ if $x_s < 5$; Z^0 polarization helps. $5 \times 10^5 B_u$ $10^7 B_u$ High p_B or $10^7 B_d$ High p_B or $10^7 B_d$ Beam constrained fit Beam constrained fit Preferable at $\Upsilon(4S)$ High p_B Secondary B vertex helps; $\Upsilon(5S)$ possible High energy and $10^6 Z^0$ High energy and $10^7 Z^0$
Rare B decays: $b \rightarrow s\gamma, sg$	$Br < 10^{-3,-4}$	Br to $10^{-4,-5}$	$10^{5,6} B$

[†]See Ref. 23.

[‡]Preliminary CLEO result. See Ref. 4.

5. Summary and Conclusions on B Physics from Z Decays

Z^0 decays into $\bar{b}b$ jets is seen to be a fruitful process for studying a variety of B physics topics. Many of the key features of both the charged and the neutral current predictions of the standard model may be tested. Deviations from these predictions can be interpreted as signatures of “new physics” which may be the only probe of certain high mass states prior to their actual discovery with higher energy colliders.

A good case can be made that the best process for studying B physics is from Z decays produced in e^+e^- interactions. The cross section for $\bar{b}b$ production at the Z^0 pole is about a factor of five times the value at the $\Upsilon(4S)$. The chief disadvantage relative to B 's produced near threshold energy—at the Υ 4S or 5S resonances—is the reduced mass resolution. Near threshold, the beam energy constraint is extremely important for isolating most of the final states and determining the relative branching ratios. However, for many other studies, the ability to isolate decay vertices will be crucial—and the higher energy affords the possibility of accessing high mass b -quark states. Specific examples of such physics studies are summarized in the previous chapter.

The challenge for SLD and SLC will be to fully utilize the two important features where it has an advantage over LEP : electron beam polarization and high precision vertex detection. Naturally, overwhelming statistics coupled with future detector improvements (and/or improvements in specific data analysis procedures) at LEP could outweigh the special advantages of SLD/SLC . Indeed, if LEP sustains an instantaneous luminosity of the order of $10^{32}\text{cm}^{-2}\text{sec}^{-1}$, and with the factor of five improvement in $\bar{b}b$ cross section over the $\Upsilon(4S)$, it could serve as a B factory that could challenge the utility of some of the proposed dedicated B factories.

We conclude from our preliminary simulations of SLD data that the potential exists for timely studies based on the special advantages of SLD/SLC . An important part of our conclusions is that B physics with SLD will require at least 10^5 $\bar{B}B$ pairs for the most significant work.

REFERENCES

1. See, for example, F.J. Gilman, *Prospects in B Physics*, SLAC-PUB-4829, Dec. 1988; F.J. Gilman, *Heavy Quark Physics*, SLAC-PUB-4955, April 1989; also, lecture notes by Gilman at SLAC Summer Institute, 1989.
2. W.B. Atwood, *B Meson Physics With Polarized Electron Beams at the SLC*, SLAC-PUB-4668, Sept. 1988; also, W.B. Atwood, I. Dunietz, and P. Grosse-Wiesmann, *CP Violation at the Z^0 with Polarized Beams*, SLAC-PUB-4544, April 1988.
3. The subject of *CP* violation in *B* decay and the need for *B* factories is discussed in some detail in the following two Snowmass '88 reports: G.J. Feldman et al., *Report of the B-Factory Group: I. Physics and Techniques*, SLAC-PUB-4838, CLNS 89/884, LBL-26790, and R.H. Siemann et al., *Report of the B-Factory Group: II. Accelerator Technology*, SLAC-PUB-4839, CLNS 89/883, LBL-26791, January 1989.
4. Talk by D.L. Kreinick, *B-Physics from CLEO*, XIV International Symposium on Lepton and Photon Interactions, Stanford—August 7-12, 1989; also, for recent results from *ARGUS* and *CLEO*, respectively, see lecture notes from 1989 *SLAC Summer Institute* by H. Kolanoski and by P. Baringer.
5. V. Barger, *Search for the Fourth Generation: Present and Future Prospects*, University of Wisconsin Preprint, MAD/PH/500, June 1989.
6. See, for example, J. Rosner, *Heavy Flavor Physics*, Preprint EFI 88-37-Draft, July, 1988.
7. U. Schneekloth, *τ Physics at the Z^0* , these preceedings.
8. K. Berkelman, *Results on b -Decay with Emphasis on CP Violation*, Prelecture Notes distributed at the 1988 *SLAC Summer Institute*, July 18—29, 1988.
9. See, in particular, T. Atomari and L. Wolfenstein, *Constraints on Semileptonic B Decays from the Measurement of the D^* Polarization in $B \rightarrow D^* e \bar{\nu}$* , Phys. Rev. **D 37** (1988) 681; B. Grinstein and M. B. Wise, *Polarization Effects in $B \rightarrow D^* e \bar{\nu}$* , Phys. Lett. **197B** (1987) 249 ; and K. Hagiwara, A.D. Martin and M.F. Wade, *Exclusive semileptonic B Meson Decays*, DTP/89/20, June 1989; see also, most recent paper by Isgur et al., since they acknowledge an error in their earlier paper—i.e., N. Isgur, D. Scora, B. Grinstein, and M.B. Wise, Phys. Rev. **D39**, 799 (1989).
10. J.S. Korner, *Exclusive Semileptonic B and D Decays*, University of Mainz preprint, MZ-TH/88-12, Oct. 1988.
11. D. Blockus, et al., *Proposal for Polarization at the SLC*, Polarization Group Proposal, SLAC Report SLAC-PROP-1 (1986).
12. H. Band, et al., *A Study on Neutrino Counting with the SLD Detector*, SLD Physics Report - 1, (1988).
13. T.W. Reeves, R.S. Panvini, and G.B. Word, *\bar{B}_s, B_s Oscillations Seen From $e^+ e^- \rightarrow Z^0 \rightarrow \bar{b} b$* , paper submitted to Workshop on *B-Factories and Related Physics Issues*, Blois, France,

- June 26—July 1, 1989; T.W. Reeves, $\bar{B}_s B_s$ Oscillations Seen From $e^+e^- \rightarrow Z^0 \rightarrow \bar{b}b$ with SLD at SLC, these proceedings.
14. R. Schindler, *Overview and Issues*, these proceedings.
 15. A. Snyder and S. Wagner, "Measurement of the B^0 Meson Lifetime", paper submitted to Workshop on B -Factories and Related Physics Issues, Blois, France, June 26—July 1, 1989. Also SLAC-PUB-5107, in progress.
 16. S. Fajfer, R.J. Oakes, *Signal for Bottom Baryon Production in Electron Positron Colliding Beams*, Phys. Rev. D **24** (1981) 781. H. Noda, T. Tashiro, K. Kinoshita, *Baryon, Anti-Baryon and Heavy Flavored Hadron Productions in e^+e^- Annihilation and Quark-Diquark Cascade Model*, Prog. Theor. Phys. **74** (1985) 1084. See also CLEO Collab., (M. Alam, *et al.*), *Evidence for Charmed Baryons in B Meson Decay*, Phys. Rev. Lett. **59** (1987) 22. CLEO Collab., (M. Alam, *et al.*), *Observation of Baryons in B Meson Decay*, Phys. Rev. Lett. **51** (1983) 1143.
 17. T. J. Weiler, private communication.
 18. L. Clavelli, *Associated heavy-vector-meson production in e^+e^- annihilation*, Phys. Rev. D **26** (1982) 1610.
 19. I. I. Bigi and L. Clavelli, *Detecting Beauty Baryons and Heavy Beauty Mesons with the J/Ψ Trigger*, SLAB-PUB-4350, UA HEP 873, (1987).
 20. M. Adler, M. Wise, private communication.
 21. N. Isgur, D. Scora, B. Grinstein, and M. Wise, Phys. Rev. D **39** (1989) 799.
 22. For a recent review, see A. Soni, *Physics of the Fourth Family*, in Proceedings of the 8th International Conference on High Energy Physics at Vanderbilt, "Collider Physics: Current Status and Future Prospects", Nashville, TN, eds. J. Brau and R. Panvini (Singapore: World Scientific, 1987).
 23. B. Gittleman and S. Stone, "B Meson Decay," CLNS 87/81-Rev., (1987).

CP Violation at the Z^0 *

S. Manly

Yale University, New Haven, Connecticut, 06511

Abstract

The prospect of observing CP violation in the decay of the Z^0 boson at SLC and LEP is briefly reviewed. Particular attention is given to pointing out ways in which the SLD detector at SLC can contribute to studies of CP violation.

I INTRODUCTION

CP violation was found at the 10^{-3} level in the K^0 system in 1964 [1]. In the last 25 years much progress has been made toward developing an understanding of this phenomenon, both theoretically and experimentally. However, CP violation is still not fully understood. This year, SLC and LEP have started producing Z^0 bosons in a clean environment. It is appropriate to review the subject of CP violation and discuss the potential impact of measurements that can be made at these two new accelerators.

This work was undertaken as part of a larger effort to identify those areas of physics that are particularly well-suited to be investigated by SLD. So, throughout this paper special mention is made of ways that SLD might contribute toward an understanding of the physics of CP violation. Potential contributions of SLD are contrasted to potential contributions of other detectors where appropriate.

In Section II, some standard model phenomenology concerning CP violation is reviewed. Also, the expectation that CP violation is most easily observable in the B meson system is discussed. Section III describes the various types of CP violation that might be observed at the Z^0 . In Section IV, estimates of the sample size necessary to observe CP violation in Z^0 decays are given. In Section V, the search for CP violation in Z^0 decays is briefly compared to other experimental techniques. Finally, the conclusions of this review are presented in Section VI.

*Presented at the SLD Kirkwood Physics Meeting in Kirkwood, California, July 31-August 4, 1989.

II PHENOMENOLOGY

CP violation can be understood in terms of the standard model ($SU(2)_L \times U(1)_Y$) of the electroweak interaction with three or more generations. For three generations there are three weak isospin doublets of quarks,

$$\begin{pmatrix} u \\ d' \end{pmatrix}_L, \begin{pmatrix} c \\ s' \end{pmatrix}_L, \begin{pmatrix} t \\ b' \end{pmatrix}_L.$$

u , c , and t are mass eigenstates. d' , s' , and b' are weak interaction eigenstates that transform to the corresponding mass eigenstates d , s , and b via the 3×3 unitary K-M (Kobayashi-Maskawa) matrix [2].

$$\begin{pmatrix} d' \\ s' \\ b' \end{pmatrix} = \begin{pmatrix} V_{ud} & V_{us} & V_{ub} \\ V_{cd} & V_{cs} & V_{cb} \\ V_{td} & V_{ts} & V_{tb} \end{pmatrix} \begin{pmatrix} d \\ s \\ b \end{pmatrix}$$

This matrix is completely determined by three mixing angles and a complex phase. A non-zero value of the complex phase in the K-M matrix gives rise to CP violation. This will be covered in more detail in Section III. There are many possible choices for parameterizing this matrix that do not change the physics content. A short review of the different parameterizations in use in the literature is given in reference [3].

The three angles and phase of the K-M matrix must be experimentally determined since they are free parameters of the standard model. Presently, they are constrained by measurements of the values of the nine elements of the K-M matrix and the need to satisfy unitarity [3]. Accurate measurements of the various K-M matrix elements are critical to studies of CP violation. Such measurements test and refine the three generation standard model, which is generally assumed in predicting the size of CP violating effects.

In the standard model, CP violation and flavor mixing are expected to occur in all the heavy quark systems. These phenomena have been extensively studied in the kaon system [4]. It is hoped that their observation in an analogous system will help resolve many of the remaining questions.

In general, the hadrons containing b quarks are thought to hold the most promise to exhibit observable CP violation in their decays. This is due to several (not completely independent) reasons. First, CP violation can only occur in a process that involves more than three K-M elements, no three of which are chosen from the same row or column [5]. This is necessary to bring out a relative CP violating phase in the decay amplitude that cannot be rotated away. B meson decays start in the third generation and work down, easily bringing in matrix elements from all over the K-M matrix. Also, B decays are

necessarily K-M suppressed to first order. This enhances the relative abundance of rare decays (which might exhibit CP violation). In addition, there is a much richer spectrum of states in which a B meson can decay relative to a D or K meson. This weakens constraints due to CPT which is generally thought to hold even in CP violating decays. Finally, flavor mixing is required to bring about many types of CP violation. The degree of mixing is thought to be larger in the B^0 - \bar{B}^0 systems than in the D^0 - \bar{D}^0 system [5].

There are several reasons to be optimistic about the eventual observation of CP violation in the B meson systems. The B lifetime is long enough ($\sim 10^{-12}$ seconds) to be observable using current vertex detector technology. A large value for B_d^0 - \bar{B}_d^0 mixing has been observed [6]. Finally, a recent measurement of ϵ'/ϵ in the kaon system is consistent with the standard model [7].

III TYPES OF CP VIOLATION

CP violation in the B meson system potentially can occur in many different ways. It can occur in either in the decay amplitudes or because the mass eigenstates are not CP eigenstates or both. Some possibilities involve mixing, some do not. In some cases the time integrated CP asymmetry is small relative to the time dependent asymmetry. In other cases this is not true. For clarity the different possibilities are broken down into four classes in this review.

Class I — Mixing where the mass eigenstates are not CP eigenstates. Assuming CPT, the B meson states with definite mass (m_1 and m_2) and width (Γ_1 and Γ_2) can be written as linear combinations of the strong interaction eigenstates [8]

$$\begin{aligned} |B_1(t)\rangle &= p |B(t)\rangle + q |\bar{B}(t)\rangle = e^{-\frac{\Gamma_1 t}{2}} e^{im_1 t} |B_1(0)\rangle \\ |B_2(t)\rangle &= p |B(t)\rangle - q |\bar{B}(t)\rangle = e^{-\frac{\Gamma_2 t}{2}} e^{im_2 t} |B_2(0)\rangle. \end{aligned}$$

p and q are defined by

$$p = \frac{1 + \epsilon_B}{\sqrt{2(1 + \epsilon_B^2)}} \quad \text{and} \quad q = \frac{1 - \epsilon_B}{\sqrt{2(1 + \epsilon_B^2)}},$$

where ϵ_B is the degree of CP violation. After eliminating the weak interaction eigenstates from the above equations, the time evolution of the strong interaction eigenstates can be written as

$$|B(t)\rangle = e^{-\frac{\Gamma t}{2}} \left[\cos \frac{\Delta m t}{2} |B(0)\rangle + i \frac{q}{p} \sin \frac{\Delta m t}{2} |\bar{B}(0)\rangle \right]$$

and

$$| \bar{B}(t) \rangle = e^{-\frac{\Gamma t}{2}} \left[i \frac{p}{q} \sin \frac{\Delta m t}{2} | B(0) \rangle + \cos \frac{\Delta m t}{2} | \bar{B}(0) \rangle \right],$$

where

$$m = \frac{m_1 + m_2}{2}, \quad \Gamma = \Gamma_1 \sim \Gamma_2, \quad \text{and} \quad \Delta m = m_1 - m_2.$$

From these expressions we get

$$\text{Prob}[B(0) \rightarrow \bar{B}(t)] = \left| \frac{p}{q} \right|^2 e^{-\Gamma t \sin^2 \frac{\Delta m t}{2}}$$

and

$$\text{Prob}[\bar{B}(0) \rightarrow B(t)] = \left| \frac{q}{p} \right|^2 e^{-\Gamma t \sin^2 \frac{\Delta m t}{2}}.$$

If $|p/q| \neq 1$, then the system violates CP. The CP asymmetry is given by

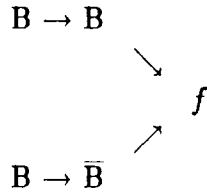
$$\frac{\text{Prob}[B(0) \rightarrow \bar{B}(t)] - \text{Prob}[\bar{B}(0) \rightarrow B(t)]}{\text{Prob}[B(0) \rightarrow \bar{B}(t)] + \text{Prob}[\bar{B}(0) \rightarrow B(t)]} = \frac{|p|^4 - |q|^4}{|p|^4 + |q|^4}$$

An experimental example of such an asymmetry is the charge asymmetry in same sign dilepton production given by

$$\frac{\sigma(B^0 \bar{B}^0 \rightarrow l^+ l^+ X) - \sigma(B^0 \bar{B}^0 \rightarrow l^- l^- X)}{\sigma(B^0 \bar{B}^0 \rightarrow l^+ l^+ X) + \sigma(B^0 \bar{B}^0 \rightarrow l^- l^- X)}.$$

This asymmetry is no larger than 10^{-2} in the K-M ansatz [9].

Class II — Mixing with interference to non-flavor-specific final states. Because the final state, f , is non-flavor-specific (i.e., both $B \rightarrow f$ and $\bar{B} \rightarrow f$ can occur), mixing provides two separate paths to f .



Amplitudes for these decay chains can interfere causing an asymmetry between $\Gamma(B \rightarrow f)$ and $\Gamma(\bar{B} \rightarrow f)$.

Suppose f is a CP eigenstate such as ψK_s or $\psi \pi^+ \pi^-$. Then [9]

$$\Gamma[B^0(\bar{B}^0) \rightarrow f] \sim e^{-\Gamma t} [1 \pm \sin(\Delta m t) \text{Im}(\frac{p}{q} \rho)],$$

where ρ is the ratio of the amplitudes for $B \rightarrow f$ and $\bar{B} \rightarrow f$. The CP asymmetry is given by

$$\frac{\Gamma(B \rightarrow f) - \Gamma(\bar{B} \rightarrow f)}{\Gamma(B \rightarrow f) + \Gamma(\bar{B} \rightarrow f)} = \sin(\Delta mt) \text{Im}\left(\frac{p}{q}\rho\right).$$

Since f is a CP eigenstate, the hadron dynamics tends to cancel out of ρ . This means the CP asymmetry is relatively easy to calculate in the standard model. It is estimated to range from 10% to 60% depending on the final state.

If f is not a CP eigenstate things get a little more complicated. In this case, the interference between $B \rightarrow f$ and $\bar{B} \rightarrow f$ can be of opposite sign to that for $\bar{B} \rightarrow \bar{f}$ and $\bar{B} \rightarrow B \rightarrow \bar{f}$. The CP asymmetry takes the form

$$\frac{\Gamma(B\bar{B} \rightarrow f) - \Gamma(B\bar{B} \rightarrow \bar{f})}{\Gamma(B\bar{B} \rightarrow f) + \Gamma(B\bar{B} \rightarrow \bar{f})}$$

A physical example of this process is $B_d^0(\bar{B}_d^0) \rightarrow D^-\pi^+, D^+\pi^-$, shown in Figure 1. In this

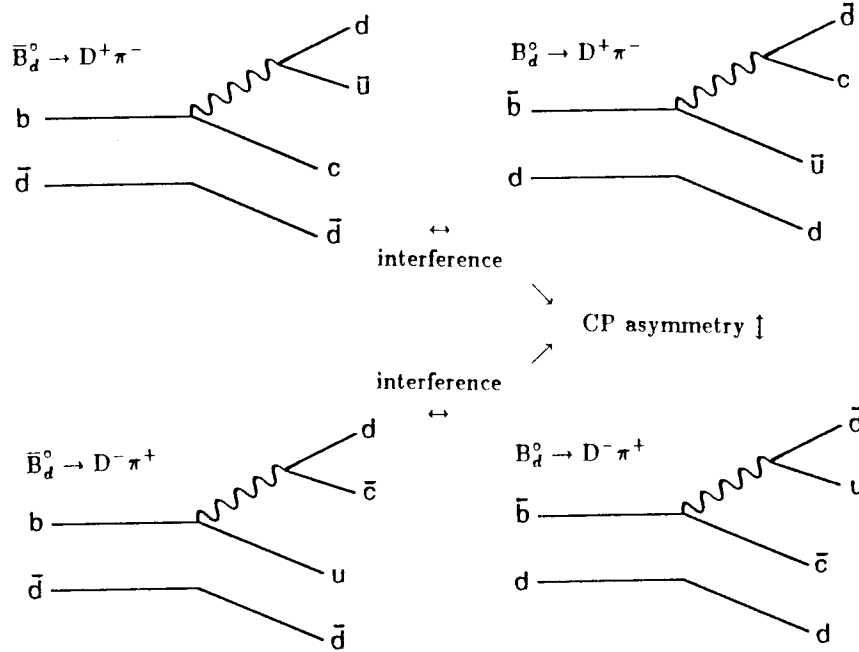


Figure 1: A possible example of a Class II CP asymmetry where f is not a CP eigenstate.

case the ratio of the decay amplitudes [10],

$$\rho = \frac{B \rightarrow f}{\bar{B} \rightarrow f},$$

depends on hadron dynamics. Thus, the theoretical expectation for the size of the CP asymmetry is uncertain.

Class III — Interference in decays to flavor-specific final states. In processes where two diagrams contribute to the same final state, interference terms can arise that contribute oppositely for $\Gamma(B \rightarrow f)$ and $\Gamma(\bar{B} \rightarrow \bar{f})$. Figure 2 shows several examples of this type of CP violation. It is important to note that mixing is not necessary for CP violation to occur in this way. It can happen for charged mesons as well as neutral ones. This class of CP asymmetries are thought to be fairly large ($\sim 10\%$); but the theoretical estimates are uncertain [9].

Class IV — Time dependent CP violation. Up to this point, all the CP asymmetries discussed in this review are time-integrated asymmetries. However many of the asymmetries that involve mixing have a time dependence that can be quite striking [11], [12]. As an example, recall that in Class II CP violation where f is a CP eigenstate,

$$\Gamma[B^0(\bar{B}^0) \rightarrow f] \sim e^{-\Gamma t} [1 \pm \sin(\Delta m t) \text{Im}(\frac{p}{q}\rho)].$$

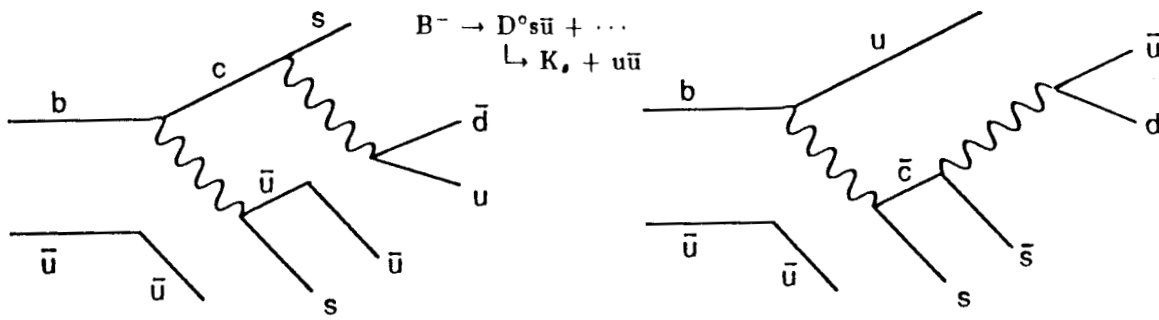
Figure 3, taken from reference [12], shows the time-dependent asymmetry for the process $B_d^0(\bar{B}_d^0) \rightarrow \psi K_s$. The solid line represents what happens when the initial state is a B_d^0 , while the dashed line represents what occurs if the initial state is a \bar{B}_d^0 . $\Delta m/\Gamma$ is 0.78 in this example. Another even more dramatic example is given in Figure 4 taken from the same reference. Here the solid lines represent an initial state B_s^0 decaying into ρK_s , and the dashed lines show what happens when an initial \bar{B}_s^0 goes into the same final state. The three figures differ only by the value of $\Delta m/\Gamma$ that was used for the calculation. In Figure 4a, $\Delta m/\Gamma=1$, while in figures 4b and 4c, $\Delta m/\Gamma=5$ and 15, respectively. Looking at figures 4b and 4c, it is easy to imagine the time-integrated CP violation asymmetry washing out completely. Since the values of $\Delta m/\Gamma$ used in these plots are quite plausible, it is conceivable that that the only way CP violation could ever be observed in the B_s^0 - \bar{B}_s^0 system is through its time dependence.

IV EXPERIMENTAL ESTIMATES

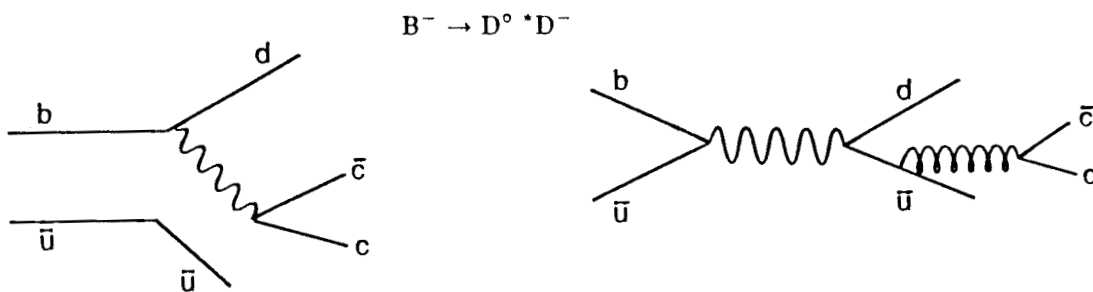
In order to determine the feasibility of studying CP violation at the Z^0 it is necessary to determine the amount of data required to see an effect. To establish an effect of s standard deviations for an asymmetry of the form

$$a = \frac{N(B) - N(\bar{B})}{N(B) + N(\bar{B})}$$

interference of cascade processes



interference of quark decay and weak annihilation



interference of penguin and spectator decay

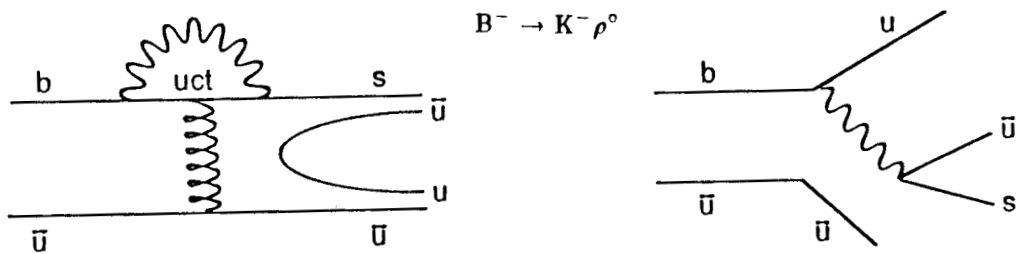


Figure 2: Examples of decays to a given flavor-specific final state where interferences can give rise to a CP asymmetry.

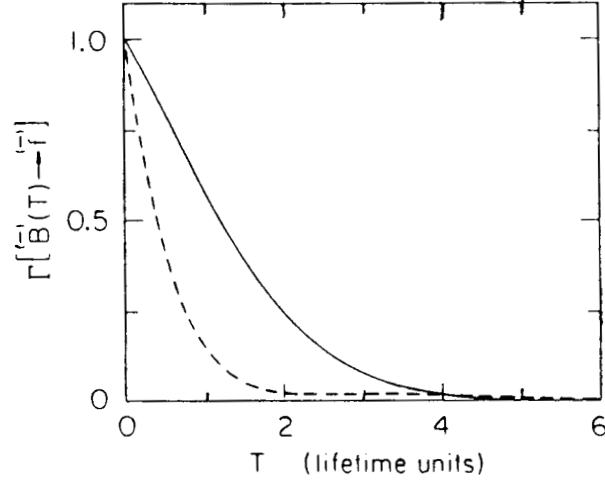


Figure 3: Time-dependent CP asymmetry in the $B_d^0(\bar{B}_d^0) \rightarrow \psi K_s$ system. The solid line is for an initial B_d^0 . The dashed line is for an initial \bar{B}_d^0 .

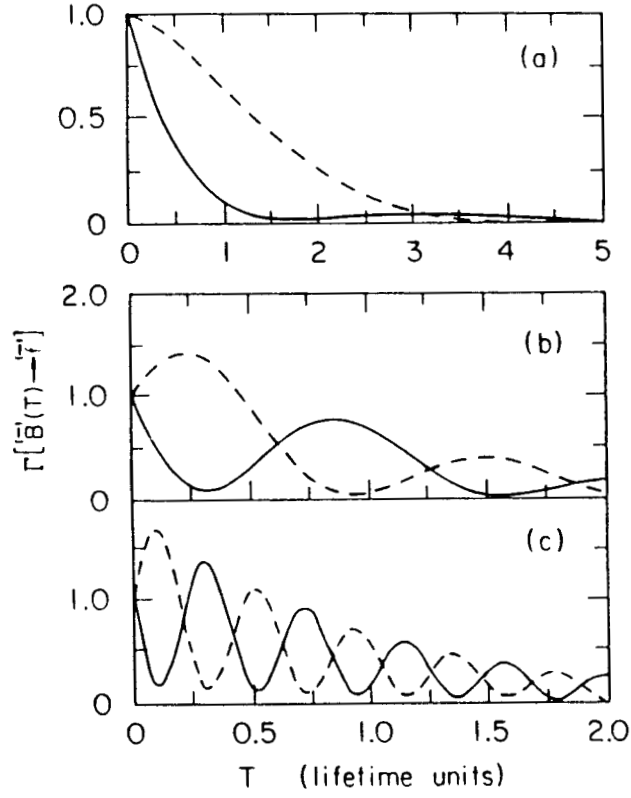


Figure 4: Time-dependent CP violation in the $B_s^0(\bar{B}_s^0) \rightarrow \psi \rho$ system. The solid line is for an initial B_s^0 . The dashed line is for an initial \bar{B}_s^0 .

requires a sample of size

$$N = \left(\frac{s}{a}\right)^2.$$

To get a realistic estimate for a given physical process, efficiencies and branching ratios must be folded in. Thus the number of $B\bar{B}$ events required is given by [9]

$$N(B\bar{B}) = k \left(\frac{s}{a}\right)^2 \left(\frac{1}{\epsilon_{tag} \cdot BR(B \rightarrow f) \cdot BR(f \rightarrow X_{ch}) \cdot F(B)} \right),$$

where k is 1 or 1/2 depending on whether or not opposite side tagging is required, ϵ_{tag} is the tagging efficiency, if required, $BR(B \rightarrow f)$ is the branching ratio of the B meson into the CP violating decay mode, f , $BR(f \rightarrow X_{ch})$ is the branching ratio for f into final state particles that can be detected, and $F(B)$ is the fraction of events produced containing the B meson species of interest.

Table 1 gives predicted numbers of $B\bar{B}$ events required to give a three standard deviation effect at the SSC for a given mode of CP violation. This table was taken from reference [9] with only small changes. The most notable thing about this table is the sheer magnitude of the estimated numbers of events required to see a CP violating effect. At least 10^7 events $B\bar{B}$ are needed to see an effect in any given mode. This is driven by the fact that when the CP asymmetry is large, the branching ratio is small and when the branching ratio is large, the CP asymmetry is small. This ‘conspiracy of nature’ occurs because a large CP asymmetry requires the involvement of all three generations in the amplitude, thus bringing in small K-M matrix elements. This, in turn, leads to a small branching ratio.

The following is a list some of the assumptions used in constructing Table 1 as well as a few points relevant to SLD:

- The list of modes in this table is not exhaustive. A creative graduate student might find a better way to look for CP violation.
- Many of the branching ratios listed in the third column are theoretical estimates. They have not been measured yet.
- The estimates do not take into account detection efficiencies except for ϵ_{tag} , which is the efficiency for tagging the accompanying B meson. This is not relevant for Class III where the decays are self-tagging. Background effects are also not taken into account.
- The magnitude of the CP asymmetries are estimates. Many are uncertain even if the assumed standard model of CP violation is correct. The predictions rely on

Class	Modes	Branching Ratio	Asymmetry	# $B\bar{B}$ Events Required
I. Mixing with Mass Eigenstates Not CP Eigenstates	$B_d \bar{B}_d \rightarrow l^\pm l^\pm + X$ $B_s \bar{B}_s \rightarrow l^\pm l^\pm + X$	0.01 0.02	10^{-3} 10^{-4}	6×10^9 2×10^{12}
II. Mixing with Interference in Decays to Non-Flavor Specific States	$B \rightarrow \psi K_s$ $B \rightarrow \psi K_s X$ $B \rightarrow D \bar{D} K_s$ $B \rightarrow \pi^+ \pi^-$ $B \rightarrow D^{*+} D^-, D^+ D^-, D^* D^+$	5×10^{-4} 2×10^{-3} 5×10^{-3} 5×10^{-5} 3×10^{-3}	0.05-0.3 0.05-0.3 0.05-0.3 0.05-0.5 0.05-0.03	$(1-34) \times 10^8$ $(2-85) \times 10^7$ $(3-100) \times 10^7$ $(0.3-32) \times 10^8$ $(0.7-26) \times 10^8$
<i>f = cp eigenstate</i>				
<i>f ≠ cp eigenstate</i>	$B_d \rightarrow D^+ \pi^-$ $B_d \rightarrow D^0 K_s$ $B_s \rightarrow D_s^+ K^-$	6×10^{-3} 6×10^{-5} 3×10^{-4}	0.001 0.01 0.5?	3×10^{11} 7×10^{11} 5×10^7
III. Interference in Decays to Flavor-Specific Final States	$B^- \rightarrow D^0 K^- + X$ $\hookrightarrow K_s + Y$	10^{-5}	0.1?	9×10^8
<i>cascade decays</i>				
<i>spectator vs annihilation</i>	$B^- \rightarrow D^{*0} D^-$	3×10^{-3}	0.01	2×10^9
<i>spectator vs penguin</i>	$B^- \rightarrow K^- \rho^0$ $\bar{B}_d \rightarrow K^- \pi^+$	$\sim 10^{-5}$ $\sim 10^{-5}$	0.1 0.1	1×10^8 1×10^8

Table 1: Predicted numbers of $B\bar{B}$ events required to see CP violation.

knowing the magnitude of the various K-M matrix elements, the mass of the top quark, and something about hadron dynamics in decays that have not yet been observed. A change in the asymmetry estimate can have a large effect because the number of required events goes as the inverse square of the asymmetry.

- $F(B)$ was taken to be 0.38 for B_d^0 and B^+ and 0.15 for B_s^0 .
- One way to reduce the number of events required to see a CP violating effect is to sum over many different decay channels or look at inclusive decays. This must be done with care. The sign of the CP asymmetry can vary in different decay modes, washing out the overall asymmetry. For example, one might be tempted to look at the inclusive decay $B(\bar{B}) \rightarrow \psi X$ [13]. One problem with this search strategy is that

$$\text{Asym}(B \rightarrow \psi K_s) = -\text{Asym}(B \rightarrow \psi K_L),$$

giving

$$\text{Asym}(B \rightarrow \psi + X^0) \sim 0.$$

- These estimates are for complicated SSC events. The calculations assumed D and D_s detection in all charged particle modes. The events will be considerably cleaner in SLD at the Z^0 . With good vertex detection, one might imagine using D tagging in modes that contain neutral particles as well.
- There could be surprises. The estimates are based on the three generation standard model. Models containing a fourth generation of quarks, supersymmetric models, theories with multiple Higgs, and left-right symmetric models all predict some effect on CP violation [14]. It is also possible that there is some surprise that even the theorists have not foreseen!
- Classes I and II require tagging the B meson on the other side of the event to determine if the B of interest is a B or a \bar{B} . For the listed estimates, the tag of choice was the semileptonic decay $B \rightarrow D + l + X$, where l is an electron or muon. The tagging efficiency used was $\text{BR}(B \rightarrow D + l + X) \cdot \text{BR}(D \rightarrow \text{all charged particles}) \sim (0.2) \cdot (0.2) \sim 0.04$. This is considerably smaller than the comparable tagging efficiency that might be expected at SLD. To get some idea of how SLD might do, it is more appropriate to look in reference [15]. Aleksan *et al.* have done a careful study of the possibility of observing CP violation in the $J/\psi + K$ system using a detector with good vertexing and particle ID at an asymmetric e^+e^- collider. They combine lepton tagging with charged kaon tagging to get a tagging efficiency of 48%. This is an order of magnitude better than the efficiency used in the SSC study. So, the estimates listed in Table 1 for Classes I and II are a factor of 10 too high for SLD.

- Polarized beams can also help by reducing the need for tagging [16]. Atwood *et al.* estimate this can reduce the number of events necessary to establish CP violation in Classes I and II by an order of magnitude. One can imagine using tagging when available and information from polarized beams when tagging is not possible to gain the largest usable sample.

V POSSIBILITIES

There are a number of different techniques being considered to look for CP violation in the B system. It is important to briefly review and contrast these different methods in order to fully grasp the potential of searching for CP violation in e^+e^- collisions at the Z°. This discussion concentrates on methods involving e^+e^- collisions. The immediate future for studying high statistics B physics in fixed target experiments [17] or in ep [18] or p \bar{p} [19] collisions is not good; although this may not always be the case. Six different techniques for looking for CP violation in e^+e^- collisions were considered in a careful study at Snowmass '88 [20]. Brief descriptions of each of the methods along with some of their advantages and disadvantages are listed below:

- **Symmetric e^+e^- collisions at the $\Upsilon(4s)$.** This is the simplest case. The advantages are multiple. The final state consists of $B_d^0\bar{B}_d^0$ or $B_u^+\bar{B}_u^-$ pairs created at rest in the center-of-mass. The resonant cross section for $b\bar{b}$ production is 3 to 4 times higher than in the surrounding continuum. Also the beam energy constraint is useful in improving the mass resolution and reducing backgrounds. The primary disadvantage of looking for CP violation using this technique is that it is not possible to measure the time development of the $B\bar{B}$ system. B and \bar{B} mesons are produced as coherent pairs at the $\Upsilon(4s)$. The asymmetry varies with the difference in the decay time. The rate goes as

$$R(B\bar{B} \rightarrow f) \sim e^{-\Gamma(t-\bar{t})}[1 \pm \sin\alpha\Gamma(t-\bar{t})].$$

Since the CP asymmetry is odd in $(t-\bar{t})$ it integrates to zero if no time information is used. Also, the fact that the B's are produced at rest increases the combinatoric background.

It should be noted that even without time information, this technique can be used to look for CP violation in dileptons and in charged B decays. In the case of the dileptons, the CP violation occurs in the mass matrix and is time independent. However, the asymmetry is expected to be small. For the charged B's there is no mixing involved. Therefore there is no time dependence. The asymmetry can be large but the calculations are uncertain.

- **Asymmetric e^+e^- collisions at the $\Upsilon(4s)$.** Colliding beams of unequal energies at the $\Upsilon(4s)$ is a technique that creates a BB system with a moving center-of-mass in the laboratory. The moving center-of-mass allows the time development of the system to be measured while retaining the advantages of running on the $\Upsilon(4s)$. The primary disadvantage of this method is the potential difficulty in building the accelerator and detector [21].
- **Symmetric e^+e^- collisions above the $\Upsilon(4s)$.** In this method the center-of-mass energy is above that for $B_d^0\bar{B}_d^0$ and below that for $B_d^+\bar{B}_d^-$. In this case, the time-integrated asymmetry is nonzero. Thus, it is possible to use this method to study CP violation using neutral B's. The disadvantage with this method is that the $b\bar{b}$ production cross section is down by a large factor from that at the $\Upsilon(4s)$.
- **Symmetric e^+e^- collisions in the continuum.** At higher center-of-mass energies (20-30 GeV) the B's have a sufficient velocity for the time development of the asymmetry to be measured. However all of the advantages of running on the $\Upsilon(4s)$ are lost. Other disadvantages are that the production cross section falls as E^{-2} and the final state is more complicated. Also, there is enough energy to create many different species of B mesons and baryons as well as to create other particles coming from the primary vertex.
- **Z^0 decay without polarization.** At the Z^0 resonance the production cross section for $b\bar{b}$ pairs is 5 times that at the $\Upsilon(4s)$. In addition, the large transverse momentum of the B mesons helps in reconstruction because the B's travel further in the laboratory and the multiple scattering is decreased for the B decay products. In this case, as in continuum production, there is a mix of b-containing hadrons created. This is a disadvantage in that there is increased difficulty in tagging each species. However it is a distinct advantage over production at the $\Upsilon(4s)$ if one wants to study the heavier hadrons, i.e., the B_s^0 . The high multiplicity of the events is a potential difficulty. However the use of a 3-dimensional vertex detector (like that in SLD) should effectively eliminate this problem.
- **Z^0 decay with polarization.** As mentioned in Section IV, longitudinal electron polarization leads to a large forward-backward asymmetry for the b and \bar{b} created in a Z^0 decay. This can be used effectively for B tagging, reducing the required sample size for a CP violation measurement.

In the Snowmass '88 report [20], the relative difficulty of searching for CP violation in a specific B decay mode ($B \rightarrow \psi K_s^0$) was evaluated using each of the methods listed above. The conclusions of the Snowmass study are presented in Table 2, which is taken

Factor/Case	Asymmetric $\Upsilon(4S)$	Symmetric $\Upsilon(4S)+$	$\sqrt{s} = 16 \text{ GeV}$	Z $\mathcal{P} = 0$	Z $\mathcal{P} = 0.9$ ($\mathcal{P} = 0.45$)
$b\bar{b}$ cross section, σ (nb)	1.2	0.3	0.11	6.3	6.3
Fraction of B^0 , f_0	0.43	0.34	0.35	0.35	0.35
ψK_s reconstruction efficiency, ϵ_r	0.61	0.61	0.61	0.46	0.46
Tag efficiency, ϵ_t (and method)	0.48 (ℓ, K)	0.48 (ℓ, K)	0.30 (ℓ, D)	0.18 (ℓ, D)	0.61 (A_{FB})
Wrong tag fraction, w	0.08	0.08	0.08	0.08	0.125 (0.27)
Asymmetry dilution, d	0.61	0.63	0.45	0.45	0.61
$\int \mathcal{L} dt$ needed for 3σ effect (10^{40} cm^{-2}) *	0.45-16	2.1-77	18-640	0.68-25	0.14-5.0 (0.37-13)
Relative $\int \mathcal{L} dt$ needed	1.0	4.7	40	1.5	0.3 (0.8)

*peak luminosity needed in units of $10^{33} \text{ cm}^{-2} \text{ sec}^{-1}$ for 10^7 seconds of fully efficient running at peak luminosity.

Table 2: Comparison of B-factory techniques.

directly from their report. The main result of their investigation is shown in the last line of the table. This line gives the relative integrated luminosity needed to observe a CP violating effect. Note that the technique of e^+e^- collisions at the Z^0 with a large polarization requires the smallest integrated luminosity by a factor of 3.

VI CONCLUSIONS

The standard model of CP violation predicts that CP violation occurs in all of the heavy quark systems that can be observed in Z^0 decays. It is thought to be most easily observable in B mesons. Estimates of the size of CP violating effects are dependent on knowledge of the mass of the top quark, the magnitude of the various K-M matrix elements, and the size of the different B meson branching ratios. It is estimated that it will take a sample of at least 10^6 - 10^7 BB pairs to observe a statistically significant effect. The sheer size of this number makes it unlikely that CP violation in the B's will be observed at SLC or LEP in the near future. It is also doubtful that any other current generation accelerator/detector can observe such an effect.

The most powerful method to look for CP violation in the B system is to use polarized e^+e^- collisions at the Z^0 . The advantages of running at the Z^0 with polarization coupled with the good vertex detection and particle ID of SLD would make SLD/SLC the ideal place for observing CP violation if SLC could provide sufficient luminosity.

In the near future, it is important to make careful measurements of the magnitudes of B_u^0 and B_d^0 mixing, B branching ratios, and K-M matrix elements. Such measurements will help refine CP violation estimates and detection strategies. With good vertex detection, particle ID, and polarized beams, SLD will be able to make a significant contribution to this database. In addition, these same characteristics put SLD in a good position to look for surprises. SLD should take advantage of this. After all, surprises do happen in physics ... CP violation was discovered!

VII ACKNOWLEDGEMENTS

The author would like to thank Michael Schmidt for several fruitful conversations and some helpful comments on the manuscript. This work was supported by the U.S. Department of Energy.

References

- [1] J.H. Christenson, J.W. Cronin, V.L. Fitch, and R. Turlay, Phys. Rev. Lett. **13**, 138 (1964).
- [2] M.Kobayashi and K.Maskawa, Prog. Theor. Phys. **49**, 652 (1973).
- [3] Particle Data Group, Phys. Lett. **B204**, 1 (1988).
- [4] K. Kleinknecht, *CP Violation in the K^0 - \bar{K}^0 System*, in **CP Violation**, C. Jarlskog, editor, World Scientific, 1989.
- [5] A.B. Carter and A.I. Sanda, Phys. Rev. **D23**, 1567 (1981).
- [6] H. Albrecht *et al.* (ARGUS), Phys. Lett. **192B**, 245 (1987).
- [7] A.J. Buras and J.M. Gérard, Phys. Lett. **B203**, 272 (1988).
- [8] K. Berkelman, *Results on b -decay in e^+e^- Collisions, with Emphasis on CP Violation*, given at the SLAC Summer Institute, Stanford University, July 18-29, 1988.
- [9] K.J. Foley *et al.*, *Bottom and Top Physics*, in **Experiments, Detectors, and Experimental Areas for the Supercollider**, R Donaldson and M.G.D. Gilchriese, editors, Berkeley, 1987.
- [10] I.I. Bigi and A.I. Sanda, Nucl. Phys. **B281**, 41 (1987).
- [11] I. Dunietz and J.L. Rosner, Phys. Rev. **D34**, 1404 (1986).
- [12] F. Gilman, *B Physics*, in **Proceedings of the Workshop on High Sensitivity Beauty Physics at Fermilab**, A.J. Slaughter, N. Lockyer, and M. Schmidt, editors, FNAL, 1987.
- [13] I.I. Bigi, *The Question of CP Noninvariance — as Seen Through the Eyes of Neutral Beauty*, in **CP Violation**, C. Jarlskog, editor, World Scientific, 1989.
- [14] For examples, see articles in **CP Violation**, C. Jarlskog, editor, World Scientific, 1989.
- [15] R. Aleksan, J. Bartelt, P.R. Burchat, and A.Seiden, Phys. Rev. **D39**, 1283 (1989).
- [16] W.B. Atwood, I. Dunietz, and P. Grosse-Wiesmann, Phys. Lett. **B216**, 227 (1989).

- [17] P.H. Garvinius, *Fixed Target Beauty Physics Experimental Programs*, in **Proceedings of the Workshop on High Sensitivity Beauty Physics at Fermilab**, A.J. Slaughter, N. Lockyer, and M. Schmidt, editors, FNAL, 1987.
- [18] M. Derrick, *Heavy Quark Production in ep Collisions at HERA*, in **Proceedings of the Workshop on High Sensitivity Beauty Physics at Fermilab**, A.J. Slaughter, N. Lockyer, and M. Schmidt, editors, FNAL, 1987.
- [19] A. Kernan, *B-Physics with Existing Collider Detectors*, in **Proceedings of the Workshop on High Sensitivity Beauty Physics at Fermilab**, A.J. Slaughter, N. Lockyer, and M. Schmidt, editors, FNAL, 1987.
- [20] See G.J. Feldman *et al.*, *Report of the B-Factory Group: I. Physics and Techniques*, SLAC-PUB-4838, 1989, (contributed to Snowmass '88) and M.S. Witherell, *Prospects for B Physics*, given at the SLAC Summer Institute, Stanford University, 1988.
- [21] See G.J. Feldman *et al.*, *Report of the B-Factory Group: I. Physics and Techniques*, SLAC-PUB-4838, 1989, (contributed to Snowmass '88) and R.H. Siemann *et al.*, *Report of the B-Factory Group: II. Accelerator Technology*, SLAC-PUB-4839, 1989, (contributed to Snowmass '88).

SUSY and the SLD

Scott Whitaker

Boston University Physics Department, Boston MA 02215

Abstract

This paper presents a brief overview of the concept of Supersymmetry and its experimental implications that are relevant to the physics regime of the SLD.

Introduction

The principle of supersymmetry (SUSY) holds that the spectra of fundamental scalars and fermions are related by a discrete symmetry. SUSY is attractive because it offers solutions to some bothersome problems common to the Standard Model and many other theories:

- the hierarchy problem, or why should scalars be as light as they must be in order to avoid strong self-coupling: scalar masses are related to fermion masses by the SUSY symmetry, and fermion masses are small due to chiral symmetry.
- the naturalness problem, or how to avoid quadratic divergence of the scalar masses: scalar loops enter with the opposite sign from fermion loops in radiative corrections, and SUSY guarantees the loop contributions come in pairs to cancel one another.
- unification: SUSY offers a means to incorporate gravity into particle physics.

SUSY has been the subject of $\sim 10^4$ publications; for reviews see references [1-3] and the references therein. The purpose of the present paper is to *briefly* review the low energy phenomenology that is relevant to the physics regime in which the SLD will operate. To that end, signatures and rates for the production of SUSY particles, current limits on SUSY particle masses, and SLD's advantages in searching for SUSY particles are discussed below.

SUSY comes in many guises. The number of SUSY generators can vary, as can the method by which SUSY is broken to reach the present energy scale. There can be mixing among various SUSY particles. The present discussion will be restricted to considering $N = 1$ SUSY (a single generator) with the minimal low energy phenomenology. Polarization will not be considered; see reference [3], Appendix F for a discussion.

The SUSY Particle Spectrum

For each familiar spin-1/2 fermion, SUSY provides a spin-0 boson partner. For each helicity state of the fermion there corresponds a scalar particle, so there are equal numbers of fermionic and bosonic states. The scalars are labeled with a tilde to denote their SUSYness and a subscript to denote the fermion helicity state with which they are associated. The scalar name is the fermion name preceeded with an *ess*.

The gauge bosons give rise to spin-1/2 partners, which are denoted by a SUSY tilde over the usual symbol and for which the name is formed by adding "ino" to the familiar name. This nomenclature itself is referred to as a "slanguage" (M. Gell Mann) or a "languino" (S. Weinberg).

The Higgs particles of the Standard Model have SUSY partners too. A special feature of SUSY is that at least two complex scalar doublets are required for the Higgs mechanism to give masses to both up-type and down-type particles. The minimal SUSY Higgs sector after symmetry breaking then includes two charged higgs scalars and three neutral higgs scalars, and the higgsino spin-1/2 partners of each.

Rates and Signatures

Manifestly, SUSY is a broken symmetry. In the unbroken symmetry the sparticle masses are equal to the particle masses, and we do not observe scalar electrons or spin-1/2 photons in our experiments. How much we don't see them will be discussed below. However, the discrete nature of the SUSY symmetry means that even in the broken symmetry the sparticles retain their quantum numbers. Thus the couplings of SUSY particles are completely specified (modulo mixing, which we are ignoring here). For example, the ratio of branching fractions for Z^0 decays to sleptons compared to leptons is given by

$$\frac{\Gamma(Z \rightarrow \tilde{l} \tilde{l})}{\Gamma(Z \rightarrow l \bar{l})} = \frac{\beta^3}{2}$$

where it is assumed that the left and right SUSY particles are degenerate in mass. The factor of 1/2 is related to the angular distribution $d\sigma/d\Omega \sim \sin^2(\theta)$. The β^3 term is the usual phase-space term for the production of scalars; it is plotted in figure 1 versus the ratio of the slepton mass to the Z^0 mass. It is clear from these general considerations that SUSY particles can be produced in Z^0 decays rather copiously for masses up to of order 80% of the beam energy.

Conservation of angular momentum, baryon number, and lepton numbers gives rise to a multiplicatively conserved quantity in the production and decay of SUSY particles. This quantity, called "R-parity", is expressed for a given particle as $R = (-1)^{3B+L+2S}$. There are two important consequences of the conservation of R-parity:

- sparticles are produced in pairs;
- the lightest SUSY particle, called the LSP, is stable.

We know from experimental constraints that the LSP is electrically and color neutral, and so a massive LSP will interact only weakly with matter. SUSY particles produced in a collision or a decay will rapidly undergo a decay cascade to regular particles and the LSP. The LSP will carry away energy from the detecting apparatus, giving the characteristic "missing

energy signature" for the production and decay of SUSY particles. In a contribution to these proceedings, R. Dubois studies the exploitation of this missing energy signature in the SLD to search for decays of the Z^0 to sparticle pairs.

In the Higgs sector, SUSY predicts that Z^0 decay to Higgs scalars is possible and may be kinematically allowed.[4] This decay, interesting because it is predicted within the SUSY framework but lacks the characteristic missing energy signature, is discussed in these proceedings in contributions from S. Whitaker and from C. Baltay, S. Manly, and J.1 Turk.

The decay of the Z^0 to sneutrino pairs, $Z \rightarrow \tilde{\nu}\tilde{\nu}$, could represent a contribution to the invisible decays of the Z^0 . This decay occurs with a branching fraction of 1/4 to 1/2 of the $\sim 6\%$ branching fraction per family for $Z \rightarrow \nu\bar{\nu}$, depending on the masses of the sneutrinos. The sneutrino, if not the LSP itself, is likely (but not guaranteed [5]) to decay to neutrinos plus the LSP and to escape detection. It will be of considerable interest to push the limit on the number of neutrino generations as close to the bound of 3 as possible to extend the search for neutral scalar production in Z^0 decays.

Present Limits on Masses of SUSY Particles

There is no experimental evidence for SUSY particles. From the non-observation of their production in electron-positron annihilation, mass limits for the smuon and the stau are near the available beam energy; the limits are presently ~ 20 GeV and should increase soon as TRISTAN limits are reported. Higher limits can be placed on the masses by considering more complex production processes; however, the limits are usually model dependent and may be in the form of a bound on some combination of sparticle masses. For example, the ASP experiment studied the radiative production of photino pairs, mediated by selectron exchange. The rate is determined by the selectron mass, which appears in the propagator, and by the photino mass, which determines the final state phase space. The results of that experiment,[6] shown in figure 2, are in the form of a bound in the selectron-mass *vs* photino-mass plane. If the photino mass is small, the selectron mass is greater than about 60 GeV; for increasing photino mass the selectron mass limit drops. Similar results are shown in the figure for the bounds on the wino and the sneutrino masses.

SUSY particles with color charge, such as squarks or gluinos, can be produced in hadron-hadron collisions. The analysis is complicated by the difficulty of calculating production cross-sections and by the model dependence of the decays. Results from the UA1, UA2, and CDF(1987) experiments give lower limits for squark and gluino masses in the vicinity of 76

to 107 GeV.[7] Higher limits from the CDF should be forthcoming soon.

For the higgsinos, the photino, and the sneutrinos, the best limits available come from astrophysical arguments. See reference [2] for a discussion. The higgsino and photino masses are believed to be either greater than about 2 GeV, or, if they are stable, less than about 100 eV. Similarly, sneutrino masses should be greater than 10 MeV or less than 100 eV.

What Can the SLD Do?

The mass limits given above do not rule out SUSY. Rather, they are a sort of "lamp post" result – we set limits where we can, but not necessarily where we expect to find the SUSY particles. In order to accomplish the desired cancellations, SUSY particles should have masses below the TeV scale. There is clearly still some room for SUSY particles yet to appear within the reach of the SLD.

The missing energy resolution of the SLD is discussed in the contribution to these proceedings from Richard Dubois. To exhibit the strength of the SLD detector in this respect, We have done a study of the importance of hadronic calorimetry for the missing energy resolution of a Z^0 detector. Using the Lund Monte Carlo codes to simulate the hadronic decays of the Z^0 , we find that 22% of the events will contain at least one neutrino in the final state. For events with at least one neutrino, the average total energy carried away by neutrinos is 8 GeV. This sets the limit on performance that could be expected from any detector – but note that in 78% of the decays of Z^0 to quarks there are no neutrinos in the final state. However, neutrons or K_L 's are produced more copiously; 89% of the events have at least one neutrino, neutron, or K_L in the final state, and the average neutral energy in those events is over 12 GeV. In order to exploit the missing energy signature, it is crucial for a detector to be as hermetic as possible and to be able to observe neutrons and K_L 's.

Some of the energy of neutrons and K_L 's will be deposited in the electromagnetic calorimeter; in the SLD the EM calorimeter is 21 radiation lengths thick, or 69% of a hadronic interaction length. To assess the value of the hadronic calorimeter, we analyzed hadronic decays of the Z^0 both including and excluding the energy deposited in the hadronic section of the calorimeter. Figure 3 shows the difference of the missing energy – what would be observed without the hadronic calorimeter minus what would be observed with the hadronic calorimeter – on an event-by-event basis. Almost 80% of the events have a significantly increased missing energy. The average increase in missing energy is 7 GeV, and there is a long tail of events out past 30 GeV. Clearly, the hadronic calorimeter is essential for acceptable

performance in missing energy resolution.

Conclusion

Supersymmetry remains an attractive feature of particle theories, and experimental results do not seriously restrict the range of the masses of SUSY particles. There is still room for discovery of SUSY particles in Z^0 decays, and the SLD is well-equipped for the task. The hadronic calorimetry of the SLD proves to be particularly important in the characteristic missing energy signature. To the extent that SUSY can exemplify the features of other new physics that might arise in Z^0 decays, our studies demonstrate the strength and the flexibility of the SLD.

References

- [1] Proceedings of the 13th SLAC Summer Institute on Particle Physics, Eileen C. Brennan, editor. SLAC Report 296, July 1985.
- [2] I. Hinchliffe, *Ann. Rev. Nucl. Part. Sci.* 36 (1986) 505.
- [3] "Physics at LEP", CERN 86-02, Vol 1 (1986) 349-422.
- [4] J. F. Gunion and H. E. Haber, *Nucl. Phys.* B278 (1986) 449-492.
- [5] R. M. Barnett, K. S. Lackner, and H. E. Haber, *Phys. Lett.* 126B (1983) 64.
- [6] C. Hearty *et. al.*, *Phys. Rev.* D39 (1989) 3207.
- [7] R. K. Ellis, conference summary talk, 8th Topical Workshop on Proton-Antiproton Collider Physics, Castiglione d. Pescaia, Italy, 5 September 1989.

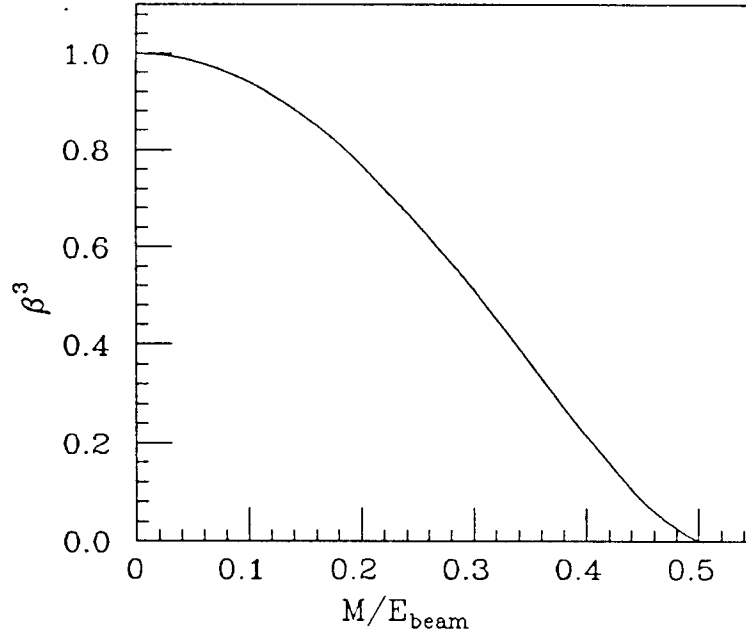
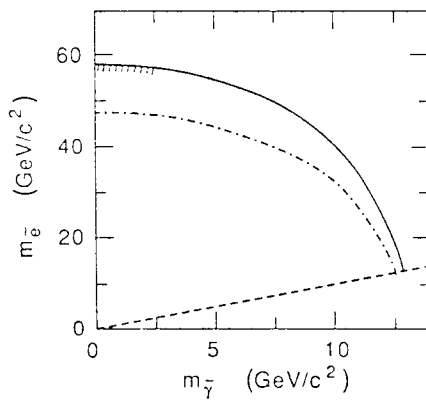
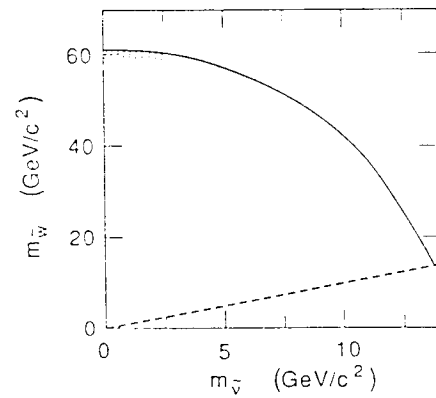


Figure 1. The β^3 factor *vs* the ratio of SUSY particle mass to the beam energy.



90%-C.L. limits placed on the scalar-electron and photino masses. The solid line applies if the scalar-electron mass states are degenerate, while the dashed-dotted line applies if one is much heavier than the other. The dashed line is $m_{\tilde{e}} = m_{\tilde{\gamma}}$.



90%-C.L. limits placed on the W-ino and scalar-neutrino masses. The calculation assumes three degenerate scalar-neutrino generations. The dashed line is $m_W = m_{\tilde{\nu}}$.

Figure 2. ASP limits on SUSY particle masses.

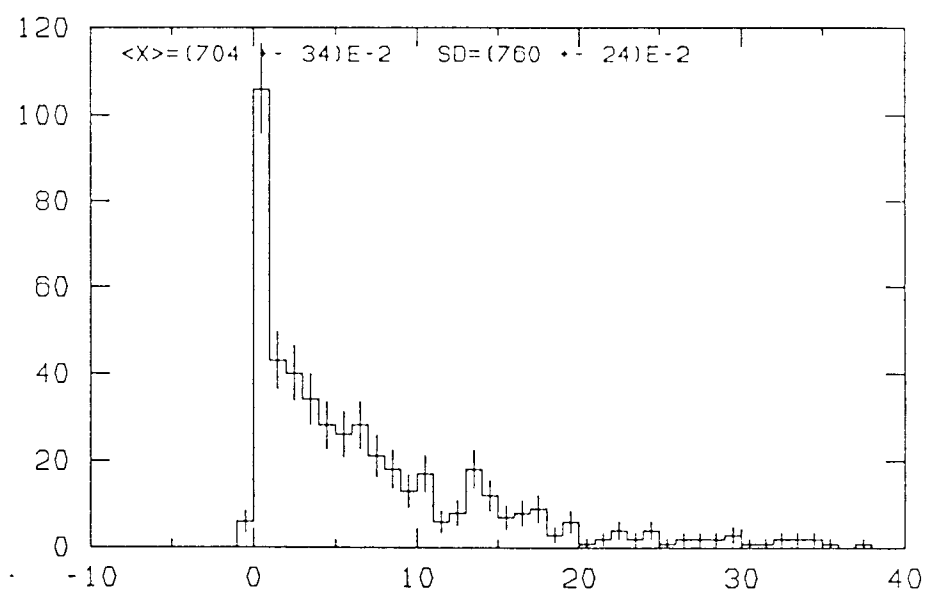


Figure 3. Energy deposited in the SLD hadronic calorimeter in hadronic Z^0 decays.

SUSY Searches for \tilde{e} , $\tilde{\mu}$, \tilde{q}

R.DUBOIS

University of Victoria, P.O. Box 1700, Victoria, BC Canada V8W 2Y2

Abstract

It is expected that SLD will be able to set limits on slepton production above about 45 *GeV*. Squarks are more demanding of the detector capabilities, but similar limits to the sleptons should be obtained.

1. Outline

This talk describes searches performed using the SLD Fast Monte Carlo (FASTMC) to determine possible limits that SLD might be able to set on slepton and squark masses. An outline follows:

1. SUSY properties
2. Relevant variables
3. Backgrounds and Cuts
4. Efficiencies and Limits
5. Conclusions

2. SUSY Properties

One of SUSY's appealing features is that the hypothesis of a symmetry linking fermions and bosons determines the couplings and properties (except for mass!) of the sparticles. The sleptons and squarks are scalars, so that they exhibit a $\sin^2\theta$ angular distribution, and a β^3 suppression. This means that our sensitivity drops off as the sparticle mass approaches the kinematical limit, just over 45 GeV .

It is assumed that the lightest supersymmetric particle (LSP) is the photino ($\tilde{\gamma}$) and, to choose a mass, weighs in at 6.8 GeV in these studies. Sparticles are assumed to decay exclusively to their particle partners and $\tilde{\gamma}$. Such decays are illustrated in Figure 1.

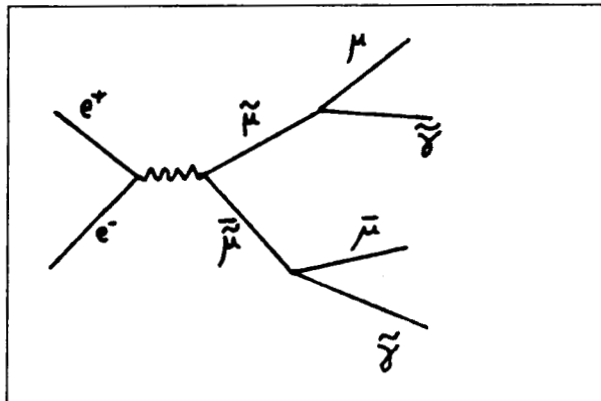


Figure 1. Sample of Sparticle Production. The diagram for the production and decay of smuons is shown. The smuons are produced in pairs and decay to muon plus photino.

Limits from Tristan were presented at the 1989 SLAC Summer Institute indicating that slepton and squark masses were above about 25 GeV . For that reason, this study has been limited to looking at 40 GeV masses. For such masses, one expects from $100\text{-}300$ sparticles for 2.5 pb^{-1} or about 100k Z^0 's. Numerology will be discussed in more detail when limits are presented.

3. Relevant Variables

Since the photino behaves like a massive neutrino, characteristic signatures of large missing energy and p_t imbalance result. Additionally one can see that the final state particles are not collinear nor coplanar (for squarks, one could look at the jet axes to see this), illustrated in Figure 2. Typical examples of such distributions are shown in Figure 3.

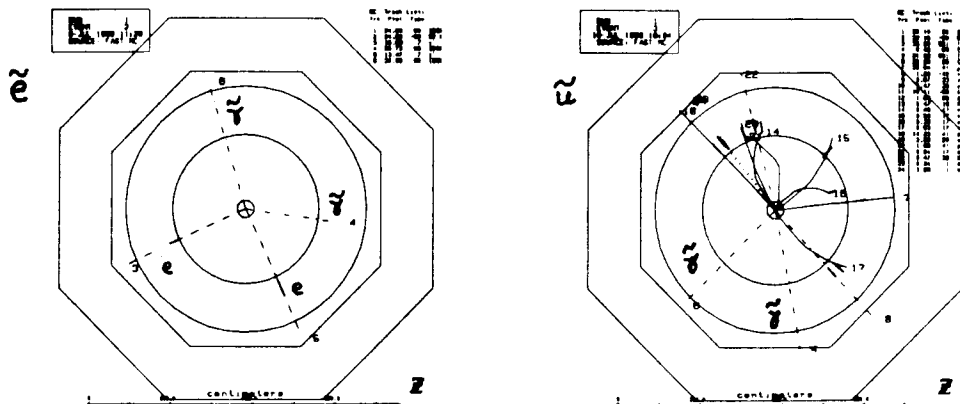


Figure 2. Event Displays of Typical Squarks and Smuons. The observed particles are very acollinear and acoplanar due to the photino.

4. Backgrounds: Sleptons

Backgrounds are quite different for the slepton as opposed to the squark channels. S sleptons have very striking signatures of large momentum lepton pairs which are acoplanar and acollinear. The only backgrounds to these channels are radiative pair production of their particle partners and τ 's.

Initial cuts are

1. exactly two tracks and two calorimeter clusters,
2. each track is associated to a calorimeter cluster,
3. combined particle ID from the calorimeter and CRID indicate good probability that the particles are the right sleptons (checking that the quality code is 4 or greater in PHPART; see G.Gladding, Analysis & Techniques, 5/5/89) leading up to cuts on acollinearity and acoplanarity and Σp_t . Figure 4 shows plots of these variables for the various background processes, and indicates the cuts used.

Backgrounds of 7500 events in each channel were generated: MCBREM5 was used for s-channel Bhabhas; MCLEPT was used for μ 's and τ 's. After these cuts (the most effective of which was the acollinearity cut in almost all cases), no background events survived. Two thirds of the signal events passed.

5. Backgrounds: Squarks

Hadronic Z^0 decays are the principal background to this search. Though it has

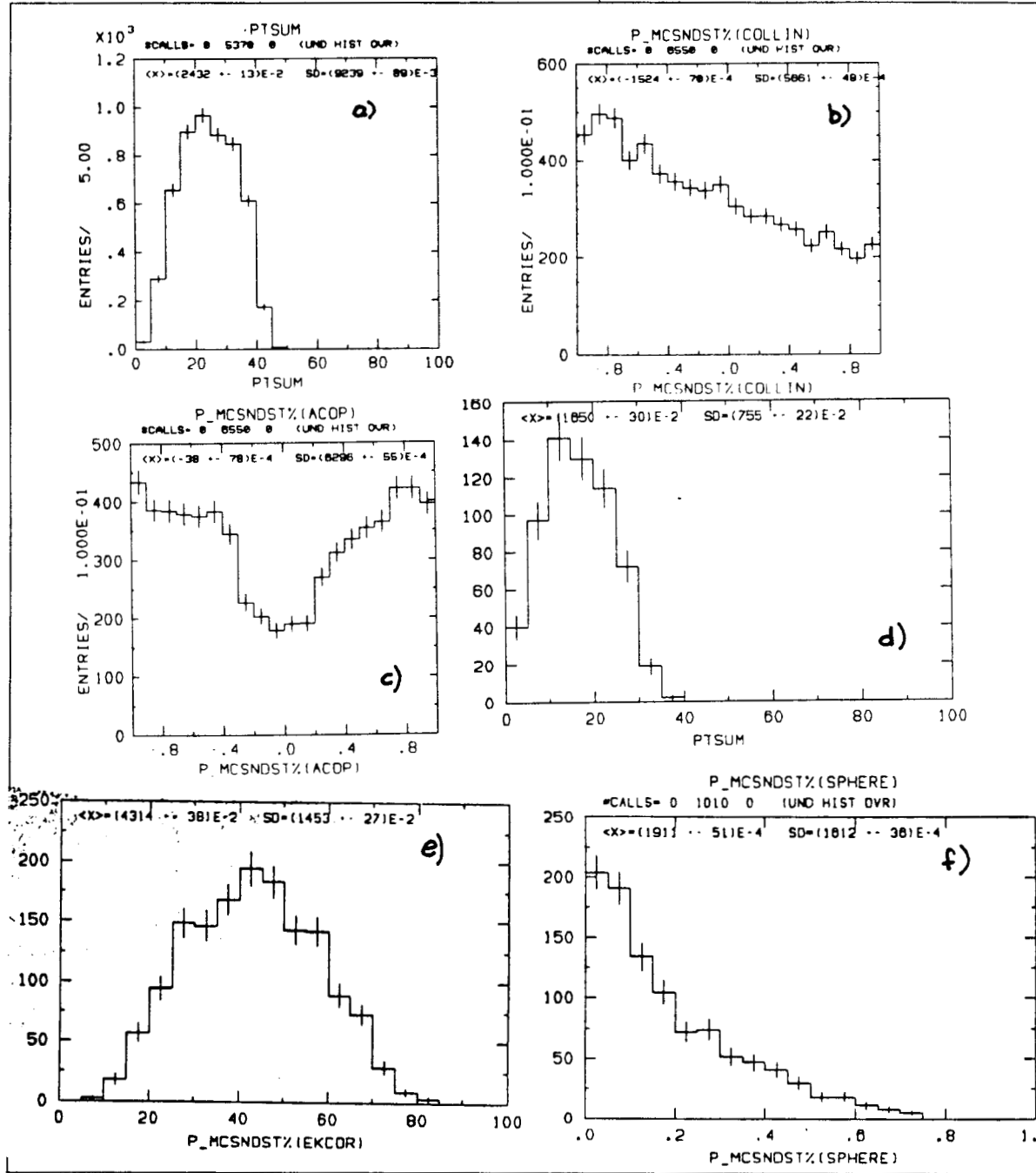


Figure 3. Various Kinematic Quantities. a) Smuon p_t imbalance. b) Smuon acollinearity. c) Smuon acoplanarity. d) Squark p_t imbalance e) Squark total energy f) Squark sphericity.

not been explicitly studied, it is expected that a minimum multiplicity and p_t imbalance cut would effectively eliminate the $\gamma - \gamma$ background. The study concentrated on hadronic decays as the only background.

The large mass of the squarks should lead to large sphericities in their decays.

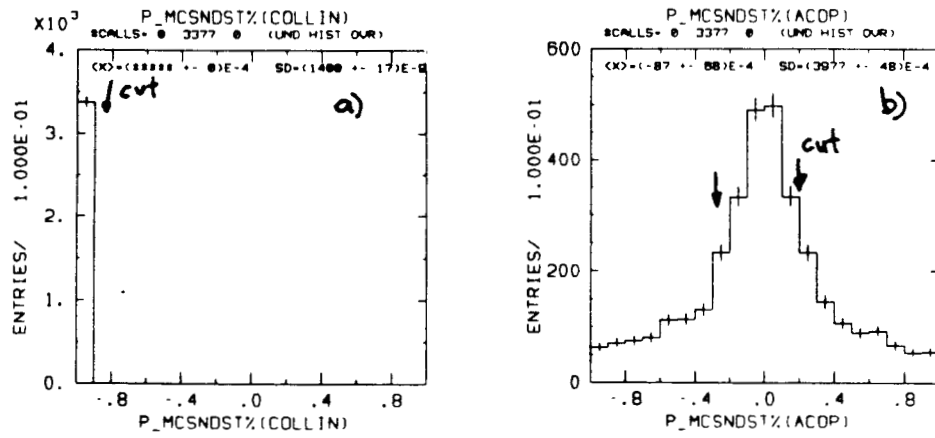


Figure 4. Slepton Background Distributions. a) Tau acollinearity. b) Muon acoplanarity.

The signature for these decays is expected to be large missing energy, large p_t imbalance and large sphericity. Examples of these distributions for the background events are shown in Figure 5. Cut values are indicated.

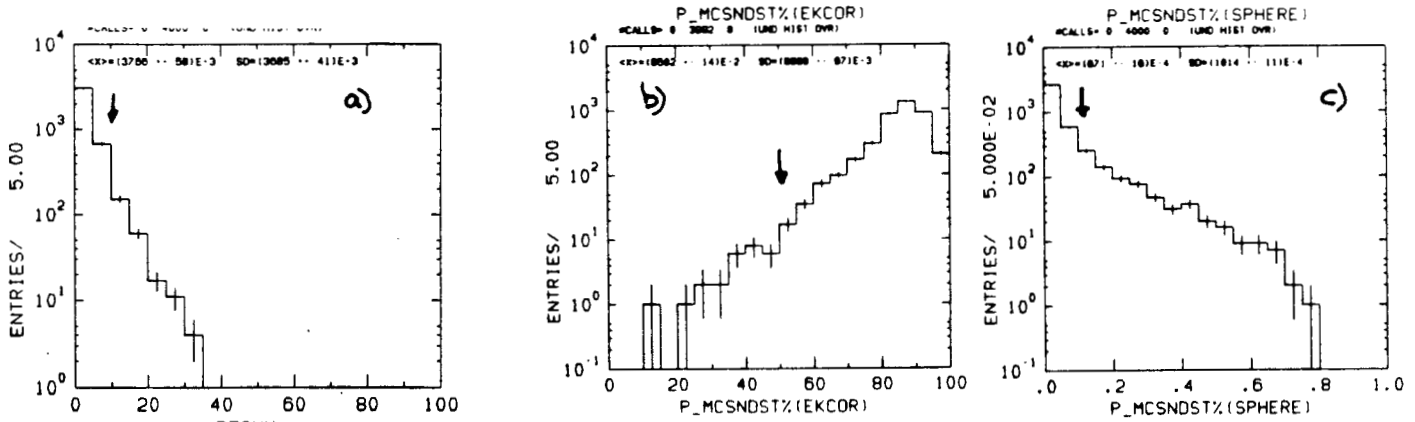


Figure 5. Squark Background Distributions. a) $Z^0 \rightarrow \text{All } p_t$ imbalance b) Total Energy c) Sphericity. Note the semilog scales.

Initial studies found that there was a long tail in the total energy distribution from the calorimeter. This was traced to energy lost in the vicinity of the beam pipe: at this stage of simulation in the FASTMC, the luminosity monitors had not been taken in account. It was found that the tail could be significantly reduced by their inclusion, as shown in Figure 6. Table 1 gives an energy audit of where energy goes in the simulation. It is possible to recover the energy within about a GeV of the total (neutrino and muon energies were not corrected for in this test). It is worth noting that the simulation still does not include intermodule gaps in the calorimeter, nor the overlap region of the barrel and endcap.

For 100k background Z^0 events, 8 passed the cuts applied.

6. Efficiencies and Limits

Table 2 lists the production cross-sections, and efficiencies for seeing the parti-

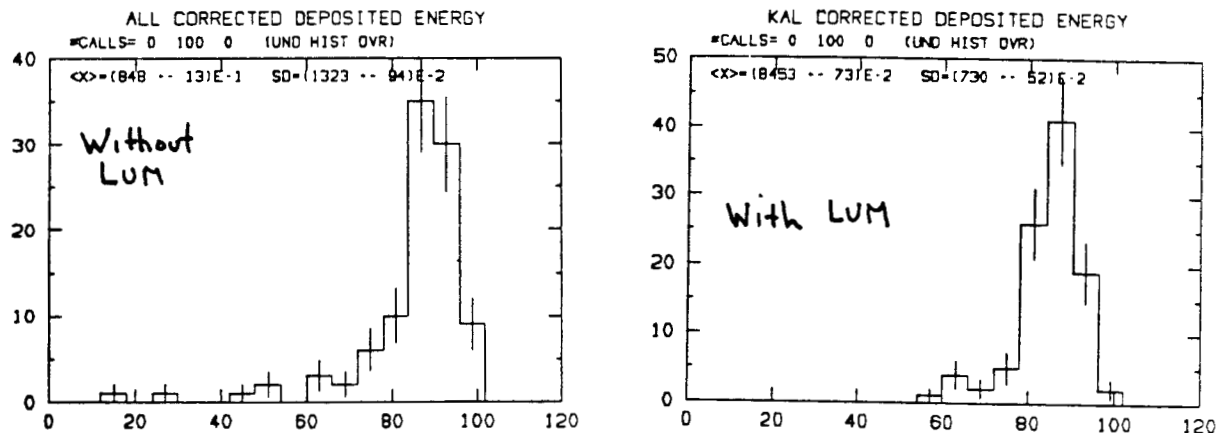


Figure 6. Missing Energy. The low energy tail is much more pronounced without the LUM simulated.

Table 1.

Energy Audit	
Description	Energy Deposit (GeV)
dead regions	3.3
beam pipe (no LUM)	6.5
beam pipe	2.2
uncorrected KAL/no LUM energy	77
corrected KAL energy	84.5
width of Z^0 peak	6

cles. The striking nature of the sleptons leads to very high efficiencies of about $2/3$, while the hard cuts on the missing energy tail leads to a squark efficiency of about $1/3$. One expects then to see from 100-200 sparticles after the search is done. Using the β^3 scaling to find where we would see 3 events leads to limits on all sparticles searched for of over 45 GeV .

7. Conclusions

SLD should be able to easily set limits of up to about 45 GeV for the sleptons, $\tilde{\mu}$ and \tilde{e} (and probably $\tilde{\tau}$ also, though not studied here). However, Mark II and the LEP detectors should have about as easy a time as well.

Squark limits are more difficult to set; tails of the missing energy distribution are important. It may be that other cuts may make the dependence on the missing energy less important (eg number of jets, jet-jet acollinearity and acoplanarity). These remain to be investigated. Mark II would have difficulties due to their lack of solid

Table 2.

Efficiencies and Limits				
Sparticle	σ (pb)	$\# / 2.5 \text{pb}^{-1}$	Efficiency	# Expected
$\tilde{\mu}$	57	143	0.67	95
\tilde{e}	90	225	0.67	151
\tilde{u}	290	725	0.32	232

angle coverage and hadron calorimetry. It is not so clear that the LEP detectors would be at a serious disadvantage, since other handles may be available to help out the missing energy.

It would also be worthwhile to study the problem with the full Monte Carlo and reconstruction to verify whether the tails are believable from the FASTMC or not.

Production of Supersymmetric Higgs Scalars in Z^0 Decays

Scott Whitaker

Boston University Physics Department, Boston MA 02215

C. Baltay, S. Manly, and J.D. Turk

Yale University Physics Department, New Haven CT 06511

Abstract

Supersymmetric scalar Higgs particles could be produced in association in Z^0 decays with branching fractions as high as several percent. If sufficiently massive, each of these scalars would decay to a b and a \bar{b} quark, leading to an event signature of four b-quark jets. The SLD's high acceptance and good calorimetric resolution will allow us to reconstruct the jet-jet masses. By using the SLD's excellent particle identification and vertexing capabilities, background four-jet events from hadronic Z^0 decays can be dramatically reduced, leading to an observable signal for SUSY Higgs production in as little as 50,000 observed Z^0 decays.

Introduction

Supersymmetric particle theories require at least two Higgs scalar doublets, in order to give mass to both up and down-type quarks.[1] In minimal theories with two doublets, the particle spectrum after symmetry breaking includes two charged and three neutral scalar particles. In the notation of reference [1], in this minimal scenario the scalar H_1 is necessarily heavier than the Z^0 and the scalar H_2 is lighter than the Z^0 . The third neutral Higgs particle, H_3 , is distinguished from H_1 and H_2 in having pseudoscalar-like couplings to fermions. The H_3 is heavier than H_2 , but it may be lighter than the Z^0 . In fact, it is possible that the masses of H_2 and H_3 are sufficiently low that the decay $\Gamma(Z^0 \rightarrow H_2 H_3)$ can be kinematically allowed. At tree level, the couplings of the neutral Higgs particles are determined by their masses. In this case, the ratio of the partial width for $Z^0 \rightarrow H_2 H_3$ to the partial width for Z^0 decay to neutrinos (of one generation) can be expressed as

$$\frac{\Gamma(Z^0 \rightarrow H_2 H_3)}{\Gamma(Z^0 \rightarrow \nu \bar{\nu})} = 4 \left(\frac{P_{CM}}{M_Z} \right) \times \frac{M_Z^2 (M_Z^2 - M_2^2)}{M_3^2 (M_Z^2 + M_3^2 - 2M_2^2)}$$

where $M_{2,3}$ are the masses of the H_2 and H_3 scalars. The branching fraction for $Z^0 \rightarrow H_2 H_3$ approaches 3% for nearly equal H_2 and H_3 masses lower than 20 GeV or so, but can be of order half a percent or larger for masses different by up to 15 GeV.

If they are sufficiently massive, H_2 and H_3 will each decay to a b quark and a \bar{b} quark. The signature of the $Z^0 \rightarrow H_2 H_3$ decay would then be a final state with four b jets, with jet-jet masses that reconstruct to the H_2 or H_3 masses. This process is the subject of the remainder of this paper. It is distinguished from Z^0 decays to the usual supersymmetric particles in that it lacks the characteristic missing energy signature.[2] In the case where the H_2 or the H_3 mass were less than about eleven GeV but more than four GeV, that scalar would decay to $c\bar{c}$ or to $\tau\bar{\tau}$. The final states involving τ 's would be very distinctive and will be the subject of a separate study.

The usual limits on Higgs masses (the relevance of which is unclear for supersymmetric theories) lie below the roughly 11 GeV threshold for $b\bar{b}$ decays. Thus we are confronted with the possibility that the only Z^0 decays to supersymmetric particles could lack the usual missing energy signature but would be characterized by the presence of four b jets in the final state. The work below will attempt to demonstrate that the particle identification and vertexing capabilities of the SLD will allow it to perform a very sensitive search for this process.

Monte Carlo Simulation

H_2 , H_3 production and decay were simulated using the SLD FASTMC Monte Carlo. The masses were arbitrarily set to $M_2 = 16$ GeV and $M_3 = 30$ GeV, corresponding to a 0.5% branching fraction of the Z^0 . Three hundred $Z^0 \rightarrow H_2 H_3$ events (appropriate for a data sample of 50,000 visible Z^0 decays) were generated with the $\sin^2(\theta)$ distribution characteristic of scalar production. The H_2 and H_3 were each decayed to $b\bar{b}$ isotropically in their rest frames, and the quarks were passed to Lund for hadronization. Detected particles were then simulated in the FASTMC fashion, which uses knowledge of the SLD geometry and detector performance to apply experimental acceptance and resolution smearing to the Lund-generated particles. To study backgrounds to the signal process, the Lund codes were used to generate 43,000 Z^0 decays to quarks according to the usual couplings. These events were passed through the FASTMC simulation as described above. A beam's-eye view of a representative $Z^0 \rightarrow H_2 H_3$ event is shown in Figure 1.

Event Analysis

The same code was used to analyze both signal and background events. Jets were found using the YCLUS algorithm with the "detected" particle bank PHPART as input. The yclus parameter was set to 0.01, a value selected to provide high efficiency for finding four jets in the signal event sample while keeping the fraction of background four-jet events from hadronic Z^0 decays small. Efficiencies will be tabulated below. With this value for yclus, the YCLUS algorithm's four-jet event fractions in both the signal and the background samples were in good agreement with the results from applying the LUCLUS jet-finding algorithm with its default parameters.

Only four-jet events were kept for further analysis. A cut on event sphericity was found to be effective in improving the signal to background ratio. Further analysis was done using the jet parameters; see the contributions of Jeffl Turk and Steve Manly to these proceedings for further details.

The thrust axis of the event was found by determining which jet-jet pairing gave the maximum value for $|\vec{P}_{pair\ 1} - \vec{P}_{pair\ 2}|$. For H_2 and H_3 masses low enough that the branching fraction for their production would be acceptably large, of order half a percent, the quarks from the H_2 will be closer to each other than they are to the quarks from H_3 decay. The thrust axis is then an estimator of the axis of the original Z^0 decay, and the jet-jet pairing

that has the maximum thrust is likely to be the right combination out of the three possible. Selection of the pairing with maximum thrust eliminates the combinatoric background to the jet-jet mass plots.

A cut on the angle of the thrust axis of $|\cos(\theta_{Thrust})| < 0.7$ was applied. The principal motivation for this cut is to require that the jets be directed into the central acceptance of the SLD, where particle identification in the CRID and vertex finding in the CCD vertex detector can be used to tag b quark jets. Since the signal is distributed as $\sin^2(\theta)$ while the background hadronic Z^0 decays are mostly distributed as $1+\cos^2(\theta)$, there is also some enhancement of the signal to background ratio.

At this point, accepted events have identified jet-jet pairings, and the lower and higher jet-jet masses $M_{JJ,low}$ and $M_{JJ,high}$ can be separately plotted for each event. Figure 2a shows the distributions in $M_{JJ,low}$ and $M_{JJ,high}$ for the 144 surviving events from the $Z^0 \rightarrow H_2 H_3$ sample (with thrown masses $M_2 = 16$ GeV and $M_3 = 30$ GeV). The reconstructed masses peak up about 15% lower than the thrown masses. This is due to neutral particles that overlap in the calorimeter with charged particles; charged particle tracking has priority in the particle detection process and so these neutrals are lost.

Energy and momentum conservation can be used to improve the jet-jet mass resolution.[3] Multiplicative constants for the momentum of each jet can be determined by requiring that each momentum component sum to zero and the total energy (calculated assuming the b quark mass for each jet) sum to the Z^0 mass, i.e. by solving

$$\sum A_i \vec{P}_i = 0$$

$$\sum \sqrt{A_i^2 P_i^2 + m_b^2} = M_Z$$

for the constants A_i for the jets $i = 1, 2, 3, 4$. This technique improves the jet-jet mass resolution by a factor of two, as shown in figure 2b. This Monte Carlo study did not include initial state radiation, final state radiation, or finite Z^0 width, so the actual improvement by this technique may be less in practice.

Figure 3 shows the distributions in $M_{JJ,low}$ and $M_{JJ,high}$ for the 2,606 background events that have passed the analysis cuts. Figure 4 shows the signal events superposed on the background distribution. While the signal events are well resolved, the background events are sufficiently numerous that detection of the signal in the presence of background would require a very large event sample.

The background can be reduced by tagging b quark jets. Two schemes are possible: search for high energy kaons, and search for secondary vertices. A requirement that an event have at least two charged kaons with momentum above 3 GeV gave a factor of two improvement in the S/B ratio but at the cost of a reduction of the number of signal events by a factor of three. The mass plots after this cut are shown in figure 5; signal and background are superposed. This cut has the virtue that the FASTMC does an adequate job of simulating it, but it is clearly expensive in terms of statistical sensitivity. A signal at the 0.5% level is at the margin of detectability in this event sample.

The alternative approach of vertex tagging is difficult to quantify now because the codes for vertex finding are not advanced enough to simulate the performance of the vertex detector. However, reasonably careful estimates of the performance to be expected have been done; see the contributions to these proceedings from David Williams and from Jeff Richman. A back-of-envelope calculation will serve to demonstrate the power of vertex finding. Let the probability that a b quark jet is correctly tagged be denoted $\epsilon_{b \rightarrow b}$, and similarly denote the probability that a non- b jet is incorrectly tagged as a b quark jet by $\epsilon_{q \rightarrow b}$. Reasonably conservative values for these performance parameters are $\epsilon_{b \rightarrow b} \approx 0.7$ and $\epsilon_{q \rightarrow b} \approx 0.1$. Using these values, the efficiency for signal events to pass a requirement of ≥ 3 tagged b jets is then

$$\epsilon_{signal} = \epsilon_{b \rightarrow b}^4 + 4\epsilon_{b \rightarrow b}^3(1 - \epsilon_{b \rightarrow b}) \approx 0.7 .$$

Of the background events that have passed the cuts so far, 20% are $b\bar{b}q\bar{q}$ events; since $\epsilon_{b \rightarrow b}$ is large compared to $\epsilon_{q \rightarrow b}$, these events will dominate the background event sample passing a three- b -tag requirement. The fraction of the event sample that passes this cut can then be estimated as

$$\epsilon_{background} = .2 \times \epsilon_{b \rightarrow b}^2(\epsilon_{q \rightarrow b}^2 + 2\epsilon_{q \rightarrow b}(1 - \epsilon_{q \rightarrow b})) \approx 0.02 .$$

The very salutary effect of requiring at least three tagged b jets is shown in Figure 6, which presents distributions in lower and higher jet-jet masses after this cut is applied; the signal has been superimposed on the background. The signal events stand out very clearly above the background – so clearly in fact that a smaller event sample would suffice to establish the presence of a signal.

Summary of the Analysis

Efficiencies and event counts are shown in Table 1 for the analysis of a data set corresponding to 50,000 visible Z^0 decays with the process $Z^0 \rightarrow H_2 H_3$ occurring with a branching

fraction of 0.5%. While the tracking and calorimetry performance are clearly important, it is the particle identification and vertexing capabilities of the SLD that are crucial to the detection of this supersymmetry signal.

References

- [1] J. F. Gunion and H. E. Haber, Nucl. Phys. B278 (1986) 449–492.
- [2] The SUSY missing energy signature is discussed by Richard Dubois in these proceedings.
- [3] See the contribution by C. Baltay, J. Turk, and S. Manly for a fuller discussion of the fitting procedure.

Table. The number of events in the Signal class, $Z^0 \rightarrow H_2 H_3$ with $M_2=16$ GeV and $M_3=30$ GeV, and in the Background class, $Z^0 \rightarrow Quarks$, at each stage of the analysis. The final two cuts are mutually exclusive: either the charged kaon requirement or the tagged b-jet requirement is imposed.

	$Z^0 \rightarrow H_2 H_3$	$Z^0 \rightarrow Quarks$
total events	300	43,408
4-jet events	226	8,485
sphericity $> .1$	156	4,322
$ \cos(\theta_{Thrust}) < .7$	144	2,606
$\geq 2 K^\pm$ at > 3 GeV	46	506
≥ 3 tagged b jets	98	58

RUN 1
 EVENT 31
 21-JUL-1989 08:36
 SOURCE: FAST MC

#	Ptot	Type
1	1.34	-17 π^-
2	5.16	-41 p^-
3	1.33	17 π^+
4	7.90	41 p^+
5	3.96	17 π^+
6	8.74	17 π^+
7	1.25	17 e^-
8	2.07	-17 π^-
9	2.10	-17 π^-
10	2.41	-17 π^-
11	0.30	-17 π^-
12	1.40	-17 π^-
13	0.57	-17 π^-
14	0.95	17 π^+
15	1.11	17 π^+
16	0.95	-17 π^-
17	2.68	-17 π^-
18	2.97	-9 μ^-
19	0.55	17 π^+
20	1.70	-17 π^-
21	1.18	-18 K^-
22	0.99	-17 π^-
23	2.39	-17 π^-
24	2.52	17 π^+
25	0.26	1 δ^-
26	0.85	1 δ^-
27	0.16	1 δ^-
28	0.86	1 δ^-
29	0.50	1 δ^-
30	0.29	1 δ^-
31	0.19	1 δ^-
32	0.72	38 K_L^0
33	7.30	1 δ^-
34	0.07	4 δ^-
35	0.48	38 K_L^0
36	0.20	1 δ^-
37	0.35	1 δ^-
38	0.11	1 δ^-
39	1.10	1 δ^-
40	1.1	38 K_L^0
41	0.9	38 K_L^0
42	0.0	4 δ^-
43	0.4	38 K_L^0

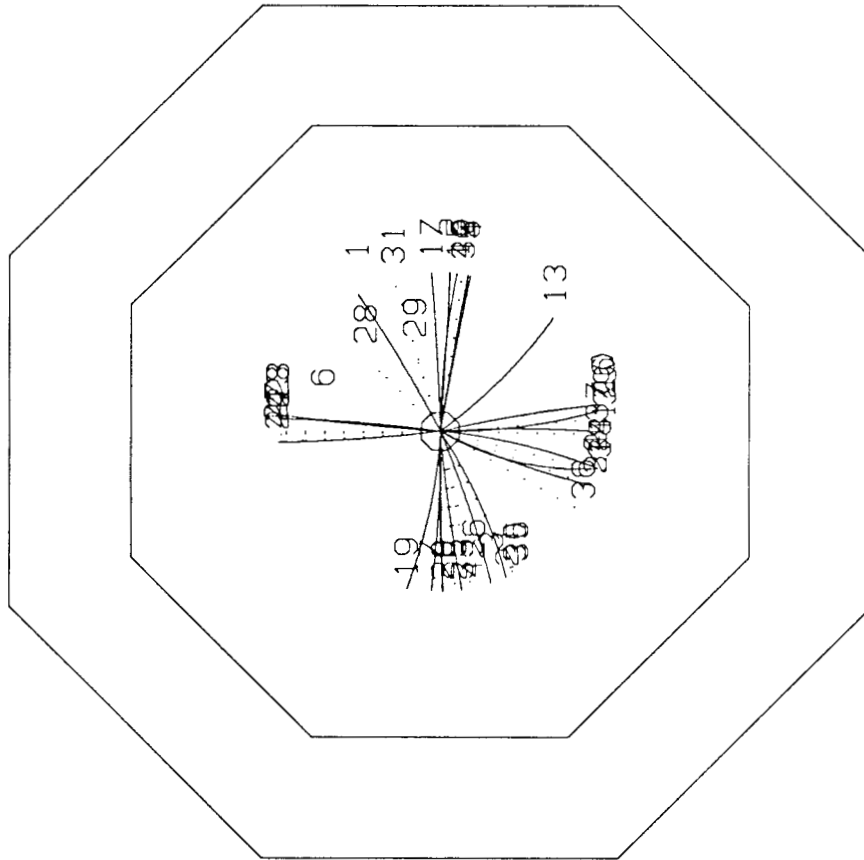


Figure 1. A representative event

92

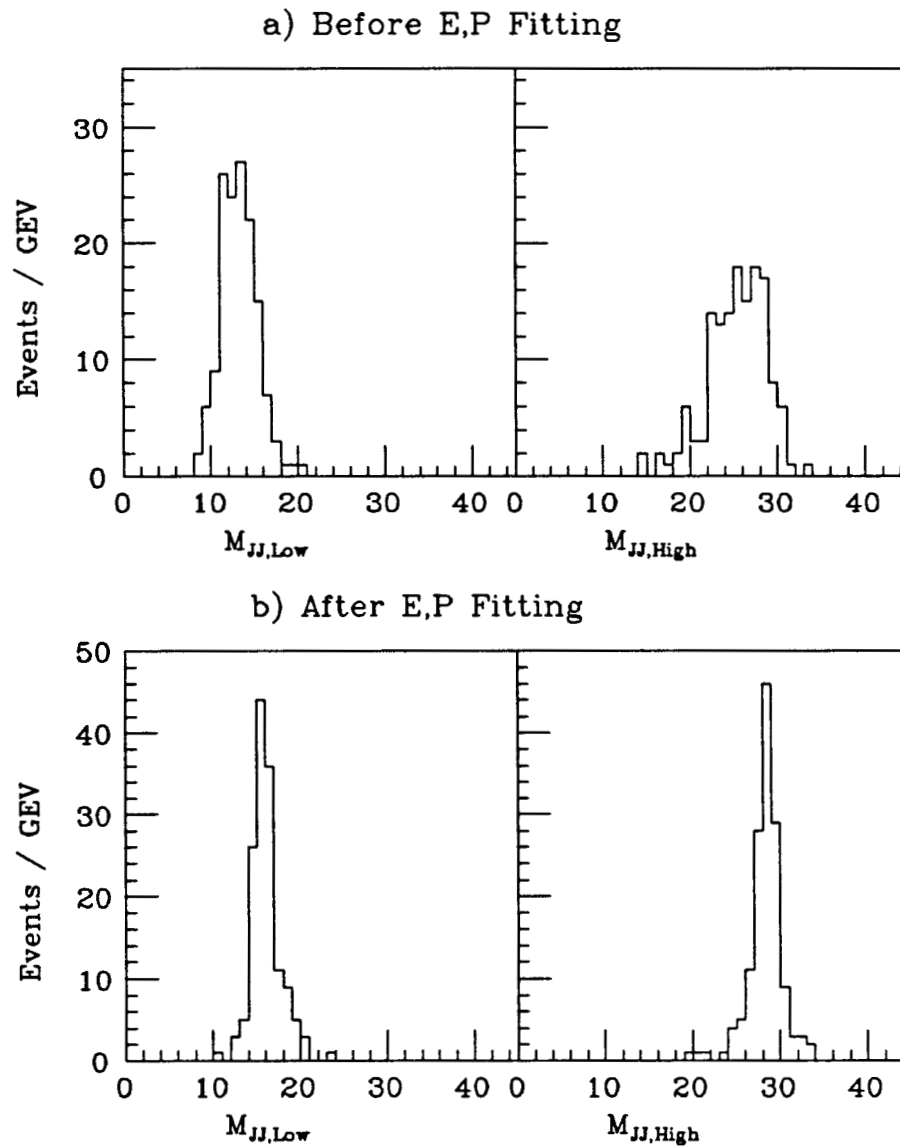


Fig. 2 $Z^0 \rightarrow H_2 H_3$ jet-jet mass distributions

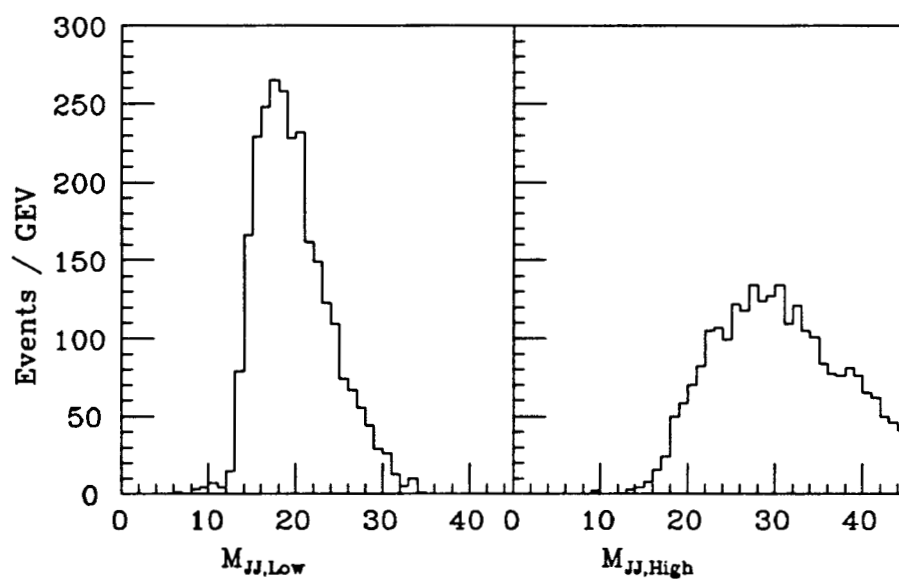


Fig. 3 $Z^0 \rightarrow \text{Quarks}$ jet-jet mass distributions

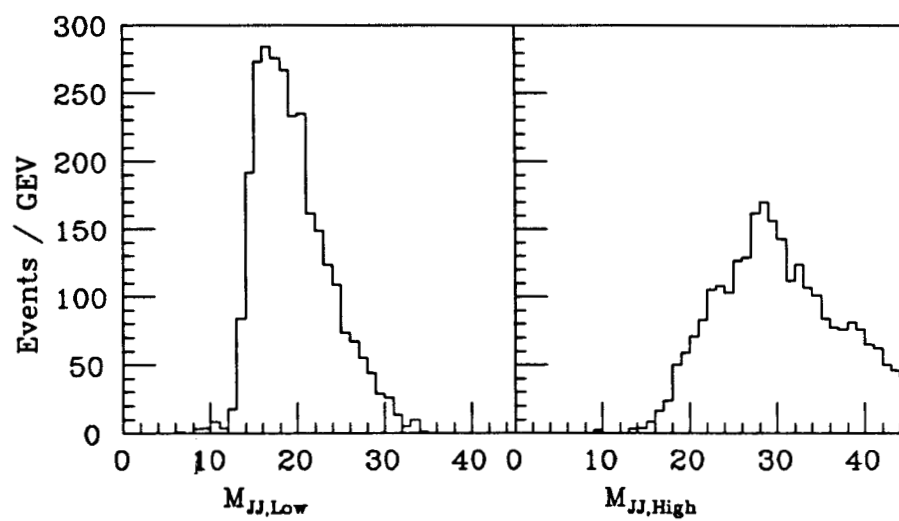


Fig. 4 Signal plus background jet-jet mass distributions.

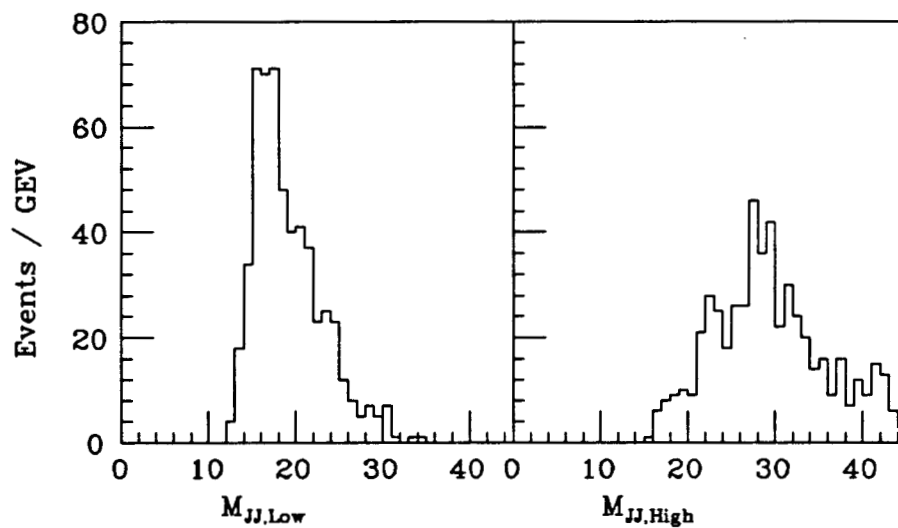


Fig. 5 Signal plus background jet-jet masses with ≥ 2 charged Kaons

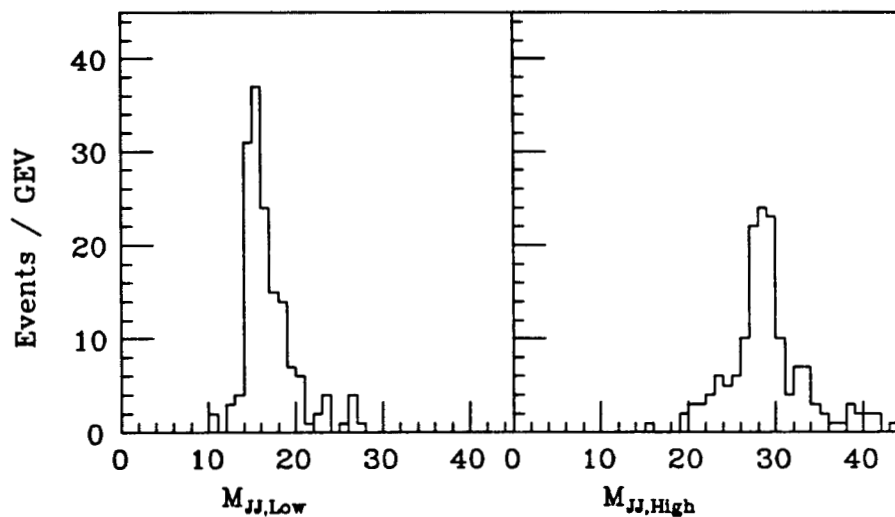


Fig. 6 Signal plus background jet-jet masses with ≥ 3 tagged b quarks.

Search for Higgs Bosons using a Missing Energy Signature

A.S. JOHNSON

Boston University

Abstract

A missing energy analysis has been used as a method of searching for evidence of Higgs Boson decays in the SLD detector. Particular attention has been given to combining information from the tracking and calorimetric detectors in order to fully exploit the advantages of the SLD.

Missing energy is a clear signature for a number of possible new particles, in particular SUSY particles and Higgs bosons. In this paper we will study how the SLD detector can be used for missing energy studies in general, and in particular to search for evidence of a standard Higgs boson by way of the reaction

$$\epsilon^+ \epsilon^- \rightarrow H^0 Z^{0*} \rightarrow q\bar{q}\nu\bar{\nu} \quad (1)$$

SLD has very good solid angle coverage with both calorimetry (electromagnetic and hadronic) and tracking chambers. While the good calorimetry is essential for the detection of neutral particles the tracking chambers can also be used as an important tool in missing energy studies since they give generally superior energy resolution for charged particles. In this paper we will be particularly interested in finding an optimal way to combine information from the calorimetric detectors and tracking chambers.

To study backgrounds to process (1) a sample of approximately 100,000 events were generated using the LUND generator. These events were fed through the SLD parameterized FASTMC program to simulate their detection by the SLD detector. The FASTMC used for this study differed from the standard SLD FASTMC in that the simulation of the calorimeter was improved in a number of areas important for the study of missing energy¹. The improvements were in the following areas:

- The luminosity monitor was included in the simulation of the calorimetry. The luminosity monitor extends the coverage of calorimetry down to 28 mrad which is important for vetoing events where significant energy is scattered at small angles.
- The material in the coil has been treated as the first sampling layer for the WIC.
- The effects of the barrel/endcap overlap region in the LAC have been simulated using a parameterization of the effect seen using the detailed GEANT Monte-Carlo program. The effects of the intermodule gaps in ϕ were also simulated.

A standard algorithm is build into the FASTMC to build a list of detected particles (stored in the PHPART banks) and assign energies to them. The algorithm works as follows: First any particles found by one or more tracking chambers (vertex chamber, central drift chamber and endcap drift chambers) are handled. The tracks are extrapolated to the point of closest approach to the interaction point, and the momentum here ($p_{charged}$) is calculated based on the measured momentum after a correction for the effect of dE/dx energy loss. The energy of the particle is then calculated as

$$E = \sqrt{p_{charged}^2 + m_{PID}^2} \quad (2)$$

where m_{PID} is the mass of the particle calculated from the result of a particle identification algorithm using input from the CRID and the calorimetry. The correction due to different particle masses does not significantly effect the missing energy studies presented here so charged particle identification is not strictly necessary for this analysis.

Once all of the charged tracks have been found the clusters of energy found in the calorimeter are treated. Each charged track is extrapolated to its point of entry

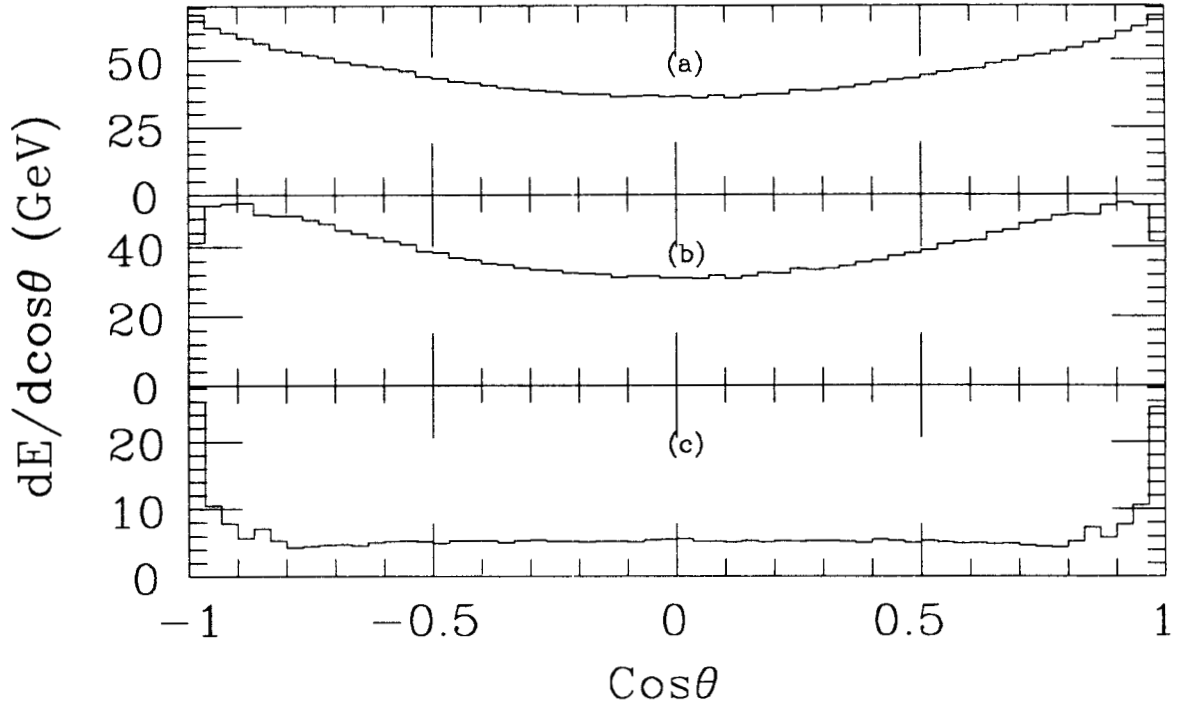


Figure 1. Energy Flow as a Function of θ . The average energy flow for a large sample of generated Lund events (a) together with the energy flow after simulation by the FASTMC (b). The difference between these two distributions (c) shows the average missing energy.

into the LAC. If the angle of the track in θ and ϕ is consistent with any of the energy clusters (taking into account the errors on θ and ϕ of the cluster) then that cluster is “associated” to the charged track. The energy of the charged track is not adjusted from the previously calculated value however. After all the charged tracks have been extrapolated then any remaining unassociated energy clusters are assumed to have been formed by neutral particles. These neutral particles are then added to the list of charged tracks already in PHPART. The energy measured by the calorimeter (E_{raw}) is corrected for e/π ratio based on a parameterization of the calorimeter’s ability, based on longitudinal shower profile, to differentiate showers caused by hadrons from those formed by electromagnetic particles. For electromagnetic showers the energy assigned to the particle is given by $E_{cal} = E_{raw}$ while for hadronic showers $E_{cal} = E_{raw}/0.85$. This is then the energy assigned to neutral particles.

The average energy flow as a function of θ is shown in figure 1 for Lund events as generated, and for the same events after simulation using the FASTMC algorithm discussed above. Subtracting the second plot from the first gives the third plot, which shows where the missing energy goes on average as a function of θ . As would be expected some energy (a little over 2 GeV on average) is lost down the beampipe, and the effects of the barrel/endcap overlap region can also be seen at $\cos \theta = \pm 0.85$.

but as the plot shows, another 6 GeV of energy is lost spread evenly over all θ . Further study of the events shows that this energy loss is primarily due to energy clusters in the calorimeter formed from a charged particle plus one or more overlapping neutral particles. Using the algorithm described above only the charged particle energy is used, while the neutral particle(s) energy gets “lost”.

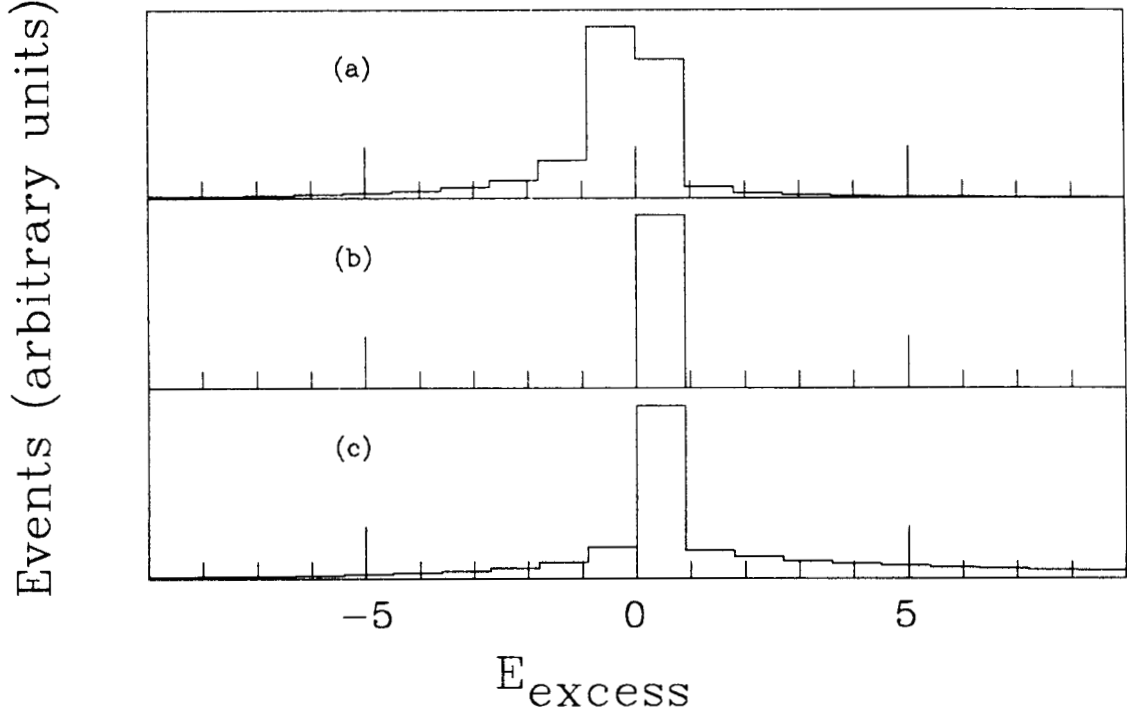


Figure 2. Excess Calorimeter Energy. The excess calorimeter energy, E_{excess} , is shown for three classes of calorimeter cluster: (a) A cluster formed from a single charged track, (b) A cluster formed from a single neutral track and (c) A cluster formed from a charged track and one or more overlapping neutral tracks.

In an attempt to recover this energy we can define an “excess calorimeter energy”, E_{excess} , as

$$E_{excess} = (E_{cal} - E)/\sigma(E_{cal}) \quad (3)$$

where the calorimeter resolution, $\sigma(E_{cal})$, can be approximated as $0.6/\sqrt{E_{cal}(GeV)}$. Figure 2 shows the excess energy for three classes of calorimetry showers, those formed from single charged tracks, those formed from single neutral tracks (where by definition $E = E_{cal}$), and those formed from one charged track and one or more overlapping neutral tracks. The assignment of clusters into these categories is based on Monte-Carlo information.

It can be seen that for the third category of tracks there is a tail at large E_{excess} which suggests that much of the lost energy can be recovered by making a suitable cut

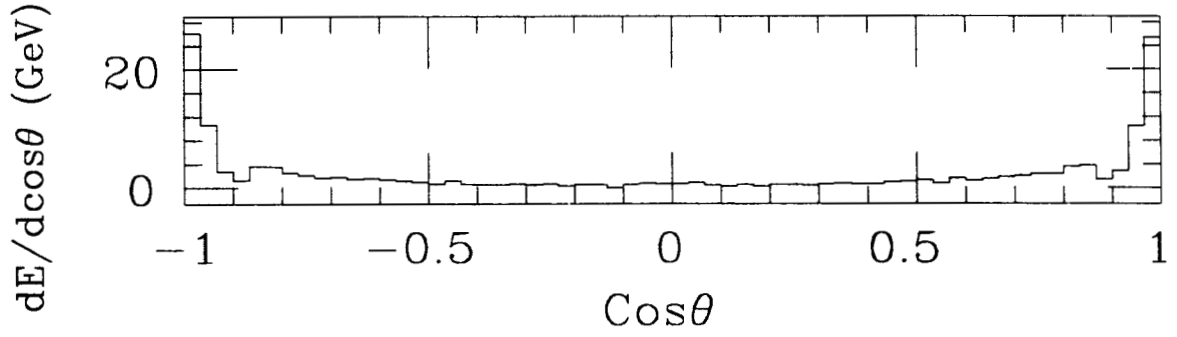


Figure 3. Corrected Missing Energy Flow as a function of θ . This figure shows the same plot as figure 1(c) but after applying the correction for charged-neutral overlap described in the text.

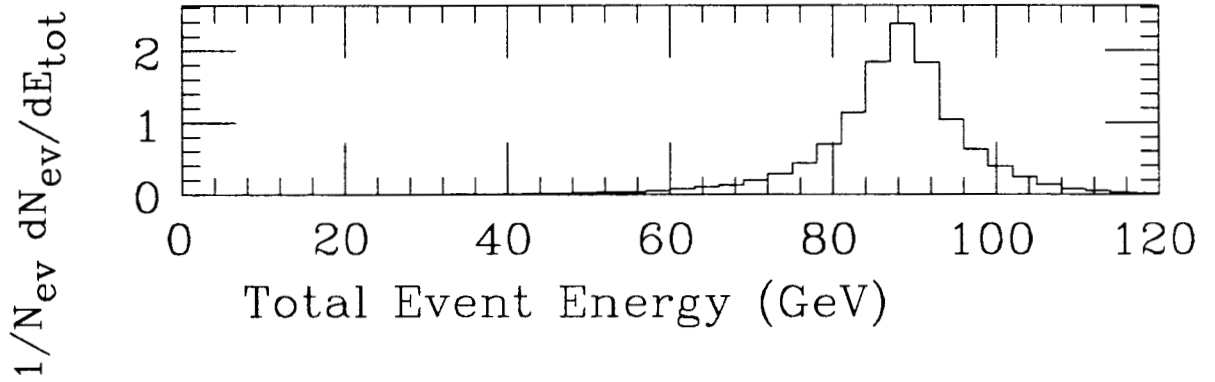


Figure 4. Total Event Energy. The total event energy after application of the algorithm described in the text for a sample of 100,000 Lund events. Only 197 events remain after application of a cut $E_{tot} < 40 \text{ GeV}$.

on this quantity, while at the same time only slightly distorting the energy measured for non-overlapping clusters. Figure 3 shows the new missing energy flow after the energy of particles have been corrected using the following prescription:

$$E_{corr} = E_{cal} \text{ for } E_{excess} > 3; E_{corr} = E \text{ for } E_{excess} \leq 3 \quad (4)$$

Figure 4 shows the total event energy, E_{tot} , formed by summing the energy of all particles in an event after applying the method described above for calculating the energy of each particle. After applying a cut,

$$E_{tot} = \sum E_{corr} < 40 \text{ GeV} \quad (5)$$

only 197 of the original 100,000 events remain.

When (5) was applied to samples of Higgs events generated² according to (1) for various Higgs masses between 8 and 20 GeV all of them passed the cut. Figure 5 and

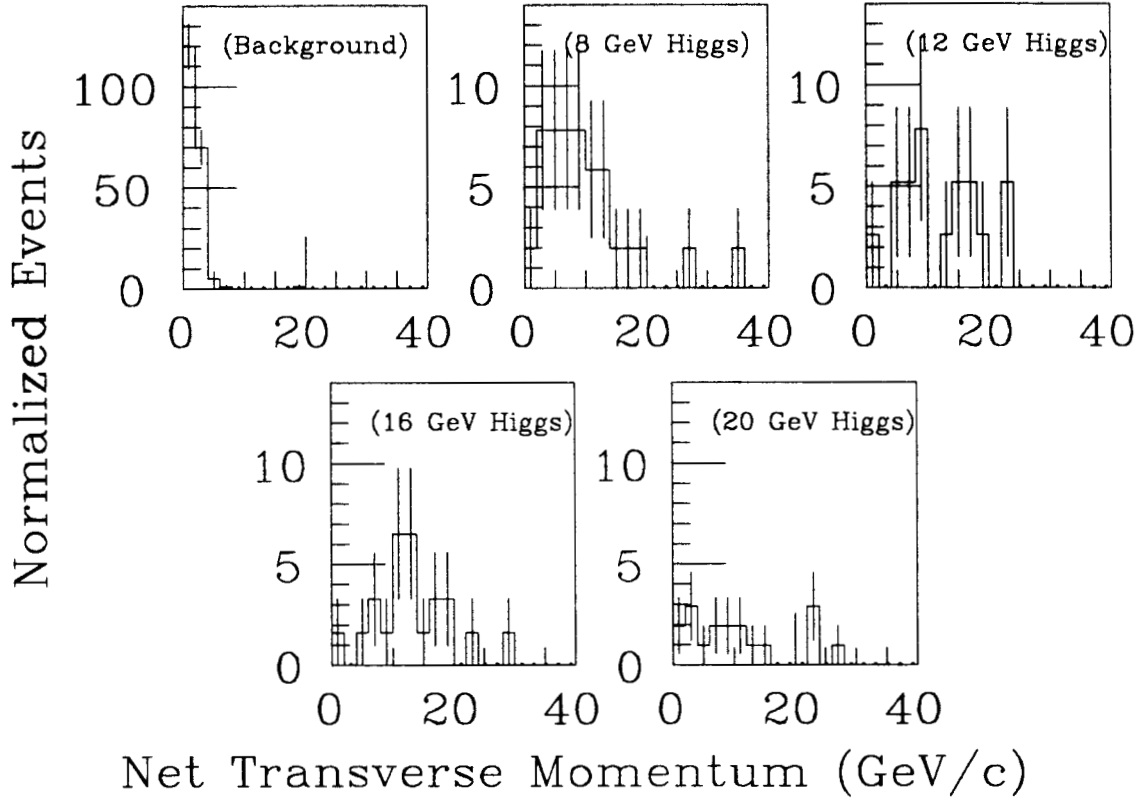


Figure 5. Net p_t for events containing 8,12,16 and 20 GeV Higgs and for background Lund events. Each distribution has been normalized to correspond to 100,000 visible Z^0 decays.

figure 6 compare the total transverse momentum, P_t , and the folded cosine of the event axis, $\cos A$, for each sample of Higgs events compared to the remaining background events where

$$P_t = \sum \sqrt{p_x^2 + p_y^2} \quad (6)$$

and

$$\cos A = \frac{\sum |p_z|}{\sqrt{(\sum p_x)^2 + (\sum p_y)^2 + (\sum |p_z|)^2}} \quad (7)$$

where the sums are over all particles in the event and p_x, p_y and p_z are the components of the particle's momentum derived from E_{corr} . As can be seen from the plots it is then a comparatively easy job to eliminate the remaining background events by applying the cuts:

$$P_t > 4 \text{ GeV}/c; \cos A < 0.98 \quad (8)$$

These cuts are at least 80% efficient for each sample of Higgs events but eliminate all but three of the background events. Finally figure 7 shows the invariant mass distribution for each sample of events after the above cuts have been applied. The

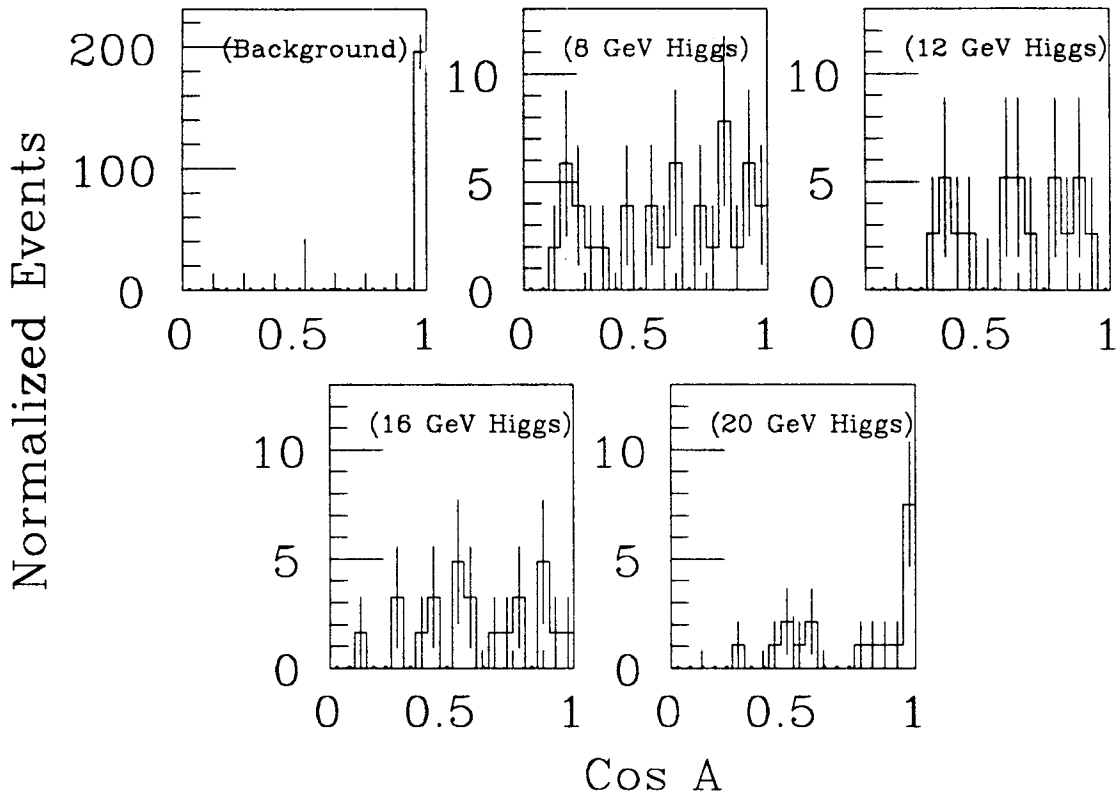


Figure 6. $\cos A$ (see text) for events containing 8, 12, 16 and 20 *GeV* Higgs and for background Lund events. Each distribution has been normalized to correspond to 100,000 visible z^0 decays.

invariant mass peaks for the Higgs events are now easily distinguished above the three remaining background events.

The entire analysis presented here has used the SLD FASTMC. This MC is only a relatively crude parametrized Monte-Carlo, and many effects which may be important for successfully isolating a missing energy signal are not well handled by the current FASTMC. Effects which should certainly be studied further include:

- Inefficiencies and mistracking in the tracking chambers. The FASTMC currently assumes a 100% efficiency for finding charged particles provided they traverse a sufficient length of the active region of the chamber, and does not simulate confusion due to noise or close tracks.
- Energy loss in discreet chunks of material such as the CRID ribs. In the current FASTMC structures such as the CRID are treated as homogeneous as far as energy loss is concerned, so effects such as certain particles losing significant energy due to ribs etc. is not simulated.
- The calorimeter response in the FASTMC is fairly idealized. Effects such as the variation of e/π suppression as a function of energy are not included.

The above items can be fairly easily simulated by using the detailed SLD Monte-

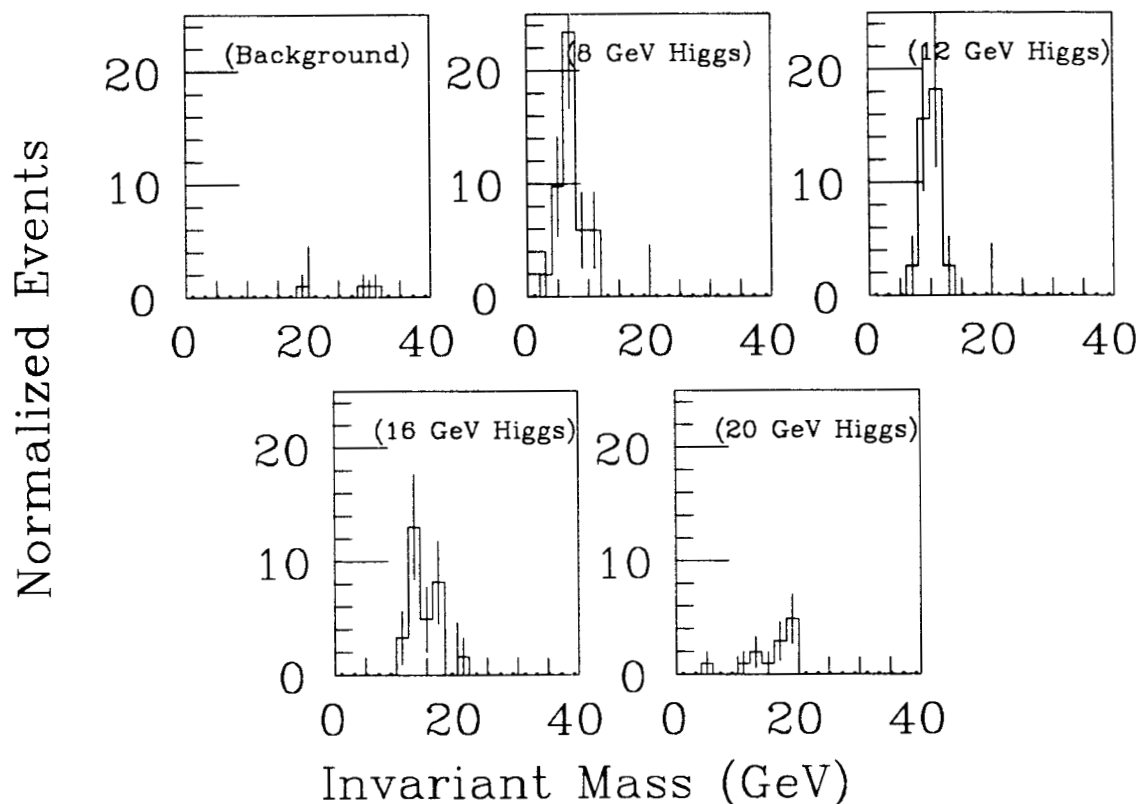


Figure 7. Invariant Mass for events containing 8,12,16 and 20 *GeV* Higgs and for background Lund events. Each distribution has been normalized to correspond to 100,000 visible z^0 decays.

Carlo in the future. This is clearly desirable since the FASTMC is also not to be trusted in predicting backgrounds as small as those studied here since it is clear that the tails of distributions simulated by the FASTMC are not reliable at this level.

There are other types of inefficiencies and backgrounds which will be much harder to simulate, for example the effects of dead wires and towers, beam-gas background and background noise, especially in the luminosity monitor and tracking chambers. Effects such as these will probably have to wait until we have real data before they can be realistically studied.

Finally if we do ever see an anomalous missing energy signal it will be very important that we have confidence in our hardware. If we see 10 events with missing energy will we be able to show without doubt that the HV was turned on for all of the calorimeter modules?

CONCLUSIONS

By combining the information from the tracking chambers with the calorimetry it has been possible to eliminate backgrounds while maintaining a very high efficiency for detecting Higgs decays. Initial studies indicate that SLD could easily detect standard

Higgs Bosons up to 20 GeV and beyond, but more detailed studies need to be done with a more complete Monte-Carlo program. While it seems unlikely that MARK II will be competitive in this kind of analysis due to their lack of a hadronic calorimeter, the capabilities of the LEP detectors are more difficult to predict, again needing a detailed Monte Carlo study to provide meaningful results.

REFERENCES

1. The improvements to the FAST MC were made by Richard Dubois and Dave Gurd.
2. The Higgs events used here were generated by Eric Vella using a program written by Alan Mincer. Cross sections here are from the LEP Yellow book, Vol. 1, p. 322.

A Search for Technicolor Particles Using the SLD Detector

Iris Abt^c, Charles Baltay^f, George Chadwick^e, Steven Manly^f
Uriel Nauenberg^b, Uwe Schneekloth^d, Michael Sokoloff^a,
Jeff Turk^f, Ron Webber^a, L. C. R. Wijewardhana^a

a) U. of Cincinnati

b) U. of Colorado

c) U. of Illinois

d) Massachusetts Institute of Technology

e) Stanford Linear Accelerator Center

f) Yale University

TABLE OF CONTENTS

I) Overview of Technicolor

- (1) The Motivation for Technicolor.
- (2) The Technicolor Mass Scale.
- (3) Possible Signals in the SLC Energy Regime.
- (4) Production Rates of Technicolor Particles in the SLC Energy Regime.
- (5) Present Status of Technicolor Searches.
- (6) Discovery Potential of Various Accelerators.

II) Study of Technicolor Signals in the SLD Detector

III) Search for Charged Scalar Particles Decaying into τ Leptons

IV) The Effect of Technicolor on Angular and Polarization Asymmetries

v) The Production and Decay of Techni-glueballs

Overview of Technicolor

1.1 THE MOTIVATION FOR TECHNICOLOR

The present standard version of the electroweak theory depends on the existence of the Higgs, a neutral scalar particle. Within our present understanding, such scalar particle theories are beset by a fundamental flaw which up to now has no satisfactory solution. The calculation of the mass of the scalar particle is subject to major divergent corrections due to the vacuum polarization type Feynman diagrams shown in Fig. 1. The diagram 1(b) is only present in the field theory of scalar particles, not in fermion based theories. This diagram gives rise to quadratic divergences which are, apparently, non-renormalizable. The expression for the mass correction is the order of

$$\delta m^2 \sim 8g^2 \int \frac{d^4 k}{(k^2 - m^2)}$$

Arguments concerning the size of this mass correction lead to fundamental issues that are usually discussed under the heading of “The Mass Hierarchy Problem”: namely, the correction is given by $\sim (g\kappa)^2$ where κ could be of the order of the Planck scale ($g\kappa \sim 10^{15}$ to 10^{19} GeV). Since the mass of the Higgs can be at most \sim a TeV, there must be very delicate cancellations between the bare mass and the corrections. This “fine tuning” is difficult to comprehend and is one of the difficulties with scalar theories.^[1]

Solutions to this problem divide into 2 categories:

1) One of these is the Supersymmetry theory which states that for every particle whose existence is known or suspected (like the Higgs) there is a partner. For each fermion there is a scalar partner and vice versa. Under these conditions the mass correction Feynman diagrams are shown in Fig. 2. The mass correction for diagram 2(c) exactly cancels the corrections due to the diagrams in Fig. 1(b) or 2(b) and we are left only with the corrections due to the diagrams of Figs. 1(a) or 2(a) which

are logarithmic in nature. These corrections are very insensitive to the magnitude of the cut-off κ and hence are manageable.

2) The other is the Technicolor theory. It states that there are no fundamental scalars (Higgs) in the electroweak theory. The mass of the gauge bosons are generated by vacuum polarization diagrams of the nature shown in Fig. 3 associated with the existence of a new scale of massive quark anti-quark pairs bound by a new force. It predicts that this new dynamics would produce new massive scalar particles.^[2] The scalar particles that are generated and remain observable are known as technipions. Because the theory must satisfy the known experimental features of the Electroweak theory it is constrained to have the same “group and gauge structure” as the electroweak theory. For example, the mass generated for the W and Z gauge bosons must satisfy the Weinberg angle relation

$$\cos\theta_w = \frac{M_W}{M_Z}$$

The calculation of the mass of the W gauge boson follows from Fig. 3; namely,

$$M_W^2 = M_{W_0}^2 + \frac{g_2^2}{4} F_\pi^2$$

where F_π is the technipion analog of our ordinary pion structure (decay) constant associated with the pion decay as shown in Fig. 4. Because the bare mass of the W is 0, in accordance with the electroweak gauge theory, the full mass is the result of the corrections due to Fig. 3. The coupling constant g_2 must satisfy the electroweak relation

$$g_2 = \frac{8}{\sqrt{2}} M_W^2 G_F = 0.67$$

Using these results one can determine the dynamical scale of the technicolor theory. This is discussed in the next section

One of the faults of the present version of the technicolor theory is that, given the requirements that it generate the gauge boson masses, it can not, at the same

time, generate correctly the masses of the quarks and leptons. The extensions of the theory that attempt to correct these defects run into difficulties in the form of results that contradict experimental observations. This problem is, so far, unsolved and remains a negative cloud on the theory.

1.2 THE TECHNICOLOR MASS SCALE

The value of the ordinary pion decay constant, f_π , as determined from a measurement of the pion lifetime time, is 93 MeV. If we equate F_π to this value and we use the above equations for M_W , we obtain that the mass of the W should be 30 MeV. This is far short of the measured value of 80.4 GeV.^[3] To accomodate this larger value we must require that F_π be considerably higher. This value follows from the relation

$$F_\pi = \frac{80\text{GeV}}{30\text{MeV}} f_\pi = 250 \text{ GeV}$$

Because of this larger value, we expect the technicolor scale to be much higher and the particles produced by this dynamics to be heavier than the regular pion. We need to remark that the results we have obtained apply only to the case where we have one techniquark, anti-techniquark pair. If the number of families of such particles increases then more of these contribute to the mass corrections shown in Fig. 3 and the value of F_π decreases accordingly,

$$F_\pi = \frac{250}{\sqrt{r}} \text{ GeV}$$

where r is the number of such techniquark families.

The gauge fields that produce the technicolor force are called technigluons in analogy to the regular gluons which are the carriers of our regular strong force. In the same way as the low energy theory predicts the existence of glueballs, technicolor predicts the existence of techni-glueballs. These are discussed at the end of this report. The masses of both technipions and techni-glueballs could be in the SLC energy range (10-50 GeV). Hence the Z^0 could decay into them. The decay modes and the possibility of their observation is the main topic of this report.

1.3 POSSIBLE SIGNALS IN THE SLC ENERGY REGIME

In the decay of the Z^0 into technipions, a possible matrix element is given by^[4]

$$M \propto \{I_3 - 2Q\sin^2\theta_w\}$$

This matrix element describes the most likely decay modes into technipions. Various technipion scenarios predict different families of technipions; we describe the two most often discussed cases. In the case that only two neutral singlet technipion exist ($t^o, t^{o'}$), we do not expect that the Z^0 will decay into them because both I_3 and Q are 0 for these and the main matrix element vanishes. In the case that there exists a triplet of technipions ($t_\pi^+, t_\pi^0, t_\pi^-$), we expect that the Z^0 will decay into a pair of these charged technipions. It can not decay into a pair of neutrals because the spin-statistics argument forbids such decays.

The technipions are expected to decay mainly into the heavy members of the lepton and quark families because the coupling is thought to be proportional to the masses of the particles the technipion decays into. This is in analogy with the decay properties of the fundamental scalar of the electroweak theory, the Higgs. If so, the main decay modes would be^[5]

$$\begin{aligned} t_\pi^+ &\rightarrow \tau^+ + \nu_\tau \\ t_\pi^+ &\rightarrow \bar{b} + c \\ t_\pi^+ &\rightarrow \bar{s} + c \end{aligned}$$

In the case of Z^0 decays into techni-globes we expect the main decay to be into the techni-globe and a photon because a decay into a pair of neutral techni-globes is forbidden by the same spin-statistics argument that applies to neutral technipions.

The main ($\sim 100\%$) decay mode of the techni-globe is into a pair of photons, because the decay into a quark-antiquark pair is heavily suppressed by a helicity suppression factor and by the large mass of the extended technicolor scale.^[6] These facts make the signal for techni-globe in the SLD very striking. Nevertheless,

this decay of the Z^0 into techni-globballs is expected to be rare and will be difficult to observe.

Hence, the signals for the technicolor states we have discussed are divided into the following patterns:

$$\begin{aligned} Z^0 &\rightarrow 4 \text{ jets} \\ Z^0 &\rightarrow 2 \text{ jets} + \tau + \text{missing energy} \\ Z^0 &\rightarrow 2 \tau\text{s} + \text{missing energy} \\ Z^0 &\rightarrow 2 \gamma\text{s} + 1 \text{ monoenergetic } \gamma \end{aligned}$$

1.4 PRODUCTION RATES OF TECHNICOLOR PARTICLES IN THE SLC ENERGY REGIME

In Fig. 5 we show the Feynman rules^[4] which can be used to calculate the expected technipion production rates in e^+e^- machines. The differential cross section is given by

$$\frac{d\sigma}{d\Omega}(e^+e^- \rightarrow \gamma \rightarrow t_\pi^+ t_\pi^-) = \frac{\alpha^2}{8s} \sin^2(\theta) \beta^3 \quad (1.4.1)$$

This leads to the integrated rate

$$\frac{\text{Rate}(e^+e^- \rightarrow \gamma \rightarrow t_\pi^+ t_\pi^-)}{\text{Rate}(e^+e^- \rightarrow \gamma \rightarrow \mu^+ \mu^-)} = \frac{1}{4} \beta^3 \quad (1.4.2)$$

and

$$\frac{\text{Rate}(e^+e^- \rightarrow \gamma \rightarrow t_\pi^+ t_\pi^-)}{\text{Rate}(e^+e^- \rightarrow \gamma \rightarrow \text{all})} = 3.6\% \beta^3 \quad (1.4.3)$$

where β is the velocity of the technipion in units of the velocity of light. Similarly, in the Z energy regime

$$\frac{Rate(e^+e^- \rightarrow Z \rightarrow t_\pi^+ t_\pi^-)}{Rate(e^+e^- \rightarrow Z \rightarrow \mu^+ \mu^-)} = \frac{1}{2} \frac{(1 - 2\sin^2\theta_w)^2}{(1 - 4\sin^2\theta_w + 8\sin^2\theta_w)} \beta^3 \quad (1.4.4)$$

$$\frac{Rate(e^+e^- \rightarrow Z \rightarrow t_\pi^+ t_\pi^-)}{Rate(e^+e^- \rightarrow Z \rightarrow all)} \simeq 1\% \beta^3 \quad (1.4.5)$$

Given these results, in general, we can expect the technipion signal to appear at the level of 1 % of Z's produced. In the Table 1 below we present the number of charged technipions produced as a function of the technipion mass for a sample of 10^5 Z's.

TABLE 1

Number of Technipions per 10^5 Z's

M_{t_π} (GeV/c ²)	$\beta=(1-4 M_{t_\pi}^2/M_Z^2)^{1/2}$	β^3	$N_{t_\pi} (\times 10^3)$
10	0.98	0.93	1.9
20	0.90	0.73	1.5
30	0.75	0.42	0.8
40	0.48	0.042	0.08
45	0.15	0.0012	0.002

The estimates for the technipion branching ratios^[5] are quite varied. A reasonable average of these various estimates is about 15% for the τ decay mode, 50% for the decay into $\bar{b}c$ quarks and 35% into $\bar{s}c$ quarks. It is clear from the table and from the expected branching ratios that the upper mass limit that we can reach is about 40 GeV/c².

In the case of the search for techni-glueballs the signal is quite unique and hence we do not expect any background. There could be both scalar and pseudoscalar techni-glueballs. The rate into these is such that it would be difficult to observe them. The calculations of the production process^[6] shows that the branching ratio is expected to be

$$\frac{Rate(Z^0 \rightarrow \phi_s + \gamma)}{Rate(Z^0 \rightarrow all)} \approx 1.0 \times 10^{-5}$$

Even though the rate is small, the signature is so unique that the observation of a few events in a sample of 10^6 Z s may signal their presence.

1.5 PRESENT STATUS OF TECHNICOLOR SEARCHES

All of our present limits on Technipions come from the experimental searches at PEP and PETRA^[7,8]. As shown in Fig. 6 the lower limits on the mass of the technipions is presently about 19 GeV/c². Although no results have been presented by the experiments at Tristan, we can expect that they are sensitive to a technipion signal up to a mass of ≈ 25 GeV/c².

Study of Technicolor Signals in the SLD Detector

A Monte Carlo study was performed in order to determine the sensitivity of the SLD detector to the production of charged technipions, t_π^\pm , in Z^0 decays. In this study, as in the searches described above, some general characteristics of the production and decay of technipions had to be assumed. These characteristics have been presented in the previous chapter. For this work the following assumptions were made:

1. $\sigma(e^+e^- \rightarrow Z^0 \rightarrow t_\pi^+ t_\pi^-) \sim 1\% \beta^3$
2. $\frac{d\sigma}{d\Omega} \sim \sin^2\theta$,
3. the t_π^\pm lifetime is so short that only the decay products can be seen in the detector,

4. the t_π^\pm couples to the mass of fermion decay products.

Because of the coupling to fermion mass, the technipions are assumed to decay into the heaviest available fermion pairs, i.e., $c\bar{b}(\bar{c}b)$, $c\bar{s}(\bar{c}s)$, or $\tau\nu$. The exact branching ratios are highly model dependent. For this study, it was assumed that $\text{BR}[t_\pi^\pm \rightarrow c\bar{b}(\bar{c}b)] = 70\%$, $\text{BR}[t_\pi^\pm \rightarrow c\bar{s}(\bar{c}s)] = 15\%$, and $\text{BR}[t_\pi^\pm \rightarrow \tau^+\nu_\tau(\tau^-\bar{\nu}_\tau)] = 15\%$.

It should be noted that these general assumptions are identical to those that could be made in a study of charged Higgs pair production at the Z^0 . The conclusions derived from this work are applicable to charged Higgses as well as charged technipions.

For the purely hadronic modes of decay, the signature for charged technipion production is quite striking. The technipions are produced back-to-back since the Z^0 is at rest. They each decay into a quark and a different flavor antiquark. The fragmentation of these quarks produces 4 jets in the detector. The main background to this process comes from the standard Z^0 decay into two quarks with gluon bremsstrahlung. The general method for an experimental search that maximizes the signal above background follows:

1. Find 4 jet events.
2. Pair the jets and plot the jet-jet invariant mass for the separate combinations.
A peak should appear at the mass of the technipion.
3. Reduce the background by angular cuts and heavy quark tagging.

For this study, ~ 300 Z^0 decays into technipion pairs were generated at each of six masses, ranging from 15 to 40 GeV/c^2 . The technipions were generated with a $\sin^2\theta$ dependence. They were allowed to decay into $c\bar{b}(\bar{c}b)$, $c\bar{s}(\bar{c}s)$, or $\tau\nu$ with the branching ratios given above. The decays into fermions were isotropic in the center-of-mass frame of the technipion. The quarks were fragmented by the LUND Monte Carlo package which uses string fragmentation^[9]. Finally, the detector simulation was accomplished by the SLD Parameterized (or Fast) Monte Carlo^[10].

The background sample of 35,000 Z^0 decays into $q\bar{q}$ pairs was also generated by LUND. The detector was simulated by the SLD Parameterized Monte Carlo for this sample as well.

Having generated the necessary samples, only those events with 4 jets were chosen. The techniques that were used for finding jets and reconstructing the jet-jet invariant mass are described in the work of Baltay et al.^[11] Prior to the 4 jet event selection, the expected number of signal events at the Z^0 for different technipion masses (normalized to 35,000 Z^0 's) is shown in Table 2 below.

TABLE 2

Number of Technipions for 35 K Zs

$M_{t_\pi}(\text{GeV}/c^2)$	N_{t_π}
15	296
20	256
25	207
30	152
35	96
40	42

The signal to background for 30 GeV/c^2 technipions is 0.004. Fig. 7 shows the reconstructed jet-jet invariant mass spectrum for the 30 GeV/c^2 technipion sample after the 4 jet event selection. For this case, 4 jet events were chosen with the "ycut"^[11] parameter set to 0.03. The combinatoric background from the jet-jet invariant mass reconstruction was removed by requiring the 4-momenta of the reconstructed technipions to lie along (or close to) the thrust axis for the event. This method works well for technipion masses below $\sim 35 \text{ GeV}/c^2$, since for low masses the 2 jets associated with a given technipion are thrust forward in the

direction of motion of the technipion. For larger masses, it often picks the wrong combination of tracks because the thrust axis is no longer well defined. Information from both tracking and calorimetry was used. The 4-momentum of each of the 4 jets was rescaled individually so that energy and momentum were conserved. The signal is normalized to 35,000 Z^0 decays. Fig.8 shows the corresponding plot for the background sample normalized to the same number of Z^0 decays. At this stage, the signal to background ratio for the 30 GeV/c² mass data sample is 0.12. There were several other cuts that were useful to improve the signal to background in this search. The first took advantage of the fact that charged technipions produced by the Z^0 have the same mass. Requiring the reconstructed jet-jet invariant mass of one pair of jets to be within 2.0 GeV/c² of the other pair's mass in a given event increased the signal to background ratio to 0.23. Another useful cut made use of the fact that the technipions are spin-0 particles with an angular dependence that goes as $\sin^2\theta$ while the background comes from the production of spin-1/2 particles with a $1 + \cos^2\theta$ dependence. An angular cut of $60^\circ < \theta < 120^\circ$ increased the signal to background to 0.39. Finally, one can take advantage of the fact that the technipions decay into heavy quarks. Requiring the presence of at least one charged kaon with a momentum greater than 3.5 GeV/c in the event increased the signal to background for the 30 GeV/c² sample to 0.64 while 27 events of the original 300 remained in the signal peak. Additional cuts making use of vertex detector information might be useful as well, although no use of that information was made here. Figs. 9 and 10 show the 30 GeV/c² signal and the background, respectively, after the three cuts described above. The technipion detection efficiency after all these cuts was $\sim 9\%$. In Figs. 11, 12, 13, and 14 the normalized signal added to the background for 35,000 Z^0 decays is given for 4 different technipion masses. The events in these plots met the following requirements:

1. there are 4 jets ($y_{\text{cut}}=0.03$),
2. the jet-jet association is chosen to be that where the 4-momenta for the two combinations lie closest to the thrust axis,

3. the thrust axis for the event satisfies $60^\circ < \theta < 120^\circ$,
4. the difference between the reconstructed invariant masses on the two sides is less than $2 \text{ GeV}/c^2$,
5. there is at least one charged kaon with $P_K > 3.5 \text{ GeV}/c$.

The search for charged technipions becomes more difficult as the mass of the technipion approaches the kinematic limit. There are two reasons for this. First, there is a β^3 factor in the production cross section; as one approaches the kinematic limit there are fewer and fewer Z^0 decays into technipions. Second, it becomes harder to associate the correct jets with the correct technipion that produced them, forcing one to keep the combinatoric background. This occurs because the technipions from the Z^0 decay have a smaller boost in the lab. In addition, the quark jets have a larger boost in the center-of-mass of the decaying technipion. This means that the quark jets come out at a larger angle than in the case where the technipion has a smaller mass. As the technipion mass increases, the two jet pairs tend to merge into one another, making it hard to choose the correct jet pairing. Therefore, one is forced to accept the jet-jet combinatoric background. On the other hand, the increased distance between the jets allows the “ycut” parameter in the jet finding^[11] to be increased with no loss of signal. This decreases the background from standard 4 jet $q\bar{q}$ events. Figs. 15, 16, 17 show the normalized signal on background for technipion masses of 30, 35, and 40 GeV/c^2 , respectively. The events in these plots satisfy the following cuts:

1. There are 4 jets (ycut=0.08),
2. the difference between the reconstructed invariant masses on the two sides is less than $2 \text{ GeV}/c^2$,
3. there is at least one charged kaon with $P_K > 3.5 \text{ GeV}/c$.

Recapitulating, we can safely say that we can detect the presence of the Z^0 decay into charged technipions in the SLD detector. This is an easier task the lower the mass of the technipion.

Search for Charged Scalar Particles Decaying into τ Leptons

The existence of charged scalar particles, S^\pm , is predicted in a number of models, e.g. supersymmetry, technicolor, or electroweak models with a non-minimal Higgs sector. Charged Higgs particles or technipions are assumed to decay predominantly into heavy particles,^[5] i. e. decay into τ leptons are favored among leptonic decays, ($S^\pm \rightarrow \tau^\pm \nu_\tau(\bar{\nu}_\tau)$). In this section, we present the prospects for searching for charged scalar particles with the SLD detector. The analysis is restricted to the case where both scalar particles decay into τ 's: $e^+e^- \rightarrow S^+S^- \rightarrow (\tau^+\nu_\tau)(\tau^-\bar{\nu}_\tau)$. It is assumed that the scalar particle has a short lifetime, and in the case of a supersymmetric model, where S is replaced by a stau ($\tilde{\tau}$), that the photino ($\tilde{\tau} \rightarrow \tau\tilde{\gamma}$) or the goldstino ($\tilde{\tau} \rightarrow \tau\tilde{G}$) mass is zero and the particle is stable.

S^+S^- events can be searched for by applying cuts similar to the selection of τ pair events. The following selection criteria were applied to a data sample of τ pair and S pair Monte Carlo events:

- 1) The number of charged tracks was required to be at least 2 and less than 10.
- 2) The tracks were combined into 2 'jets' (at least one track in each jet), and all tracks were required to lie within a cone of 40° opening angle with respect to the jet-axes.
- 3) The total visible energy, including charged tracks and all calorimeter clusters, had to be greater than 0.2 of the center of mass energy.
- 4) The energy measured in the electromagnetic part of the calorimeter was required to be less than 0.8 of the beam energy (E_b), and the energy of the highest electromagnetic shower less than $0.9 E_b$.
- 5) The invariant mass of all tracks and clusters in each hemisphere (jet) had to be smaller than $3 \text{ GeV}/c^2$.
- 6) For 2 prong events, the acoplanarity angle was demanded to be greater than 10 mrad .

74% of all τ Monte Carlo events passed these selection criteria. The background of $q\bar{q}$ and two-photon events was estimated to be of the order of 1%. The detection efficiency for scalar particles of 40 GeV/c² with subsequent τ decay was 67% as determined by the Monte Carlo simulation. After these cuts, the only significant background to S pair production is expected to be τ pair production. Experimental variables that can be used to distinguish between both processes are $\cos\theta$ (θ is the angle between the jet thrust axis and the beam direction) and the acoplanarity angle. A cut on $\cos\theta$ is, however, only effective for small m_S . The $\sin^2\theta$ distribution is smeared out for large S masses, since the neutrinos are not observed. The acoplanarity distribution of τ pair and S pair Monte Carlo events with a mass of 40 GeV/c² is shown in Fig. 18 and Fig. 19, respectively. An acoplanarity cut of 30° removes all τ pair events, while keeping a considerable fraction of S pair events; notice the overflow at acoplanarities greater than 100° in Fig. 19. The efficiency after all cuts was calculated for S masses from 25 to 45 GeV/c² in 5 GeV/c² steps and for 43 GeV/c². It varied from 38% at low to 57% at high masses. The statistical error was typically 5%.

If no event is observed after applying all cuts, a limit on the branching ratio of the scalar particle decaying into τ , $BR(S^\pm \rightarrow \tau^\pm \nu_\tau(\bar{\nu}_\tau))$, can be calculated. Assuming the ratio of the cross sections to be:

$$\frac{\sigma(e^+e^- \rightarrow Z^0 \rightarrow S^+S^-)}{\sigma(e^+e^- \rightarrow Z^0 \rightarrow \mu^+\mu^-)} \simeq \frac{1}{4}\beta^3,$$

a region in the $BR(S^\pm \rightarrow \tau^\pm \nu_\tau(\bar{\nu}_\tau))$ m_{S^\pm} plane can be excluded. The result for 1,000 produced τ pair events, corresponding to 30,000 produced Z^0 events ($\sqrt{s} = m_{Z^0} = 91$ GeV/c²), is shown in Fig. 20. One can conclude that scalar particles with masses up to 43 GeV/c² can be excluded at 95% CL, if the branching ratio is equal to one, e.g. a stau. Table 3 shows the 95% CL mass limit that can be obtained as a function of the number of produced Z^0 events.

TABLE 3

Number of Zs Needed to Obtain the Given Mass Limit at 95% CL

$$\text{for } \text{BR}(S \rightarrow \tau \nu_\tau) = 1$$

$$M_Z = 91 \text{ GeV}/c^2$$

$m_S \text{ (GeV}/c^2\text{)}$	$N_{Z^0} (\times 10^3)$
25	1.8
30	2.7
35	3.1
40	8.0
43	20.0
44	44.0
45	233.0

The Effect of Technicolor on Angular and Polarization Asymmetries

The basic idea of Technicolor^[1] is to replace the Higgs sector with a dynamical mechanism to generate the masses of the gauge bosons. However, that leaves the fermions massless and flavour changing neutral currents [FCNC] are almost unavoidable in these simple models. Generally fermions are given mass by inventing a new gauge interaction linking the technifermions to the ordinary fermions [Extended Technicolor Models].^[17] In ETMs the FCNCs still cause problems, but with STI [Standard Theoretician's Ingenuity] they can be overcome. There are a variety of approaches to create "realistic" technicolor models. One, about which a number of publications have come out, is the composite technicolor standard model [CTSM].^[12] All these "realistic" models have a tendency to be rather complicated. In CTSM, for instance, quarks, leptons and technifermions are composite and the basic gauge group^[15] is $(SU(3)_C \times SU(2)_W \times U(1)_Y \times SU(n)_{TC}) \times (SU(3) \times U(1))$.

Actually, it is possible, that the preons involved respect a symmetry as large as $SU((45) + 4n)$.

All these models are, at present, in the “experimental” stage. As there is no hint as to which of these models is correct, it is difficult to decide which direction to pursue experimentally. Statements like “Compositeness is not an essential ingredient of composite technicolor standard models”^[12] seem to indicate a degree of confusion in this field.

Very understandably, it is rather hard to find firm predictions, but generally all the technicolor models predict a variety of new particles in the 10 GeV to 10 TeV range. Light particles accessible to SLC/SLD are not a necessity at all for technicolor models. Even in the simplest technicolor model with 2 techniquarks the technipions are eaten by the gauge bosons and the lightest particle is the technirho around 2 TeV. As technicolor was invented to replace the Higgs sector, it has to recreate all the benefits of the Higgs. In doing that, it might mimic a Higgs. Many models contain a 0^{++} state, that might look exactly like the standard $H^{0[1]}$.

Given that the predictions of these models do not make it certain that we may observe the expected particles, it behooves us to look for other effects of technicolor, such as in polarization and angular asymmetries.

Two asymmetries that can be measured on the Z^0 peak are the forward backward asymmetry A_{FB} and the left right asymmetry A_{LR} . As LEP will most likely not have longitudinally polarized beams for the next couple of years, A_{LR} is something that can exclusively be done at SLC.

The standard model has firm predictions for the asymmetries in lowest order and the radiative corrections are well understood.^[13,14] However, as discussed elsewhere in these proceedings, the radiative corrections are dependent on a number of input parameters $[m_T, M_H, m_Z, \sin^2\theta_W]$, some of which are not known at this point in time. Therefore there is a range of predictions for the standard model.

Let us define δA_{LR} :

$$\delta A_{LR} = A_{LR} - A_{LR}|_0$$

where $A_{LR}|_0$ is the leading order calculation in perturbation theory.

There are two types of contributions to δA_{LR} : so called oblique and direct corrections. Oblique corrections are all those corrections that do not involve any external particles. Direct corrections involve external particles. In all theories (including the standard model) δA_{LR} is calculated separately for the two classes of corrections. Generally it is easier to calculate the oblique corrections. For technicolor models with no light extra particles, there are only oblique corrections.

With the above mentioned uncertainties in the input parameters for the standard model the uncertainties in the standard model predictions are a couple of percent. However, the contributions from new physics could very well be large. Whatever phenomenon might show up in the asymmetries, it will show up much clearer in A_{LR} than in A_{FB} . As recent measurements tell us that m_Z is around 91 GeV, for one loop corrections, δA_{FB} is only about 15 % of δA_{LR} . That makes SLC/SLD comparable with LEP even with substantially lower luminosity.

In technicolor models^[13,15] the symmetry-breaking produces a model dependent number of pseudo Goldstone bosons. These influence the vacuum polarization amplitudes and thus cause radiative corrections different from those predicted by the standard model. The pseudo Goldstone bosons are described by effective Lagrangians which are only valid well below the relevant cutoff Λ_{TC} of the model considered. All calculations done are cutoff dependent. The effective theory of technicolor bosons is actually not renormalizable from the point of view of $SU(2) \times U(1)$ which leads to large radiative corrections of the order of $\ln(\Lambda_{TC}^2/m_Z^2)$. In addition the mass matrix of the usually rather large variety of pseudo Goldstone bosons should break global $SU(2)$ rather badly, as some particles have to be very heavy while the others are restricted to be the longitudinal components of the W^\pm and Z^0 . The resulting values for δA_{LR} can be as high as 10% .

In CTSM another effect^[12] could indirectly influence δA_{LR} . CTSM could in-

produce a correction to G_F of the order of a few percent. Then G_F would not accurately describe the scale of electro-weak symmetry breaking. This also would lead to large deviations in δA_{LR} from the predictions of the standard model. However, this effect is only a possibility in CTSM and not a prediction.

Other new physics like SUSY or SUGRA or extra generations potentially also have large effects on δA_{LR} .^[13,16] In case there is a deviation from the standard model prediction it will not at all be easy to determine what causes it. However, the left right asymmetry is definitely the place to look for the effects of new physics that is not directly accessible because the masses may be so large that they can not be produced at present accelerators. That may be the case with technicolor.

The Production and Decay of Techni-glueballs

The standard model of electro-weak and strong interactions has proven to be a remarkable phenomenological success. The only aspect of the theory that has not been verified experimentally is the mechanism of electro-weak symmetry breaking and fermion mass generation. The standard Higgs model, which relies on the existence of elementary scalar fields to break the symmetry and to generate fermion masses, is known to suffer from serious theoretical problems. Elementary scalar theories require unnatural fine tunings of parameters to maintain hierarchies.^[1] This has motivated investigations of alternatives to the Higgs method of symmetry breaking. Technicolor theories are among the most promising of such alternatives.^[1]

In these theories, symmetry breaking is assumed to come from a new non-abelian gauge interaction, technicolor, acting among a new set of fermions, techni-quarks. The techni-gauge force is exactly like QCD, but it becomes strong at a scale much higher than 200 MeV. The chiral flavor symmetry breaking in technicolor theories leads to Goldstone bosons which are techni-quark/anti-techni-quark bound states.

In a generic technicolor theory with r $SU_L(2)$ doublets of techni-quarks, the techni-Goldstone boson decay constant F_π must be $250/\sqrt{r}$ GeV to give the W^\pm

and Z^0 their measured masses (see the discussion in sections 1.1 and 1.2). In QCD, the non-abelian gauge theory we know best, the pion decay constant f_π , and the confinement scale are roughly the same. If the same holds true for technicolor, then the techni-confinement scale must be hundreds of GeV. Therefore, such technicolor theories are indistinguishable from the standard Higgs theories of symmetry breaking at energy scales within the reach of existing particle accelerators.

In the standard model the only observable excitation coming from the symmetry breaking sector is the Higgs scalar. In technicolor theories we can excite techni-mesons, baryons, and also glueballs once we pass the confinement scale. Therefore, once we have particle accelerators with sufficient energy to probe the technicolor confinement scale, we can definitely test the validity of the technicolor hypotheses.

To generate masses for quarks and leptons within the framework of technicolor one must assume the existence of an extra set of interactions, Extended Technicolor (ETC),^[17] at a scale of order 1000 TeV. Below this scale the effect of the ETC interactions can be summarized by a set of effective 4-fermion interactions among techni-ordinary, techni-techni, and ordinary-ordinary quarks. These interactions generate flavor changing neutral currents among ordinary quarks. To be consistent with the experimental limits on such processes, the ETC scale must be above approximately 1000 TeV. In earlier discussions, technicolor was deemed phenomenologically deficient because $M_{ETC} = 1000$ TeV generated ordinary quark masses much smaller than observed. More recently, technicolor theories with walking coupling strengths have been proposed^[18] which resolve this problem. It has also been noted that when the 4-fermion coupling among techni-quarks is sufficiently strong to directly affect the chiral symmetry breaking of techni-quarks, the ordinary fermion masses are automatically enhanced.^[19] Either of these two possibilities can be utilized in building viable technicolor models.

Physics will be more interesting if it is possible to build such models with confinement scales much smaller than 250 GeV. Several approaches leading to this

conclusion have been discussed recently. Eichten and Lane^[20] have entertained the possibility of putting some techni-fermions in representations higher than the fundamental representation (N) of $SU(N)$, where $SU(N)$ is the techni-gauge group. As pointed out by Marciano,^[21] such an assumption leads to the generation of a hierarchy between the confinement scale Λ_c and the Goldstone boson decay constant F_π , with $F_\pi/\Lambda_c > 1$. Therefore, in such technicolor models it is possible to have Λ_c in the 10's of GeV with $F_\pi = 250$ GeV, provided that the quadratic Casimir $C_2(R)$ of the fermion representation R is large enough. Another possibility, pointed out by Appelquist, Einhorn, Takeuchi, and Wijewardhana,^[19] is that the 4-fermion couplings among the techni-quarks generated at the ETC scale can dominate the technicolor chiral symmetry breaking when the couplings exceed some critical value. This tends to push F_π towards M_{ETC} , allowing the possibility that $F_\pi/\Lambda_c \approx 10$ with $F_\pi/M_{ETC} \ll 1$ and $F_\pi = 250$ GeV.

If we have a theory with small Λ_c , then we have the possibility of light techni-glueballs. Here we assume that some technicolor theory predicts techni-glueballs lighter than the Z^0 . Without considering the specific details of that theory we can calculate the production of these techni-glueballs at the Z^0 resonance and their subsequent decays. In this discussion we also assume that techni-quarks do not carry ordinary color.

First we calculate the decay rate $Z^0 \rightarrow \phi\gamma$ for a techni-glueball ϕ at the one techni-quark loop level. This decay proceeds via a virtual techni-quark loop. We make the approximation that the effective coupling g' of the techni-glueball to the techni-quark is point-like and of strength $g'^2/4\pi = 0.1$. For the purpose of this calculation we also assume that the techni-quark mass is a hard mass (*ie.*, we neglect the dynamical variation of the mass with momentum). Then the calculation is straight-forward and the Z^0 radiative decay widths into scalar and pseudo-scalar techni-glueballs (ϕ_s and ϕ_{ps}) are:

$$\Gamma(Z^0 \rightarrow \phi_s \gamma) = \frac{\alpha G_F}{12\sqrt{2}\pi^3} \left(\frac{g'^2}{4\pi} \right) \left[\frac{4}{81} N_{TC}^2 N_F^2 \right] M_Z^3 \times \left\{ \frac{\gamma(\beta - \gamma)}{\beta} \left[-1 + \left(1 + \frac{\beta\gamma}{\beta - \gamma} \right) (\omega^2 - z^2) + \frac{2\beta}{\beta - \gamma} \left(\frac{\omega}{c} - \frac{z}{a} \right) \right]^2 \right\} \quad (5.1)$$

and

$$\Gamma(Z^0 \rightarrow \phi_p \gamma) = \frac{\alpha G_F}{12\sqrt{2}\pi^3} \left(\frac{g'^2}{4\pi} \right) \left[\frac{4}{81} N_{TC}^2 N_F^2 \right] M_Z^3 \left\{ \frac{\gamma(\beta - \gamma)}{\beta} (\omega^2 - z^2) \right\} \quad (5.2)$$

where

$$\begin{aligned} \beta &= \frac{4M_T^2}{M_\phi^2} & a &= \frac{1}{\sqrt{\beta - 1}} & z &= \tan^{-1} a \\ \gamma &= \frac{4M_T^2}{M_Z^2} & c &= \frac{1}{\sqrt{\gamma - 1}} & \omega &= \tan^{-1} c \end{aligned} \quad (5.3)$$

Here we have used N_{TC} to denote the dimension of the techni-quark representation and N_F to denote number of techni-quark families. M_T is the techni-quark mass, which we have assume to be independent of techni-quark flavor.

Once it is produced, the techni-glueball must decay predominantly to two photons via a techni-quark loop. As the techni-glueball carries no ordinary color, it couples predominantly to techni-quarks. We assume that techni-quarks and techni-pions (pseudo-Goldstone bosons) are sufficiently massive that they will not appear as techni-glueball decay products. The decay of techni-glueballs to ordinary quark/anti-quark pairs (of opposite helicity) proceeds via the effective 4-fermion interaction with coupling strength $\approx 1/M_{ETC}^2$. Because of the magnitude of M_{ETC} the resulting decay width is highly suppressed, and is small compared to $\phi \rightarrow \gamma\gamma$.

The decay width for $\phi \rightarrow \gamma\gamma$ can be estimated by calculating a triangle diagram. For the pseudoscalar case the calculation is similar to that of $\pi^0 \rightarrow \gamma\gamma$ and is straightforward. For the scalar case the calculation is similar to that of $H \rightarrow \gamma\gamma$.^[22] After summing over all the techni-quarks and including the appropriate

techni-color factors, the techni-glueball decay widths are:

$$\Gamma(\phi_s \rightarrow \gamma\gamma) = \frac{\alpha^2}{4\pi^2} \left(\frac{g'^2}{4\pi} \right) \left[\frac{25}{81} N_{TC}^2 N_F^2 \right] \frac{M_\phi^3}{M_T^2} \left\{ \frac{\beta}{2} [(1-\beta)z^2 + 1] \right\}^2 \quad (5.4)$$

and

$$\Gamma(\phi_p \rightarrow \gamma\gamma) = \frac{\alpha^2}{25\pi^2} \left(\frac{g'^2}{4\pi} \right) \left[\frac{4}{81} N_{TC}^2 N_F^2 \right] \frac{M_\phi^3}{M_T^2} \left\{ \frac{\beta}{2} z^2 \right\}^2 \quad (5.5)$$

The $Z^0 \rightarrow \phi\gamma$ decay rate calculated from equations 5.1 and 5.2 are plotted as functions of M_ϕ for various values of M_T in Figure 21 (for scalar techni-glueballs) and Figure 22 (for pseudoscalar techni-glueballs). We have assume $N_{TC} = 8$, $N_F = 3$, and $g'^2/4\pi = 0.1$. The decay rates are shown as Z^0 branching ratios times 10^5 for $M_Z = 91.1$ GeV and $\Gamma_{Z^0} = 2.4$ GeV. This is the number of $Z^0 \rightarrow \phi\gamma$ events we might hope SLC would produce in a year's run. The decay widths for $\phi \rightarrow \gamma\gamma$ are 10's of keV or less. These widths are very narrow given detector resolutions, so constrained fitting of exclusive three photon events (to conserve beam energy and momentum) would provide the best sensitivity. The techni-glueball production rates calculated for the parameters given are too low to produce a large number of events, but the signal is so striking that it might be possible to detect these events in a sample of 10^6 Zs. In all cases, larger values of the model dependent parameters N_{TC} and N_F will lead to larger Z^0 decay rates and, hence, detectable signals.

REFERENCES

1. L. Susskind, Phys. Rev. D 20, 2619 (1979)
S. Weinberg, Phys. Rev. D 19, 1277 (1979)
R. D. Peccei, Proceedings of the Second Lake Louise Winter Institute, 564 (1987)
2. E. Farhi, L. Susskind, Phys. Reports 74, No. 3, 277 (1981)
3. The CDF Collaboration. Results presented at the XIV International Symposium on Lepton and Photon Interactions at High Energies, Stanford, CA. 1989
4. S. Chadha, M. Peskin, Nuclear Phys. B185, 61 (1981)
5. E. Eichten, I. Hinchliffe, K.D. Lane, C. Quigg, Phys. Rev. D34, 1547 (1986)
6. See the chapter on the production of Techni-glueballs. This work is the contribution of M. Sokoloff, R. Weber, and L. C. R. Wijerwardhana
7. C. A. Blocker et. al. Phys. Rev. Letters 49, 517 (1982)
W. Bartel et. al. Phys. Letters 114B, 211 (1982)
B. Adeva et. al. Phys. Letters 115B, 345 (1982)
M. Althoff et. al. Phys. Letters 122B, 95 (1983)
8. H. J. Behrend et. al. Phys. Lett. B193, 376 (1987)
9. T. Sjöstrand, Comp. Phys. Comm. 27, 243 (1982), and 28 (1983). Jetset 6.3 was used for this work.
10. The SLD Monte Carlo was developed by the SLD Software Group
11. C. Baltay, S. Manly, and J. D. Turk, "The Jet-Jet Invariant Mass Reconstruction", contribution to these proceedings
12. R. S. Chivkila and H. Georgi, Phys. Rev.D 36, 2102 (1987)
13. B. W. Lynn, M. E. Peskin, and R. G. Stuart, Physics at LEP, [CERN report 86-02], 90 (1985)

14. B. W. Lynn and R. G. Stuart, Nucl. Phys. B253, 216 (1985)
15. B. W. Lynn and M. E. Peskin, SLAC-PUB 3724 (1985)
16. B. W. Lynn, SLAC-PUB 3358 (1984)
17. E. Eichten and K. Lane , Phys. Lett. 190B, 125 (1980)
18. T. Appelquist, D. Karabali, and L. C. R. Wijewardhana, Phys. Rev. Lett. 57, 957 (1986)
T. Appelquist and L. C. R. Wijewardhana, Phys. Rev. D 36, 568 (1987)
19. T. Appelquist, M. Einhorn, T. Takeuchi, and L. C. R. Wijewardhana, Phys. Lett. 220B, 223 (1989)
20. E. Eichten and K. Lane, Phys. Lett. 222B, 274 (1989)
21. W. Marciano, Phys. Rev. D 21, 245 (1980)
22. L. Resnick, M. K. Sundaresan, and P. J. S. Watson, Phys. Rev. D 8, 172 (1973)
T. G. Rizzo, Phys. Rev. D 22, 178 (1980)
L. B. Okun, *Leptons and Quarks*, North Holland, (1982)

FIGURE CAPTIONS

- 1) Feynman Diagrams for Mass Corrections in Scalar Theories
- 2) Feynman Diagrams that lead to the Scalar Mass Corrections in the Supersymmetric Theory
- 3) The W Mass Diagrams in the Technicolor Theory
- 4) The π Decay Feynman Diagram
- 5) The Feynman Rules that Apply to the Production of Technipions in the Z^0 Energy Regime
- 6) Present Experimental Limits of the Technipion Mass
- 7) Reconstructed Invariant Mass Spectrum for $M_{t_\pi} = 30 \text{ GeV}/c^2$. Combinatoric background has been removed
- 8) Reconstructed Invariant Mass Spectrum for the Background Normalized to the Same Number of Z^0 Decays. Only the two jet combination that gives the lowest mass is kept
- 9) Reconstructed Invariant Mass Spectrum for $M_{t_\pi} = 30 \text{ GeV}/c^2$ after the cuts described on page 12 have been applied
- 10) Reconstructed Invariant Mass Spectrum for the Background after the cuts described on page 12 have been applied
- 11) Signal and Background Mass Spectrum After Cuts for $M_{t_\pi} = 20 \text{ GeV}/c^2$
- 12) Signal and Background Mass Spectrum After Cuts for $M_{t_\pi} = 25 \text{ GeV}/c^2$
- 13) Signal and Background Mass Spectrum After Cuts for $M_{t_\pi} = 30 \text{ GeV}/c^2$
- 14) Signal and Background Mass Spectrum After Cuts for $M_{t_\pi} = 35 \text{ GeV}/c^2$
- 15) Signal and Background Mass Spectrum After Cuts for $M_{t_\pi} = 30 \text{ GeV}/c^2$
- 16) Signal and Background Mass Spectrum After Cuts for $M_{t_\pi} = 35 \text{ GeV}/c^2$
- 17) Signal and Background Mass Spectrum After Cuts for $M_{t_\pi} = 40 \text{ GeV}/c^2$

- 18) Acoplanarity Distribution of τ pair Monte Carlo Events
- 19) Acoplanarity Distribution of S pair Monte Carlo Events for $m_S = 40 \text{ GeV}/c^2$
- 20) Limit on the Branching Ratio ($S \rightarrow \tau \nu_\tau$) at 95% CL as a Function of the Scalar Particle Mass ($\sqrt{s} = M_Z = 91 \text{ GeV}/c^2$)
- 21) Z^0 Decay Rates into Scalar Techni-glueballs for Various Techni-quark masses
- 22) Z^0 Decay Rates into Pseudo-scalar Techni-glueballs for Various Techni-quark masses

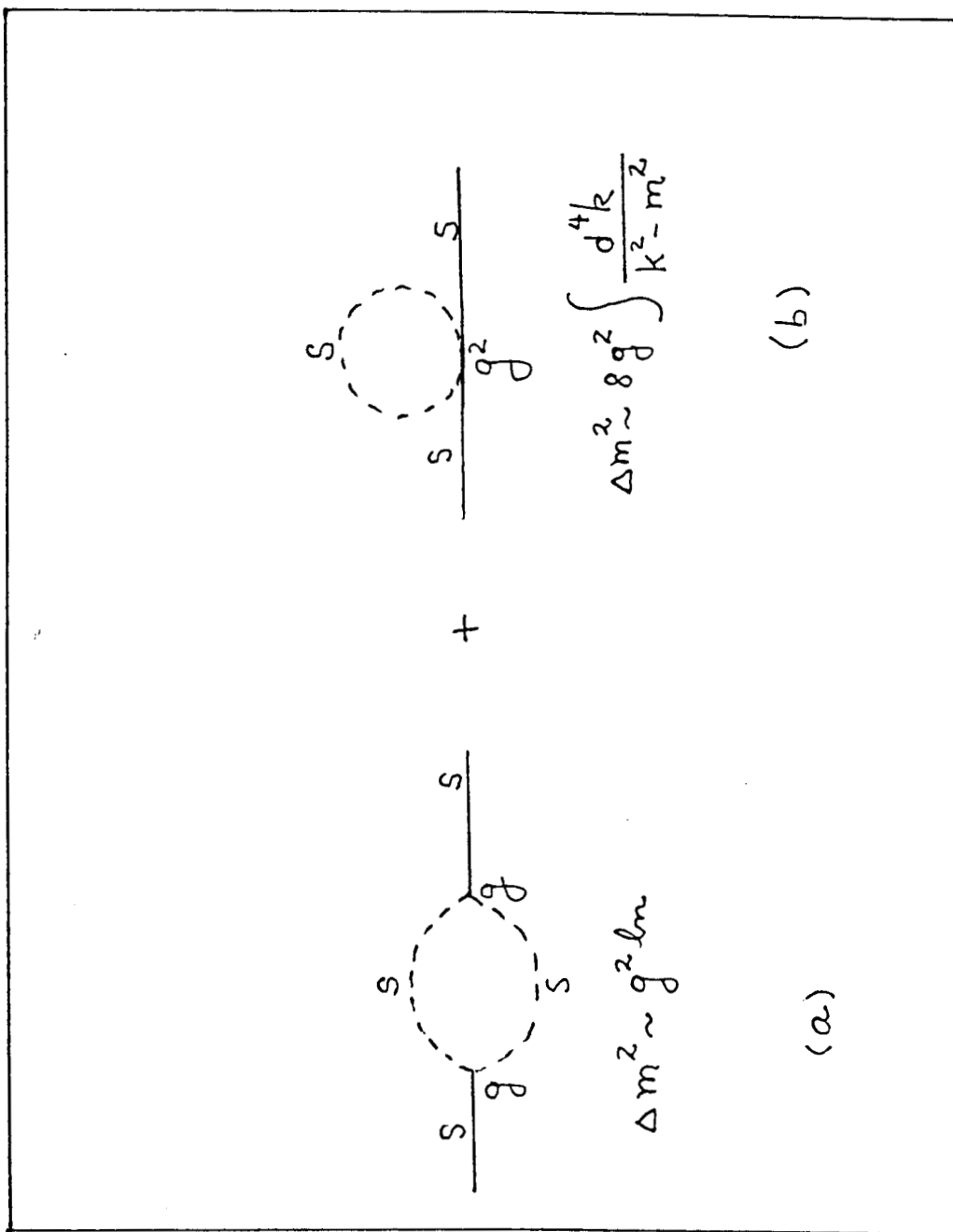


Fig. 1

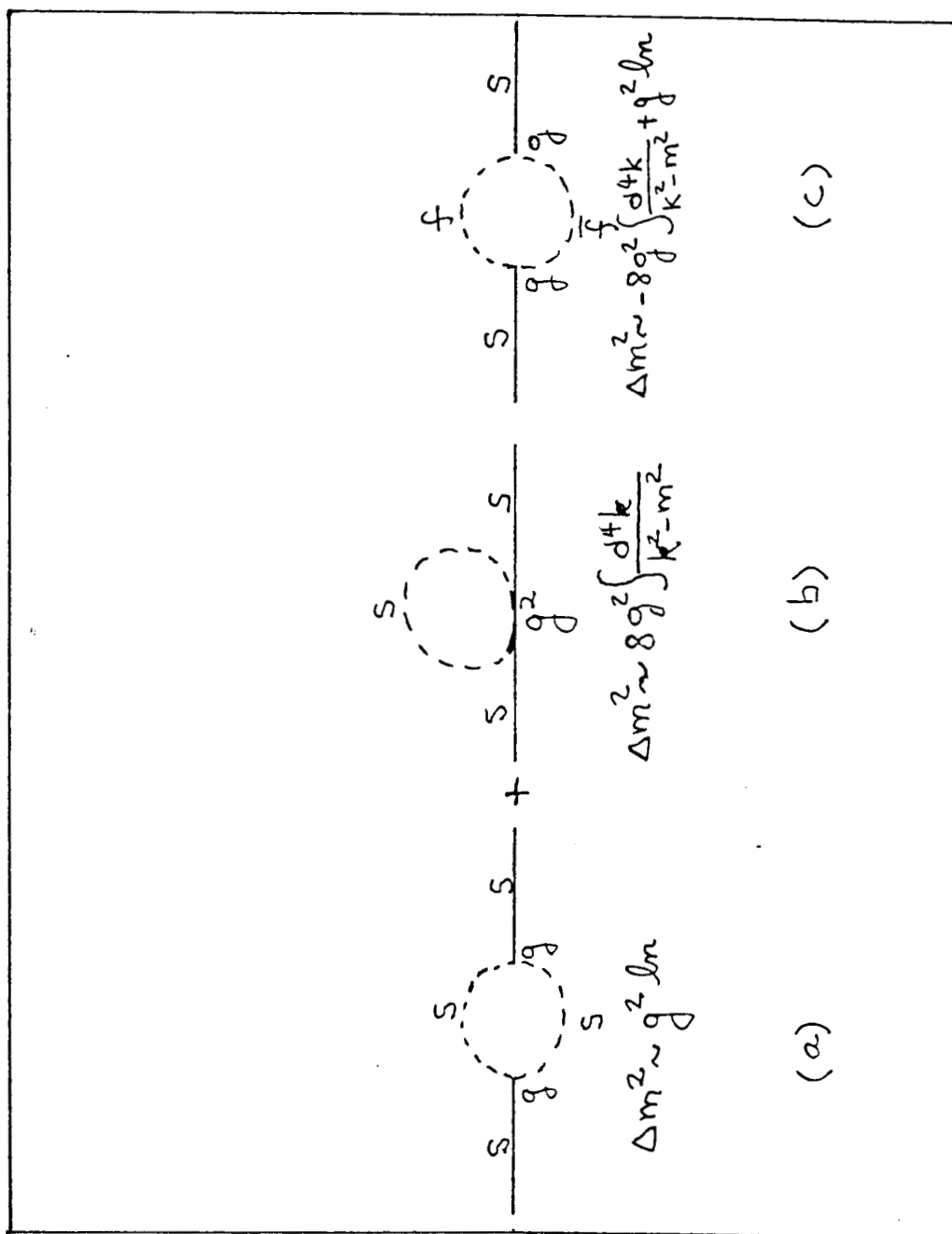


Fig. 2

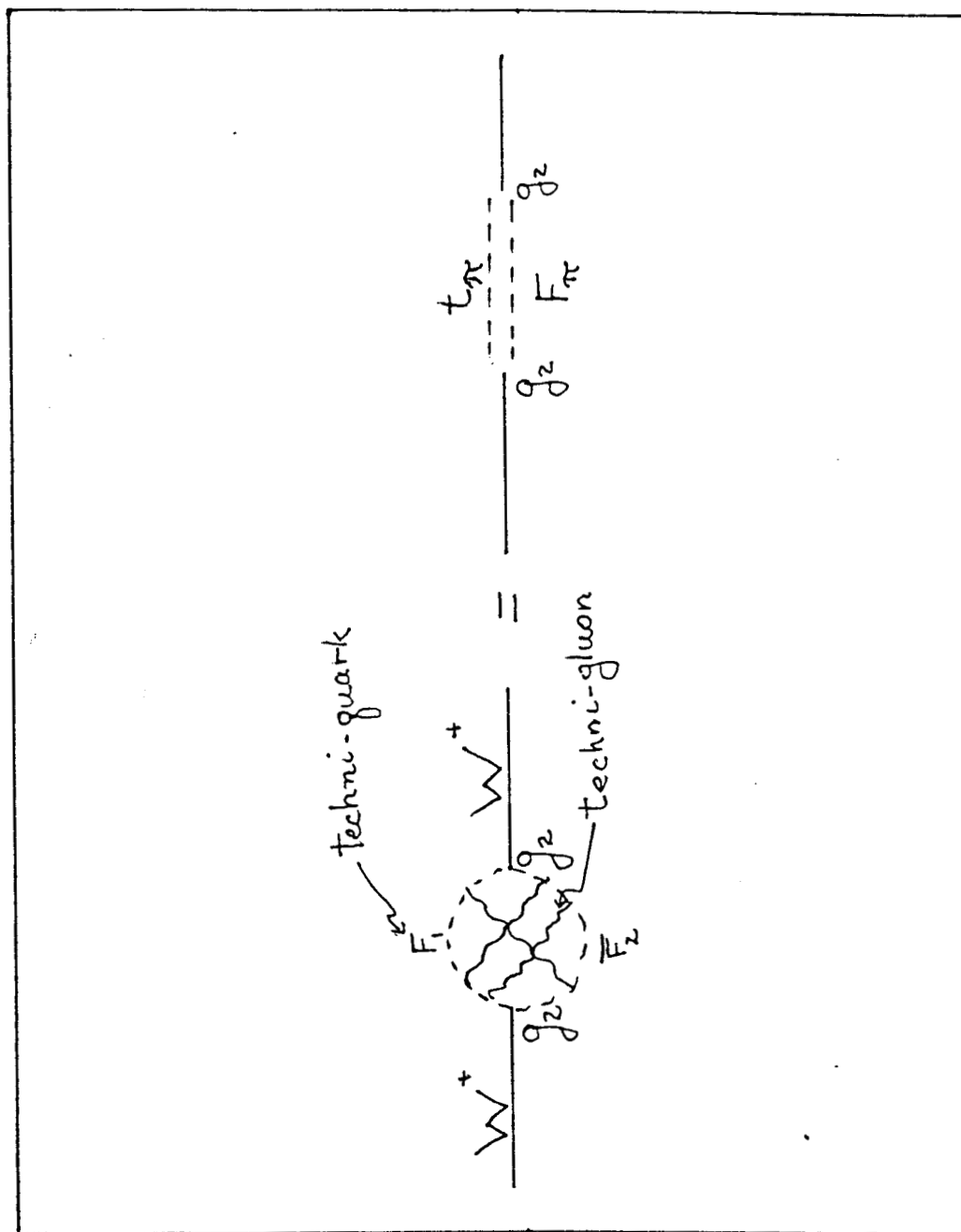


Fig. 3

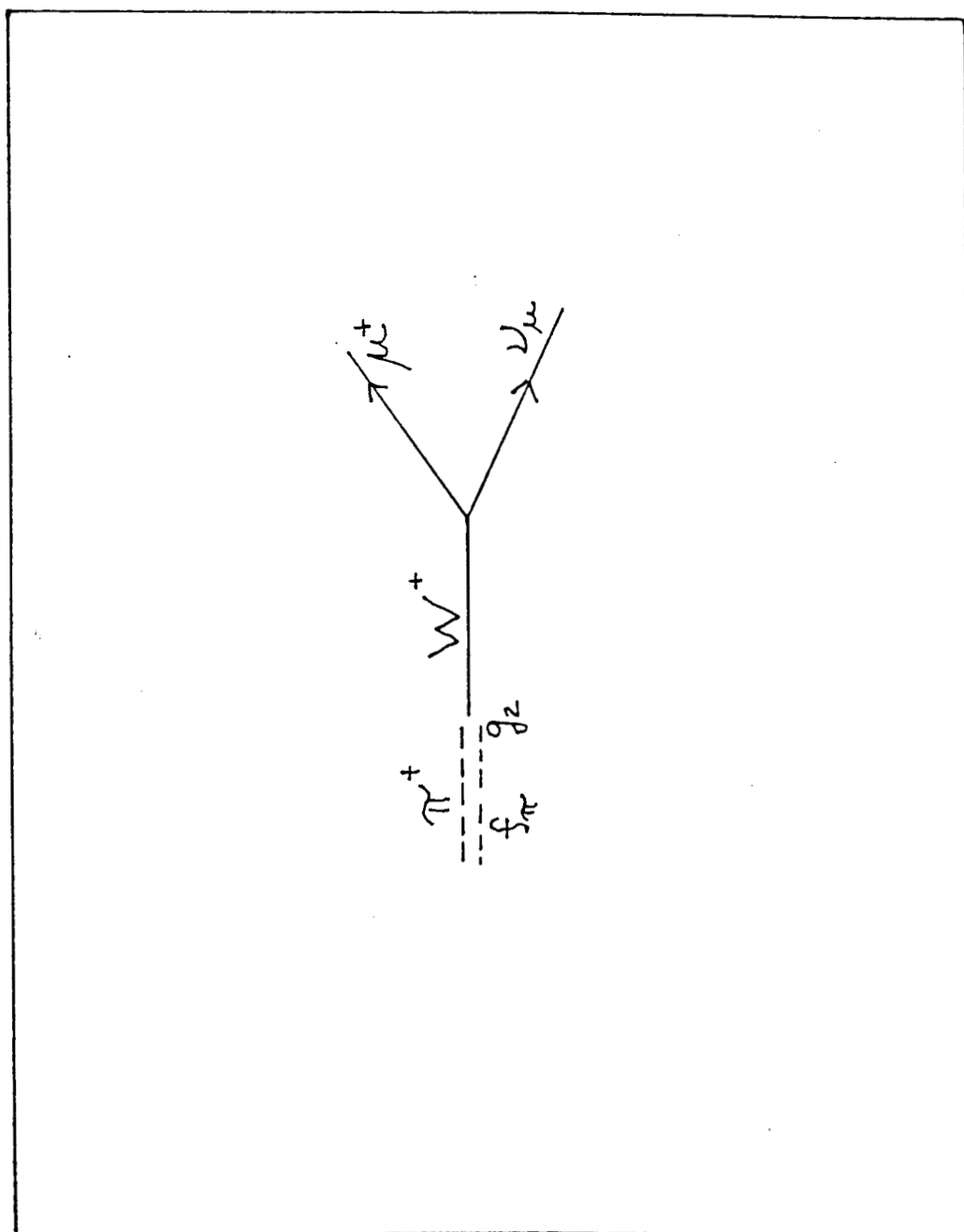


Fig. 4

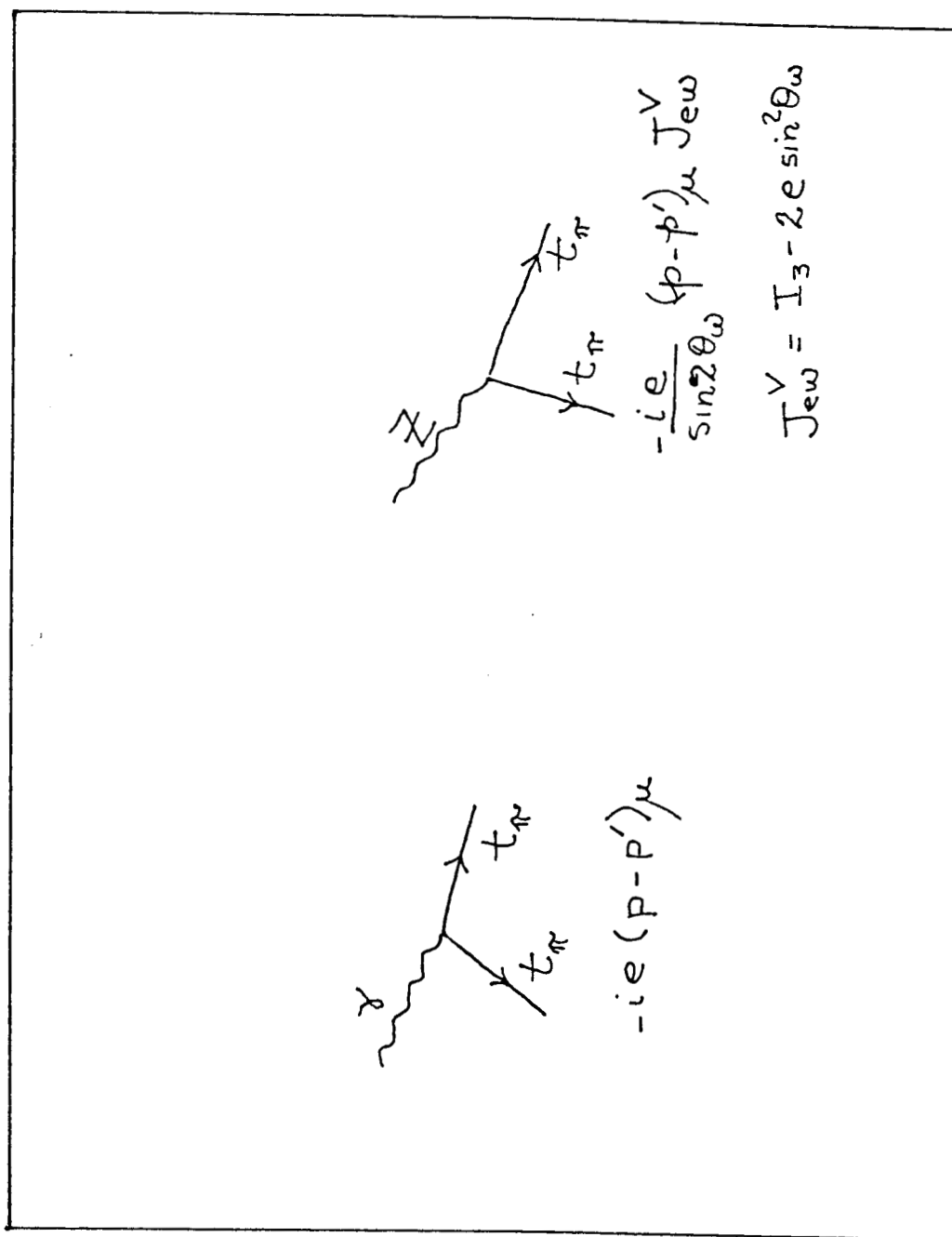


Fig. 5

PRESENT LIMITS

$$e^+ e^- \longrightarrow t_{\pi}^+ t_{\pi}^-$$

CELLO

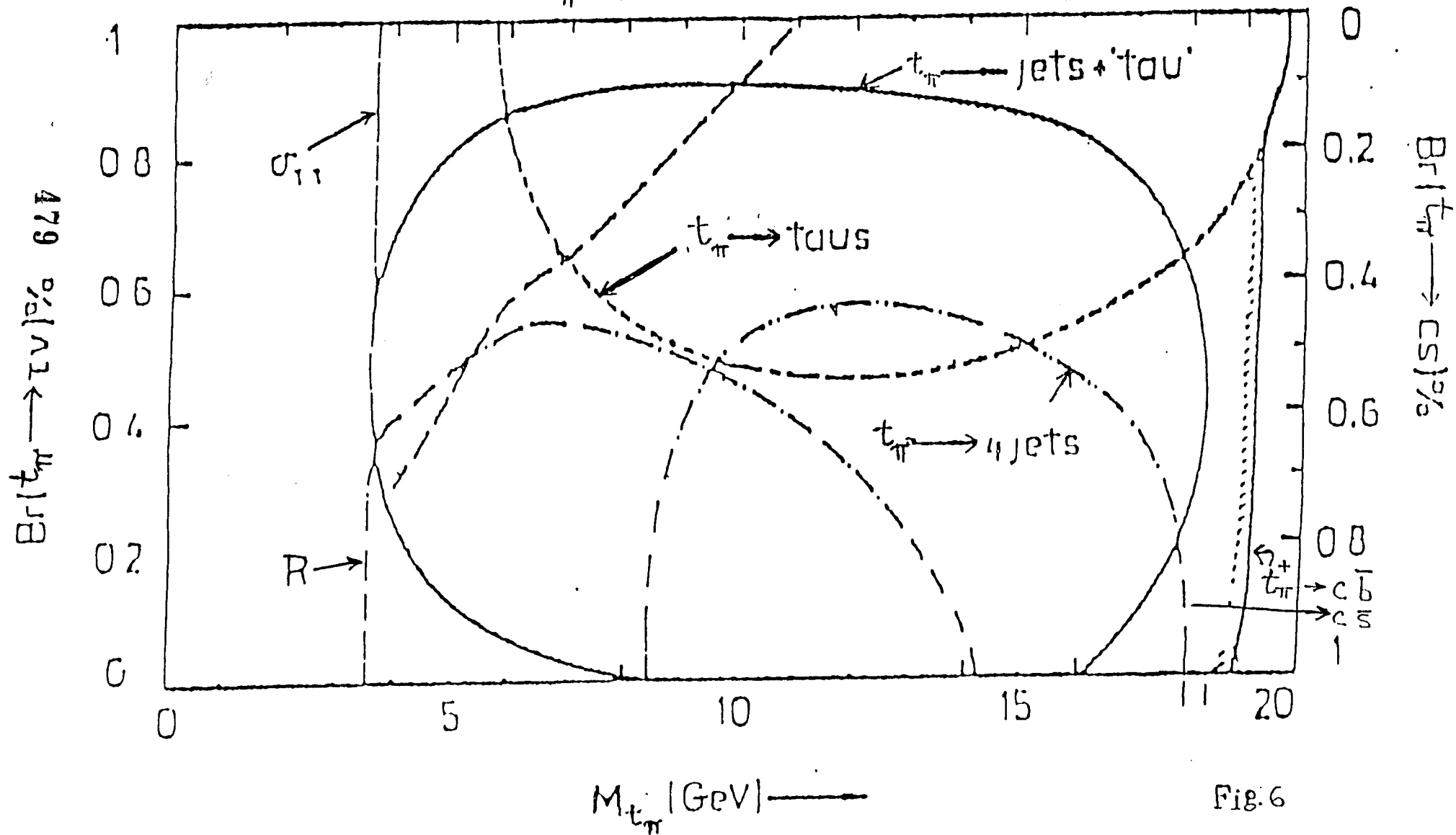


Fig.6

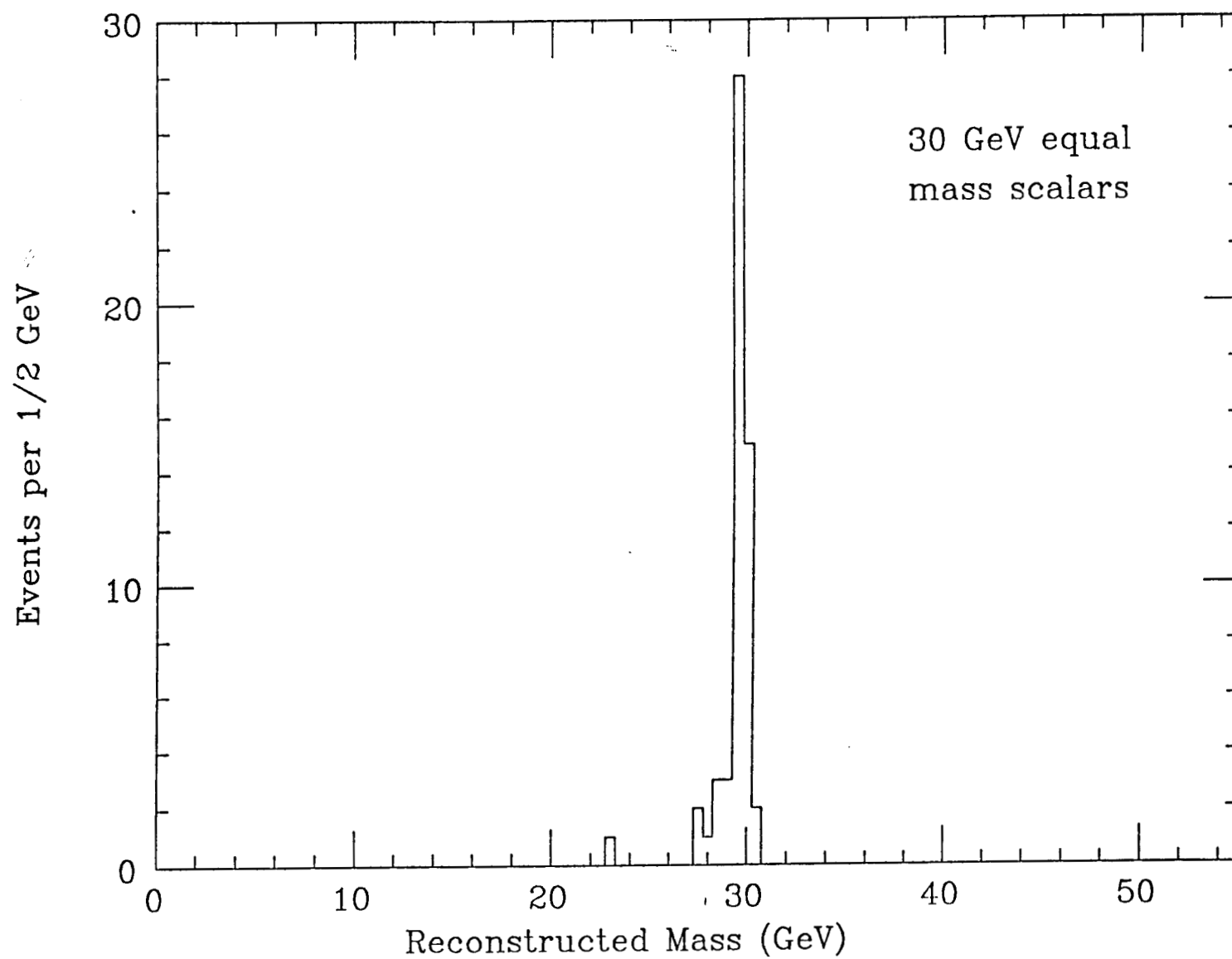


Fig. 7

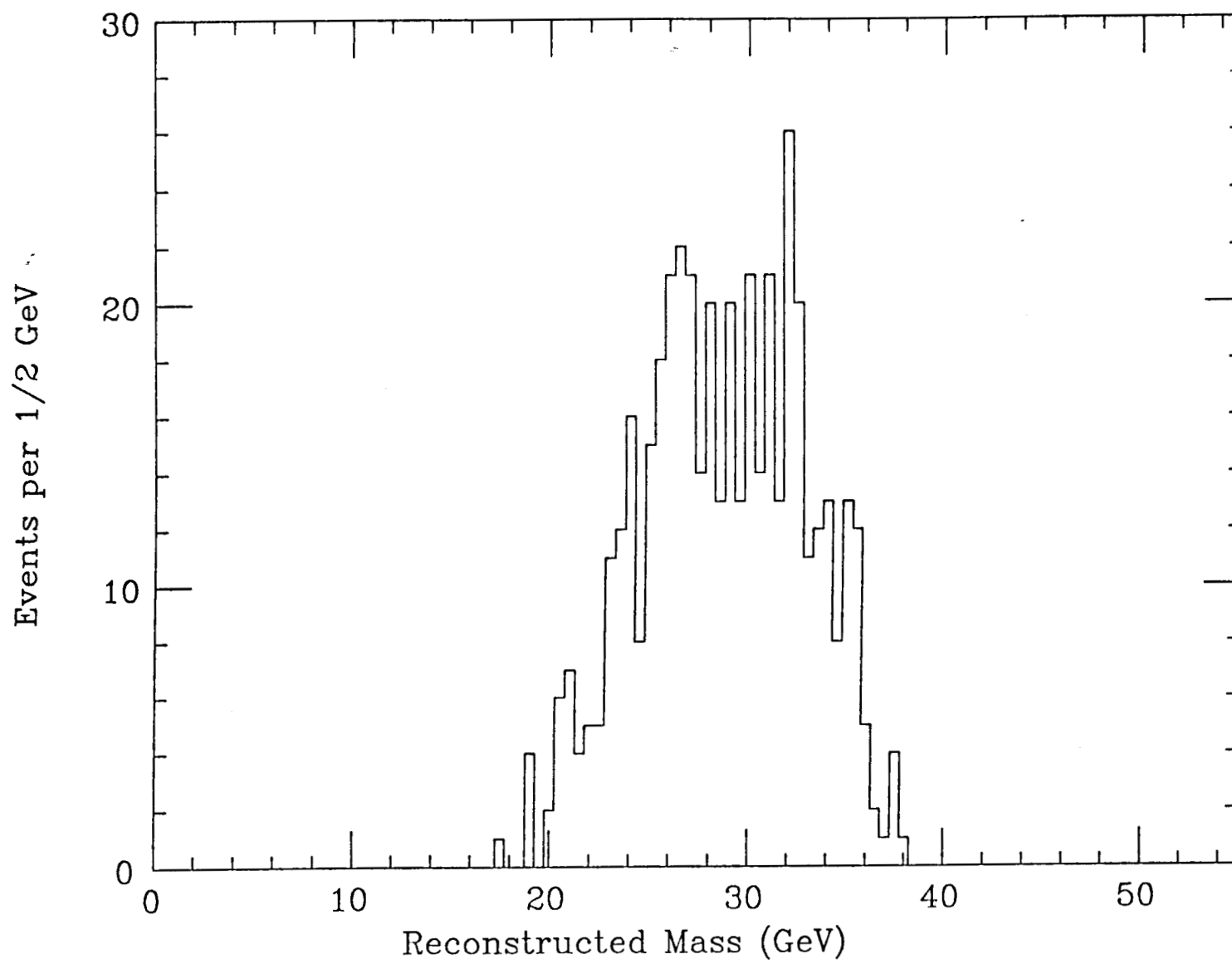


Fig. 8

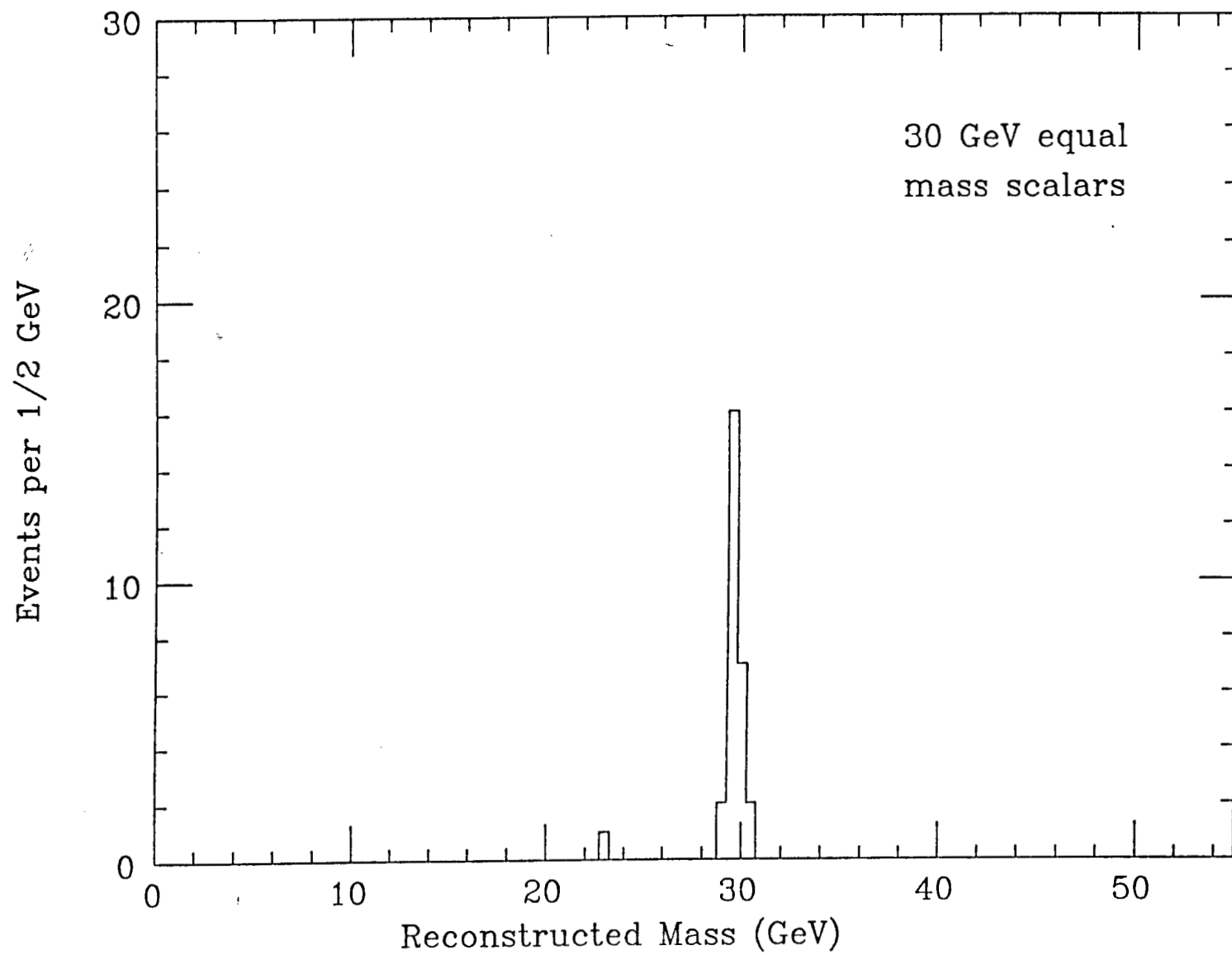


Fig. 9

887

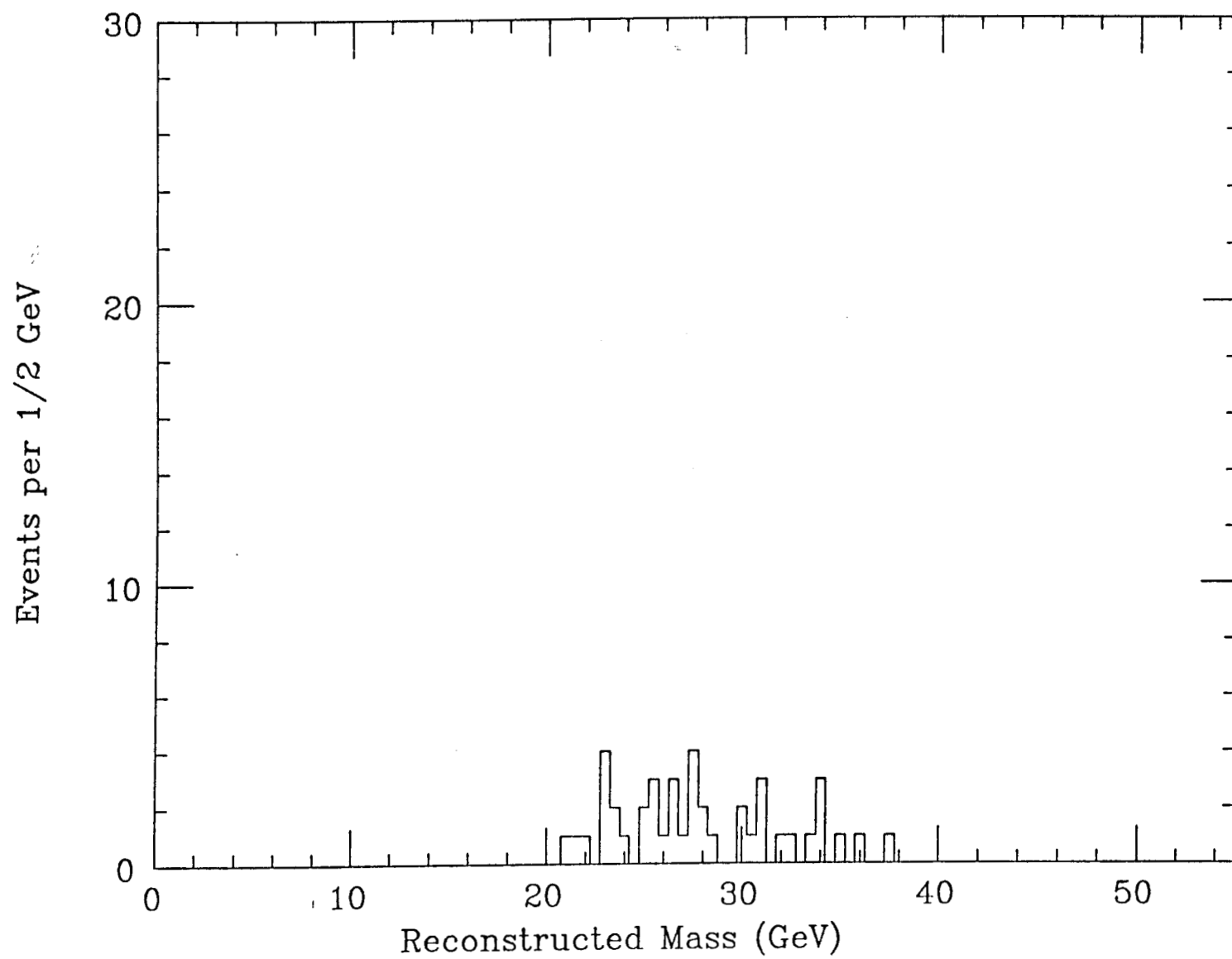


Fig. 10

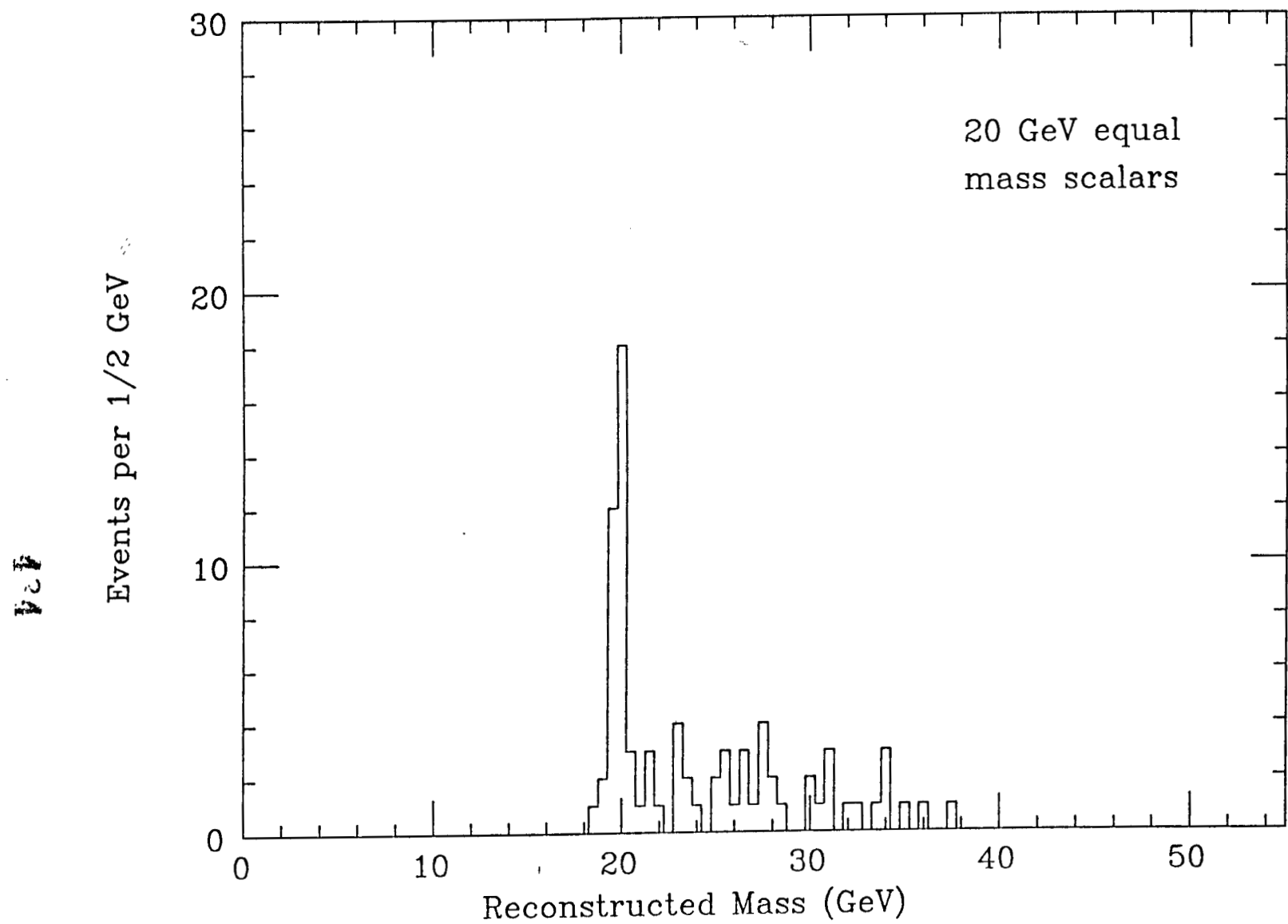


Fig. 11

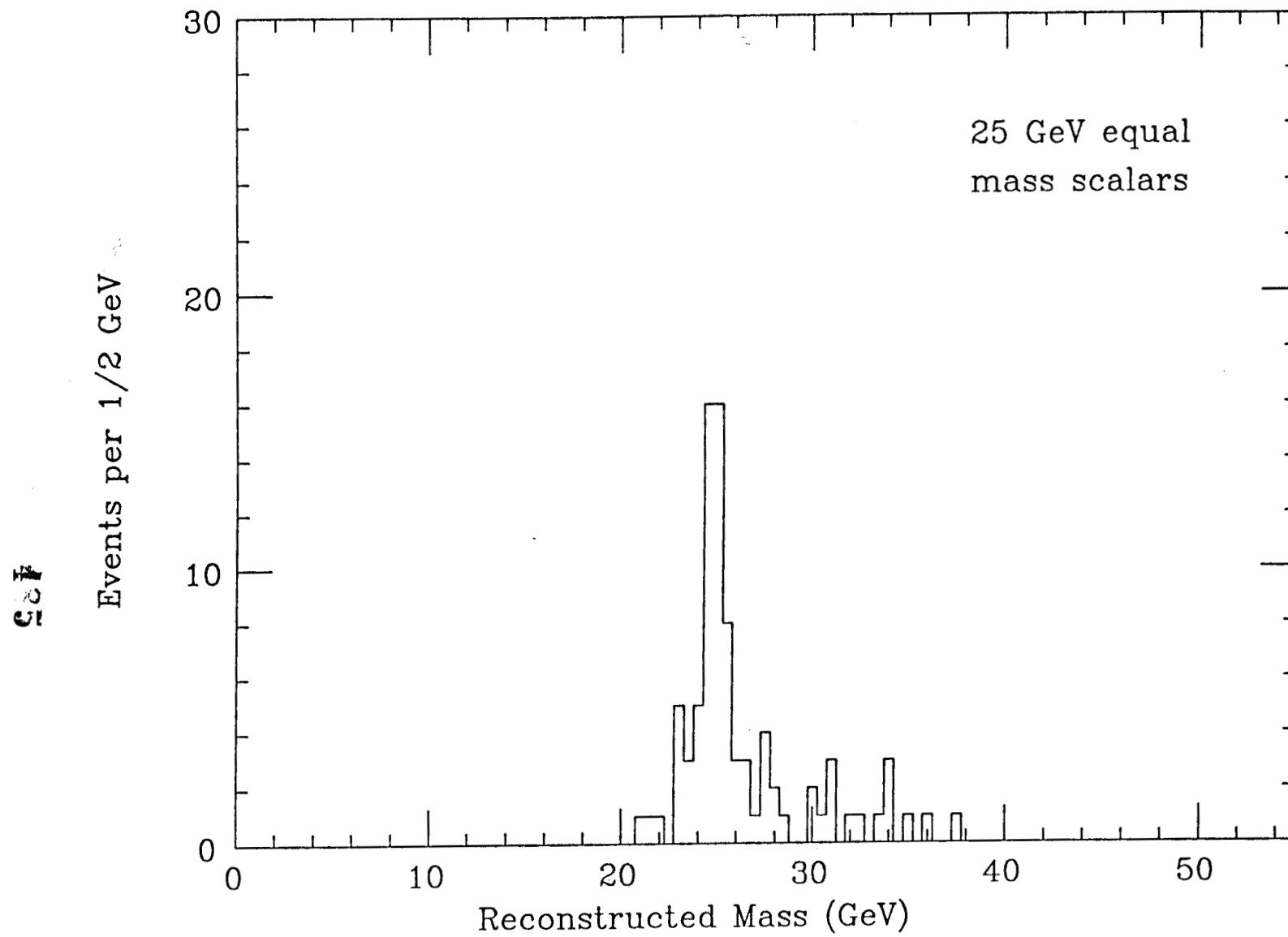


Fig. 12

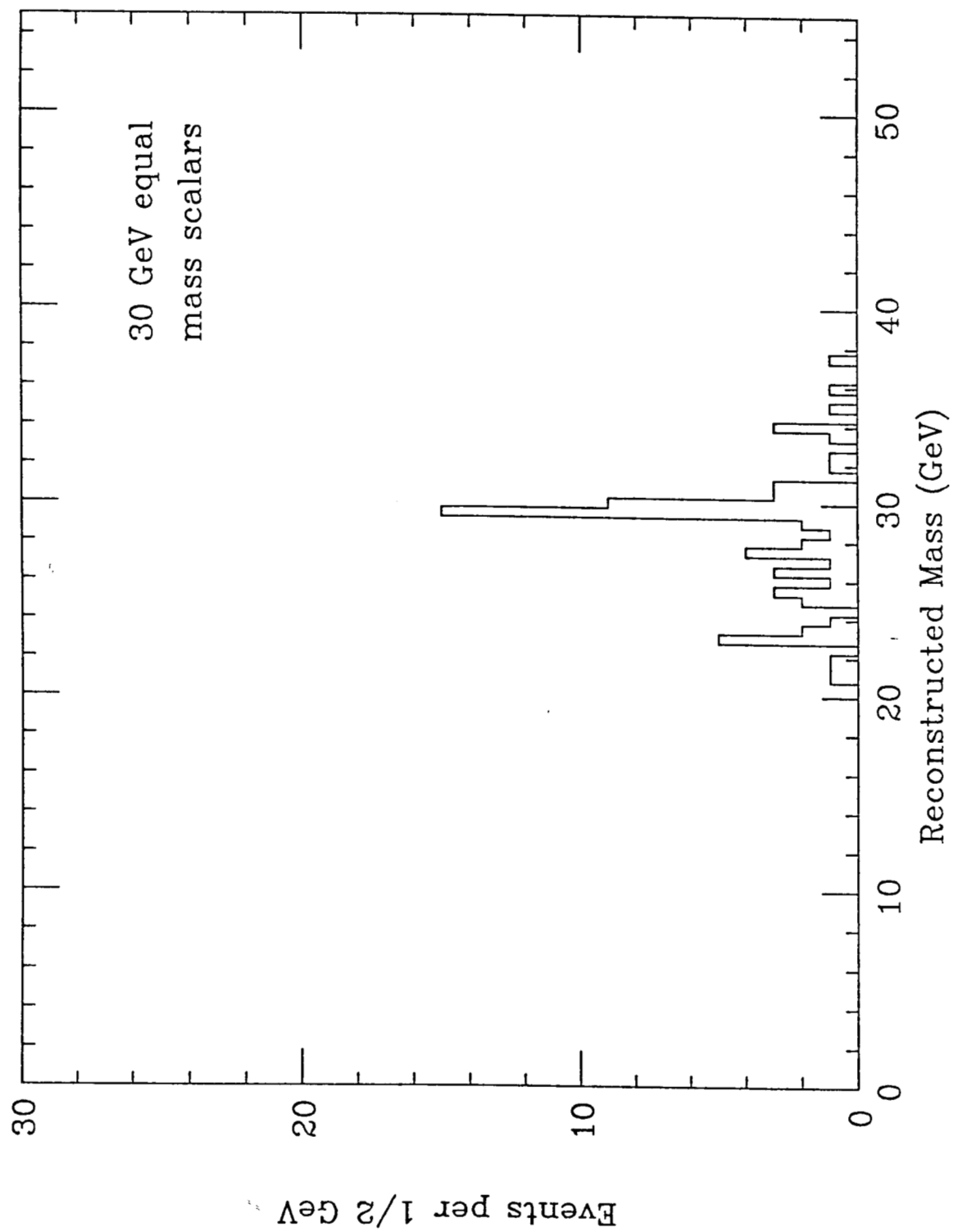


Fig. 13

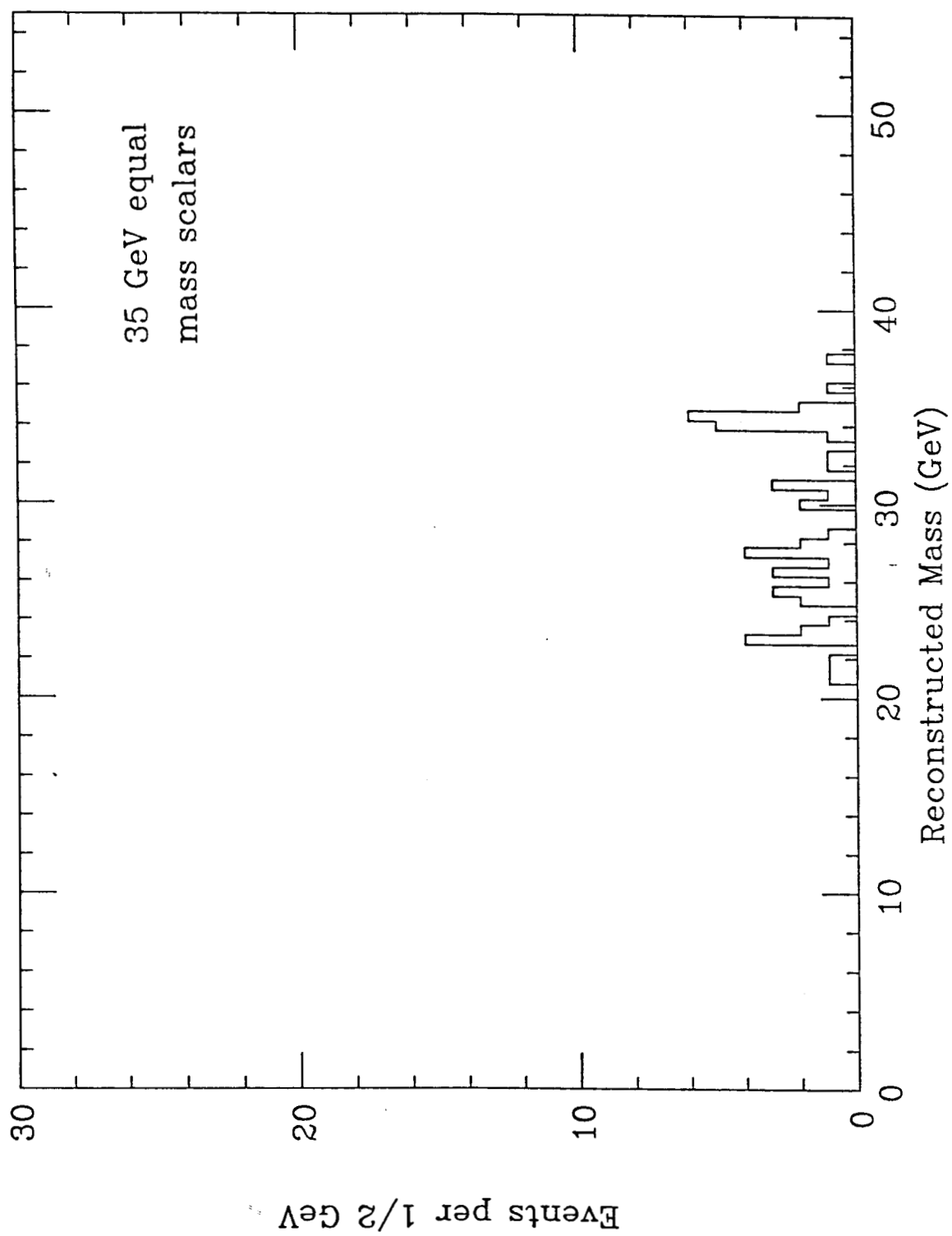


Fig. 14

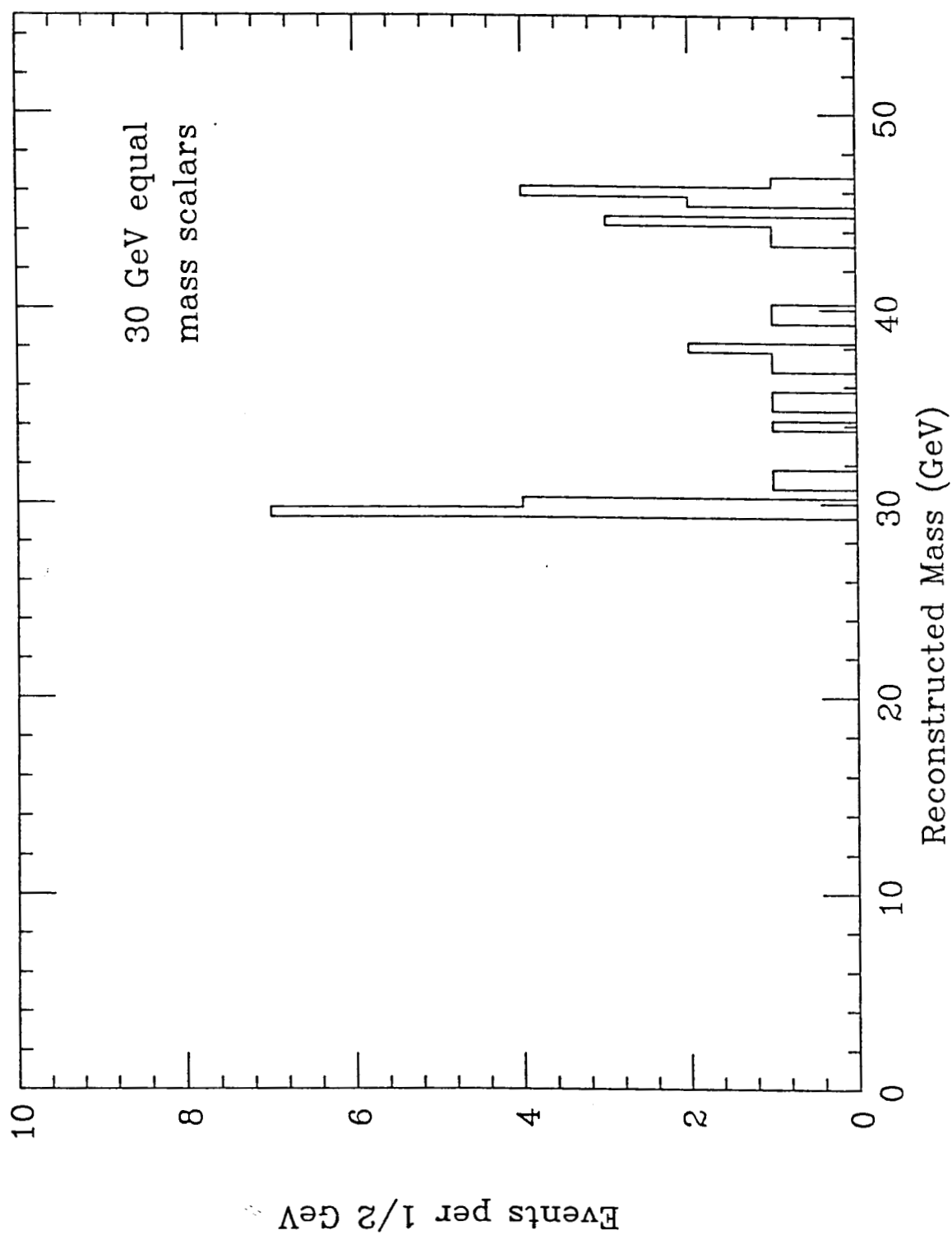


Fig. 15

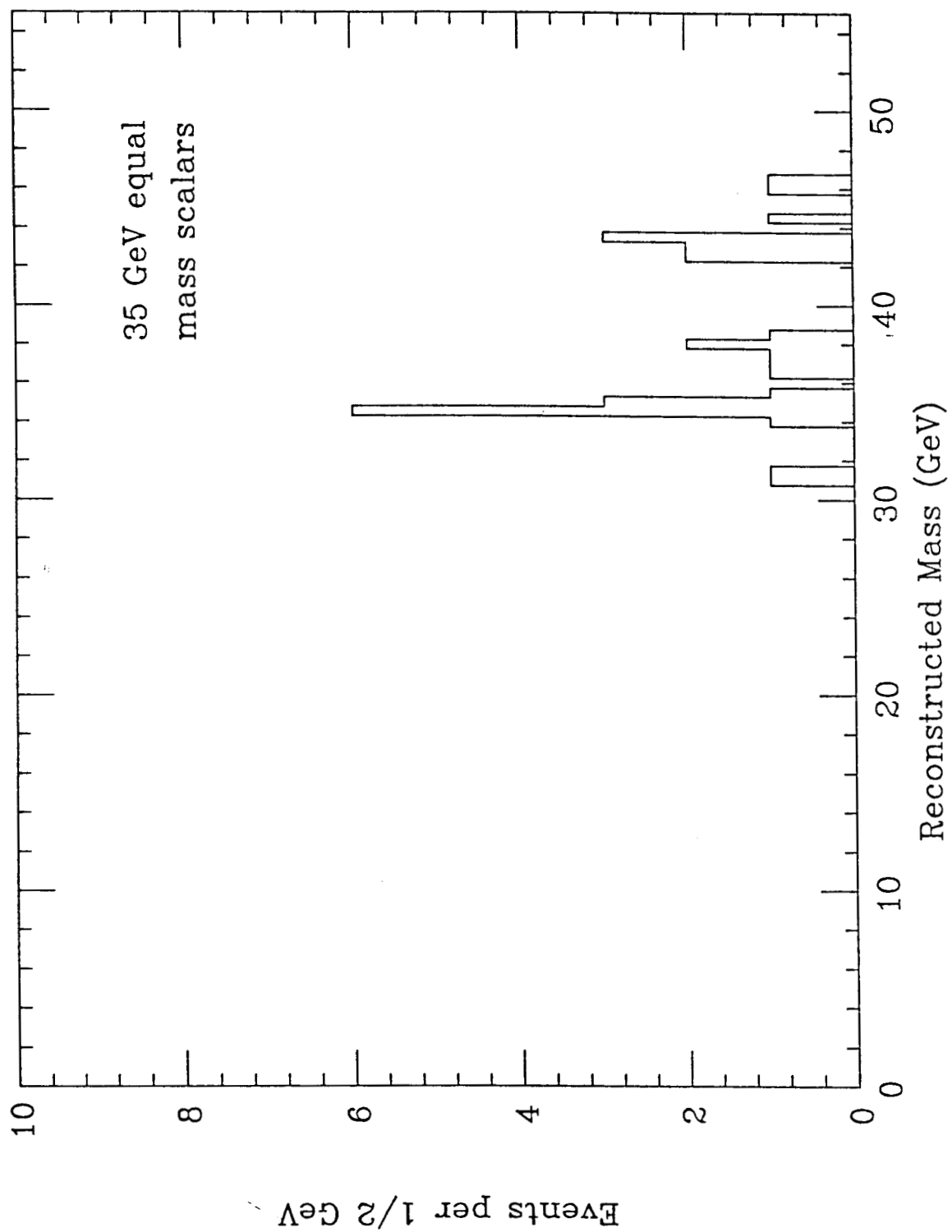


Fig. 16

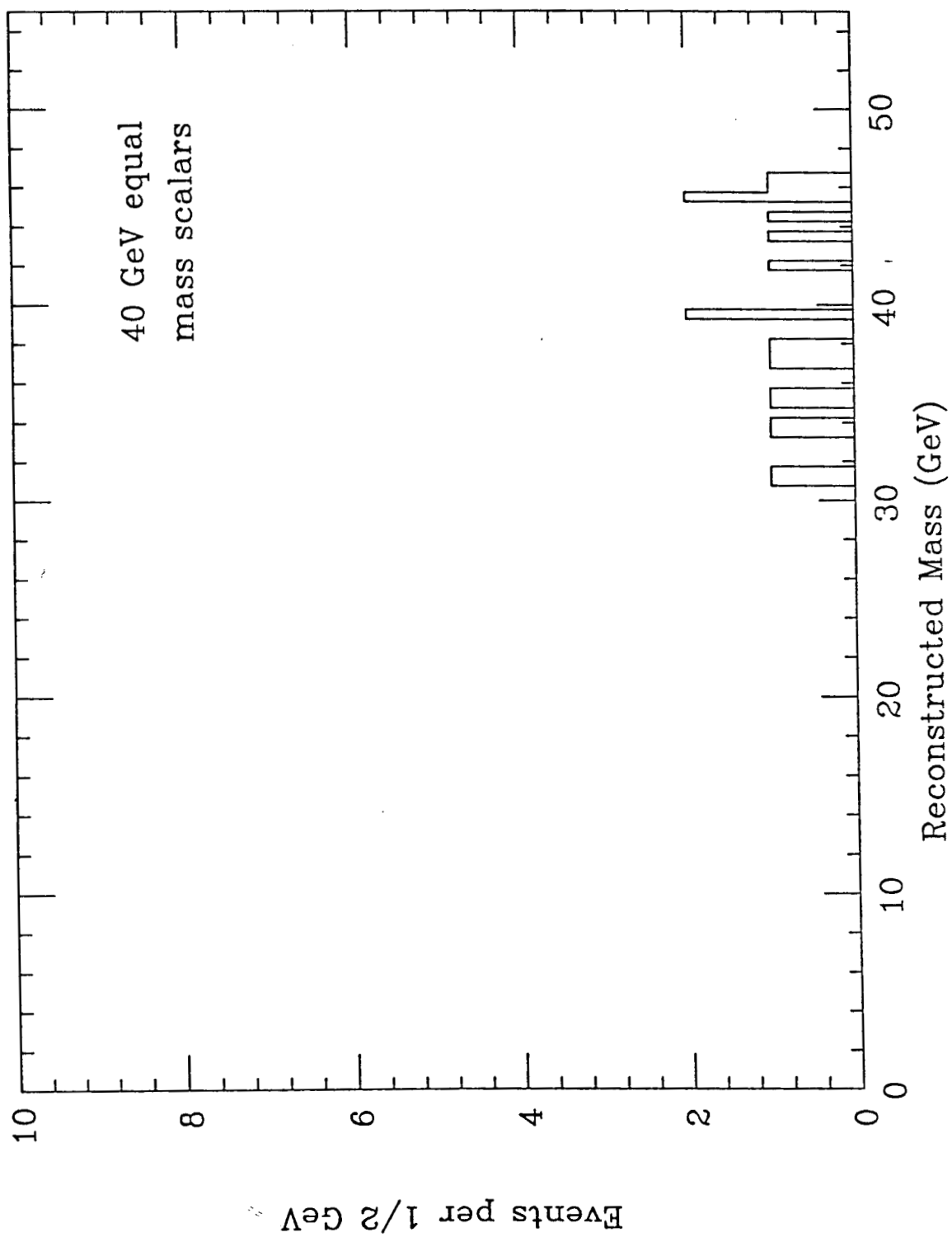


Fig. 17

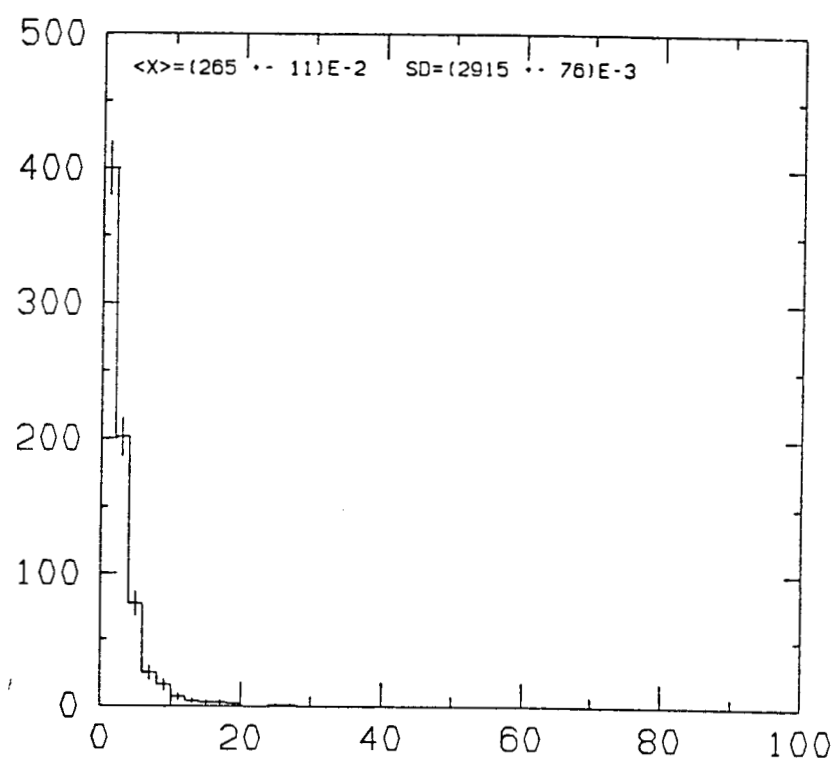


Figure 18

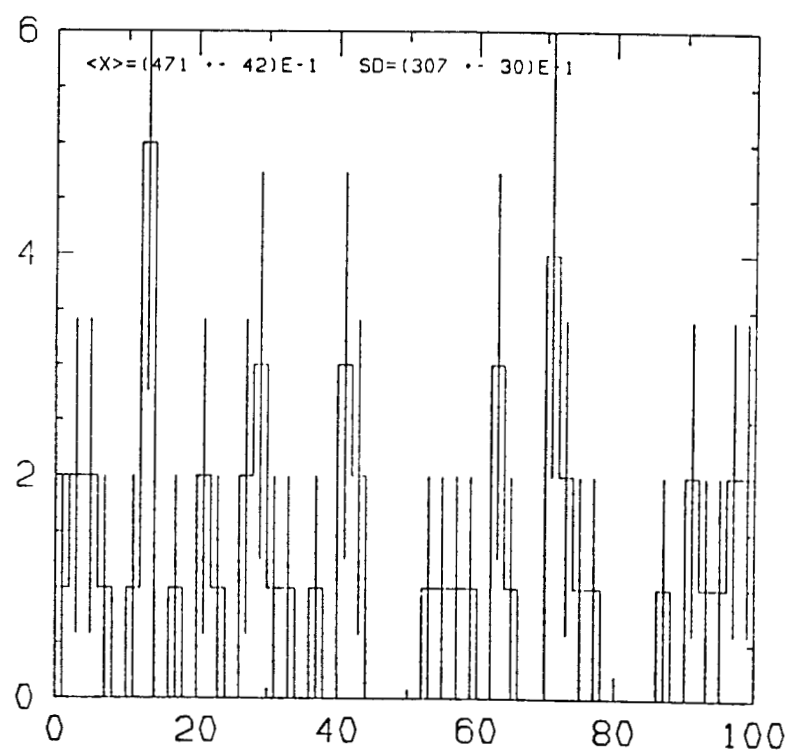


Figure 19

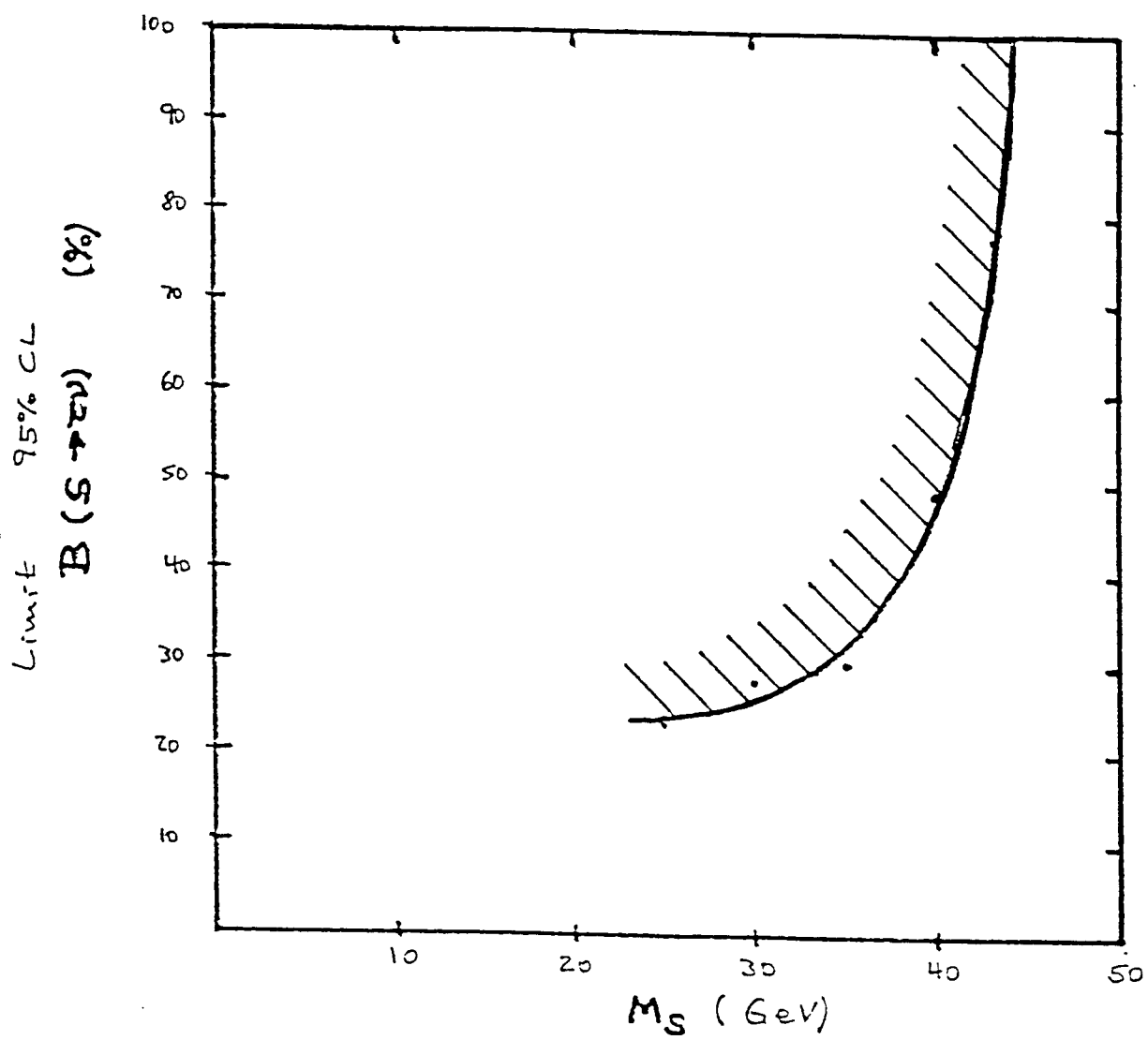


Figure 20

Scalar Production Rates

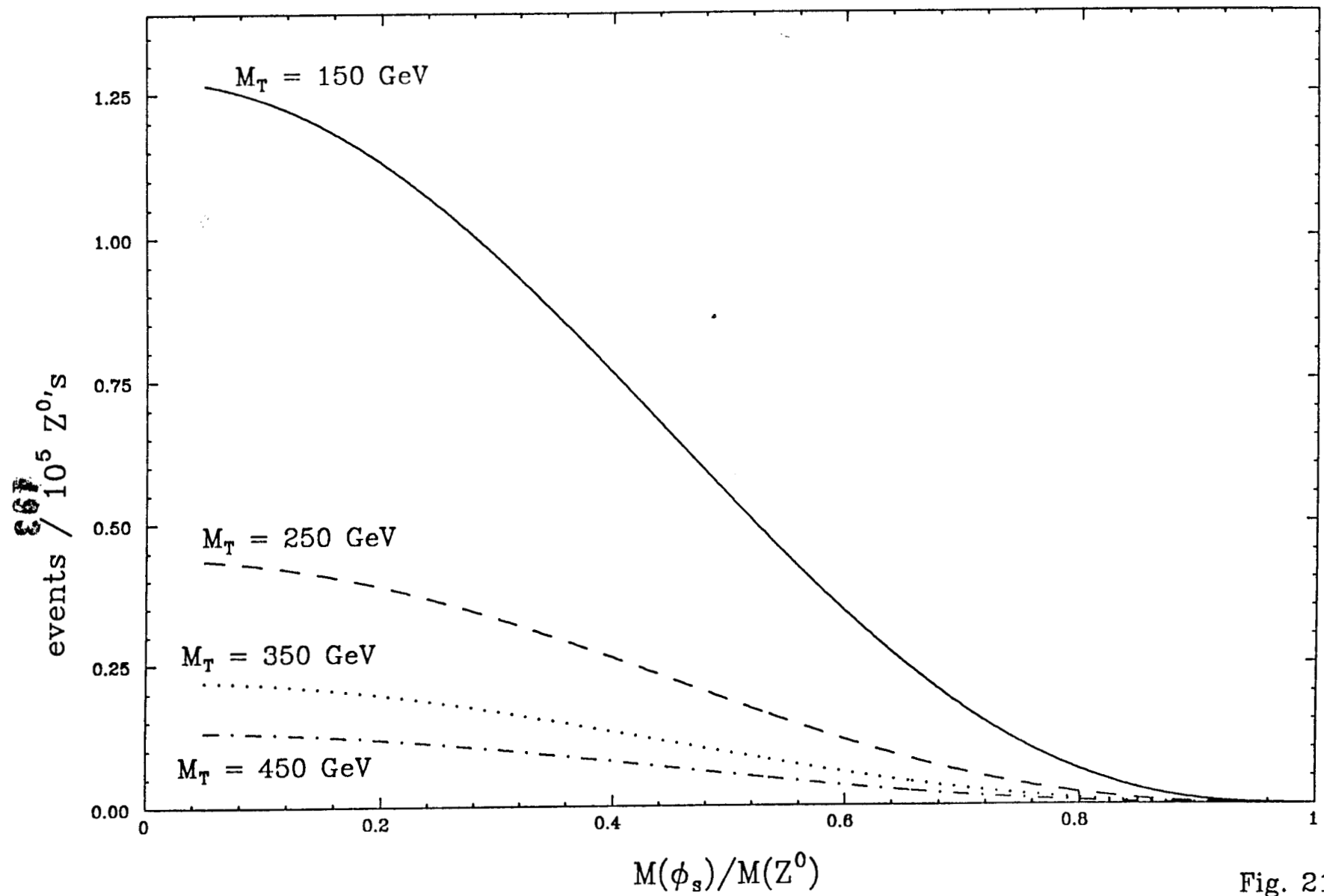


Fig. 21

Pseudocalar Production Rates

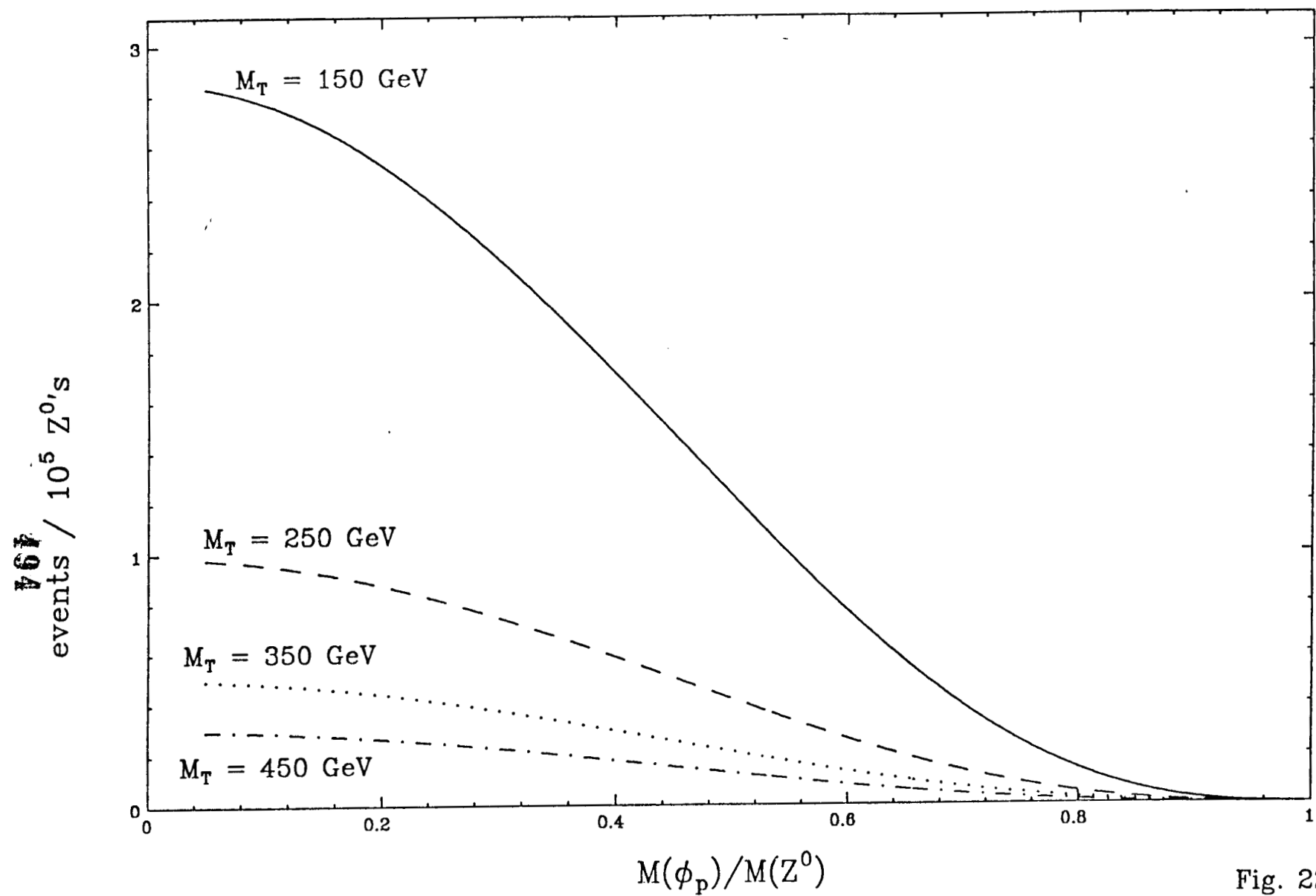


Fig. 22

Jet-Jet Invariant Mass Reconstruction

C. Baltay, S. Manly, and J.D. Turk

Department of Physics, Yale University, New Haven, Connecticut 06520

ABSTRACT

A Monte Carlo study was undertaken to determine the mass resolutions attainable, using the SLD detector, in the reconstruction of events where a Z decays into spinless particles that decay to quark pairs. Preliminary results indicate that for equal mass particles, $\sigma_m/m \sim 1\%$. For unequal masses, the resolution is $\sim 5\%$.

A powerful tool in the search for new particles is the technique of jet-jet invariant mass reconstruction.¹ This is particularly useful in searches for particles presumed to decay into quark jets, such as neutral Higgs scalars² and technipions.³ The events of interest have four well-separated jets. This topology comes about by the Z decaying into two back-to-back spinless particles, not necessarily of the same mass. These particles are then assumed to have sufficient mass to cause good separation of the two jets from their quark-antiquark decays. An invariant mass can be constructed for each scalar by taking the norm of the sum of the 4-momenta for its correct pair of decay jets. This study examines methods of scaling the jets, using constraints from e^+e^- precision and Z decay kinematics, so that the best resolution of the scalar masses is achieved.

The Z bosons for this study are made to decay with a $\sin^2\theta$ distribution into spinless particles, for both equal and unequal mass particles. For the equal mass particles (assumed charged scalars), samples were produced for six masses from 15 to 40 GeV/c^2 . For unequal masses (assumed neutral scalars), only one sample was produced. In this sample the Z decays to two scalars, one at 20 and the other at 30 GeV/c^2 . In both the equal and unequal mass cases the scalars are decayed isotropically in their own center-of-mass frame. The charged scalars are assumed to decay into $b\bar{c}$ ($c\bar{b}$) quark-antiquark pairs $\sim 80\%$ of the time, and the remainder decay to c and s pairs. The neutral scalars are assumed to decay only to $b\bar{b}$ pairs. At this point 4-momenta are generated for each of the four quarks. No radiative corrections are done. The quarks form jets via string fragmentation in the LUND⁴ Monte Carlo package. The standard LUND package for heavy quark decays has been used in this analysis. The hadronized final state particles are

passed through the SLD Fast Monte Carlo detector simulation. This simulation uses simple algorithms for detector components, and does not model effects for tracking inefficiencies. The overall simulation, however, is adequate for this study.

An important consideration is what detector subsystem information should be used. This study starts by using only calorimeter information. The benefits of using particle ID and tracking for the charged track momenta are then made clear by the improved resolution. The biggest problem with using tracking is that 60% of the of the charged tracks with momentum over 3 GeV/c have neutral particles within 5° . Since tracks bend by $\sim 10^\circ/p$ in the SLD magnetic field, and the calorimeter segmentation is $\sim 3^\circ$, there can be an overlap of the calorimeter signals for charged and neutral particles. If the charged track momentum is taken from tracking, then that hidden neutral energy is lost. One correction that can be done is to use tracking information if the tracking and calorimetry agree within errors, but use the calorimeter information if it shows energy larger (beyond the errors involved) than that from tracking.

It is interesting to consider how much the resolution benefits from *hadronic* calorimetry. Since photons are stopped within the electromagnetic portion of the calorimeter, and hadronic signals associated with charged tracks are ignored (if tracking is used), the only particles that require hadronic calorimetry are neutrons and long-lived neutral kaons. Since heavy quarks tend to produce many kaons, these account for more than 8% of the energy in these samples. As a simple way to estimate the effects of not having hadronic calorimetry, particles tagged as K_L^0 s can be removed from the analysis (neutrons or any other track with more than 1 GeV of energy in the hadronic calorimeter, unassociated with a charged track, are

tagged as K_L^0 s). There are problems with this simple way of estimating the loss in resolution. One is that 50% of the photons with energy below 1 GeV are also tagged as kaons. Another problem is that even particles that interact hadronically can leave a substantial amount of energy in the 0.7 interaction lengths of the electromagnetic calorimeter.

Once the particle momenta are determined, the Yclus algorithm⁵ is used to group them into jets. The algorithm works by iteratively combining tracks with low invariant masses between them, where the invariant mass is the norm of the sum of the 4-momenta of the two tracks. The combining of tracks is done by simply adding their 4-momenta to define a new track. Jets are formed in this way. The combining of jets continues until the lowest invariant mass (M) between any two jets satisfies: $(M/E_v) > Y_{cut}$, where Y_{cut} is a variable input parameter to the algorithm, and E_v is the total visible energy in the event. The Y_{cut} is chosen to pick the lowest invariant mass allowed between jets. Y_{cut} is set between 0.015 and 0.030 to get good four-jet events from the generated samples in this study.

Having four-jet events, reconstruction begins. In fig. 1 is plotted the average reconstructed mass for each of the three possible pairings of the four jets. The reconstructed mass is simply the norm of the sum of the 4-momenta of the two jets taken as pairs on one side of the event. An invariant mass is calculated similarly for the opposite two jets, and the two invariant masses are averaged. The sample used is of 30 GeV/ c^2 equal mass charged scalars which decay to bc (80%) or cs (20%) quark-antiquark pairs. The Y_{cut} in the jet-finding algorithm was set to 0.030. Fig. 1 uses only calorimeter information for particle 4-momenta. To reduce the combinatorics (two of the three entries per event in fig. 1 are from incorrect jet

pairings), the thrust axis of the event is used to pair the jets into combinations that maximize the longitudinal momenta of the pairs. The result is fig. 2. This method always selects the lowest invariant mass pairing of jets. This works well for scalar masses below $35 \text{ GeV}/c^2$, but selects the wrong pairing for higher masses, becoming useless. Because the measured jet energies tend to be low, the reconstructed masses fall well below the $30 \text{ GeV}/c^2$ original mass. To correct for this, the reconstructed masses can be scaled by half the true event energy divided by the sum of the measured energies of the two jets used in the reconstruction of the mass. This simple scaling is justified only when assuming equal masses for the scalars from the Z decay. Each then takes half of the event energy. The much improved results are in fig. 3. To further improve the peak, another method of reconstruction can be employed in which all of the kinematic information available for the event is used. The jets are scaled individually so that the sum of the momenta of each of the jet pairs is equal to half of the true event energy, and the sum of the 3-momenta of the four jets is minimized (should be zero). An initial state hard photon lost down the beampipe would weaken these assumptions, but these effects were not considered. The scaling factor distribution for this method is shown in fig. 4. The mass peak is plotted in fig. 5. Fig. 6 is the same plot, except that full particle identification was implemented and tracking information was used for charged particle momenta. The resolution is very much improved and is about $1/3$ of a GeV/c^2 . As an attempt to determine the resolution without hadronic calorimetry, the same analysis is run with particles tagged as K_L^0 s removed. The resulting peak is shown in fig. 7. The resolution is worse by roughly a factor of two.

For the study of unequal mass scalar pairs, a sample of 20 and $30 \text{ GeV}/c^2$

neutral particles is used. Momentum conservation is again required in the reconstruction, but now the energy conservation constraint is weakened by not having equal masses. Since the energy will not be shared equally by the two scalars, the equal mass constraint that each side have half of the true event energy now only requires that both sides added together have the full energy. A solution can still be found for the scaling factors for each jet. The scaling factor distribution is depicted in fig. 8. The two mass peaks for this sample are plotted in fig. 9. For this analysis, Y_{cut} is set to 0.020, the thrust axis is again used to select the correct pairing of jets, full particle identification is implemented, and tracking is used for the charged particle momentum determination. Because these neutral scalars are assumed to decay to $b\bar{b}$ pairs, the b mass can be used in the energy constraint: $E^2 = p^2 + m_b^2$. The improved results are shown in fig. 10. The resolution is between 1 and 2 GeV/c^2 for the two peaks. If particles tagged as K_L^0 s are removed to simulate the lack of hadronic calorimetry, the resolution is degraded by roughly a factor of two, as is shown in fig. 11.

The conclusions of this study are that resolutions of $\sigma_m/m \sim 1\%$ for equal mass pairs of particles, and $\sigma_m/m \sim 5\%$ for unequal mass pairs, can be achieved by the SLD detector using jet-jet invariant mass reconstruction and the precision of e^+e^- kinematics in Z decays. The loss of hadronic calorimetry hurts the resolution by roughly a factor of two, as indicated by the approximate simulation used. Possible refinements to this study include modelling the effects of initial state radiation, using the more precise Slow Monte Carlo, and implementing a more accurate heavy quark decay package. This work would not have been possible without the software assistance of Richard Dubois and Tony Johnson.

REFERENCES

1. A good discussion of a similar analysis at TASSO can be found in S. M. Ritz, Univ. of Wisconsin-Madison Ph.D. Thesis (1988).
2. A study of neutral Higgs detection at SLD, done by Scott Whitaker, is included in these proceedings.
3. The results of the technicolor group's analysis of four-jet technipion events are included as part of the technicolor report in these proceedings.
4. T. Sjöstrand, Comput. Phys. Commun. **27**, 243 (1982); T. Sjöstrand, Comput. Phys. Commun. **28**, 229 (1983).
5. Authored by S. Bethke for JADE, now part of the SLD software package.

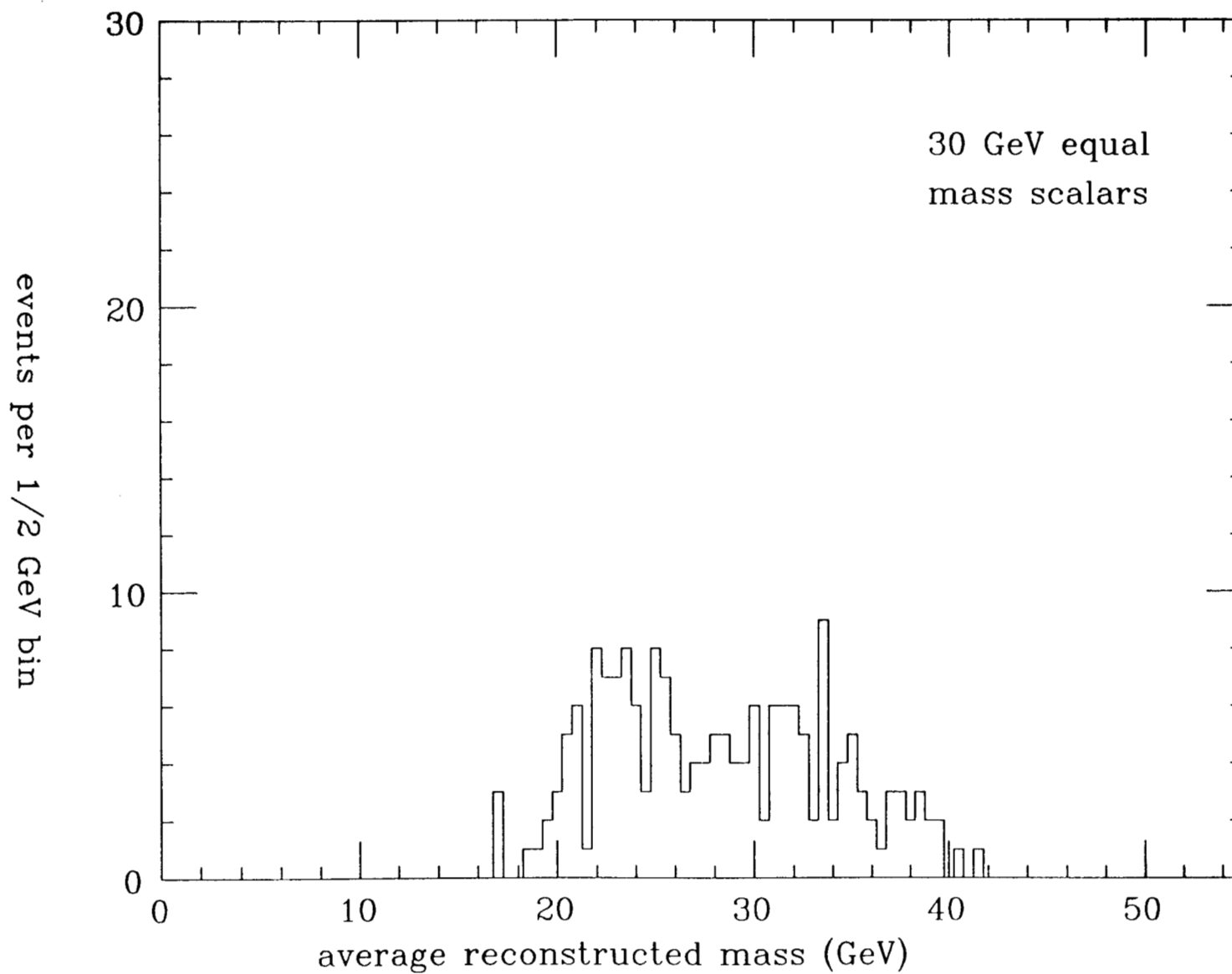


Fig. 1. The reconstructed masses for all pairings of UNSCALED jets is shown. Only calorimetry data is used. $Y_{\text{cut}} = 0.020$.

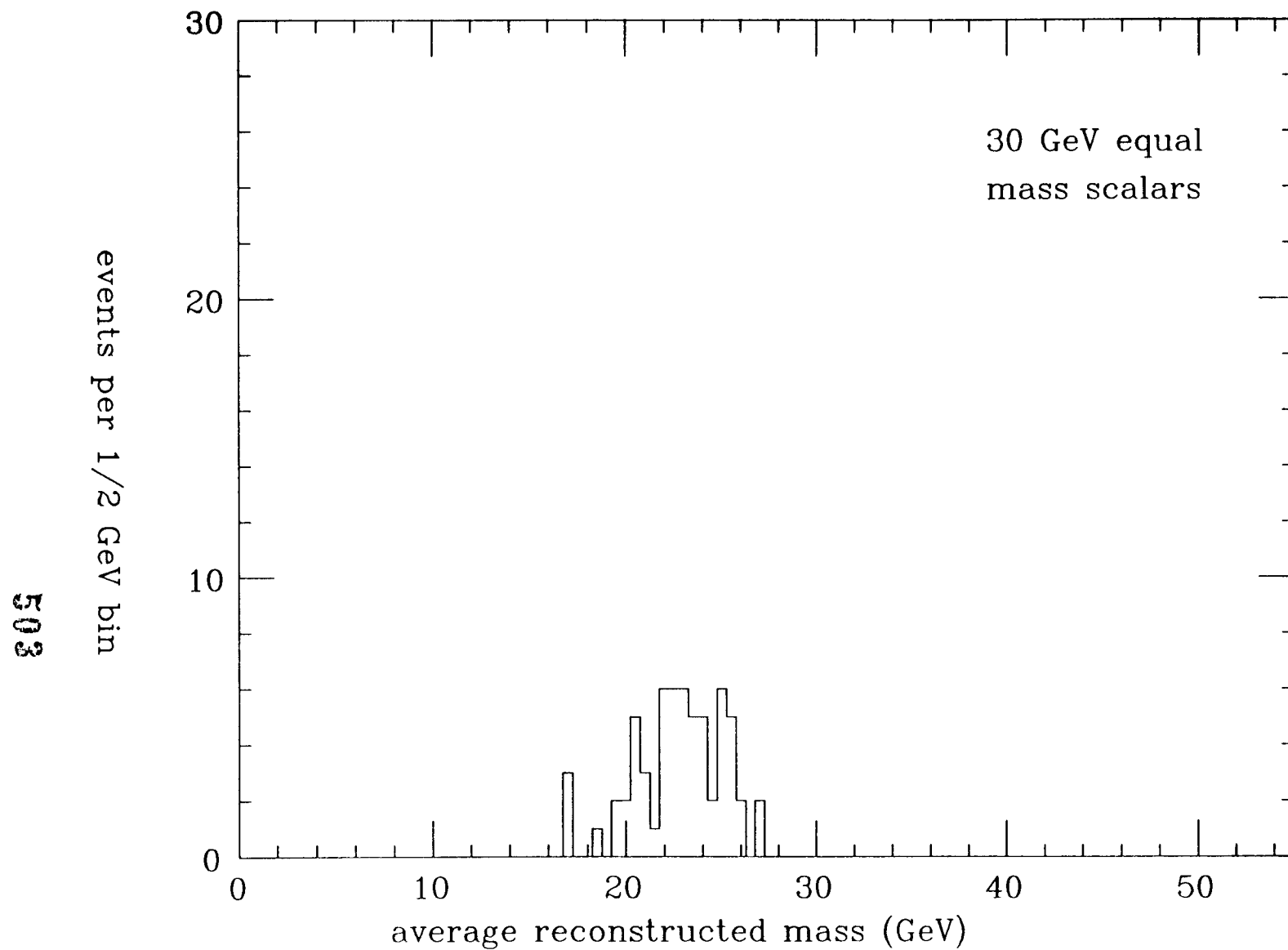


Fig. 2. The thrust axis is used here to pair the jets. Otherwise, this is the same analysis as in fig. 1.

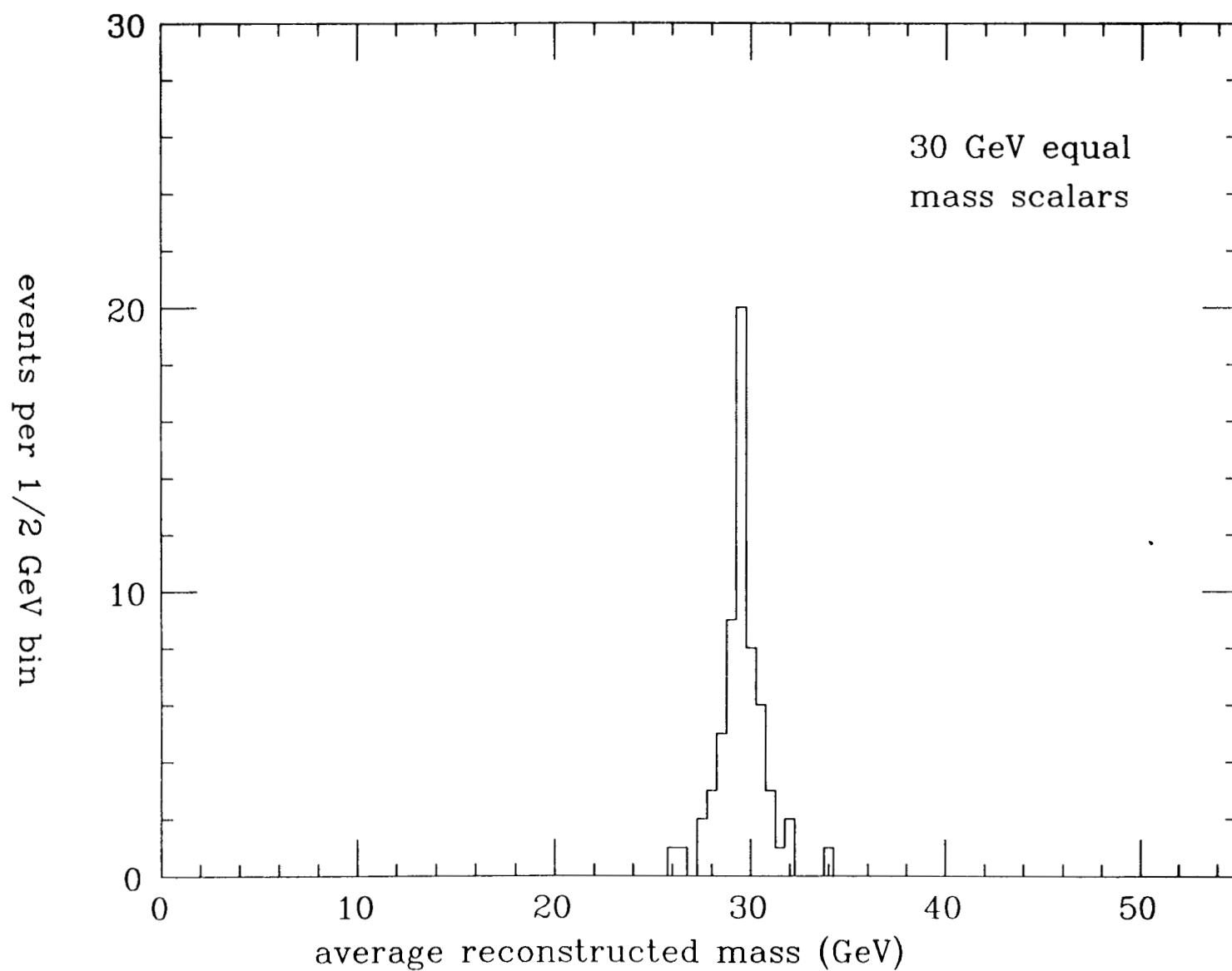


Fig. 3. The reconstructed mass is scaled by the true energy divided by the measured energy in the two jets used for the mass.

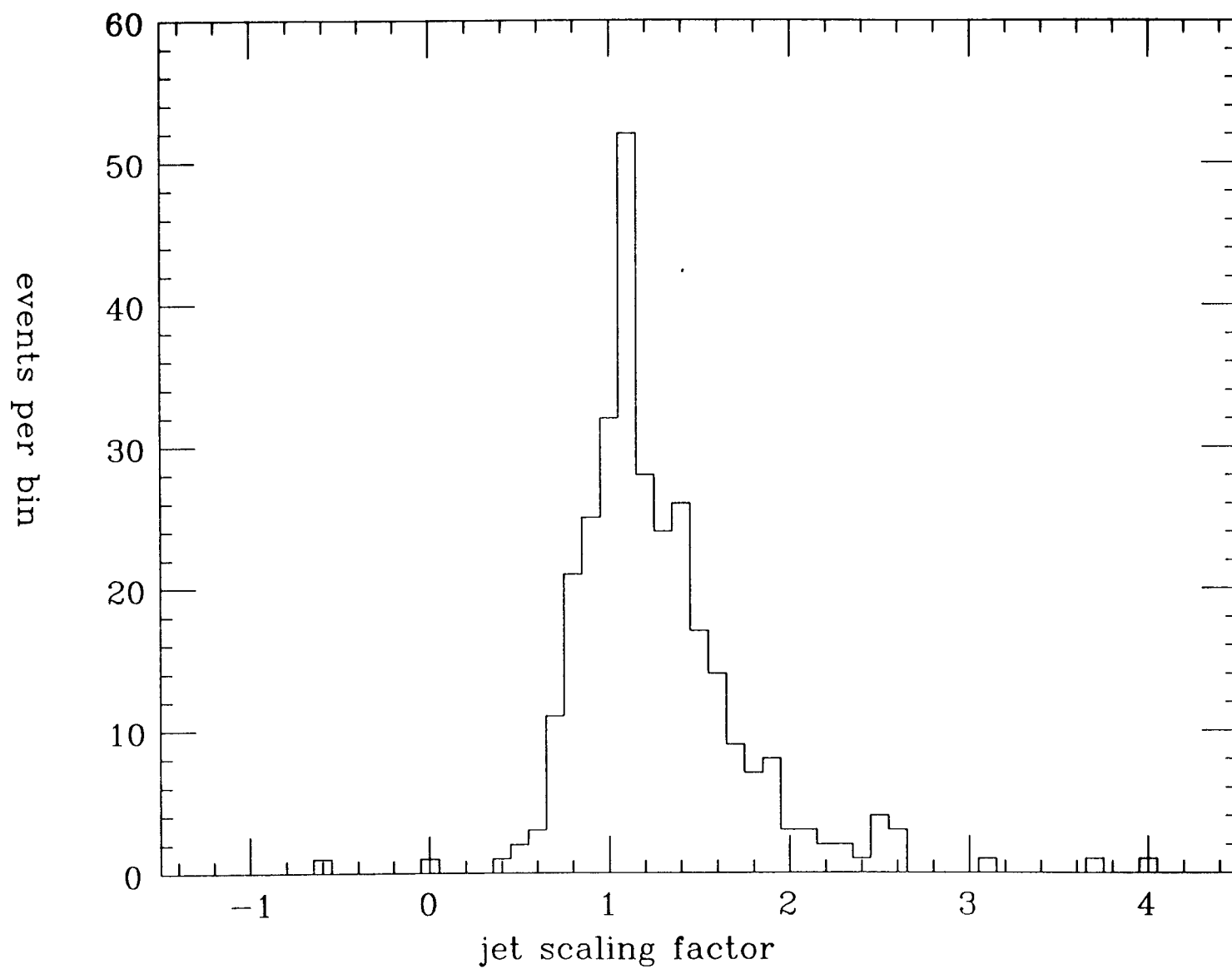


Fig. 4. This is the distribution of jet 4-momentum scaling factors using the full kinematic reconstruction for equal masses.

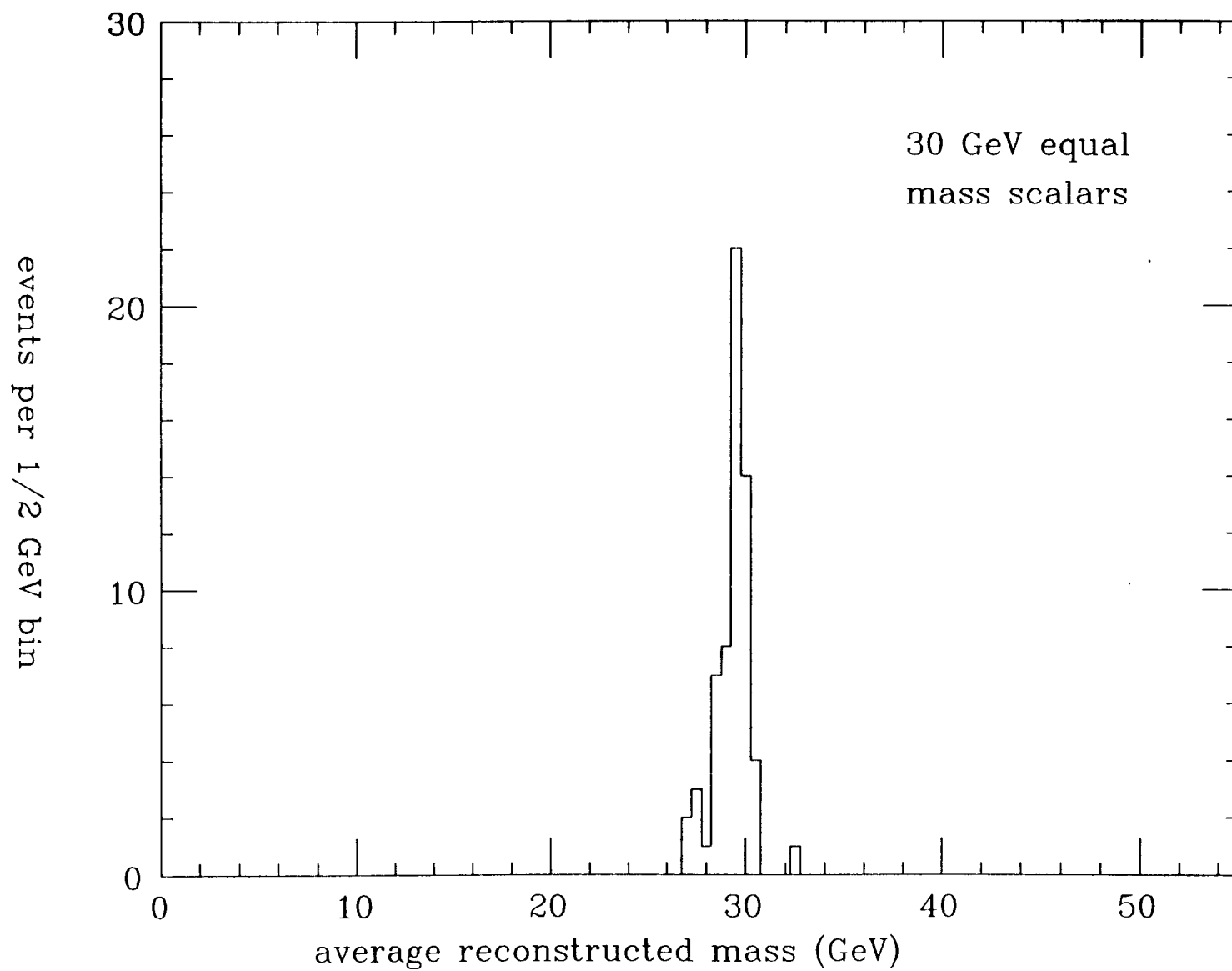


Fig. 5. The full reconstruction is implemented with, as in fig. 2-3, calorimeter data, thrust axis jet pairing, and $Y_{\text{cut}} = 0.020$.

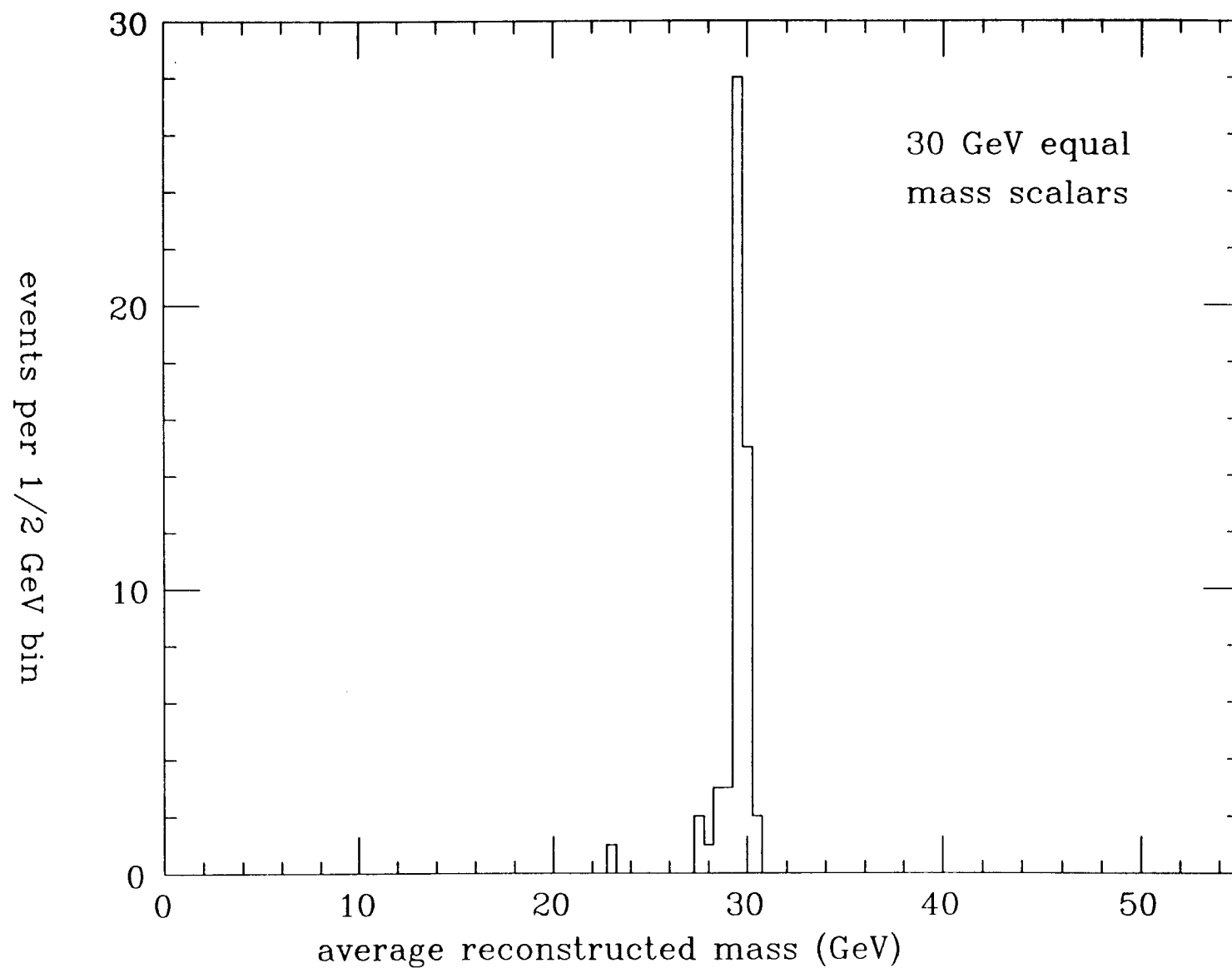


Fig. 6. Particle ID is used here, and tracking for charged particle momenta. This gives the best SLD reconstruction.

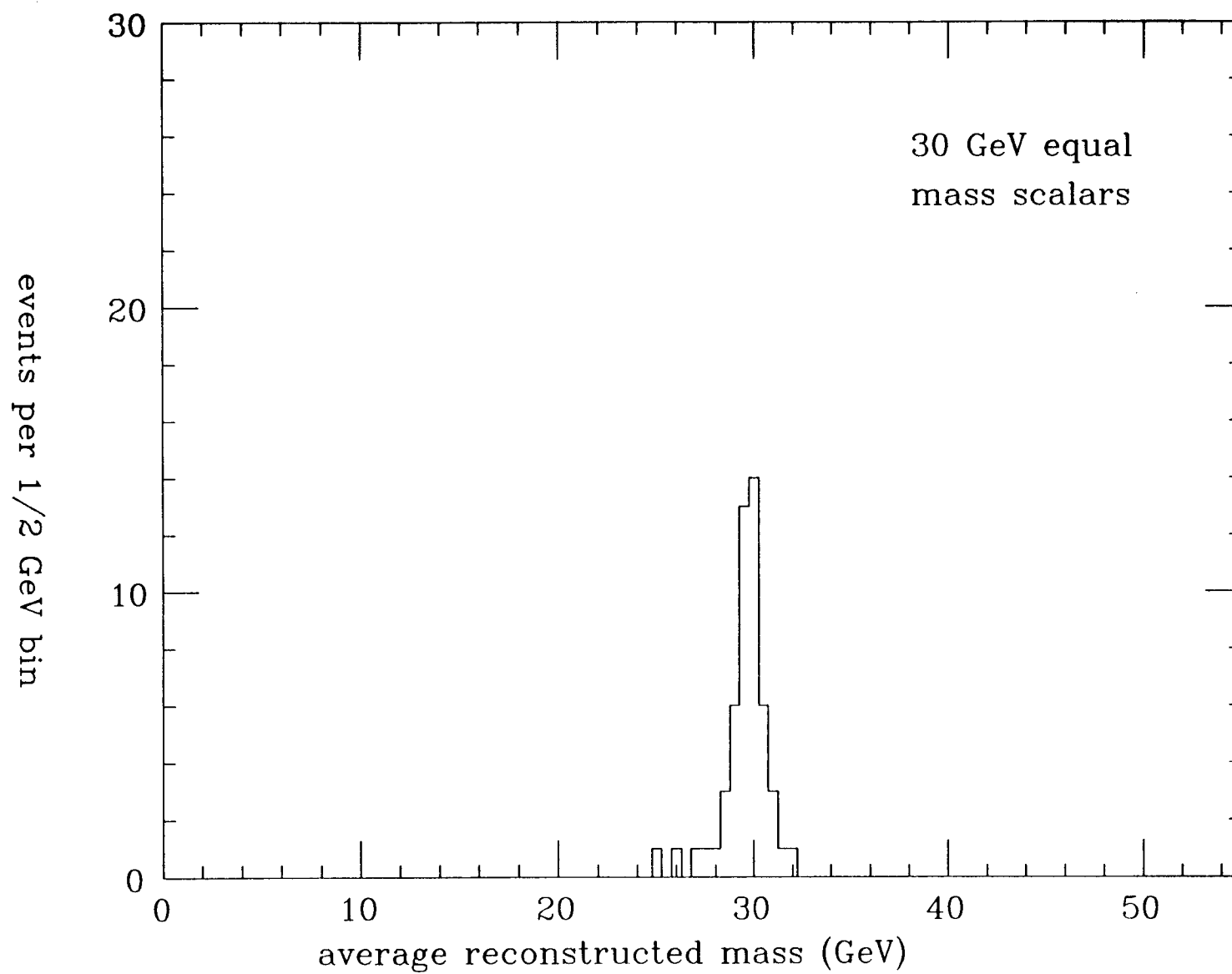


Fig. 7. Particles tagged as K-longs are removed from the analysis of fig. 6. Lack of hadronic calorimetry is thus simulated.

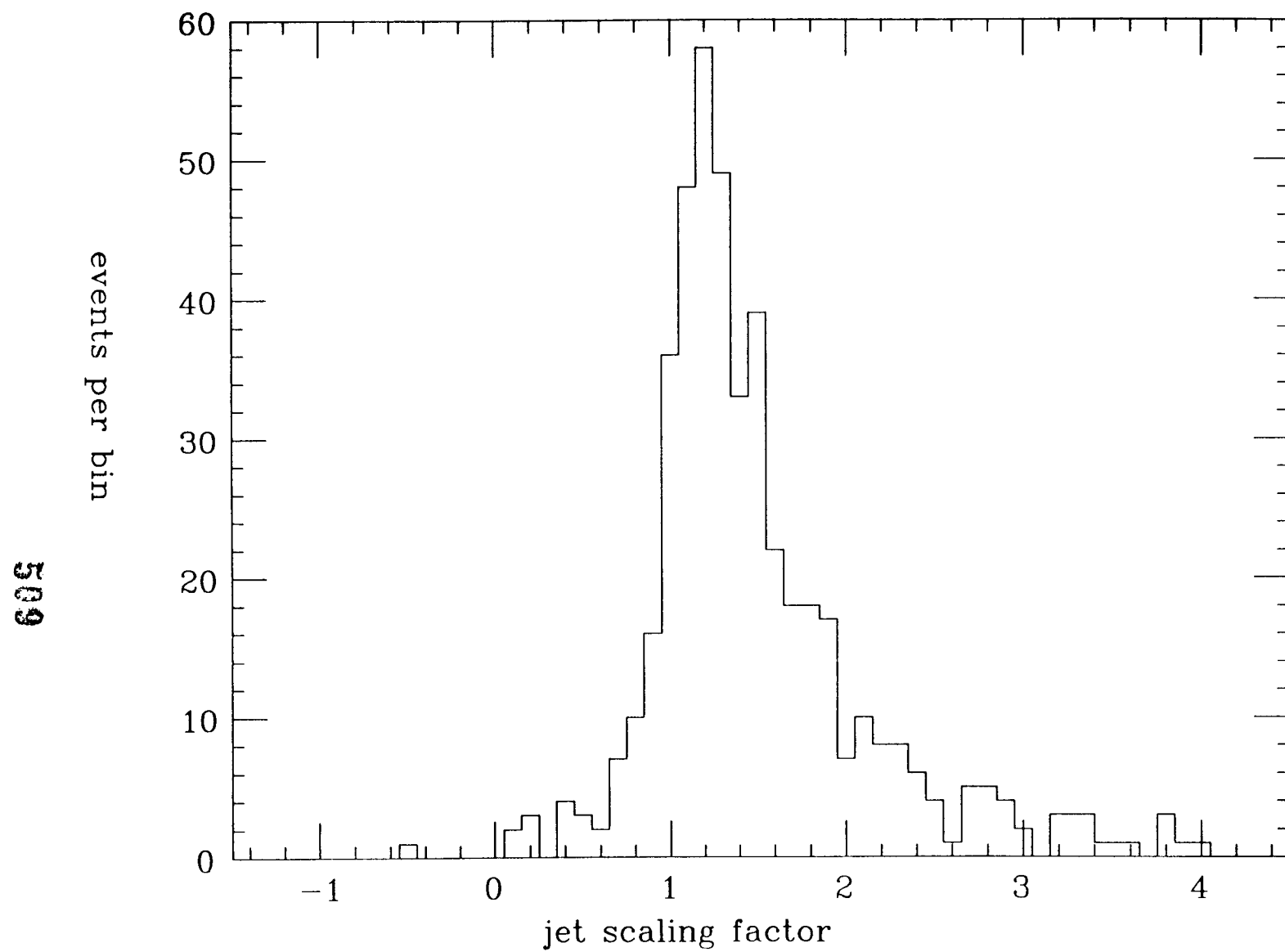


Fig. 8. This is the distribution of jet 4-momentum scaling factors using the full reconstruction for UNEQUAL masses.

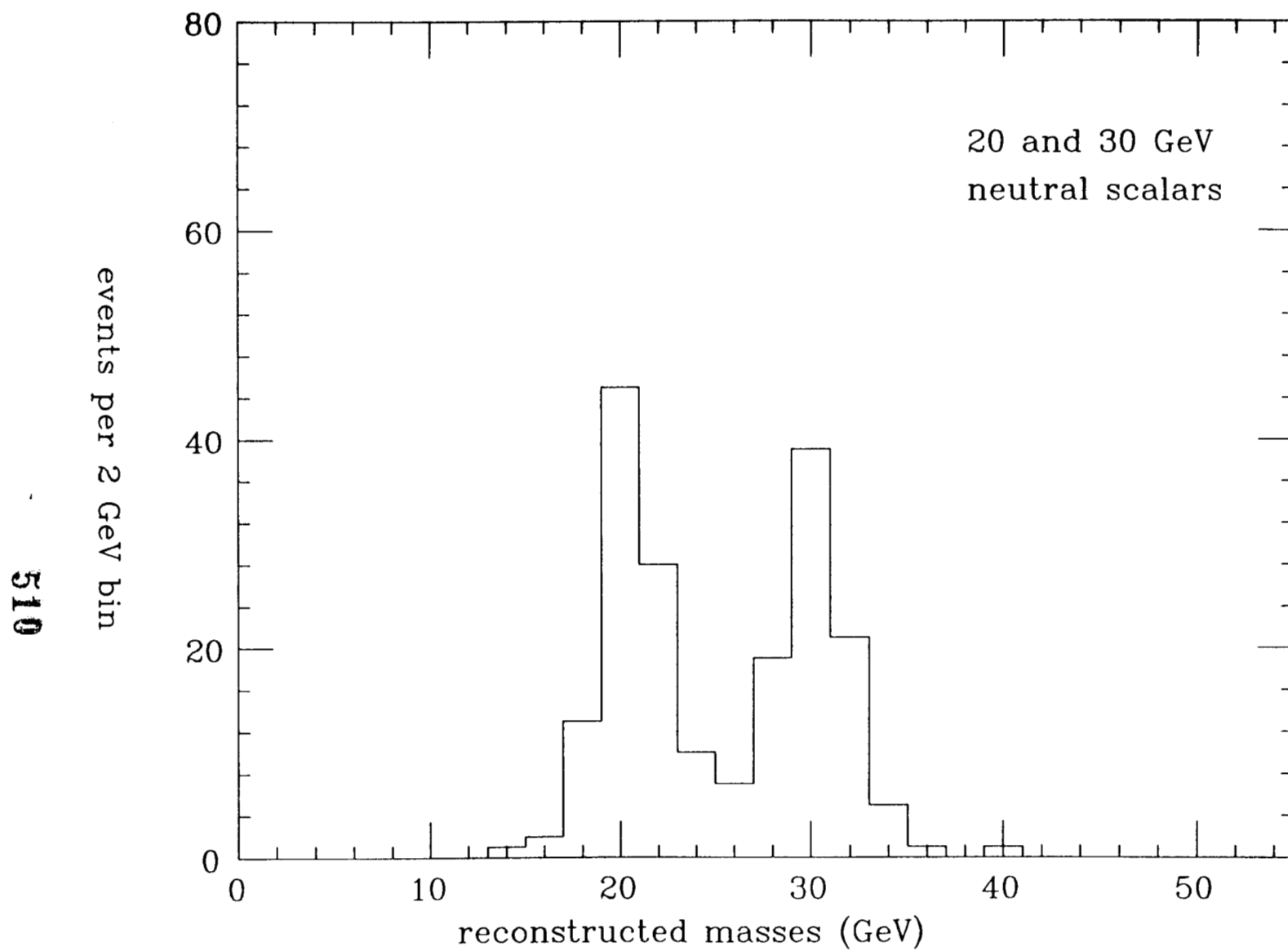


Fig. 9. The reconstruction is done with the jet energies scaled by the same factor as the momenta. Tracking and ID are used.

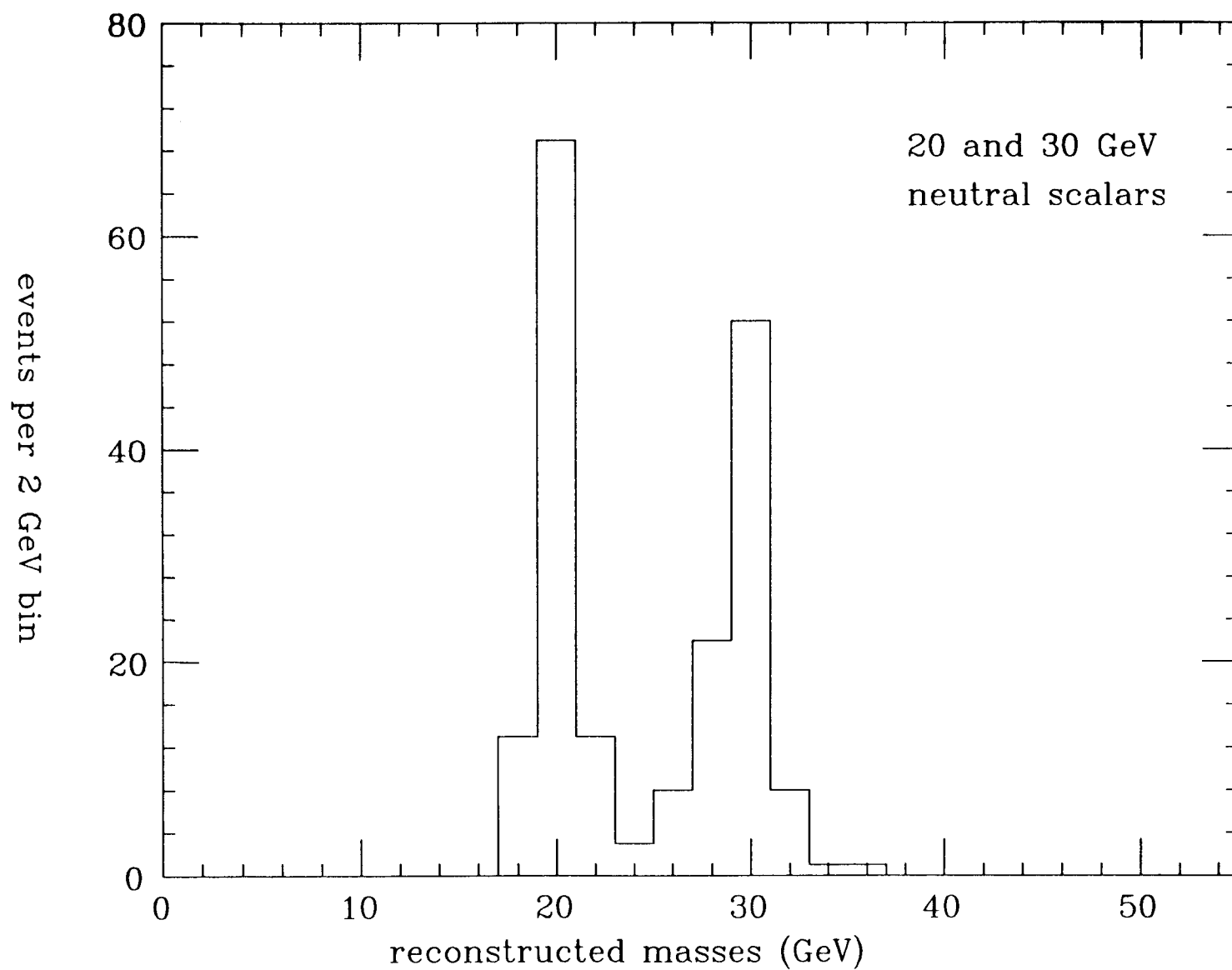


Fig. 10. The analysis for fig. 9 is repeated, but with the energies instead constrained by the b quark mass (SLD best).

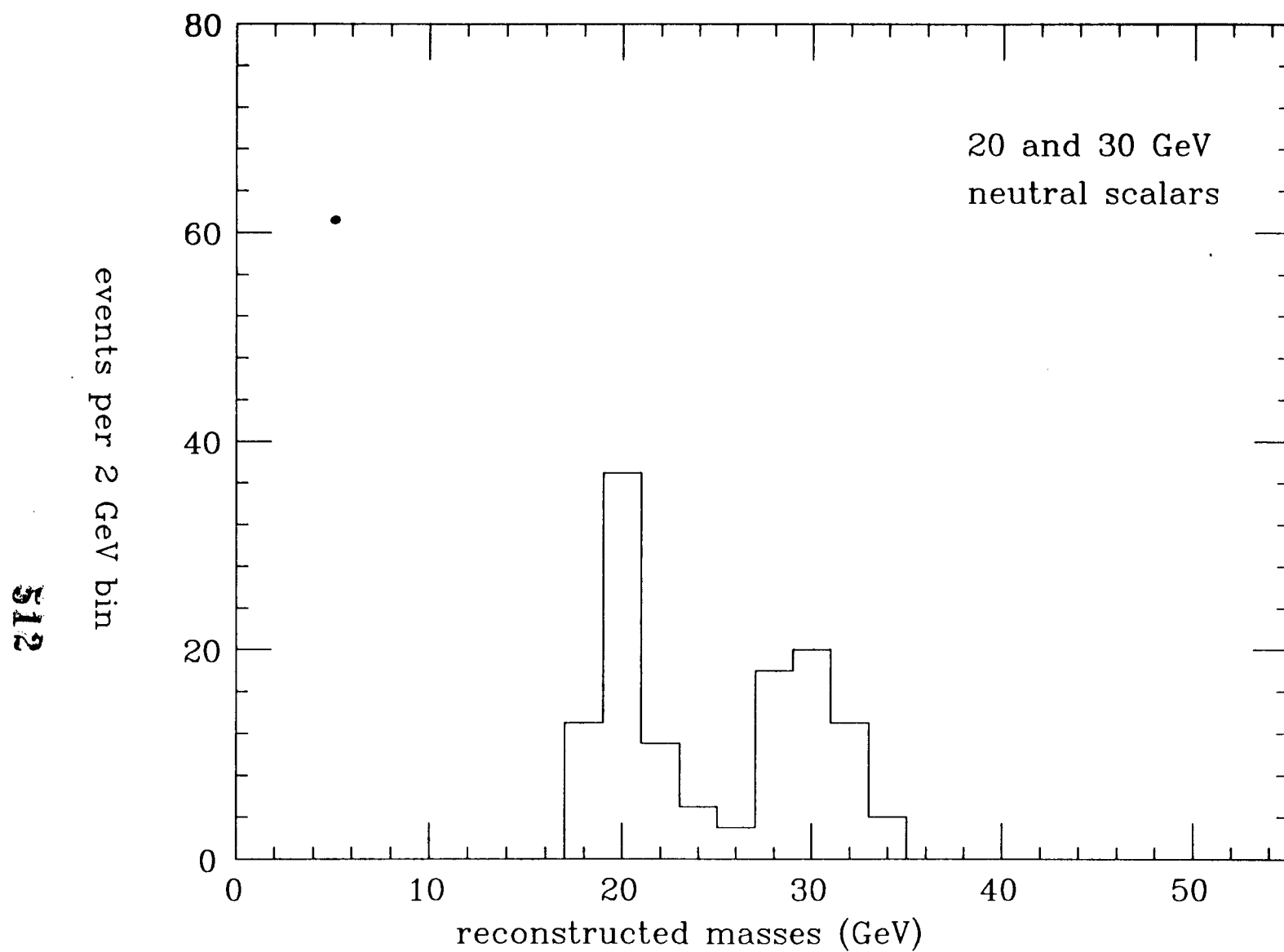


Fig. 11. To simulate not having hadronic calorimetry, particles tagged as K-longs are removed from the Fig. 10 analysis.

The Search for New Particles with the SLD at the Stanford Linear Collider

P.C. ROWSON¹

C. ARROYO¹, A.O. BAZARKO¹, T. BOLTON¹, J. BRAU²,
M.H. SHAEVITZ¹, S.R. SMITH¹, R.V. STEINER¹,
A. WEIDEMANN³, R. WHITE¹, C. ZEITLIN²

¹Department of Physics, Columbia University, NY, NY 10027

²Department of Physics, University of Oregon, Eugene, OR 97403

³Department of Physics, University of Tennessee, Knoxville, TN 37996

Introduction

A primary function of any colliding beam experiment at a new energy range is to search for new states and to extend limits in the event that these states are not seen. For an e^+e^- experiment operating in the Z^0 resonance region, assuming it is kinematically allowed, a variety of new particles are expected to be produced copiously and with distinctive experimental signatures; examples include top hadrons and hadrons due to the production of a fourth generation down-type quark (b'). If favorable decay mechanisms are assumed, significant mass limits can be extracted for these particles from very small data sets, as the Mark II collaboration has demonstrated with fewer than 400 Z^0 decays. At the other extreme, there are hypothetical states for which direct detection will be challenging even for event samples of 10^4 Z^0 's, and states that will require high precision measurements to observe indirectly. Exotic leptons produced via potentially small mixing effects or weak couplings are an example of the former, while massive neutral vector bosons are in the latter category.

Presumably, by the time the SLD begins its physics run the Mark II will have already studied the most accessible topics and the focus of new particle searches at the SLC and LEP will be on the more exotic species. However, in the following report our working group has examined several topics of interest with an eye towards clearly establishing the capabilities of the SLD in both the low and high statistics realms. Due to the multiplicity of models that predict new fermions our study is not exhaustive, nevertheless the chosen topics are representative of both minimal extensions of and phenomena beyond the Standard Model.

Sequential Quarks and Leptons

For the purpose of this study, we will assume that the top quark is above threshold at the SLC. In fact, the best available lower mass limit from the CDF experiment at the Tevatron is $m_t > 76$ GeV at 95% confidence¹. The recent e^+e^- result from the Mark II is more directly interpretable in terms of the SLD experiment and is $m_t > 40.7$ GeV at 95% confidence²; fairly close to half the Z^0 mass (45.6 GeV)³. With the top quark inaccessible to our experiment, new sequential fermions must derive from a fourth generation.

A well known free parameter of the Standard Model is the number of generations of weak isodoublets of fermions; at SLC and LEP the effort to determine this parameter will proceed on several fronts. A precision measurement of the Z^0 resonance width is sensitive to the production of new particles, as are proposed “neutrino counting” measurements that are capable of detecting new weakly interacting neutral states. Our concern will be with direct searches, though we will make reference to the limits that are expected to derive from other analyses.

Within the minimally extended standard model all couplings to the Z^0 , both vector and axial vector, are uniquely specified. These couplings are given in Table 1 where the right-hand column refers to hypothetical heavy charged leptons (L^\pm), neutrinos (ν_L), top-type quarks (t) and bottom-type quarks (b').

Final State	v_f	a_f	New Heavy Fermions
$e^+e^-, \mu^+\mu^-, \tau^+\tau^-$	$-\frac{1}{2}[1 - 4\sin^2\theta_W]$	$-\frac{1}{2}$	L^\pm
$\bar{\nu}_e\nu_e, \bar{\nu}_\mu\nu_\mu, \bar{\nu}_\tau\nu_\tau$	$\frac{1}{2}$	$\frac{1}{2}$	ν_L
$\bar{u}u; \bar{c}c$	$\frac{1}{2}[1 - \frac{8}{3}\sin^2\theta_W]$	$\frac{1}{2}$	t
$\bar{d}d, \bar{s}s, \bar{b}b$	$-\frac{1}{2}[1 - \frac{4}{3}\sin^2\theta_W]$	$-\frac{1}{2}$	b'

Table 1: fermion couplings

Pair production of heavy fermions is suppressed by the phase space factor given below, where β is the fermion speed.

$$BR(Z^0 \rightarrow f\bar{f}) = BR(Z^0 \rightarrow \mu\mu) \times \frac{v_f^2(\frac{3\beta-\beta^3}{2}) + a_f^2\beta^3}{v_f^2 + a_f^2}$$

From this expression one can see how the production of weak isospin $-\frac{1}{2}$ fermions is more severely limited than it is for the $+\frac{1}{2}$ weak isospin partners; near threshold one has, for example, $BR(L^+L^-) \sim \beta^3$ while $BR(\nu_L\bar{\nu}_L) \sim \beta$. Relative to the leptons, quark production is enhanced by a factor of ≈ 3 due to color statistics. Hence, compared to other sequential fermions, the largest data samples will be needed to set limits on the production of new charged leptons.

Sequential Leptons

The decays of new sequential leptons proceed via the charged weak current, where the allowed modes depend on the relative masses of the charged and neutral leptons and on possible lepton generation mixing effects. Several scenarios are possible:

- $m_L > m_{\nu_L}$ and both are $< m_Z/2$

$L^- \rightarrow W^- \nu_L$ decays occur.

ν_L is stable in the absence of mixing and detectable via neutrino counting.

With mixing, $\nu_L \rightarrow W^+ l^-$ with rate proportional to mixing parameter $|U_{Ll}|^2$.

- Only m_{ν_L} OR m_L is $< m_Z/2$

$L^- \rightarrow W^- \nu_l$ via mixing, or ...

$\nu_L \rightarrow W^+ l^-$ via mixing,

where in both cases the decay rate is proportional to mixing parameter $|U_{Ll}|^2$.

For our studies we have chosen the following complementary cases for charged and neutral leptons:

$$L^- \rightarrow W^- \nu_L \text{ without mixing, and } \nu_L \rightarrow W^+ l^- \text{ via mixing}$$

For the charged lepton decays, the difference $m_L - m_{\nu_l}$ is assumed to be large, and for the neutral decays, the charged lepton is taken to be too massive to be produced at the Z^0 .

The best available limits on heavy charged leptons are $m_L > 41 \text{ GeV}/c^2$ from the UA1 collaboration⁴, and $m_L > 28 \text{ GeV}/c^2$ from the TRISTAN experiments⁵. We have taken the easily interpretable e^+e^- result as a benchmark; our studies consider $m_L \geq 30 \text{ GeV}/c^2$. For the charged lepton analysis three methods have been studied. The second and third techniques require respectively a single isolated lepton in the event and a final state “ $e\mu$ ” signature; we will not discuss these methods here, and instead refer the reader to the chapter on sequential leptons written by Tim Bolton. The method best suited to the analysis of data samples of $10^4 Z^0$ events does not require lepton identification, and thus does not suffer the statistical loss due to the leptonic decay rate of $\approx 15\%$. In this approach, a measure of the non-planar topology of an event, the “acoplanarity”, is calculated for each event, and is defined by:

$$\cos \theta_A = \frac{(\hat{n}_1 \times \hat{t}) \cdot (\hat{n}_2 \times \hat{t})}{|\hat{n}_1 \times \hat{t}| \cdot |\hat{n}_2 \times \hat{t}|}.$$

Here \hat{t} is the thrust direction used to divide the event in half, and the \hat{n}_i are visible energy unit vectors on the two sides of the event. The electromagnetic and hadronic calorimeters are used to determine both the energy vectors and the thrust, with the addition of drift chamber data used for minimum ionizing tracks.

Our monte-carlo studies generated heavy leptons of masses from 30 to 45 GeV/ c^2 , as well as conventional quark production hadronic, two-photon and tau lepton events. The massive lepton decays produce highly acoplanar events; for properly chosen cuts background from conventional sources is entirely due to detector acceptance limitations. We have chosen a cut at $\theta_A > 0.3$ radians, supplemented by the requirement that the polar angle of the thrust axis satisfy $|\cos \theta_{thrust}| < 0.8$. Due to the high degree of hermiticity in the SLD, the background has been found to be small. For 10^4 produced Z^0 's, 7.5 background events are expected, all due to hadronic events. The efficiency for the signal is 0.51, independent of the lepton mass, and the number of detected events is found to be 53, 31 and 9.6 for $m_L = 30, 35$ and 40 GeV/ c^2 respectively. The conclusion of this study is that with 10^4 Z^0 events the SLD should be able to set mass limits on the production of sequential charged leptons at about 40 GeV/ c^2 . We have also used a parameterized simulation of the Mark II detector⁶ to estimate that with a similar calorimetric analysis the Mark II could set mass limits at < 35 GeV/ c^2 , where the optimal cuts were found to be relatively tight ($\theta_A > 0.5$ and $|\cos \theta_{thrust}| < 0.5$) due to the limited acceptance of this device and its lack of hadronic calorimetry.

The search for heavy fourth generation neutrinos assumes that decays occur via lepton family mixing. As mentioned earlier, we have assumed that the charged lepton partner is heavier than the neutrino. We therefore can expect the following experimental signatures:

$$\nu_L \rightarrow l^- + \text{hadrons} \quad \text{or} \quad \nu_L \rightarrow l^- + l'^+ \nu_{l'},$$

where the purely leptonic mode occurs $\approx 25\%$ of the time. Due to the fact that the heavy neutrino lifetime scales as

$$\tau \sim \tau_\mu \left(\frac{m_\mu}{m_{\nu_L}} \right)^5 |U|^{-2},$$

$$\text{with } |U|^2 = |U_{Le}|^2 + |U_{L\mu}|^2 + |U_{L\tau}|^2,$$

lifetimes are very short and decay vertices are not visible unless the mixing param-

eter $|U|^2 < 10^{-8}$. The interesting case where the heavy neutrino decay can be seen has not been studied in detail, however such behavior is likely to give a spectacular signature.

Theory provides little guidance for a choice of mixing scenarios, though a reasonable assumption is $|U_{Le}| < |U_{L\mu}| < |U_{L\tau}|$. We have focused on the experimentally most challenging case where mixing is entirely to τ leptons. Our procedure was then to attempt to cover as large a region of the m_{ν_L} versus $|U|^2$ plane as possible. Complementing any direct search for heavy neutrinos, measurements of the Z^0 resonance width will provide limits which are independent of mixing angles. For a sample of 10^5 events, the width measurement should exclude new heavy neutrinos with masses of $< 41 \text{ GeV}/c^2$. Neutrino counting measurements, by virtue of the fact that stable neutral objects are included by the search, are sensitive to the small mixing region, but are limited in mass reach. Together, these methods will eventually cover the kinematically available parameter space.

Our preferred method to search for a fourth generation neutrino is to look for isolated electrons or muons opposite to a jet, since this mode will constitute $\approx 44\%$ of all decays and is a fairly clean signature. Additional cuts on the event are designed to assure that the lepton side of the event contains only the expected decay products of a leptonic neutrino decay, and that the opposite side of the event is consistent with semi-leptonic neutrino decay; the reader is referred to T. Bolton's chapter for details. It is found that efficiencies vary from around 15% at the smallest masses ($5 \text{ GeV}/c^2$) to 1% at the kinematic limit. Backgrounds for 10^4 Z^0 's are estimated at 1.7 events from hadronic production, and less than 1.0 event due to two-photon processes. Due to the high production rates of heavy neutrinos, this allows detection of neutrinos with masses just over $40 \text{ GeV}/c^2$, and with the limit improved if mixing to electrons and muons is allowed. The best available limit is based upon a search for isolated tracks; the Mark II collaboration has announced 95% C.L. limits at $42.4 \text{ GeV}/c^2$ using 310 hadronic Z^0 decays², where full mixing to τ leptons is assumed. It is clear that the Mark II and LEP experiments may exhaust the topic of heavy neutrinos, and it is possible that this

topic will no longer be of interest by the time SLD begins data taking.

Sequential Quarks

The possibility exists that the fourth generation weak isospin $-1/2$ quark, usually known as the b' quark, is less massive than the third generation top quark. If this is the case $\bar{b}'b'$ production will be copious at the Z^0 resonance, and their decays will be distinctive. For this reason it is evident from the start that the search for b' quarks will most likely be accomplished by the Mark II or by LEP. Nevertheless, we have undertaken a study of the SLD's capabilities in this measurement for the purposes of comparison, and with an eye towards any possible decay processes that might require the unique capabilities of our detector.

We are assuming that $m_t > M_Z/2$ so that top is not produced, and that $m_{b'} < M_Z/2$. If this unusual mass hierarchy occurs, then the b' will undergo the KM suppressed charged current decay to charm

$$b' \rightarrow W^- c.$$

In the plausible circumstance that the KM matrix elements satisfy

$$\frac{|V_{b'c}|}{|V_{bt'}||V_{b't'}|} < 10^{-2},$$

effective flavor-changing neutral currents (FCNCs), which occur at the one loop level, may be the dominant modes (here, the t' refers to the massive weak isospin partner of the b'). The effective FCNC modes include, for example,

$$b' \rightarrow b \text{ gluon}, \text{ and } b' \rightarrow b\gamma,$$

where the first channel would lead to multi-jet events and the second to isolated high energy photons.

The production cross section for b' is large, about 6% of the total Z^0 cross section for b' masses of 40 GeV/ c^2 , allowing one to establish good mass limits with small data sets. The Mark II lower limits on $m_{b'}$ range from a high of 45 GeV/ c^2 if purely charged current decays to charm are assumed, or if one takes $BR(b' \rightarrow b\gamma) > 40\%$, to a low of 41 GeV/ c^2 if the decays are purely $b' \rightarrow b \text{ gluon}^2$. Our studies show that the SLD cannot improve significantly on these results for the case of the charged current decay. Details of an analysis based on an isolated lepton signature are given in the chapter by A. Weidemann and C. Zeitlin, where it is found that background contamination can be held below 5%, with better than 10% efficiency for the signal. It may possible to exploit the superior capabilities of the SLD with respect to bottom hadron detection in the $b' \rightarrow b \text{ gluon}$ channel; this avenue has not yet been investigated.

Non-standard Leptons

Various extensions of the Standard Model require the existence of exotic new leptons; grand unified theories (GUTs), supersymmetry (SUSY), composite models and left-right symmetric theories are a few prominent examples. The new leptons suggested by these models are characterized by non-standard production mechanisms at Z^0 energies and unusual decay properties. We have chosen to study two specific classes of new leptons in order to ascertain the capabilities of the SLD for a set of widely different experimental challenges.

Singly-produced Neutral Heavy Leptons

If weak isospin *singlet* neutral leptons exist, and they couple to ordinary leptons via mixing, the GIM mechanism that forbids flavor changing neutral currents at tree level no longer applies (this is true because the GIM mechanism will only work if all neutral leptons belong to the same representation of weak isospin). Under these circumstances, neutral heavy leptons (NHLs) can be singly produced, and it is possible to probe lepton masses up to M_Z . A new feature of this process is that the production process $Z^0 \rightarrow L^0 \nu$ is suppressed by a phase space term and

by the mixing parameter :

$$\sigma(Z^0 \rightarrow L^0 \nu) = \sigma(Z^0 \rightarrow \nu_l \bar{\nu}_l)(1 - m_L^2/s)^2(1 + m_L^2/2s)^2|U_{Ll}|^2.$$

Pair production of these NHLs is doubly suppressed, and was ignored in this study. The decays of singlet NHLs may occur via charged currents or FCNCs,

$$L^0 \rightarrow W^+ l^- \text{ or } L^0 \rightarrow Z^0 \nu_l,$$

in the ratio 1 : 2 where in both cases the matrix element is proportional to $|U_{Ll}|^2$. Hence if production is reduced by small mixing, the lifetime of the NHL is necessarily increased.

In our analysis we have taken advantage of two useful experimental signatures: 1) single production of NHLs will, for NHL masses up to 80 GeV/ c^2 or so, lead to a distinctive “monojet” topology as the decay of the heavy lepton recoils against the unseen neutrino, and 2) the class of charged current decays where the W boson decays hadronically have small missing energy and may be used to reconstruct a NHL mass peak if $m_L < M_Z/2$. Present limits are due to beam dump experiments⁷ which exclude masses below ≈ 1.5 GeV/ c^2 , fixed target neutrino experiments⁸ which exclude the region $|U|^2 > 3 \times 10^{-4}$ for low masses up to $|U|^2 > 10^{-2}$ for $m_L = 10$ GeV/ c^2 , and “monojet” searches at the e^+e^- storage rings PEP and PETRA⁹ that exclude a region up to masses just below 20 GeV/ c^2 for $|U|^2 > 10^{-2}$. Mixing above $|U|^2 \approx 10^{-2}$ is ruled up by precision beta decay measurements.

The details of our monte-carlo study are given in the chapter by A. Bazarko and M. Shaevitz. To summarize, events are selected by the following three classes of cuts:

- Monojet cuts, that require a jet opposite to very small visible energy.
- Acceptance cuts, which are fairly loose owing to the SLD’s good hermiticity, particularly at small angles with respect to the beam direction.

- $\tau^+\tau^-$ and two-photon cuts, which require a minimum track multiplicity and jet invariant mass.

Both the case where mixing occurs equally to all lepton families and only to τ leptons were studied. The signal efficiency peaks at about 60% for $m_L \sim 20 \text{ GeV}/c^2$, dropping to 10% for masses of either a few GeV/c^2 or $\sim 80 \text{ GeV}/c^2$. Backgrounds due to hadronic events, tau pair production and two-photon events are small; the total background is less than 5 events per $10^5 Z^0$'s. Clean mass peaks were reconstructed for $m_L = 25 \text{ GeV}/c^2$ even if mixing was exclusively to τ , albeit with $\approx 30\%$ the efficiency of the "democratic mixing" case.

It is found that significant improvements on existing limits for NHL masses above $10 \text{ GeV}/c^2$ are possible with a sample of $10^5 Z^0$'s. Due to improved angular coverage and calorimetry, the SLD is found to have a slight ($\approx 20\%$) advantage in efficiency over the Mark II for data samples of 10^5 events. No advantage over a typical LEP detector is expected.

Excited Muons

The idea that leptons are composite objects that exhibit a spectrum of excited states follows a line of reasoning dating back to atomic physics. Without recourse to a specific constituent model, one can appeal to general principles and study a class of models of excited leptons via an effective Lagrangean, where a constant with the dimensions of mass incorporates what is unspecified about the mechanism of compositeness. The Lagrangean describes spin 1/2 fermions with effective magnetic dipole coupling to the vector fields¹⁰:

$$\mathcal{L}_{eff} = \sum_V \frac{e}{\Lambda} \bar{f}^* \sigma_{\mu\nu} (1 - \gamma_5) f \partial_\mu V_\nu + h.c.$$

Here the sum is over vector fields (A,W,Z) and Λ is the compositeness scale in TeV.

We have examined the special case of the electromagnetic decays of an excited muon, μ^* , singly produced as in

$$e^+e^- \rightarrow \mu\mu^* \rightarrow \mu\mu\gamma,$$

where one searches for a $\mu\gamma$ mass peak. The experimentally clean $\mu\mu\gamma$ final state simplifies the analysis and results in a well understood background that is entirely due to QED processes, after our cuts. The best available limits on the production of excited muons are from the TRISTAN experiments¹¹, which have presently excluded the region in the mass versus coupling plane from $m_{\mu^*} < 58 \text{ GeV}/c^2$ with $\Lambda < 10^{-3}\text{TeV}$ to $\Lambda < 3 \times 10^{-1}\text{TeV}$ for masses just above the pair production threshold (about $30 \text{ GeV}/c^2$). Below threshold, pair production analyses exclude excited muons for all values of Λ , since pair production occurs at full strength.

The analysis proceeded by demanding that only $\mu^+\mu^-\gamma$ is detected, with an additional requirement that the missing energy in the event be less than 11 GeV in order to eliminate the expected $\tau\tau\gamma$ background; details may be found in the chapter by C. Arroyo and R. Steiner. The QED background was simulated with the MCBREMUS monte carlo. The invariant mass was formed for each $\mu\gamma$ pair, and the resulting mass spectrum was studied for several values of m_{μ^*} up to $80 \text{ GeV}/c^2$ and for integrated luminosities from 10^4 to 10^6 Z^0 's. A significant improvement in mass resolution from $3 \text{ GeV}/c^2$ to $0.2 \text{ GeV}/c^2$ was made by applying a beam energy constraint on the final state 4-vectors. The background due to $\tau\tau\gamma$ and hadronic events was found to be negligible over the full range of sample sizes that were studied.

The absence of any signal will allow the SLD to exclude a large region of the Λ versus m_{μ^*} plane for 10^4 Z^0 's; for 10^5 events masses up to $80 \text{ GeV}/c^2$ with Λ approaching 1 TeV are ruled out. A measurement of this type, particularly due to the fact that the beam energy constraint provides much of the precision, is not expected to show significant dependence on the apparatus. Our study reveals only a small advantage over the Mark II for the SLD; LEP experiments can be expected to do as well as we can.

Additional Z Bosons

Various models postulate gauge symmetries beyond the $SU(3) \times SU(2) \times U(1)$ of the Standard Model; examples include left-right symmetric theories, E_6 based GUT's and minimal modifications of the SM in which quarks and leptons transform under separate gauge groups¹². In general, additional $U(1)$ symmetries in these models lead to additional vector bosons with non-standard coupling to Standard Model fermions, and these new couplings modify measurable electroweak parameters. New neutral vector bosons " Z' " will have the same quantum numbers as the the Standard Model Z^0 and can therefore quantum mechanically mix with the Z^0 ; the strength of the mixing can be characterized by a model dependent mixing angle θ_{mix} . Expected experimental effects include:

- Shifts of M_Z and Γ_Z .
- Modifications of the hadronic and leptonic partial widths and cross sections in Z decays.
- Measurable effects on the forward-backward (FB) and and polarized left-right (LR) production asymmetries.

Present neutral current data allows a region in $M_{Z'}$ versus θ_{mix} space from about 130 GeV/ c^2 for large mixing to just below 400 GeV/ c^2 for $|\theta_{mix}| > 0.02$ ¹³. Unless the the Z' boson is light enough to be observed directly at the SLC or LEP (a possibility that is essentially excluded by present data), only high precision measurements of the type listed above can reveal the presence of additional vector bosons at present e^+e^- colliders. The experimetal picture is complicated by the effects of radiative corrections, particularly those effects due to a heavy top quark. Until the magnitude of these electroweak loop corrections are known (for example once the mass of the top quark has been measured), any search for Z' bosons based on a determination of electroweak parameters will be beset by ambiguities. However, it has been recognized for some time that one should be able to minimize the confusion by a propitious choice of a set of observables and a measurement of their correlations¹³. By an appropriate linear combination of observables, one can

construct a measurable quantity for which the troublesome “oblique” radiative corrections due to top quark vacuum polarization loops nearly cancel. For example, it may be possible to combine measurements of the LR asymmetry with measurements of the polarized FB asymmetry since their respective oblique corrections are the same up to a known proportionality constant. The reader is referred to the chapter by P.C. Rowson for details.

One’s ability to make precision measurements of electroweak parameters such as the Z^0 mass, width, partial widths and LR asymmetries depends more strongly on the performance of the accelerator (luminosity, energy spread and polarization) than it does on the detector used. Thus the SLD will enjoy an advantage over the LEP experiments only to the extent that the SLC will provide longitudinally polarized beams and LEP will not. The advantage of polarization is equivalent to a factor of ≈ 100 in effective luminosity.

The search for Z' bosons might proceed in two stages, as successively larger data samples become available:

1. Observation of non-standard Z^0 partial widths (e.g. $\Gamma_{\mu\mu}$, $\Gamma_{hadrons}$, and their ratio). A dramatic signature allowed in some models is a *downshifted* total width.
2. Establishment of a less ambiguous effect by precision measurements of weak asymmetries using polarized beams. At this stage, specific models can be distinguished and their parameters determined.

It should be possible to probe mixing angles $|\theta_{mix}|$ less than 0.02 with 10^5 events using the LR asymmetry. Shifts of M_Z will be detectable for $M_{Z'}$ up to perhaps $400 \text{ GeV}/c^2$, though these results will be hard to interpret until precise $M_Z - M_W$ measurements and the mass of the top quark are available from the hadron colliders. Mixing angles smaller than 0.01 will be probed with 10^6 events.

Summary

The following table summarizes our findings for all new particles that were studied; sensitivities for the indicated sample sizes are shown. A \star indicates a possible advantage for the SLD over the LEP experiments.

New Particle	Sensitivity	# Z^0 's
L^-	$m_L < 40 \text{ GeV}/c^2$	10^4
ν_L	$m_{\nu_L} < 40 \text{ GeV}/c^2, \tau \text{ mixing only}$	10^4
b'	$m_{b'} < 45 \text{ GeV}/c^2$	10^4
L^0	$m_L < 10, 50 \text{ GeV}/c^2, U ^2 > 10^{-3}, 10^{-2}$	10^5
μ^*	$m_{\mu^*} < 80 \text{ GeV}/c^2, \Lambda < 1 \text{ TeV}/c^2$	10^5
$\star Z'$	$M_{Z'} < 400 \text{ GeV}/c^2 \text{ for } \theta_{mix} > 0.02$	10^5

Table 2: New particle searches with the SLD

References

1. CDF Collaboration, Lepton/Photon Symposium, August 1989, Stanford, CA.
2. Mark II Collaboration, HEP'89, September 1989, Madrid, Spain.
3. G.S. Abrams *et al.*, Phys.Rev.Lett.,63:724,1989.
4. UA1 Collaboration, Phys.Lett.,198B:271,1989.
5. AMY Collaboration, Lepton/Photon Symposium, August 1989, Stanford, CA. VENUS Collaboration, Phys.Rev.Lett.,61:915,1988.
6. T. Bolton, "A Simple Mark II Detector Simulation", SLD note in preparation, September 1989.
7. For example: BEBC Collaboration, PITHA 81/01,1981.
8. S.R. Mishra *et al.*, Phys.Rev.Lett.,60:1618,1988.
9. Two representative examples are:
MAC Collaboration, Phys.Rev.Lett.,54:2477,1985.. and JADE Collaboration, Phys.Lett.,155B:288,1985.
10. K. Hagirawa *et al.*, Z.Phys.C, 29:115,1985.
11. For a review, K. Hiragawa & S. Komamiya, KEK-TH-145,1987.
12. H. Georgi *et al.*, Phys.Rev.Lett.,62:2789,1989.
13. See, for example, B. Lynn *etal*, Nucl.Phys.B310:237,1988.

Fourth Generation Sequential Lepton Searches at SLD

T. BOLTON

Department of Physics, Columbia University, NY, NY 10027

1. Fourth Generation Leptons

A simple extension to the standard model is the addition of a fourth doublet of leptons (ν_4, L_4). The existence of such leptons with mass $< 45 \text{ GeV}/c^2$ will likely be decided by Z^0 experiments.

SLD is well suited for these studies. However, LEP will most likely blow our doors off if Mark II and CDF don't do it first.

2. Charged Sequential Leptons

2.1. BASIC FORMULAE

To first order:

$$B(Z^0 \rightarrow L_4^+ L_4^-) = B(Z^0 \rightarrow \mu^+ \mu^-) \frac{g_v^{\mu^2} \frac{(3\beta - \beta^3)}{2} + g_a^{\mu^2} \beta^3}{g_v^{\mu^2} + g_a^{\mu^2}}.$$

Since $g_v^{\mu^2} = (\frac{1}{2} - 2 \sin^2 \theta_W)^2 \simeq 0.002 \ll g_a^{\mu^2} = 0.5^2$, the rate falls off as β^3 over most of the range.

Assuming a heavy top quark and neglecting KM suppressed transitions, the L_4 decay width is:

$$\Gamma_{L_4} = \frac{G_F^2 m_{L_4}^5}{192\pi^3} (1 + 1 + 1 + 3 + 3),$$

where the three lepton and two quark families contribute as shown. Thus $B_{c\nu} = B_{u\nu} = 3B_{\tau\nu} = 3B_{\mu\nu} = 3B_{e\nu}$. The event topologies break up into three classes, lepton-lepton, lepton-jets, and jets-jets, in the approximate ratio 1:4:4.

2.2. EXISTING AND PROJECTED SEARCH RESULTS.

A UA1 result^[1] of $m_{L_4} > 41 \text{ GeV}/c^2$ is the best published limit; however, the methodology employed is complicated. A more unambiguous result is $m_{L_4} > 28 \text{ GeV}/c^2$ by the Tristan experiments.^[2] Tristan should have little trouble probing lepton masses up to half the center-of-mass energy, which might be $m_{L_4} \gtrsim 35 \text{ GeV}/c^2$ by the time SLD runs in 1990.

Mark II projects a sensitivity to L_4 masses of 20,25,30 and 35 GeV/c^2 with a data sample of $\sim 1000, \sim 1500, \sim 2500$, and $\sim 4000 \text{ } Z^0$, respectively. They will need 10-20 thousand Z^0 to reach $m_{L_4} = 40 \text{ GeV}/c^2$ and $\sim 50,000 \text{ } Z^0$ to reach 45 GeV/c^2 .^[3]

As will be shown, SLD can do better than Mark II with $10^4 \text{ } Z^0$. It is, however, difficult to see how any of the LEP experiments will do much worse than SLD. UA1, UA2, or CDF could also preempt this topic by 1990.

2.3. MONTE CARLO DETAILS

We have used the Monte Carlo generator TIPTOP, written by S. Jadach and J. Kuehn^[4] and SLD-ized by A. Wiedeman, to simulate heavy lepton production and decay. This program, called MCTIPT in SLD,^[5] includes the standard production and decay matrix elements, effects from initial state radiation, beam polarization, finite fourth generation neutrino masses, and W -propagator effects.

MCLUND was used for simulating hadronic event backgrounds. Specifically, the $\sim 90\text{K}$ events on the data sets DSTUDS, DSTC, and DSTB were used. These

events were generated with the Parton Shower option and the Peterson c and b quark fragmentation functions with $\epsilon_c = -0.075$ and $\epsilon_b = -0.03$. For two-photon simulation, the generator MCTWOG,^[6] SLD-ized from Mark II's GGDEPA via a TPC intermediate state by C. Zeitlin was used. Tau backgrounds were generated using MCLEPT,^[7] an SLD-ized version of Mark II's LULEPT.^[8]

Detector simulation of SLD was performed using FSIM. A parametric version of a Mark II simulator was also written and used for comparison purposes.^[9]

2.4. INCLUSIVE ANALYSES

The main analysis focuses in on the 88% of the topologies that have jets in the final state. As a backup, we have also performed separate analyses of the clean all-lepton final state topologies and of the lepton-jet topology. Only $m_{L_4} \geq 30\text{GeV}/c^2$ was considered.

The key ingredient in these analyses is a cut on event *acoplanarity*,^[10] which is defined by:

$$\cos \theta_A = \frac{(\hat{n}_1 \times \hat{t}) \cdot (\hat{n}_2 \times \hat{t})}{|\hat{n}_1 \times \hat{t}| \cdot |\hat{n}_2 \times \hat{t}|}.$$

Here, \hat{t} is the thrust axis, which is used both to divide the event into two halves and to define planes in the two halves; and \hat{n}_1 and \hat{n}_2 are the visible energy vectors in each half of the event.

The thrust axis and visible energy vectors are calculated using the calorimeter cluster information, supplemented with the drift chamber for minimum ionizing tracks.^[11] The calorimetry particle identification is used, when available, to correct for the π/e ratio (taken as 0.85). If a cluster cannot be identified as hadronic or electromagnetic, then the energy in the first two sections of the calorimeter is treated as electromagnetic, and the remaining energy is treated as hadronic.

We also determined the thrust axis and visible energy only from particle (PHPART) information, using the drift chamber for charged tracks and the calorimeter for photons and neutral hadrons.^[12]

The Mark II detector would have to follow this latter kind of procedure, except that no neutral hadrons would be detected. This lack of neutral particle detection, coupled with their reduced solid angle coverage should reduce their ability to reject hadronic backgrounds. To attain a quantitative comparison, the MARKII simulator was used.^[13]

Table I shows the number of background events passing different acoplanarity cuts from various $q\bar{q}$ final states, assuming 10,000 produced Z^0 . "Par" implies that quantities were calculated only from PHPART "particle" properties; "kal" means that PHKAL calorimeter clusters were used. Figures 1 and 2 show some important kinematic distributions for Lund events passed through FSIM and the MARKII simulator, respectively.

Table I. Background Estimates for $L_4^+ L_4^-$

$q\bar{q}$	SLD _{kal} $ \cos \theta_{th} < 0.8$ $\theta_A > 0.3$	SLD _{kal} $ \cos \theta_{th} < 0.8$ $\theta_A > 0.5$	SLD _{par} $ \cos \theta_{th} < 0.8$ $\theta_A > 0.5$	"M2" $ \cos \theta_{th} < 0.7$ $\theta_A > 0.3$	"M2" $ \cos \theta_{th} < 0.5$ $\theta_A > 0.5$
$u\bar{u}, d\bar{d}, s\bar{s}$	1.1	0.4	2.9	41.1	11.8
$c\bar{c}$	1.8	0.4	0.6	7.6	1.3
$b\bar{b}$	4.6	1.3	0.6	6.9	1.6

Several interesting features emerge from the table. First, a thrust axis cut is necessary to keep events with large missing energy down the beam pipe from dominating the background. Relaxing the $|\cos \theta_{th}| < 0.8$ requirement increases the background level by a factor of 4-5 for SLD. The MARK II detector, mainly because of its inability to measure charged particle energy outside its drift chamber acceptance, is

much more susceptible to high acoplanarity events caused by lack of acceptance. To get the Mark II background to the level of SLD, the thrust axis cut had to be reduced to $|\cos \theta_{th}| < 0.5$. For SLD, the PHPART and PHKAL methods yield similar total backgrounds; however, the PHPART based cuts allow in more light quark background. These extra background events all contain a high energy neutral shower that overlaps with a charged particle. The neutral shower is associated with the charged track, but the particle energy is taken from the drift chamber momentum. The net result is a spurious high missing energy/momentum. Mark II will suffer the same problem, but even more so since they cannot pick up the neutral hadrons. To compensate, the acoplanarity cut had to be boosted to $\theta_A > 0.5$ for Mark II.

For the analysis of the signal, the cuts $|\cos \theta_{th}| < 0.8$ and $\theta_A > 0.3$ were adopted. This resulted in a detection efficiency of 0.51 for $m_{L_4} > 30 \text{ GeV}/c^2$, essentially independent of mass. The “Mark II” cuts, $|\cos \theta_{th}| < 0.5$ and $\theta_A > 0.5$, yielded an average efficiency of 0.18. These numbers and the branching ratio formula yield Table II, which gives the number of detected events vs. mass for 10,000 produced Z^0 events.

Table II.Inclusive $L_4^+ L_4^-$ Analysis

m_{L_4}	produced/ $10^4 Z^0$	detected-SLD	detected-M2
30.0	105	53.	19.
32.5	84	43.	15.
35.0	60	31.	11.
37.5	39	20.	7.0
40.0	19	9.6	3.9
42.5	9	4.6	1.6
45.0	2	0.9	0.3

A few checks were performed to see whether the background estimates were sensitive to Lund fragmentation parameters. No significant differences were observed between the estimate obtained from the default Lund values and three other cases: Lund parton shower with Λ raised to 0.75 GeV, second order QCD matrix elements with Λ raised to 0.75 GeV, and default shower parametrizations but the Peterson fragmentation parameters lowered to $\epsilon_c = -0.03$ and $\epsilon_b = -0.01$.

To conclude this section, SLD could have a statistically significant observation of $L_4^+ L_4^-$ pair production with $10^4 Z^0$ up to 40. GeV/ c^2 in mass. If Mark II were to attempt this sort of calorimeter based analyses, they would be limited to masses < 35 GeV/ c^2 for the same number of Z^0 .

2.5. LEPTON-JET ANALYSIS

A possible problem with the inclusive search for $L_4^+ L_4^-$ based on high acoplanar events is the dependence on the estimate of the background. A real analysis requires a careful study of the effects of fragmentation model parameters on the final answer. A way to avoid this problem is to search for events in which one L_4 decays to $\ell\nu\nu$ and the other to $jets + \nu$. This topology is preferred by Mark II.

For this analysis, the thrust axis is first used to divide the event in half. Next, a search is performed for isolated leptons (e or μ). The isolation criteria are that the lepton be identified as such in PHPART, that its energy be greater than 2. GeV, and that it be at least 12.8° from any other charged track or neutral cluster. The half of the event containing the highest energy lepton is considered as the “lepton” half. The lepton half of the event is required to have at least half of its visible energy taken up by the lepton. The opposite “jet” half is required to have at least 5 GeV of visible energy and at least 5 total particles from PHPART. The reason that the lepton half is allowed to have more than just the charged lepton is to take into account that the two event halves can mix with each other at the masses of interest ($m_{L_4} > 30$ GeV/ c^2). This selection procedure results in detection efficiencies and number of detected events shown in Table III.

The estimated background is 1.9 events from Z^0 hadronic decays and $\lesssim 1$ event from two-photon interactions per 10^4 produced Z^0 .

Table III. Lepton vs. Jet $L_4^+ L_4^-$ Analysis

m_{L_4}	efficiency	detected/ $10^4 Z^0$
30.0	0.187	19.6
32.5	0.175	14.7
35.0	0.161	9.6
37.5	0.149	5.8
40.0	0.138	2.6
42.5	0.126	1.1
45.0	0.115	0.2

The sensitivity at SLD in the lepton-jet mode is $\sim 37.5 \text{ GeV}/c^2$ with $10^4 Z^0$. Mark II should have a slightly lower sensitivity due to their smaller acceptance, particularly for muons; however, the lepton-jet mode is their preferred search strategy.

2.6. ALL LEPTON MODES

The classic search mode for new charged leptons is the $e\mu$ final state. This mode can be detected with high efficiency and no background. The problem is that only 2/81 of the $L_4^+ L_4^-$ events will appear as $e\mu$. Actually, the number is a bit higher, since $e\tau$, $\mu\tau$ and $\tau\tau$ topologies all have $e\mu$ components. The total observed $e\mu$ branching fraction is 3.4% rather than 2.5%.^[14]

The requirements were that there be exactly one identified electron and one identified muon in the event, that each lepton have an energy of 2 GeV or greater, and that the two leptons be acolinear by at least 25.8° . The detection efficiency, determined almost entirely by solid angle coverage, was 0.8 for all masses above 30

GeV/ c^2 . The predicted number of detected events are given in Table IV. Within the limit of Monte Carlo statistics, no backgrounds were detected from $(\gamma)\tau\tau$ or $\gamma\gamma$ sources.

Table IV. All Lepton $L_4^+ L_4^-$ Analysis

m_{L_4}	efficiency	detected/ $10^4 Z^0$
30.0	0.80	3.1
32.5	0.80	2.3
35.0	0.80	1.7
37.5	0.80	1.1
40.0	0.80	0.6
42.5	0.80	0.2
45.0	0.80	0.05

2.7. OTHER POSSIBILITIES

The possibility that the fourth generation neutrino may have a non-zero mass has not been considered. As long as $m_{L_4} - m_{\nu_4}$ is large compared to the heaviest decay products, $m_c + m_s$ or m_τ , nothing important will change. The $L_4^+ L_4^-$ events will look even more distinct since the neutrinos will carry away more energy. As the neutrino mass approaches the charged lepton mass, phase space effects will modify the decay patterns of the L_4 . This is the “close-mass-pair” case considered first by Mark II at PEP.^[15] SLD should do well in this type of search for low multiplicity final states with high missing energy, especially since we should be less susceptible to the dominant two-photon backgrounds.

2.8. CHARGED SEQUENTIAL LEPTON SUMMARY

The SLD should be able to discover a charged sequential lepton with a mass $\leq 40 \text{ GeV}/c^2$ with a sample of $10^4 Z^0$. With this sample, our mass reach is probably 3-5 GeV/c^2 higher than Mark II. However, the β^3 threshold behavior mandates a sample of $> 10^5 Z^0$ to push up to the kinematic limit. Unfortunately, LEP has a virtual lock on this topic.

3. Sequential Heavy Neutrinos

3.1. BASIC FORMULAE

To leading order:

$$B(Z^0 \rightarrow \nu_4 \bar{\nu}_4) = B(Z^0 \rightarrow \nu_e \bar{\nu}_e) \frac{3\beta + \beta^3}{4}.$$

We use the notation “ ν_4 ” rather than “ ν_L ” because the neutrino mass eigenstates may differ from the neutrino flavor eigenstates. Neutrino mixing can thus occur, which allows the ν_4 to decay. The rate is analogous to the charged particle case:

$$\Gamma_{\nu_4} = \frac{9G_F^2 m_{\nu_4}^5}{192\pi^3} |U|^2.$$

The new feature is the mixing element:

$$|U|^2 = |U_{e4}|^2 + |U_{\mu 4}|^2 + |U_{\tau 4}|^2.$$

If there is no mixing, the neutrinos will be stable unless ν_4 is heavier than L_4 . This unusual case has not been studied in detail here. The unique signature of a pair of heavy stable “muon-like” particles would be hard to miss. We assume henceforth that ν_4 is less massive than L_4 , with the most interesting situation being $m_{L_4} > m_{Z^0}/2$.

Searches for ν_4 probe different regions of a plane of mixing angle vs. mass, usually $|U_{e4}|^2$ or $|U_{\mu 4}|^2$ vs m_{ν_4} . The best point on existing limit plots corresponds to $|U_{\mu 4}|^2 \sim 10^{-8}$, $m_{\nu_4} = 15 \text{ GeV}/c^2$. Since the neutrino branching fraction per species is large at the Z^0 , the threshold behavior is a mild linear β dependence, and the mass reach large, a vast area of mixing vs mass can be explored.

Unfortunately, SLD will arrive late again. The distinct decay signatures and robust production should enable even Mark II to exclude most of the available parameter space.

3.2. DIRECT SEARCHES VS. INDIRECT SEARCHES

We are concerned with directly observing heavy neutrinos which decay in the detector. Width measurements of the Z^0 and neutrino counting measurements also test for the existence of ν_4 .

Neutrino counting measurements generally probe low ν_4 mass and small $|U|^2$; a neutrino which decays in the detector obviously ruins the usual single photon signature. Width measurements are independent of mixing. Hence, in the absence of new physics, the ν_4 mass limit will eventually be pushed up $m_{Z^0}/2$.

An estimate has been made of the sensitivity of the various measurements. This is summarized in Fig. 3, along with the best existing limits. Obviously the width measurements are most powerful. Any measurement of a fractional number of neutrino generations requires a direct search to identify the source of the extra width. In this case, direct searches complement neutrino counting.

3.3. MONTE CARLO GENERATORS

There are a couple of subtleties for ν_4 decay generators. First, low masses are still of interest, so some attention has to be paid to thresholds. Second, small mixing can lead to long ν_4 lifetimes. A generator call MCNHL has been written to take care of both these effects.^[16] This generator uses formulae taken from a paper on close-mass lepton pairs^[15] to adjust ν_4 branching fractions as a function

of mass. The branching fractions are then fed into SLDPDG and the Lund Monte Carlo is then allowed to manage the decays. Correct production distributions are incorporated, including an allowance for polarization. However, the generator does not include initial state radiation, production-decay spin correlations, or W propagator effects.

3.4. DECAY SIGNATURES

High mass ν_4 will decay to $\ell^-\ell^{+\prime}\nu$ or $\ell^-\bar{Q}q$ in the ratio 1:3. Analogous to the charged lepton case, 11% of the events will be all lepton, 44% lepton vs. jets, and 44% jets vs jets. All events will have at least two leptons, but the types of leptons depend on the unknown mixing. We assume that ν_4 mixes only with τ since naively that possibility is the most likely and since experimentally it is the worse case. Because of this assumption, the very distinct $e^+e^-e^+e^-$, $\mu^+\mu^-\mu^+\mu^-$, $e^+e^-e^\pm\mu^\mp$, $\mu^+\mu^-\mu^\pm e^\mp$, and $\mu^+\mu^-e^+e^-$ final states constitute in sum only 0.9% of the total $\nu_4\bar{\nu}_4$ final states.

The jets vs jets final state will be harder to pick out than the analogous mode in the charged lepton case because large missing energy/momentum is not guaranteed. High mass $\nu_4\bar{\nu}_4$ events will be spherical, however, lower mass $\nu_4\bar{\nu}_4$ will appear similar to $b\bar{b}$ or $c\bar{c}$ final states.

The preferred search topology is thus the leptons vs jets mode. Candidate events are required to have $|\cos\theta_{th}| < 0.8$ and to have at least one “isolated” e or μ . The isolation criteria are that the lepton has an energy of at least 2 GeV and that it be separated by at least 12° from the nearest charged and neutral particles. An isolation criteria based on nearest jets might be better, but the technique was not developed for this study.

The event is then divided in half with the thrust axis. The half with the highest energy lepton is called the “lepton half”, and the other half is called the “jet half”. The lepton half must have exactly 2 charged particles and at most 3 neutral particles. The extra neutral particles are to allow for the two event halves

mixing with each other at high ν_4 mass. The jet half is required to have at least 5 particles and at least 10 GeV of visible energy.

Table V. shows the number of produced events, detection efficiency, and number of detected events for different ν_4 masses, assuming 10^4 produced Z^0 .

Table V. $\nu_4\bar{\nu}_4$ Event Selection Results

m_{ν_4}	produced/ $10^4 Z^0$	efficiency	detected/ $10^4 Z^0$
5	606	0.148	90
25	452	0.110	50
35	315	0.062	20
45	75	0.008	0.8

The estimated background from hadronic Z^0 events is $1.7/10^4 Z^0$ and that from $\gamma\gamma$ events $\lesssim 1.0/10^4 Z^0$.

We conclude that with $10^4 Z^0$ ν_4 up to mass 40 GeV/ c^2 that decayed promptly and mixed mainly with τ could be discovered at SLD. If the mixing with μ or e is significant, the sensitivity would be even greater.

In the event that the mixing is small enough to give the neutrinos a finite lifetime, the analysis would probably be unaffected if the ν_4 decayed before reaching the drift chamber. If the ν_4 decayed in the drift chamber or LAC, the signature would be so spectacular that a single event would constitute a major discovery. One small concern is that the SLD may not be able to trigger on non-interacting neutral particles which live long enough to reach the LAC or even the WIC.

With $10^5 Z^0$, it is fairly clear that the majority of the mass range for ν_4 can be ruled out.

4. Conclusion

With $10^4 Z^0$, SLD should be able to discover L_4 and ν_4 with masses up to 40 GeV/ c^2 . With this data sample, we would be significantly better than Mark II for these topics. However, $10^5 Z^0$ will allow *any* detector to find heavy sequential leptons up to nearly the kinematic limit. It is very likely that Mark II will get a good start on this physics and LEP will finish it before SLD takes any data.

REFERENCES

1. UA1 Collaboration, Phys. Lett. **198B**, 271, 1987.
2. AMY Collaboration, Phys. Rev. Lett **61**, 911, 1988.
TOPAZ Collaboration, Phys. Rev. **D37**, 1339, 1988.
VENUS Collaboration, Phys. Rev. Lett.**59**, 2915, 1987.
3. J. Dorfan, SLAC-PUB-4816B, 1989.
4. S. Jadach and J. Kuehn, MPI Preprint MPI-PAE/PTh-64/86, Oct. 1986.
5. This program resides on the NEWPAR disk.
6. This program currently resides on Zeitlin 191.
7. This program resides on the ELECWEAK disk.
8. Written by D. Stoker.
9. The program is called MARKII and sits on TAB 191. Use it in lieu of FSIM.
10. This is not the most common definition of this quantity.
11. A routine called MCJKAL can be called from IDA to fill a useful bank called MCJETK. MCJKAL uses PHKAL and PHKPID except for minimum ionizing clusters, in which case PHPART is used.
12. A routine called MCJETPM can be called from IDA to fill a useful bank called MCJETP. MCJETPM uses only PHPART information.
13. MCJETPM can be called after MARKII to fill MCJETP with shape parameters, etc.
14. This analysis was performed by Richard White, a Hampshire College undergraduate working for Columbia.
15. D.P. Stoker *etal*, SLAC-PUB-4590, 1988.
16. This program resides on TAB 191.

FIGURE CAPTIONS

- 1) Acoplanarity vs $\cos \theta_{th}$, E_{vis} vs $\cos \theta_{th}$, thrust axis distribution, and acoplanarity distribution after $|\cos \theta_{th}| < 0.8$ cut for 10^5 Lund events passed through FSIM.
- 2) Acoplanarity vs $\cos \theta_{th}$, E_{vis} vs $\cos \theta_{th}$, thrust axis distribution, and acoplanarity distribution after $|\cos \theta_{th}| < 0.7$ cut for 10^5 Lund events passed through MARKII simulator.
- 3) Estimate of sensitivities of different methods of searching for ν_4 . The solid line shows the existing excluded region (assuming $|U|^2 = |U_{\mu 4}|^2$). The dashed lines show the excluded regions based on width measurements with 10^4 and 10^5 Z^0 . The dotted lines show the excluded regions from neutrino counting for the same event samples. The dot-dashed line shows the region excluded from direct searches for 10^4 and 10^5 Z^0 .

$\langle \text{ACOS}(_MCJETK\%(ACOPLA)) \rangle$

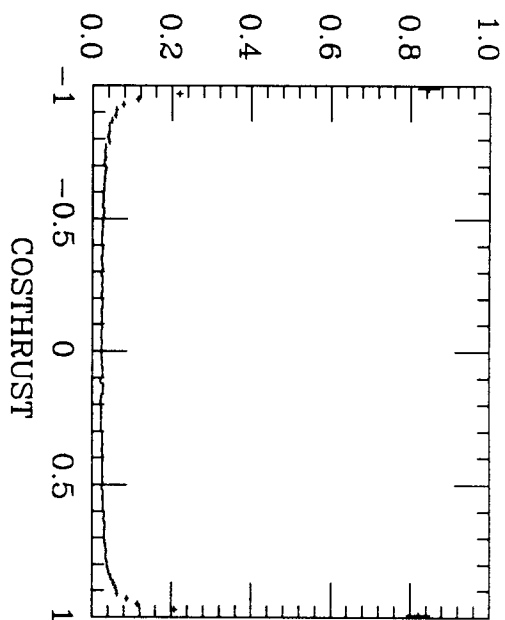


FIG. 1a.

$\langle \text{EVIS} \rangle$

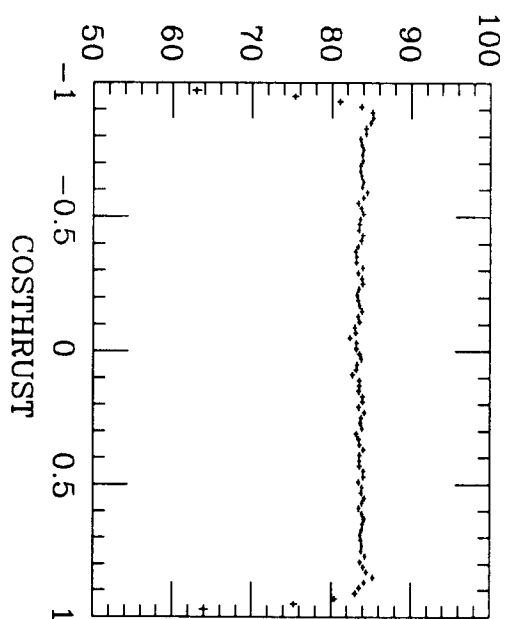


FIG. 1b.

ENTRIES/ 2.000E-02

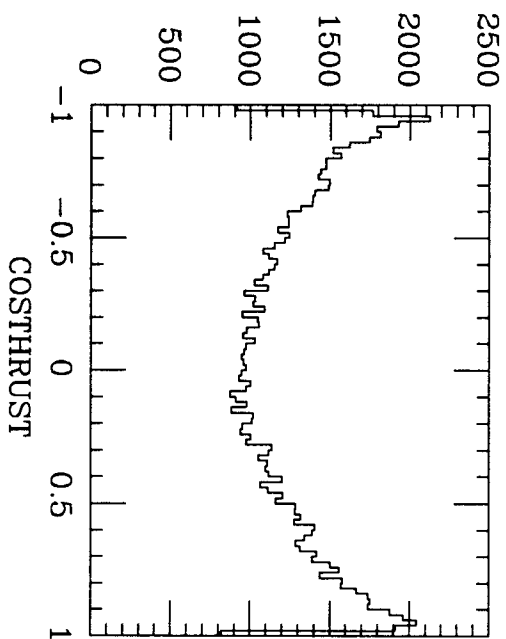


FIG. 1c.

ENTRIES/ 1.000E-02

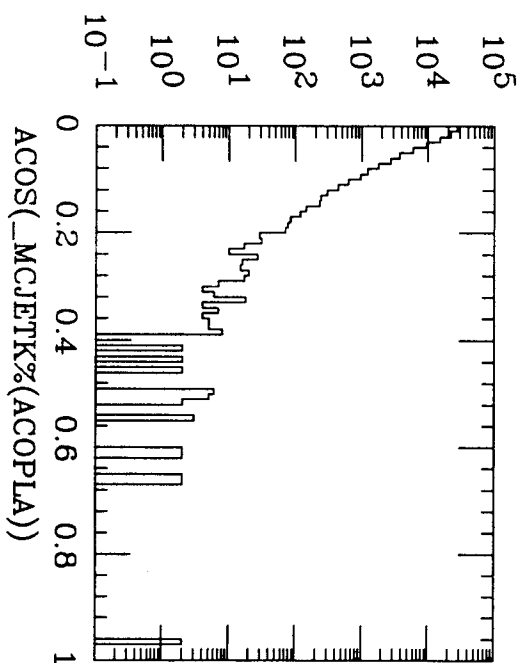


FIG. 1d.

$\langle \text{ACOS}(_MCJETP\%(ACOPLA)) \rangle$

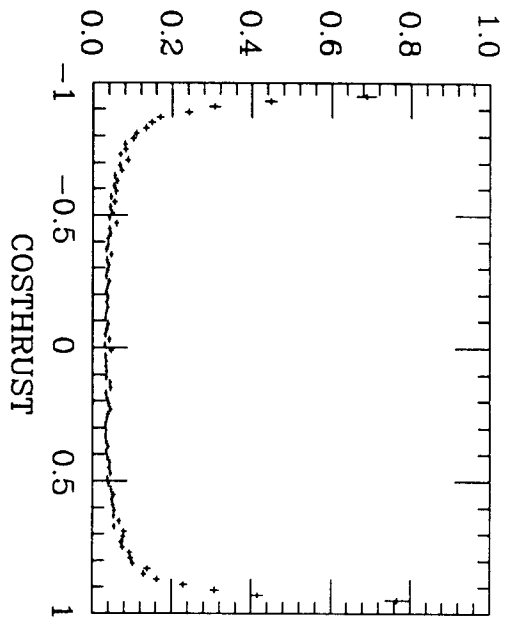


FIG. 2a.

$\langle \text{EVIS} \rangle$

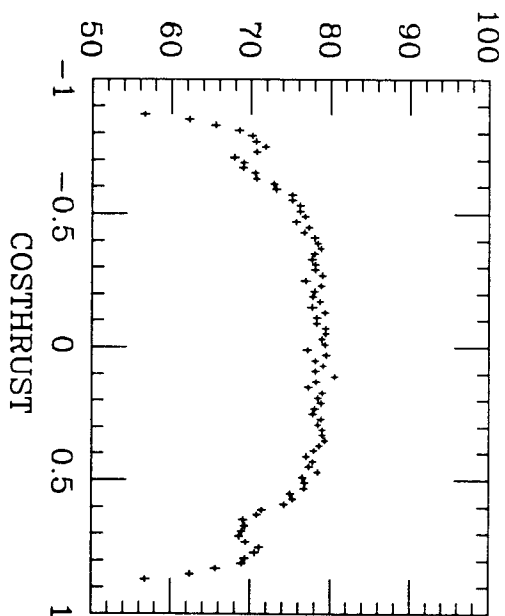


FIG. 2b.

ENTRIES/ 2.000E-02

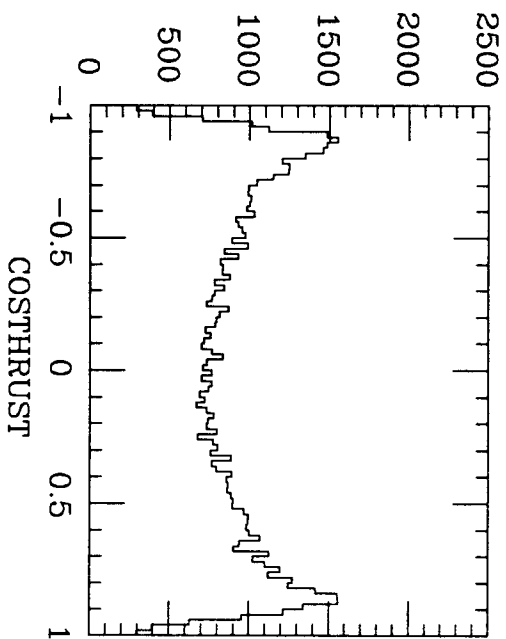


FIG. 2c.

ENTRIES/ 1.000E-02

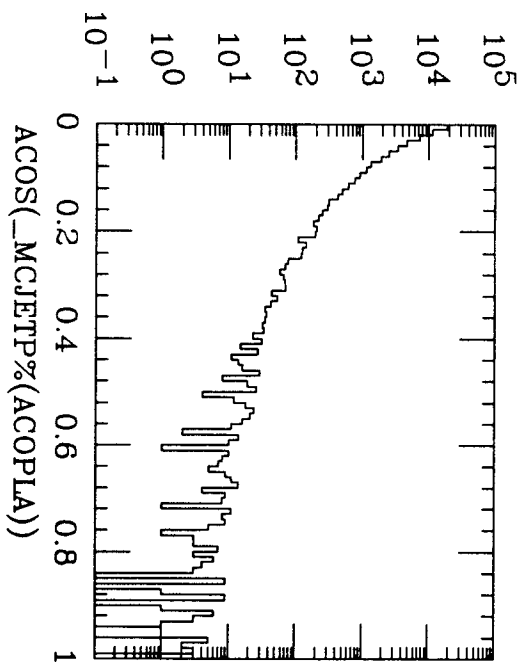
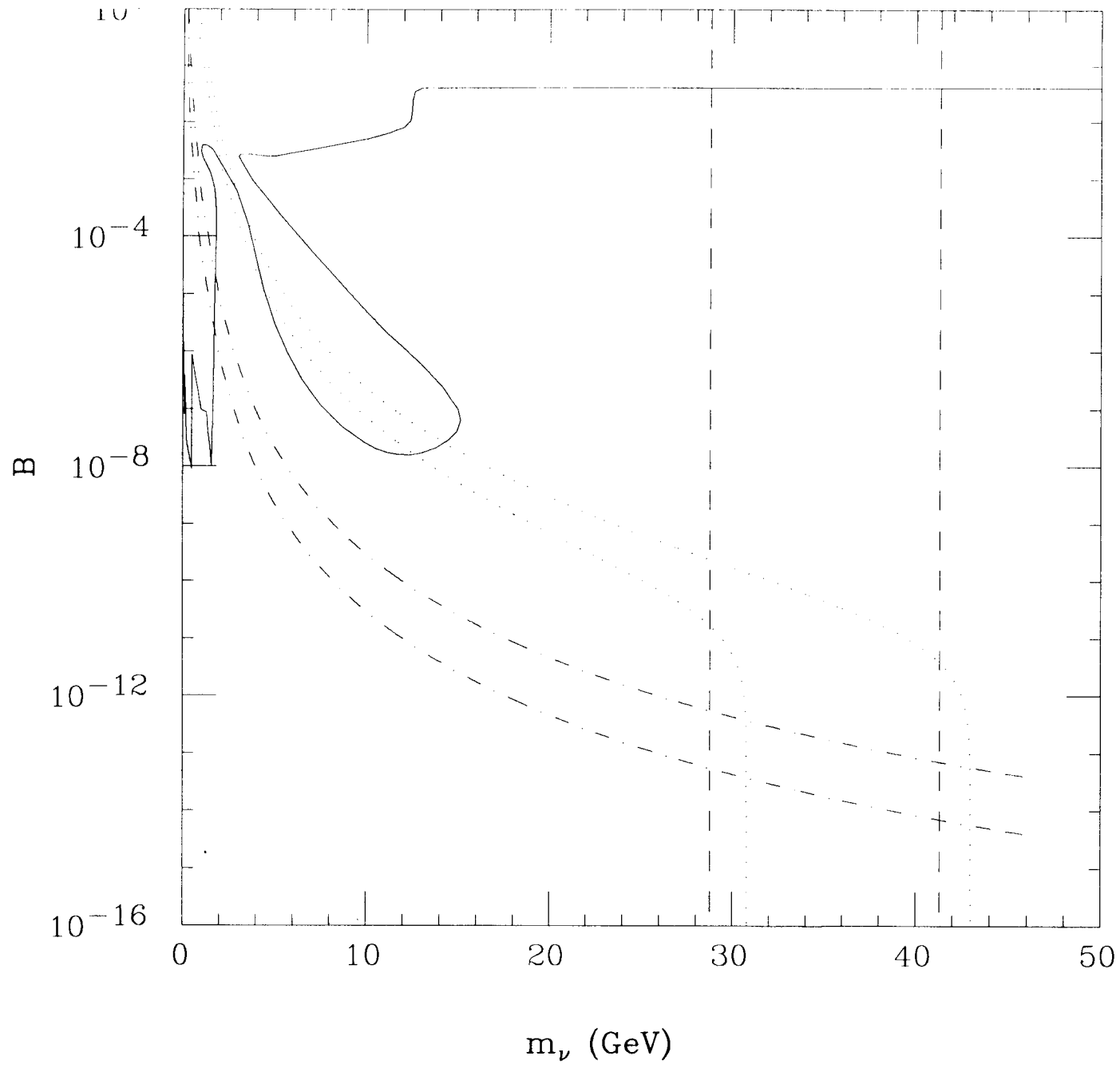


FIG. 2d.



A Fourth-Generation Charge $-\frac{1}{3}$ Quark at SLD

ACHIM W. WEIDEMANN

University of Tennessee, Knoxville[†]

CARY J. ZEITLIN

University of Oregon, Eugene

I. Introduction

A fourth generation of quarks and leptons is not presently excluded by astrophysical arguments or theoretical prejudice. The possibility that the mass of a fourth-generation quark is below the top quark mass opens the (however remote) possibility to observe the former at SLC energies, which is considered in this note. In Section II. known limits on such new quarks are given, in Sect. III. possible reactions and signatures. Sect. IV gives some Monte Carlo results indicating how some of these signatures would look at SLD, and how they could be distinguished from background.

II. Nomenclature and Known Limits

Following Barger *et al.* we label the fourth-generation quarks here a, v , where a has the charge $+\frac{2}{3}$ and v , $-\frac{1}{3}$. These authors write that "this notation is suggested by the alphabetic labels used for the other quarks (*viz.* $a, b, c, d, \dots, s, t, u, v$)" and furthermore that "the names audio and video have been proposed for these quarks, after the gods of the present generation!"³ Other authors refer to the a, v quarks as b', t' ; in LUND,¹¹ they are called h and l .

The top quark mass is known to lie between 76 GeV and 200 GeV, where the lower limit comes from CDF¹², and the upper one from loop corrections (different for NC and CC, and excluded by experiment).

[†] Address: Bin 94, SLAC, P.O.B. 4349, Stanford, CA 94309. Bitnet: ACHIM @ SLACVM

For m_ν , UA1 gives 34 GeV as lower limit, and VENUS⁶, 27.5 GeV (AMY⁷, 27.2 GeV). Combined Cello, Jade, Mark J and Tasso data gave 22.7 GeV.[‡] Theoretical prejudice (*i.e.* the renormalization group equations of N=1 supergravity³, assuming that couplings remain perturbative up to the GUT scale of 10^{16} GeV) suggests the upper bounds $m_a \leq 140$ GeV, $m_\nu \leq 135$ GeV (and also $m_L \leq 70$ GeV, where L denotes a fourth-generation lepton).

III. Reactions and Signatures

III.1 Cross-section and Decays.

The production cross section for ν at the Z^0 , $\sigma(e^+e^- \rightarrow Z^0 \rightarrow \nu\bar{\nu})$, is about 3 nb for $m_\nu = 40$ GeV, about 1 nanobarn more than that for a t of the same mass (that for a 4th generation lepton, L or its neutrino, ν_L , is about $\frac{1}{2}nb$). For comparison, the μ production cross section at the Z^0 is 1.8 nb. As $\sigma(e^+e^- \rightarrow Z^0 \rightarrow \text{anything}) \approx 30nb$, the ν production cross section is appreciable; one would expect about 1,000 $\nu\bar{\nu}$ events in 10,000 Z^0 events.

III.2 Threshold in hadronic cross-section.²

The existence of the known heavy quarks was shown by a resonance and step in $R = \frac{\sigma(e^+e^- \rightarrow \text{hadrons})}{\sigma(e^+e^- \rightarrow \mu^+\mu^-)}$. The ratio R increases by $3e_q^2 * (\text{electro} - \text{weak and QCD corrections})$ as the energy is increased above the threshold for production of a new quark q . The corrections lead to a step in R by only 1.0 for a ν , 0.68 for a t -quark of $m_q = 40$ GeV. Without a new quark, R is already almost 16 at 80 GeV, so the relative change is small and is getting smaller as you approach the Z^0 peak. Furthermore, the ν -quark signature at the Z^0 peak is clear with relatively few events, as will be shown below. Thus, we do not intend to look for ν -quarks by enhancement of R.

‡ After this note was completed, Mark II announced 45 GeV as their limit for m_ν ^{13,14} for CC decays and FCNC decays with an isolated photon.

III.3 Weak Charged Current (CC) Decays of the v -Quark.

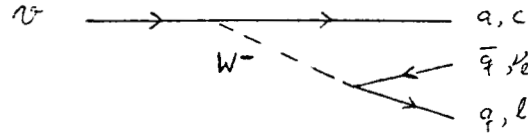


Fig. 1. CC decays of the v -quark.

The condition $m_v < m_t$ (and assumption $m_a > m_v$) makes the charged current (CC) decays $v \rightarrow t + W^-$ and $v \rightarrow a + W^-$ kinematically forbidden; in that case the transition $v \rightarrow c + W^-$ dominates, but is strongly KM suppressed (as the decay goes from 4th to 2nd generation with the square of the mixing V_{cv} , which is expected to be small). From the $v \rightarrow c$ and $v \rightarrow cs\bar{c}$ decay modes, a high multiplicity of charmed particles is expected. The fraction of $v\bar{v}$ events with 2,3,4 charmed particles is $\sim 100\%, 44\%, 11\%$, unlike $b\bar{b}$ events with fractions $\sim 100\%, 12\%, \frac{1}{2}\%$, as $b \rightarrow cs\bar{c}$ is phase space suppressed.³

III.4 Flavor-Changing Neutral Current (FCNC) Decays.

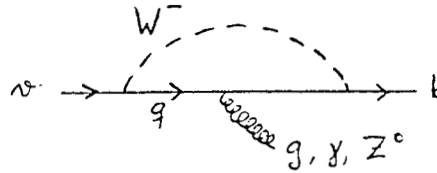


Fig. 2. FCNC decay of the v -quark ($q = t, a, c, u$).

The v -quark decays may be dominated by the decay $v \rightarrow b + g$ which proceeds via a loop involving a W^- and an a or t quark (which radiates a gluon), as the relevant CKM matrix elements, $V_{av}V_{ab}^*$ and $V_{tv}V_{tb}^*$, are expected to be less suppressed than V_{cv} , and also as the loop amplitude grows with the mass of the virtual a or t quark in the loop. The branching fraction $v \rightarrow b + g$ may be as large as 5 to 10%. The ratio of the branching fractions for FCNC to CC decays is proportional to $|\frac{V_{tv}V_{tb}^*}{V_{cv}}|^2$, but these CKM matrix elements are unknown. The distinctive decay $v \rightarrow b + \gamma$ might also have a detectable branching fraction.

III.5 CC Signature 1: Jet Broadening.

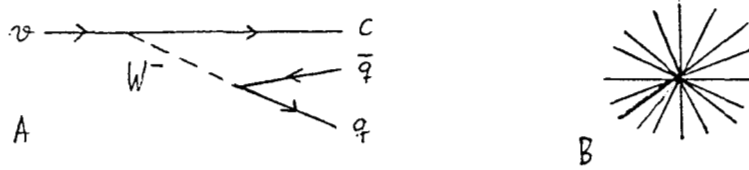


Fig. 3. A: hadronic CC decay of the ν -quark; B: Schematic signature.

The large energy release in ν decay should produce jets which are broader than those of $q\bar{q}$ events for lighter quarks (except for those with several non-collinear gluons). These events will have low thrust, $T < 0.9$ for $> 85\%$ of the events.

The broadening of jets from a heavy quark can be used to measure the quark mass. According to Barger⁵, $\langle \sum p_i^2 \rangle \approx (\pi/4)m_q$, where p_i^2 is the momentum of the i^{th} particle transverse to the jet axis. In the real world, missing neutrinos will reduce the sum a bit.

III.6 CC Signature 2: Semileptonic decays of the ν .

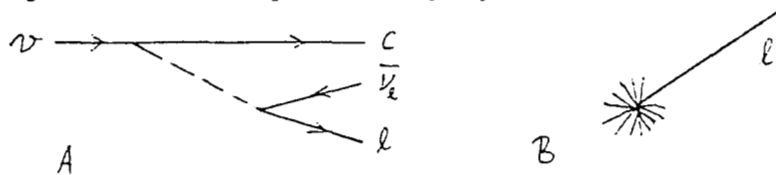


Fig. 4. A: Semileptonic CC decay; B: Schematic signature.

Semileptonic decays provide a convenient tag for heavy flavor production. At the Z^0 , the average number of electrons per hadronic event is expected to be 0.14; the existence of a 40 GeV ν quark would increase this average to 0.17, a small but observable difference. *Isolated leptons* from ν decay will be much more common than those coming from either b or c decays. Adopting Barger's definition of an isolated electron being one with $p > 10$ GeV and less than 8 GeV of hadronic energy within 15° , 16–19% of $\nu\bar{\nu}$ events are expected to have an isolated lepton, compared to 1% ($< 0.1\%$) for $b\bar{b}$ ($c\bar{c}$).

III.7 FCNC signatures.

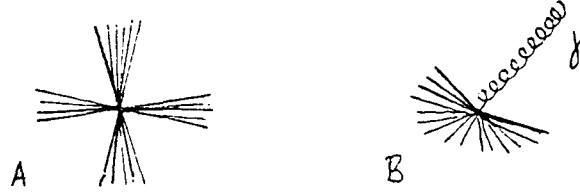


Fig. 5. FCNC schematic signatures A: 4 jets; B: Isolated photon.

The signature for the FCNC decay $v \rightarrow b + g$ (and similar for the \bar{v}) would be four back-to-back planar jets; for $v \rightarrow b + \gamma$, a high-energy isolated photon.

III.8 Decay vertices for long-lived v .

Due to the CKM suppression of both CC and FCNC decays, the v lifetime might be quite long and of order 10^{-13} to 10^{-12} . The decay length of a v with $m_v = 40$ GeV would be $190\mu m$ and could be resolved by the vertex detector.²

IV. Monte Carlo Results

IV.1 Generation of events.

We studied the generation and decay of v -quarks using the LUND¹¹ and LULEPT¹⁰ generators. Whereas $v(l)$ quarks can be generated directly in LUND, LULEPT includes the polarization and spin correlation in the production and decay of these quarks and is therefore preferable.

We studied so far only the charged-current decays of a v -quark with $m_v = 40$ GeV (and $m_a = 200$ GeV, $m_t = 42.5$ GeV) and assumed the usual branching ratios

$$\begin{aligned} v &\rightarrow ce^- \bar{\nu}_e : 11\% \\ &\rightarrow c\mu^- \bar{\nu}_\mu : 11\% \\ &\rightarrow c\tau^- \bar{\nu}_\tau : 11\% \\ &\rightarrow c\bar{u}d : 34\% \\ &\rightarrow c\bar{c}d : 33\%. \end{aligned}$$

1000 such v -quark pair events were generated with LULEPT; and simulated

with the SLD Fast Monte Carlo FSIM. For the background, we took 10000 events from the 5-flavor LUND data set DSTUDSCB. (for the figures shown; as part of the data set was unavailable later, I took the 6793 events still available to find the efficiencies of the cuts, and scaled up to 10000 events). Event shape quantities were calculated using routines originally written by T. Bolton, which in turn use the LUND routines LUSPHE and LUTHRU¹¹. An over-all cut of $|\cos(\hat{z}, thrust\ axis)| < 0.8$ was applied; this cut was passed by 83.4% of the ν -quark events (or 834 out of the 1000 generated) and 73.1% of the 5-flavor LUND events. Below, we give always the number of events passing a given cut for 1000 generated ν -quark events and 10000 5-flavor LUND events analysed (or 834 ν -quark events, 7305 5-flavor LUND events which passed the above cut on the cosine of the thrust axis).

IV.2 Event shape variables and suggested cuts.

IV.2.1 Thrust

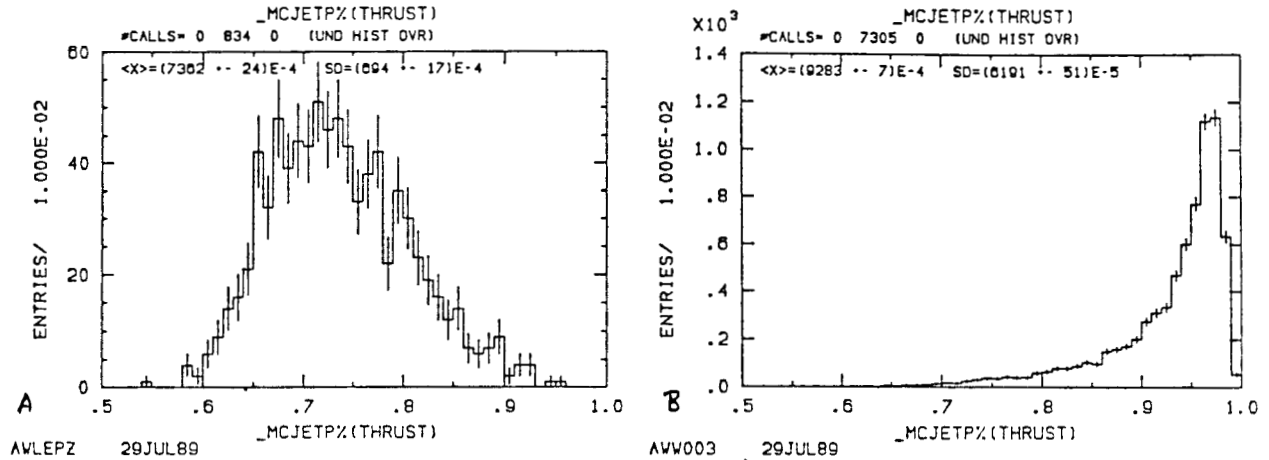


Fig. 6. Thrust. A: For 1000 CC ν decays; B: for 10000 5-flavor LUND events.

A cut at $thrust < 0.9$ (combined with the over-all cut) will keep 822 of the ν -quark events, but only 1600 of the 5-flavor LUND events.

IV.2.2 Aplanarity

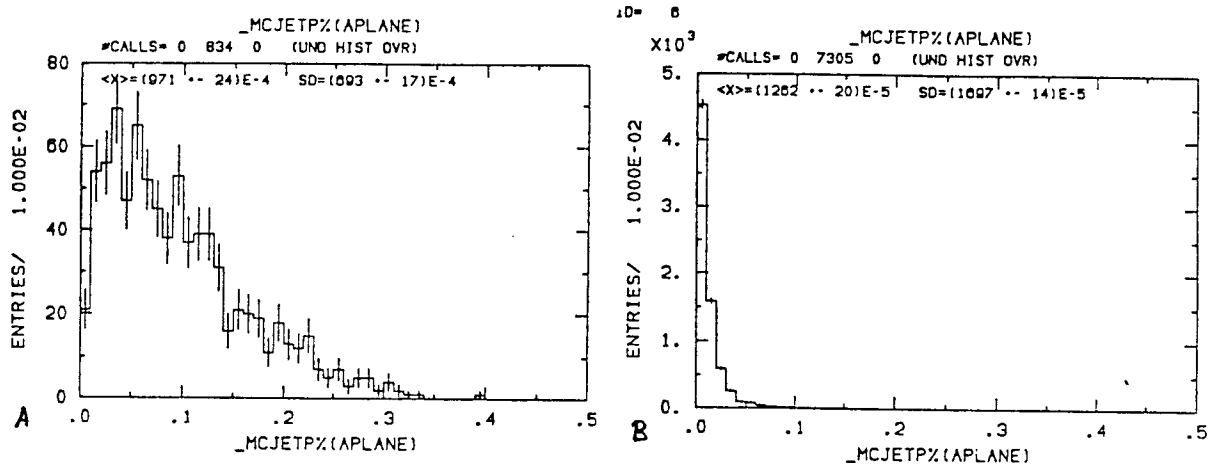


Fig. 7. Aplanarity. A: For 1000 CC ν decays; B: for 10000 5-flavor LUND events.

Requiring *aplanarity* > 0.1 keeps 334 ν events, but only about 50 5-flavor LUND events.

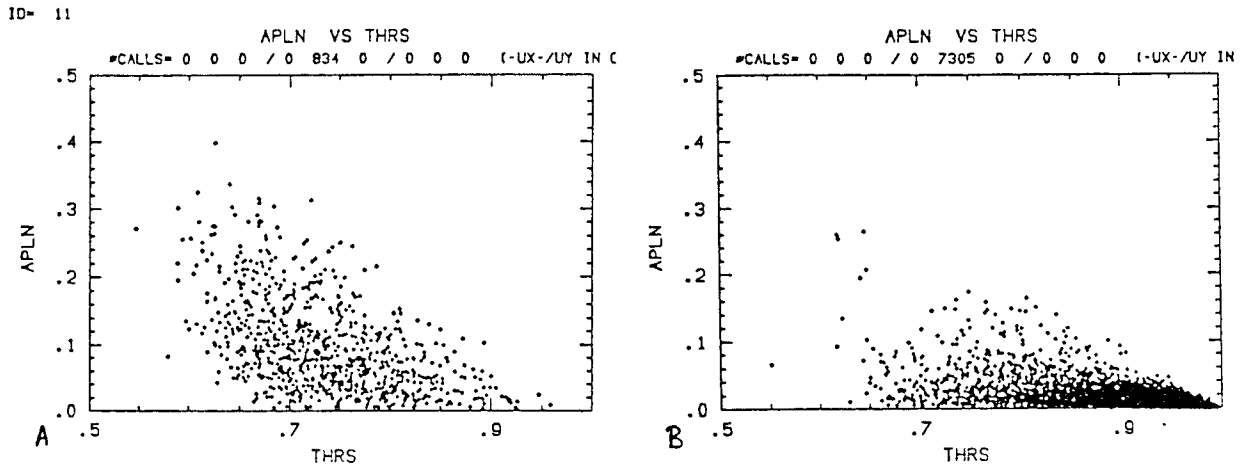


Fig. 8. Aplanarity vs. Thrust. A: For 1000 CC ν decays; B: for 10000 5-flavor LUND events.

The above aplanarity cut eliminates also all background events with *thrust* > 0.9 .

IV.2.3 Sphericity

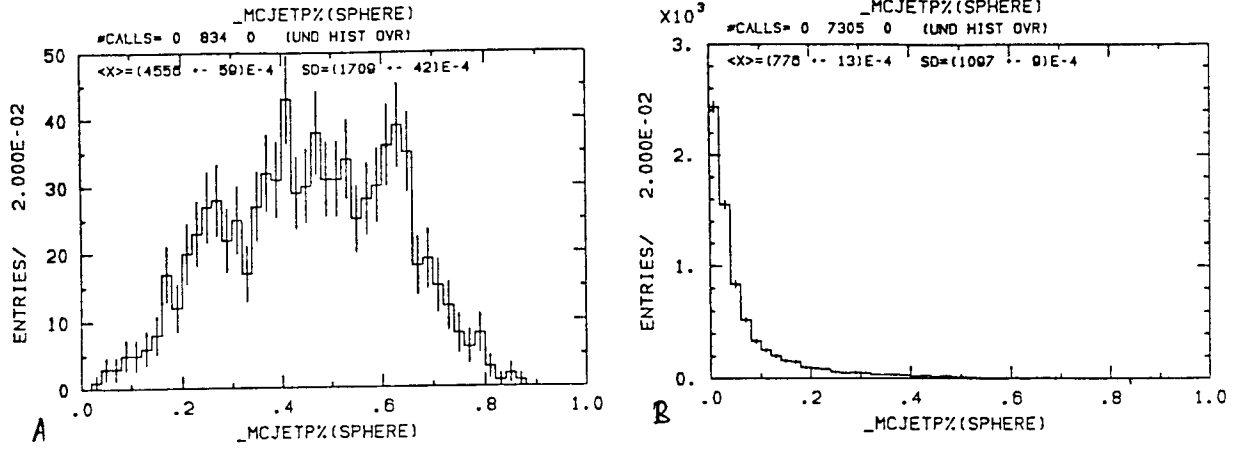


Fig. 9. Sphericity. A: For 1000 CC ν decays; B: for 10000 5-flavor LUND events.

Requiring *sphericity* > 0.2 leaves 774 ν -quark, and only 755 5-flavor LUND events.

IV.2.4 Oblateness

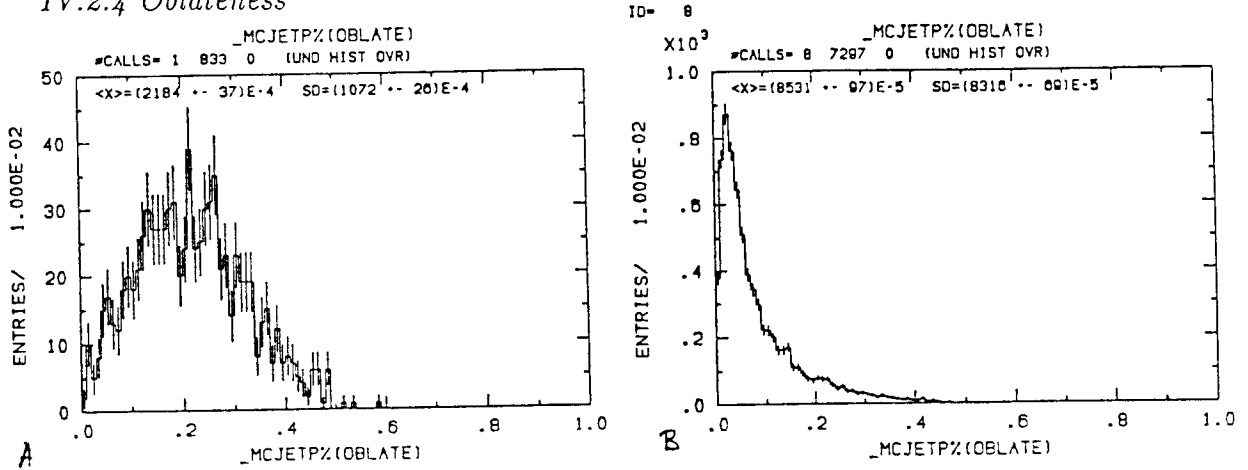


Fig. 10. Oblateness. A: For 1000 CC ν decays; B: for 10000 5-flavor LUND events.

Requiring *oblateness* > 0.2 leaves 456 ν -quark, and only 517 5-flavor LUND events.

IV.3 Isolated leptons

A lepton is considered isolated, if the angle α between the lepton's and any other (charged or neutral) track obeys $\cos(\alpha) < 0.95$ (or $\alpha > 18.2^\circ$).

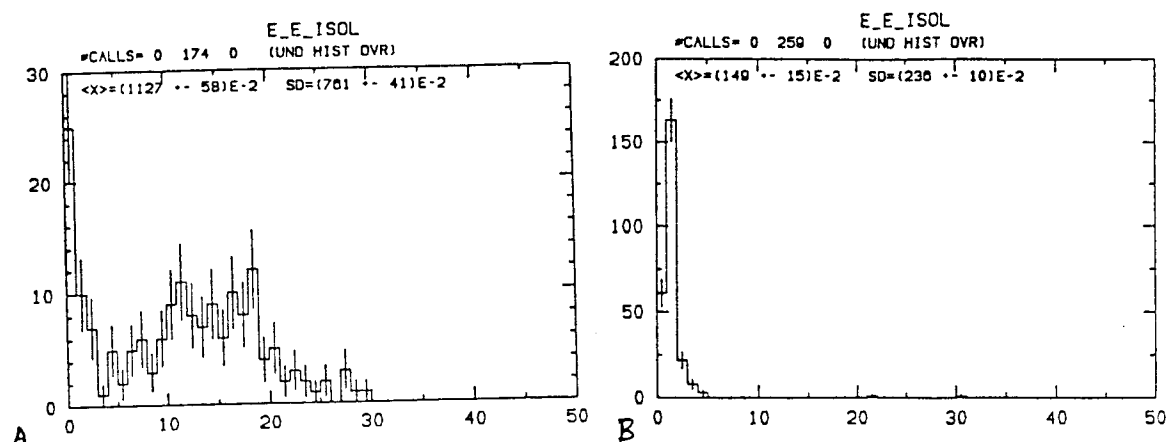


Fig. 11. Isolated electron energy.

A: For 1000 CC ν decays; B: for 10000 5-flavor LUND events.

In the 1000 (10000) generated ν -quark (5-flavor LUND) events, there are a total of 680 (6411) electrons (after over-all cut), of which 174 (275) fit the above definition of isolated-ness. However, 126 of the isolated electrons from ν -quark events, but only 3 of those from 5-flavor LUND events have an energy of more than 5 GeV.

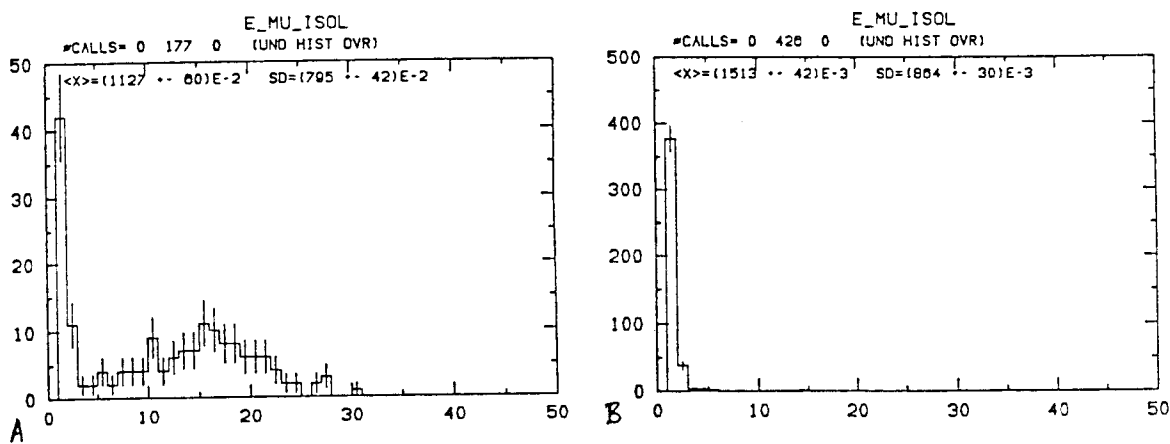


Fig. 12. Isolated muon energy.

A: For 1000 CC ν decays; B: for 10000 5-flavor LUND events.

Similarly, there are a total of 904 (5090) muons (after over-all cut), of which 177 (428) fit the above definition of isolated-ness. And again, 120 of the isolated

muons from ν -quark events, but only 5 of those from 5-flavor LUND events have an energy of more than 5 GeV.

Another measure of isolation is the minimum half-angle of a cone around the direction of the lepton momentum, which contains a visible energy of, say, 10 GeV, excluding the lepton energy. This angle will be larger for isolated leptons. Fig. 13 below shows a scatterplot of this angle *vs.* energy for electrons with *thrust* < 0.9.

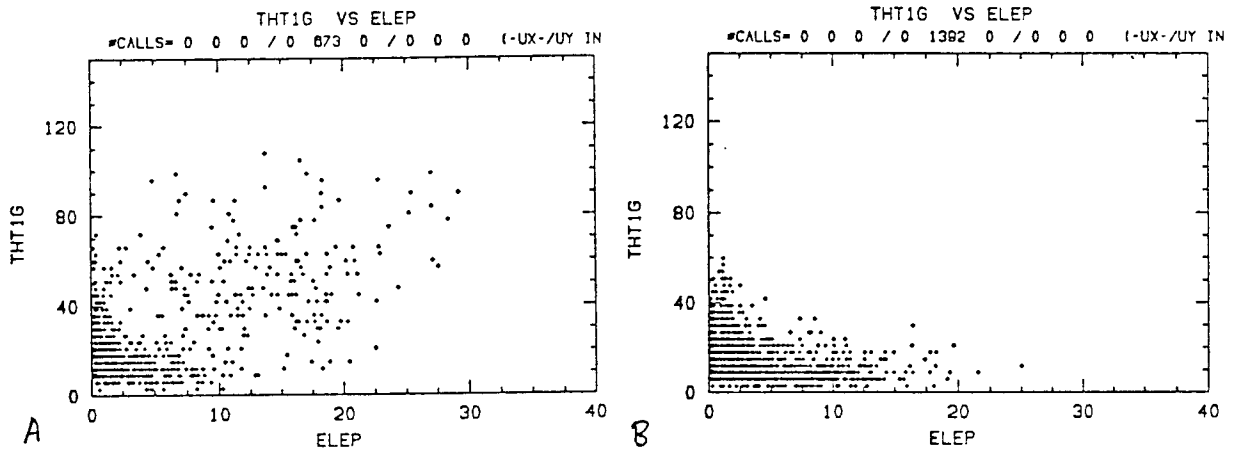


Fig. 13. $\Theta(10 \text{ GeV})$ vs. electron energy.

A: For 1000 CC ν decays; B: for 10000 5-flavor LUND events.

One sees that the background is in the lower left-hand corner; a possible cut requiring $\Theta(10 \text{ GeV}) > (80. - 4 \cdot (E/\text{GeV}))^\circ$ (the straight line from $E = 0, \Theta = 80^\circ$ to $E = 20, \Theta = 0^\circ$) leaves from the 145 (15) electrons from the 673 (1354) electrons with *thrust* < 0.9 produced by ν -quark (5-flavor LUND) events.

IV.4 Conclusion from Monte Carlo results.

The cuts on shape variables and isolated leptons shown above indicate, that a ν -quark decaying by CC should easily be seen by SLD (or any other detector with reasonable efficiency). Nonobservation of a signal (no events above the background using the above cuts) would allow to set a lower mass bound of 40 GeV on a ν -quark which decays by CC: the existence of FCNC decays is ignored here and could change the limits⁷.

V. Conclusion

It is easy for SLD to find a ν -quark dominantly decaying by CC, if its mass allows its production at SLC; unfortunately, however, we expect a ν -quark of less than 40 GeV already to be excluded by CDF or MarkII and also LEP before SLD turns on. The scenario of dominant FCNC has not yet been investigated as thoroughly, but the SLD detector is well suited to measure this decay mode as well.

VI. Acknowledgement

We thank Dr. David Stoker on his advice on the use of LUND and LULEPT, and Dr. Tim Bolton for his useful routines.

VII. References

1. V.BARGER, H.BAER, K.HAGIWARA & R.J.N. PHILLIPS, *Fourth-generation Quarks and Leptons*, Phys. Rev. D30, 947-960 (1984).
2. V.BARGER, R.J.N. PHILLIPS & A.SONI, *Possible v -Quark Signatures at e^+e^- Colliders*, Phys. Rev. Lett. 57, 1518 (1986).
3. V.BARGER, & R.J.N. PHILLIPS, *Collider Physics*, Addison Wesley Publishing Company, Menlo Park, California, 1987.
4. WEI-SHU HOU & ROBIN G. STUART, *Possibility of Discovering the Next Charge $-\frac{1}{3}$ Quark through its Flavor-Changing Neutral-Current Decays*, Phys. Rev. Lett. 62, 617 (1989).
5. V.BARGER, H.BAER, A.D. MARTIN & R.J.N. PHILLIPS, *Systematic procedures for identifying t quarks....*, Phys. Rev. D29, 887 (1984).
6. K. ABE *et al.*, VENUS COLLABORATION, *Search for a fourth-generation quark....*, Phys. Rev. D39, 3524-3527 (1989).
7. S. ENO *et al.*, AMY COLLABORATION, *Search for a fourth-generation Charge $-1/3$ quark*, KEK Preprint 89-46 AMY 89-08, July 1989.
8. WEI-SHU HOU & ROBIN G. STUART, *Flavor Changing Neutral Currents Involving Heavy Fermions: a General Survey*, MPI-PAE/PTh 55/88 (October 1988).
9. WEI-SHU HOU & ROBIN G. STUART, *Flavor Changing Decays of the Z^0 Boson to Massive Quarks in the 2 Higgs Doublet Model*, MPI-PAE/PTh 54/88 (December 1988).
10. D. STOKER, *A new Monte Carlo generator for t and b' quarks*, Mark II/SLC Physics Working Group Note #3-25, (August 1987).

11. T. SJÖSTRAND & M. BENGTSON, *The LUND Monte Carlo for Jet Fragmentation and e^+e^- Physics - Jetset Version 6.3 - An Update*, Comp. Phys. Comm. **43**, 367 (1987); see also Comp. Phys. Comm. **39**, 347 (1986).
12. P. SINERVO, *Search for new particles at CDF*, Invited Talk at the XIV International Symposium on Lepton and Photon Interactions, Stanford, August 6-12, 1989.
13. A. WEINSTEIN, *Decays of the Z^0 (Mark II)*, Invited Talk at the XIV International Symposium on Lepton and Photon Interactions, Stanford, August 6-12, 1989.
14. W. INNES, *A Search for New Particles in Z Decay*, Invited Talk at the International Conference on High Energy Physics, Madrid, September 6-13, 1989.

Singly Produced Neutral Heavy Leptons and the Search for Monojets

A.O. BAZARKO & M.H. SHAEVITZ

Department of Physics, Columbia University, NY, NY 10027

The search for a weak isospin singlet neutral heavy lepton is motivated by models beyond the standard model. These models include GUTs, left-right symmetric models, and mirror lepton models.^{[1] [2]}

A weak isospin singlet can couple to the standard Z^0 because of mixing with the standard neutrinos, with a mixing strength factor $|U_{L^0\nu}|^2$. Since the standard light neutrinos and the heavy neutral lepton belong to two different representations of weak isospin, there is no GIM mechanism and flavor changing neutral currents are allowed. At the SLC, the L^0 can be produced by the process $Z^0 \rightarrow L^0\nu$, where the standard neutrino does not interact in the detector and the L^0 decays via both charged or neutral current. The decay of the L^0 produces a one sided jet opposed by a quiet hemisphere.

L^0 production depends on the mixing factor and the phase space factor:

$$\frac{\sigma(Z^0 \rightarrow L^0\nu)}{\sigma(Z^0 \rightarrow \nu\bar{\nu})} = |U_{L^0\nu}|^2 \left(1 - \frac{M_{L^0}^2}{s}\right)^2 \left(1 + \frac{M_{L^0}^2}{2s}\right)$$

Analysis

Our present analysis uses FSIM to simulate the SLD, assuming charged particle tracking for $|\cos\theta| < 0.96$ and particle veto for $\theta < 0.027$ radians. We study the

cases where L^0 mixes with all three lepton flavors and where L^0 mixes only with tau neutrinos.

The analysis implements the following cuts:

- Monojet cut:

Divide the event into two hemispheres by finding the plane perpendicular to the thrust axis and demanding that there be a quiet hemisphere with visible energy below a specified value. We perform the analysis demanding that the quiet hemisphere have either $E_{vis} < 1$ GeV or $E_{vis} < 5$ GeV.

- Acceptance cuts:

The angle of the thrust axis: $|\cos(\theta_{Thr})| < 0.8$

Total $p_{\perp} > (E_{cm} - E_{vis})\sin\theta_{veto}$ (To eliminate missing energy near the beam)

The visible energy of the monojet: $E_{vis} > 10$ GeV

- Background cuts:

Charged track multiplicity ≥ 2 (A visible track has $p_{tot} > 100$ MeV and $|\cos\theta| < 0.96$)

Invariant mass of the monojet > 2 GeV

For the decay of a neutral particle one would expect an even number of charged tracks. However, since it is easy to “lose” a track, a less strict requirement of \geq two charged tracks is employed.

The signal analysis for a $25 \text{ GeV}/c^2$ L^0 is shown in figures 1 - 8. Histogrammed quantities are presented with cuts superimposed. The angular distribution of the monojet events is fairly flat, so the thrust axis cut does not unduly effect the signal. The E_{vis} and p_{\perp} acceptance cuts do not remove much signal. L^0 events often have a relatively large charged track multiplicity and effective mass, and the final background cuts do not decrease the signal by much.

Backgrounds

Possible backgrounds to this signal which were studied are $q\bar{q}$, $\tau^+\tau^-$, and two photon processes going to hadron or $\tau^+\tau^-$ final states. Ordinary $q\bar{q}$ events (figures 9-10) may fake a monojet if half of the event is lost down the beampipe. This background is almost eliminated by the thrust axis acceptance cut. The $\tau^+\tau^-$ background (figures 11-12), where one or more neutrinos carry away most of the associated tau energy, is characterized by a low invariant mass. Most of this background is eliminated by demanding that the monojet invariant mass be at least 2 GeV. Of the six background events that remain from our study of 5.6×10^4 $\tau^+\tau^-$ events, five would be eliminated by raising the final mass cut to 3 GeV. Two photon processes (figures 13-14) produce a background at a rate of 2 events per $10^6 Z^0$. These background events have invariant mass below 10 GeV so that if the search is for M_{L^0} greater than this, then two photon background can be eliminated. For low M_{L^0} searches, two photon background must be accounted for, albeit at a very low rate.

Background summary			
background	MC events generated	Z^0 equiv.	background events observed
$q\bar{q}$	7.1×10^4	10^5	3
$\tau^+\tau^-$	5.6×10^4	1.7×10^6	6
$\gamma\gamma \rightarrow \tau^+\tau^-$	2.7×10^4	3.2×10^6	6
$\gamma\gamma \rightarrow \text{hadrons}$	0.7×10^4	2.5×10^4	0

Other possible backgrounds from beam-gas or cosmic ray events are expected to be small and can be eliminated by requirements on the event vertex.

Signal efficiency and experimental sensitivity

The signal efficiency over the range of neutral lepton masses is plotted in figure 15. The peak efficiency is approximately 60% near $M_{L^0}=17$ GeV, falling to approximately 10% at $M_{L^0} = 80$ GeV. The efficiency falls off above $M_{Z^0}/2$ because heavy L^0 masses produce more spherical decays. At low M_{L^0} the efficiency also

falls due to the 2 GeV mass cut. Without this final mass cut, the efficiency would remain at its plateau value. In the case of a search for low mass L^0 , the monojet would be tightly collimated, making it improbable that a track would be lost in the quiet hemisphere, allowing a tighter even number track cut to eliminate the one and three prong tau background.

This analysis is fairly insensitive to detector noise as indicated by our studies of E_{vis} cuts between 1 and 5 GeV.

The region of experimental sensitivity is plotted in the $|U_{L^0\nu}|^2$ vs. M_{L^0} plane (figure 16). The straight limit line on the left follows from the requirement that the L^0 decay within the detector. The rest of the curve follows from L^0 production, with signal efficiency folded in, and the requirement that there be at least five observed decays. We can begin to significantly extend the present experimental limits with $> 10^5 Z^0$.

Mass measurement

For L^0 masses below $M_{Z^0}/2$, the invariant mass distribution of the monojet hemisphere would show a mass peak due to the charged current decay mode $L^0 \rightarrow lq\bar{q}$ which has little missing energy and a high branching ratio ($\sim 22\%$). After the basic analysis cuts, two additional cuts: demanding that there be one charged lepton track and a monojet visible energy greater than 40 GeV, allow for a sharp mass peak to emerge. The peak is formed from about 25% of the of the analysed events (figures 17-18).

If the L^0 mixes only with tau, the overall efficiency of our analysis remains the same. However, it is more rare to produce events with low missing energy. The mass peak is not as sharp and is gathered from only about 9% of the analysed events (figure 19-20).

A heavy lepton search using the SLD relies heavily on large particle acceptance and uniform hadronic calorimetry. A comparison with MarkII was studied using a parametric MarkII simulator^[3] and with the analysis cuts changed to: $|\cos(\theta_{Thr})| <$

0.7 and charged particle tracking for $|\cos\theta| < 0.85$. For this analysis, MarkII's relative signal efficiency is 85% of SLD's with comparable backgrounds.

Summary

The SLD is sensitive to singlet neutral heavy lepton production for $5 < M_{L^0} < 80$ GeV with mixing $10^{-2} < |U_{L^0\nu}|^2 < 10^{-4}$. Extensions to present experimental limits can be made with $10^5 Z^0$.

The backgrounds to this search are small.

If a signal is observed then we can search for a mass peak, taking advantage of the decay mode $L^0 \rightarrow lq\bar{q}$. Also, polarized beams would allow the study of L^0 production dynamics.

A slight advantage over MarkII is evident from this analysis.

REFERENCES

1. Gilman, F., Comments Nucl. Part. Phys. **16**, 231 (1986).
2. Gronau, M., Leung, C.N., Rosner, J.L., Phys. Rev. **D29**, 2539 (1984).
3. Bolton, Tim. "A simple MarkII detector simulator," SLD Note in preparation.

Sample signal analysis

$$M_{L0} = 25 \text{ GeV}$$

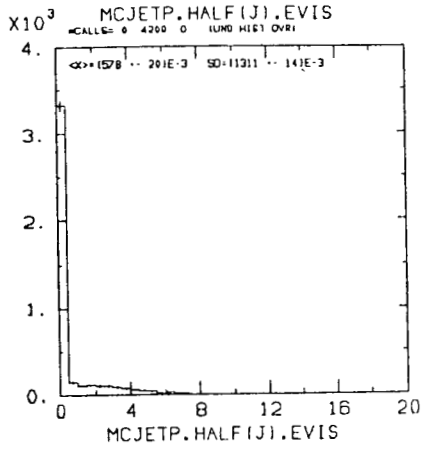


Fig. 1

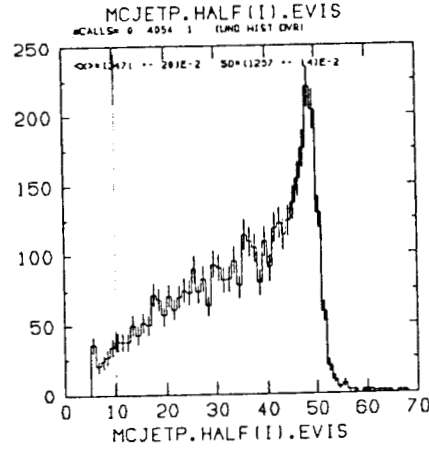


Fig. 2

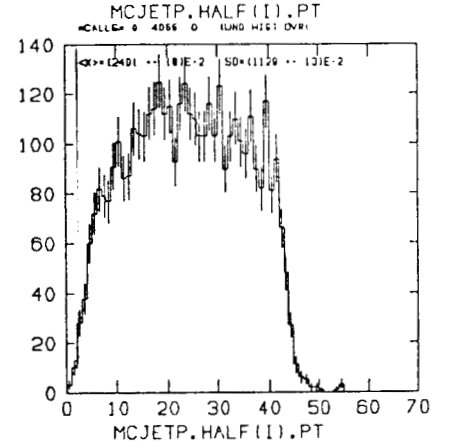


Fig. 3

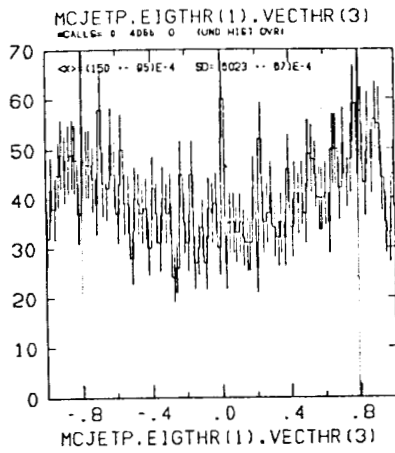


Fig. 4

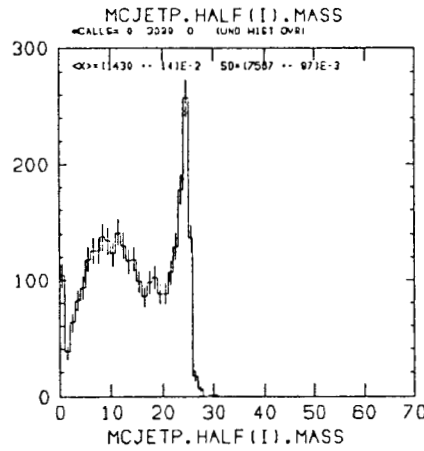


Fig. 5

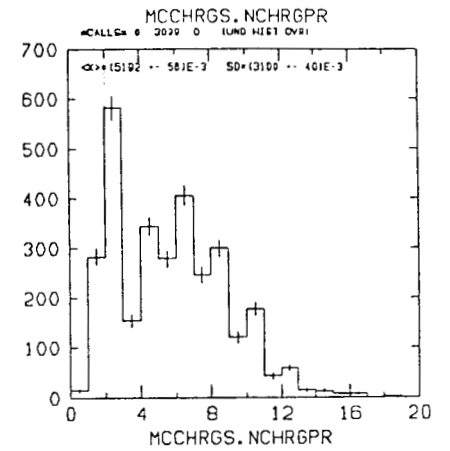


Fig. 6

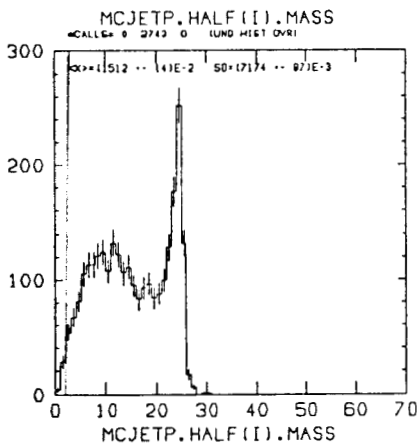


Fig. 7

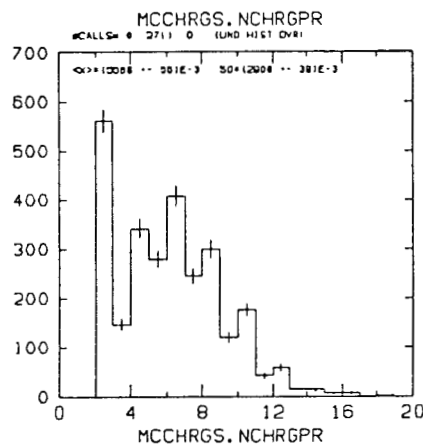


Fig. 8

Fig. 1 - E_{vis} of the quiet hemisphere. Fig. 2 - E_{vis} of the monojet. Fig 3. - p_{\perp} of the monojet. Fig 4. - $\cos(\theta_{Thr})$ of the monojet. Fig 5. - after the acceptance cuts, the invariant mass of the monojet. Fig. 6 - the number of visible charged tracks. Fig. 7 - after demanding that there be at least 2 visible charged tracks, the invariant mass of the monojet. Fig. 8 - after demanding that the invariant mass be $> 2 \text{ GeV}$, the number of visible charged tracks.

backgrounds

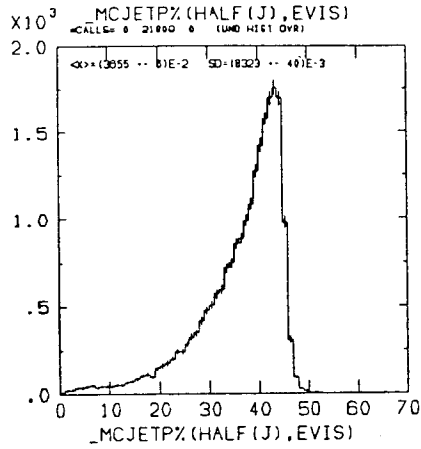


Fig. 9

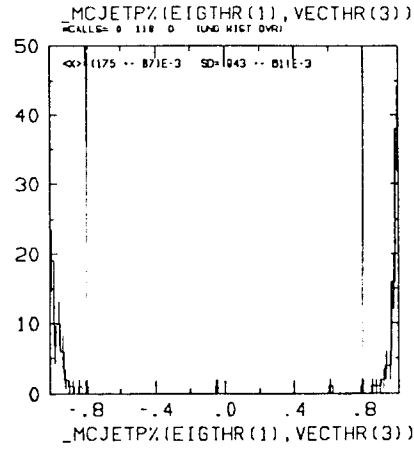


Fig. 10

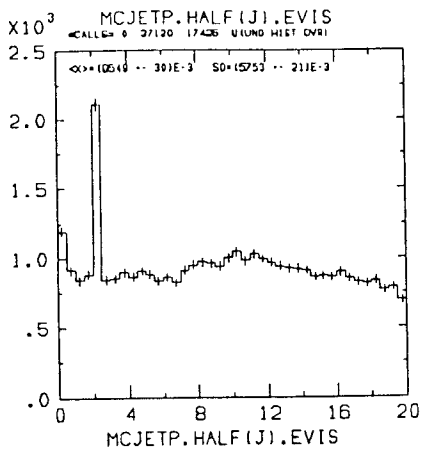


Fig. 11

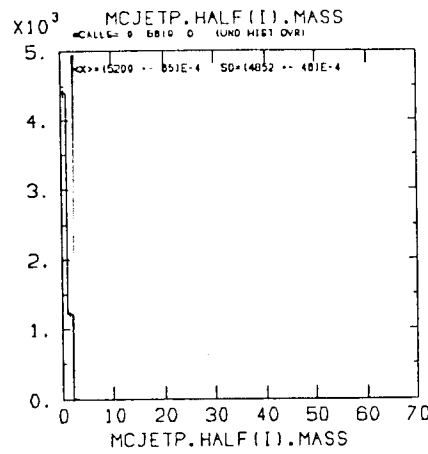


Fig. 12

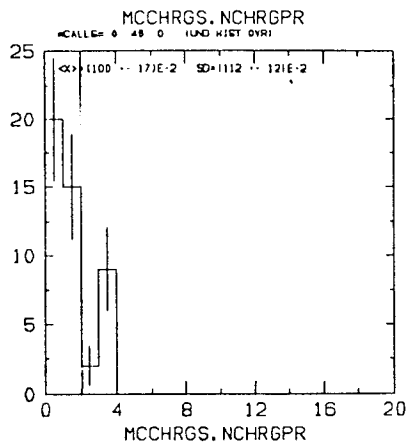


Fig. 13

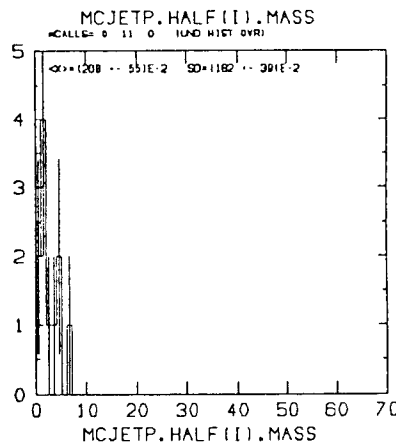


Fig. 14

Fig. 9 - $q\bar{q}$ background, E_{vis} of quiet hemisphere. Fig. 10 - $\cos(\theta_{Thr})$ of monojet. Fig. 11 - $\tau^+\tau^-$ background, E_{vis} of quiet hemisphere, the peak is due to the energy deposited in the endcap calorimeter by minimally ionizing particles without endcap tracking information. Fig. 12 - after acceptance cuts, monojet invariant mass. Fig. 13 - $\gamma\gamma \rightarrow \tau^+\tau^-$ background, after acceptance cuts, visible charged track multiplicity. Fig. 14 - after visible charged track cut, monojet invariant mass.

EFFICIENCY

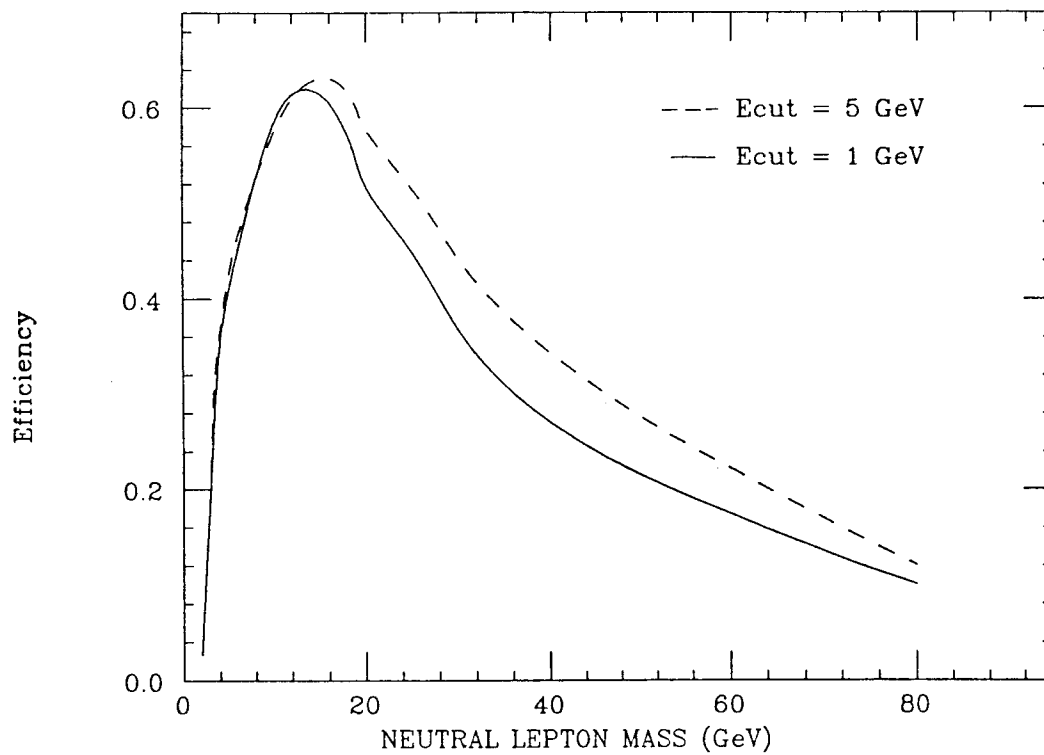


Fig. 15

Sensitivity; U^{*2} vs. Mass

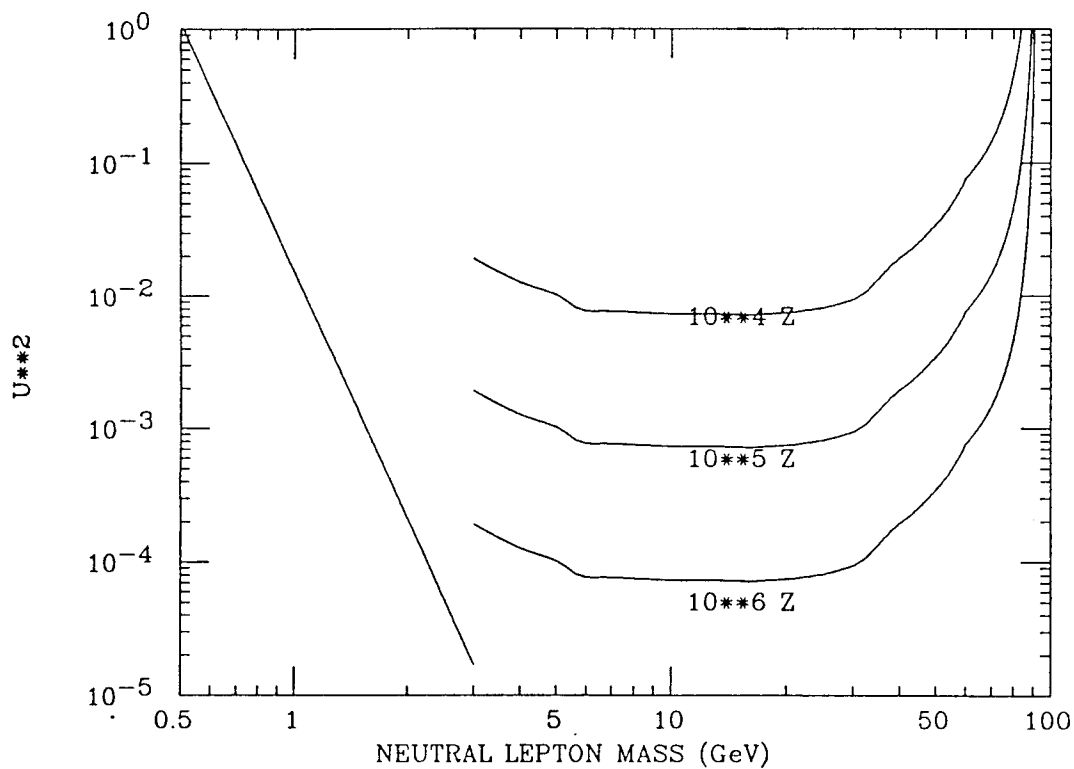


Fig. 16

mass measurement

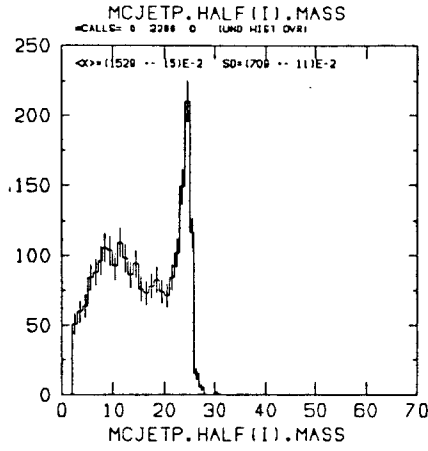


Fig. 17

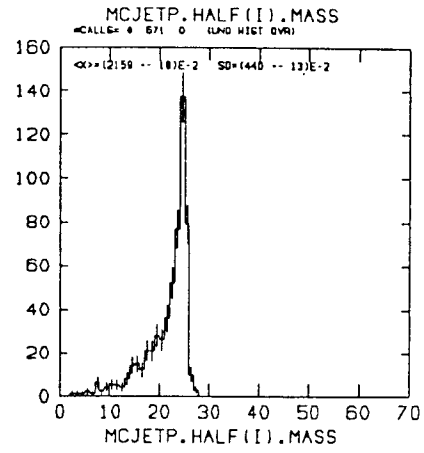


Fig. 18

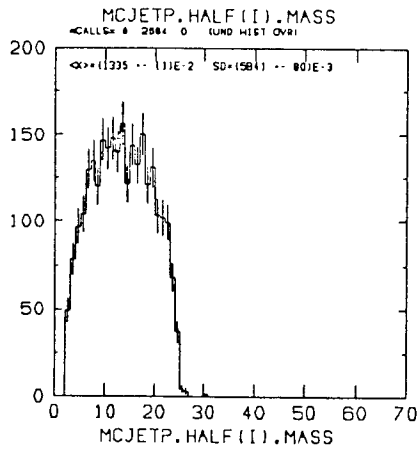


Fig. 19

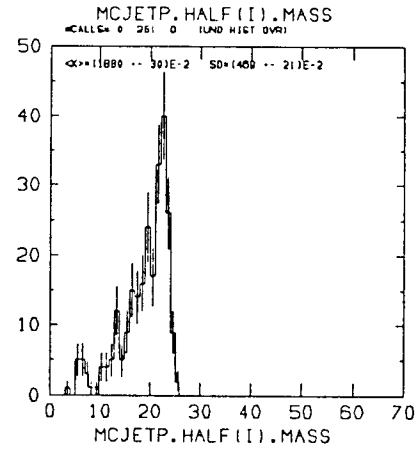


Fig. 20

Fig. 17 - the monojet invariant mass after the analysis. Fig. 18 - after demanding that there be one charged lepton track and $E_{vis} > 40$ GeV, the monojet invariant mass for $M_{L^0} = 25$ GeV. Fig. 19 - the monojet invariant mass for L^0 coupling only to tau. Fig. 20 - after demanding lepton track multiplicity = 1 and $E_{vis} > 40$ GeV, the monojet invariant mass.

Search For Excited Muons in SLD

C.G. ARROYO & R.V. STEINER

Department of Physics, Columbia University, NY, NY 10027

1. Introduction

In spite of the success of the $SU(2) \times U(1)$ electroweak theory, it is believed that a threshold for new physics exists at about the 1 TeV energy scale. The two scenarios generally offered are: (1) *supersymmetry*—predicting a large number of new particles and interactions; and (2) *compositeness*—predicting a substructure to the quark and/or lepton. The compositeness scenario leads naturally to the prediction of excited quarks and leptons. Considerable experimental effort has gone into searches for these objects. Unfortunately, the value of the mass scale which characterizes the strength of the binding interactions within the quark/lepton is unknown. Hence, the experimental limits that have been set generally depend upon the assumed mass and couplings of these objects to normal fermions. In this note, we report on the capabilities of SLD to search for excited muons under two different production scenarios.

There are several different possibilities for excited lepton production in general, summarized in the set of diagrams of Figure 1, which is taken from a review by Hagiwara and Komamiya¹. As indicated by that figure, excited leptons may be either singly or pair produced in e^+e^- interactions. Note that, if lepton number is conserved, only excited *electrons* may appear in the t-channel diagrams of that figure. The open circle of Fig. 1(a) represents the possible existence of a form factor, while the solid circle vertex is described by the Lagrangian

$$L = \frac{\epsilon}{2\Lambda} \bar{l}^* \sigma^{\mu\nu} (c_\gamma - d_\gamma \gamma_5) l F_{\mu\nu} + h.c.$$

where Λ is the scale of compositeness. Hagiwara and Komamiya note that electronic chirality is preserved only when $c_\gamma = d_\gamma = \pm 1$. One must look closely at the assumed couplings in studying the literature, as most analyses do in fact assume the non-chiral coupling $d_\gamma = 0$.

As indicated, both single and double excited lepton production are possible. For both cases, theory provides little guidance as to the expected masses or couplings of these objects to normal fermions. Hence, the predicted cross sections for these processes are highly model-dependent. The current experimental limits on these process are summarized in Figure 2. We note that while the single excited lepton processes have a higher mass reach than the corresponding double excited lepton process, the backgrounds are generally more severe.

2. Single Excited Muon Production

2.1. SIMULATION

Event Simulation

Simulated events of the type $e^+e^- \rightarrow \mu^*\mu, \mu^* \rightarrow \mu\gamma$ were generated according to the model of Hagiwara *et al.*² This model assumes the occurrence of charged and neutral excited leptons within weak doublets, assumes that $SU(2) \times U(1)$ invariance is preserved for both left and right-handed excited fermions and assumes no anomalous magnetic moments of the excited leptons. The coupling used corresponds to $\Lambda = 1$ TeV, and excited muon masses of 40, 60 and 80 GeV were studied. The excited μ was assumed to decay immediately via $\mu^* \rightarrow \mu\gamma$ with 100% branching fraction. For further details, refer to section III of Hagiwara *et al.*

Background Simulation

For single excited muon production, the principal backgrounds are from third order electroweak processes in which a photon is emitted from either the initial or final state, yielding a final state consisting of two oppositely charged muons and one photon. Such processes were simulated using the BREMMUS generator for radiative lepton pair production. Detector acceptance cuts to simulate the beam pipe were applied to this sample, but no further attempt was made to interface BREMMUS to the SLD detector geometry. From the generated events, kinematic quantities of interest (muon and photon energies, angles, etc.) were plotted in order to determine which data cuts could be used to distinguish between the signal and background samples.

A background also exists from radiative tau pair production, in which both taus decay via $\tau \rightarrow \mu \nu_\tau \bar{\nu}_\mu$, with a photon radiated somewhere in the process. This processes were simulated using the generator LULEPT. In addition possible backgrounds from quark-antiquark pair production were studied using MCLUND.

Detector Simulation and Event Reconstruction

The SLD detector simulation used GEANT to simulate the detector geometry and tracking, the fast shower parameterization to simulate the showering of electrons and photons and the standard calorimeter and event reconstruction programs. However, as will be described later in this paper, use of the beam energy constraint made use of the detector energy information only in a marginal way. A parametrized simulation of the MarkII³ was used to estimate the performance of this detector in an excited muon search.

2.2. DATA ANALYSIS

Candidates for $e^+e^- \rightarrow \mu^*\mu$, where $\mu^* \rightarrow \mu\gamma$, were required to satisfy the following data cuts:

- (1) Exactly one photon of energy > 0.1 GeV and two muons of opposite charge in the final state.

- (2) The missing energy $E_{missing} < 11\text{GeV}$, where $E_{missing} = 2 * E_{beam} - (E_{\mu+} + E_{\mu-} + E_{\gamma})$ with $E_{beam} = 46.5\text{GeV}$, and the μ and γ energies determined from the output data banks of the Monte Carlo.
- (3) $\cos(\theta_{\mu\gamma}) < -.98$, where $\cos(\theta_{\mu\gamma})$ is the angle between the photon and either of the two muons.

The first requirement assured high detection efficiency for the photons of the data sample. The second cut was used to exclude either undetected or poorly measured particles, and was also used to reduce background contributions from radiative τ pair production and from Lund backgrounds. The third cut stemmed from the fact that for high mass μ^* (greater than 20 GeV), the $\cos(\theta_{\mu\gamma})$ distribution of the radiative muon pair background, which is highly peaked near $\cos(\theta_{\mu\gamma}) = -1$, can be effectively isolated from the signal.

Although the muon and photon angles are relatively well-measured by SLD, considerable improvement can be attained in the excited muon mass resolution through use of the beam energy constraint. Hence, an event passing the above cuts was subject to a redetermination of the energies of the particles using only the angles measured with the detector, assuming a possible missing photon emitted along the beampipe direction and using energy-momentum conservation to obtain the four unknown total momenta.

$$P_{\mu+} + P_{\mu-} + P_{\gamma} + P_{\gamma missing} = (E_{cm}, 0, 0, 0)$$

where the Ps are the four momenta and $E_{cm} = 2 * E_{beam}$. A consistence check chi square was constructed using the redetermined and detected values of the total momenta and using for the standard deviations the values found in the SLD design report. The energy redetermination was considered acceptable for values of chi-squared less than 30.

The existence of μ^* is signaled by a mass peak in the $\mu\gamma$ invariant mass. Each event contributes two entries to the invariant mass histogram, one for each $\mu\gamma$.

It was found that our cuts reduced the background to:

BREMUS		5208 events/ $10^6 Z^0$
LULEPT	with 95%CL	1 events/ $10^6 Z^0$
LUND	with 95%CL	122 events/ $10^6 Z^0$

Invariant mass plots showing both signal and background are shown in Fig. 2 for the limit case with 95%CL. for excited muon masses of 40, 60 and 80 GeV. In the absence of evidence of the existence of μ^* we will be able to discard a region in the Λ -Mass of the excited muon plane.

3. Pair Production of Excited Muons

The event selection for pair production of excited muons, $e^+e^- \rightarrow \mu^*\mu^*$, in which *each* excited muon decays via $\mu^* \rightarrow \mu\gamma$ was the requirement of only two photons and two opposite charged muons in the final state. The production of a pair of excited muons is equivalent to that of muons of the corresponding masses. That is there is no Λ dependence.

The double mass constraint provides a distinctive signature for this process in which both $\mu\gamma$ invariant mass combinations are plotted in a scatter plot. The dominant background is from fourth order QED and leptonic decay of tau pairs, where the taus retain most of the event energy. We expect these backgrounds to be small but did not have at our disposal a generator to study them in detail.

The contribution of this mode to Figs.3 and 4 is the steep line at the beam energy.

4. Summary

We have examined here only a small subset of the various modes in which excited leptons may appear. Depending upon the masses and couplings, copious production could be seen in a sample of as little as 10,000 Z^0 decays. On the basis of the preliminary study done here, SLD would appear to have only a slight advantage over Mark II in its detection ability for single excited muon production. It should be noted that a beam energy constraint significantly enhances the ratio of signal to background in the invariant mass (typically 15 times).

5. Acknowledgements

We would like to thank the other members of the SLD New Leptons/Quarks Group for many helpful contributions to this work.

6. References

- (1) K. Hagiwara, S. Komamiya, Search for New Particles at e^+e^- Colliders, KEK
- (2) K. Hagiwara, S. Komamiya and D. Zeppenfeld, Excited Lepton Production at LEP and HERA, Z.Phys.C, 29, 115-122(1985).
- (3) T. Bolton, A Simple MarkII Detector Simulator, SLD preprint.
- (4) See, for example, the discussion on p.224-5 of Bartel *et al.*, Observation of Radiative e^+e^- Annihilation Into $\mu\mu\gamma$ and $\mu\mu\gamma\gamma$, Z.Physik C, 24 223-229(1984).

7. Figures

1. Feynman diagrams for excited lepton production
2. $\mu\gamma$ invariant mass μ^* masses of 40,60 and 80GeV. Case of $10^6 Z^0$.
3. Excluded region 95% CL. for SLD.
4. Excluded region 95% CL. for MKII.

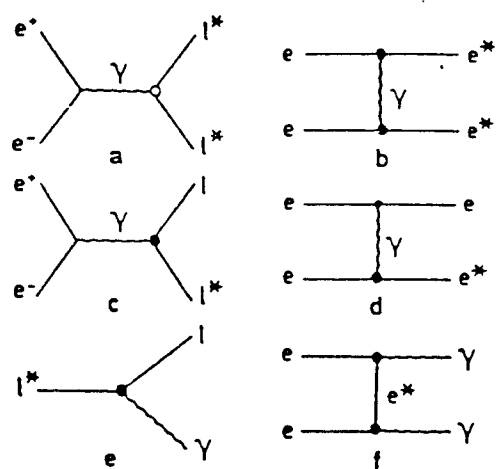
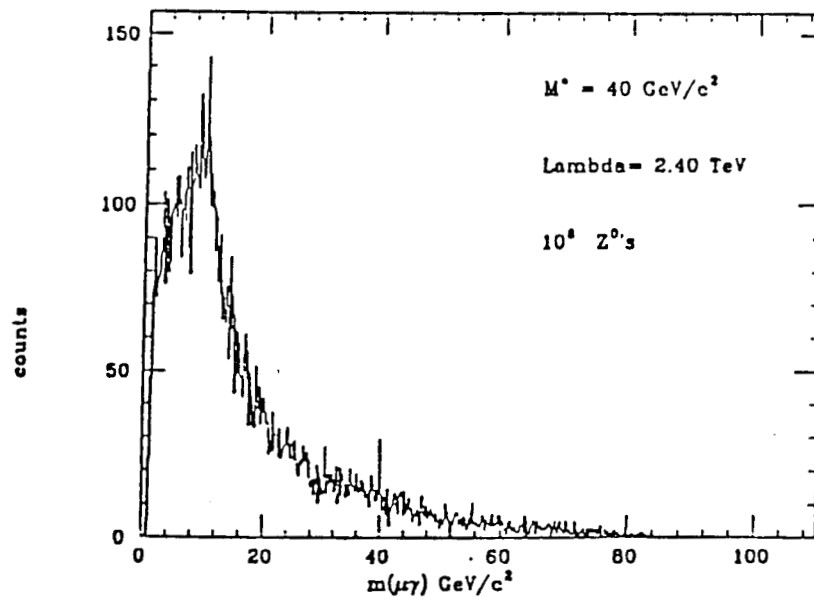
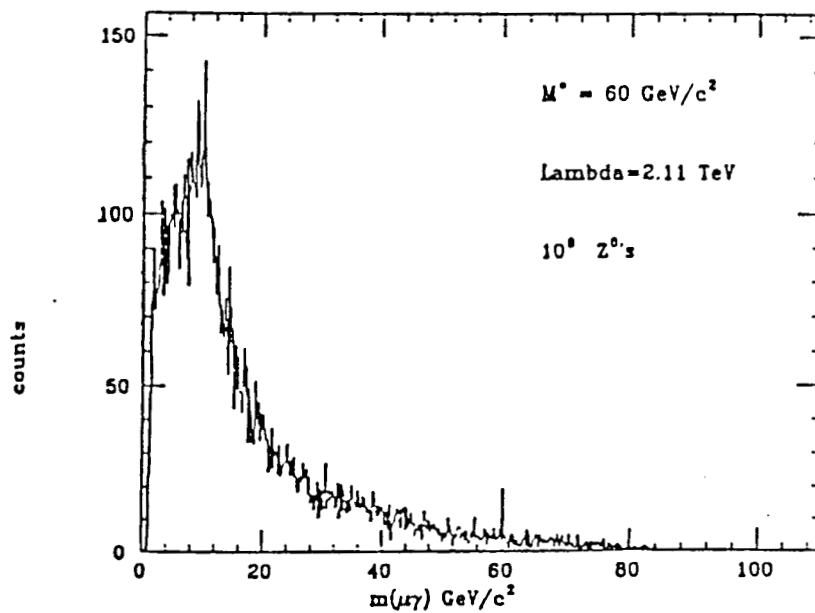


Figure 1

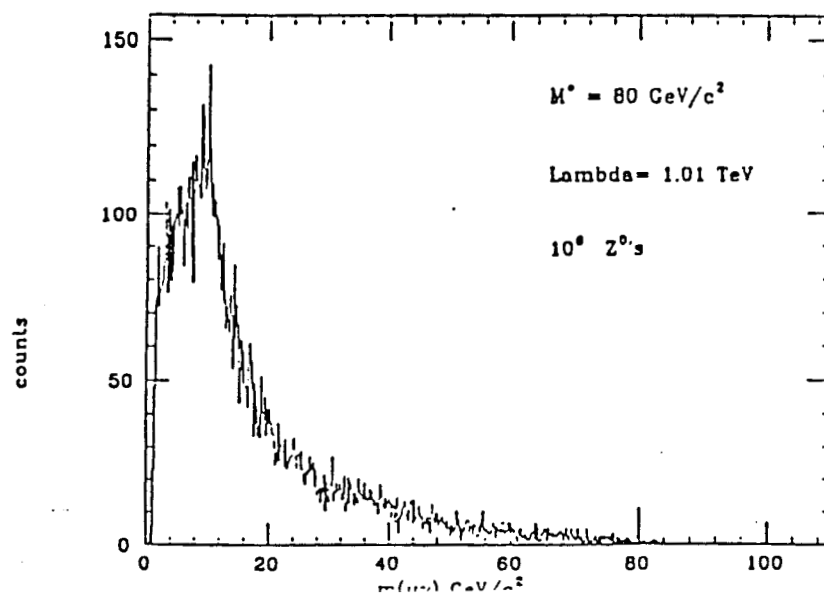
Photon - Muon invariant mass



Photon - Muon invariant mass



Photon - Muon invariant mass



Excluded Region : 95 % C.L. SLD

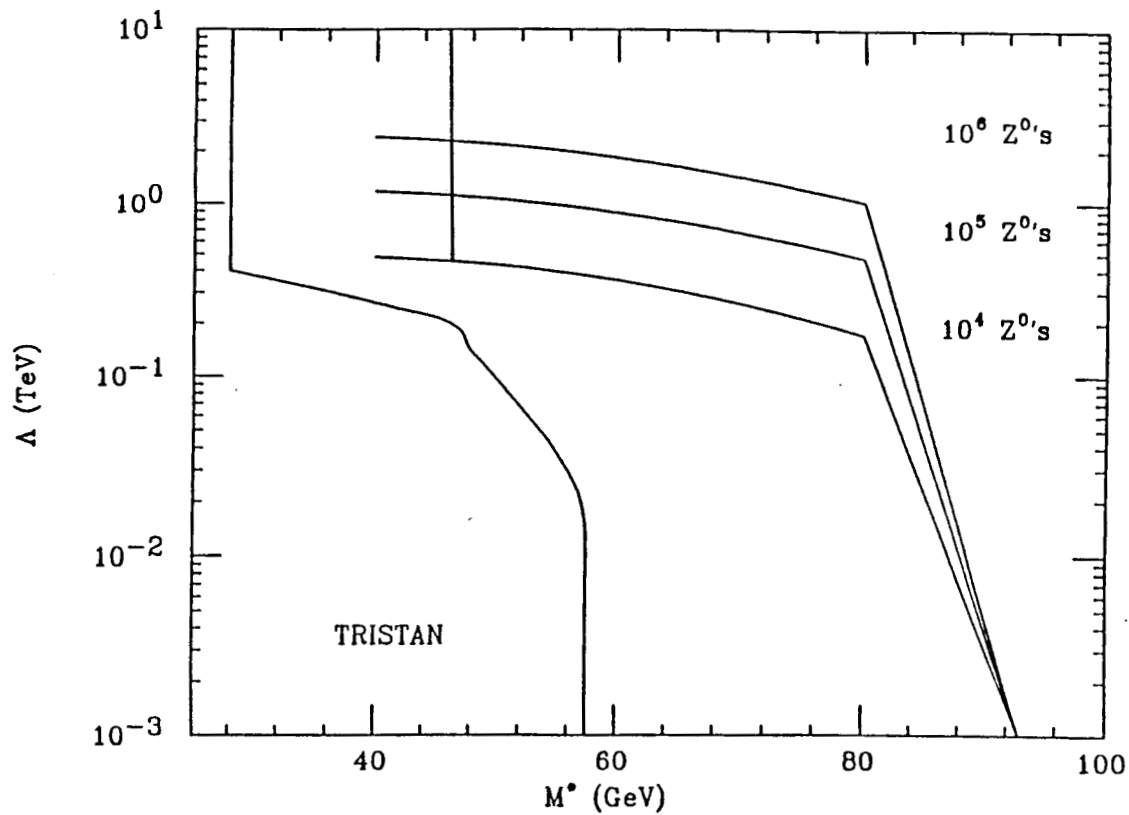


Figure 3

Excluded Region : 95 % C.L. MKII

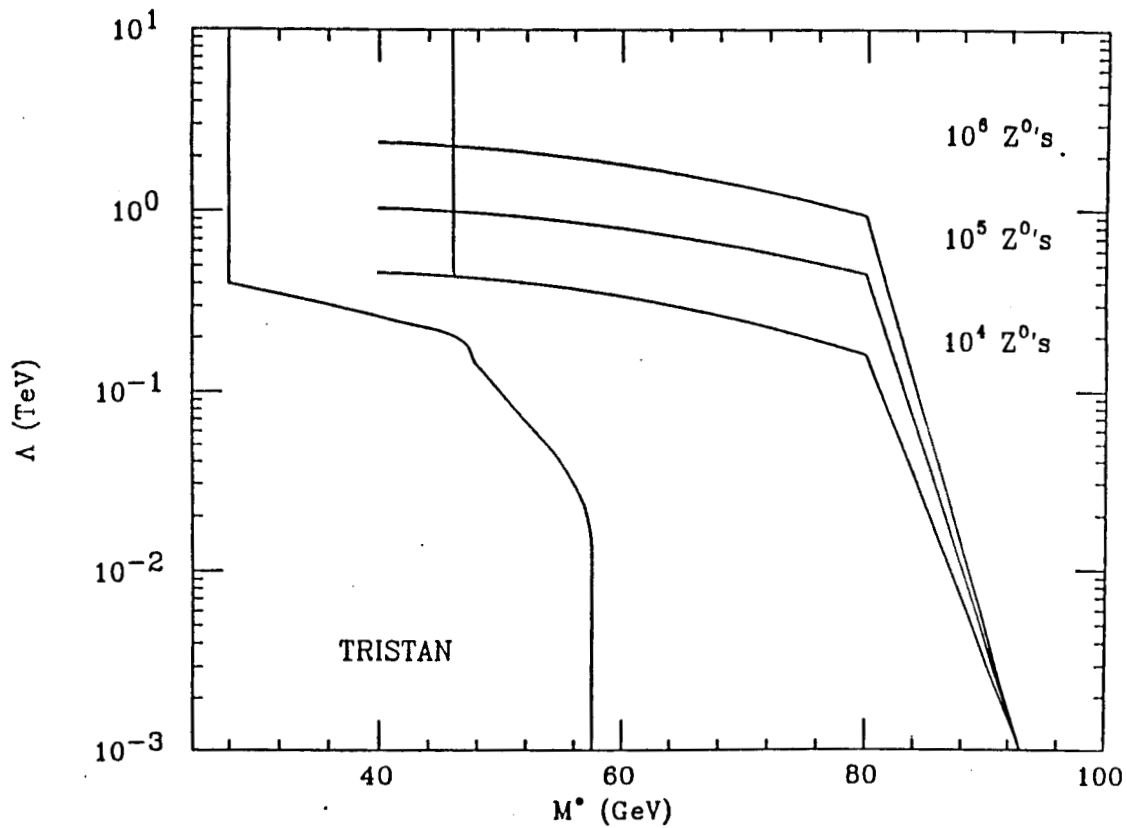


Figure 4

Additional Neutral Vector Bosons

P.C. ROWSON

Department of Physics, Columbia University, NY, NY 10027

Introduction

New neutral vector bosons beyond the familiar Z^0 arise in several models characterized by extended gauge symmetry groups. Theories which incorporate gauge symmetries beyond the $SU(3) \times SU(2) \times U(1)$ of the Standard Model include left-right symmetric theories, E_6 based grand unified theories and minimal modifications of the Standard Model in which quarks and leptons transform under separate gauge groups¹.

Basic Phenomenology

We will here describe the simple phenomenological consequences of an additional Z' boson, where for definiteness we will refer to a specific model with extended gauge symmetry. A grand unified theory (GUT) based on the exceptional Lie group E_6 has been extensively studied in the context of Z' physics². The E_6 symmetry breaking pattern is given by :

$$E_6 \rightarrow SU(5) \times U(1)_\chi \times U(1)_\psi \quad \text{and} \quad SU(5) \rightarrow SU(3) \times SU(2) \times U(1)$$

The $U(1)$ groups are each associated with a neutral vector boson:

$$U(1)_\chi \rightarrow Z_\chi \quad U(1)_\psi \rightarrow Z_\psi \quad U(1) \rightarrow Z,$$

where Z is the boson of the Standard Model. The new Z' is in fact a linear

combination of the Z_χ and Z_ψ ,

$$Z' = Z_\psi \cos \theta_6 + Z_\chi \sin \theta_6 \quad (1)$$

where θ_6 is an E_6 induced mixing angle³. The neutral current Lagrangian now takes the form:

$$\mathcal{L}_{NC} = e A_\mu J_E^\mu M + g_Z Z_\mu J_Z^\mu + g'_Z Z'_\mu J_{Z'}^\mu, \quad (2)$$

where the new weak current couplings of the Z' to the known fermions are specified uniquely for the E_6 model.

Since the Z' will have the same quantum numbers as the the Standard Model Z , quantum mechanical mixing will occur. The physical Z^o and $Z^{o'}$ (the “mass eigenstates”) will actually be a linear combination of the Z and Z' discussed above. The mixed states are found by diagonalizing the mass matrix,

$$\begin{pmatrix} M_Z^2 - i M_Z \Gamma_Z & \delta M^2 \\ \delta M^2 & M_{Z'}^2 - i M_{Z'} \Gamma_{Z'} \end{pmatrix},$$

where the size of the off-diagonal element of the mass matrix specifies the strength of the mixing. The off diagonal element depends on the details of the Higgs mechanism that is responsible for the Z and Z' masses, and on the weak mixing parameter $\sin \theta_W$. For small mixing, the diagonalization is achieved via a rotation through an angle

$$\theta_{mix} \approx \frac{\delta M^2}{M_{Z'}^2 - M_Z^2}. \quad (3)$$

The mass of the Z^o will be downshifted from its Standard Model value (the $Z^{o'}$ mass increases by the same amount), where for small mixing the mass shift is given by:

$$\delta M_Z \approx \frac{M_Z^2 - M_{Z'}^2}{2M_Z} \theta_{mix} \quad (4)$$

Since the coupling constants g_Z and g'_Z are also mixed by a rotation through θ_{mix} ,

and

$$\Gamma_Z \sim g_Z^2 M_Z,$$

the total and partial widths of the Z^0 are shifted as well. *In general, $Z - Z'$ mixing effects modify measurable electroweak parameters.*

Experimental Issues

The expected experimental effects due to $Z - Z'$ mixing include:

- Shifts of M_Z and Γ_Z .
- Modifications of the hadronic and leptonic partial widths and cross sections in Z decays.
- Measurable effects on the forward-backward (FB) and and polarized left-right (LR) production asymmetries.

Unless the Z' boson is light enough to be observed directly at the SLC or LEP (a possibility that is essentially excluded by present data), only high precision measurements of the type listed above can reveal the presence of additional vector bosons at present e^+e^- colliders. The experimental picture is complicated by the effects of radiative corrections, particularly those effects due to a heavy top quark. If we take α , G_F and M_Z as the fundamental parameters of the electroweak model, the W boson mass is given by⁴

$$M_W = \frac{M_Z}{\sqrt{2}} \left[1 + \left(1 - \frac{4\pi\alpha}{\sqrt{2}M_Z^2 G_F (1 - \Delta r)} \right)^{1/2} \right]^{1/2}, \quad (5)$$

where Δr contains what is known about loop corrections and is dominated by contributions due to the top quark. We take the definition of the weak mixing angle to be

$$\sin^2 \theta_W = 1 - \frac{M_W^2}{M_Z^2}. \quad (6)$$

Thus shifts of M_Z will not be interpretable until precision values for M_W and Δr become available. Figure 1 illustrates the relationship between M_Z and M_W

for several values of the top mass⁵, where the present experimental values are overlaid⁶.

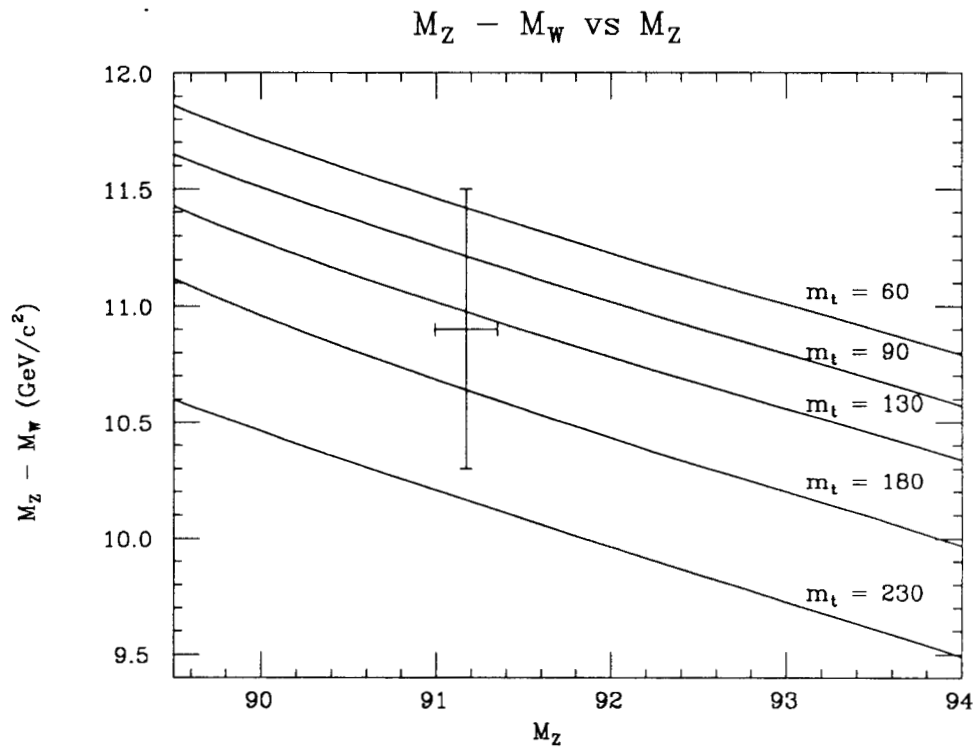


Figure 1.

From figure 1 it is clear that significant information about the top mass will require much better M_W measurements.

The best available limits on Z' bosons derive from neutrino scattering neutral current data⁷ which allow a region in $M_{Z'}$ versus θ_{mix} space from about 130 GeV/c² for large mixing to just below 400 GeV/c² for $|\theta_{mix}| > 0.02$. The allowed region is shown in figure 2.

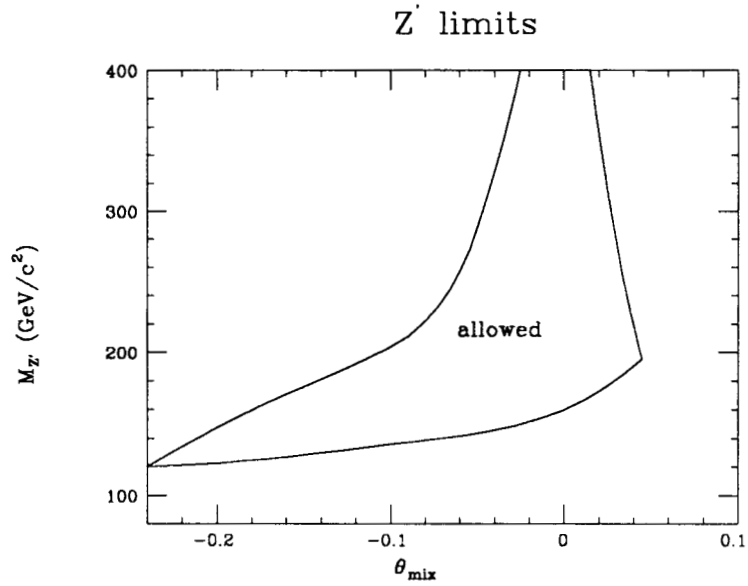


Figure 2.

We can illustrate the present limits by comparison with the expected mass shifts of the Z^0 due to $Z - Z'$ mixing; here we have taken the "premixing" Z^0 mass to be 92 GeV/c^2 .

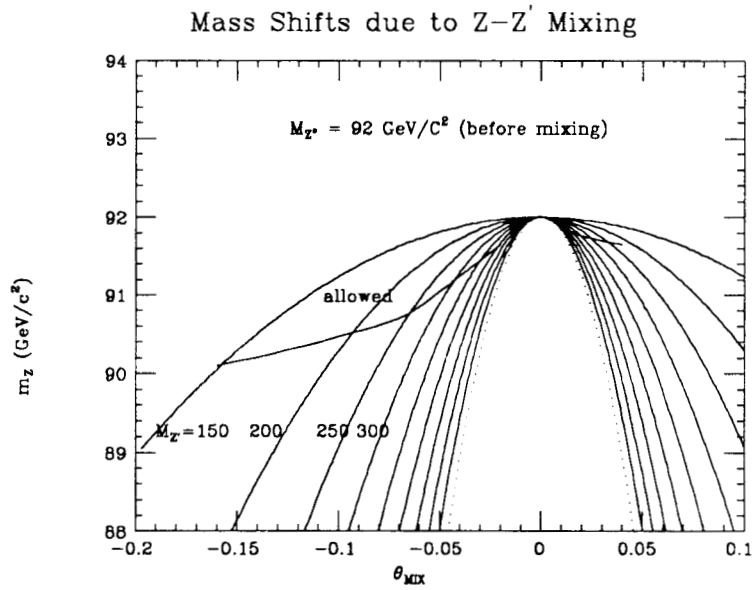


Figure 3.

From this figure, we see that for large Z' masses, large mass shifts are ruled out

for all but the smallest mixing angles. As hadron colliders will probably exclude Z' masses up to just over $300 \text{ GeV}/c^2$ in the near future⁸, it is not likely that a search for small Z^o mass shifts will be the most effective approach at the SLC. A better technique is to exploit the high sensitivity to weak parameters made available with a polarized e^- beam. The search for Z' bosons might proceed in two stages, as successively larger data samples become available:

1. Observation of non-standard Z^o partial widths (e.g. $\Gamma_{\mu\mu}$, $\Gamma_{hadrons}$, and their ratio). A dramatic signature allowed in some models is a *downshifted* total width.
2. Establishment of a less ambiguous effect by precision measurements of weak asymmetries using polarized beams. At this stage, specific models can be distinguished and their parameters determined.

In figure 4, the variation of the LR asymmetry versus the ratio of the Z^o leptonic and hadronic partial widths⁹ is shown as a function of both the E_6 mixing angle and θ_{mix} . Also shown is the Standard Model variation expected for top masses from 40 to $180 \text{ GeV}/c^2$. The measurement errors shown correspond to a data sample of 10^5 events and a 5% polarization error; if polarization measurement errors are reduced from 5% to 1%, the error for the LR asymmetry will be reduced proportionately.

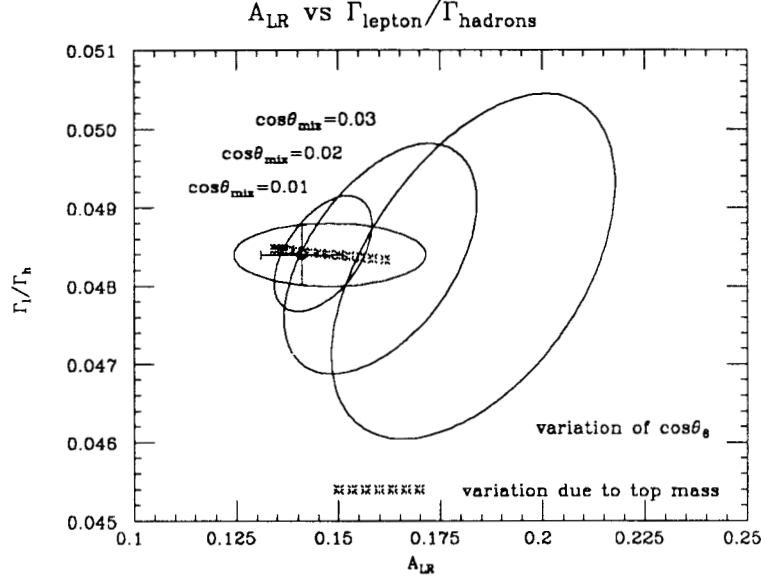


Figure 4.

As evidenced by figure 4, the detection of effects due to small mixing will be challenging. Until the magnitude of electroweak loop corrections are known (for example once the mass of the top quark has been measured), any search for Z' bosons based on a determination of electroweak parameters will be beset by ambiguities. It has been recognized for some time that one should be able to minimize the confusion by a propitious choice of a set of observables and a measurement of their correlations. By an appropriate linear combination of observables, one can construct a measurable quantity for which the troublesome “oblique” radiative corrections due to top quark vacuum polarization loops nearly cancel. An example of this idea is due to Lynn, Renard and Verzegnassi¹⁰. These authors consider the LR asymmetry (A_{LR}) and the polarized FB asymmetry for bottom quarks ($A_{FB}^{pol(b)}$),

$$A_{FB}^{pol(b)} = \frac{1}{\mathbf{P}} \frac{(N_{\mathbf{P}F}^b - N_{-\mathbf{P}F}^b) - (N_{\mathbf{P}B}^b - N_{-\mathbf{P}B}^b)}{(N_{\mathbf{P}F}^b + N_{-\mathbf{P}F}^b) + (N_{\mathbf{P}B}^b + N_{-\mathbf{P}B}^b)}, \quad (7)$$

where $\mathbf{P} = -P_e$ (the positron beam is unpolarized).

Both A_{LR} and $A_{FB}^{pol(b)}$ are particularly useful due to their insensitivity to QED and strong interaction corrections. The oblique corrections for these two asymmetries are proportional:

$$\delta A_{FB,oblique}^{pol(b)} = \frac{1}{15} \delta A_{LR,oblique}, \quad (8)$$

suggesting the construction of a “correction-free” quantity,

$$\tilde{A}_{FB}^{pol(b)} = A_{FB}^{pol(b)} - \frac{1}{15} A_{LR} \quad (9)$$

The experimental difficulties associated with properly identifying the bottom jet (as opposed to the anti-bottom jet) have not been conclusively studied, but preliminary work within the SLD collaboration¹¹ indicates that it should be possible to measure $A_{FB,oblique}^{pol(b)}$ to within 7-8% with 10^5 events. At the moment it is unclear whether or not the techniques suggested by Lynn *et al.* will be practical.

Comparisons and Conclusions

One’s ability to make precision measurements of electroweak parameters such as the Z^0 mass, width, partial widths and LR asymmetries depends more strongly on the performance of the accelerator (luminosity, energy spread and polarization) than it does on the detector used. Thus the SLD will enjoy an advantage over the LEP experiments only to the extent that the SLC will provide longitudinally polarized beams and LEP will not.

At the SLC, it should be possible to probe mixing angles $|\theta_{mix}|$ less than 0.02 with 10^5 events using the LR asymmetry. Mixing angles smaller than 0.01 will be probed with 10^6 events. One study¹² has estimated that the LEP experiments will be sensitive to $|\theta_{mix}| \geq 0.025$ with 10^6 events, and that nearly 10^8 events will be needed to achieve precisions comparable to those possible with 10^6 events and polarization. The advantage of polarization is equivalent to a factor of ≈ 100 in effective luminosity.

References

1. A theory of this type is given in H. Georgi *et al.*, Phys.Rev.Lett.,62:2789,1989.
2. See, for example, P.J. Franzini, thesis, Stanford University, SLAC-Report-308, 1987.(Our discussion of phenomenology is taken in part from this work).
3. A often referred to special case is $Z_\eta = -\sqrt{\frac{5}{8}}Z_\psi + \sqrt{\frac{3}{8}}Z_\chi$, inspired by super-string phenomenology.
4. A. Sirlin, Phys.Rev.D22,971,1980.
W. Marciano and A. Sirlin,Phys.Rev.D22,2695,1980.
5. B. Lynn and R. Stuart, Nucl.Phys.B253,216,1985.
6. G.S. Abrams *et al.*, Phys.Rev.Lett.,63:724,1989, for the Z^0 mass of 91.17 ± 0.18 GeV $/c^2$ and CDF Collaboration, Lepton/Photon Symposium,1989, Stanford, CA,. for the Z^0 and W masses of $90.9 \pm 0.3 \pm 0.2$ (*scale*) GeV $/c^2$ and $80.0 \pm 0.5 \pm 0.3$ (*scale*) GeV $/c^2$ respectively.
7. L. Durkin and P. Langacker, Phys.Lett.166B,436,1986.
8. G. Altarelli *et al.*, CERN-TH.5323/89,1989.
9. The author acknowledges useful calculations and assistance from M. Peskin, and refers the reader to his lecture from the SLAC Summer Institute, 1989.
10. See, for example, B. Lynn *etal*, Nucl.Phys.B310:237,1988.
11. W.B. Atwood, SLAC-PUB-4827,1988.
12. C. Verzegnassi, CERN-TH.5438/89,1989.

SLD PHYSICS REPORT - 1

December, 1988

A Study of Neutrino Counting with the SLD Detector

H. Band^l, W. Buggⁱ, G. Chadwick^h, D. Coyne^c, M. Gyure^d, S. Hertzbach^g,
R. Messner^h, A. Mincer^b, P. Mockett^k, U. Nauenberg^d, P. Reutens^h,
J. Rothberg^k, P. Rowson^e, M. Shaevitz^e, R. Sobie^j,
J. Thaler^f, B. Wilson^a, C. Young^h, K. Young^k

- a) Boston University
- b) California Institute of Technology
- c) University of California at Santa Cruz
- d) University of Colorado at Boulder
- e) Columbia University
- f) University of Illinois at Urbana-Champaign
- g) University of Massachusetts
- h) Stanford Linear Accelerator Center
- i) University of Tennessee
- j) University of Victoria
- k) University of Washington
- l) University of Wisconsin

TABLE OF CONTENTS

- I) Introduction
- II) Determination of N_ν from the Z_0 Width.
 - (1) Calculation of the Z_0 Width and Its Dependence on the number of Neutrinos.
 - (2) Effect of the Uncertainty in the Measurement of the Luminosity and Beam Energy Spectrum.
 - (3) Effect of the Uncertainty in the Mass of the Top Quark.
 - (4) Effect of the Presence of Toponium at the Z_0 .
 - (5) Dependence of the Z_0 Width on Decays into Supersymmetric Particles.
 - (6) Dependence of the Z_0 Mass and Width on Radiative Corrections.
- III) Determination of N_ν by Directly Measuring the Fraction of the Z_0 Width due to $Z_0 \rightarrow \nu + \bar{\nu}$ Decays.
- IV) Determination of N_ν Using the Reaction $e^+ + e^- \rightarrow Z_0 \rightarrow \nu + \bar{\nu} + \gamma's$
 - (1) The Cross Section and Expected Number of Events.
 - (2) The Effect of Radiative Corrections on the Reliability of the Cross Section Calculation.
 - (3) Limits on the accuracy of N_ν obtained by measuring the Absolute Cross-section.
 - (4) The Background due to Radiative Bhabha Scattering.
 - (5) The Background due to the 3 γ 's final state.
 - (6) The Measurement of N_ν with a Polarized e^- Beam.
 - (7) Limits on the Accuracy of N_ν obtained by measuring the Branching Ratio $\frac{e^+ + e^- \rightarrow \nu + \bar{\nu} + \gamma's}{e^+ + e^- \rightarrow \mu^+ + \mu^- + \gamma's}$.
 - (8) The Effect of the Processes $e^+ + e^- \rightarrow Z_0 \rightarrow \tilde{\nu} + \tilde{\bar{\nu}} + \gamma's$ and $e^+ + e^- \rightarrow \tilde{\gamma} + \tilde{\gamma} + \gamma's$.

v) Photon Detection in the SLD Calorimeter.

- (1) Angular Resolution of the SLD Calorimeter for Low Energy Photons.
- (2) Energy Resolution of the SLD Calorimeter for Low Energy Photons.
- (3) Beam Related Photon Background.
- (4) Cosmic Ray Related Background.
- (5) Veto Efficiency of the Luminosity Monitor.

vi) Resolution in the Determination of N_ν Based on Various Cuts and Running Conditions.

1. Introduction

Ever since the 1970's when the "standard model"^[1] began to emerge, one of the interesting questions which arose was whether there were more than the known three families or generations (doublets) of leptons and quarks. The neutrinos are each a member of a lepton generation. These neutrinos are assumed to be the only particles among the leptons and quarks to be very light, even massless; certainly, the measured upper limits on the masses are quite small^[2]. Given our present understanding of the particle generations pattern, a measurement of the number of types of neutrinos would tell us the number of lepton and quark doublets. This number is a crucial element in the understanding of the structure of matter. In addition, the number of light neutrinos is an important parameter in the determination of the abundance of light chemical elements in the universe^[3]. In fact, the best upper limit on the number of neutrinos, derived from these calculations is four^[3].

Because the known neutrinos are light, a reasonable assumption is that new generations of these are also light. Since the Z_0 can decay into pairs of neutrinos, its decay rate into them measures the number of generations. Obviously, we can only determine the number of neutrino generations with masses less than half the Z_0 mass. Since accelerators are being built that will produce a very large number of Z_0 's^[4], this experiment is feasible. This measurement can be done in one of four ways, each depending on a comparison with theoretical expectations based on the "Electroweak Theory"^[1]. The four methods are:

1. Compare the expected integrated decay rate of the Z_0 (its mass width), based on the number of neutrino types, with the measured value.
2. Measure directly the fraction of the Z_0 width due to its decay into neutrinos and compare it with the expected value.
3. Measure the cross-section of the process $e^+ + e^- \rightarrow Z_0 \rightarrow \nu + \bar{\nu} + \gamma$'s and compare it with the predicted dependence on the number of neutrino types.

4. Compare the rate of the process $e^+ + e^- \rightarrow Z_0 \rightarrow \nu + \bar{\nu} + \gamma's$ with the process $e^+ + e^- \rightarrow Z_0 \rightarrow \mu^+ + \mu^- + \gamma's$ and compare the ratio with the predicted dependence on the number of neutrinos. This method is the least sensitive to errors that appear in the calculation of the rate since they appear equally in both processes and hence cancel out in the ratio.

It is the purpose of this note to discuss, in detail, the difficulties encountered in making these measurements; namely, the expected limits of the accuracy in the determination of the number of neutrinos from each type of measurement.

2. Determination of N_ν from the Z_0 Width

2.1 THE EXPECTED Z_0 WIDTH AND ITS DEPENDENCE ON THE NUMBER OF NEUTRINOS.

The determination of the number of neutrinos by studying the properties of Z_0 decays depends crucially on the correctness of the "electroweak" theory^[1]. Based on the electroweak lagrangian that describes the Z_0 decay^[4],

$$\mathcal{L}(Z_0 \rightarrow f + \bar{f}) = i\sqrt{2}G_F M_Z \{\bar{\psi}_f \gamma^\mu (v_f - a_f \gamma_5) \psi_f\} Z_\mu \quad (2.1.1)$$

one can calculate the decay rate of the Z_0 into any fermion anti-fermion pair of the lepton and quark families. The decay rate is given by^[4,5]

$$\Gamma(Z_0 \rightarrow f + \bar{f}) = \frac{cM_Z^3}{6\pi} \frac{G_F}{\sqrt{2}} \{v_f^2 + a_f^2 - \frac{2m_f^2}{M_Z^2}(2a_f^2 - v_f^2)\} \{1 - 4\frac{m_f^2}{M_Z^2}\}^{\frac{1}{2}} \quad (2.1.2)$$

where the color factor $c=1$ for leptons and 3 for quarks.

In Table 1 we define the various parameters in (2.1.2) and we relate the values of v_f and a_f to $\sin^2 \theta_w$; we also calculate the decay rates, and the branching ratio of decays into various final states.

Radiative effects can alter the observed results quite markedly^[6], but we assume that these corrections will be understood at the time that the measurements will take place. In any case, we discuss these in various sections of this work and point out where uncertainties still exist and additional calculations need to be done.

We can summarize the results presented in Table 1 by the following expression describing the dependence of the Z_0 width on M_Z, N_ν , and $\sin^2 \theta_w$ in the limit $m_f=0$:

$$\Gamma_Z = \frac{M_Z^3}{24\pi} \frac{G_F}{\sqrt{2}} \{21.7 + N_\nu - 49.4 \sin^2 \theta_w + 65.6 \sin^4 \theta_w\} \quad (2.1.3)$$

Using the values of the parameters presented in Table 1, the dependence on N_ν

alone can be expressed by:

$$\Gamma_Z = 2.65 + 0.172 \times (N_\nu - 3) \text{ GeV} \quad (2.1.4)$$

The effect of an error in the known value of $\sin^2\theta_w$ ($\pm .001$) on the value of M_Z is 0.15 GeV and on the expected value of Γ_Z is $\delta\Gamma_Z = .017$ GeV or about $0.1N_\nu$ which can be neglected for the purpose of determining the number of neutrinos. A good figure of merit on the accuracy needed in the determination of the Z_0 width is the requirement that we know N_ν to about $0.2 N_\nu$. This implies a measurement error $\delta\Gamma_Z \approx 0.035$ GeV.

TABLE 1
 Z_0 Decay Rates

Final State	v_f	a_f	$\Gamma(GeV)$	Branching Ratio (%) per final state
$e^+e^-, \mu^+\mu^-, \tau^+\tau^-$	$-\frac{1}{2}[1 - 4\sin^2\theta_w]$	$-\frac{1}{2}$	0.087	3.3
$\bar{\nu}_e\nu_e, \bar{\nu}_\mu\nu_\mu, \bar{\nu}_\tau\nu_\tau$	$\frac{1}{2}$	$\frac{1}{2}$	0.172	6.5
$\bar{u}u, \bar{c}c$	$\frac{1}{2}[1 - \frac{8}{3}\sin^2\theta_w]$	$\frac{1}{2}$	0.298	11.2
$\bar{d}d, \bar{s}s$	$-\frac{1}{2}[1 - \frac{4}{3}\sin^2\theta_w]$	$-\frac{1}{2}$	0.383	14.4
$\bar{b}b$	$-\frac{1}{2}[1 - \frac{4}{3}\sin^2\theta_w]$	$-\frac{1}{2}$	0.379	14.3
$\bar{t}t$	$\frac{1}{2}[1 - \frac{8}{3}\sin^2\theta_w]$	$\frac{1}{2}$	0.060	2.3
$\sum_i \bar{q}_i q_i g$			0.072	2.7
Total			2.65	100.0

We used the following parameters:

$$\begin{aligned}
 \sin^2\theta_w &= 0.226 \\
 M_Z &= \left\{ \frac{\pi\alpha_R}{\sqrt{2}G_F} \right\}^{1/2} \times \frac{1}{\sin\theta_w \cos\theta_w} = 92.2 GeV \\
 \alpha_R^{-1} &= 137.036 - 171/6\pi \\
 m_t &= 40.0 GeV \\
 m_b &= 5.0 GeV \\
 G_F &= 1.166 \times 10^{-5} GeV^{-2} \\
 Z_0 \rightarrow \bar{q}_i q_i g &= .04 \quad Z_0 \rightarrow \bar{q}_i q_i^{[4]}
 \end{aligned}$$

2.2 EFFECT OF THE UNCERTAINTY IN THE MEASUREMENT OF THE LUMINOSITY AND BEAM ENERGY SPECTRUM.

The beam energy spectrum of the SLC at the collision point is expected to have a low energy tail owing to the beam spectrum at the end of the linac and the bremsstrahlung of the beam going around the arcs. A typical spectrum at the end of the linac, provided by the accelerator group, is shown in Fig. 1. Like the initial state radiation corrections in the individual collisions, the non gaussian tails shown in the figure will cause an upward shift in the measured peak center and an increase in the measured width. These effects must be corrected for.

The uncertainty in the luminosity measurement will not induce a systematic shift in the peak center, but will increase the measured width due to the relative uncertainty at the various energy scan points. Of course, an absolute error in the luminosity will have no effect on these matters. We assign an error to the luminosity of 3%, as suggested by other studies.

The above effects were included in an extensive Montecarlo simulation of an energy scan over the Z_0 peak of the process $e^+e^- \rightarrow f\bar{f}$. Various beam energy spectra of the type shown in Fig. 1 were used to smear the initial energies of the colliding beams. The total number of events recorded was equivalent to an integrated luminosity of $1.6 \times 10^{37} \text{ cm}^{-2}$, approximately a 1 year run at expected SLC beam fluxes. At each scan point we generate the number of events equivalent to a given value of the luminosity (the integrated luminosity divided by the number of scan points). Also, at each scan point we randomly smear the beam energy a few hundred times, simulating the non-gaussian beam energy spectrum, as shown in Fig. 1. We determined the cross section expected at the calculated center of mass energy using the values of the parameters given in Table 1 and recorded the expected number of events using the luminosity determined after it was varied randomly by 3%. This number of events found at each scan point was saved and used in a 2 dimensional Chi-Square fit in which the Z_0 mass and width were allowed to vary. These fits were done for different number of

scan points, anywhere from 6 to 16 such points. The results of the fit varied only slightly as the number of scan points across the resonance were varied. The results of the fit were $M_Z = 92.35$ GeV and Γ_Z from 2.52 to 2.80 GeV. The error of the fits were $\delta M_Z \approx 0.02$ GeV and $\delta \Gamma_Z \approx 0.03$ GeV. The Chi-Square of the fit usually was between 0.7 and 1.5 per degree of freedom. The conclusion of this preliminary study is that a non-gaussian low energy tail in the beam spectrum can shift upward the value of M_Z by 0.15 GeV and affect the value of Γ_Z by $\approx \pm 0.15$ GeV. From the Chi-Square of the fit we cannot tell that the beam has a low energy tail. Hence, knowing the energy distribution of the interacting beams is essential in this study.

We need to note that we did not include beam bremsstrahlung distortions of its energy spectrum nor radiative correction effects on the shape of the resonance, which will affect the measurement of the mass and width of the Z_0 in this study in a similar fashion. This is discussed later on.

2.3 EFFECT OF THE UNCERTAINTY IN THE MASS OF THE TOP QUARK

In Fig. 2 we show the decay rate of $Z_0 \rightarrow \bar{t}t$ as a function of the top quark mass, assuming the electroweak parameters shown in Table 1. The latest results from the UA1 experiment indicate that the top quark mass is greater than 40 GeV^[7]. As seen from Fig. 2, this implies at best an uncertainty in the number of neutrinos, due to the decay into a possible heavy top quark pair ($M_t \geq 40$ GeV), of 0.3 neutrino generations.

In addition, even if the top quark mass is larger than $M_Z/2$ it will still have an effect on the Z width because the Z propagator will be modified by loop (also called oblique) corrections. The magnitude of these corrections have been already described elsewhere^[8] and is shown in Fig. 2 also. As can be seen, this correction increases the width of the Z and for a top mass of ≈ 100 GeV it corresponds to about .09 N_ν .

2.4 EFFECT OF THE PRESENCE OF TOPONIUM AT THE Z_0 .

Because Toponium, the bound state of the top quark anti-quark pair, has the same quantum numbers as the Z_0 , we can expect to observe interference effects in the e^+e^- annihilation process into these final states. This effect has been studied in detail^[9]. The Feynman diagram that describes the process for the interference is shown in Fig. 3. This phenomena leads to changes in the mass and width of the Z_0 . The effect on the mass has been determined to be small while it is significant on the width if

$$|M_Z - M_{t\bar{t}}| \leq 2\Gamma_Z$$

The analysis of the off-diagonal elements of the mass matrix, which are responsible for the mass and width changes, indicate that

$$\delta M_Z = -\delta M_{t\bar{t}}$$

$$\delta \Gamma_Z = -\delta \Gamma_{t\bar{t}} < 0$$

Most of the effect on the width changes is due to the 3S_1 ($n=1,2,3,\dots$) states but not the corresponding P states. The shift in the Z_0 mass and width due to the 3S_1 states depends on the value of the wave function at the origin which is not negligible. On the other hands the contribution from the P states depends on the radial derivative of the wave function at the origin which has a much smaller value. Hence, the P states do not contribute significantly to these effects.

If the $M_{t\bar{t}}$ is very close to the M_Z then the shift in the width due to the $n=1$ 3S_1 state is -18 MeV. If one adds the contribution from all the radial excitations ($n=2,3,\dots$) one gets a net shift of -40 MeV or about 1/4 of a neutrino generation. This shift is significant and needs to be considered in the study of the number of neutrino generations in nature.

2.5 DEPENDENCE OF THE Z_0 WIDTH ON DECAYS INTO SUPERSYMMETRIC PARTICLES.

If supersymmetric particles exist and their mass is small enough such that the Z_0 can decay into them, then we can expect an increase in the nominal Z_0 width. The magnitude of the contribution to this width depends on the masses of the particles involved due mainly to the phase space factor $\beta = (1 - 4m^2/s)^{1/2}$. Possible supersymmetric particles that can add significantly to the width are the sneutrinos which contribute $3\beta^3\%$ (1/2 of a neutrino generation for $\beta = 1$) of the standard width; neutralinos (neutral supersymmetric gauge bosons) which can contribute as much as $\approx 10\%$; sleptons that contribute $\approx 10\beta^3\%$ of the leptons contribution or $.3\beta^3\%$ of the nominal width; and squarks with a similar contribution. The contribution from photino or gluino production is much smaller^[10]. Hence, the contribution to the total Z_0 width from such final states can be quite significant and could be equivalent to a few neutrino generations.

2.6 DEPENDENCE OF THE Z_0 MASS AND WIDTH ON RADIATIVE CORRECTIONS.

In this section we discuss the effects of radiative corrections on the determination of the Z_0 mass and width. The effect of gluon emission in the final state in which quarks are present increases the width of the Z_0 . This has already been pointed out in Table 1 and we will not discuss it any further here. The effect of loop corrections involving the top quark on the Z_0 propagator and its effect on the Z_0 width has been discussed briefly in Sect. 2.3. In general, this effect is of the order of $.1 N_\nu$ and we will not discuss them in this section. Our main topic of discussion in this section is the effect of the electromagnetic radiative corrections, both internal and external, on the shape of the Z_0 resonance and how it affects the determination of the Z_0 mass and width.

One effect, that we neglected to include in Table 1, is the correction to the Z_0 width due to the contribution to the total decay rate of processes with an

external photon in the final state. In general this requires a contributing factor for each charged final state of^[8]

$$1 + \frac{3\alpha}{4\pi}(Q_i/e)^2$$

This leads to a width increase of ≈ 0.005 GeV which can be neglected for our purposes. The fact that final state radiation does not contribute to large logarithmic corrections like initial state radiation is due to the cancellation between the internal photon exchange processes and the photon emission processes^[11]. In addition, radiation from final state particles does not affect the shape of the resonance and, hence, the measurement of the Z_0 mass and width.

Hence, the main topic of this section is the change in the Z_0 mass and width due to the radiation by the incident electron and positron. In Fig. 4 and 5 we present the line shape as predicted by the electroweak theory^[4] with the parameters in Table 1. The figures show the distortion generated by the initial state radiation. The “radiative” curves were generated using the technique of Kuraev and Fadin^[12] and described by Cahn^[12] but without Cahn’s approximations. We have included the renormalization of α_{em} due to the propagator loop corrections in the main process. We use $\alpha_{em} = 128$ to describe the electromagnetic coupling in the annihilation process but not in the photon emission process that distorts the resonant line shape. This renormalization just changes the magnitude of the cross section but does not change the distortion of the shape.

The net effect of these distortions is to shift upward the location of the peak of the cross section by 0.115 GeV while the width increases by 0.056 GeV, equivalent to 1/3 of a neutrino generation. In addition, the magnitude of the cross section at the peak decreases by a factor of 0.735. These results are only slightly different from those in Cahn’s paper. Of course, in principle, these effects can be corrected if we know the beam energy spectrum. Hence, the ultimate errors can be much smaller.

3. Determination of N_ν by Directly Measuring the Fraction of the Z_0 Width due to $Z_0 \rightarrow \nu + \bar{\nu}$ Decays.

Recently it has been pointed out^[13] that one can achieve a reasonable measurement of the number of neutrino generations by directly measuring the difference between the total Z_0 width and that fraction of the width due to Z_0 decays into charged leptons and hadrons. This difference is a direct measurement of the contribution to the width due to Z_0 decays into neutrinos. This, of course, assumes there are no new Z_0 decays into particles that leave no signal in the detector, like decays into some types of supersymmetric particles. One can show, that with a few thousand Z_0 decays, one can reach an error limit of ≈ 0.5 of a neutrino generation (for 90% c.f.). It is difficult to reach error limits below this level because other non statistical errors, like the luminosity error, become significant.

4. Determination of N_ν Using the Reaction

$$e^+ + e^- \rightarrow Z_0 \rightarrow \nu + \bar{\nu} + \gamma's$$

Measuring the cross section for Z_0 directly into neutrinos would be the most definitive way to determine the number of neutrino generations, but the neutrinos are defacto undetectable. However, the radiative process produces at least one detectable photon, as has been pointed out by several authors^[14]. Thus, the presence of a single photon in the detector signals the annihilation into neutrinos. We have to include the observation of more than 1 γ in order to reduce the uncertainty in the calculation of the cross section. This uncertainty is due to the radiative correction^[6,15]. This is discussed in more detail later on.

In the following sections, we discuss this process and the possible sources of background affecting this measurement. In particular, we derive the statistical and systematic limitations of the measurement of N_ν .

4.1 THE CROSS SECTION AND EXPECTED NUMBER OF EVENTS.

The process with 1 γ is described by the Feynman diagrams shown in Fig. 6. The major contributor to this process is the annihilation via the Z_0 channel, diag. (a). Only this diagram depends on the number of neutrinos in nature. The other contributors to this process is the W exchange term, diag. (b), and the interference between these two. The double differential cross section has been calculated^[14] and is given by

$$\begin{aligned} \frac{d^2\sigma}{dx dy} &= \frac{G_F^2 \alpha}{6\pi^2} \frac{s(1-x)}{x(1-y^2)} [(1-x/2)^2 + x^2 y^2 / 4] \\ &\times \left\{ \frac{N_\nu (v_e^2 + a_e^2) + 2(v_e + a_e)[1 - s(1-x)/M_Z^2]}{[s(1-x)/M_Z^2 - 1]^2 + \Gamma_Z^2/M_Z^2} + 2 \right\} \end{aligned} \quad (4.1.1)$$

where

$$\begin{aligned}
x &= E_\gamma/E_{beam} \\
s &= 4E_{beam}^2 \\
y &= \cos \theta_\gamma \\
v_e &= -\frac{1}{2}[1 - 4 \sin^2 \theta_w] \\
a_e &= -\frac{1}{2}
\end{aligned}$$

Recently a more accurate treatment^[13] of the W exchange diagram in Fig. 6 has lead to a more accurate expression for eq. 4.1.1. Nevertheless, the differences are no more than 2 – 3% at $E_{cm} = M_Z$ and even less at 96 GeV. Hence, all our results have been determined using the expression above.

Using these results we display in Figs. 7,8 the cross section of the process for the case where there are 3 or 4 neutrinos and for various cuts on the detected photon. These cuts describe the geometrical and sensitivity cuts of the SLD detector. In Fig. 7 we cut on the transverse momentum and the angle of the photon relative to the beam direction. In Fig. 8 we cut on the energy and angle of the photon. The importance of these cuts, especially the transverse momentum, as we will discuss in the next section, is that they reduce the background from radiative Bhabha scattering. In Figs. 9,10 we display the photon energy and angular distribution for various center of mass energies and for a cut in the transverse momentum of the photon.

The following observations can be made from these distributions:

1. The cross section for 4 neutrinos is $\approx 27\%$ higher than the cross section for 3 neutrinos. This difference varies a few percent as one varies the center of mass energy. It also varies slightly depending on whether one cuts on the photon energy or the photon transverse momentum.
2. The angular distribution of the photon is fairly broad showing a substantial flux of photons at large angles to the beam direction. The energy distribution of the photon shows that most of the photons are very low energy (≤ 2 GeV) unless the center of mass energy of the collisions is around 96 GeV.

3. A cut on the photon momentum instead of the transverse momentum at 1 GeV leads to an $\approx 125\%$ increase in the cross section at a center of mass energy of 92.2 GeV and an $\approx 45\%$ increase at 96 GeV; hence, it results in a better statistical separation between the existence of 3 or 4 neutrinos. Nevertheless, as we will discuss later on, it leads to a substantially larger background from radiative Bhabhas.
4. The cross section for radiative neutrino production has a marked energy dependence on the center of mass energy between 91 and 95 GeV. Hence, to distinguish between the existence of 3 or 4 neutrino generations from measurements in this energy regime requires a precise knowledge of the collision energy ($\approx .1\%$). Above the Z_0 mass, at ≈ 96 GeV, the cross section becomes relatively large and less sensitive to variations in the center of mass energy; therefore, this becomes a more propitious region in which to carry out this measurement.

Assuming a 1 year run with a luminosity of $10^{30} \text{ cm}^{-2} \text{ sec}^{-1}$ and a 50 % data logging efficiency we can collect data with an integrated luminosity of 18 pb^{-1} . Using Fig. 8 and including a correction factor of .78 for radiative corrections (see next section) we can deduce the number of observed events for the case of 3 neutrinos. We expect 1500 single photon events at a center of mass energy of 92.2 GeV and 3200 events at a center of mass energy of 96 GeV. This number is $\approx 27\%$ higher for the case of 4 neutrinos.

4.2 THE EFFECT OF RADIATIVE CORRECTIONS ON THE RELIABILITY OF THE CROSS SECTION CALCULATION.

Recently, a series of studies^[16] have pointed out that, at the Z_0 energy, the existence of additional box and triangle Feynman diagrams in the $e^+ + e^-$ annihilation process, as shown in Fig. 11, lead to sizable corrections that reduce the cross section anywhere from 10 to 40 %. Nevertheless, recently^[17] it was pointed out that if one includes the corrections due to the emission of a second

soft photon these corrections can be reduced. The result of these calculations show that the cross section can be written in the form

$$\frac{d^2\sigma}{dxdy} = \left(\frac{d^2\sigma}{dxdy} \right)_0 \left(1 - \frac{\alpha}{\pi} \ln(s/m_e^2) \ln(s/4w_0^2) \right) \quad (4.2.1)$$

where $\left(\frac{d^2\sigma}{dxdy} \right)_0$ is equation (4.1.1) and w_0 is the maximum energy of the second soft photon. For $w_0 = 1$ GeV this expression leads to a correction of 22 % at $E_{cm} = M_Z$. Except where explicitly stated this correction has not been included. Recently, a more accurate treatment of these corrections^[15] using kinematical cuts that are more realistic conclude that these corrections reduce the cross section by 17%. It is expected that these corrections become even smaller if one includes the observation of multi-photon ($N > 2$) events. Hence, it is important that SLD's solid angle coverage be large enough that we can record these multi-photon events.

Because these corrections are large at these energies, the present first and second order calculations may not be accurate enough. This is particularly important in the study of neutrino counting since the corrections are of a magnitude similar to the differences in the cross section between 3 and 4 neutrino generations. Hence, it is necessary to calculate the higher order corrections to determine their contribution to the cross section. This work is now in progress^[16].

4.3 LIMITS ON THE ACCURACY OF N_ν OBTAINED BY MEASURING THE ABSOLUTE CROSS-SECTION.

A Montecarlo study was carried out to determine the degradation in the statistical significance of the observed number of events given: (1) a non gaussian low energy tail in the beam energy distribution, as shown in Fig. 1; (2) a 3 % random error in the luminosity measurement. The conclusions are shown in Fig. 12. It shows clearly the quick degradation of the resolving power in the energy region below 96 GeV due to the sharp energy dependence of the cross section.

It also shows that the resolving power at 93 GeV is only 5 standard deviations without including other errors like those due to background and resolution of the detector for low energy photons (≈ 1 to 2 GeV). This degradation due to the detector photon energy resolution and the effect of the background due to radiative Bhabhas is discussed in the next section. All the effects that relate to the resolution in the separation between the signals due to 3 and 4 neutrinos are discussed in detail in section VI.

In order to understand and determine how the energy resolution of our detector affects our ability to distinguish between 3 and 4 neutrino generations we display the change in the radiative neutrino pair cross section as we change the minimum allowed photon energy, Fig. 13, or as we change the minimum allowed transverse photon momentum, Fig. 14. We determined the effect of the SLD detector calorimeter resolution ($\delta E = 9\sqrt{E}\%$, $\delta\theta = 1^\circ$) on the observed number of events. This was done at $E_{cm}=92.2$ GeV and for the cuts on the photon of $E_{min}=1$ GeV or $P_{tmin}=1$ GeV, and $\theta = 10^\circ$. Using Montecarlo techniques we generated the events according to the differential cross section and determined how many events were observed above the cuts assuming a perfect resolution and assuming the resolution given above. We found that, due to the finite resolution of the calorimeter, there was a 0.6% increase in the number of observed events both in the case of cuts in the photon energy or transverse momentum. Given that one extra neutrino generation increases the cross section by 27%, this effect gives rise to a 0.02 neutrino generation. Hence it can be neglected. The size of this effect can be surmised to be even smaller at $E_{cm}=96$ GeV. Because the radiative Bhabha background can be reduced substantially relative to the $\nu\bar{\nu}\gamma$ signal if we cut on the photon transverse momentum instead of the energy, the transverse momentum is the variable that should be used.

These results are an indicator that the determination of the number of neutrinos is best done at a center of mass energy near 96 GeV instead of near the Z_0 mass. The improvement in the resolution at 96 GeV as compared to 93 GeV is shown in section VI.

4.4 THE BACKGROUND DUE TO RADIATIVE BHABHA SCATTERING.

Several processes may produce single photons with characteristics similar to the γ 's from the $\nu\bar{\nu}\gamma$ final state. Such a situation can occur for the γ associated with the final states $e^+e^-\gamma$ (Radiative Bhabha), $\mu^+\mu^-\gamma$, and $\tau^+\tau^-\gamma$ when the charged particles may escape undetected down the beam pipe or into inefficient areas of the detector. The transverse momentum (p_\perp) of the observed γ must be balanced by the p_\perp of the unseen particles. If efficient particle detection occurs down to small angles around the beam axis, the p_\perp of the observed γ is limited by the maximum angle that the charged particles can have without triggering the veto counters which, in our case, is the luminosity monitor. This limit is given by the relation

$$p_{\perp\gamma} \leq (E_{cm} - E_\gamma)\sin\theta_{veto} \quad (4.4.1)$$

Previous neutrino counting experiments at PEP and PETRA^[19] have shown that efficient photon detection above several hundred MeV and efficient charged particle detection down to small angles (≈ 10 's of mrad.) is sufficient to achieve the desired hermiticity.

The SLD detector has luminosity monitor coverage down to 22 mrad. For this veto angle and $E_{cm} = M_Z = 92.2$ GeV we get $p_{\perp\gamma} \leq 2.02$ GeV. Because the photon transverse momentum is almost always balanced by either the electron or positron alone instead of by both simultaneously, most of the photons have $p_\perp \leq 1$ GeV. Also, the radiative Bhabha process has a large "t" channel contribution to the cross section at small angles which is not present in the other processes mentioned above. Hence it is by far the dominant background. In fact, given a θ_{veto} angle of 22 mrad, the $\mu^+\mu^-\gamma$ and $\tau^+\tau^-\gamma$ backgrounds are totally suppressed and are neglected here.

A recent Montecarlo program by Mana and Martinez (MM)^[20] was optimized specifically to calculate the cross section and generate $e^+e^-\gamma$ events with the e^\pm at small angles to the beam axis and the γ satisfying the experimental detection

cuts. The MM Montecarlo has been successfully cross checked^[21] against other calculations^[22]. In Fig. 15 we show the differential cross section as a function of $P_{\perp\gamma}$ of radiative Bhabhas for different photon cuts and for $E_{cm}=95$ GeV. The bins at the very highest gamma transverse momentum suffer from poor Montecarlo statistics and only should be used as trends of the total cross section. The radiative Bhabha cross section for single photons drops only slowly with increasing energy^[20]. Hence, to avoid excessive CPU usage, the distributions for $E_{cm} = M_Z$ and 96 GeV were estimated by suitably scaling a sample of events corresponding to a luminosity of 62.6 pb^{-1} generated by the MM Montecarlo program at 95 GeV. Comparison of a statistically smaller sample generated at these three energies showed no significant differences.

The energy and angular resolution of the SLD liquid Argon calorimeter, $\delta E = 9\sqrt{E}\%$ and $\delta\theta = 1^\circ$, will smear out the photon transverse momentum in the observed events. We generated events smeared with this resolution. The effect of the smearing at these energies is to increase the number of observed radiative Bhabhas for a p_\perp cut of 1 GeV by 2% at 95 GeV. Hence the resolution effects are small and can be easily corrected for in the analysis stage.

In Fig. 16 we show the cross section as a function of the minimum photon transverse momentum cut for both the $\nu\bar{\nu}\gamma$ and the $e^+e^-\gamma$ final states. Using these, we calculate the number of expected γ 's of each type in a data sample corresponding to a luminosity of 10 pb^{-1} . This data sample corresponds to 4.1×10^5 Z's at $E_{cm}=92.2$ GeV and 9.1×10^4 Z's at 96 GeV. The results are presented in Table 2. In the calculation of the number of $\nu\bar{\nu}\gamma$ events we reduce the calculated number from eqn. 4.1.1 by a factor of .78 (see sect. 4.2) to account for the radiative corrections. The numbers in Table 2 show that the background from radiative Bhabhas can be substantial except when you make a photon transverse momentum cut above 1.5 GeV. Also, it shows that it is best to take the data at $E_{cm}=96$ GeV instead of at M_Z .

A similar study was done cutting on the photon energy instead of the trans-

verse momentum. In Fig. 17 we present the cross section dependence on a minimum photon energy cut for the $\nu\bar{\nu}\gamma$ and the $e^+e^-\gamma$ final state. The results, indicating the signal and background, are shown in Table 3. They indicate that the background is much more severe when we use the photon energy instead of the photon transverse momentum.

TABLE 2

Signal and Background for Pt_γ Cuts.

Integrated Luminosity = 10 pb^{-1}

E_{cm} GeV	Min. θ_γ deg.	Veto θ_{e^\pm} mrad.	Min. $P_{\perp\gamma}$ GeV	$N_{\nu\bar{\nu}\gamma}$	$N_{e^+e^-\gamma}$
92.2	10	22	0.8	480	640
92.2	10	22	0.9	450	310
92.2	10	22	1.0	390	54
92.2	10	22	1.5	234	≤ 1
96.0	10	22	1.0	1250	51
96.0	10	22	1.5	940	≤ 1

TABLE 3

Signal and Background for E_γ Cuts.

Integrated Luminosity = 10 pb^{-1}

E_{cm} GeV	Min. θ_γ deg.	Veto $\theta_{e\pm}$ mrad.	Min. E_γ GeV	$N_{\nu\bar{\nu}\gamma}$	$N_{e^+e^-\gamma}$
92.2	10	22	1.0	900	5940
92.2	10	22	1.5	430	3870
92.2	10	22	2.0	270	2540
92.2	10	22	2.5	195	1700
96.0	10	22	1.0	1760	5460
96.0	10	22	2.5	1130	1570

4.5 THE BACKGROUND DUE TO THE 3 γ 'S FINAL STATE.

We determined the single photon background for this process. The only Feynman diagram that contributes is the one where we have a t-channel electron exchange. The Z_0 s-channel exchange can not contribute because a spin 1 particle can not decay into 2 photons. We determined the cross section under the following conditions: The high energy photons angle has to be less than 22 mrad relative to the beam, the soft photon has a transverse momentum greater than 1 GeV, and an angle greater than 10 deg. relative to the beam. The cross section was determined using the Montecarlo program developed by Berends and Kleiss. The calculation shows that the cross section, with these cuts, is less than 2 pb. This cross section is small when compared with our signal cross section of 40 pb at $E_{cm} = M_Z$. Using the results from Table 2 we note that this background is about one third as large as the background from radiative Bhabhas.

4.6 THE MEASUREMENT OF N_ν WITH A POLARIZED e^- BEAM.

The schedule for SLC improvements calls for the availability of longitudinally polarized electron beams near the time the SLD is installed. It is expected that, initially, the polarization "P" will be $\approx .45 \pm .02$, with future improvements approaching perhaps 100 % with an error of 1 %.

We discuss here the advantages and disadvantages of using a polarized e^- beam^[23]. We assume throughout this discussion that the luminosity, energy stability, and reliability of the SLC will not change in the presence of accelerated polarized electron beams.

In the case where the electron and positron helicities are explicitly included, with h_e and h_p taking on the values ± 1 for the two possible values of helicity of the electron and positron, the same cross-section expression given in eq. (4.1.1) becomes:

$$\frac{d^2\sigma_{pol}}{dx dy} = (1 - h_e h_p) \frac{G_F^2 \alpha}{6\pi^2} \frac{s(1-x)}{x(1-y^2)} [(1-x/2)^2 + x^2 y^2 / 4]$$

$$\times \left\{ \frac{N_\nu(v_e^2 + a_e^2 - 2h_e v_e a_e) + 2(1 - h_e)(v_e + a_e)[1 - s(1-x)/M_Z^2]}{[s(1-x)/M_Z^2 - 1]^2 + \Gamma_Z^2/M_Z^2} + 2(1 - h_e) \right\} \quad (4.6.1)$$

Since the positron beam in the SLC is unpolarized, we must average over h_p which is equivalent to setting it to 0. We replace h_e^- with $P_1 \approx -0.5$, the polarization of the beam when the helicity is negative, h_e^+ with $P_2 \approx +0.5$ and the luminosity for each case as L_1 and $L_2 = 1/2L$, where L is the luminosity of the full run. We can calculate the expected number of events, for each longitudinal polarization of the electron beam, in a 1 year run with an integrated luminosity of 18 pb^{-1} . These are shown in Fig. 18 for the same conditions discussed with an unpolarized beam.

The following comments can be made about the advantages and disadvantages of measuring the number of neutrino generations using this technique:

1. The advantage of using polarized beams is that the background due to the QED radiative Bhabhas and $\gamma\gamma\gamma$ processes cancels out when one takes the difference in the observed rates due to the possible longitudinal polarization states of the incident electron beam. The helicity dependent γ/Z_0 interference contribution is expected to be smaller than the dominant QED term by $\approx 10^4$. This is the reason for considering this avenue in measuring the number of neutrino generations.
2. One disadvantage derives from the fact that the difference in the observed number of events leads to a small signal with a larger associated statistical error. This can be determined from Fig. 18. Comparing the statistical error associated with the difference in the signals with that associated with

the signal from an unpolarized beam we can see that, for a center of mass energy of 96 GeV, the statistical percentage error increases by a factor

$$\frac{(2024 \pm 45) - (1640 \pm 40)}{3665 \pm 61} = \frac{384 \pm 60}{3665 \pm 61} = 9.4$$

3. The study based on the difference of the rates depends on how well we know the polarization of the electron beam. Hence, the error in the observation will include a contribution from this uncertainty which could be 5%. This is smaller than the statistical error from the observed number of events after one year of running (13%) with an integrated luminosity of 18 pb^{-1} . Nevertheless, it becomes significant if further running takes place. Reducing the uncertainty in the polarization to 1 % is significant for this measurement.
4. The signal due to the difference in the cross section for the two polarization states of the electron beam is more sensitive to the value of $\sin^2\theta_w$ than the cross section due to an unpolarized beam. This is shown in Fig. 19, where we plot these two cases as a function of $\sin^2\theta_w$. Curves (a) refer to the unpolarized beam condition while curves (b) refer to the difference in the number of observed events from the two longitudinally polarized beam conditions. The contributions to the statistical error in the signal due to the expected number of events and due to a value of $\sin^2\theta_w = 0.220 \pm .002$ are shown in Table 4 for two data gathering conditions. We can observe that in the case of the unpolarized beam condition the contribution to the total error due to an error in $\sin^2\theta_w$ is negligible, while in the case of the polarized beam conditions the contribution from this error is noticeable.

TABLE 4

Statistical Errors in a 1 Year Run

$$\sin^2\theta_w = 0.220 \pm .002$$

Signal Type and Associated Errors	$E_{cm}=93$ GeV	$E_{cm}=93$ GeV	$E_{cm}=96$ GeV	$E_{cm}=96$ GeV
	$N_\nu=3$	$N_\nu=4$	$N_\nu=3$	$N_\nu=4$
N (unpol.) per year	2143	2718	4284	5209
$Error = N^{\frac{1}{2}}$	46.3	52.1	65.4	72.2
$\frac{dN}{d\sin^2\theta_w} \delta\sin^2\theta_w$	3.3	4.6	7.9	9.4
N_- (neg. pol.) per year	1178	1501	2394	2912
N_+ (pos. pol.) per year	965	1218	1889	2297
$N_- - N_+$	213	283	505	614
$\delta(N_- - N_+) = (N_- + N_+)^{\frac{1}{2}}$	46.3	52.1	65.4	72.2
$\frac{d(N_- - N_+)}{d\sin^2\theta_w} \delta\sin^2\theta_w$	17.3	21.8	33.7	51.2

In conclusion, in order to distinguish between 3 and 4 neutrino generations (27 % difference in the observed number of events) using the difference between the observed number of events of the two longitudinal beam polarizations, we need to use the data collected over a 3 year period and the value of $\sin^2\theta_w$ needs to be known with an error of $\approx \pm .001$. This conclusion is made tenuous by the observation that the statistical error is increased by the background of radiative Bhabhas included in the observed number of events in each state of beam polarization.

4.7 LIMITS ON THE ACCURACY OF N_ν OBTAINED BY MEASURING THE BRANCHING RATIO $\frac{e^+ + e^- \rightarrow \nu + \bar{\nu} + \gamma}{e^+ + e^- \rightarrow \mu^+ + \mu^- + \gamma}$.

We have discussed the statistical error limits, the dependence of the rates on various parameters, and the reliability of the radiative corrections. We still need to confront the error limits that result from understanding the detection efficiency of low energy single photons in the SLD detector. This last study will be presented in a latter section. Here we investigate the sensitivity that the relative branching ratio of radiative annihilation into neutrinos to radiative annihilation into muons has to the value of $\sin^2\theta_w$ and to the photon detection efficiency. The premise is that, since both processes may have a similar dependence on the electroweak parameters and on the photon spectrum, the value of this relative branching ratio would be insensitive to the electroweak parameters or to the photon detection efficiency. In addition, and most important, the radiative corrections due to the virtual photon exchange diagrams are quite large and not well calculated in these processes^[16,17]. They are expected to be quite similar for both neutrino and muon radiative final states; hence they should cancel in the expression for the relative branching ratio. These facts are the main reason why a measurement of this relative branching ratio has the greatest potential to achieve the lowest total uncertainty in the determination of the number of neutrino generations.

We first describe the process $e^+ + e^- \rightarrow \mu^+ + \mu^- + \gamma$ and then discuss how insensitive the relative branching ratio to $\nu + \bar{\nu} + \gamma$ is to various effects. In Fig. 20 we present the cross section^[24]. We describe the contribution from the radiation of the incident electrons, the contribution from the radiation of the outgoing muons, and the total cross section which includes the interference effects between the radiation from the incident and outgoing particles. It is clear from the figure that the major contribution to the total cross section is due to the radiation from the muons. This surprising result is due to 2 effects: 1) The photon emission from the muons does not change the sharp rise in the cross section due to the

Z_0 pole unlike the effect of photon emission from the incident particles; this is clearly seen as the difference in the energy dependence of the two cross sections shown in the figure. 2) The cross section has a $\sin^{-2}\theta$ dependence, where θ is the angle between the photon and the emitting particle. Since we can only observe photons with an angle greater than 10° to the beam direction, this cut reduces by ≈ 2 the observed contribution from initial state photon emission relative to the final state emission where no such cut relative to the muon direction is applied. The effect of this angle cut on the initial state radiation is also observed in Fig. 8. Hence, the number of events that we can expect from this final state can be quite substantial and it will have a strong energy dependence that is different from the $\nu\bar{\nu}\gamma$ channel.

We studied this angular dependence to determine whether, by making selective cuts, we could reduce the differences in the various spectra between the case when there are neutrinos in the final state and muons in the final state. Such a reduction would improve the accuracy in the determination of neutrino generations using the method being described in this section. The effect of the $\sin^{-2}\theta$ dependence is best shown in Fig. 21 where we show the cross section after we require that the angle between the photon and either muon be greater than 20° . The decrease in the contribution to the total cross section from the final state muons radiation has decreased markedly, while the initial state radiation contribution is only slightly lower.

In Fig. 22 and 23 we show the photon energy distribution from the contributing initial and final states. In Fig. 23 we see clearly the effect of the Z_0 pole increasing the cross section for higher energy photons radiated by the incident particles. No such effect is seen for the photons radiated by the outgoing muons.

In Fig. 24 we plot the ratio of the cross sections as a function of the center of mass energy for different cuts in the angle between the photon and either muon (0° and 20°), but for one value in the cut of the minimum photon energy (1 GeV). In Fig. 25 and 26 we plot this same ratio for a particular value of the center of

mass energy, but varying the allowed minimum value of the photon energy. This is done for two values of the minimum angle between the photon and either muon. It is clear that this ratio is most stable to errors in the minimum photon energy at a center of mass energy of 96 GeV as compared to 93 GeV. It is also noted that a cut in the angle between the photon and either muon of 20° improves the separation in the expected signal for 3 and 4 neutrino generations by a factor ≈ 1.7 .

Finally, in Fig. 27 and Fig. 28 we show, for two values of the center of mass energy, how the cross section ratio changes as we vary the value of $\sin^2\theta_w$. For a value of .226 the variation is substantial at 93 GeV and much less so at 96 GeV. Again, a cut in the minimum angle between the photon and muon of 20° improves the separation in the 3 and 4 neutrino generation signal by a factor of ≈ 1.5 .

We can determine the effect of errors in the center of mass energy, the minimum photon energy, and the value of $\sin^2\theta_w$ on the determination of the number of neutrino generations using this method. An error of .1 GeV ($\approx .1\%$) in the center of mass energy gives rise to an uncertainty of .3 N_ν at $E_{cm}=93$ GeV and .08 N_ν at $E_{cm}=96$ GeV. For the SLD detector resolution in the photon energy of $.09\sqrt{E}$ we obtain an uncertainty of .02 N_ν at 93 GeV and .01 N_ν at 96 GeV. Similarly, for $\sin^2\theta_w=.226$ with an error of .001 we have an uncertainty of .3 N_ν at 93 GeV and .1 N_ν at 96 GeV. These are the results for no cut in the angle between the photon and either muon. Making such a cut reduces these uncertainties further as discussed before.

The background from radiative Bhabhas is reduced substantially when one makes a cut on the transverse momentum of the photon instead of the energy. This was discussed in the section describing this source of background. Because of this we also did the same study based on the requirement that the photon transverse momentum be ≥ 1 GeV.

Making such a cut reduces the difference in the signal between 3 and 4

4 neutrinos. This deterioration is due to two effects: 1) The total cross sections decrease, and 2) The part of the cross section due to radiation from the initial state decreases more than the part due to radiation from the final state in the case of the $\mu\mu\gamma$ final state and this degrades the comparison with the $\nu\nu\gamma$ final state as discussed before.

In Fig. 29 through 36 we present the various distributions as before but making the cut on the photon transverse momentum. The various distributions are similar to the previous ones.

In general, the measurement of the number of neutrinos using this method is best done at 96 GeV where we are less sensitive to variations in the center of mass energy, to the determination of the photon energy given the calorimeter resolution, and to the value of $\sin^2\theta_w$. Using either the photon energy or the photon transverse momentum has very similar effects on the determination of N_ν as a result of the measurement errors. Using the photon transverse momentum leads to a lower number of $\mu^+\mu^-\gamma$ events observed and we would have to collect data for a larger period of time; at the same time it leads to a lower number of Radiative Bhabhas and hence reduces the background due to these events. The effect of all the errors on the determination of the number of neutrino generations is presented in detail in section VI.

4.8 THE EFFECT OF THE PROCESSES $e^+ + e^- \rightarrow Z_0 \rightarrow \tilde{\nu} + \bar{\tilde{\nu}} + \gamma's$ AND $e^+ + e^- \rightarrow \tilde{\gamma} + \bar{\tilde{\gamma}} + \gamma's$.

The differential cross section for the radiative sneutrino pair production process^[25] has been calculated^[26]. In the center of mass energy domain of the SLC the main process that contributes is the s-channel Z_0 exchange with a small contribution from the t-channel Wino (Supersymmetric partner of the W Boson) exchange. The expression for the cross section, if we neglect the small Wino exchange contribution, is^[26]

$$\frac{d^2\sigma}{dxdy} = \frac{1}{2} \left(\frac{d^2\sigma}{dxdy} \right)_0 \left[1 - \frac{4m_{\tilde{\nu}}^2}{s(1-x)} \right]^{3/2}$$

where $\left(\frac{d^2\sigma}{dxdy} \right)_0$ is eqn. 4.1.1

with the W exchange contribution excluded.

$$x = E_\gamma / E_{beam}$$

$$y = \cos\theta_\gamma$$

Hence, for sneutrino masses small compared with the available center of mass energy and assuming there are as many sneutrinos as neutrinos, we expect the cross section for single γ to increase by 50%.

The process $e^+ + e^- \rightarrow \tilde{\gamma} + \bar{\tilde{\gamma}} + \gamma's$ can only occur via a t-channel selectron (the supersymmetric partner of the electron) exchange. In general, this cross section is small compared to the one for a gamma together with neutrino pairs^[27] for center of mass energies within ≈ 5 GeV of the Z_0 mass. Therefore, this process should not contribute significantly to our signal.

5. Photon Detection in the SLD Calorimeter.

In order to understand the response of the detector to photons with energy less than ≈ 5 GeV we have studied method by which we can calibrate the SLD calorimeter's behavior to these photons. This chapter discusses our rather superficial understanding of this issue.

5.1 ANGULAR RESOLUTION OF THE SLD CALORIMETER FOR LOW ENERGY PHOTONS.

The position and angular resolution for 2 GeV photons has been studied using the EGS4 photon shower simulator in an approximate geometry of the SLD electromagnetic calorimeter. This geometry includes the correct thickness for the lead, the liquid argon, and the aluminum dewar wall. The calorimeter cells or towers are assumed to be square with 6 cm. sides. We assume photons from the interaction point are incident normal(90°) to the calorimeter towers while those coming from possible background sources, ≈ 1 meter from the interaction region, are incident at 20° . This angular separation represents the realistic situation when the photons strike near the middle of the barrel calorimeter. This angular separation becomes much smaller when the photons are incident on the end cap calorimeters. Hence the results presented in this study refer to the best situation in which to separate the signal from the background by determining how well they point to the interaction region. In addition, the effect of electronic noise is investigated by adding simulated noise of various amounts to the deposited energies.

The position resolution is determined with an algorithm that uses the relative energies deposited in adjacent towers in the first few layers of the calorimeter (EM1) and the next series of layers (EM2). By looking at the energy deposited to the right and to the left of the main tower one can determine the central position of the energy deposition in EM1 and EM2. This position resolution in EM1 and EM2 are then used to determine the photon angular resolution. The

position resolution for 2 GeV photons in EM1 and EM2 is found to be 9.6 mm and 7.6 mm respectively. The longitudinal separation between the showers in EM1 and EM2 is 68 mm. Using these results we determine that the angular resolution of 2 GeV photons is 9.6° . These results were obtained in the case that the electronic noise is equivalent to 8 MeV of energy deposited in a given cell. If no noise had been included the resolution would have been 9.0° .

In Table 5 we show the results indicating what fraction of the signal and of the background are kept depending on the angular cut applied to the observed photon. This angle cut is indicative of how well this photon is required to point to the interaction region. These results show that if we have a sizable photon background it could lead to a significant contamination of the signal. The magnitude of this background can be determined by determining the number of kinematically uncorrelated photons observed in events in which there is also an electron or muon pair in the final state.

TABLE 5
Study of Photon Detection Efficiency

Angular Cut deg.	Efficiency for 90° Photons %	Efficiency for 20° Photons %
5.0	40.0	2.7
6.5	50.0	5.0
8.5	60.0	8.4
10.5	70.0	13.7
13.5	80.0	23.0
17.5	90.0	36.0

We should note that a 20° error in the photon direction translates into a ± 35 cm. error in the interaction point while the nearby MASKS are located as close as ± 20 cm. Hence, the photon background problem will need to be studied carefully.

5.2 ENERGY RESOLUTION OF THE SLD CALORIMETER FOR LOW ENERGY PHOTONS.

The energy resolution of the SLD calorimeter is expected to be $9\sqrt{E}\%$. This expectation must be determined under actual running conditions. We have studied the possibility of determining this resolution using radiative electron pair (Bhabhas) and muon pair production. From Tables 6 and 10 of the next chapter we can tell that in a standard run we expect to have thousands of such events. Most of these have low energy photons (a few GeV) associated. Using the angular and momentum resolution of the drift chambers we can calculate the expected photon energy associated with the charged lepton pair. Given the expected angular resolution of 0.1 mrad and a charged particle momentum resolution of 3.2 GeV (for 46 GeV charged particles), we can expect to determine the photon momentum with an error of $\approx 10\%$. Using a constrained fit we can reduce this error substantially. Hence we can calculate the expected magnitude and direction of the photon with a resolution which is smaller than that of the calorimeter. These photons can be used to map the response of the calorimeter to the type of low energy photons which are used in the study of the number of neutrino generations. In section 4.3 we have already discussed the implications of the predicted resolution; namely, it will have a very small effect on our ability to determine the number of number of neutrino generations in nature.

A detail Monte Carlo study of this issue can be carried out with the BREMUS and YFS radiative muon pair generators. Such a study has not yet been carried out but will be.

5.3 BEAM RELATED PHOTON BACKGROUND.

A major concern of a single photon counting experiment is the possibility that beam gas interactions or off beam electrons striking a beam line component could produce photons that can enter the SLD detector. These photons become the background of the experiment. To model this process by computer techniques is very difficult and can not be trusted. Nevertheless, past experience with the MAC and ASP detectors which studied single photon events is valuable in determining an expectations for the magnitude of this background.

In the ASP experiment the beam gas interaction background of single photons, as determined from the reconstructed source distribution of these photons, was slightly less than the single photon from the three neutrino generation signal. This should imply that the background from the SLC beam gas interactions should be much smaller since the cross section for the signal increases substantially while the beam gas cross section should not change much. The experience of the MAC detector was similar.

In the case of both ASP and MAC, photons from off beam electrons hitting mask elements in the beam line were observed by noting that the reconstructed source position of these photons had peaks away from the beam crossing region. In the case of SLD the masks are closer to the beam crossing region so that it will be more difficult to eliminate this background source. This type of background will have to be studied in detail by observing photons present with electron and muon pairs that do not fit kinematically with the hypothesis that this is a radiative lepton pair case.

5.4 COSMIC RAY RELATED BACKGROUND.

The ungated cosmic ray rate through the liquid Argon Calorimeter in the SLD detector is

$$.024Hz/cm^2 \times (600)^2 cm^2 \approx 10^4 Hz$$

The SLC duty factor ($3\mu\text{sec}$ per $5\text{ msec} = 6 \times 10^{-4}$) reduces this rate to a few hertz. Making a cut requiring that there be no tracks in the outer muon chambers, that no more than 30% of the photon energy be deposited in the hadron calorimeter, and that the photon energy deposition pattern describe a photon coming from the interaction region should reduce this source of background to a very low level. In the case of the MAC detector these simple requirements reduced the cosmic ray background to insignificant levels.

5.5 VETO EFFICIENCY OF THE LUMINOSITY MONITOR.

The luminosity monitor can detect particles down to an angle of 22 mrad. By this means we can detect the electron and positron from the radiative Bhabha process and, by this means, reduce substantially the single photon background from this process. The radiative Bhabha background is described in Tables 2,3 and shown in Figs. 15,16,17. It is clear that this background is very sensitive to the veto angle. Hence determining the angle at which the luminosity monitor begins to detect the secondaries becomes crucial. It is likely that the luminosity monitor may not be very efficient down to such a small angle; it may even be possible that the present design may need to be modified because of beam related constraints such that the lowest veto angle may be larger. We have calculated the increase in the cross section of the radiative Bhabhas as the veto angle increases from 22 to 28 mrad. If we require that the photon transverse momentum be greater than 1 GeV, the cross section increases from 3.8 pb for a veto angle of 22 mrad, to 19.4 pb for an angle of 24 mrad, to 36.1 pb for an angle of 26 mrad, to 38.2 pb for an angle of 28 mrad. Hence, increasing the veto angle by a couple of mrad substantially increases the single photon background from radiative Bhabhas. On the other hand, the background can be reduced an equal amount by increasing the minimum transverse momentum cut from 1.0 to 1.2 or 1.5 GeV. The signal, under these new cuts, would only decrease by $\approx 30\%$. A detailed study of the luminosity monitor efficiency versus angle will need to be done with the various detector elements in place to determine the most effective

sets of cuts to maximize the signal versus the background and to keep the amount of data needed to a minimum.

6. Resolution in the Determination of N_ν Based on Various Cuts and Running Conditions.

Making use of the results discussed in the previous sections we have calculated how well we can determine the number of neutrino generations. These results are obtained under the following assumptions:

1. The effective average luminosity is $0.5 \times 10^{30} \text{ cm}^{-2} \text{ sec}^{-1}$.
2. The cross section for $e^+ + e^- \rightarrow \mu^+ + \mu^-$ at $E_{cm} = M_Z$ is 1.34 nb. This is shown in Fig. 5. The branching ratio is 3.27%.
3. The beam energy distribution is gaussian and the center of mass energy resolution is 50 MeV.
4. The calorimeter in the SLD detector has a photon energy resolution given by $\delta E = 9\sqrt{E}\%$.
5. The angular resolution of the calorimeter is good enough that it does not contribute to the overall error.
6. The ratio in the cross section for $e^+ + e^- \rightarrow \nu + \bar{\nu} + \gamma$ between the case for $4N_\nu$ and $3N_\nu$ is 1.30 at $E_{cm} = M_Z$ and 1.23 at $E_{cm} = 96.0 \text{ GeV}$.
7. The theoretical uncertainty in the magnitude of the cross section for $e^+ + e^- \rightarrow \nu + \bar{\nu} + \gamma$ is 5%. This is an optimistic assumption since, at present, the radiative corrections are large ($\approx 22\%$). Nevertheless, we expect that the third order corrections will be calculated soon and will reduce the uncertainty in the magnitude of this cross section.
8. The theoretical uncertainty in the magnitude of the cross section for $e^+ + e^- \rightarrow e^+ + e^- + \gamma$ (Radiative Bhabha) is 1%.
9. The theoretical uncertainty in the magnitude of the cross section for $e^+ + e^- \rightarrow \mu^+ + \mu^- + \gamma$ is less than 1%.
10. The uncertainty in the luminosity measurement is 3%.

11. The veto angle for radiative Bhabhas is 22 mrad.

The results of this study are shown in Tables 6 to 13. The results are obtained assuming that we run for the same integrated luminosity at a given run setting. We conclude that the best determination is achieved running at a center of mass energy near 96 GeV, requiring that the photon transverse momentum be greater than 1 GeV, and using the ratio method. When we are in the regime of low statistics (60 day running or less) the resolution is limited mainly by statistics. In Figs. 37 and 38 we show the limits achievable under various running conditions given the running time at an average luminosity of $0.5 \times 10^{30} cm^{-2} sec^{-1}$.

TABLE 6

Method used is Comparison of the Observed Number of $\nu\nu\gamma$ Events with the Expected.

Run Conditions: $E_{cm} = M_Z$, $E_\gamma \geq 1$ GeV, No P_t Cut, $\theta_{\gamma beam} \geq 10^\circ$.

For 1 Additional Neutrino $\delta\sigma/\sigma = 30\%$.

All Errors Stated in Units of N_ν .

Running Time (days)	0.6	6	30	60	600
# of Z_0 's Ev.	1×10^3	1×10^4	5×10^4	1×10^5	1×10^6
# of $\nu\nu\gamma$ Ev.	2	21	103	207	2070
# of Rad. Bhabhas Ev.	13	134	670	1340	1.34×10^4
$\delta\sigma$ (due to number of events)	6.4	2.0	0.92	0.67	0.29
$\delta\sigma$ (due to beam energy resol.)	0.14	0.14	0.14	0.14	0.14
$\delta\sigma$ (due to photon energy resol.)	0.02	0.02	0.02	0.02	0.02
$\delta\sin^2\theta_w$	0.001	0.0003	0.0003	0.0002	0.0001
$\delta\sigma$ (due to $\delta\sin^2\theta_w$)	0.31	0.09	0.09	0.06	0.03
$\delta\sigma$ (due to Rad. Corr. Uncertainty)	0.17	0.17	0.17	0.17	0.17
$\delta\sigma$ (due to Luminosity Uncertainty)	0.10	0.10	0.10	0.10	0.10
$\delta\sigma$ Total	6.4	2.0	0.95	0.72	0.38

TABLE 7

Method used is Comparison of the Observed Number of $\nu\nu\gamma$ Events with the Expected.

Run Conditions: $E_{cm} = M_Z$, $Pt_\gamma \geq 1$ GeV, $\theta_{\gamma beam} \geq 10^\circ$.

For 1 Additional Neutrino $\delta\sigma/\sigma = 30\%$.

All Errors Stated in Units of N_ν .

Running Time (days)	0.6	6	30	60	600
# of Z_0 's Ev.	1×10^3	1×10^4	5×10^4	1×10^5	1×10^6
# of $\nu\nu\gamma$ Ev.	1	9	44	88	879
# of Rad. Bhabhas Ev.	0.1	1	7	13	134
$\delta\sigma$ (due to number of events)	3.5	1.0	0.50	0.35	0.12
$\delta\sigma$ (due to beam energy resol.)	0.13	0.13	0.13	0.13	0.13
$\delta\sigma$ (due to photon energy resol.)	0.02	0.02	0.02	0.02	0.02
$\delta\sin^2\theta_w$	0.001	0.0003	0.0003	0.0002	0.0001
$\delta\sigma$ (due to $\delta\sin^2\theta_w$)	0.34	0.10	0.10	0.07	0.03
$\delta\sigma$ (due to Rad. Corr. Uncertainty)	0.17	0.17	0.17	0.17	0.17
$\delta\sigma$ (due to Luminosity Uncertainty)	0.10	0.10	0.10	0.10	0.10
$\delta\sigma$ Total	3.5	1.0	0.57	0.42	0.27

TABLE 8

Method used is Comparison of the Observed Number of $\nu\nu\gamma$ Events with the Expected.

Run Conditions: $E_{cm} = 96.0$ GeV, $E_\gamma \geq 1$ GeV, No P_t Cut, $\theta_{\gamma beam} \geq 10^\circ$.

For 1 Additional Neutrino $\delta\sigma/\sigma = 23\%$.

All Errors Stated in Units of N_ν .

Running Time (days)	0.6	6	30	60	600
# of Z_0 's Ev.	186	1860	9290	18600	1.86×10^5
# of $\nu\nu\gamma$ Ev.	4	43	218	436	4360
# of Rad. Bhabhas Ev.	13	130	640	1290	1.29×10^4
$\delta\sigma$ (due to number of events)	4.5	1.3	0.59	0.43	0.18
$\delta\sigma$ (due to beam energy resol.)	0.04	0.04	0.04	0.04	0.04
$\delta\sigma$ (due to photon energy resol.)	0.01	0.01	0.01	0.01	0.01
$\delta\sin^2\theta_w$	0.001	0.0003	0.0003	0.0002	0.0001
$\delta\sigma$ (due to $\delta\sin^2\theta_w$)	0.10	0.03	0.03	0.02	0.01
$\delta\sigma$ (due to Rad. Corr. Uncertainty)	0.22	0.22	0.22	0.22	0.22
$\delta\sigma$ (due to Luminosity Uncertainty)	0.13	0.13	0.13	0.13	0.13
$\delta\sigma$ Total	4.5	1.3	0.64	0.50	0.32

TABLE 9

Method used is Comparison of the Observed Number of $\nu\nu\gamma$ events with the Expected .

Run Conditions: $E_{cm} = 96.0\text{GeV}$, $Pt_\gamma \geq 1\text{ GeV}$, $\theta_{\gamma beam} \geq 10^\circ$.

For 1 Additional Neutrino $\delta\sigma/\sigma = 23\%$.

All Errors Stated in Units of N_ν .

Running Time (days)	0.6	6	30	60	600
# of Z_0 's Ev.	186	1860	9290	18600	1.86×10^5
# of $\nu\nu\gamma$ Ev.	3	30	150	300	3000
# of Rad. Bhabhas Ev.	0.1	1	7	13	130
$\delta\sigma$ (due to number of events)	2.6	0.81	0.36	0.25	0.080
$\delta\sigma$ (due to beam energy resol.)	0.01	0.01	0.01	0.01	0.01
$\delta\sigma$ (due to photon energy resol.)	0.01	0.01	0.01	0.01	0.01
$\delta\sin^2\theta_w$	0.001	0.0003	0.0003	0.0002	0.0001
$\delta\sigma$ (due to $\delta\sin^2\theta_w$)	0.03	0.009	0.009	0.006	0.003
$\delta\sigma$ (due to Rad. Corr. Uncertainty)	0.22	0.22	0.22	0.22	0.22
$\delta\sigma$ (due to Luminosity Uncertainty)	0.13	0.13	0.13	0.13	0.13
$\delta\sigma$ Total	2.6	0.85	0.45	0.36	0.27

TABLE 10

Method used is Comparison of the Observed Number of $\nu\nu\gamma$ with $\mu\mu\gamma$ Events.

Run Conditions: $E_{cm} = M_Z$, $E_\gamma \geq 1$ GeV, No P_t Cut, $\theta_{\gamma beam} \geq 10^\circ$.

$R = N(\nu\bar{\nu}\gamma)/N(\mu^+\mu^-\gamma)$, For 1 Additional Neutrino $\delta R/R = 44\%$.

All Errors Stated in Units of N_ν .

Running Time (days)	0.6	6	30	60	600
# of Z_0 's Ev.	1×10^3	1×10^4	5×10^4	1×10^5	1×10^6
# of $\nu\nu\gamma$ Ev.	2	21	103	207	2070
# of Rad. Bhabhas Ev.	13	134	670	1340	1.34×10^4
# of $\mu\mu\gamma$ Ev.	4	43	214	428	4280
δR (due to number of events)	4.7	1.4	0.65	0.47	0.20
δR (due to beam energy resol.)	0.08	0.08	0.08	0.08	0.08
δR (due to photon energy resol.)	0.02	0.02	0.02	0.02	0.02
$\delta \sin^2 \theta_w$	0.001	0.0003	0.0003	0.0002	0.0001
δR (due to $\delta \sin^2 \theta_w$)	0.84	0.25	0.25	0.17	0.08
δR (due to Rad. Corr. Uncertainty)	0.0	0.0	0.0	0.0	0.0
δR (due to Luminosity Uncertainty)	0.0	0.0	0.0	0.0	0.0
δR Total	4.7	1.4	0.70	0.51	0.23

TABLE 11

Method used is Comparison of the Observed Number of $\nu\nu\gamma$ with $\mu\mu\gamma$ Events.

Run Conditions: $E_{cm} = M_Z$, $Pt_\gamma \geq 1$ GeV, $\theta_{\gamma beam} \geq 10^\circ$.

$R = N(\nu\bar{\nu}\gamma)/N(\mu^+\mu^-\gamma)$, For 1 Additional Neutrino $\delta R/R = 48\%$.

All Errors Stated in Units of N_ν .

Running Time (days)	0.6	6	30	60	600
# of Z_0 's Ev.	1×10^3	1×10^4	5×10^4	1×10^5	1×10^6
# of $\nu\nu\gamma$ Ev.	1	9	44	88	879
# of Rad. Bhabhas Ev.	0.1	1	7	13	134
# of $\mu\mu\gamma$ Ev.	4	37	185	370	3700
δR (due to number of events)	2.4	0.82	0.37	0.26	0.08
δR (due to beam energy resol.)	0.06	0.06	0.06	0.06	0.06
δR (due to photon energy resol.)	0.02	0.02	0.02	0.02	0.02
$\delta \sin^2 \theta_w$	0.001	0.0003	0.0003	0.0002	0.0001
δR (due to $\delta \sin^2 \theta_w$)	0.94	0.28	0.28	0.19	0.09
δR (due to Rad. Corr. Uncertainty)	0.0	0.0	0.0	0.0	0.0
δR (due to Luminosity Uncertainty)	0.0	0.0	0.0	0.0	0.0
δR Total	2.6	0.87	0.47	0.33	0.14

TABLE 12

Method used is Comparison of the Observed Number of $\nu\nu\gamma$ with $\mu\mu\gamma$ Events.

Run Conditions: $E_{cm} = 96.0\text{GeV}$, $E_\gamma \geq 1\text{ GeV}$, No P_t Cut , $\theta_{\gamma beam} \geq 10^\circ$.

$R = N(\nu\bar{\nu}\gamma)/N(\mu^+\mu^-\gamma)$, For 1 Additional Neutrino $\delta R/R = 30\%$.

All Errors Stated in Units of N_ν .

Running Time (days)	0.6	6	30	60	600
# of Z_0 's Ev.	186	1860	9290	18600	1.86×10^5
# of $\nu\nu\gamma$ Ev.	4	43	218	436	4360
# of Rad. Bhabhas Ev.	13	130	640	1290	1.29×10^4
# of $\mu\mu\gamma$ Ev.	1	11	56	113	1130
δR (due to number of events)	5.0	1.4	0.64	0.46	0.17
δR (due to beam energy resol.)	0.02	0.02	0.02	0.02	0.02
δR (due to photon energy resol.)	0.01	0.01	0.01	0.01	0.01
$\delta \sin^2 \theta_w$	0.001	0.001	0.0003	0.0003	0.0001
δR (due to $\delta \sin^2 \theta_w$)	0.06	0.06	0.02	0.02	0.006
δR (due to Rad. Corr. Uncertainty)	0.0	0.0	0.0	0.0	0.0
δR (due to Luminosity Uncertainty)	0.0	0.0	0.0	0.0	0.0
δR Total	5.0	1.4	0.64	0.46	0.17

TABLE 13

Method used is Comparison of the Observed Number of $\nu\nu\gamma$ with $\mu\mu\gamma$ Events.

Run Conditions: $E_{cm} = 96.0$ GeV, $Pt_\gamma \geq 1$ GeV, , $\theta_{\gamma beam} \geq 10^\circ$.

$R = N(\nu\bar{\nu}\gamma)/N(\mu^+\mu^-\gamma)$, For 1 Additional Neutrino $\delta R/R = 28\%$.

All Errors Stated in Units of N_ν .

Running Time (days)	0.6	6	30	60	600
# of Z_0 's Ev.	186	1860	9290	18600	1.86×10^5
# of $\nu\nu\gamma$ Ev.	3	30	150	300	3000
# of Rad. Bhabhas Ev.	0.1	1	7	13	130
# of $\mu\mu\gamma$ Ev.	1	9	45	91	914
δR (due to number of events)	4.6	1.4	0.60	0.42	0.13
δR (due to beam energy resol.)	0.03	0.03	0.03	0.03	0.03
δR (due to photon energy resol.)	0.01	0.01	0.01	0.01	0.01
$\delta \sin^2\theta_w$	0.001	0.001	0.0003	0.0003	0.0001
δR (due to $\delta \sin^2\theta_w$)	0.14	0.14	0.04	0.04	0.01
δR (due to Rad. Corr. Uncertainty)	0.0	0.0	0.0	0.0	0.0
δR (due to Luminosity Uncertainty)	0.0	0.0	0.0	0.0	0.0
δR Total	4.6	1.4	0.60	0.42	0.13

REFERENCES

1. S. Weinberg, Phys. Rev. Letters 19, 1264 (1967) and Phys. Rev. D5, 1412 (1972).
 A. Salam in Elementary Particle Theory, edited by N. Svartholm, Nobel Symposium No. 8 (Wiley, New York, 1969) p. 361.
 S. L. Glashow, Nuclear Physics 22, 579, (1969) and S. L. Glashow et. al. Phys. Rev. D2, 1285, 1970.
2. Particle Properties Data Booklet, April, 1986.
3. Cosmology and Particle Physics. M. S. Turner Fermilab Conf. 84/60-A. June, 1984.
4. J. Ellis, M. K. Gaillard Annual Reviews of Nuclear and Particle Science Vol. 32, 443, 1982.
5. Proceedings of the SLC Workshop on Experimental Use of the SLAC Linear Collider. SLAC-247.
 Physics at LEP, CERN 86-02
 Z_0 Decay Modes Experimental Measurements. J. M. Dorfan SLAC-PUB 3407
 The Physics in the Z_0 Energy Regime. U. Nauenberg, COLO-HEP 107, Springer Tracts in Modern Physics, Vol. 108, 1986, p. 191.
6. Y. S. Tsai SLAC-PUB 3129.
 D. C. Kennedy and B. W. Lynn SLAC-PUB 4039.
 F. A. Berends, G. J. H. Burgers, and W. L. Van Neerven Phys. Lett. B, 191, 1986.
 F. A. Berends, G. J. H. Burgers, C. Mana, M. Martinez, and W. L. van Neerven, CERN-TH. 4865/87.
 O. Nicrosini and L. Trentadue, Phys. Lett. B, 551, 1987.
7. UA1 Collaboration report at the XXIV International Conference in Munich, Germany, 1988.

8. Patricia Rankin, Physics Working Group Note # 1-9 Report. Proceedings of the Third MARK II Workshop on SLC Physics. SLAC-Report-315, 1987.
B. W. Lynn, M. E. Peskin, and R. G. Stuart, SLAC-PUB-3725, 1985.
9. Mixing of Toponium with the Z_0 Boson. Paula J. Franzini, and Fred. J. Gilman, SLAC-PUB 3541, (1985).
Toponium Physics at LEP. W. Buchmuller, A. Martin, J. H. Kuhn, F. Richard, P. Roudeau, G. Coignet, L. Rolandi, MPI-PAE/Pth 85/85.
Toponium Z Mixing. L. J. Hall, S. F. King, S. R. Sharpe, Nucl. Phys. B260, 510, (1985).
Z Decays to Top Quarks. J. H. Kuhn, A. Reiter, P. M. Zerwas, SLAC-PUB 3746, (1985).
Toponium Physics. A. Martin, CERN-th. 4060/84.
The Last Hurrah for Quarkonium Physics. The Top System. E. Eichten, Fermilab-Conf. 85/29-T.
10. H. Baer et. al. , Physics at LEP, CERN 86-02 Vol. 1, (1986).
11. T. Kinoshita J. Math. Phys. 3, 650, (1962).
T. D. Lee and M. Nauenberg, Phys. Rev. 133, 1549, (1964).
12. E. A. Kuraev and V. S. Fadin, Sov. J. Nucl. Phys. 41,466, (1985).
Robert N. Cahn, LBL-22601, (1986); also published in Phys. Rev. D36, 2666, (1987).
13. G. Feldman, MARK II/SLC-Physics Working Group Note # 2-24.
14. E. Ma and J. Okada, Phys. Rev. Letters 41, 287, (1978). Errata, Phys. Rev. Letters 41, 1759, (1978).
K. J. F. Gaemers, R. Gastmans, and F. M. Renard, Phys. Rev. D 19, 1605, (1979).
G. Barbiellini, B. Richter, and J. L. Siegrist, Phys. Letters 106B, 414, (1981).
Proceedings of the SLC Workshop on Experimental Use of the SLAC Linear Collider, SLAC-247, CONF-811233, pages 122 and 237, (1982).

15. F. A. Berends, G. J. H. Burgers, C. Mana, M. Martinez, and W. L. Van Neerven, Nuclear Physics B301, 583, (1988).
16. M. Igarashi and N. Nakazawa, TKU-HEP 86/01 or KUDP 86/02, (1986).
N. Dombey, J. Cole, and F. Boudjema, Phys. Letters 167B, 108, (1986).
17. F. A. Behrends, G. J. H. Burgers, and W. L. Van Neerven, Leiden Preprint 86-0458, 1986 at SLAC., also published Phys. Lett. 177B, 191, (1986).
O. Nicrosini and L. Trentadue, Phys. Lett. 196B, 551, (1987).
F. A. Berends, G. J. H. Burgers, C. Mana, M. Martinez, and W. L. van Neerven, CERN preprint TH.4865/87, (1987).
18. B. W. Lynn private communication.
19. W. T. Ford et al. (MAC Collaboration), Phys. Rev. D33, 3472 (1986).
E. Fernandez et al. (MAC Collaboration), Phys. Rev. Lett. 54, 1118, (1985).
C. Hearty et al. (ASP Collaboration), Phys. Rev. Lett. 58, 1711, (1987).
G. Bartha et al. (ASP Collaboration), Phys. Rev. Lett. 56, 685, (1986).
H. Behrend et al. (CELLO Collaboration), Phys. Lett. B176, 247, (1986).
20. C. Mana and M. Martinez, Nucl. Phys. B287, 601, (1987).
21. H. R. Band, SLD Note 176, (1988).
22. M. Caffo, R. Gatto, and E. Remiddi, Phys. Lett. B173, 91, (1986).
23. Neutrino Counting in e^+e^- Collisions, M. Caffo, R. Gatto, E. Remiddi UGVA-DPT 1986/09-514.
24. Montecarlo Simulation of Radiative Processes in Electron- Positron Scattering, Thesis report by R. P. Kleiss, 1982.
25. C. Hearty et. al. (ASP Collaboration), SLAC-PUB-4684, (1988).
26. J. S. Hagelin, G. L. Kane, and S. Raby, Nucl. Phys. B241, 638, (1984).
27. J. Ellis and J. S. Hagelin, Phys. Lett. B122, 303, (1983).

FIGURE CAPTIONS

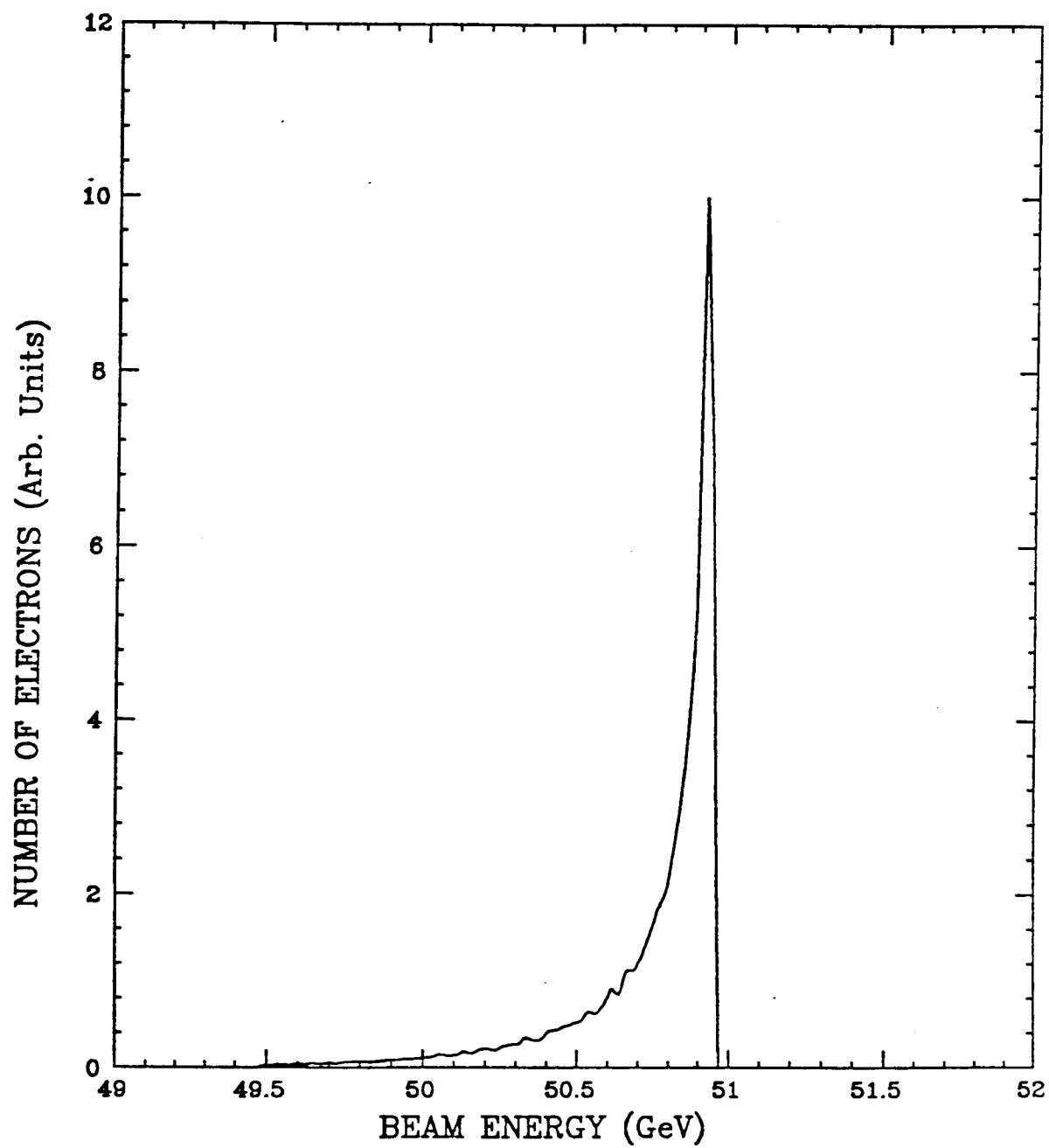
1. A possible beam energy spectrum with a low momentum tail.
2. The expected Z decay rate into a pair of charge $2/3$ e quarks as a function of the quark mass. For the case of a top quark mass of 40 GeV the decay rate is equivalent to a 0.3 neutrino generation.
3. The Feynman diagram that describes the process that leads to the interference between Z_0 and Toponium production.
4. The shape of the resonance as a function of the center of mass energy before you include initial state radiation and after.
5. Detail of the shape of the resonance around the peak.
6. The Feynman diagrams that describe the process $e^+ + e^- \rightarrow Z_0 \rightarrow \nu + \bar{\nu} + \gamma$.
7. The cross section for the process $e^+ + e^- \rightarrow Z_0 \rightarrow \nu + \bar{\nu} + \gamma$ for the case of 3 and 4 neutrino generations and for cuts in the photon transverse momentum and angle.
8. The cross section for the process $e^+ + e^- \rightarrow Z_0 \rightarrow \nu + \bar{\nu} + \gamma$ for the case of 3 and 4 neutrino generations and for cuts in the photon momentum and angle.
9. The photon energy distribution in the process $e^+ + e^- \rightarrow Z_0 \rightarrow \nu + \bar{\nu} + \gamma$ for various conditions.
10. The photon angular distribution in the process $e^+ + e^- \rightarrow Z_0 \rightarrow \nu + \bar{\nu} + \gamma$ for various conditions.
11. Feynman diagrams that represent the main radiative corrections to the first order process.
12. The number of standard deviations away from the expected signal for 4 neutrinos after 1 year of running with an integrated luminosity of 18 pb^{-1} assuming that the observed signal comes from the 3 neutrino case. Curve

- (a) assumes that the beam energy distribution is gaussian with a $\sigma = 250$ MeV and there is no error in the luminosity. Curve (b) considers the case that the beam energy distribution has a low energy tail like in Fig. 1. Curve (c) is for the same conditions as (b) and, in addition, has a 3 % statistical error in the value of the luminosity.
13. The cross section for the radiative neutrino production process as we vary the minimum acceptable photon energy. The parameters used are those in Table 1. For the case of 4 neutrinos we increased the Z_0 width accordingly (2.82 GeV). The photon angle relative to the beam is greater than 10°
 14. Same as in Fig. 13 but now we vary the minimum allowed transverse photon momentum. In addition we still require that the photon energy be greater than 1 GeV.
 15. The differential cross section of the Radiative Bhabha process as a function of the photon transverse momentum for various photon cuts at a center of mass energy of 95 GeV
 16. A comparison of the cross section dependence on a minimum photon transverse momentum cut from Radiative Bhabhas at a center of mass energy of 95 GeV and from the $\nu\bar{\nu}\gamma$ process at 92 and 96 GeV. Since the Radiative Bhabha process only varies slowly with energy, the characteristics at 95 GeV apply equally to all energies in the vicinity.
 17. Same as Fig. 17 but using a minimum photon energy cut.
 18. The number of events expected in a 1 year run with an integrated luminosity of $18pb^{-1}$. Curve (a) refers to the case of an unpolarized beam and curve (b) represents the difference in the signals with the two possible longitudinal polarization states of the electron assuming we used equal integrated luminosity (1/2 the total luminosity) in obtaining each signal.
 19. The sensitivity in each of the signals to the value of $\sin^2\theta_w$. Curve (a) is the case of an unpolarized beam and curve (b) refers to the case of the difference

in the signals from the two longitudinally polarized electron beams.

20. The cross section for the process $e^+ + e^- \rightarrow \mu^+ + \mu^- + \gamma$. We show the total cross section for $E_\gamma > 1$ GeV; the contribution to it from radiation by the incoming electron and positron and from the radiation by the outgoing muons.
21. The cross section for the process $e^+ + e^- \rightarrow \mu^+ + \mu^- + \gamma$. after we require that the angle between the photon and either muon be greater than 20° . The effect of this cut is to reduce markedly the contribution from the final state radiation, as expected.
22. The photon energy spectrum in the process $e^+ + e^- \rightarrow \mu^+ + \mu^- + \gamma$ at the center of mass energy of 92 GeV. We show the total energy spectrum and that spectrum of the photons coming from the radiation of the incident electron and positron, and the radiation from the outgoing muons.
23. The photon energy spectrum in the process $e^+ + e^- \rightarrow \mu^+ + \mu^- + \gamma$ at the center of mass energy of 96 GeV. We show the total energy spectrum and that spectrum of the photons coming from the radiation of the incident electron and positron, and the radiation from the outgoing muons.
24. Expected value of the ratio $\frac{e^+ + e^- \rightarrow \nu + \bar{\nu} + \gamma}{e^+ + e^- \rightarrow \mu^+ + \mu^- + \gamma}$ as a function of the center of mass energy for two cuts in the angle between the photon and either muon.
25. Dependence of the ratio $\frac{e^+ + e^- \rightarrow \nu + \bar{\nu} + \gamma}{e^+ + e^- \rightarrow \mu^+ + \mu^- + \gamma}$ on the cut of the minimum photon energy acceptable at a center of mass energy of 92 GeV.
26. Dependence of the ratio $\frac{e^+ + e^- \rightarrow \nu + \bar{\nu} + \gamma}{e^+ + e^- \rightarrow \mu^+ + \mu^- + \gamma}$ on the cut of the minimum photon energy acceptable at a center of mass energy of 96 GeV.
27. Dependence of the ratio $\frac{e^+ + e^- \rightarrow \nu + \bar{\nu} + \gamma}{e^+ + e^- \rightarrow \mu^+ + \mu^- + \gamma}$ on the value of $\sin^2 \theta_w$ at a center of mass energy of 93 GeV.
28. Dependence of the ratio $\frac{e^+ + e^- \rightarrow \nu + \bar{\nu} + \gamma}{e^+ + e^- \rightarrow \mu^+ + \mu^- + \gamma}$ on the value of $\sin^2 \theta_w$ at a center of mass energy of 96 GeV.

29. The cross section for the process $e^+ + e^- \rightarrow \mu^+ + \mu^- + \gamma$. We show the total cross section for $Pt_\gamma > 1$ GeV; the contribution to it from radiation by the incoming electron and positron and from the radiation by the outgoing muons.
30. The photon transverse momentum spectrum in the process $e^+ + e^- \rightarrow \mu^+ + \mu^- + \gamma$ at the center of mass energy of 92 GeV.
31. The photon transverse momentum spectrum in the process $e^+ + e^- \rightarrow \mu^+ + \mu^- + \gamma$ at the center of mass energy of 96 GeV.
32. Expected value of the ratio $\frac{e^+ + e^- \rightarrow \nu + \bar{\nu} + \gamma}{e^+ + e^- \rightarrow \mu^+ + \mu^- + \gamma}$ as a function of the center of mass energy for the photon transverse momentum greater than 1 GeV.
33. Dependence of the ratio $\frac{e^+ + e^- \rightarrow \nu + \bar{\nu} + \gamma}{e^+ + e^- \rightarrow \mu^+ + \mu^- + \gamma}$ on the cut of the minimum photon transverse momentum acceptable at a center of mass energy of 93 GeV.
34. Dependence of the ratio $\frac{e^+ + e^- \rightarrow \nu + \bar{\nu} + \gamma}{e^+ + e^- \rightarrow \mu^+ + \mu^- + \gamma}$ on the cut of the minimum photon transverse momentum acceptable at a center of mass energy of 96 GeV.
35. Dependence of the ratio $\frac{e^+ + e^- \rightarrow \nu + \bar{\nu} + \gamma}{e^+ + e^- \rightarrow \mu^+ + \mu^- + \gamma}$ on the value of $\sin^2 \theta_w$ at a center of mass energy of 93 GeV.
36. Dependence of the ratio $\frac{e^+ + e^- \rightarrow \nu + \bar{\nu} + \gamma}{e^+ + e^- \rightarrow \mu^+ + \mu^- + \gamma}$ on the value of $\sin^2 \theta_w$ at a center of mass energy of 96 GeV.
37. Limit on the achievable accuracy of the value of the number of neutrino generations from the observed number of radiative neutrino pair events at (a) $E_{cm} = M_Z = 92.2$ GeV and (b) $E_{cm} = 96.0$ GeV when compared with the theoretical expectations. These curves follow from the results presented in Tables 6 to 9.
38. Limit on the achievable accuracy of the value of the number of neutrino generations when comparing the number of observed radiative neutrino pairs and radiative muon pairs at (a) $E_{cm} = M_Z = 92.2$ GeV and (b) $E_{cm} = 96.0$ GeV. These curves follow from the results presented in Tables 10 to 13.



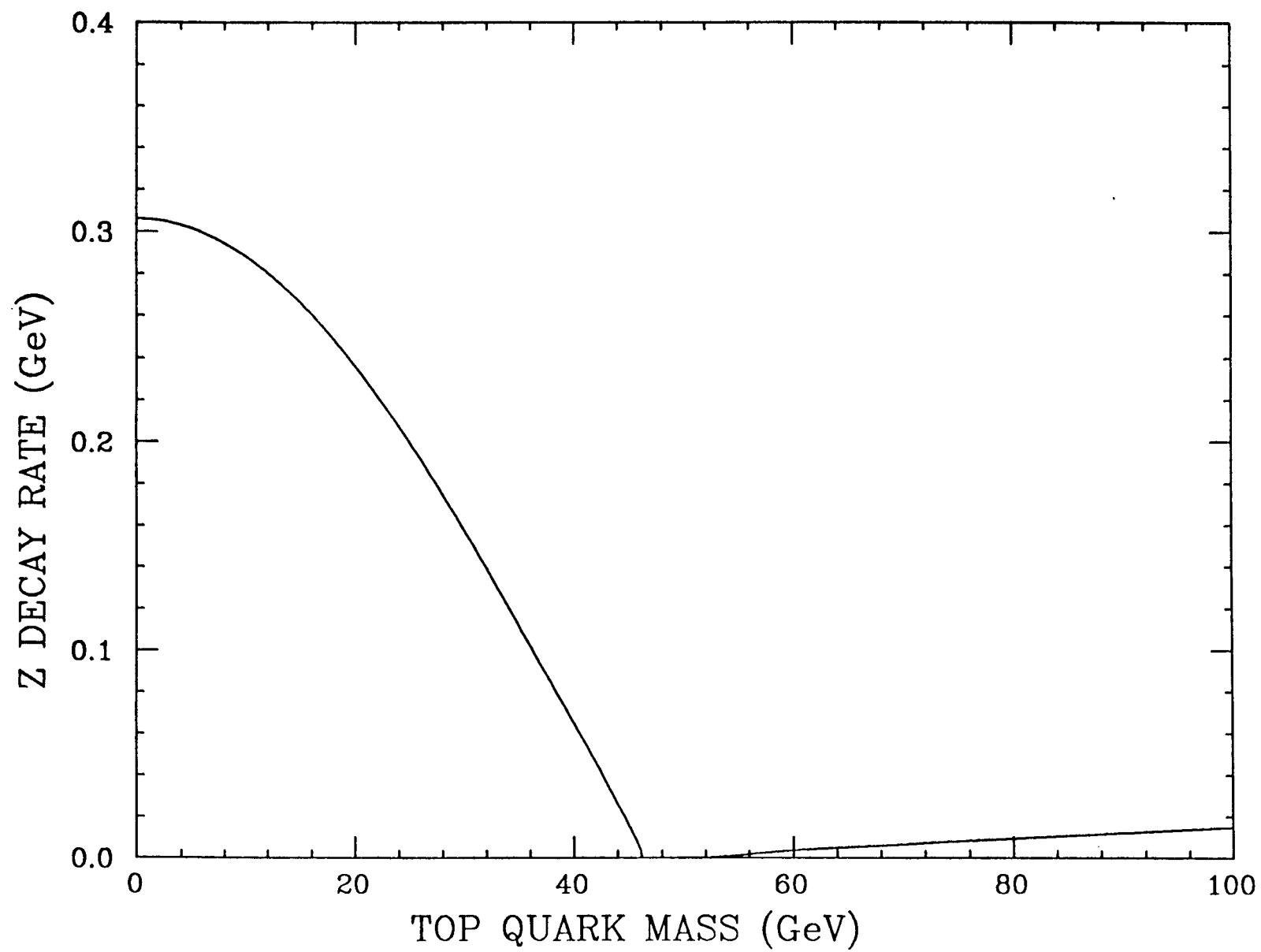
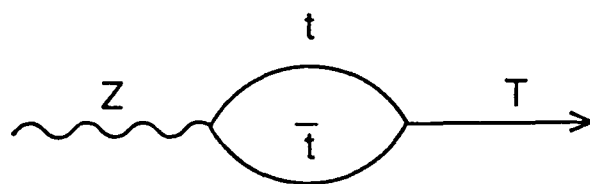


FIG. 2



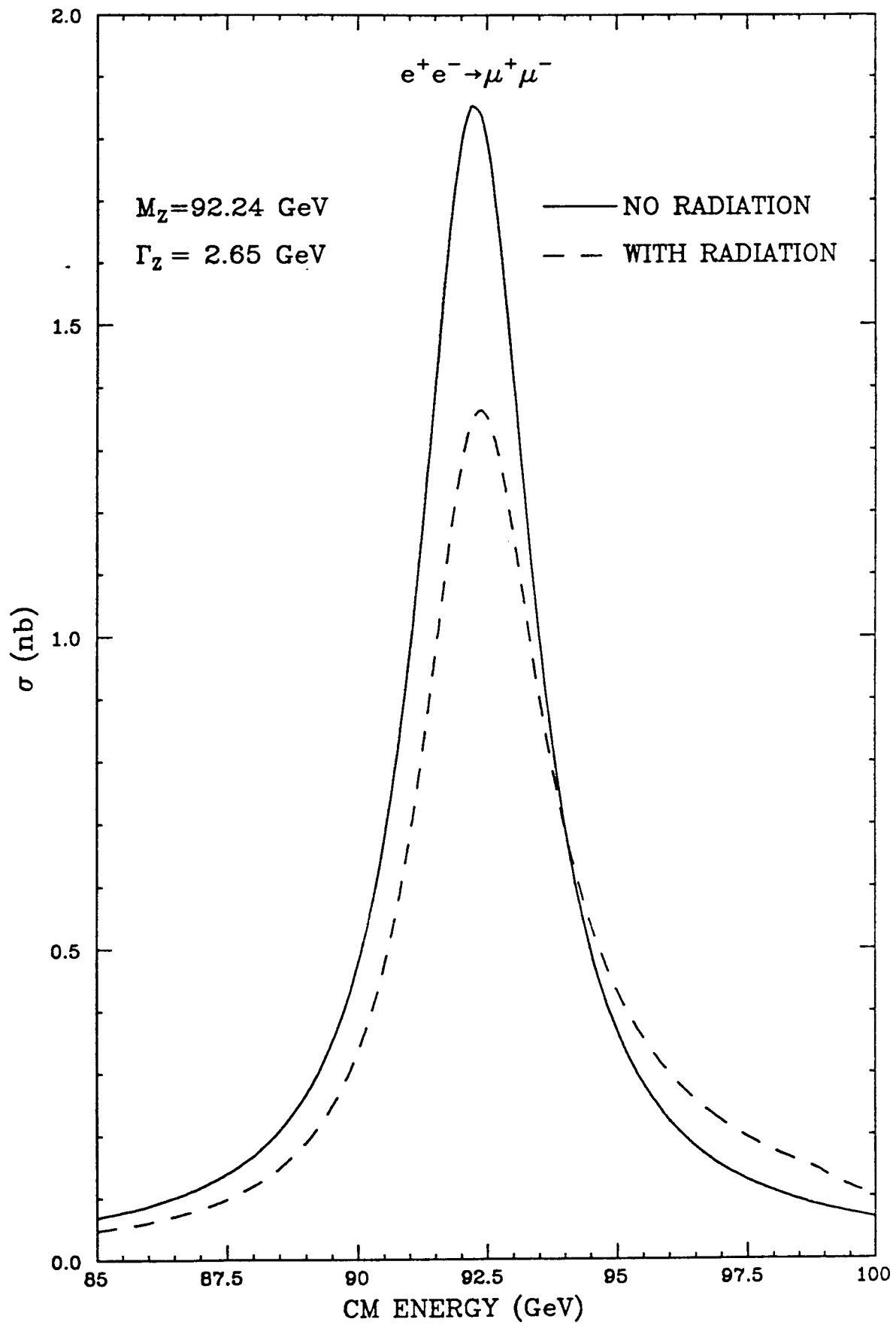
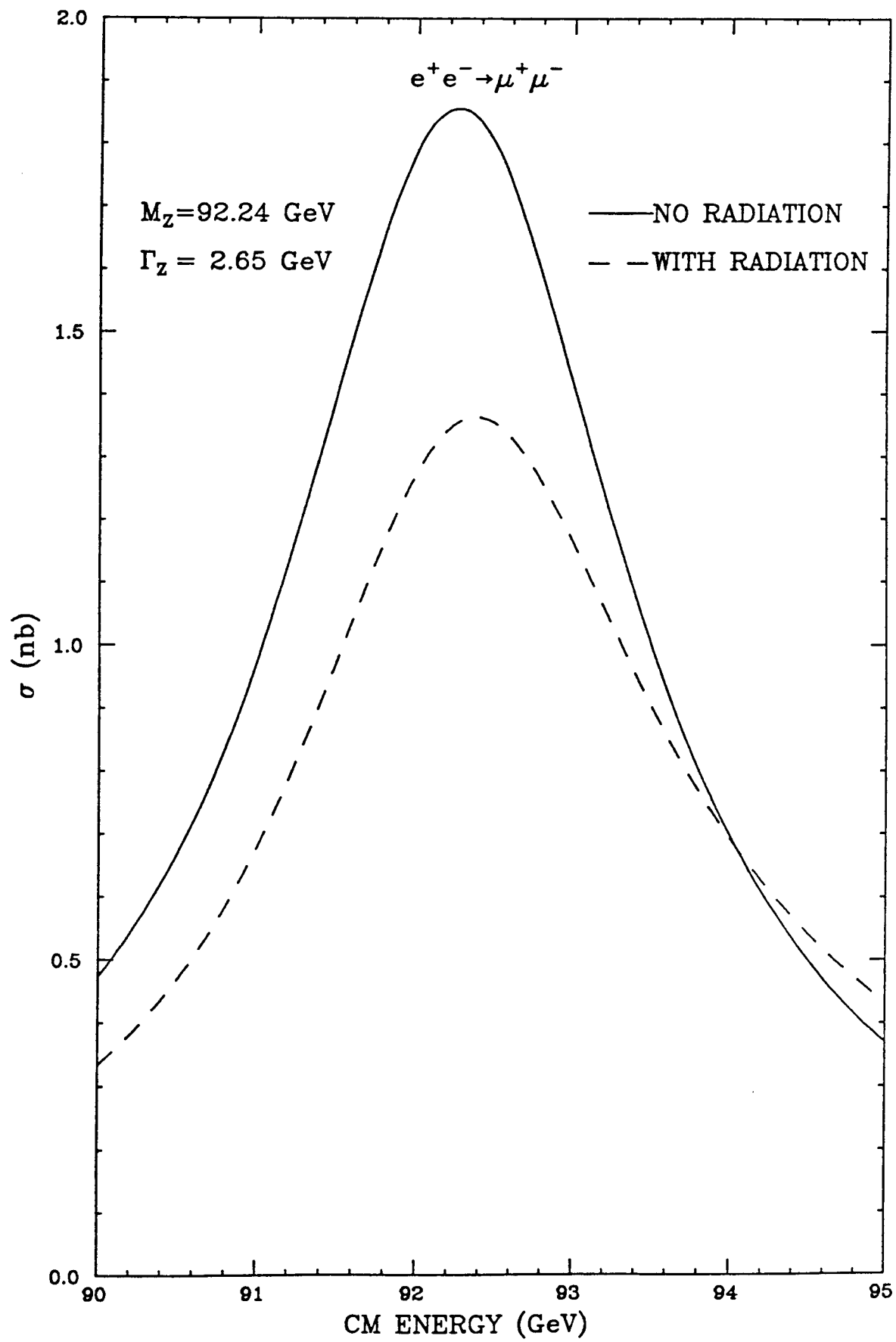


FIG. 4



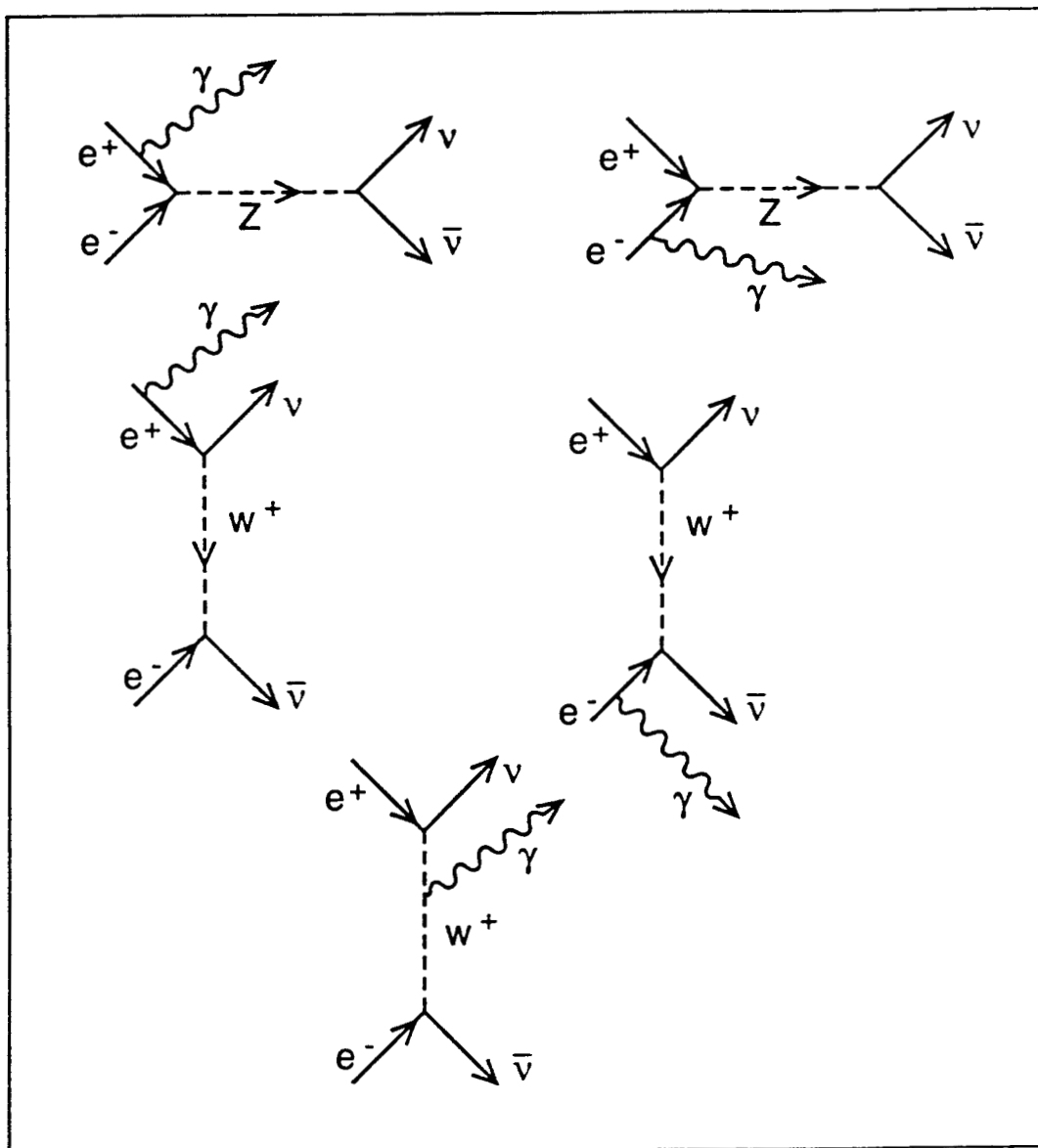
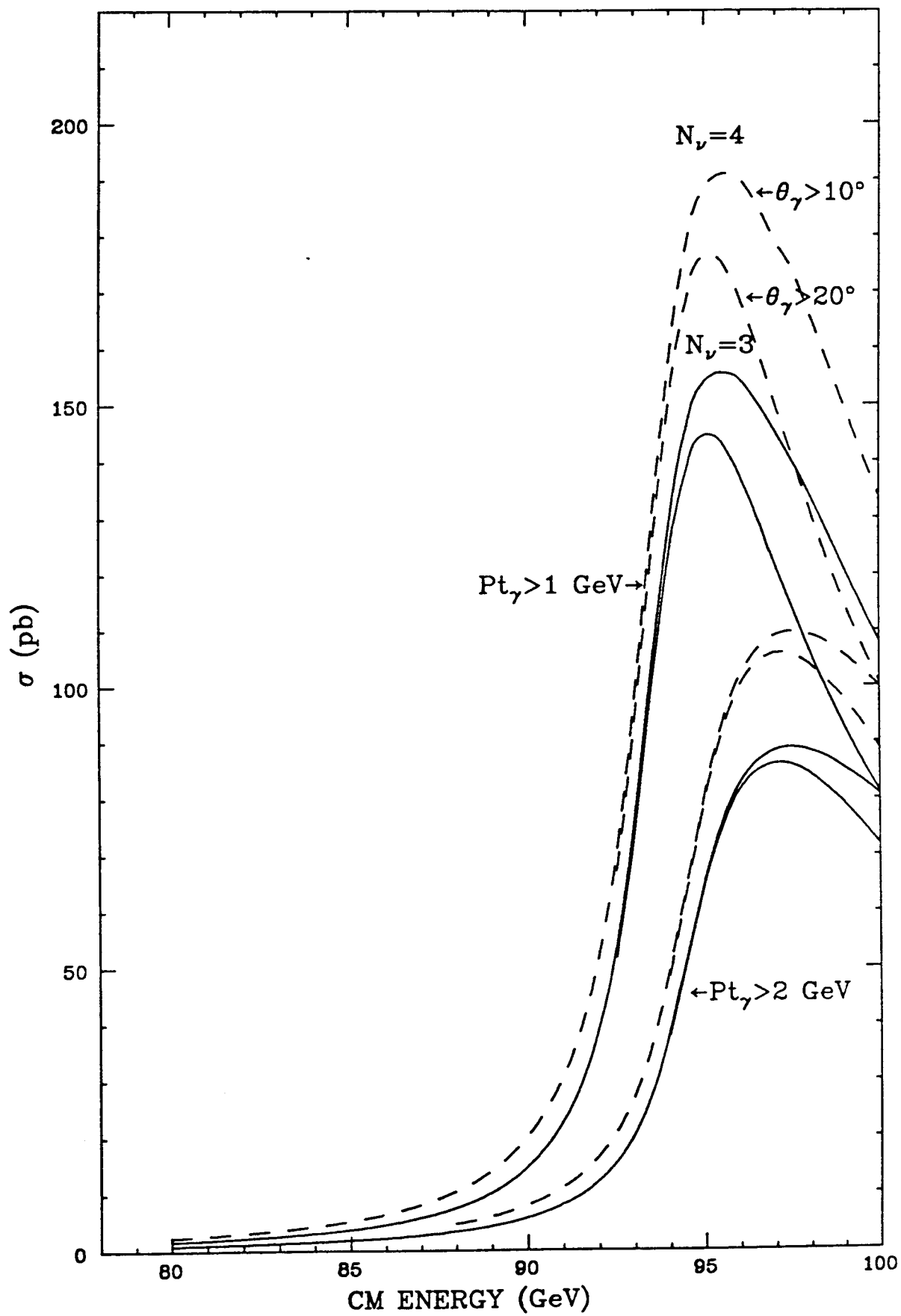
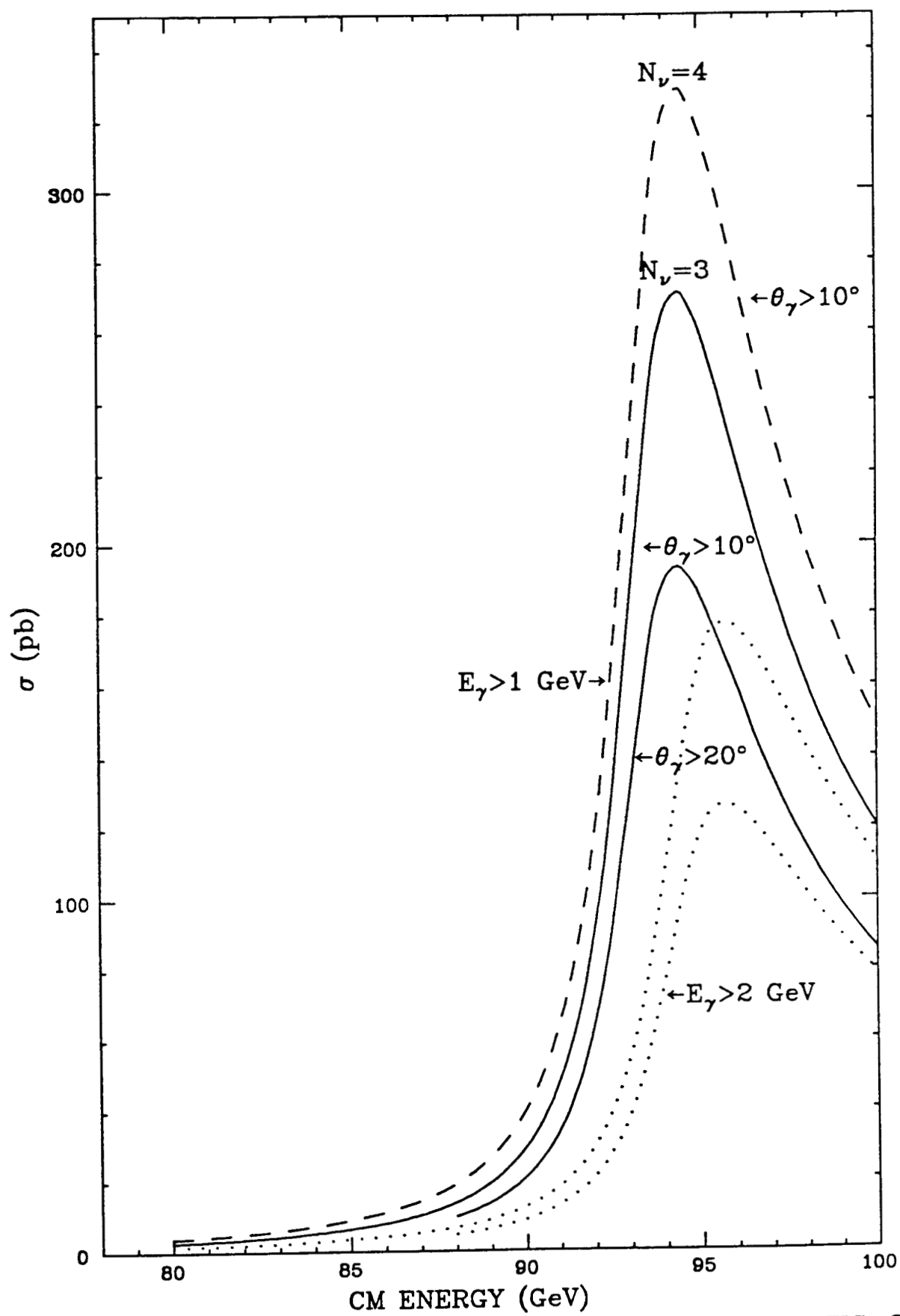


FIG. 6





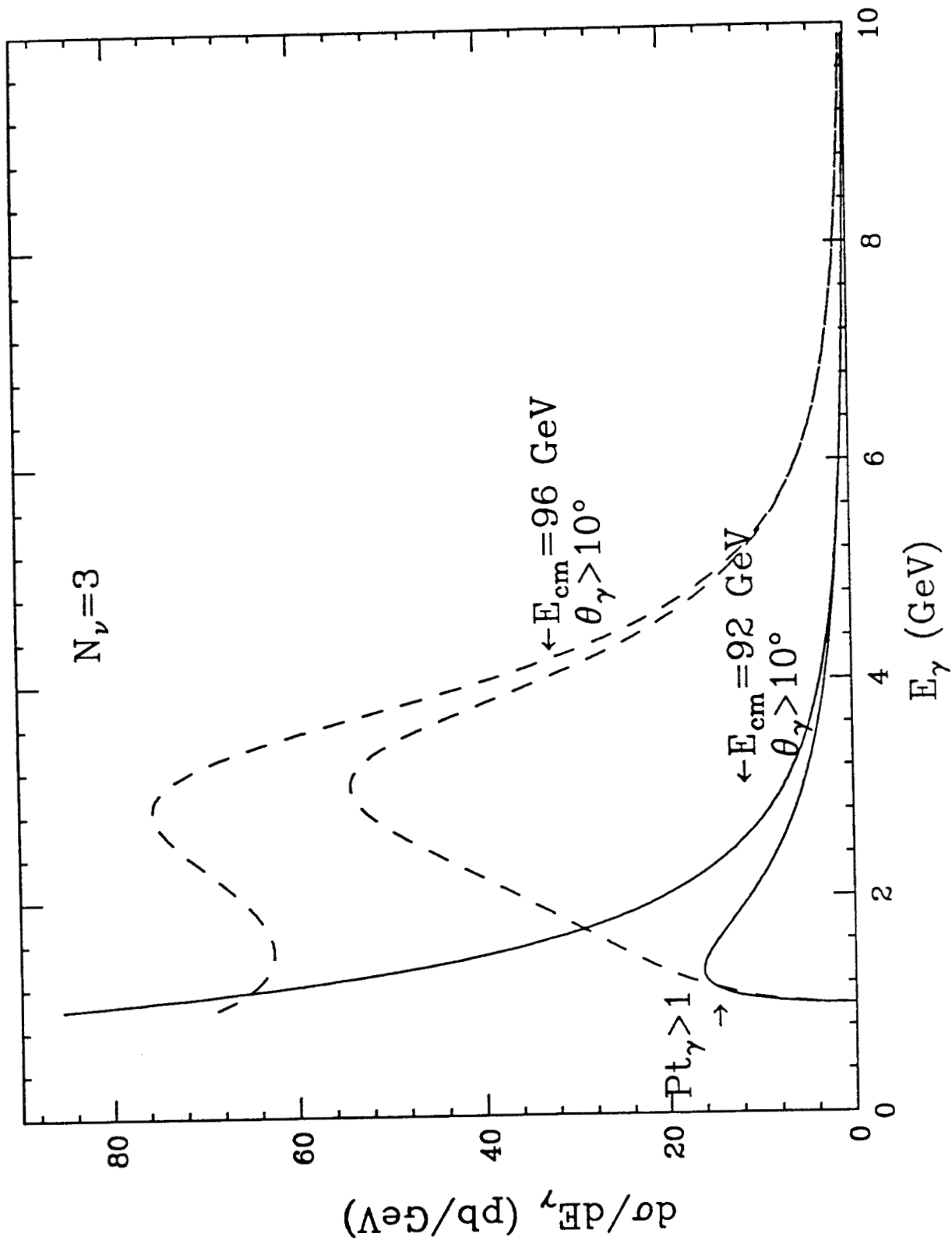


FIG. 9

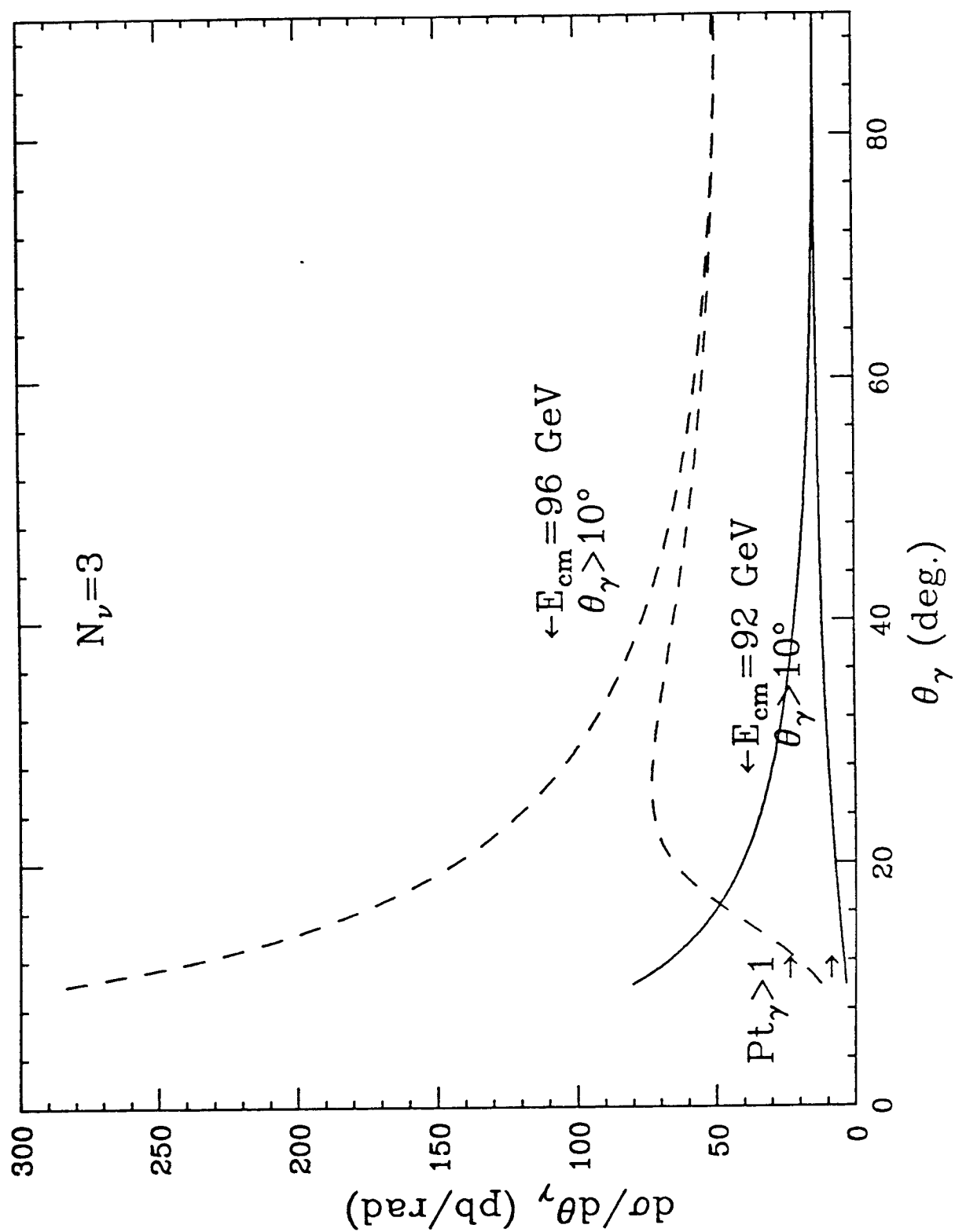


FIG. 10

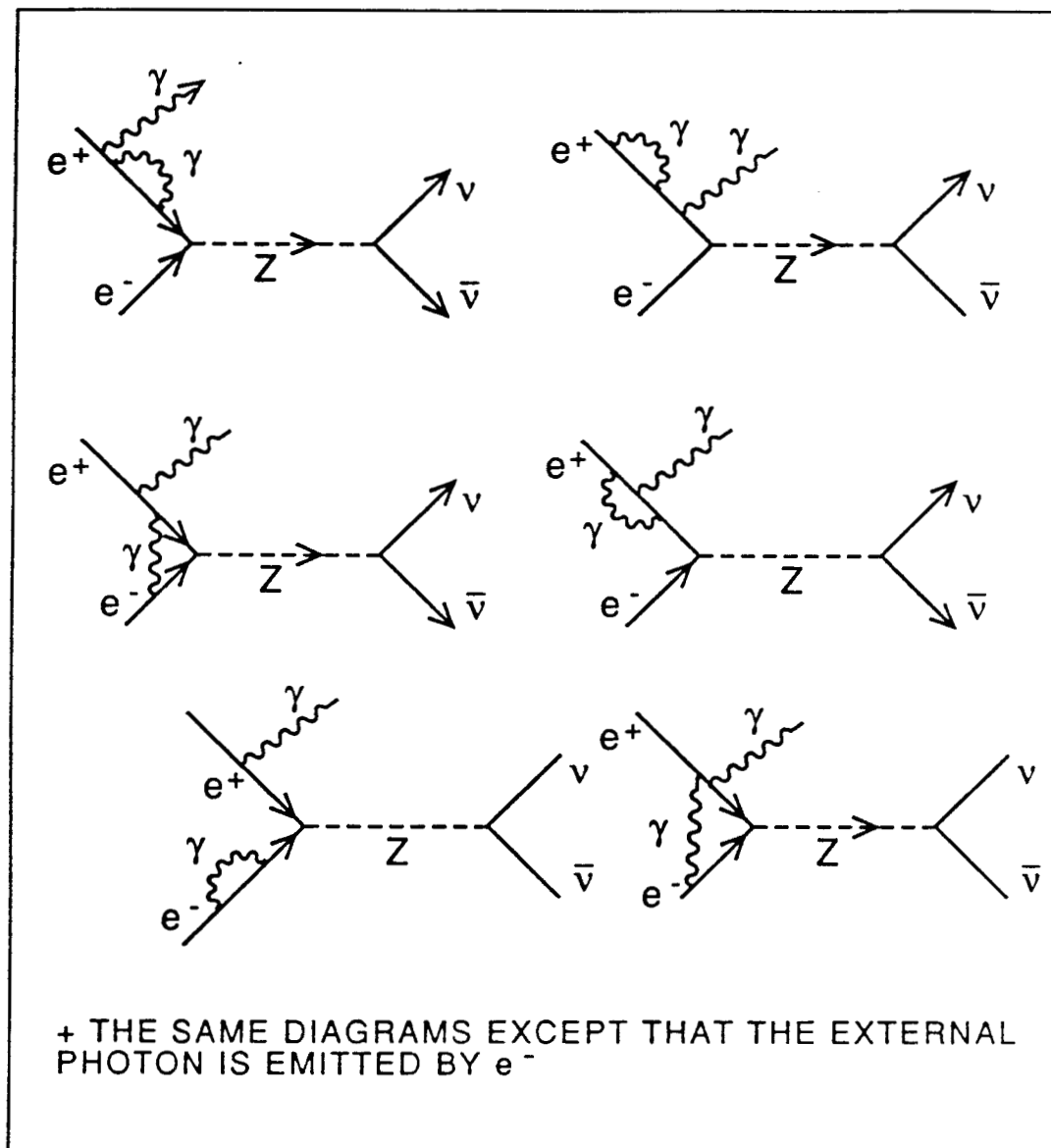


FIG 11

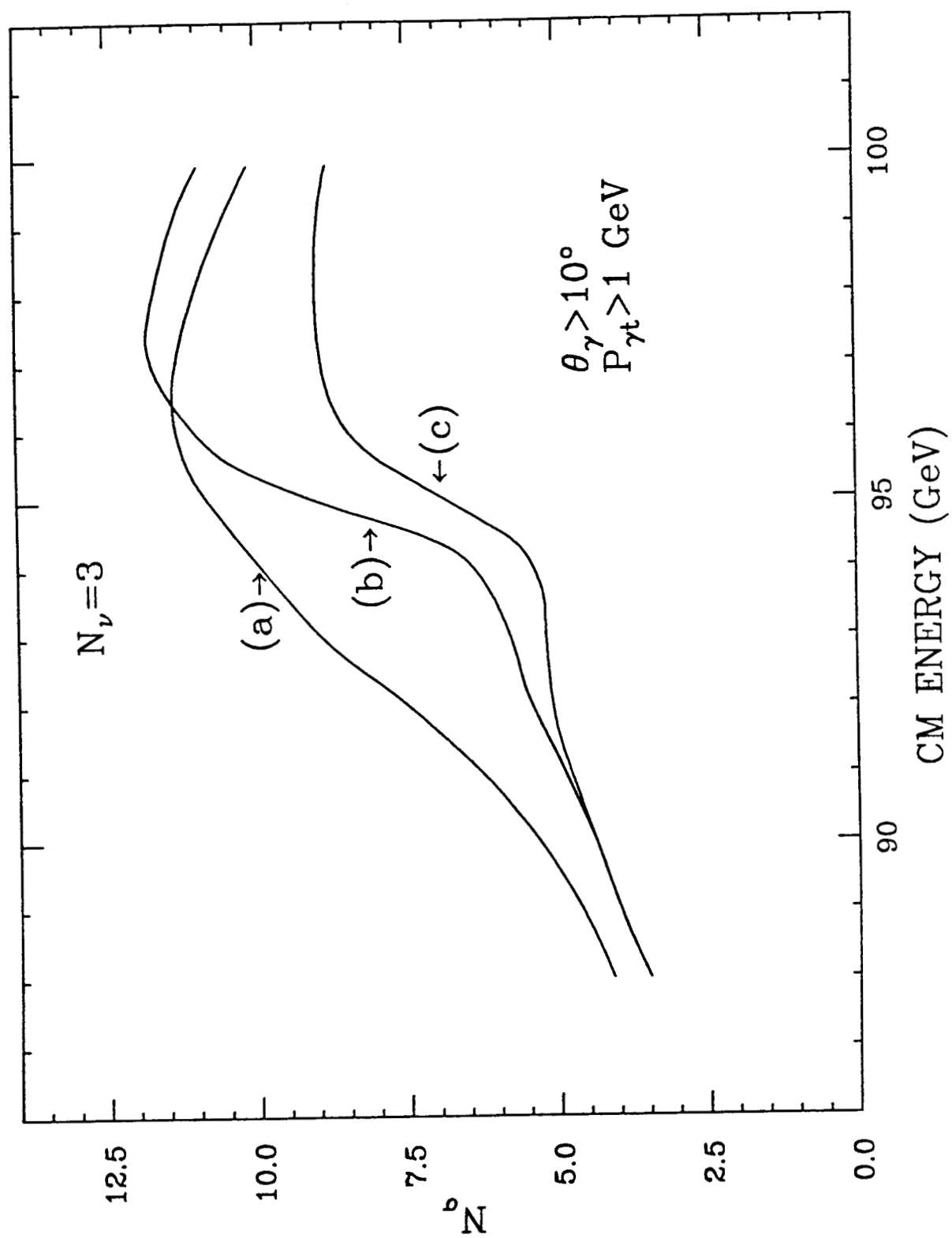


FIG. 12

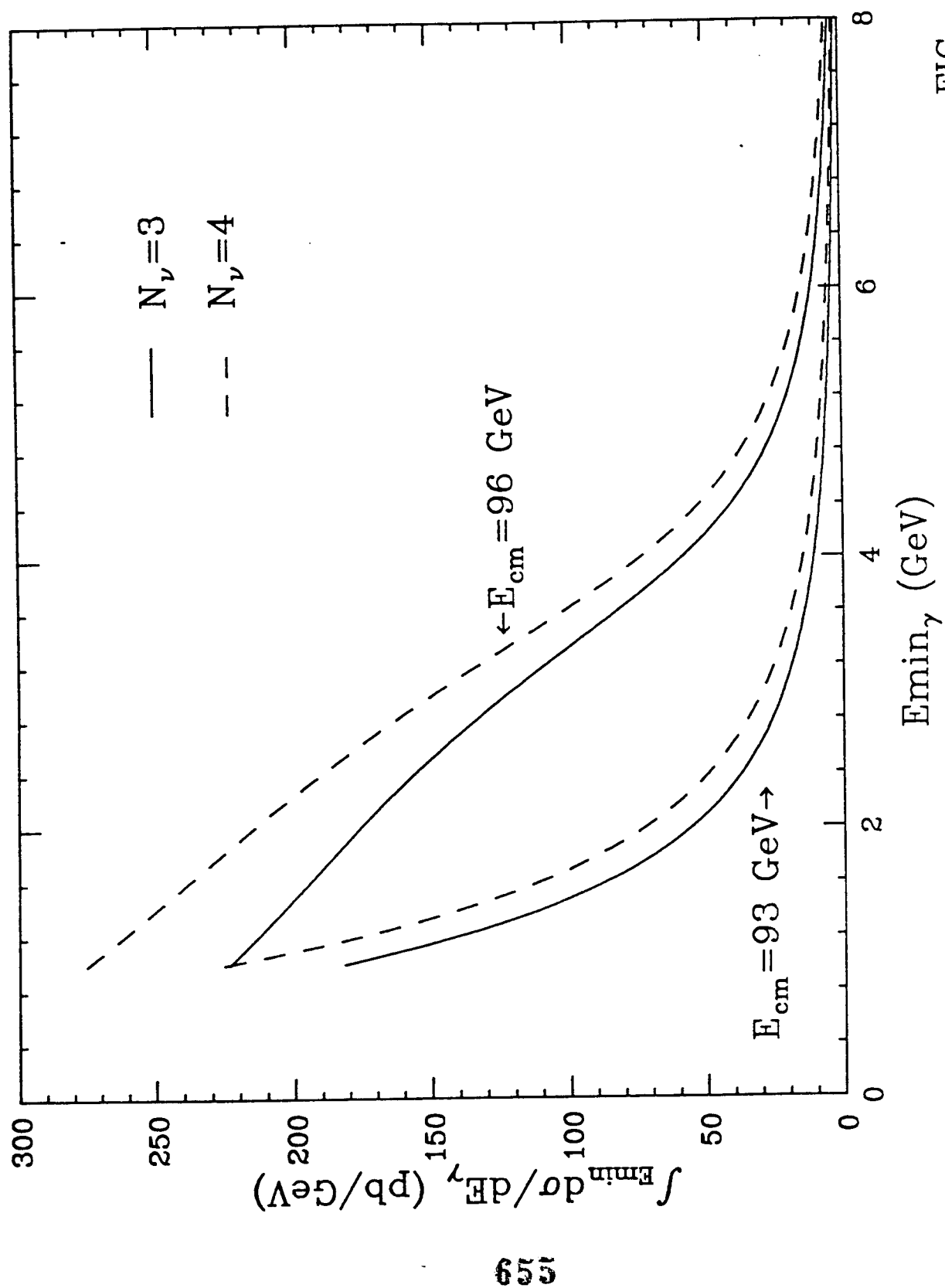


FIG. 13

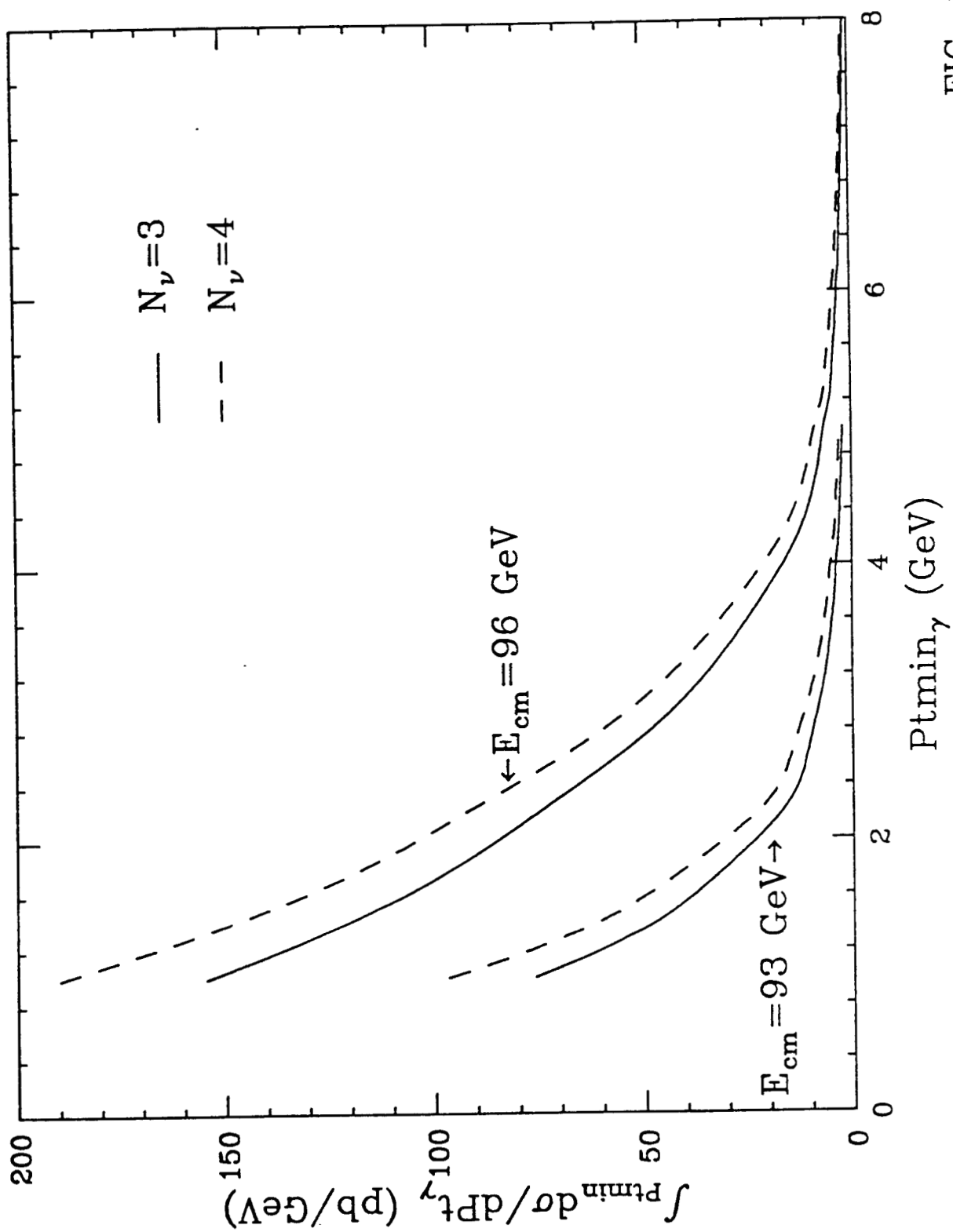


FIG. 14

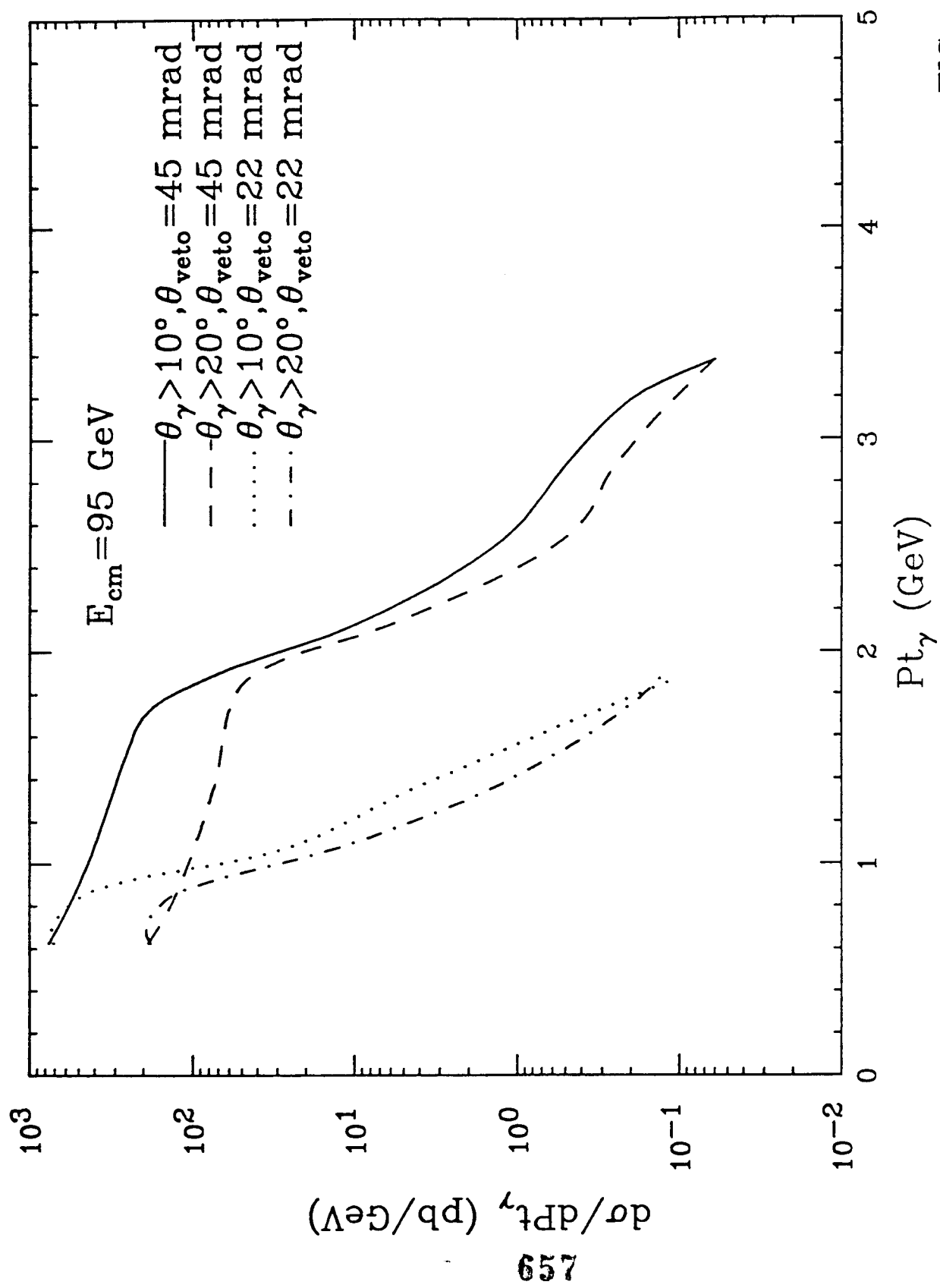


FIG. 15

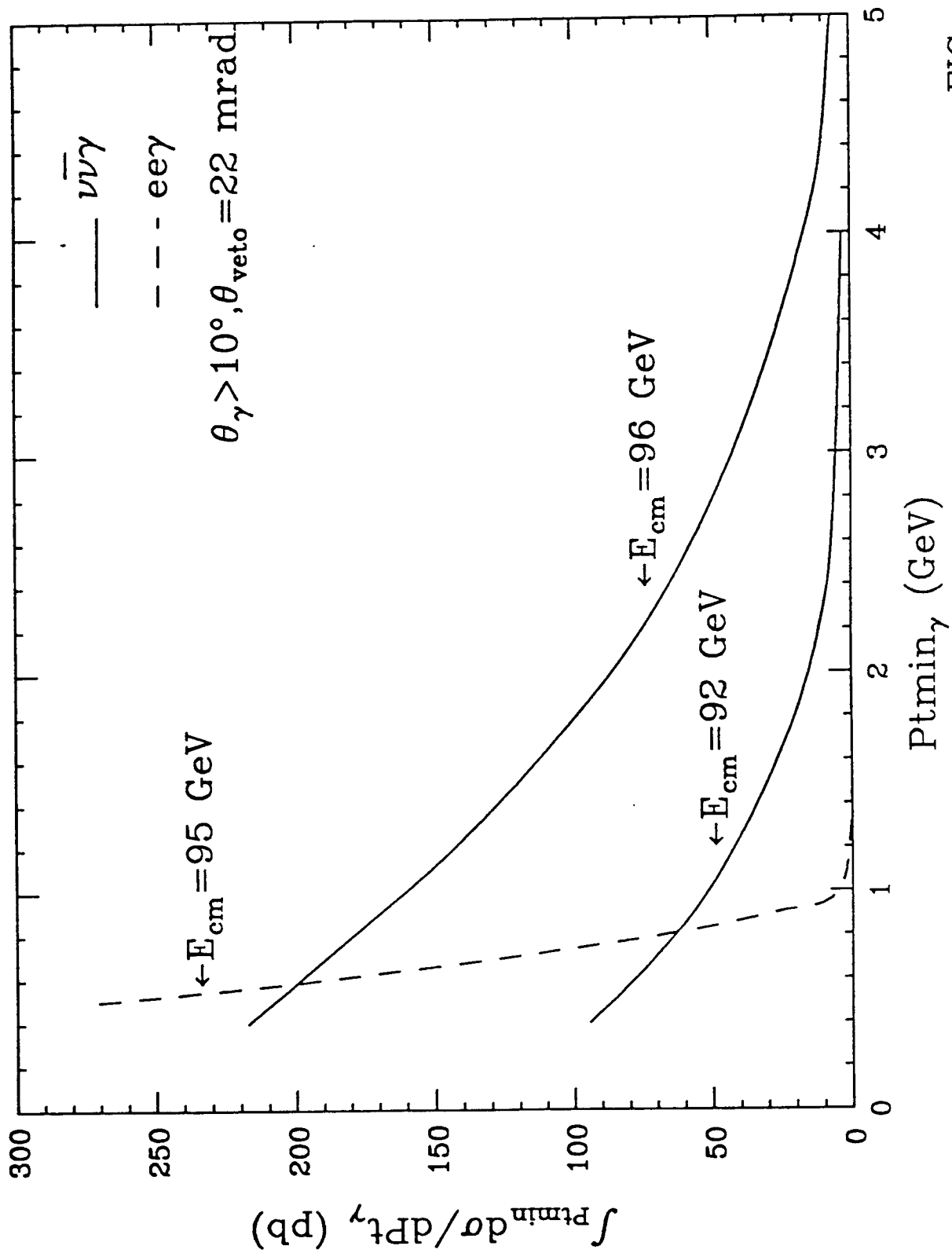


FIG. 16

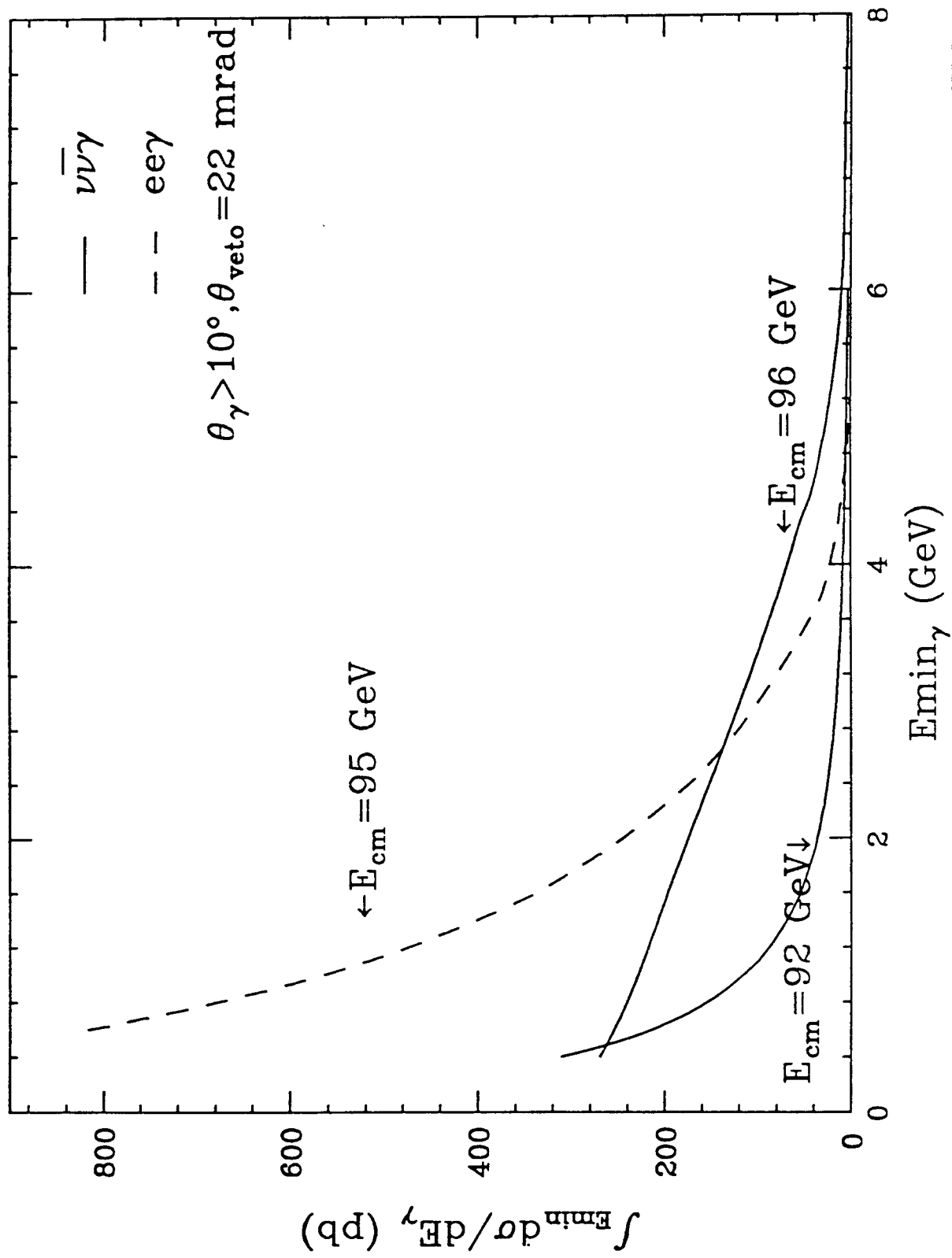


FIG. 17

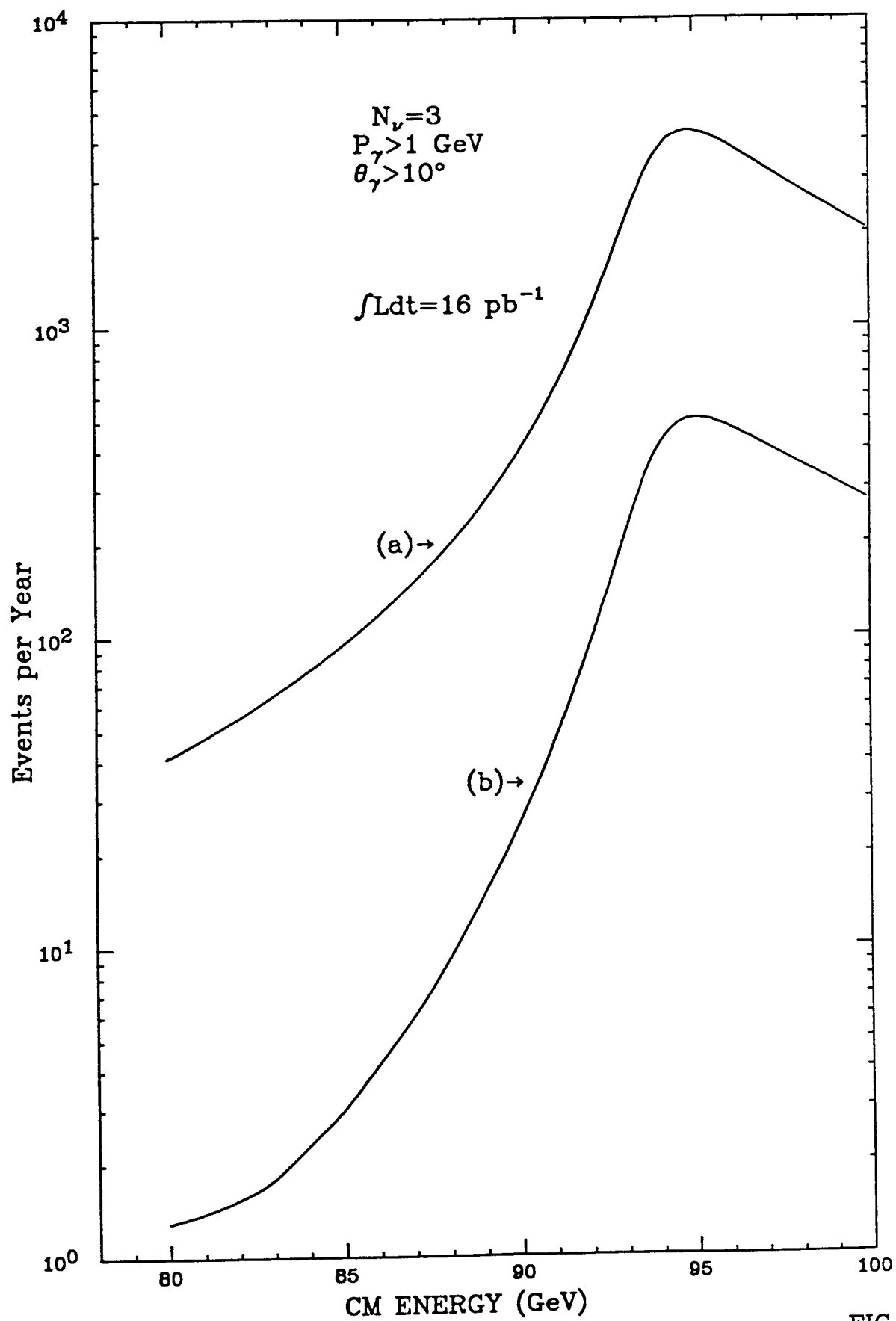


FIG. 18

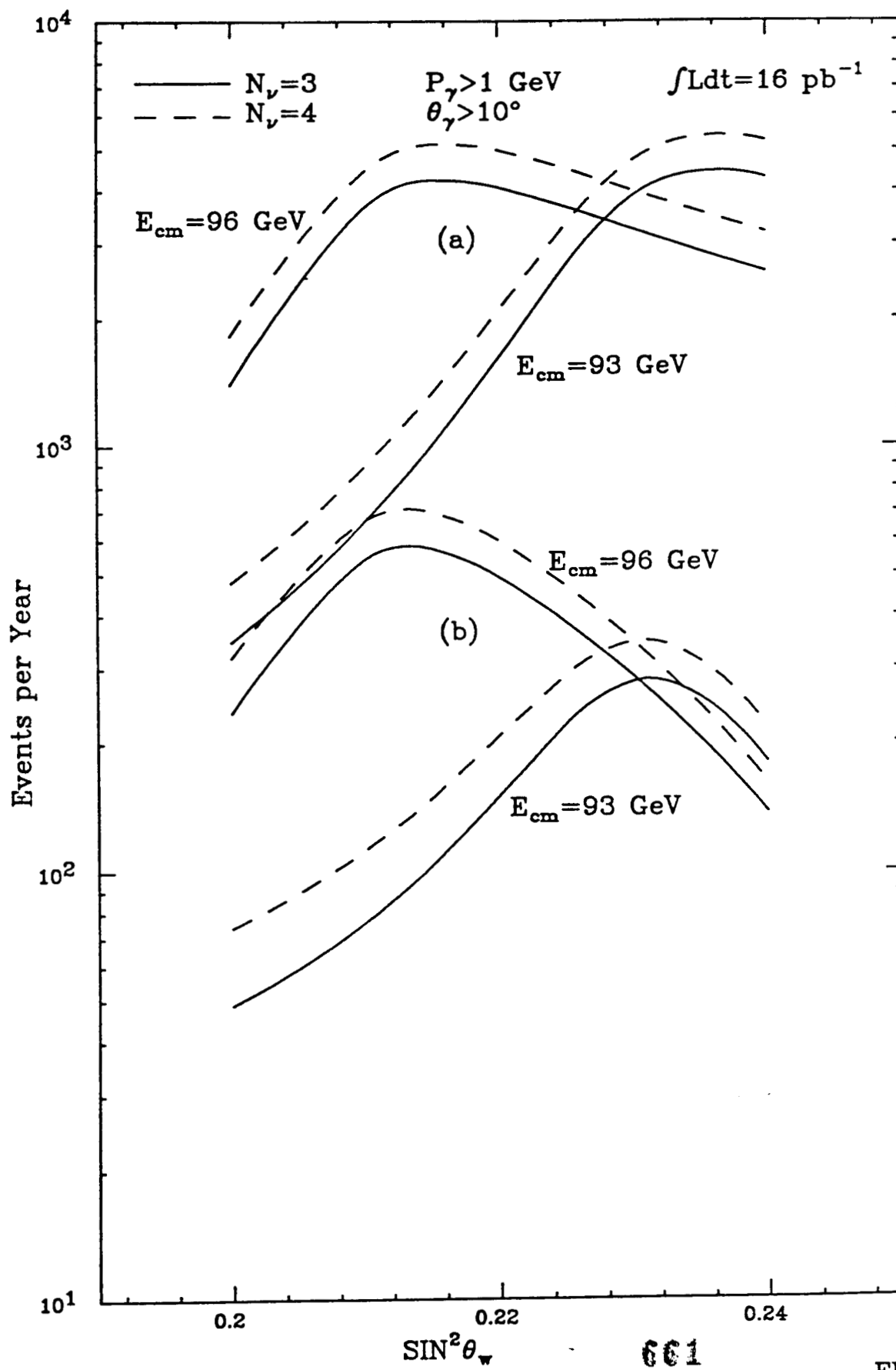
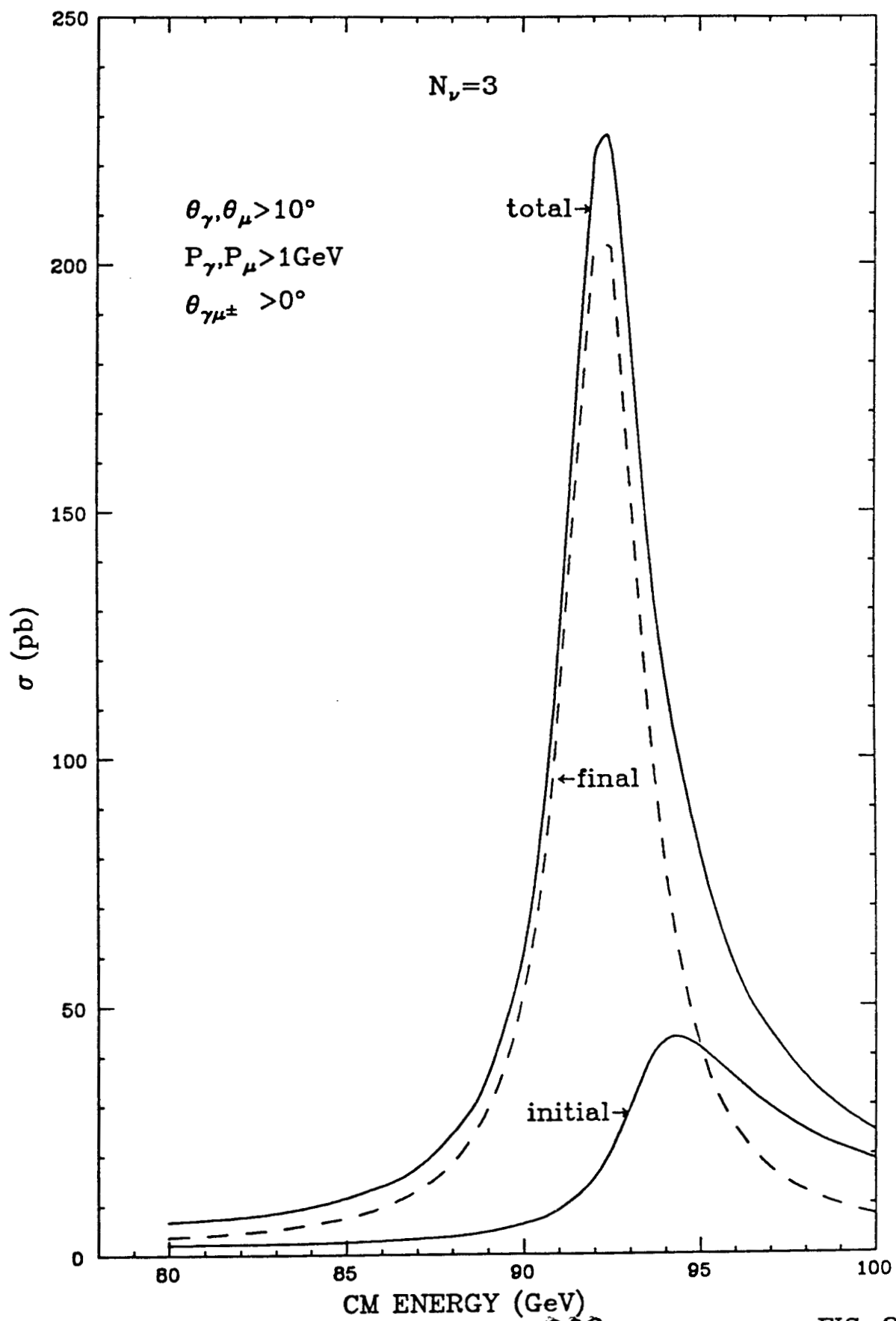
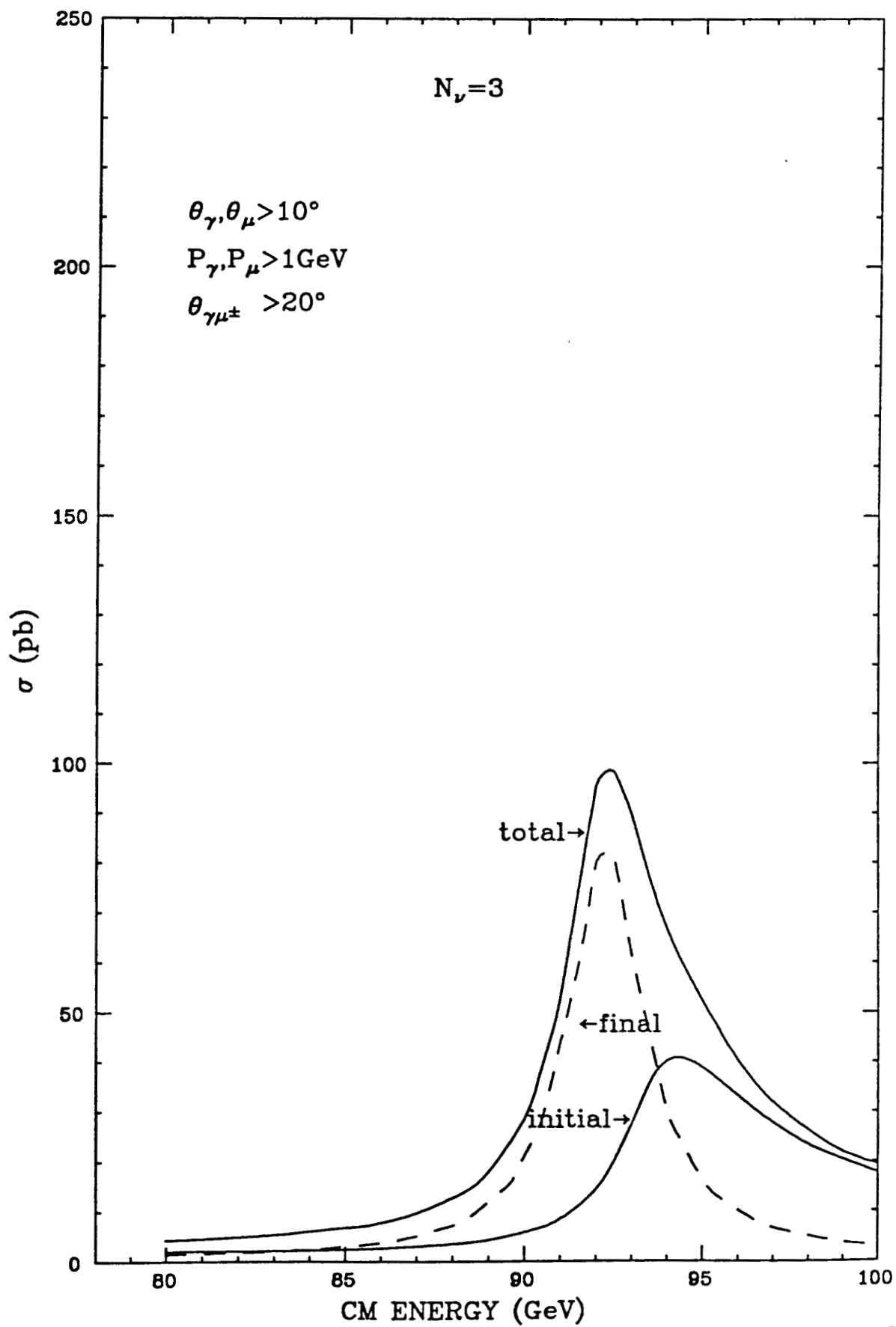


FIG. 19





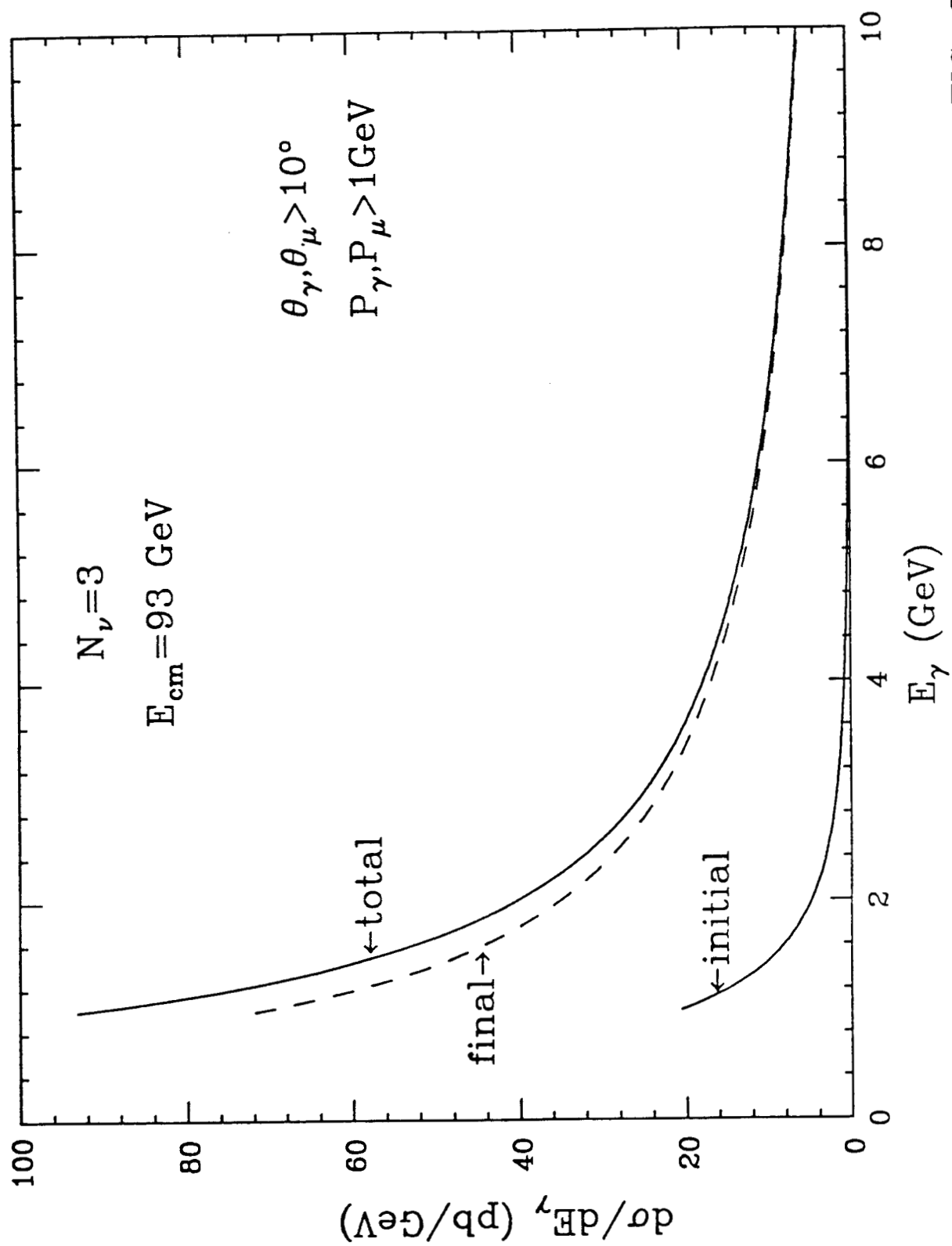


FIG. 22

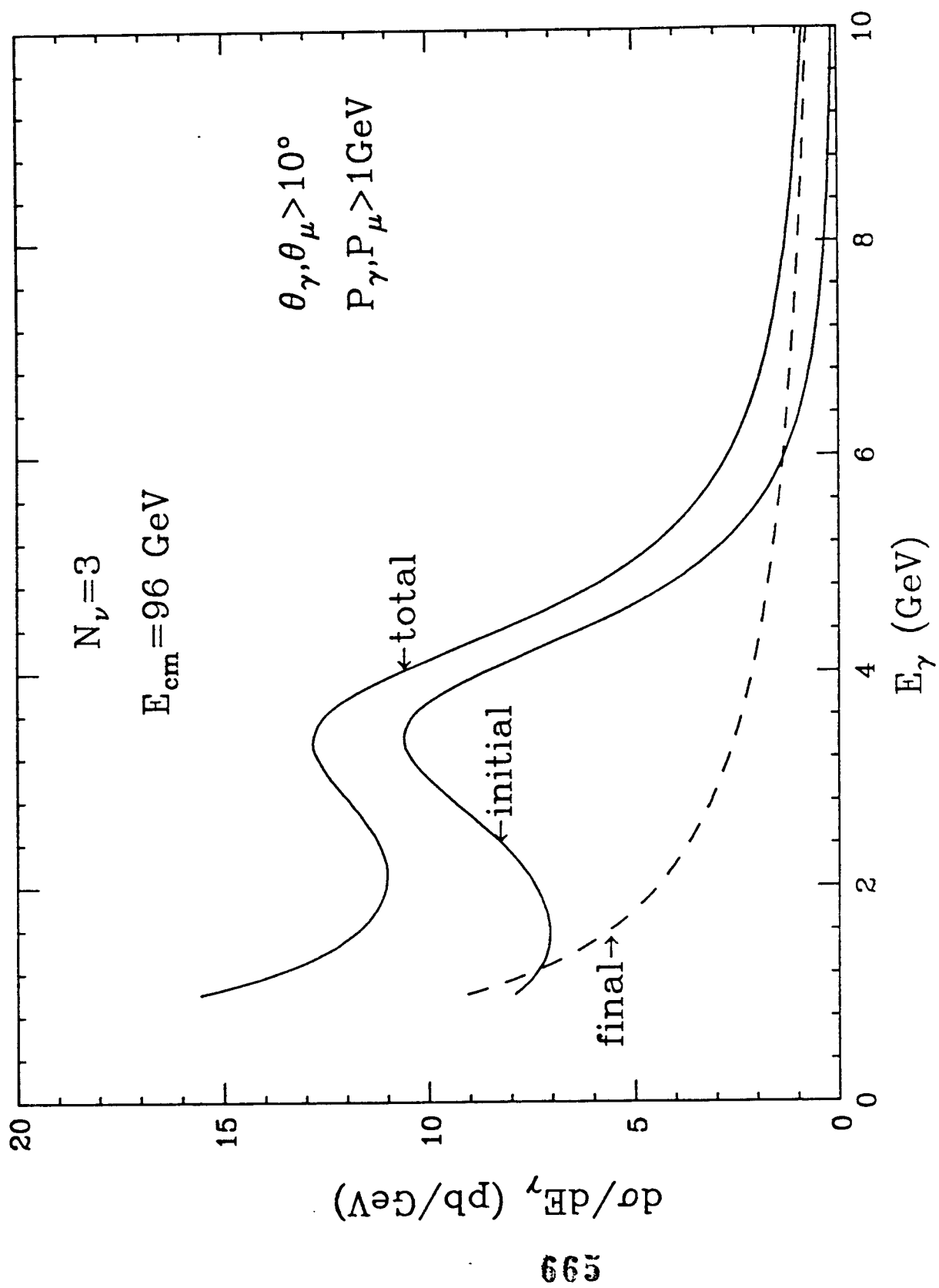


FIG. 23

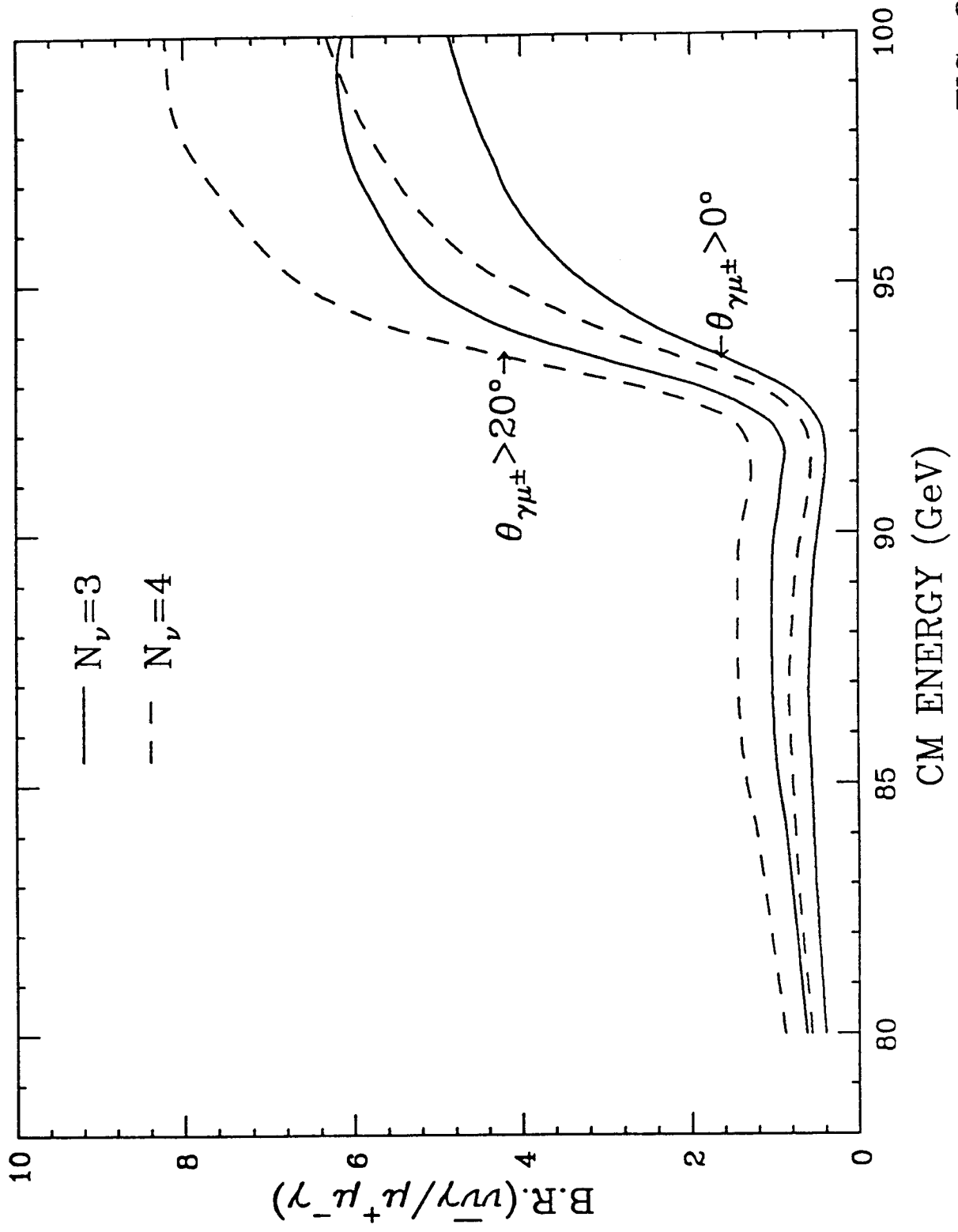


FIG. 24

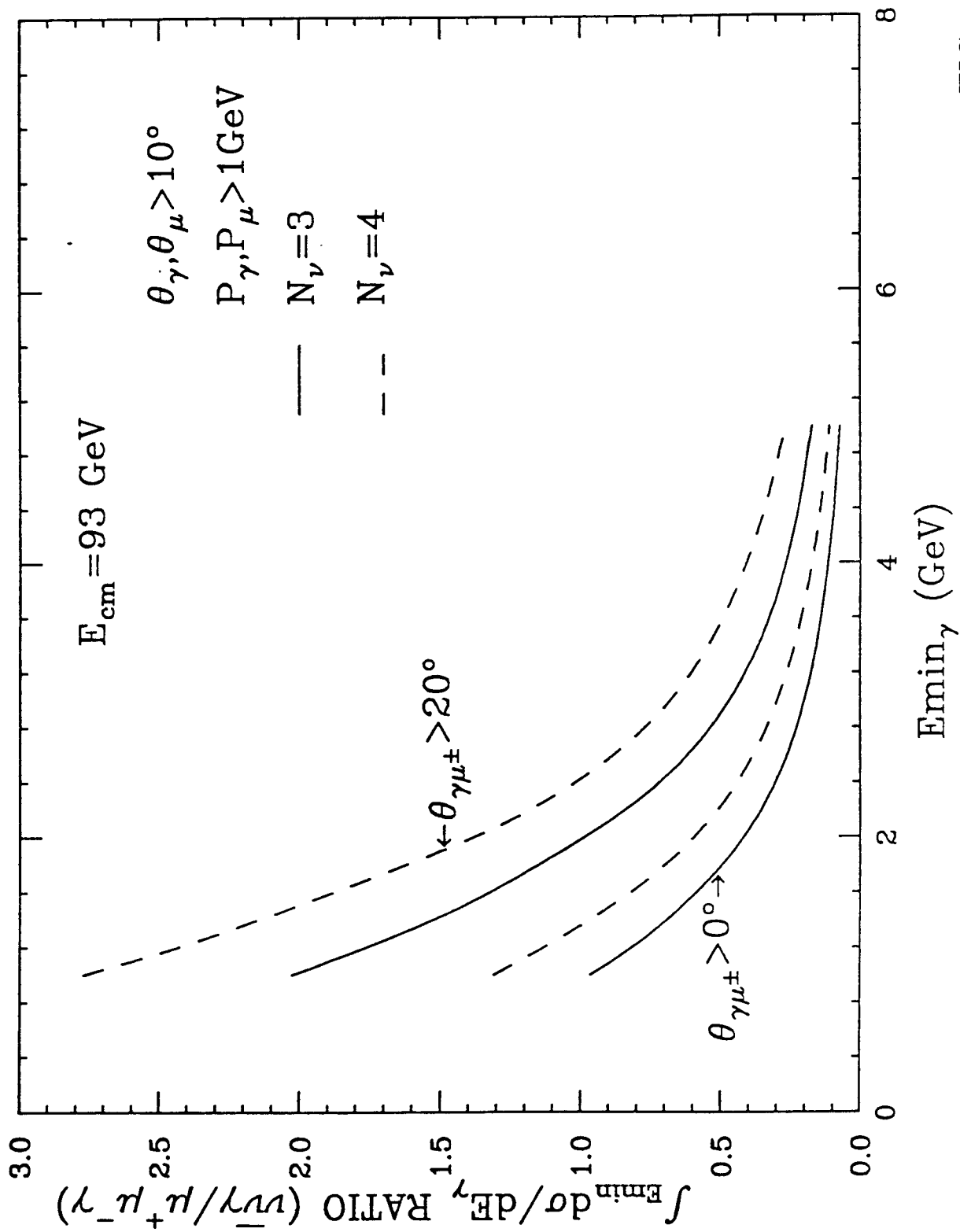


FIG. 25

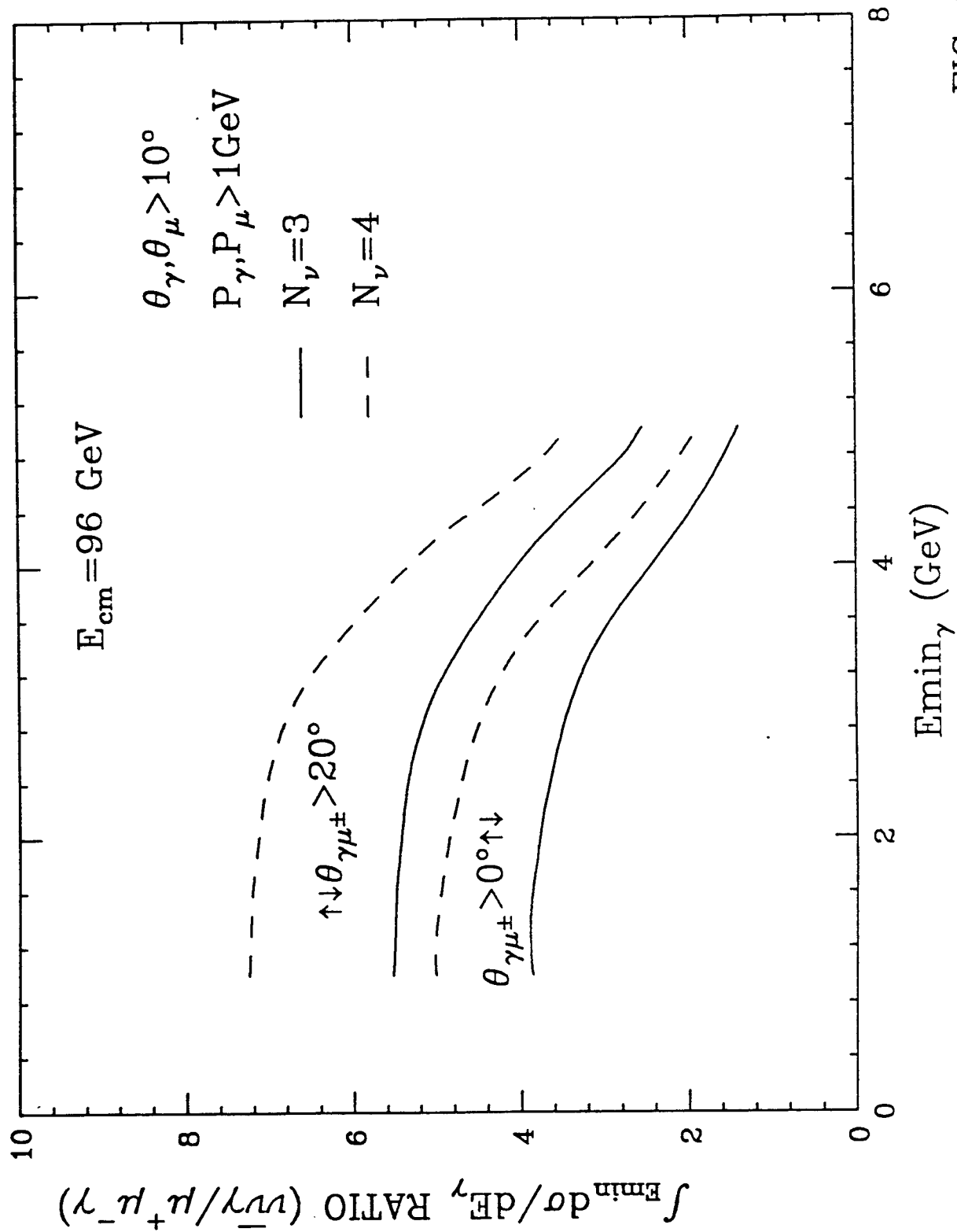


FIG. 26

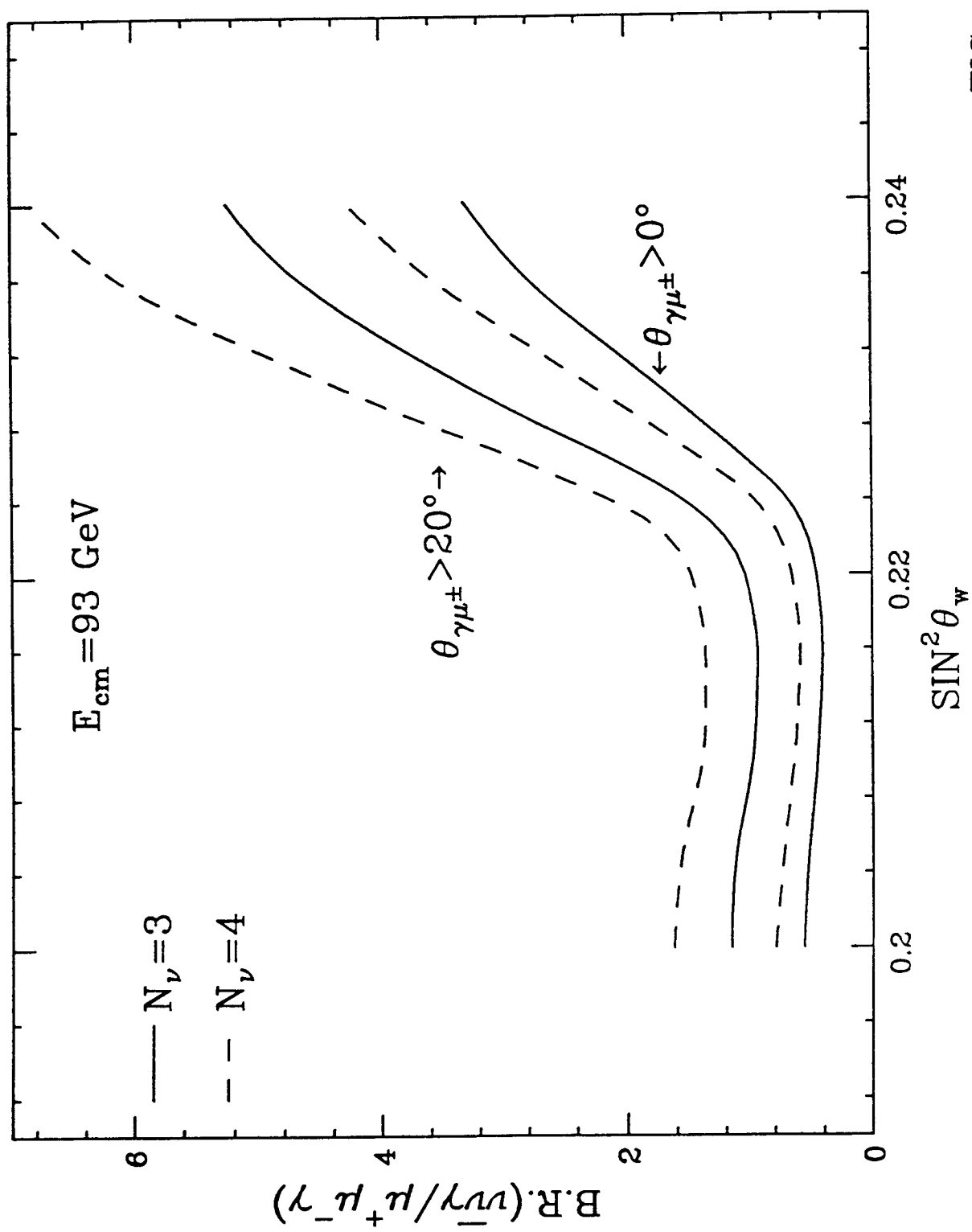


FIG. 27

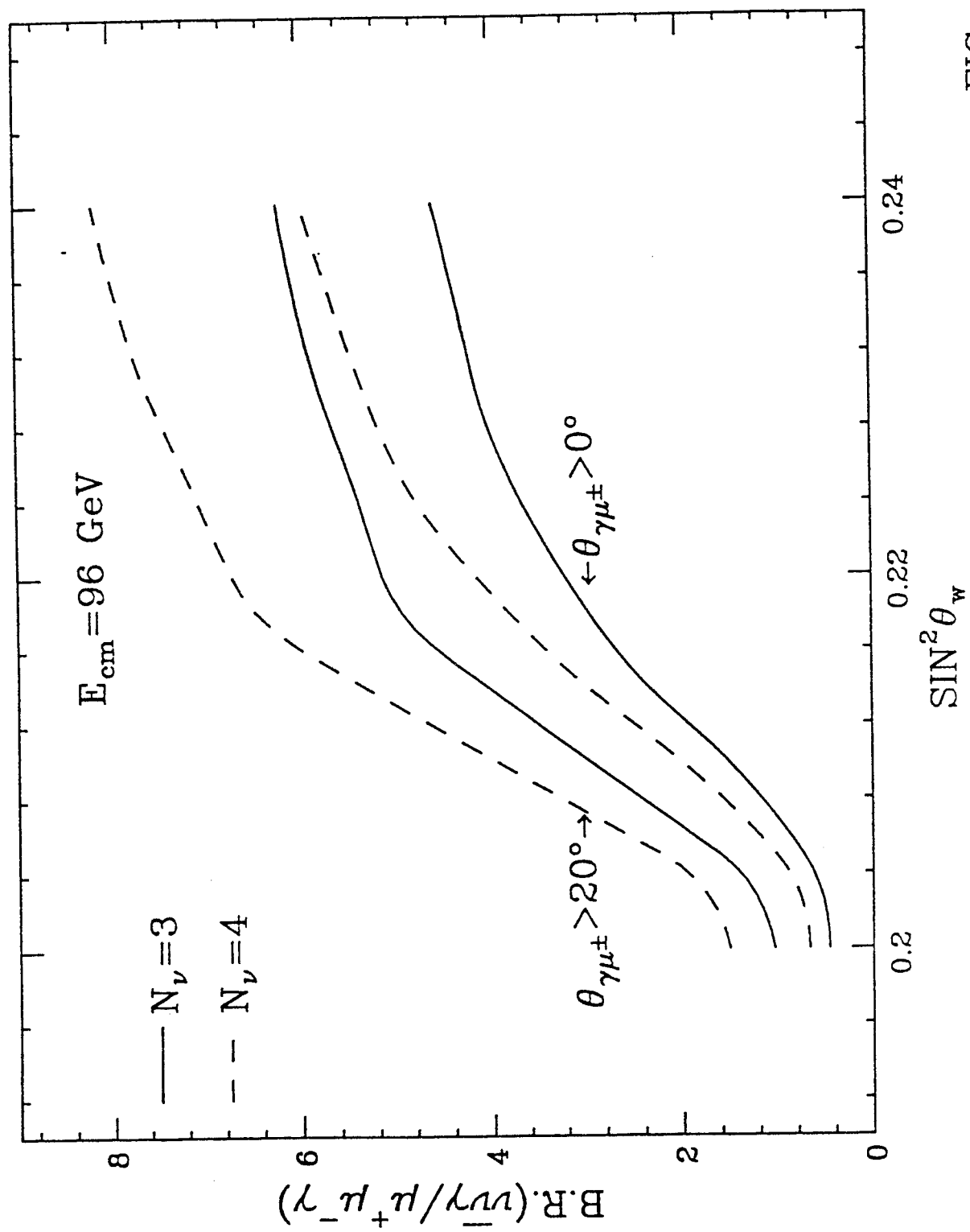
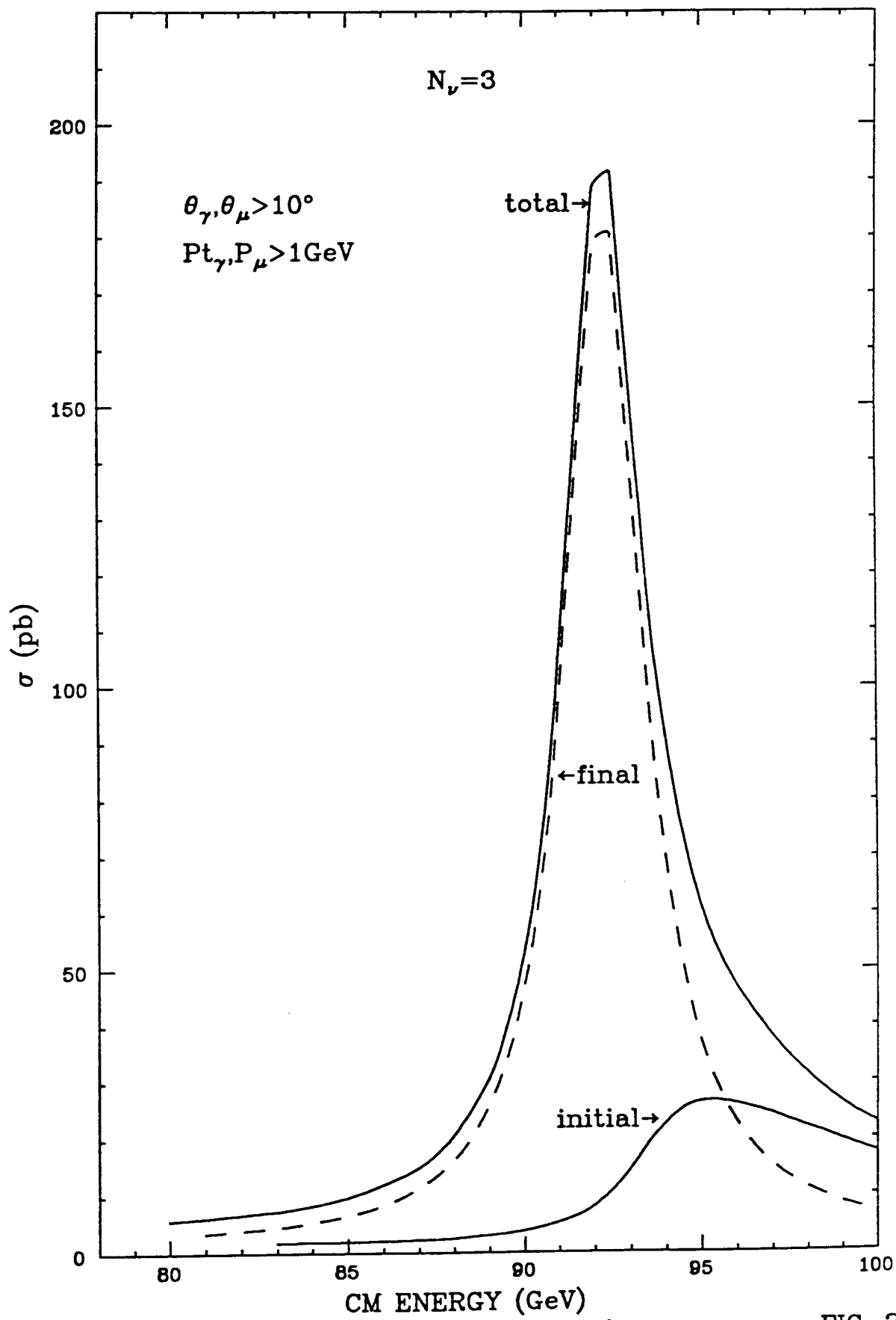


FIG. 28



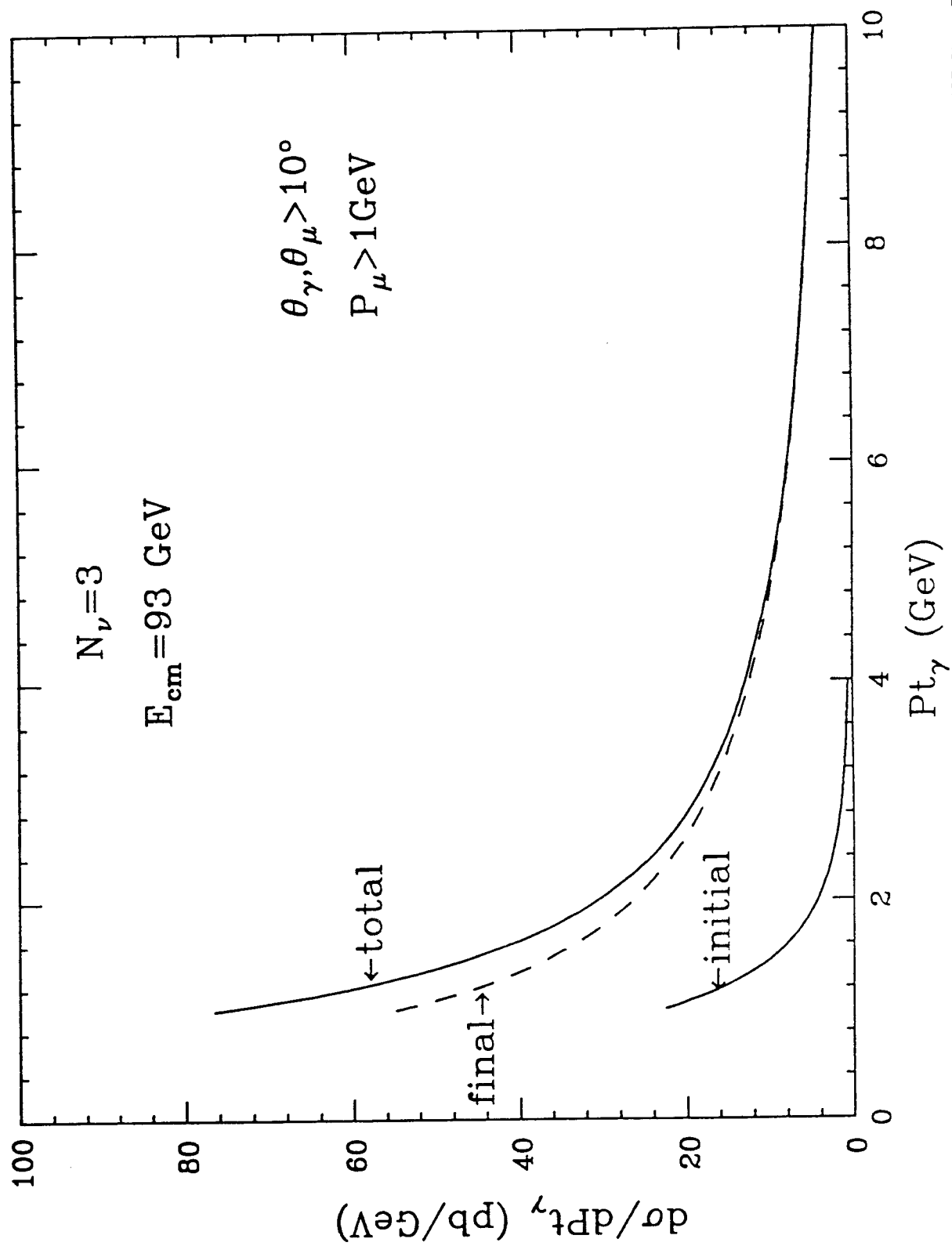


FIG. 30

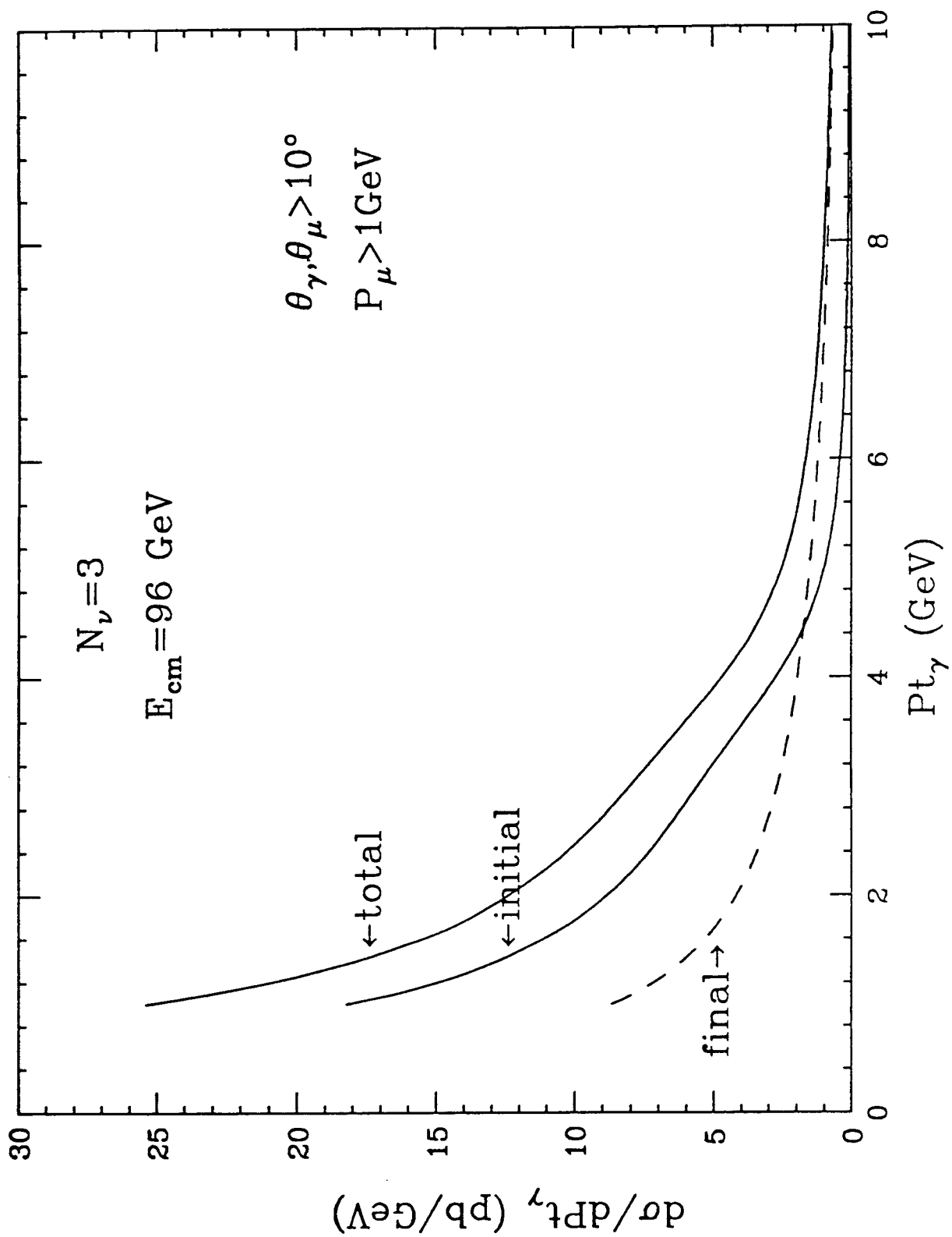


FIG. 31

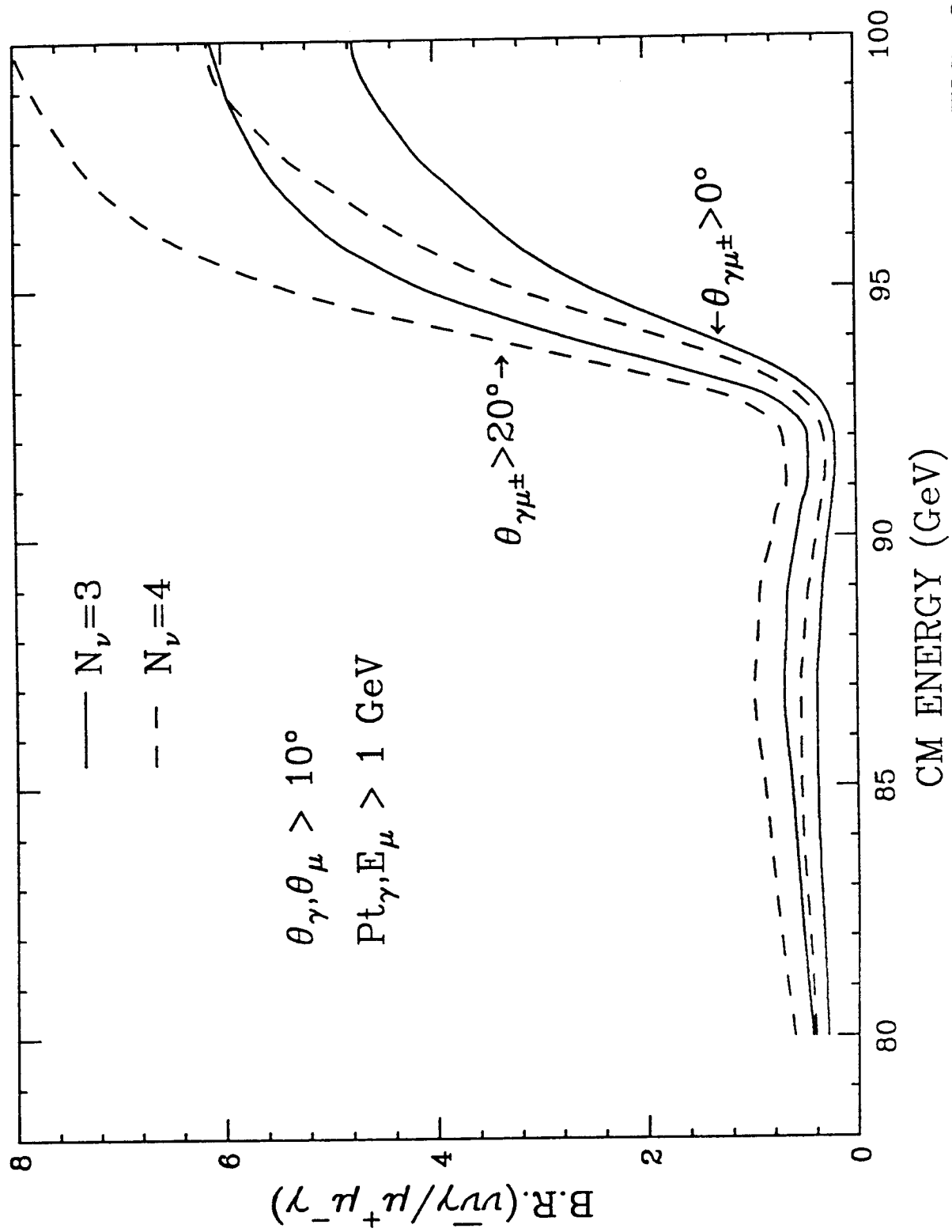


FIG. 32

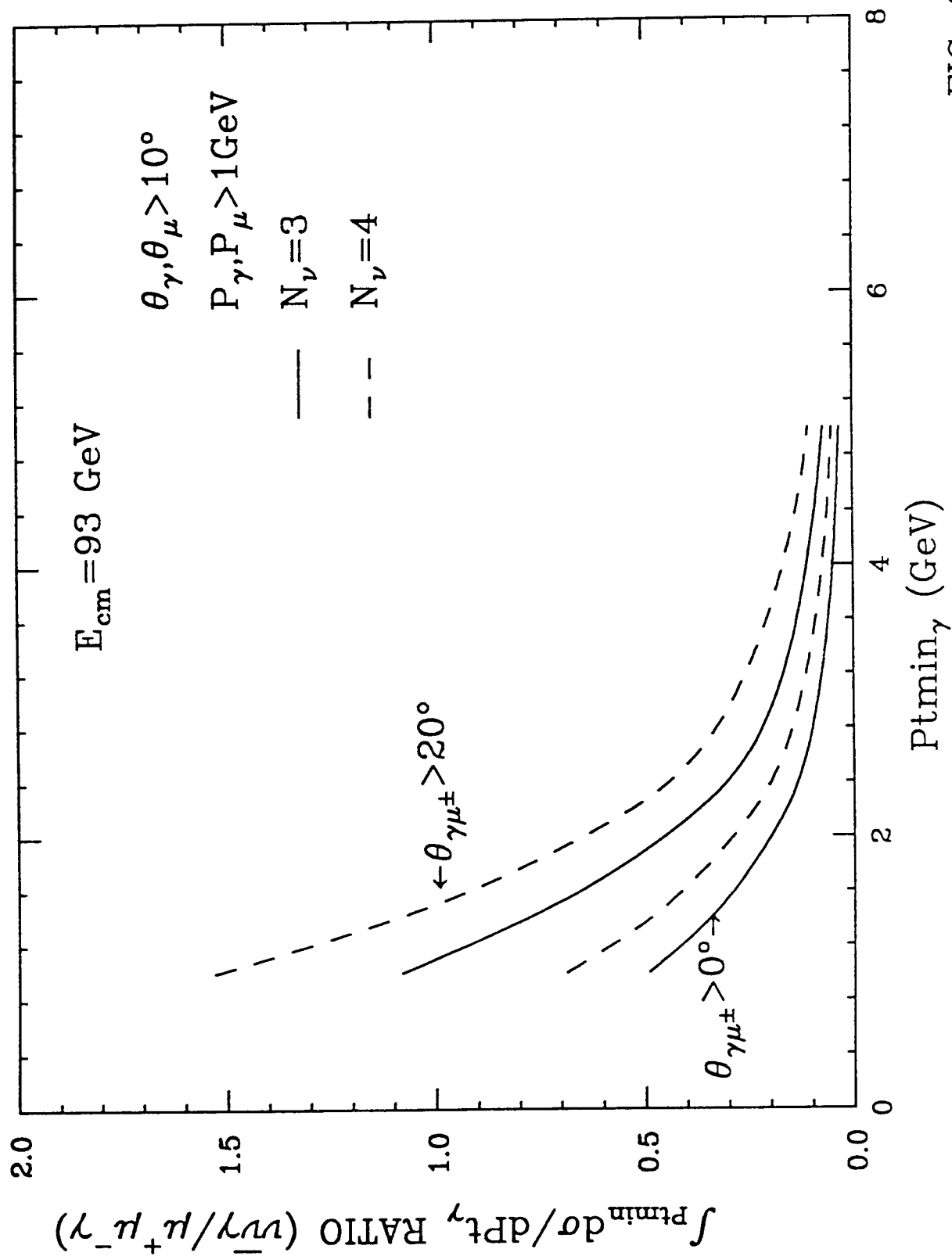


FIG. 33

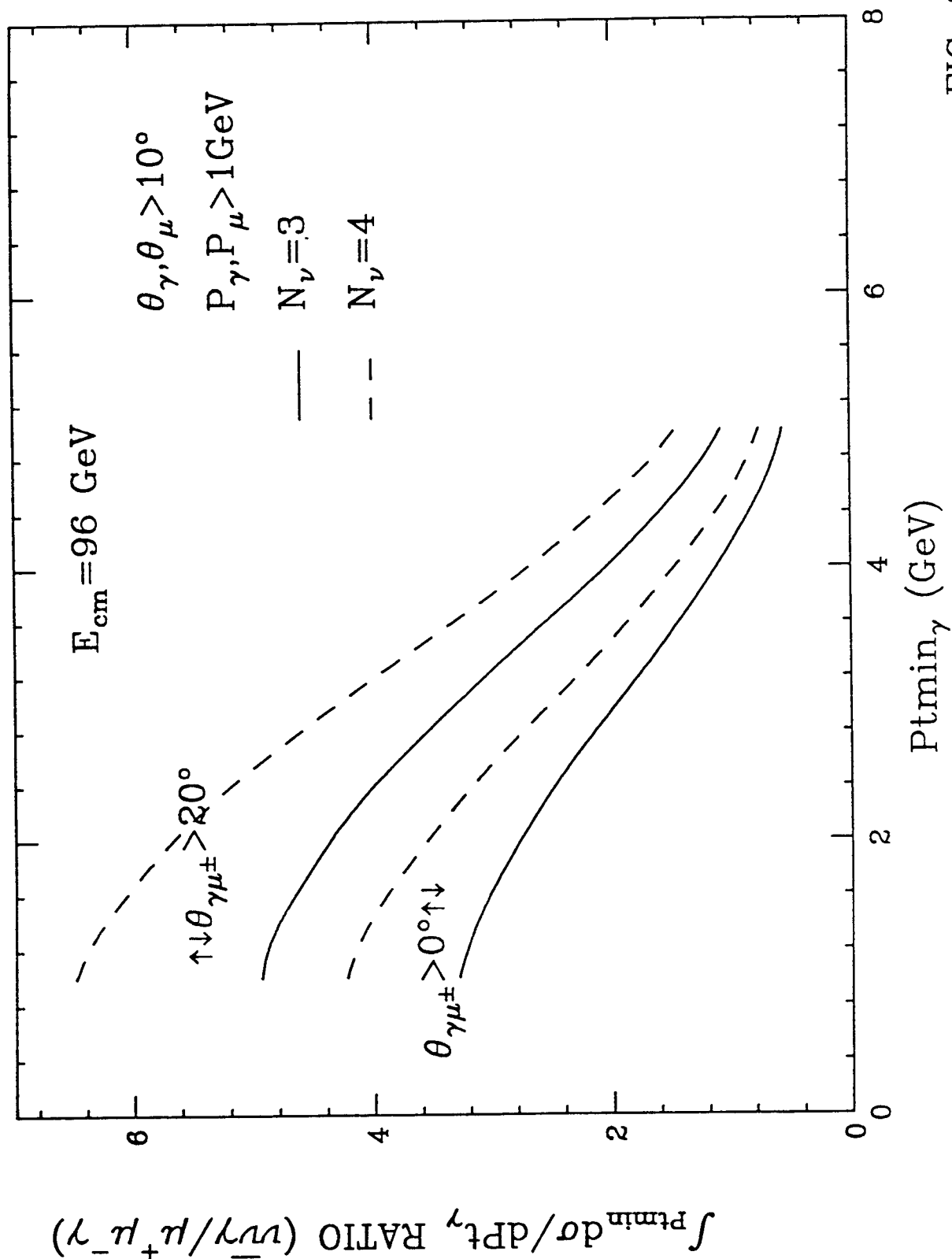


FIG. 34

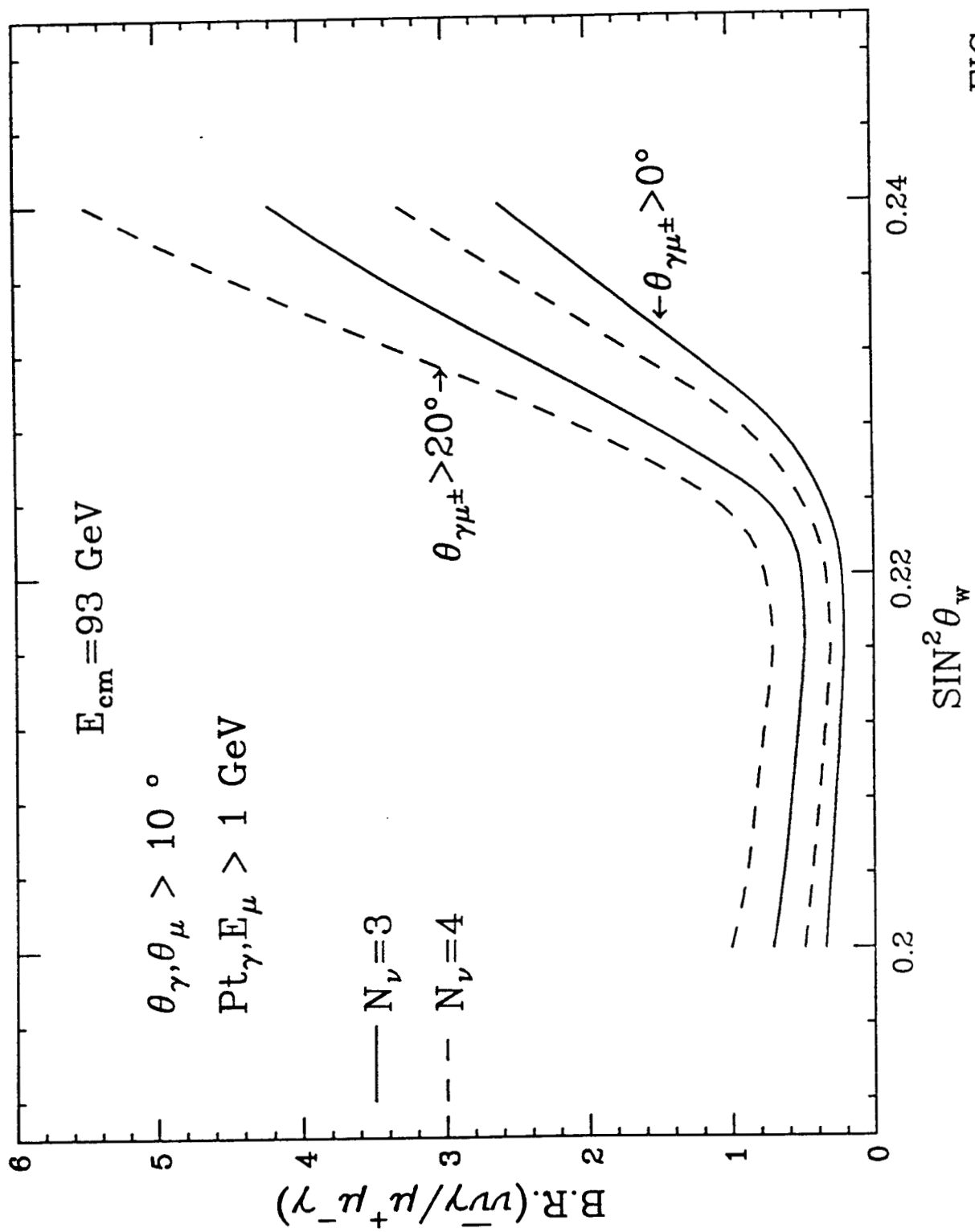


FIG. 35

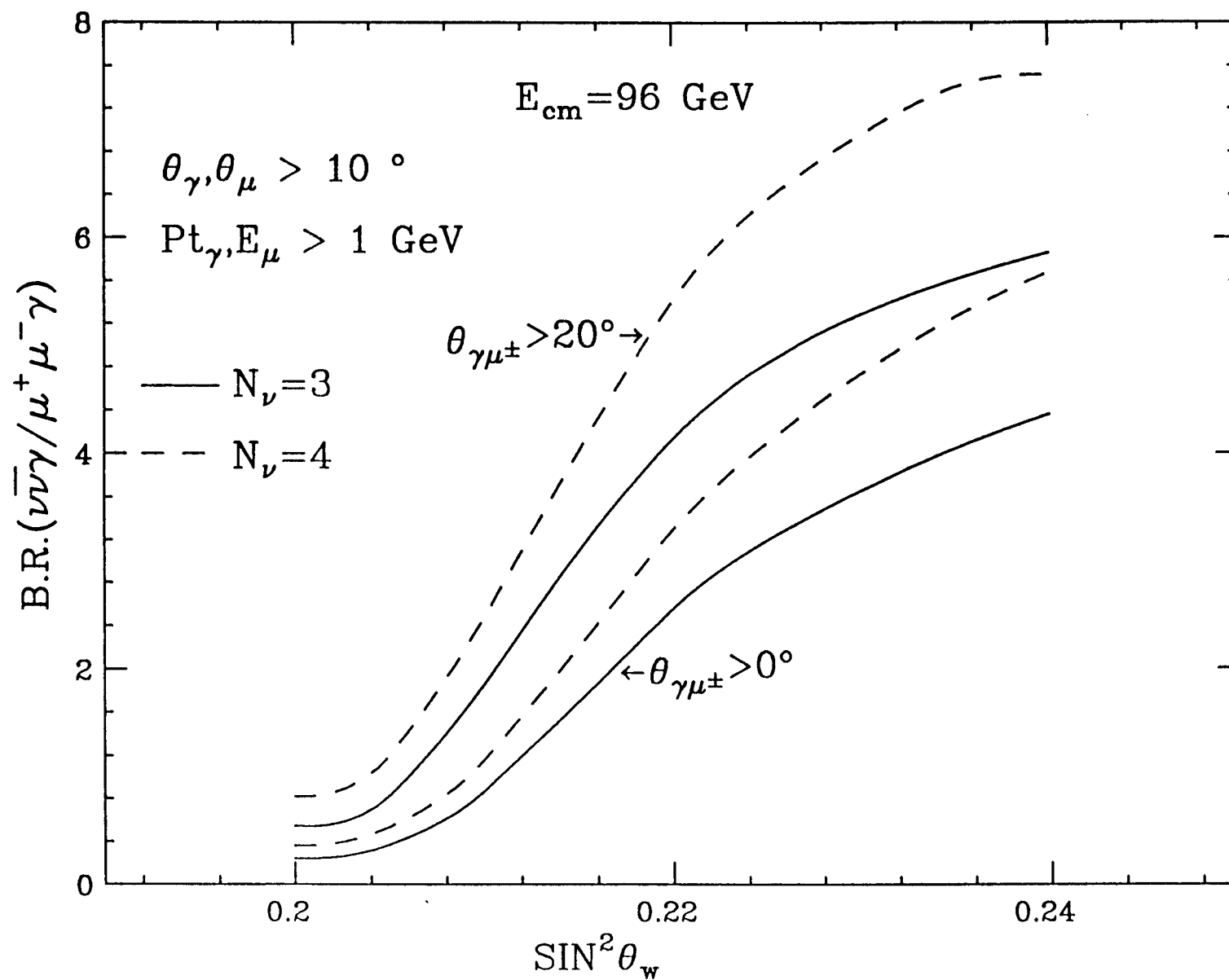


FIG. 36

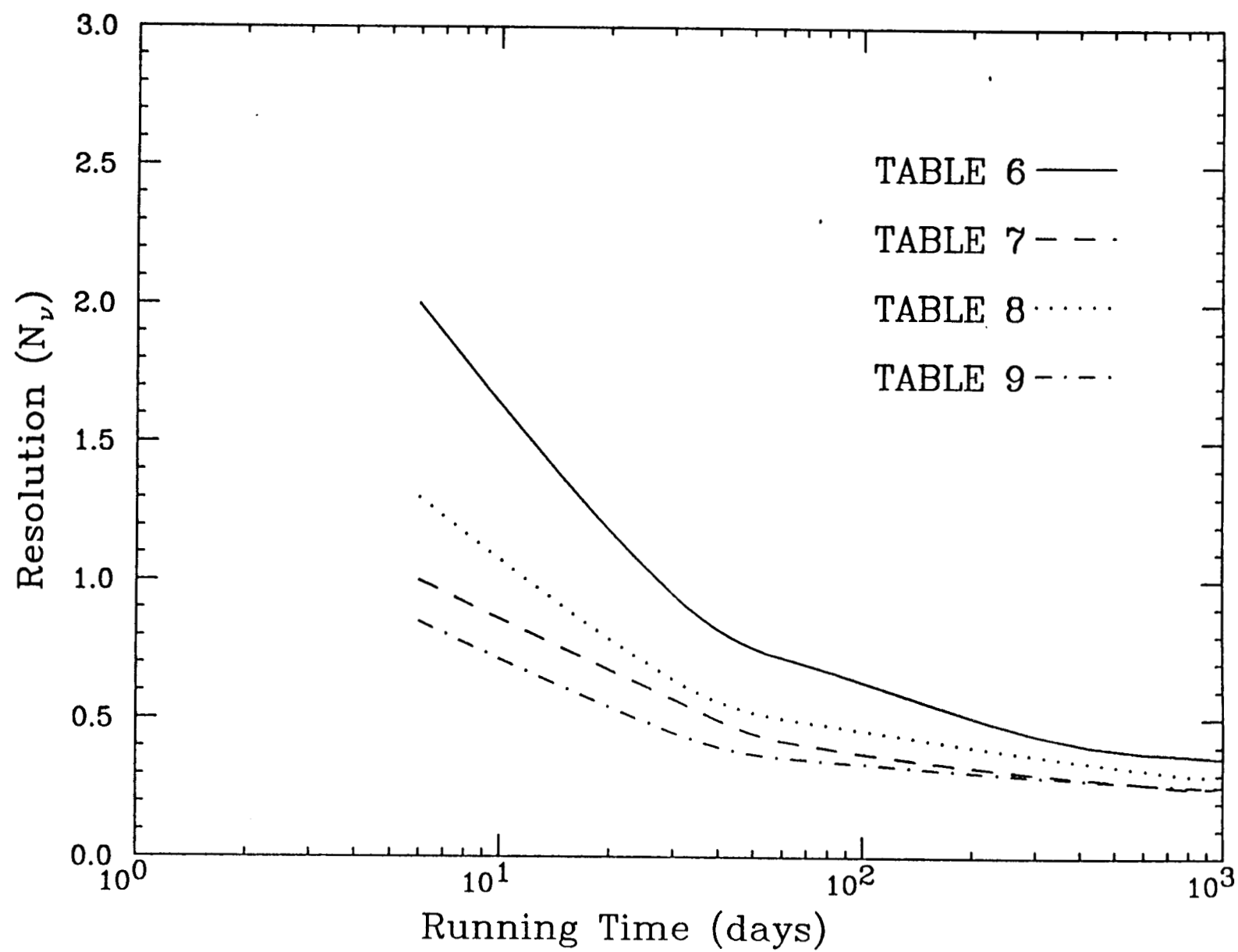


FIG. 37

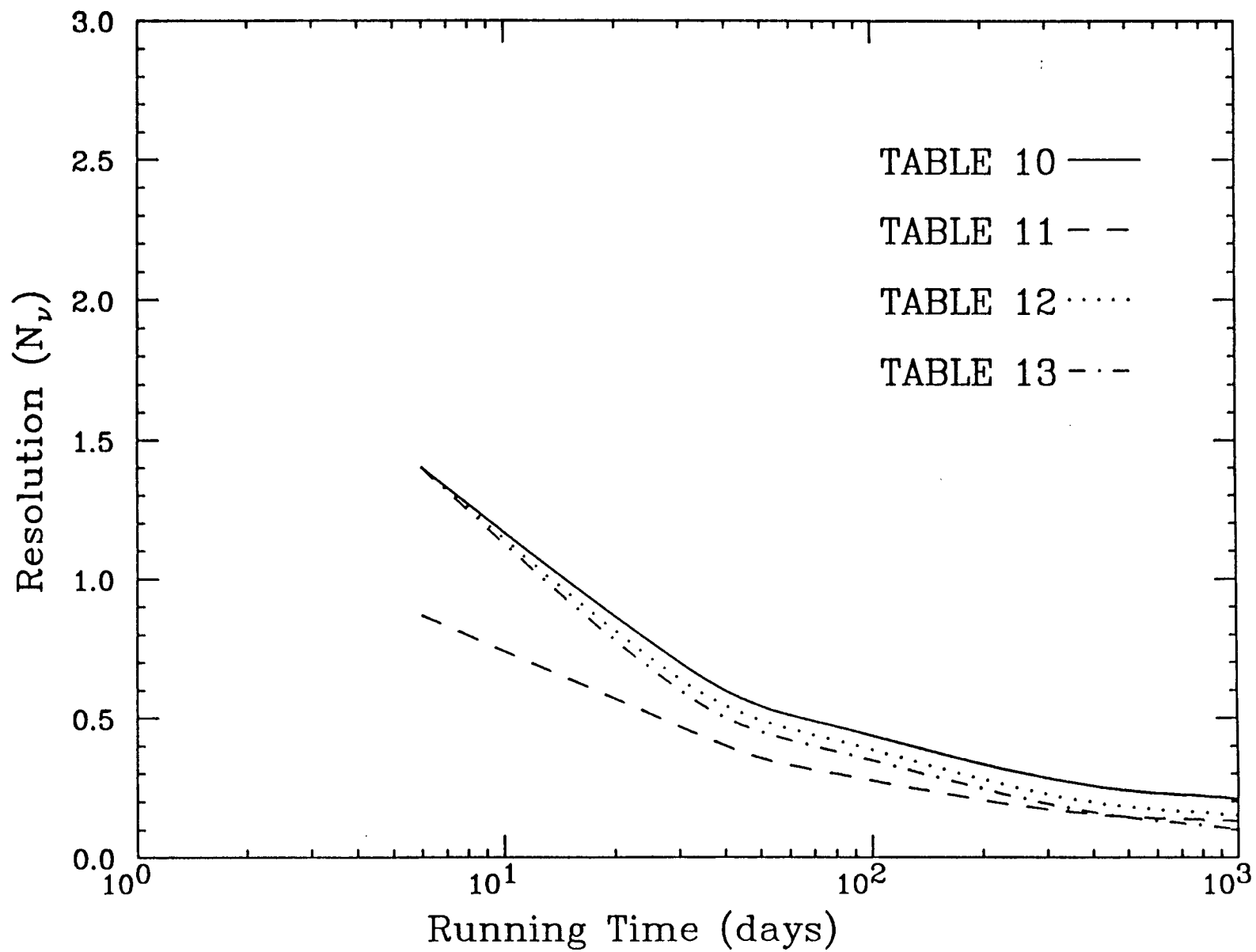


FIG. 38

Agenda for SLD Overview
Monday AM / July 31, 1989

Coffee	Conference Room	8:30 a.m. - 9:00 a.m.
SLD Overview	M. Breidenbach/C. Baltay	9:00 a.m. - 9:45 a.m.
Status of SLC	E. Paterson	9:45 a.m. - 10:45 a.m.
Plans for TLC	E. Paterson	10:45 a.m. - 11:00 a.m.
Coffee		11:00 a.m. - 11:30 a.m.
New Final Focus for SLC	K. Brown	11:30 a.m. - 12:00 p.m.
Polarization at SLC	R. Prepost	12:00 p.m. - 12:30 p.m.

Overview Talks
Monday PM / July 31, 1989

Installation & Commissioning	M. Shaevitz	2:00 p.m. - 2:45 p.m.
Electroweak & QCD Overview	T. Hansl-Kozanecka	2:45 p.m. - 3:30 p.m.
Coffee		3:30 p.m. - 4:00 p.m.
Neutrino Counting Overview	U. Nauenberg	4:00 p.m. - 4:45 p.m.
<i>B</i> Spectroscopy	M. Witherell	4:45 p.m. - 5:30 p.m.

Overview Talks
Tuesday AM / August 1, 1989

Coffee	Conference Room	8:30 a.m. - 9:00 a.m.
Higgs Search Overview	P. Mockett	9:00 a.m. - 9:45 a.m.
Technicolor Search Overview	U. Nauenberg	9:45 a.m. - 10:30 a.m.
Coffee		10:30 a.m. - 11:00 a.m.
Supersymmetry Search Overview	S. Whitaker	11:00 a.m. - 11:45 a.m.
Overview of Search for New Quarks & Leptons	P. Rowson	11:45 a.m. - 12:30 p.m.

Software Discussions
Tuesday Eve / August 1, 1989

General Philosophy of SLD Software	T. Schalk	8:00 p.m. - 8:30 p.m.
Discussion		8:30 p.m. - ?

SLD Physics Topics
Wednesday AM / August 2, 1989
(T. Hansl-Kozanecka)

Coffee	Conference Room	8:30 a.m. - 9:00 a.m.
Asymmetries in $\mu^+\mu^-$	J. Yamartino	9:00 a.m. - 9:20 a.m.
τ Physics at the Z^0	U. Schneekloth	9:20 a.m. - 9:40 a.m.
Comments on the Z^0 Width Measurement	R. Battiston	9:40 a.m. - 9:50 a.m.
Large Angle Bhabha Scattering	M. Pauluzzi	9:50 a.m. - 10:10 a.m.
Coffee		10:15 a.m. - 10:45 a.m.
Tagging B and C Quarks	D. Williams	10:45 a.m. - 11:05 a.m.
QCD at the Z^0	P. Burrows	11:05 a.m. - 11:50 a.m.
QED Radiative Corrections	R. Battiston	11:50 a.m. - 12:10 p.m.
Acceptance for Charged Particle Tracking for Hadronic Events	G. Baranko	12:10 a.m. - 12:20 p.m.

SLD Physics Topics
Wednesday PM / August 2, 1989
(Gladding/Schindler)

Overview and Issues	R. Schindler	2:00 p.m. - 2:30 p.m.
Vertexing Issues	G. Gladding	2:30 p.m. - 2:50 p.m.
Monte Carlo Overview and D/D_s Decay Models	J. Labs	2:50 p.m. - 3:00 p.m.
B Decay Models	G. Eigen	3:00 p.m. - 3:10 p.m.
Estimating Sensitivity to B_d and B_s Mixing	T. Reeves	3:10 p.m. - 3:25 p.m.

Coffee		3:30 p.m. - 4:00 p.m.
General Double Vertex Technique (topological)	P. Kim	4:00 p.m. - 4:25 p.m.
Distinguishing D^+ and D_s^+ (use of neutrals)	J. Izen	4:25 p.m. - 4:40 p.m.
Single Semileptonic Tag with Polarization	T. Browder	4:40 p.m. - 4:55 p.m.
Double Tag Method Employing Dileptons	C. Simopoulos	4:55 p.m. - 5:10 p.m.
Kaon Tagging	R. Panvini	5:10 p.m. - 5:25 p.m.
Prospects for CP Violation	S. Manly	5:25 p.m. - 5:40 p.m.

SLD Physics Topics
Thursday AM / August 3, 1989
(M. Witherell/I. Peruzzi)

Coffee	Conference Room	8:30 a.m. - 9:00 a.m.
Charm identification	M. Strauss	9:00 a.m. - 9:20 a.m.
Particle identification with the CRID	P. Antilogus	9:20 a.m. - 9:40 a.m.
B Physics Using Ψ Decays	I. Peruzzi	9:40 a.m. - 10:00 a.m.
Coffee		10:15 a.m. - 10:45 a.m.
Measuring B^0/B^+ Lifetimes Using Semileptonic Decays	T. Browder	10:45 a.m. - 11:15 a.m.
Analysis of Exclusive Semileptonic Decays	M. Witherell	11:15 a.m. - 11:35 a.m.
Tagging D_s Decays to Study the B_s	G. Eigen	11:35 a.m. - 11:55 a.m.

SLD Physics Topics
Thursday Eve / August 3, 1989
(U. Nauenberg/P. Mockett)

Reconstruction of Jet Jet Masses for Technicolor	J. Turk	7:30 p.m. - 7:50 p.m.
Study of Technicolor Signals	S. Manly	7:50 p.m. - 8:10 p.m.

Effect of Technicolor on Polar Asymmetries	I. Abt	8:10 p.m. - 8:20 p.m.
Study of Technipions Using the τ Decay Modes	U. Schneekloth	8:20 p.m. - 8:30 p.m.
Production & Decay of Techniglobes	R. Webber	8:30 p.m. - 8:50 p.m.
Break		8:50 p.m. - 9:10 p.m.
Standard Model Higgs Detection in $e^+e^- \rightarrow H\nu\bar{\nu}$	E. Vella	9:10 p.m. - 9:30 p.m.
Higgs Search in $e^+e^- \rightarrow H^0 q\bar{q}$	H. Kim	9:30 p.m. - 9:50 p.m.
Jet Mass Correction to Magnetic Field Deflection	M. Ji	9:50 p.m. - 10:05 p.m.
On the Trail of Lost Energy	A. Johnson	10:05 p.m. - 10:15 p.m.
Detection of $Z \rightarrow H\nu\bar{\nu}$	P. Mockett	10:15 p.m. - 10:30 p.m.

SLD Physics Topics
 Friday AM / August 4, 1989
 (Rowson/Dubois)

Coffee	Conference Room	8:30 a.m. - 9:00 a.m.
Sequential leptons	T. Bolton	9:00 a.m. - 9:15 a.m.
Excited muons	C. Arroyo	9:15 a.m. - 9:30 a.m.
Singly produced NHL's	A. Bazarko	9:30 a.m. - 9:45 a.m.
4th Generation quarks	A. Weidemann	9:45 a.m. - 10:00 a.m.
Comments on Z' Bosons	P. Rowson	10:00 a.m. - 10:15 a.m.
Coffee		10:15 a.m. - 10:45 a.m.
Muon id	T. Hansl-Kozanecka	10:45 a.m. - 11:00 a.m.
Electron / π^0/γ id	R. Dubois	11:00 a.m. - 11:20 a.m.
SUSY Higgs	S. Whitaker	11:20 a.m. - 11:40 a.m.
Selectrons, smuons, and squarks	R. Dubois	11:40 a.m. - 12:00 p.m.

Summary Session
 Friday PM / August 4, 1989

Physics Overview & Summary	C. Baltay	2:00 p.m. - 3:00 p.m.
Discussion		3:00 p.m. - 3:30 p.m.
Discussion continued over coffee		3:30 p.m. -

List of Attendees

Koya Abe	Sridhara Dasu
Iris Abt	Roberto Dell'Orso
Pierre Antilogus	Riccardo De Sangro
Carlos Arroyo	Patrizia De Simone
William Ash	Richard Dubois
Charles Baltay	Derrell Durrett
Henry Bank	Peter Du
Greg Baranko	Gerald Eigen
Roberto Battiston	Michael Fero
Andrew Bazarko	Gary Gladding
Alice Bean	David Gurd
Robert Bell	Traudl Hansl-Kozanecka
Ram Ben-David	T. E. Hart
Gian Mario Bilei	Katsuo Hasegawa
Tim Bolton	Stanley Hertzbach
Gary Bower	Emlyn Hughes
James Brau	Joseph M. Izen
Martin Breidenbach	Anthony Johnson
Tom Browder	James Johnson
Karl Brown	Ryoichi Kajikawa
William Bugg	Hideaki Kawahara
Toby Burnett	Michael Kelsey
Philip N. Burrows	Henry Kendall
Wit Busza	Hwi Kim
David Caldwell	Peter Kim
Massimo Carpinelli	M. Klein
John Carr	Richard Kofler
Ronald Cassell	Karen Krieger
Rino Castaldi	Robert S. Kroeger
Andrea Castro	Youngjoon Kwon
George Chdawick	Jonathan Labs
Liang Ping Chen	Amitabh Lath
Victor Cook	Jan Lauber
Hans Cohn	David Leith
Paschal Coyle	Adolph Lu
Graham Cross	Harvey Lynch

Ji Ma
Walid A. Majid
Steven Manly
Thomas Markiewicz
Hiroaki Masuda
Laurent Mathys
Edoardo Mazzucato
John McGowan
Adrian McKemey
Brian Meadows
Robert Messner
Paul Mockett
Rollin Morrison
Benoit Mours
David Muller
Tadashi Nagamine
Uriel Nauenberg
Louis Osborne
Robert Panvini
E. Paterson
Michele Pauluzzi
Ida Peruzzi
Luisa Pescara
Marcello Piccolo
Livio Piemontese
Enrico Pieroni
Richard Plano
E. Prabhaker
Richard Prepost
Charles Prescott
Blair Ratcliff
Terry Reeves
Jeff Richman
Leon Rochester
Lawrence Rosenson
Peter Rowson
Attilio Santocchia
Terry Schalk
Rafe Schindler
Uwe Schneekloth

Abe Seiden
Leonello Servoli
Michael Shaevitz
J. Shank
Steve Smith
Jeff Snyder
Michael Sokoloff
Robert Steiner
Michael G. Strauss
Dong Su
Akira Sugiyama
Shiro Suzuki
Frank Taylor
Marc Turcotte
Jeff D. Turk
Cristina Vannini
Eric Vella
John Venuti
Piero Giorgio Verdini
R.M. Webber
Achim W. Weidemann
Scott Whitaker
Sharon White
David A. Williams
David C. Williams
Robert Williams
Robert Wilson
William Wisniewski
Michael Witherell
Gary Word
Jeff Wyss
Richard Yamamoto
John Yamartino
Charles Young
Haruo Yuta
Richard Zdarko
Cary Zeitlin